

THE UNIVERSITY OF HULL

**EDIBLE SURFACTANTS AT FLUID-FLUID INTERFACES**

being a Thesis submitted for the Degree of Doctor of Philosophy in  
the University of Hull

by

Yu Liu

MEng (China University of Petroleum (East China), China)

BEng (China University of Mining and Technology, China)

June 2021

## ACKNOWLEDGEMENTS

First and foremost, I want to express my sincere gratitude to my academic supervisor, Professor Bernard P. Binks for giving me the opportunity to join his research group at the University of Hull. Amidst the 4-year PhD study, he has helped me a lot with performing experiments, data analysis, academic writing, making presentations in addition to directing the research. Without his professional supervision, I cannot finish this thesis.

I also want to thank the China Scholarship Council (CSC, No.201706450036) for sponsoring my PhD project.

Many thanks go to Mr Timothy S. Dunstan and Mrs A. Lowry for their help with cryo-SEM and TEM imaging. My thanks also go to Mr Dean A. Moore for his assistance with DSC and IR experiments, and Dr. Timothy J. Prior for XRD experiments.

I feel grateful for my colleagues and friends at the University of Hull especially in the Department of Chemistry for their help and friendship, with special mention to Ana María Bago Rodriguez, Raojun Zheng, Qianli Ma, Xin Hu and my friends on Inglemire Lane.

Lastly, I want to express my gratitude to my family especially my father and mother for their unconditional love and support. Many thanks are also given to my two best friends who I grew up with - Xianwen Shen and Deshuai Shen. Our friendship has lasted for nearly 25 years! Special thanks to my beloved girlfriend Gloria. Her unselfish love and tremendous support give me the strength to overcome difficulties encountered in both life and work. With her around, my life becomes more colourful and meaningful.

## ABSTRACT

This thesis probes into the adsorption properties of several edible surfactants/fats at a range of fluid-fluid interfaces, *e.g.* air-oil, air-water and water-oil. Based on this, various colloidal materials are fabricated including aqueous and oil foams, simple and multiple emulsions, foamed and aerated emulsions. Among these materials, oil foams are the focus. Different techniques are applied to characterise the resulting materials and reveal the underlying stabilisation mechanisms, such as differential scanning calorimetry, rheology, X-ray diffraction, infrared spectrometry, surface/interfacial tension, contact angle, dynamic light scattering, optical and cryo-scanning electron microscopy.

Ultra-stable edible oil foams can be prepared from neat vegetable oils containing mainly long-chain, unsaturated fatty acids in their triglyceride molecules in the absence of an added foaming agent. Upon cooling/warming these oils, crystals of high melting fractions form in a low melting liquid oil yielding an oil gel. Such oil gels can be whipped to fabricate oil foams stabilized by pre-formed fat crystals. Foaming behavior depends on the oil composition and the degree of supercooling. Optimum foaming yields an over-run of  $\sim 40\%$  for peanut oil and  $\sim 110\%$  for olive oil. Oil foams devoid of drainage, coarsening or coalescence are achievable. We demonstrate that high melting triglyceride crystals possess a higher fraction of saturated fatty acids than the original oil. In addition, ultra-stable oil foams can be destabilized by heating due to the dissolution of the crystals in the continuous phase and at the air-oil surface.

Very stable oil foams can also be fabricated from mixtures of hydrophobic sugar ester surfactants and vegetable oils. Nevertheless, a novel foaming strategy is adopted during which aeration is first performed in the one-phase region followed by rapid cooling and then storing at low temperature. For sucrose ester surfactants, we first study the effect of aeration temperature and surfactant concentration on foamability and foam stability cooled from an one-phase oil solution. Unlike previous reports, both foamability and foam stability decrease upon decreasing the aeration temperature into the two-phase region containing surfactant crystals. At high temperature in the one-phase region, substantial foaming is achieved within minutes of whipping, but foams ultimately collapse within a week. We show that surfactant molecules are surface-active at high temperature and that hydrogen bonds form between surfactant and oil molecules. Cooling these foams substantially increases foam stability due to both interfacial and bulk surfactant crystallisation *in situ*. The generic nature of our findings is demonstrated for a range of vegetable oil foams with a maximum over-run of 330% and the absence of drainage, coalescence and disproportionation being obtained. In analogy with sucrose esters,

long-term oil foams with a maximum over-run of  $\sim 275\%$  are yielded based on mixtures of sorbitan esters and vegetable oil.

Reasonably stable aqueous foams can be prepared from mixtures of a series of sucrose ester surfactants and water, during which the effect of surfactant HLB and pH is investigated. The foaming functionality of sucrose esters is closely linked to the physicochemical properties of bulk liquid before aeration, including aggregate morphology and size, zeta potential, viscosity, and surface tension. At the natural condition, in comparison to the micelle-forming aqueous solutions of sodium dodecyl sulfate (SDS), the foaming capacity of sucrose ester dispersions containing vesicles is lower due to slower adsorption kinetics of surfactant molecules towards the air-water surface. By contrast, the resulting foams are much more stable than SDS foams. This is attributed to the steric hindrance of giant vesicles and that electrostatic repulsion existing between adjacent vesicles within the liquid films and Plateau borders of the foam. Amidst the investigated sucrose esters, lower HLB tends to yield improved foam stability. The effect of lowering pH on the dispersion and foaming characteristics of two relatively hydrophobic sucrose esters in water is then discussed. Upon lowering pH, the morphology of surfactant aggregates in bulk liquid and the interfacial properties are altered. Meanwhile, their foamability is improved markedly due to more rapid adsorption dynamics of surfactant monomers towards the air-water surface.

As seen above, sucrose ester is versatile adsorbing readily at various fluid-fluid interfaces. Is it feasible to stabilise multiple interfaces simultaneously in the same system using sucrose ester alone? Herein we report for the first time on the preparation of a multitude of colloidal materials using one and the same sucrose ester sample through facile protocols, *i.e.* air-in-oil (a/o) and air-in-water (a/w) foams, oil-in-water (o/w), water-in-oil (w/o), and oil-in-water-in-oil (o/w/o) emulsions, air and water-in-oil (a & w/o) foamulsions and air-in-oil-in-water (a/o/w) emulsions.

Overall, the research in this thesis gives insight into the adsorption modes of several types of edible surfactants/fats at a range of fluid-fluid interfaces. Besides, various colloidal materials are fabricated *via* facile protocols. Despite this, the stabilisation mechanism of the air-oil surface with surfactants/fats of varying architecture is not fully understood yet. For the sake of application, further investigations on novel colloidal materials using oil foams as templates are needed as well.

## PUBLICATIONS AND PRESENTATIONS

The work contained within this thesis has been published and will be submitted for publication:

### Publications

1. **Y. Liu** and B.P. Binks, Foams of vegetable oils containing long-chain triglycerides, *J. Colloid Interface Sci.*, 2021, **583**, 522-534.
2. **Y. Liu** and B.P. Binks, A novel strategy to fabricate stable oil foams with sucrose ester surfactant, *J. Colloid Interface Sci.*, 2021, **594**, 204-216.
3. **Y. Liu** and B.P. Binks, Sucrose ester surfactant: foams, emulsions, foamulsions and aerated emulsions, in preparation, to be submitted to *Langmuir*.
4. **Y. Liu** and B.P. Binks, Effect of HLB and pH on aqueous dispersion and foaming behavior of sucrose ester surfactants, in preparation, to be submitted to *Langmuir*.
5. **Y. Liu** and B.P. Binks, Oil foams stabilized by sorbitan esters, to be submitted to *Langmuir*.

Oral and poster presentations have been given at the following events:

### Presentations

1. Poster presentation: “Foams of vegetable oils containing long-chain triglycerides”, Postgraduate Research Colloquium, July 2019, University of Hull, U.K.
2. Oral presentation: “Foams of vegetable oils containing long-chain triglycerides”, 33<sup>rd</sup> Conference of the European Colloid and Interface Society (ECIS), 8-13 September 2019, Leuven.

## NOTATIONS

Symbol	Meaning
$a$	Area (m <sup>2</sup> )
$A$	Hamaker constant
$c$	Solubility or concentration (mg L <sup>-1</sup> )
$C_p$	Heat capacity (J K <sup>-1</sup> )
$d$	Bubble/droplet diameter (m)
$d_H$	Hydrodynamic diameter (m)
$D$	Diffusion coefficient (m <sup>2</sup> s <sup>-1</sup> )
$D(1,0)$	Number average diameter (m)
$E$	Interfacial elasticity (mN m <sup>-1</sup> )
$f$	Frequency (Hz)
$F$	Force (N)
$g$	Acceleration due to gravity (m s <sup>-2</sup> )
$G$	Gibbs free energy (J)
$G'$	Elastic (storage) modulus (Pa)
$G''$	Viscous (loss) modulus (Pa)
$G^*$	Complex modulus (Pa)
$h$	Height or distance (m)
$H$	Enthalpy (J)
$I$	Light intensity
$K$	Permeability constant
$l$	Length (m)
$M$	Molar mass (g mol <sup>-1</sup> )
$n$	Number
$p$	Pressure (Pa)
$Q$	Volumetric flow rate (mL min <sup>-1</sup> )
$r$	Bubble/droplet radius (m)
$R$	Ideal gas constant (J K <sup>-1</sup> mol <sup>-1</sup> )
$s$	Spreading coefficient (mN m <sup>-1</sup> )
$S$	Entropy (J K <sup>-1</sup> )
$SFC$	Solid fat content (%)

(continued)

Symbol	Meaning
$t$	Time (s)
$T$	Temperature (K or °C)
$\dot{T}$	Temperature change rate (K or °C s <sup>-1</sup> )
$v$	Velocity (m s <sup>-1</sup> )
$V$	Volume (m <sup>3</sup> or mL)
$w$	Width or thickness (m)
$\gamma$	Strain
$\gamma_c$	Critical surface tension (mN m <sup>-1</sup> )
$\gamma_{oa}$	Surface tension of oil-air (mN m <sup>-1</sup> )
$\gamma_{os}$	Interfacial tension of oil-solid (mN m <sup>-1</sup> )
$\gamma_{ow}$	Interfacial tension of oil-water (mN m <sup>-1</sup> )
$\gamma_{sa}$	Surface tension of solid-air (mN m <sup>-1</sup> )
$\gamma_{ws}$	Interfacial tension of water-solid (mN m <sup>-1</sup> )
$\gamma_{wa}$	Surface tension of water-air (mN m <sup>-1</sup> )
$\kappa_B$	Boltzmann constant (J K <sup>-1</sup> )
$\kappa_H$	Henry' s constant (Pa m <sup>3</sup> mol <sup>-1</sup> )
$\dot{\gamma}$	Shear rate (s <sup>-1</sup> )
$\tau$	Stress (N)
$\lambda$	Wavelength (Å)
$\delta$	Phase angle (°)
$\eta$	Viscosity (mPa s)
$\rho$	Density (Kg m <sup>-3</sup> )
$\theta$	Contact angle or scattering angle (°)
$\pi$	Pi-number
$\omega$	Angular frequency (rad s <sup>-1</sup> )
$\mu$	Refractive index
$\phi_g$	Gas volume fraction
$\phi_l$	Liquid volume fraction

## CONTENTS

<b>CHAPTER 1 – INTRODUCTION .....</b>	<b>1</b>
1.1 Oleogels based on edible surfactants/fats.....	1
<i>1.1.1 Definition.....</i>	<i>1</i>
<i>1.1.2 Types of oleogelator .....</i>	<i>1</i>
1.2 Liquid foams .....	5
<i>1.2.1 Definition and types.....</i>	<i>5</i>
<i>1.2.2 Destabilization processes .....</i>	<i>6</i>
<i>1.2.3 Stabilization of aqueous foam.....</i>	<i>7</i>
1.2.3.1 Surfactants.....	7
1.2.3.2 Solid particles.....	10
1.2.3.3 Crystalline particles .....	13
<i>1.2.4 Stabilization of oil foam.....</i>	<i>14</i>
1.2.4.1 Surfactants.....	14
1.2.4.2 Solid particles.....	16
1.2.4.3 Crystalline particles .....	18
<i>1.2.5 Aqueous and oil foams: similarities and differences.....</i>	<i>26</i>
1.3 Emulsions.....	27
<i>1.3.1 Definition and types.....</i>	<i>27</i>
<i>1.3.2 Destabilization processes .....</i>	<i>28</i>
<i>1.3.3 Stabilization of emulsion .....</i>	<i>31</i>
1.3.3.1 Surfactants.....	31
1.3.3.2 Solid particles.....	32
1.3.3.3 Crystalline particles .....	33
1.4 Aims of current research .....	37
1.5 Presentation of thesis.....	39
1.6 References .....	41

<b>CHAPTER 2 – EXPERIMENTAL .....</b>	<b>53</b>
2.1 Materials.....	53
2.1.1 <i>Surfactants</i> .....	53
2.1.2 <i>Water</i> .....	54
2.1.3 <i>Oils</i> .....	54
2.1.4 <i>Other materials</i> .....	55
2.2 Methods.....	56
2.2.1 <i>Characterisation of neat surfactants</i> .....	56
2.2.1.1 Differential scanning calorimetry (DSC).....	56
2.2.1.2 X-ray diffraction (XRD) .....	57
2.2.1.3 Fourier-transform infrared (FTIR) spectroscopy .....	58
2.2.2 <i>Preparation of aqueous solutions/dispersions and aqueous foams</i> .....	59
2.2.3 <i>Characterisation of aqueous solutions/dispersions and aqueous foams</i> .....	60
2.2.3.1 Dynamic light scattering (DLS) and Zeta potential .....	60
2.2.3.2 Optical microscopy .....	63
2.2.3.3 Transmission electron microscopy (TEM) .....	63
2.2.3.4 Cryo-scanning electron microscopy (cryo-SEM) .....	63
2.2.3.5 Rheology .....	64
2.2.3.6 Surface tension.....	65
2.2.4 <i>Preparation of oil solutions/dispersions, oil foams, emulsions, foamulsions and aerated emulsions</i> .....	67
2.2.4.1 Oil solutions/dispersions .....	67
2.2.4.2 Oil foams.....	67
2.2.4.2.1 Whipping.....	67
2.2.4.2.2 Bubbling.....	69
2.2.4.3 Emulsions.....	71
2.2.4.4 Foamulsions .....	71

2.2.4.5 Aerated emulsions.....	72
2.2.5 <i>Characterisation of oil solutions/dispersions, oil foams, emulsions, foamulsions and aerated emulsions</i> .....	72
2.2.5.1 DSC.....	72
2.2.5.2 DLS .....	73
2.2.5.3 Solid fat content (SFC) .....	73
2.2.5.4 FTIR spectroscopy .....	74
2.2.5.5 Rheology .....	74
2.2.5.6 Surface tension.....	75
2.2.5.7 Contact angle determination .....	76
2.2.5.8 Temperature-controlled optical microscopy .....	77
2.2.5.9 Separation of surfactant crystals .....	78
2.2.5.9.1 Filtration and solvent washing .....	78
2.2.5.9.2 Centrifugation.....	79
2.2.5.10 Synthesis of FAMES and analysis by GC/MS .....	79
2.2.5.11 Cryo-SEM.....	80
2.2.5.12 XRD .....	80
2.2.5.13 Drop test and stability assessment .....	81
2.2.6 <i>Statistical analysis</i> .....	82
2.3 References .....	83
<b>CHAPTER 3 – FOAMS OF VEGETABLE OILS CONTAINING LONG-CHAIN TRIGLYCERIDES</b> .....	85
3.1 Introduction .....	85
3.2 Crystallisation and melting behaviour of vegetable oils .....	86
3.2.1 <i>Appearance</i> .....	86
3.2.2 <i>Thermal properties and SFC</i> .....	88
3.2.3 <i>Crystal morphology and rheological properties</i> .....	90

3.3 Preparation and characterisation of vegetable oil foams.....	94
3.3.1 <i>Effect of whipping time</i> .....	94
3.3.2 <i>Effect of whipping temperature</i> .....	100
3.4 Thermo-responsiveness of oil foams.....	111
3.5 Determination of fatty acid composition in oil crystals .....	114
3.6 Conclusions .....	116
3.7 References .....	117
<b>CHAPTER 4 – A NOVEL STRATEGY TO FABRICATE STABLE OIL FOAMS WITH SUCROSE ESTER SURFACTANT .....</b>	<b>121</b>
4.1 Introduction .....	121
4.2 Cooling and warming mixtures of sucrose ester and oil .....	123
4.2.1 <i>Visual observations and thermal properties</i> .....	123
4.2.2 <i>Crystal morphology and molecular interactions</i> .....	127
4.2.3 <i>Rheology</i> .....	128
4.3 Whipping mixtures of sucrose ester and oil .....	130
4.3.1 <i>Foams prepared and stored at same temperature</i> .....	130
4.3.2 <i>Protocol for fabricating very stable foams</i> .....	137
4.3.3 <i>Rheology of stable foam</i> .....	145
4.3.4 <i>Thermo-responsiveness of stable foam</i> .....	147
4.3.5 <i>Surfactant crystal structure</i> .....	151
4.4 Proposed stabilisation mechanism of oil foam by sucrose ester .....	153
4.5 Whipping other vegetable oils and sucrose ester .....	158
4.6 Whipping or bubbling a second sucrose ester and oil .....	160
4.6.1 <i>Very stable foams formed by whipping</i> .....	160
4.6.2 <i>Foams formed by bubbling</i> .....	166
4.6.2.1 <i>Bubbling mixtures of sucrose ester and oil</i> .....	166
4.6.2.2 <i>Bubbling neat oil</i> .....	171

4.6.3 Whipping versus bubbling .....	174
4.7 Conclusions .....	176
4.8 References .....	177
<b>CHAPTER 5 – FABRICATION OF OIL FOAMS WITH SORBITAN ESTERS.....</b>	<b>183</b>
5.1 Introduction .....	183
5.2 Dispersion behaviour of sorbitan monooleate-oil mixtures .....	184
5.2.1 Visual observations.....	184
5.2.2 Surface tension .....	184
5.2.3 Molecular interactions .....	186
5.3 Whipping mixtures of sorbitan monooleate and oil .....	188
5.3.1 Foams prepared and stored at same temperature.....	188
5.3.2 Protocol for fabricating stable foams.....	194
5.4 Dispersion behaviour of sorbitan monostearate-oil mixtures .....	198
5.4.1 Molecular interactions and thermal properties.....	198
5.4.2 Visual observations and crystal morphology .....	200
5.5 Whipping mixtures of sorbitan monostearate and oil .....	201
5.6 Conclusions .....	210
5.7 References .....	211
<b>CHAPTER 6 – EFFECT OF HLB AND pH ON AQUEOUS DISPERSION AND FOAMING BEHAVIOUR OF SUCROSE ESTERS .....</b>	<b>213</b>
6.1 Introduction .....	213
6.2 Systems with sucrose esters of varying HLB.....	215
6.2.1 Dispersion behaviour of sucrose ester-water mixtures .....	215
6.2.2 Foaming behaviour of sucrose ester-water mixtures .....	227
6.3 Systems with sucrose esters of varying pH.....	236
6.3.1 Dispersion behaviour of sucrose ester-water mixtures .....	236
6.3.2 Foaming behaviour of sucrose ester-water mixtures .....	238

6.4 Conclusions .....	243
6.5 References .....	244
<b>CHAPTER 7 – SUCROSE ESTER SURFACTANT: FOAMS, EMULSIONS, FOAMULSIONS AND AERATED EMULSIONS.....</b>	<b>249</b>
7.1 Introduction .....	249
7.2 Dispersion behaviour of sucrose ester-oil mixtures .....	251
7.3 Air-oil surface tension and oil-water (air) contact angle with sucrose ester .....	254
7.4 Preparation and characterisation of various colloidal materials with sucrose ester .....	255
7.4.1 <i>Oil and aqueous foams</i> .....	255
7.4.2 <i>Simple and multiple emulsions</i> .....	258
7.4.3 <i>Foamulsions and aerated emulsions</i> .....	265
7.4.4 <i>Rheology, polymorphs and thermal properties</i> .....	273
7.5 Conclusions .....	278
7.6 References .....	280
<b>CHAPTER 8 – SUMMARY OF CONCLUSIONS AND FUTURE WORK.....</b>	<b>285</b>
8.1 Summary of conclusions .....	285
8.2 Future work .....	288
8.2.1 <i>Oil foams from mixtures of sugar esters in adipate ester oils</i> .....	288
8.2.2 <i>The role of oil-soluble emulsifiers in oil foaming</i> .....	290
8.2.3 <i>Using sucrose ester and a second surfactant to prepare foamulsions</i> .....	290
8.2.4 <i>Preparation of oil-in-water-in-oil emulsions with sucrose esters</i> .....	290
8.2.5 <i>Ascending behaviour of gas bubbles in oil solutions of sucrose ester</i> .....	291
8.3 References .....	291

## CHAPTER 1 – INTRODUCTION

### 1.1 Oleogels based on edible surfactants/fats

#### 1.1.1 Definition

Fats and oils are one of the most important macronutrients in the human diet, which provide the highest fraction of total daily caloric intake.<sup>1</sup> Of particular focus in the food industry are saturated fats since they are prevalently used as an alternative to *trans* fats.<sup>2,3</sup> The use of saturated fats has two drawbacks however: (i) the long-term intake of saturated fats may cause negative cardiovascular effects, (ii) their excessive consumption may promote obesity.<sup>2,4</sup> Considering this, a dietary guideline from the Food and Agriculture Organization (FAO) recommended that the daily consumption of saturated fats should be restricted to less than 10% relative to total calories.<sup>5</sup> Thus, a great deal of effort has been devoted by food scientists to find ways to reformulate food products with a better nutritional profile (*e.g.* a lower level of saturated fats) while maintaining the desirable functionality endowed by saturated fats.

In recent years, oleogelation of edible oils using gelators of a natural or synthetic origin is gaining surging interest.<sup>6-11</sup> It has been regarded as a promising oil-structuring technique due to its potential in reducing the saturated fat content, improving nutritional and technological appeal and imparting impressive rheological and sensorial properties.<sup>6-11</sup> Commonly, an oleogelation process can convert  $\geq 90$  wt.% of a flowable edible oil into an elastic gel with relatively low gelator concentration, during which a three-dimensional (3D) gelator network is formed due to non-covalent, *e.g.* van der Waals, forces.

#### 1.1.2 Types of oleogelator

The pre-requisite for a material to act as an oleogelator is that a delicate balance between solvent-gelator and gelator-gelator interactions should be achieved.<sup>2</sup> Too strong gelator-gelator interactions will lead to gelator precipitation, *i.e.* phase separation. By contrast, dominant solvent-gelator interactions tend to yield a flowable dispersion. Apart from the above, oleogelators should also be efficient, cheap, readily available and food-grade.<sup>7</sup> Depending on the structures of mesophases formed in oil, oleogelators can be categorised into two groups: self-assembled structures and crystalline particles.<sup>6</sup> The former system goes through self-aggregation of oleogelator molecules in oil (*i.e.* reverse micelles) under certain circumstances in which hydrophobic tails are in contact with oil alongside hydrophilic heads being removed from contact with the oil. By contrast, the latter involves the nucleation and subsequent crystal growth of gelator molecules in the oil phase due to either supercooling or supersaturation,

during which gelator molecules are arrayed periodically and held together by uniform intermolecular forces.<sup>3,6</sup> Based on the number of the types of gelators involved in an oleogelation process, oleogels can be defined as mono-component or multi-component.<sup>9</sup> In this section, we are not trying to include all papers regarding oleogels; we select some of the representative and recent publications in this area and then summarise them into different tables based on the number and types of gelators used. See Table 1.1-Table 1.4.

**Table 1.1.** Mono-component oleogels.

Oil	Oleogelator	Gelation type	Morphology	Ref.
Cottonseed oil, soybean oil, sesame oil, corn oil and olive oil	Sorbitan ester	Self-assembly	Rod-shaped tubules	12
Hazelnut oil	Monoglyceride	Self-assembly/	Elongated plate-like	13,14
Olive oil	Monoglyceride	crystalline particles	Rod-like	15
Canola oil	Ceramide	Crystalline particles	Fibril-like/needle-like	16
Sunflower oil, soybean oil and rapeseed oil	Fatty acid	Crystalline particles	Lozenge-shaped	17
Sunflower oil and commercial diet oil	Fatty alcohol	Crystalline particles	Platelet-like	18
Sunflower oil and soybean oil	Fatty alcohol	Crystalline particles	Platelet-like	19
Sunflower oil	Wax ester	Crystalline particles	–	20
Sunflower oil	Dicarboxylic acid	Crystalline particles	–	20
Canola oil	Hydroxylated fatty acid	Crystalline particles	Fibril-like	21,22
Sal fat olein, palm super olein, olive oil and cocoa butter	High-melting fat	Crystalline particles	–	23,24
Salad oil and olive oil	Rice bran wax	Crystalline particles	Needle-like	25
Safflower oil	Candelilla wax	Crystalline particles	Platelet-like	26,27

**Table 1.2.** Multi-component oleogels based on lecithin.

Oil	Oleogelator	Gelation type	Morphology	Ref.
Sunflower oil	Lecithin + $\alpha$ -tocopherol	Self-assembly	Cylindrical worm-like micelles	28
Canola Oil	Lecithin + Stearic acid	Self-assembly/ crystalline particles	Fibril-like reverse micelles/spherulite-like crystals	29
Sunflower oil	Lecithin + Sorbitan tri-stearate	Crystalline particles	Needle-like	30
Sunflower oil	Lecithin + Sitosterol	Crystalline particles	Platelet-like	31
Sunflower oil	Sunflower lecithin + Sucrose ester	Crystalline particles	Ruptured globule	32
Sunflower oil	Soybean lecithin + Fruit wax	Crystalline particles	Rosette-like	33
High oleic canola oil	Lecithin + Ethyl-cellulose	—	—	34

**Table 1.3.** Multi-component oleogels based on fatty acids/alcohols/esters.

Oil	Oleogelator	Gelation type	Morphology	Ref.
Sunflower oil	Oleic acid + Sodium oleate	Self-assembly/ crystalline particles	—	35
Sunflower oil, soybean oil and rapeseed oil	Fatty acids + Fatty alcohols	Crystalline particles	Lozenge-shaped/platelet-like	17
Sunflower oil and commercial diet oil	Stearyl alcohol + Stearic acid	Crystalline particles	Elongated feather-like/ needle-like	18
Canola oil	Stearyl alcohol + Stearic acid + Ethyl-cellulose	Crystalline particles	Needle-like/feather-like	36
Sunflower oil	$\gamma$ -oryzanol + Sterol	Self-assembly	Tubules	37

(continued)

Oil	Oleogelator	Gelation type	Morphology	Ref.
Extra virgin olive oil	Fatty alcohols + Glyceryl stearate	Crystalline particles	—	38
Sunflower oil	Monoglycerides + Phytosterols	Crystalline particles	Needle-like/clustered-like/spherulite-like	39
Canola oil	Monoglycerides + native phytosterols	Crystalline particles	Fibril-like/needle-like	40
Sunflower oil	Monoglycerides + Diglycerides	Crystalline particles	—	41

**Table 1.4.** Multi-component oleogels based on natural waxes.

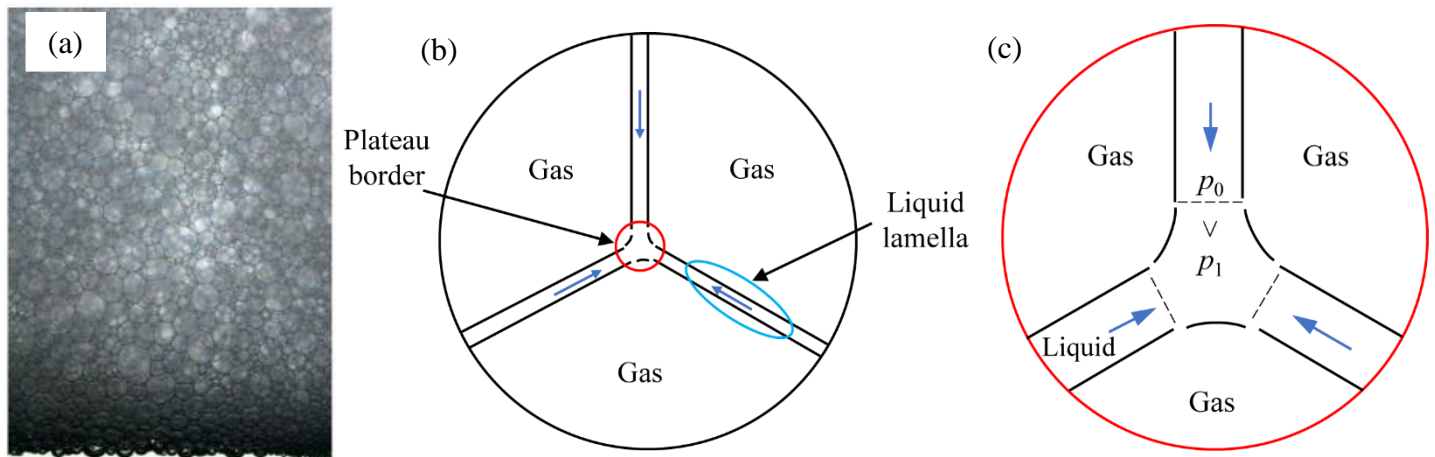
Oil	Oleogelator	Gelation type	Morphology	Ref.
Soybean oil	Candelilla wax + Sorbitan monostearate + Fully hydrogenated palm oil	Self-assembly/crystalline particles	—	42
Soybean oil	Beeswax + Rice bran wax + Sunflower wax	Crystalline particles	Needle-like	43
Pomegranate seed oil	Propolis wax + Beeswax	Crystalline particles	Needle-like	44
Soybean oil	Candelilla wax + Triglycerides	Crystalline particles	Platelet-like	45
Soybean oil	Beeswax + Sunflower Wax + Candelilla Wax	Crystalline particles	Platelet-like	46

## 1.2 Liquid foams

### 1.2.1 Definition and types

A liquid foam is a colloidal dispersion of gas in a continuous liquid phase containing foaming agents.<sup>47-50</sup> When the continuous phase is water, it is called aqueous foam. On the other hand, it is referred to as oil foam (or oleofoam) when the liquid phase is oil. Commonly, foams can be produced by simple handshaking of surfactant solutions. Foams are usually polydisperse with bubble diameters of 10  $\mu\text{m}$ -1000  $\mu\text{m}$ . Bubble rising and liquid drainage occur simultaneously on storage. In the upper part of a foam, bubbles become gradually distorted during which thin liquid films turn planar and joined at Plateau borders. In the lower part, foams are wet in which bubbles are normally spherical, see Figure 1.1.

**Figure 1.1.** (a) Photograph of an aqueous foam after initial drainage. In the upper part, the foam is dry and the bubbles within are polyhedral, whilst the lower layer is wet being composed of spherical bubbles. Taken from ref. 54. (b) Schematic of a 2D dry foam. (c) Schematic of a 2D Plateau border, at which three planar liquid films meet at 120° along a line. Liquid drainage in the thin film is driven by a capillary force due to the difference in Laplace pressure ( $p_0 > p_1$ ). Arrows indicate the direction of liquid flow. Adapted from ref. 49.



The degree of bubble packing in a foam can be characterized by the gas volume fraction  $\phi_g$ , *i.e.* the ratio of gas volume to total foam volume.<sup>50</sup> Foam bubbles are spherical in wet foams, *i.e.*  $\phi_g$  of up to 0.74, whilst they become distorted in the range  $0.74 < \phi_g < 0.83$ . In a drier foam ( $\phi_g > 0.83$ ) foam cells are polyhedral in shape.

### 1.2.2 Destabilization processes

Foams are thermodynamically unstable colloidal systems and tend to decay through three known destabilisation mechanisms, namely liquid drainage, coarsening and coalescence, Figure 1.2.<sup>47</sup> Drainage refers to the phenomenon of foam fluid flowing down through interstitial channels between bubbles and finally leading to the separation of gas and liquid due to a density difference. The initial drainage is driven by a gravitational force, whilst subsequent thin film drainage is controlled by a capillary force with the gravitational force being negligible as shown in Figure 1.1(c). The characteristic time of drainage is expressed as,<sup>51</sup>

$$t_{drain} = \frac{h\eta}{K\rho g r^2 \phi_l^\alpha} \quad (1.1)$$

where  $h$  is the foam height,  $\eta$  is the liquid viscosity,  $K$  is the permeability constant of order  $10^{-2}$ ,  $\rho$  is the liquid density,  $g$  is the acceleration of gravity,  $r$  is the average bubble radius,  $\alpha$  is an exponent between 0.5 and 1 and  $\phi_l$  is the volume fraction of liquid. It suggests that retardation of drainage can be achieved through increasing the liquid viscosity, reducing the bubble size or reducing the liquid volume fraction. The occurrence of liquid drainage leads to a reduction in liquid fraction and an increase in air fraction for a foam.

Coarsening refers to the diffusion of gas from small bubbles to large ones driven by pressure differences between bubbles of different sizes, being accompanied by an increase in the average bubble size.<sup>52</sup> The excess pressure within a spherical gas bubble in foam is given by the Laplace equation,<sup>49</sup>

$$\Delta p = \frac{2\gamma}{r} \quad (1.2)$$

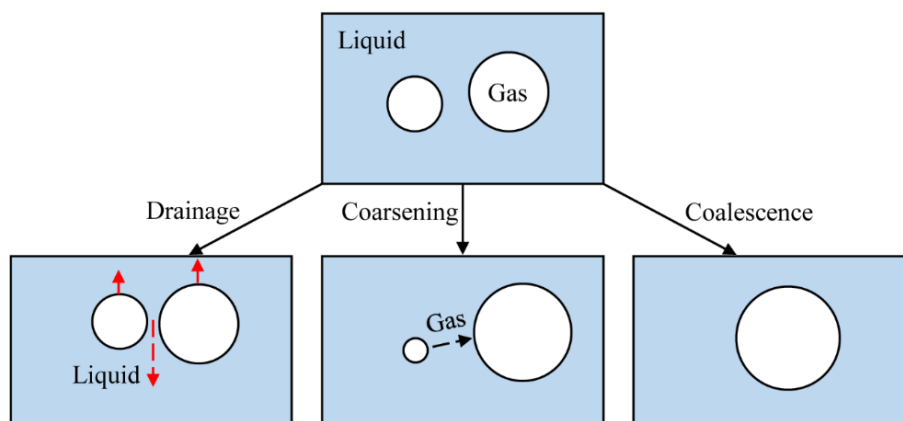
where  $\gamma$  is the surface tension of a surfactant solution. The smaller  $r$  the larger  $\Delta p$ , thus the greater the solubility of gas in continuous liquid. This leads to enhanced inter-bubble gas transfer. The characteristic time of coarsening is expressed by,<sup>53</sup>

$$t_{coarsen} = \frac{r^2}{D_{ef}(\phi_l)h} \quad (1.3)$$

where  $D_e$  is the effective diffusion coefficient being proportional to the gas diffusivity through a film,<sup>53</sup>  $f(\phi_l)$  is the fraction of total bubble area covered by thin films and  $h$  is the film thickness. Coarsening will be suppressed when the film thickness becomes thinner or the bubble size turns larger.

When drainage has finished, liquid films become very thin. In this scenario, even a small disruption can trigger the rupture of the films leading to the merging of adjacent bubbles.<sup>54</sup> This process is referred to as coalescence during which there is an increase in the bubble size alongwith a decrease in the bubble number.

**Figure 1.2.** Schematic illustrating different destabilisation processes of a foam.

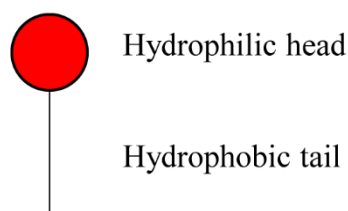


### 1.2.3 Stabilization of aqueous foam

#### 1.2.3.1 Surfactants

A surfactant is an amphiphilic molecule composed of a hydrophilic (water-loving) head and a hydrophobic (oil loving) tail(s) (Figure 1.3), which can attach spontaneously at various interfaces, *e.g.* air-water.<sup>55</sup> Surfactants can be generally categorised into four types depending on the nature of their head group: zwitterionic, anionic, cationic and non-ionic.<sup>55</sup>

**Figure 1.3.** Schematic of a typical surfactant molecule.

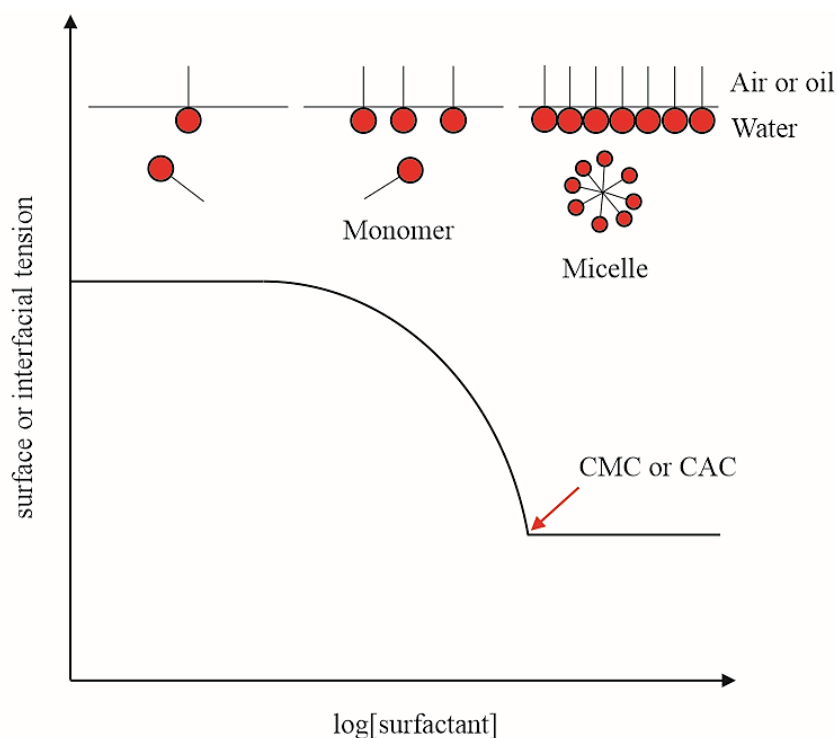


When water-soluble amphiphilic molecules are added to water, surfactant adsorption and aggregation will occur. At low concentrations, surfactant monomers are moving spontaneously from the bulk phase to an interface between two immiscible fluids due to their amphiphilic nature, thereby forming a monolayer along with a drop in the interfacial tension. When a certain concentration is reached, the interface becomes saturated and excess surfactant monomer will associate spontaneously yielding self-assembled aggregates, see Figure 1.4. This critical concentration is defined as the critical micelle/aggregate concentration (abbreviated as CMC or CAC), above which the interfacial tension remains almost constant. The driving force for the spontaneous self-assembly phenomenon is the hydrophobic effect, the mechanism

behind which is a negative entropy change associated with the process of hydrophobic tails being forced out of water.<sup>55</sup>

It is well known that the geometry of a specific surfactant molecule can be quantified by the critical packing parameter,  $CPP = \frac{V}{a_0 l_0}$ , where  $V$  is the volume occupied by per molecule,  $a_0$  is the area per hydrophilic headgroup and  $l_0$  is the critical chain length.<sup>56</sup> This parameter can be applied to predict potential self-assembled structures formed when surfactants are dissolved in water:<sup>56</sup> (1)  $CPP \leq 1/3$  – spherical micelles; (2)  $1/3 < CPP \leq 1/2$  – rod-like or worm-like micelles; (3)  $1/2 < CPP < 1$  – vesicles or tubules; (4)  $CPP = 1$  – lamellae; (5)  $CPP > 1$  – reversed micelles. In practical applications, through optimising the molecular architecture of a surfactant, surfactant concentration and external conditions, various lyotropic liquid crystalline phases can be formed in bulk.

**Figure 1.4.** Typical curve of surface or interfacial tension *versus* surfactant concentration. The arrow indicates CMC or CAC. At low concentration, few surfactant monomers are present at the interface thus surface or interfacial tension remains almost constant. With increasing concentration more surfactant monomers adsorb at the interface decreasing surface or interfacial tension significantly. Once above CMC or CAC, the interface becomes saturated and excess monomers tend to aggregate spontaneously forming different self-assemblies depending on the  $CPP$ .



The role of surfactants in stabilizing foams is clarified with respect to the three major destabilization processes:

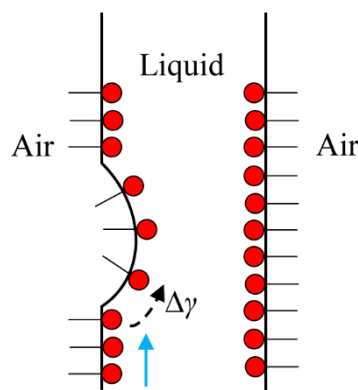
(a) Lowering surface tension

The adsorption of surfactant monomers at air-liquid surfaces leads to a decrease in the surface tension. Coarsening is prone to be suppressed due to the reduction of the dissolution of gas into the continuous liquid. In addition, the interfacial adsorption of surfactant monomers can reduce the surface free energy and protect air bubbles against coalescence.

(b) Gibbs-Marangoni effect

The interfacial adsorption of surfactant monomers can induce the Gibbs-Marangoni effect, Figure 1.5.<sup>55,57</sup> When an initially uniform liquid film is partially thinned, few surfactant molecules are present at the stretched region of the surface, so the local surface tension is higher than that of the unstretched area. This leads to a surface tension gradient inducing interfacial surfactant monomers to move towards the stretched site. Meanwhile, the liquid adjacent to the surface will flow in the same direction accompanying the surface flow, which tends to restore the film thickness of the thinned area thus driving air bubbles away from each other.

**Figure 1.5.** Schematic of the Gibbs-Marangoni effect acting on a thinned liquid film of a foam. Black arrow indicates a surface tension gradient  $\Delta\gamma$  created between stretched and unstretched areas; blue arrow denotes liquid flow accompanying surface flow. Adapted from ref. 55.



(c) Surface viscosity and surface elasticity

Surface viscosity is a parameter reflecting the relaxation speed of a surface to an equilibrium state after imposing a stress; surface elasticity is a measure of the energy stored in a surface layer due to an external stress.<sup>55</sup> According to previous studies, foam stability is

positively correlated to the viscoelastic properties of surface layers, *i.e.* the higher the surface viscoelasticity, the higher the foam stability to coalescence.<sup>55</sup>

#### (d) Disjoining pressure

The adsorption of ionic surfactants may impart a liquid surface with charges. When two charged bubbles in a foam approach each other, electrostatic repulsion tends to prevent them from approaching too close, hence reducing the occurrence of coalescence.<sup>58</sup> On the contrary, for nonionic surfactants or amphiphilic polymers, the electrostatic contribution to foam stability is negligible. When the two adsorbed layers overlap each other, short-range steric repulsive forces begin to operate.<sup>59</sup>

#### (e) Self-assembly

At surfactant concentrations above CMC/ CAC, various surfactant self-assemblies are formed depending on the *CPP*. In fact, the presence of self-assemblies in a liquid lamella contributes to a disjoining pressure by steric hindrance/electrostatic repulsion, which can limit film drainage and coarsening. According to previous studies, the morphology and size of surfactant self-assemblies significantly affect foaming properties.<sup>60</sup> Moreover, relatively bulky vesicles or lamellar phases are shown to be more effective foam stabilizers than small spherical micelles.<sup>60</sup> Of particular interest is the system reported by Fameau *et al.*<sup>61</sup> They found that the formation of multilamellar tubes (several microns in length) in the continuous phase conferred aqueous foams with long term stability which could last for several months. More importantly, the foams exhibited thermo-responsive properties, during which they were significantly destabilized at the temperature where the tubes melted into small micelles on warming, and these foams were re-stabilized when the tubes were reformed upon cooling below the transition temperature.

### 1.2.3.2 Solid particles

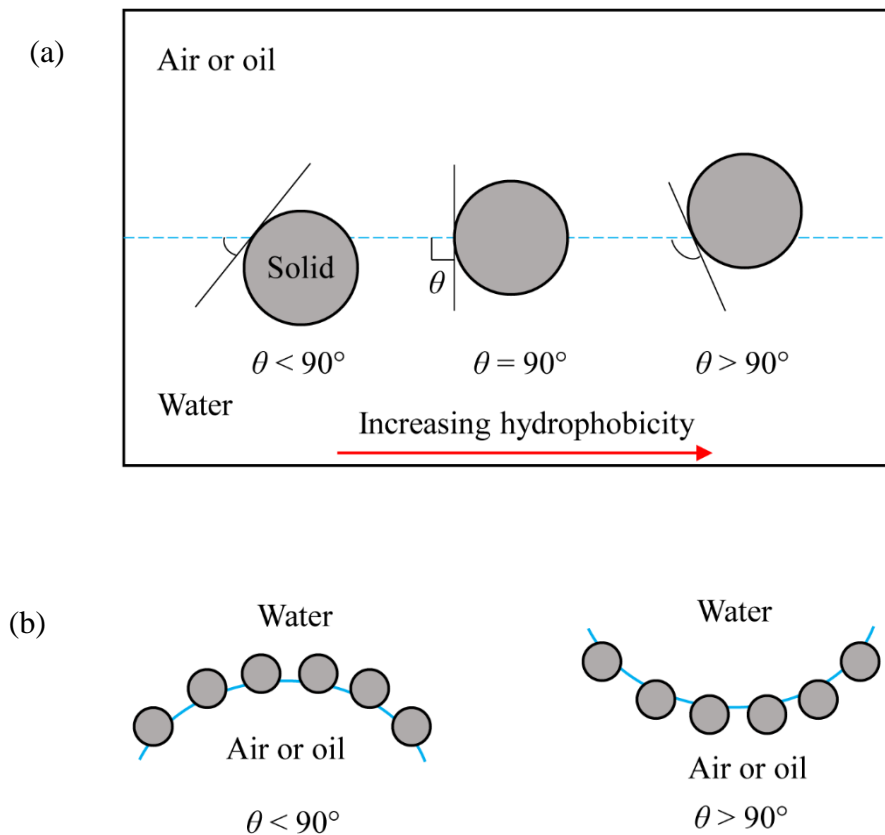
#### (a) Particle wettability

For surfactants, their hydrophile-lipophile balance (HLB) number is a vital parameter controlling whether they preferentially reside in either water, oil or a third phase. For solid particles, their potential to reside at various fluid interfaces is determined by the particle wettability, quantified by the three-phase contact angle  $\theta$  measured through a more polar phase.<sup>62-66</sup> For mixtures of solid, air and water,

$$\cos \theta = \frac{\gamma_{sa} - \gamma_{ws}}{\gamma_{wa}} \quad (1.4)$$

where  $\gamma_{sa}$ ,  $\gamma_{ws}$  and  $\gamma_{wa}$  stand for the interfacial tensions of solid-air, solid-water and air-water surfaces, respectively. For relatively hydrophilic spherical particles, they tend to reside more in water with  $0^\circ < \theta < 90^\circ$ , giving rise to aqueous foams. For comparatively hydrophobic spherical particles with  $90^\circ < \theta < 180^\circ$ , they exhibit a preference for air, which can be applied to prepare free flowing ‘dry water’ or aqueous marbles.<sup>67</sup> See Figure 1.6.

**Figure 1.6.** (a) Adsorption behaviour of a spherical particle at a planar air (oil)-water interface as a function of particle hydrophobicity. (b) Bending behaviour of a particle-adsorbed interface for more hydrophilic ( $\theta < 90^\circ$ ) or more hydrophobic ( $\theta > 90^\circ$ ) particles. Redrawn from ref. 62.



(b) Detachment energy of particles from a surface

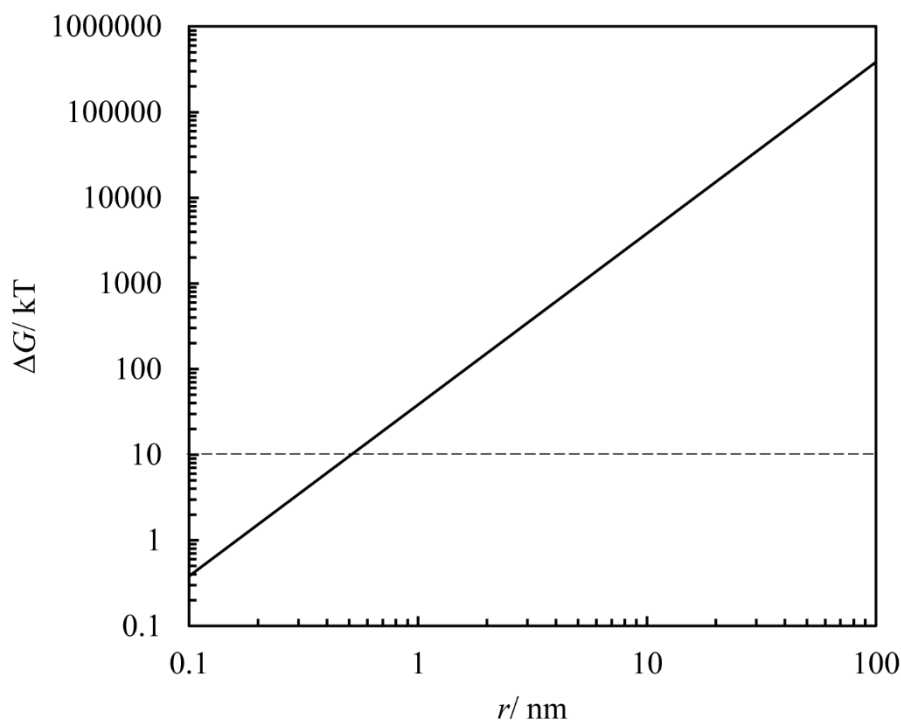
When a particle pins at an air-water surface, the minimum energy needed to remove it from the surface is described by the following equation,<sup>63</sup>

$$\Delta G = \pi r^2 \gamma_{wa} (1 \pm \cos \theta)^2 \quad (1.5)$$

where the sign ‘-’ inside the bracket indicates the removal of a particle from a surface into water for  $0^\circ \leq \theta \leq 90^\circ$  whilst ‘+’ represents entering air for  $90^\circ \leq \theta \leq 180^\circ$ , and  $r$  is the particle radius. The relationship between detachment energy and particle radius for  $\theta = 90^\circ$  is presented

in Figure 1.7. The detachment energy of sub-nanometer particles ( $r < 0.5$  nm) is less than 10 kT, being comparable to that of surfactant molecules.  $\log \Delta G$  increases linearly with  $\log r$  and the value of  $\Delta G$  can reach more than  $10^5$  kT for 100 nm. So, the ability of particle retention at the air-water surface is enhanced markedly, *i.e.* irreversible adsorption.<sup>62</sup>

**Figure 1.7.** Detachment energy for a small spherical particle from a planar air-water surface (contact angle  $90^\circ$ ) with  $\gamma_{wa} = 72$  mN m<sup>-1</sup> as a function of particle radius  $r$  at 298 K.



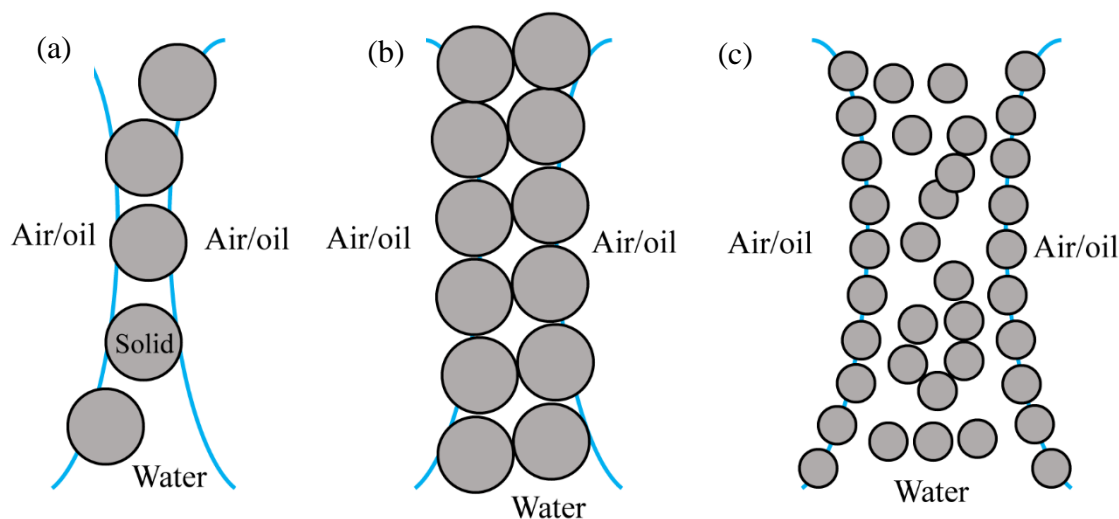
### (c) Particle-stabilized aqueous foams

Based on the above theory, very stable aqueous foams have been prepared with spherical micro- or nanoparticles.<sup>68-70</sup> In a pioneering study, Binks and Horozov investigated the effect of particle hydrophobicity on foam stability based on surfactant-free systems containing spherical fumed silica nanoparticles of varying SiOH content in water.<sup>68</sup> The foam containing relatively hydrophobic nanoparticles (32% SiOH) was demonstrated to be the most stable system devoid of coarsening/coalescence for several months. In another study, Fujii *et al.* reported the preparation of very stable aqueous foams from latex suspensions in the absence of surfactant.<sup>70</sup> The liquid films in the foam were found to be composed of a bilayer of latex particles based on the cryo-SEM images.

The stability of aqueous films separating foam bubbles is crucial for coalescence and foam collapse. The stabilization mechanisms of foam films with solid particles were well explained in a review paper by Horozov.<sup>64</sup> Liquid films were stabilized by either a bridging

monolayer, a bilayer of hexagonally close-packed particles or a network of particle aggregates (Figure 1.8).

**Figure 1.8.** Possible stabilisation mechanisms of aqueous films with solid particles. (a) monolayer of bridging particles; (b) bilayer of close-packed particles and (c) network of particle aggregates. Redrawn from ref. 64.

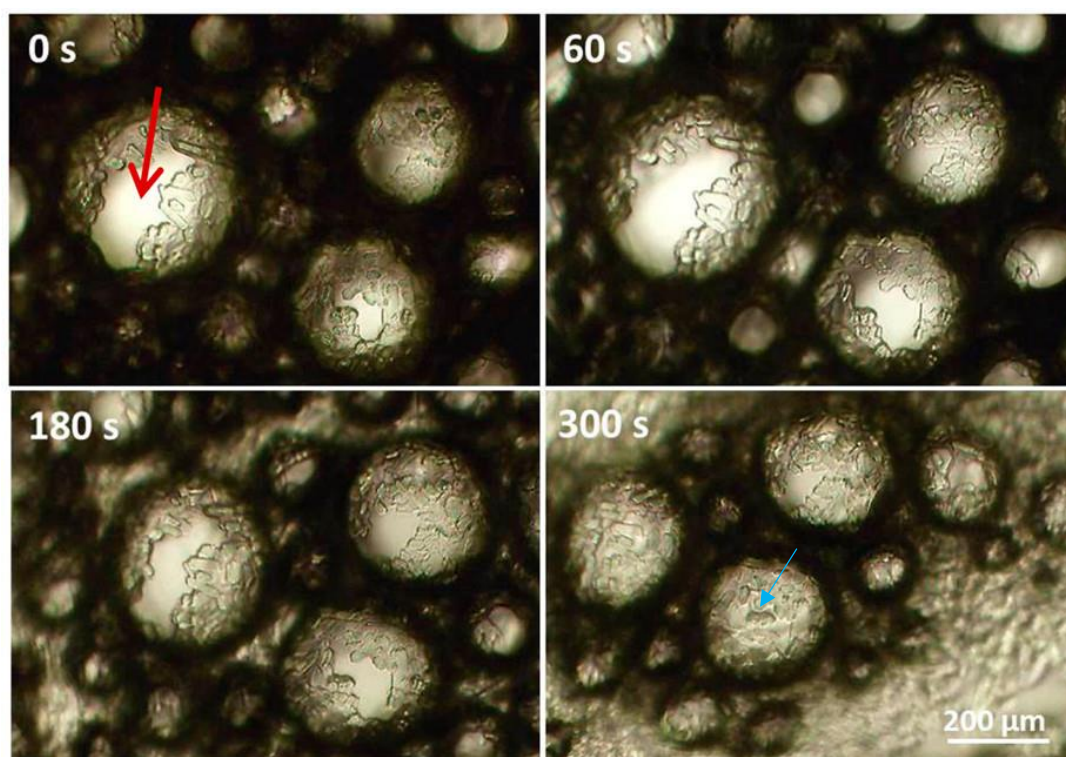


### 1.2.3.3 Crystalline particles

The stabilization of aqueous foams in the presence of surfactant crystals is sparsely studied.<sup>71-76</sup> Shrestha *et al.* showed that stable foams were prepared using diluted aqueous dispersions of pentaglycerol monostearate ( $C_{18}G_5$ ).<sup>71</sup> The long-term stability was due to the presence of small surfactant solid particles in the continuous phase leading to an increase in the liquid viscosity, which could slow down liquid drainage. Sodium dodecyl sulfate (SDS) is an anionic surfactant commonly used as a foaming agent. SDS foams are unstable however, merely surviving several hours. Interestingly, Zhang *et al.* discovered that the introduction of inorganic salts (*e.g.* NaCl and KCl) into aqueous SDS solutions with simultaneous foaming could induce the precipitation of SDS molecules *in situ* at air bubble surfaces.<sup>72-74</sup> At high salt concentrations, foams without coarsening or drainage could be formed due to the close packing of SDS crystals at the bubble surfaces alongwith the jamming of SDS crystals within the liquid films and Plateau borders. SDS tends to precipitate in the form of crystals due to a decreased solubility below the Krafft point. One example of such a foam during storage is shown in Figure 1.9. Another advantage of these foams was that they could be destabilized upon reaching the melting temperature of SDS crystals on warming. In another study,<sup>75</sup> a different protocol was

adopted to fabricate SDS crystal-stabilized aqueous foams. A divalent salt, *i.e.*  $\text{Mg}(\text{NO}_3)_2$ , was added into aqueous SDS solutions to induce SDS crystallization in bulk liquid, followed by vigorous hand shaking. Herein, the resulting aqueous foams were stabilized by pre-formed SDS crystals other than *in situ* formed ones. Most recently, a review paper by Fameau and Binks summarised all recent publications on aqueous foams containing surfactant crystals and highlighted the foaming and stabilisation mechanisms therein.<sup>77</sup> Readers can refer to this paper for more details.

**Figure 1.9.** Microscopy images of aqueous foam bubbles made with 500 mM KCl and 600 mM SDS as a function of storage time. Blue arrow indicates an SDS crystal-coated air bubble. The bubble surface is rough and textured. Taken from ref. 73.



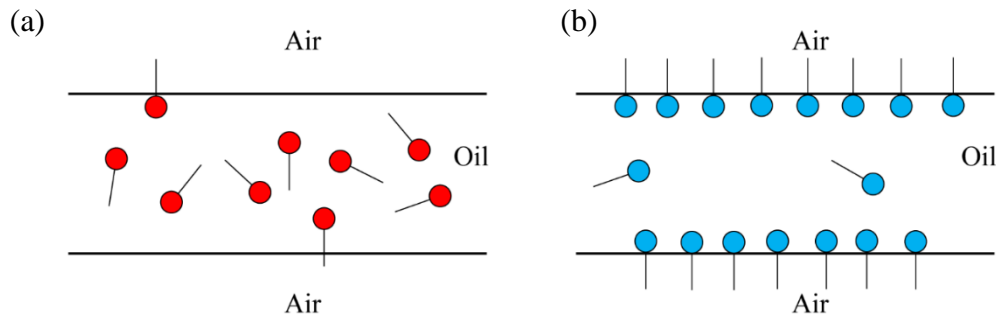
## 1.2.4 Stabilization of oil foam

### 1.2.4.1 Surfactants

The surface tensions of most hydrocarbon solvents ( $< 35 \text{ mN m}^{-1}$ ) are lower when compared to that of water ( $72 \text{ mN m}^{-1}$  at  $25^\circ\text{C}$ ). Commonly, hydrocarbon-based surfactants show no or weak adsorption tendency towards hydrocarbon-air surfaces because their surface tensions are too low to be decreased further, see Figure 1.10(a).<sup>78</sup> Fluorocarbon-based surfactants have a lower surface energy than hydrocarbon-based ones, so they are possibly

surface-active at both air-water and air-oil surfaces, Figure 1.10(b).<sup>79</sup> Based on this, fluorocarbon-based surfactants are a potential candidate for producing reasonably stable oil foams from their isotropic hydrocarbon solutions. Bergeron *et al.* found that the adsorption of fluorocarbon surfactant molecules at the dodecane-air surface resulted in a reduction of the surface tension by  $\sim 6 \text{ mN m}^{-1}$ .<sup>80</sup> The stability of bulk foams and foam films originated from a repulsive disjoining pressure due to the overlap of surfactant layers.

**Figure 1.10.** Possible adsorption behaviour of (a) hydrocarbon-based and (b) fluorocarbon-based surfactant molecules at air-oil surfaces. Adapted from ref. 78.



Air entrainment in lubricating oils is undesirable and detrimental which leads to reduced lubrication, lubricant oxidation, energy loss *etc.* The composition of lubricant-based oils is more complicated than that of alkane hydrocarbons, containing mainly base oil (*e.g.* mineral oil) and various additives. This makes the investigations on their interfacial and foaming properties difficult to carry out. The dynamic behavior of air bubbles in lubricating oils containing various solutes (*e.g.* polydimethylsiloxane) and the mechanisms therein have been studied by Ross and coworkers.<sup>81,82</sup> They found that the rising rate of an air bubble in the oil solution was inhibited to some extent depending on solute concentration and solute type. It was postulated that adsorbed solute molecules were not uniformly distributed on the surface of the ascending bubble, due to the viscous dragging force from the oil phase acting on the bubble surface. This led to the surface concentration on the upstream part of the bubble being larger than that on the downstream part. The induced surface tension gradient on the bubble surface could trigger Marangoni flow, which counteracted a fluid flow induced by the shearing stress on the bubble surface from continuous oil. The improved rigidity of the interface could inhibit an inherent air circulation within the bubble, so the terminal velocity of bubble rising was reduced. The terminal velocity can be expressed as,

$$V = 1/\kappa[2|\rho_2 - \rho_1|gr^2/9\eta_2] \quad (1.6)$$

$$\kappa = [e + b(3\eta_1 + 2\eta_2)]/[e + a(3\eta_1 + 3\eta_2)] \quad (1.7)$$

where  $r$  is the bubble radius,  $\rho_1$  and  $\eta_1$  are the density and viscosity of the bubble, respectively,  $\rho_2$  and  $\eta_2$  are the density and viscosity of continuous oil, respectively,  $e$  is the surface viscosity coefficient and  $b$  is a constant. This equation suggests that the terminal velocity can be reduced by either increasing the liquid viscosity, reducing the density difference between air and oil or decreasing the bubble size. Furthermore, they highlighted that the inability of a solute to reduce the equilibrium surface tension of an oil solution did not equal the surface inactivity of the solute.<sup>81</sup> Recently, the mechanism behind the foaming of complex lubricant base oils was further unveiled by Suja *et al.*<sup>83</sup> It was due to the solutocapillary Marangoni flow originating from the differential evaporation of different lubricant components in a thin film: evaporation caused a surface tension gradient between bulk liquid and thin film, which restored flow into the thin film from the bulk.

#### 1.2.4.2 Solid particles

For solid (s) - oil (o) - air (a) systems, the particle wettability depends on its contact angle  $\theta$  with an oil-air surface measured through oil, which can be described as,

$$\cos \theta = \frac{\gamma_{sa} - \gamma_{os}}{\gamma_{oa}} \quad (1.8)$$

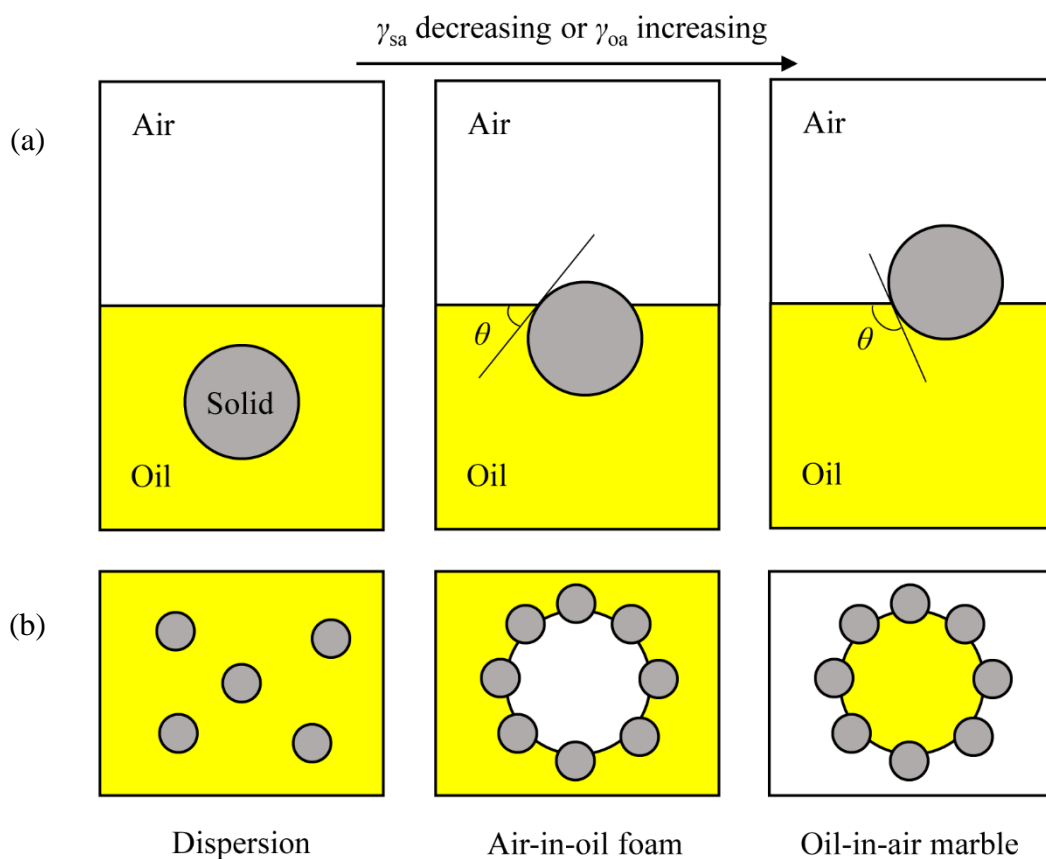
where  $\gamma_{sa}$ ,  $\gamma_{os}$  and  $\gamma_{oa}$  are the surface tensions of solid-air, solid-oil and air-oil, respectively. In the case of a spherical particle, no adsorption occurs when  $\theta = 0^\circ$  (wetting) or  $180^\circ$  (non-wetting), whereas for a moderate value of  $\theta$  varying between  $0^\circ$  and  $180^\circ$ , the adsorption of particles happens.

Early work by Fox and Zisman systematically studied the wetting behaviour of a range of liquids in air on smooth solid substrates of low surface energy, such as poly(tetrafluoroethylene) (PTFE) and modified tetrafluoroethylene polymers.<sup>84,85</sup> As a matter of fact, the contact angle  $\theta$  increased as the liquid surface tension increased. Moreover, an imaginary value, the critical surface tension  $\gamma_c$  of a solid was defined based on the relationship between the liquid surface tension  $\gamma_{la}$  and the contact angle  $\theta$ . A liquid with surface tension  $\gamma_{la} \leq \gamma_c$  of a solid could wet the solid completely ( $\theta = 0^\circ$ ), whilst those with  $\gamma_{la} > \gamma_c$  partially or fail to wet the solid ( $0^\circ < \theta \leq 180^\circ$ ). Based on the above conclusions, various colloidal materials (*viz.* oil foam, dry oil, oil liquid marble) were fabricated from solid particles in mixtures of oil and air.

Murakami and co-workers succeeded in preparing both oil foams and dry oils with oligo(tetrafluoroethylene) (OTFE) particles in the absence of surfactant.<sup>86,87</sup> More importantly, a new route was introduced to fabricate macroporous polymers using the oil foam as a template. Systematic studies performed by Binks *et al.* optimised the conditions for the stabilization of air-oil surfaces by a number of solid particle types.<sup>88-92</sup> The investigated particles were

fluoroethylene,<sup>88,89</sup> fluorinated fumed silica,<sup>90</sup> fluorinated clay<sup>91</sup> and other fluorinated particles.<sup>92</sup> The type of material formed, *e.g.* oil foam, dry oil, oil liquid marble, was influenced by the oil surface tension, the particle surface energy, the weight ratio of particle to oil and the level of mechanical energy input. The potential wetting behaviour as a function of liquid surface tension or particle surface energy is schematically shown in Figure 1.11. Most recently, Li *et al.* reported the fabrication of oil foams using fluorinated silica particles with controllable pit structures.<sup>93</sup> The particle morphology was modified *ex situ* by varying the wet etching time.

**Figure 1.11.** (a) Position of a spherical solid particle at an air-oil surface as a function of oil surface tension or particle surface energy. (b) Corresponding materials formed. Redrawn from ref. 90.



All investigations described above were carried out at room temperature. Besides, no study was available focusing on the behavior of a single air bubble in hydrocarbon oil with solid particles. For the first time, Garbin's group explored the dissolution behavior of single air bubbles coated by micron-sized clay particles in oil upon heating.<sup>94</sup> The clay particle-coated bubble in alkane was completely stable against dissolution at ambient temperature since its interfacial elasticity  $E$  could counteract the air dissolution driven by a Laplace pressure with

$E > \gamma_{oa}/2$ . Interestingly, when the temperature was submitted to a gradual increase, the bubble suffered dissolution during which its surface underwent buckling and crumpling without shedding of the adsorbed particles. The reason for this phenomenon was the unsaturation of the oil phase by air on heating. In contrast, for a colloidal particle-stabilized bubble in water bubble dissolution was enhanced during cooling.<sup>95</sup> In addition, the bubble surface went through either wrinkling or particle desorption depending on the particle-to-bubble size ratio. Thus, the dissolution behavior of an air bubble in a liquid amidst a temperature change is dependent on several parameters including the solvent type, bubble size, particle concentration *etc.*

#### 1.2.4.3 Crystalline particles

In ref. 78, Friberg and Solans clarified that by now fluorinated surfactant would be the only choice if one wanted to generate stable oil foam from an isotropic oil solution of surfactant. The use of such surfactant is restricted however due partly to its high cost and toxic nature.<sup>79</sup> so the future research on oil foams should be directed towards regions of the phase diagrams of hydrocarbon-based systems containing more than one phase.<sup>78</sup> Based on the above, Ross and Nishioka elucidated the role of the solubility phase boundary of a solute in oil on foaming.<sup>96</sup> They found a significant increase in foam stability when approaching the solubility limit of the stabilizing agent in oil, *i.e.* since it became insoluble. This was further verified by Friberg *et al.* on investigating the dispersion and foaming behavior of triethanolammonium oleate in p-xylene.<sup>97</sup> Good foam stability was obtained due to the adsorption of liquid crystalline phases at air bubble surfaces. Subsequently, by studying the foaming properties of a series of low molar mass and polymeric surfactants in poly(decene) oil, Binks *et al.* demonstrated enhanced foamability near the phase separation boundary of the solute in oil where the affinity of the former for the latter was low.<sup>98</sup> Reasonably stable oil foams from mono- and diglycerol fatty acid esters in long-chain alkanes and vegetable oils were systematically studied by Shrestha and coworkers.<sup>99-102</sup> Foamability and foam stability were determined by surfactant self-assembled aggregates formed within a two-phase region, being affected by the oil nature, surfactant concentration, surfactant architecture and temperature. Surfactant solids ( $\alpha$  or  $\beta$ ) were proven to be better foam stabilizers than the lamellar liquid crystalline phase ( $L_a$ ). Among all these studies, the gelation of oil was not achievable, however. So, their stability was relatively low (from several hours to several weeks).

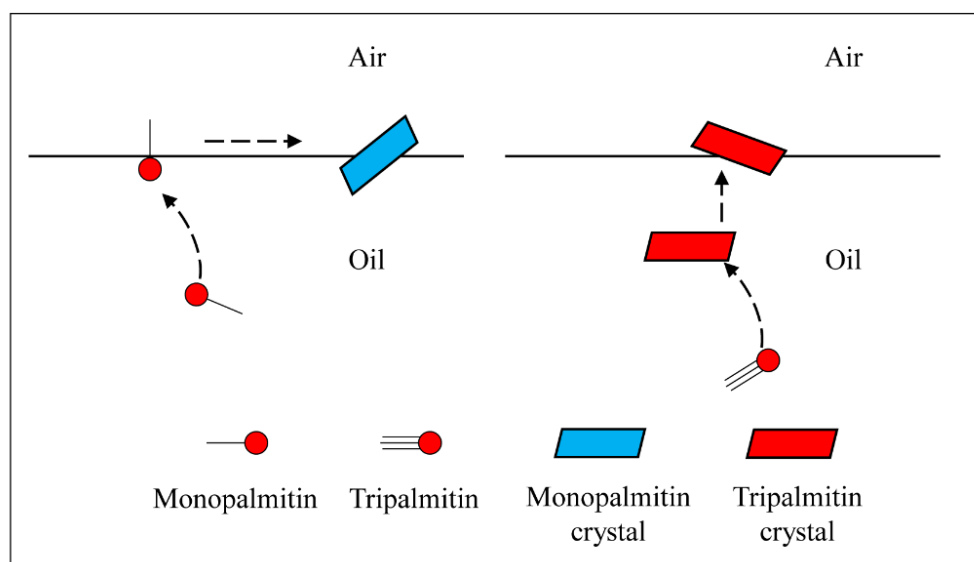
In recent years, oil foams find applications in the food industry because of their potential in reducing saturated fat intake, providing more desirable mouthfeel and reducing delivery costs.<sup>103,104</sup> The approaches for preparing ultra-stable edible oil foams are developed on the

basis of oleogels, during which a homogeneous solution of edible emulsifier in vegetable oil is first submitted to a specific tempering procedure to yield an oleogel, followed by mechanical energy input to generate an air-in-oil foam stabilized by pre-formed crystals.<sup>104-106</sup> The resulting foam is completely stable to coarsening/coalescence for several months due to a jammed layer(s) of crystalline particles surrounding air bubbles. Besides, excess crystals in the continuous oil can contribute to foam stability by arresting oil drainage. To help readers readily understand this area, some review papers are recommended herein.<sup>77,104-109</sup> By now, the investigated stabilizing agents can be categorized as: mono- and/or diglycerides,<sup>110-116</sup> fatty acids,<sup>117</sup> fatty alcohols,<sup>118</sup> high-melting triglycerides (TAG),<sup>119-124</sup> hydrocarbon waxes,<sup>125</sup> sucrose esters<sup>126,127</sup> and surfactant mixtures.<sup>40,128,129</sup> Several methods have been utilized to prepare oil foams including whipping, depressurization, hand shaking *etc.*

#### (a) Mono-/diglycerides

Brun *et al.* first reported the fabrication of ultra-stable oil foams in the system of mono- and diglycerides in rapeseed oil.<sup>110</sup> The resulting foams were stable against coalescence and Ostwald ripening because of a rigid layer(s) of surfactant crystals surrounding air bubbles. Moreover, the 3D crystal network was elastic enough to arrest gravity-driven creaming. In another study, Gunes *et al.* pointed out that the application of whipping was necessary for the creation of a compact layer(s) of crystals at bubble surfaces, thereby providing Pickering-type interfacial stabilization.<sup>111</sup> The effect of tempering protocol on the foaming behavior of mono- and diglycerides in vegetable oil was studied by Heymans *et al.*<sup>112</sup> and Li *et al.*<sup>113</sup> respectively. Subsequently, the crystallization behaviour of monopalmitin at the surface of medium-chain triglyceride oil was probed by Mishra *et al.* as shown in Figure 1.12.<sup>114</sup> Monopalmitin molecules could crystallize *in situ* at the air-oil surface on cooling, leading to the rapid formation of an elastic interfacial network. However, the adsorption configuration of monopalmitin molecules is still ambiguous. On the contrary, tripalmitin crystals were formed in the bulk phase before adsorbing towards the air-oil surface. Apart from the known aging mechanisms of foam mentioned above, ref. 116 highlighted that partial coalescence could lead to the destabilisation of oil foams containing monoglyceride crystals.

**Figure 1.12.** Proposed crystallisation behaviour of (left) monopalmitin and (right) tripalmitin at the medium-chain triglyceride oil-air surface during cooling. Monopalmitin molecules crystallise directly at the surface whilst tripalmitin crystals are formed in the bulk before moving towards the surface. Adapted from ref. 114.



#### (b) Fatty acids/fatty alcohols

In ref. 117, the solubility diagram of mixtures of myristic acid in high oleic sunflower oil was determined *via* visual observations and differential scanning calorimetry (DSC) tests. Based on this, whipping was performed as a function of whipping temperature and surfactant concentration. Stable oil foams without drainage, coarsening or coalescence were fabricated in the presence of sufficient amounts of pre-formed surfactant crystals. Fameau *et al.* reported a different method to prepare stable oil foams based on mixtures of fatty alcohols of varying alkyl chain length and sunflower oil.<sup>118</sup> Whipping was applied on the mixtures with simultaneous cooling to induce the surfactant crystallization *in situ* on bubble surfaces and in the oil phase. The obtained foams were ultra-stable below the crystallization temperature; they could be destabilized upon warming above the melting temperature.

#### (c) High-melting triglycerides

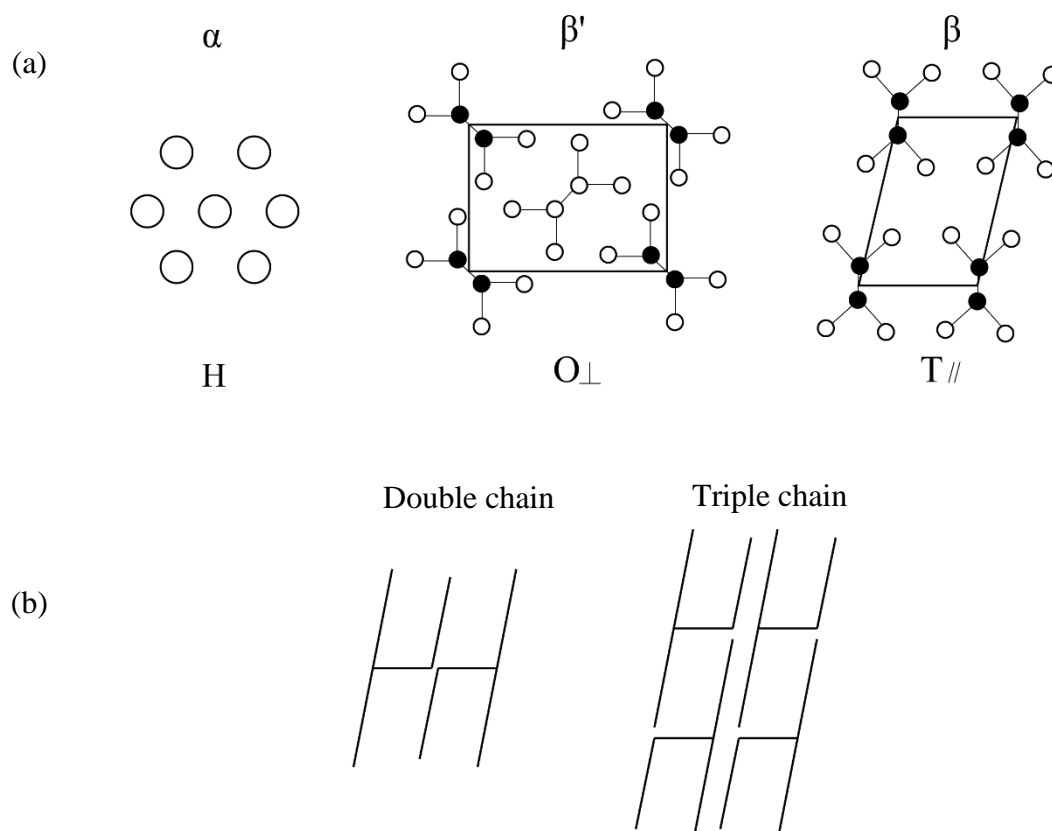
Edible fats and oils are complex multi-component mixtures, which are mainly composed of TAG formed by esterification of one glycerol group and three fatty acids.<sup>130</sup> The chemical and physical characteristics of fats and oils are affected by the type of the fatty acid, the way of positioning and the degree of saturation.<sup>130,131</sup> The length of the fatty acid normally

varies from 4 carbons (*i.e.* butyric acid) to 22 carbons (*i.e.* behenic acid). As a rule, the longer the alkyl chain length, the higher the melting temperature of TAG. On the other hand, the melting point of TAG containing more saturated fatty acids is normally higher than those composed of more unsaturated fatty acids. In the current consumption market, examples of liquid oils rich in unsaturated fatty acids are olive oil, soybean oil, rapeseed oil and peanut oil, whilst fats composed of more saturated fatty acids are coconut oil and palm oil to name just a few.

When a liquid TAG oil is cooled below its crystallisation temperature, TAG molecules tend to arrange head-to-head, forming a repetitive bimolecular layer to optimise interactions between polar groups, *i.e.* undergoing crystallisation.<sup>132</sup> The crystallisation process normally involves three individual events: nucleation, crystal growth and crystal ripening.<sup>131,133</sup> Nucleation occurs firstly followed by crystal growth. As the growth continues, secondary nucleation may initiate accompanied by crystal ripening.

Polymorphism is defined as the existence of several crystalline or liquid crystalline phases with different structures based on one chemical composition.<sup>131</sup> Depending on various external conditions, *e.g.* temperature, pressure and solvent, the most common polymorphs of TAG crystals are  $\alpha$ ,  $\beta'$  and  $\beta$ . The subcell structure of a TAG crystal is the major criterion to distinguish between different polymorphs.<sup>134</sup> The  $\alpha$  polymorph adopts a hexagonal sub-cell (H), the  $\beta'$  one has an orthorhombic-perpendicular subcell ( $O_{\perp}$ ) and the  $\beta$  one has a triclinic-parallel subcell ( $T_{\parallel}$ ), see Figure 1.13(a).<sup>135</sup> The sub-cell structures of different polymorphs can be differentiated based on their characteristic short-spacing patterns measured by X-ray diffraction (XRD). The  $\alpha$  polymorph is characterised by a short spacing near 0.42 nm. The  $\beta'$  polymorph has two evident short spacing peaks at 0.37-0.40 nm and 0.42-0.43 nm, respectively. The  $\beta$  form can be identified by a strong spacing peak at around 0.46 nm and a series of other peaks between 0.36-0.39 nm.<sup>135</sup> The chain length structures represent the repetitive sequence of the fatty acid chains in a unit cell lamella along a long-chain axis in a fat crystal. The chain length structures of TAG crystals have two typical types: double chain length and triple chain length, being associated with the chemical similarities of the fatty acid chains, see Figure 1.13(b).<sup>134</sup>

**Figure 1.13.** (a) Sub-cell structures of different TAG crystal polymorphs. (b) Chain length structures of TAG in a fat crystal. Redrawn from ref. 133.



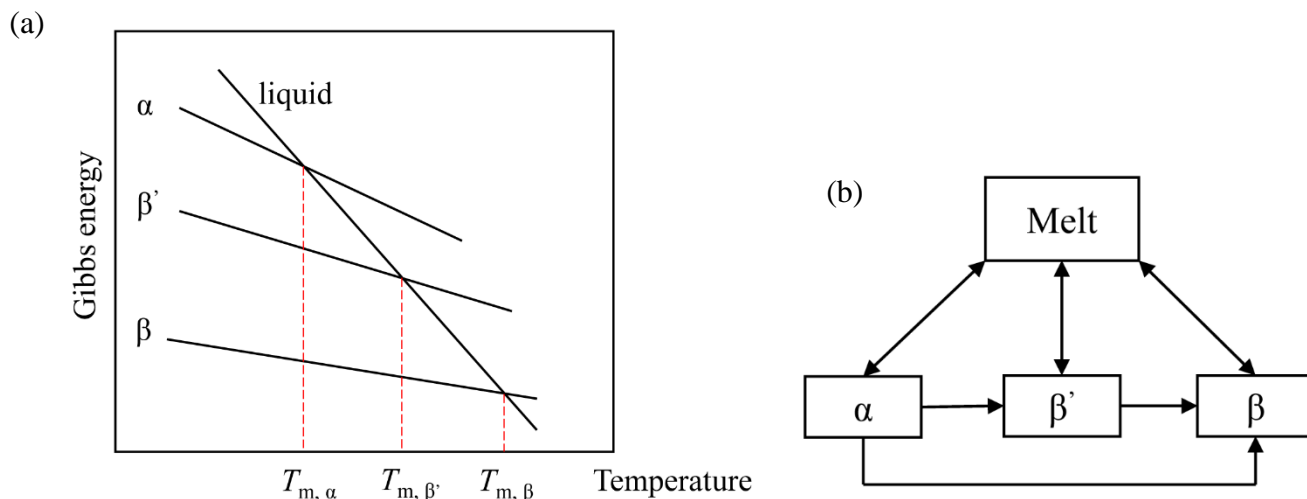
Thermodynamically, different polymorphs of TAG crystals have different stability and a less stable polymorph tends to transform into a more stable one driven by a difference in Gibbs free energy. The Gibbs free energy of different polymorphs as a function of temperature is presented in Figure 1.14(a). The relationship between Gibbs free energy ( $G$ ) and temperature ( $T$ ), enthalpy ( $H$ ), entropy ( $S$ ) is described as,

$$G = H - TS \quad (1.9)$$

With increasing temperature,  $G$  decreases linearly. On the other hand, the Gibbs free energy of the  $\alpha$ -form is the highest indicating the least stability. The system stability is intermediate for the  $\beta'$ -form while the highest for the  $\beta$ -form with the lowest  $G$ . Besides, each polymorph has its own melting point, defined as the crossover temperature of the  $G$ - $T$  lines between various polymorphs and liquid. The most stable polymorph ( $\beta$ ) has the highest melting point  $T_{m,\beta}$  whereas the least stable one ( $\alpha$ ) has the lowest melting point  $T_{m,\alpha}$ . Based on the above, the pathways of polymorphic transitions between them are displayed in Figure 1.14(b). First, the three crystal polymorphs can be formed directly from a melted state and *vice versa*. Secondly,

a less stable polymorph can transit to a more stable one irreversibly, *i.e.* the  $\alpha$ -form to the  $\beta'$ -form to the  $\beta$ -form or the  $\alpha$ -form directly to the  $\beta$ -form.

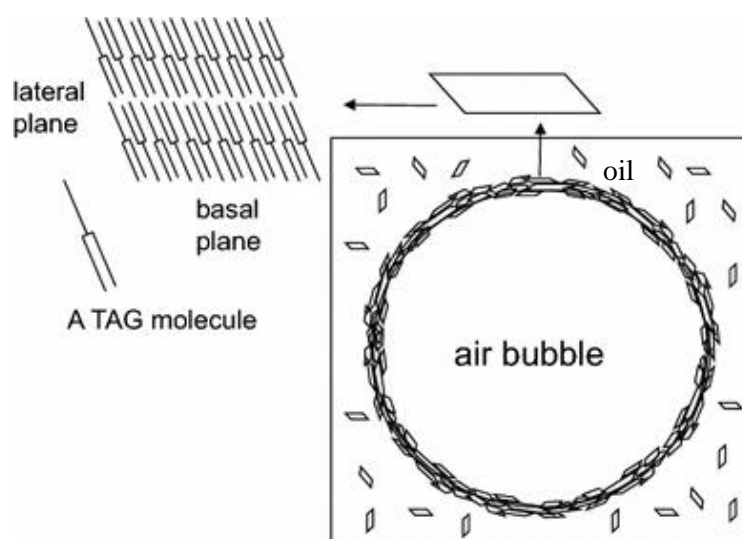
**Figure 1.14.** (a) Gibbs free energy as a function of temperature for different polymorphs of TAG crystals.  $T_{m,\alpha}$ ,  $T_{m,\beta'}$  and  $T_{m,\beta}$  are the melting points of  $\alpha$ ,  $\beta'$  and  $\beta$  forms, respectively. (b) Transition between different polymorphs. Redrawn from ref. 131.



In pioneering work, Mishima *et al.* reported the stabilization of vegetable oil foams by high-melting fat crystals containing saturated  $C_{18}$ - $C_{22}$  hydrocarbon chains.<sup>119</sup> Small  $\beta$ -fat crystals were proven to be a pre-requisite for preparing well-whipped salad oil. More importantly, the arrangement of TAG crystals near the air-oil interface was determined by synchrotron radiation microbeam X-ray diffraction (SR- $\mu$ -XRD). As shown in Figure 1.15, the faces of interfacial TAG crystals are oriented parallel to the air-oil interface, whilst crystals within the continuous oil phase are randomly distributed. An energy-favorable configuration is such that the methyl groups of TAG crystal faces interact with both air and oil, whereas their edges mainly composed of methylene and glycerol groups interact with the other edges of adjacent adsorbed TAG crystals (*via* van der Waals forces and hydrogen bonds). Later, Binks *et al.* reported on the foaming potential of neat vegetable oils composed of medium or long chain fatty acids in the absence of any additive, see also Chapter 3.<sup>120,121</sup> Subsequently, the foaming capacity of anhydrous milk fat and palm kernel oil was demonstrated.<sup>122,123</sup> Most recently, Metilli *et al.* reported on the fabrication of oleofoams by whipping oleogels containing cocoa butter and high oleic sunflower oil.<sup>124</sup> It was shown that cocoa butter concentration was the major parameter affecting foamability rather than the size and shape of cocoa butter crystals. Given the fact that the composition of natural fats/oils is rather complex, the role of intrinsic

minor species within on their oil foaming properties is worthy of further investigations. An interesting study carried out by Mishra *et al.* looked at the adsorption and network formation behavior of tripalmitin at medium chain triglyceride oil-air surfaces amidst crystallisation.<sup>114</sup> Through careful surface tension and interfacial rheological measurements, the interfacial adsorption mechanism of tripalmitin was postulated: tripalmitin molecules crystallized in the oil phase prior to migrating gradually towards the oil surface with comparatively slow adsorption kinetics, see Figure 1.12 earlier. It has been concluded that the high  $\gamma_{os}$  drove the tripalmitin crystals to the air-oil surface to minimize their contact area with the oil.

**Figure 1.15.** Schematic illustrating the arrangement behaviour of high melting fat crystals near a bubble surface and in continuous oil. Taken from ref. 119.



#### (d) Hydrocarbon waxes

In ref. 125, through investigating the rheological properties of the bulk oil phase and the air-oil interface separately, the role of interfacial and continuous phase contribution in the stabilization of oil foams with hydrocarbon wax crystals was decoupled. It was illustrated that the Pickering mechanism of stabilization alone was insufficient to arrest bubble dissolution, whereas the firmness of the continuous phase was dominant in suppressing bubble dissolution.

#### (e) Surfactant mixtures

Few papers are currently available focusing on the preparation of stable oil foams from mixtures of two or more crystallizable surfactants.<sup>40,128,129</sup> Are there any synergistic interactions between certain surfactants, potentially exhibiting improved foamability, enhanced foam stability or novel functionality compared to single surfactant? Truong *et al.* looked at the oleogelation and foaming characteristics of mixtures of saturated monoglycerides (MAG) with

native phytosterols (NPS) in canola oil.<sup>40</sup> NPS are plant-derived steroid alcohols containing sterols and stanols being beneficial to human health since they can weaken the adverse effect of cholesterol and have anti-inflammatory and anti-cancer effects. Seeking ways to introduce NPS into food products is of industrial interest. Through varying the surfactant concentration, the weight ratio of MAG:NPS and tempering protocol, oleofoams containing many crystal-coated air bubbles of different structures could be yielded. NPS were successfully introduced into potential low-density aerated food products *via* their co-crystallization with MAG. Mixing fatty acids and fatty alcohols has been adopted by some researchers to structure edible oils.<sup>17</sup> However, the potential effects on oleofoams have not been explored. Callau *et al.* probed into the foaming properties of oleogels from mixtures of behenyl alcohol (BO) and behenic acid (BA) in sunflower oil.<sup>128</sup> Oil foams of different air fraction, microstructure and stability were obtained by varying the weight ratio of BO:BA. The best foam was yielded, *i.e.* possessing the highest over-run, the highest stability, the smallest average bubble diameter and highest firmness from the system containing the smallest crystal size and highest solid content. Oleofoams based on diacylglycerol mixtures were studied by Wang's group.<sup>113,129</sup> The highlight of ref. 113 was that the adsorption of diacylglycerol fractions at bubble surfaces could facilitate the interfacial crystallization of fully hydrogenated palm oil, thereby yielding smaller bubble size and higher foam elasticity. In ref. 129, they found that diacylglycerol could interact with  $\beta$ -sitosterol *via* intermolecular hydrogen bonding improving the oleogel elasticity, possibly enhancing foam stability.

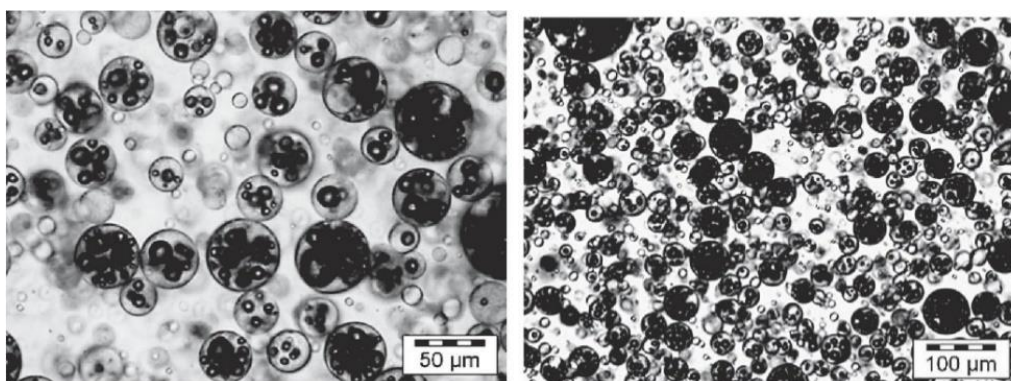
#### (f) Sucrose esters

As seen above, oil foams are stabilised by pre-formed surfactant/fat crystals. In contrast to all previous work, we recently reported a novel strategy to prepare stable vegetable oil foams from mixtures of sucrose ester and vegetable oil (see also Chapter 4).<sup>126</sup> Oil foams of high air fraction could be obtained from one-phase oil solutions at high temperature. This was due to the rapid adsorption of sucrose ester-triglyceride molecular complexes at the air-oil surface upon whipping, which was confirmed by infrared (IR) spectrometry and surface tension measurements. Due to the instability of those foams prepared at high temperature, a post-whipping protocol, *i.e.* rapid cooling, was introduced whereby ultra-stable oil foams containing many crystal-protected air bubbles were obtained. This finding could be applied to other unsaturated vegetable oil systems. Based on this finding, we succeeded in fabricating a multitude of colloidal materials using single sucrose ester surfactant, *i.e.* simple and multiple

emulsions, aqueous and oil foams, aerated emulsions and foamed emulsions.<sup>127</sup> This work has not been peer reviewed yet.

Stable oil foams by surfactant/fat crystals could be used as intermediates to prepare air-in-oil-in-water (a/o/w) emulsions.<sup>110,122,129</sup> When dispersing those foams into a viscous aqueous dispersion containing various hydrophilic emulsifiers and thickening agents, novel a/o/w emulsions are obtained. For droplet deformation and rupturing to occur, the applied shear stress  $\eta_c \dot{\gamma}$  must be sufficiently high,  $\eta_c$  being the viscosity of the aqueous phase and  $\dot{\gamma}$  being the applied shear rate. Nevertheless, it should not be excessive to avoid the disruption of air bubbles entrapped within oil globules. The major drawback of the existing systems however is that so many emulsifiers are involved during emulsification, making it difficult to probe into the underlying stabilisation mechanisms; the synergistic or antagonistic interactions between different species are far from clear.

**Figure 1.16.** Micrographs of a multiple air-in-oil-in-water emulsion. Small air bubbles (black) are stabilised by adsorbed anhydrous milk fat crystals, whereas relatively large oil globules are stabilised by 12 wt.% sodium caseinate and 0.02 wt.% sodium azide. Taken from ref. 122.



### 1.2.5 Aqueous and oil foams: similarities and differences

Aqueous foams are similar to oil foams in two aspects. Firstly, the mechanisms leading to foam destabilization are the same for both types of foams, *i.e.* liquid drainage, coarsening and coalescence. Secondly, both foam types can be stabilized by surfactants, solid particles or crystalline particles. Significant differences exist between aqueous and oil foams. The major one is surface tension. The surface tension of water is  $\sim 72 \text{ mN m}^{-1}$  at  $25^\circ\text{C}$  due to extensive hydrogen bonding. For hydrocarbon oils, their surface tensions are much lower ( $< 35 \text{ mN m}^{-1}$ ), making the adsorption of most hydrocarbon surfactants towards the air-oil surface energetically unfavorable. Secondly, most oils have low dielectric constants within which the

ionization of ionic surfactants will be suppressed. Therefore, electrostatic repulsive forces contributing to the stability of aqueous foam is insignificant in oil foam. Thirdly, when left to open air, oil foams are less likely to suffer liquid evaporation (unless the oil is volatile) compared to aqueous foams. Different methods are commonly adopted to prepare aqueous and oil foams.<sup>77</sup> In the case of oil foams, whipping is the most popular strategy, during which air entrainment followed by progressive bubble breakup under shear are involved. Oil foams can be produced *via* depressurization or bubbling as well. For aqueous foams, the most common method is hand shaking. Besides, a simple home-built foaming device has been applied, being composed of two connected plastic syringes with one containing air and the other one containing surfactant solutions.

## 1.3 Emulsions

### 1.3.1 Definition and types

A simple emulsion is a heterogeneous system containing two immiscible liquid phases in which one phase is dispersed into the other phase as drops of colloidal size.<sup>136</sup> There are two basic types of simple emulsions, *i.e.* water-in-oil (w/o) and oil-in-water (o/w) emulsions. For the former one, a water phase is dispersed into continuous oil, whilst oil is dispersed as droplets into continuous water for the latter one. One facile method to distinguish between the two emulsions is the drop test. A water continuous emulsion can mix readily with water whereas an oil continuous emulsion can easily dissolve into oil.<sup>136</sup> Another way to determine the type of an emulsion is to measure its electrical conductivity. This method is based on the fact that the conductivity of an emulsion is close to that of its continuous phase, so the electrical conductivity of an o/w emulsion is normally higher than that of a w/o emulsion. A multiple emulsion is defined as a complex emulsion system consisting of more than two dispersed phases. The simplest multiple emulsions are double emulsions, which are composed of three distinct phases. The representative types of double emulsions are water-in-oil-in-water (w/o/w) and oil-in-water-in-oil (o/w/o), Figure 1.17.<sup>137</sup> The former emulsion can mix readily with water whereas the latter one can dissolve into oil.

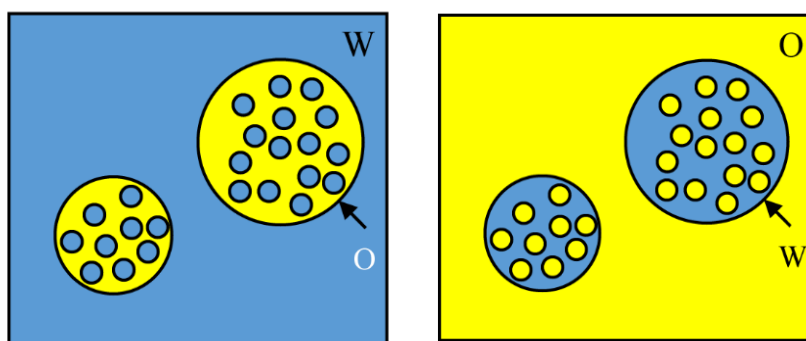
Depending on the drop size, emulsions are classified into three types: macroemulsions (500 nm-500  $\mu$ m), miniemulsions (50 nm-500 nm) and microemulsions (5 nm-50 nm). Macro- and miniemulsions are thermodynamically unstable systems requiring external energy input to form droplets. In contrast, microemulsions can be rendered spontaneously being

thermodynamically stable.<sup>55</sup> The key to the thermodynamic stability of an emulsion is the Gibbs free energy change  $\Delta G$  involved in emulsification,<sup>55</sup>

$$\Delta G = \gamma \Delta a - T \Delta S \quad (1.10)$$

where  $\gamma$  is the interfacial tension,  $\Delta a$  is the interfacial change in area,  $T$  is the absolute temperature and  $\Delta S$  is the change in entropy. It suggests that to improve the thermal stability of a system ( $\Delta G < 0$ ),  $\gamma \Delta a$  should be smaller than  $T \Delta S$ . During an emulsifying process, disorder tends to increase with  $\Delta S > 0$  contributing positively to emulsion stability. On the other hand, there is an increase in the interfacial area due to the formation of colloidal droplets with the application of mechanical energy input. This leads to an increase in  $\gamma \Delta a$ . In addition, the magnitude of  $T \Delta S$  is much lower relative to that of  $\gamma \Delta a$ . Therefore, the creation of an emulsion is energetically unfavourable with  $\Delta G$  being positive, ultimately destabilising to recover its initial state if kinetic stabilisation is not available. However, if one surfactant can reduce the interfacial tension to a very low value ( $10^{-4}$  to  $10^{-2}$  mN m<sup>-1</sup>),  $\gamma \Delta a$  will be sufficiently small favouring the spontaneous formation of a microemulsion ( $\Delta G < 0$ ). From here on, microemulsions will not be discussed further.

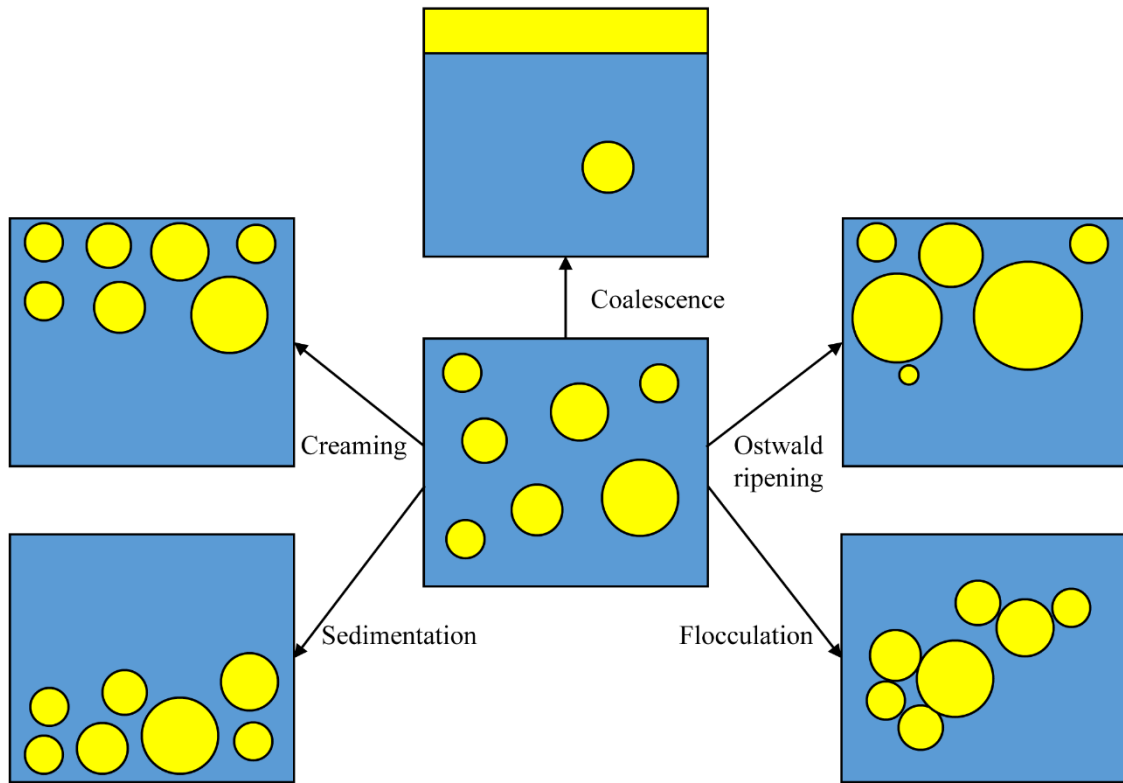
**Figure 1.17.** Schematic of a water-in-oil-in-water emulsion (left) and an oil-in-water-in-oil emulsion (right).



### 1.3.2 Destabilization processes

A macroemulsion is thermodynamically unstable tending to phase separate in the absence of stabilisers. There are several destabilisation processes therein, including creaming (or sedimentation), flocculation, coalescence and Ostwald ripening, see Figure 1.18.

**Figure 1.18.** Schematic illustrating different destabilisation processes of an emulsion. Adapted from ref. 55.



(a) Creaming or sedimentation

Creaming or sedimentation occurs when the density of a dispersed phase is not equal to that of its continuous medium. An o/w emulsion suffers creaming during which low density oil droplets tend to move upward reaching the top of the emulsion. On the contrary, sedimentation occurs in a w/o emulsion whereby high density water droplets gather progressively at the sample bottom. Creaming or sedimentation is typically a precursor to coalescence. The rate of creaming or sedimentation depends on the volume fraction  $\phi$  of the dispersed phase.<sup>55</sup> Generally, it decreases reaching almost zero with increasing  $\phi$ . For very dilute emulsions ( $\phi < 0.01$ ), the rate can be estimated by Stokes' law,

$$v = \frac{2\Delta\rho gr^2}{9\eta_c} \quad (1.11)$$

where  $\Delta\rho$  is the density difference between the dispersed phase and its continuous medium,  $r$  is the droplet radius,  $\eta_c$  is the viscosity of the continuous phase and  $g$  is the acceleration due to gravity. Stokes' law suggests that the moving rate of a droplet in liquid can be reduced by either reducing the density difference, reducing the droplet size or increasing the viscosity of the continuous phase.

#### (b) Flocculation

Flocculation refers to the formation of relatively large, three-dimensional (3D) droplet clusters without merging. This phenomenon arises from strong van der Waals attractions. For two spherical droplets of equal radii  $r$ , the van der Waals attraction force  $F_{vw}$  as a function of surface-to-surface distance  $h$  is given by the following equation,<sup>55</sup>

$$F_{vw} = -\frac{Ar}{12h^2} \quad (1.12)$$

where  $A$  is the effective Hamaker constant and the symbol '-' indicates the force is attractive. This equation suggests that the magnitude of  $F_{vw}$  increases with decreasing distance or increasing droplet size. In combination with the Stokes' equation, flocculation can lead to more rapid creaming/sedimentation due to their larger sizes compared to individual droplets.

#### (c) Ostwald ripening

Ostwald ripening is a phenomenon during which the dispersed phase diffuses molecularly from smaller to larger droplets through its continuous medium.<sup>55</sup> This is due to the fact that a smaller droplet has a higher Laplace pressure and a higher solubility than a larger one. The solubility  $c(r)$  of a spherical droplet of radius  $r$  in continuous fluid can be described by the Kelvin equation,

$$c(r) = c(\infty) \exp\left(\frac{2\gamma V_m}{rRT}\right) \quad (1.13)$$

where  $c(\infty)$  is the bulk solubility,  $\gamma$  is the interfacial tension,  $V_m$  is the molar volume of the dispersed phase,  $R$  is the ideal gas constant and  $T$  is the absolute temperature. During Ostwald ripening, larger droplets grow gradually at the expense of smaller droplets, leading to an increase in the average droplet size.

#### (d) Coalescence

Due to the occurrence of flocculation or creaming(sedimentation), liquid films surrounding droplets becomes thinner. When the film thickness is below a critical value, film rupture may happen resulting in the merging of droplets accompanied by an increase in the droplet size. Without stabilizers, this destabilization process will lead to complete phase separation of an emulsion into two original liquid phases.

### 1.3.3 Stabilization of emulsion

#### 1.3.3.1 Surfactants

The amphiphilic nature of many emulsifying surfactants can be semi-quantified by the hydrophilic-lipophilic balance (HLB) number.<sup>138</sup> A hydrophobic surfactant with a low HLB number  $< 7$  tends to stabilise a w/o emulsion. In contrast, a hydrophilic surfactant can be used to stabilise an o/w emulsion for a high HLB number  $> 7$ . The role of surfactant in facilitating emulsification or improving emulsion stability is summarised as follows:

##### (a) Lowering surface tension

The adsorption of surfactant molecules at an oil-water interface can significantly reduce its interfacial tension. From a thermodynamic perspective, the interfacial energy  $\gamma\Delta a$  is lowered due to surfactant adsorption, thereby enhancing the thermodynamic stability of an emulsion or reducing the energy barrier involved in emulsification, see equation 1.10. On the other hand, the reduction of interfacial tension can decrease the driving force for Ostwald ripening, see equation 1.13.

##### (b) Gibbs-Marangoni effect

The mechanism of the Gibbs-Marangoni effect induced by an interfacial tension gradient is well explained above, Figure 1.5. In an emulsion, the existence of the Gibbs-Marangoni effect can prevent further drainage of a thin liquid film, thus effectively hindering coalescence. In addition, the interfacial elasticity endowed by surfactant adsorption can reduce Ostwald ripening.<sup>55,58</sup>

##### (c) Electrostatic or steric barrier

The existence of an electrostatic or a steric barrier can prevent emulsion droplets from approaching too close thus reducing flocculation, Ostwald ripening and coalescence.<sup>55,58</sup>

##### (d) High viscosity

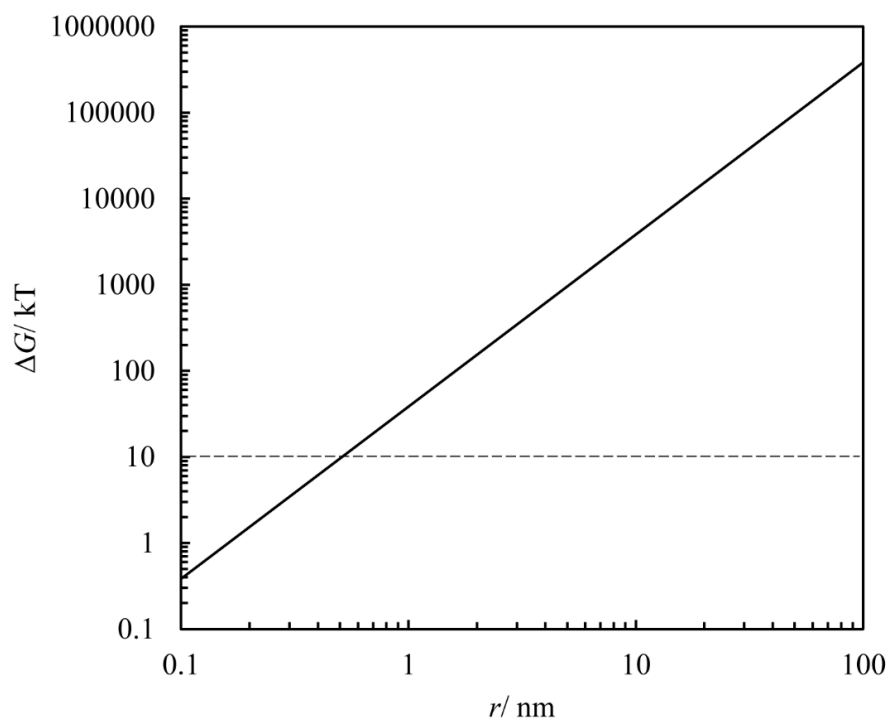
When dissolving certain surfactant into an emulsion, *e.g.* sodium carboxymethyl cellulose into an o/w emulsion, a viscous gel network may be formed. So, the rates of phase separation, Ostwald ripening, *etc.* are retarded.<sup>58</sup>

### 1.3.3.2 Solid particles

In systems containing solid, oil and water, o/w emulsions are preferred for spherical hydrophilic particles with  $0^\circ < \theta < 90^\circ$ . For spherical hydrophobic particles with  $\theta > 90^\circ$ , they tend to yield w/o emulsions. See Figure 1.6.

Figure 1.19 gives the detachment energy for a spherical solid particle from a planar alkane-water interface ( $\theta = 90^\circ$ ) as a function of particle radius at 298 K. The interfacial tension  $\gamma_{ow}$  equals  $50 \text{ mN m}^{-1}$ , being the typical value of an alkane-water interface at 298 K. The detachment energy for a 100 nm spherical particle is several orders of magnitude higher than the thermal energy (kT). Thus the particle is irreversibly adsorbed at the interface.

**Figure 1.19.** Detachment energy for a single spherical particle from a planar alkane-water interface ( $\theta = 90^\circ$ ) with  $\gamma_{ow} = 50 \text{ mN m}^{-1}$  as a function of particle radius at 298 K.



Based on the above theories, the stabilization of emulsions with hard particles has been extensively investigated. Many examples of the stabilizers are available including silica,<sup>62,63</sup> metal,<sup>139</sup> carbon<sup>140</sup> and clay<sup>141</sup> particles.

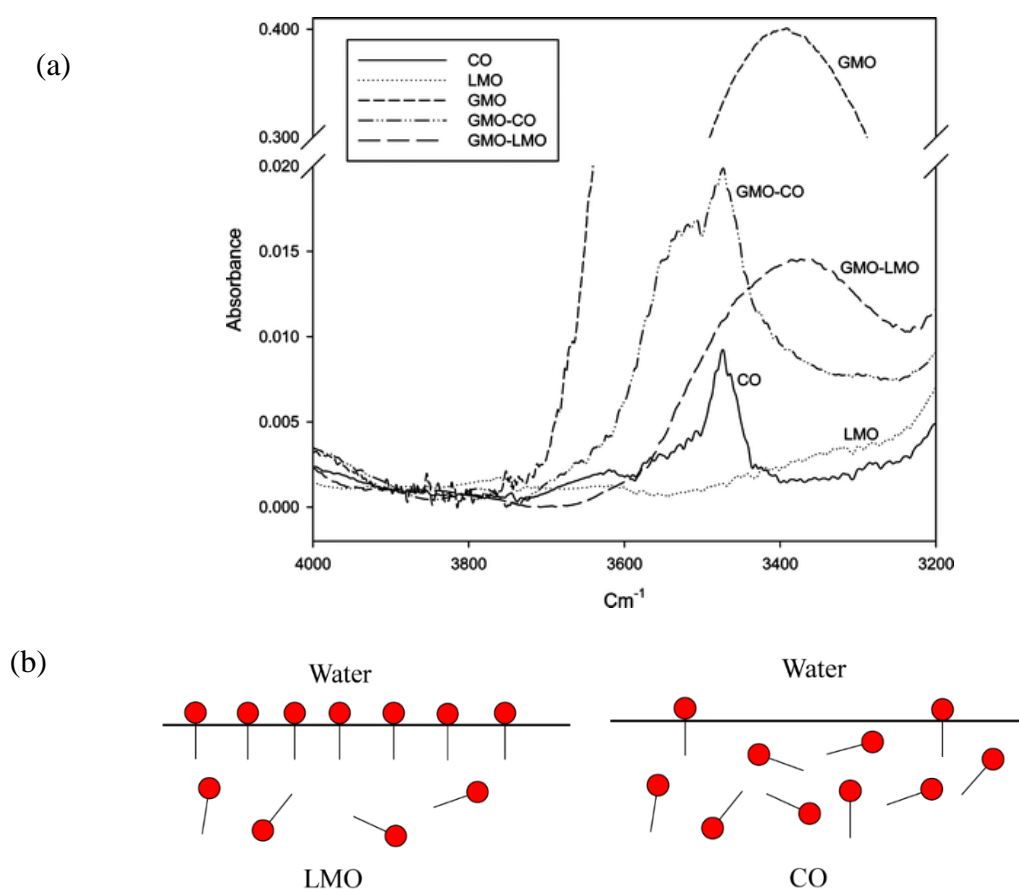
### 1.3.3.3 Crystalline particles

The review in this section on emulsions stabilized by crystalline particles is restricted to w/o only. By now the investigations on oil continuous emulsions stabilized by fat/surfactant crystals are far from enough, despite their omnipresence in the area of food.<sup>142,143</sup> Comprehensive work carried out by Rousseau and coworkers is worth highlighting.<sup>143-154</sup> They have prepared edible w/o emulsions containing various species and verified the stabilization mechanisms and molecular interactions therein. The long-term stability of such emulsions is achieved due to the adsorption of crystals (*in situ* or pre-formed) at droplet surfaces and the gelation of continuous oil by sufficient crystals formed therein. The jamming of adsorbed crystals at interfaces can prevent Ostwald ripening, flocculation and coalescence. Moreover, the continuous network stabilization can arrest droplet movement avoiding sedimentation. In early work, two strategies were adopted to prepare w/o emulsions with fat crystals: (1) TAG crystallization *in-situ* at both surfaces and in continuous oil induced by rapid cooling after emulsification at high temperature, (2) addition of pre-formed TAG crystals prior to emulsification.<sup>155</sup> The emulsions based on the former method were more stable than those based on the latter one. However, the difference in the crystal size and morphology between the two methods could not be neglected. The finding was later verified by Binks and Rocher focusing on non-edible oil emulsions with wax microparticles.<sup>156</sup> Based on the above, a popular strategy to fabricate stable w/o emulsions is summarised below. Firstly, a mixture of oil and fat/surfactant is melted at high temperature to create a homogeneous oil solution. Secondly, the solution is introduced into water followed by vigorous homogenisation or rotating to prepare an emulsion. Last, the w/o emulsion is submitted to rapid cooling under continuous stirring to avoid sedimentation and then stored at low temperature. The resulting emulsions reveal varying microstructures, rheological and thermal properties, being dependent on the additive type, fat/surfactant concentration, water content, *etc.*

Based on Rousseau's work, Pickering-type stabilization has been achieved in several ways in various systems.<sup>144,146</sup> In the case of a mixture of oil, water and high melting oil-soluble surfactant, *e.g.* glycerol monostearate (GMS), GMS molecules can adsorb readily to the water-oil interface at high temperature due to their amphiphilic nature, the configuration of which is that their polar headgroups (*e.g.* hydroxyl/carbonyl groups) are oriented towards the aqueous phase and their fatty acid tails are in contact with the oil phase. Subsequent cooling can trigger the local crystallization of interfacial GMS molecules yielding a solid crystalline shell(s) around water droplets. The crystallization temperature of glycerol monooleate (GMO) is much

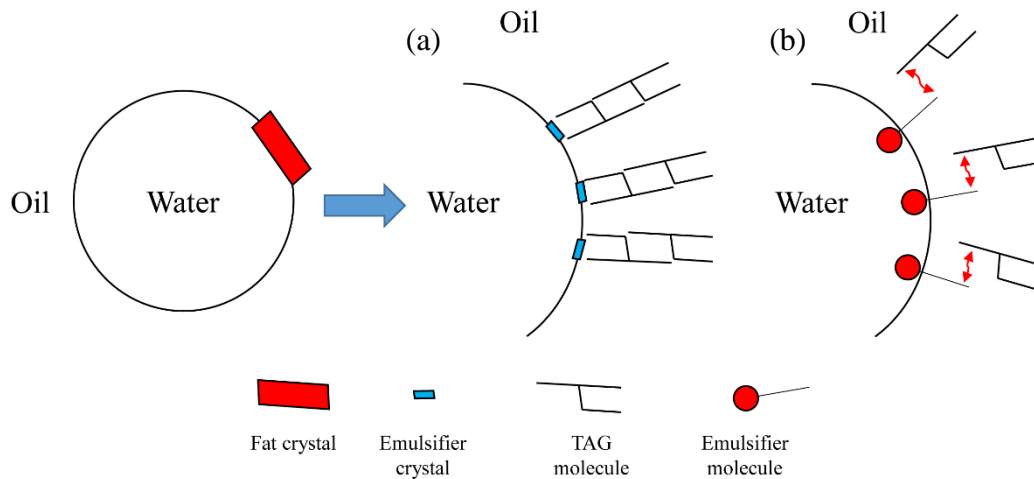
lower than that of GMS; GMO does not go through crystallization within the investigated quenching range. Thus, GMO-stabilized emulsions are not as stable as GMS-stabilized ones in the absence of Pickering-type stabilization. Apart from the crystallization temperature of surfactant, the emulsification efficiency is affected by the intermolecular interactions between surfactant and oil molecules as well. If surfactant molecules can form H-bonds strongly with continuous oil (e.g. vegetable oil), the interfacial adsorption/desorption equilibrium will be shifted towards desorption due to the fact that H-bonding between carbonyl groups in oil and hydroxyl groups in surfactant is stronger than that between hydroxyl groups in surfactant and water, Figure 1.20(a). This phenomenon was proven to be detrimental to emulsion stability, Figure 1.20(b).

**Figure 1.20.** (a) FTIR spectra of canola oil (CO), light mineral oil (LMO), glycerol monooleate (GMO) and 4 wt.% GMO in CO or LMO. Taken from ref. 144. (b) Proposed adsorption behaviour of GMO molecules at the water-LMO (left) or water-CO (right) interface. GMO molecules adsorb preferentially towards the water-LMO interface because their polar heads exhibit a strong affinity for water. For CO however, H-bonding between carbonyl groups in CO and hydroxyl groups in GMO is stronger than that formed between hydroxyl groups in GMO and water, thus retarding their interfacial adsorption.



Unlike surfactant crystals, high melting fat crystals exhibit little or no surface activity towards water-oil interfaces in w/o emulsions, so they stabilise the emulsions mainly *via* physically encasing dispersed droplets in a continuous fat matrix.<sup>145</sup> To improve the emulsifying efficiency of fat crystals, emulsifiers are commonly added. The primary function of an emulsifier is to lower the interfacial tension between water and oil facilitating emulsification. Secondly, the presence of small amounts of emulsifiers can modify the wettability of fat crystals. Thirdly, emulsifiers can affect the kinetics of TAG nucleation/crystal growth. Furthermore, emulsifiers possibly affect interfacial TAG crystallization in w/o emulsions.<sup>145</sup> Two different modes of interfacial TAG crystallization in oil continuous emulsions have been reported, relying on the crystallization temperatures of emulsifier ( $T_{ce}$ ) and fat ( $T_{cf}$ ). If  $T_{ce} > T_{cf}$ , emulsifier molecules pre-adsorbed at water-oil interfaces can crystallise *in situ* at water droplets when the temperature was lowered below  $T_{ce}$ . The crystalline emulsifier can then induce heterogeneous nucleation of neighbouring TAG molecules from continuous oil followed by crystal growth on its surface. If  $T_{ce} < T_{cf}$ , emulsifiers may remain liquid over the quenching and storage periods. If the alkyl chains of emulsifier and TAG are comparable, they may associate with each other (mainly *via* Van der Waals forces) in a molten state, which then serve as templates promoting TAG crystallization at oil-water interfaces when the temperature is cooled below  $T_{cf}$ . Nevertheless, if the fatty acid chains of emulsifier do not match those of TAG, TAG crystallisation occurs mainly in the continuous phase. The proposed mechanisms of interfacial TAG crystallisation in a w/o emulsion are illustrated in Figure 1.21.

**Figure 1.21.** Possible mechanisms of TAG crystallization at a water-oil interface in a w/o emulsion in the presence of an emulsifier. (a) The crystallization temperature of the emulsifier ( $T_{ce}$ ) is higher than that of TAG ( $T_{cf}$ ). TAG crystallization occurs by heterogeneous nucleation on the surface of the solidified emulsifier on cooling. (b)  $T_{ce} < T_{cf}$ . The fatty acid chains of the emulsifier and TAG interact with each other at high temperature, which may act as templates for TAG crystallization at the interface when the temperature is lowered below  $T_{cf}$ . Adapted from ref. 143. The sizes of molecule and crystal are not to scale.



## 1.4 Aims of current research

The aims of the research in this thesis are:

- (1) Investigate the adsorption behaviour of several edible surfactants/fats at a range of fluid-fluid interfaces, including air-oil, air-water and water-oil;
- (2) Explore the dispersion properties of surfactants/fats in various solvents;
- (3) Fabricate and characterise various colloidal materials with surfactants/fats, *e.g.* aqueous and oil foams, simple and multiple emulsions, foamed and aerated emulsions.

According to the literature summary, the investigations on stable edible oil foams and oil foam-based materials with surfactant/fat crystals are rising, during which many lipid materials have been applied as foaming and stabilising agents. Sucrose esters (SE) are nonionic surfactants consisting of sucrose as the hydrophilic group and fatty acid chains as the hydrophobic groups.<sup>157-159</sup> By now, few reports have been available regarding the physicochemical and functional properties of SE. In ref. 160, the polymorphism of a commercial grade sucrose stearate ester with HLB of 1 was determined. The sample revealed one small angle peak at 5.32 nm and one wide angle peak at 0.41 nm, indicating a double chain length structure and a hexagonal lateral packing. Its polymorph is similar to the  $\alpha$  form of sunflower oil stearins. In another study, Szűts *et al.*<sup>161</sup> discovered that hydrophilic SE with HLB of 16 showed four distinct peaks (*i.e.* 4.14 nm, 2.04 nm, 1.34 nm, 0.99 nm) in the small angle region, comparable to the scattering patterns of stearic acid. With decreasing HLB, the characteristic peaks of SE gradually diminished and the interplanar spacings increased due to the presence of polyesters.<sup>162</sup>

Moreover, several questions within or surrounding the area of oil foam remain to be answered. Previous research on the foaming potential of neat vegetable oils without additives is based on oils mainly composed of saturated fatty acids in their TAG chains. The long-term consumption of saturated fats may promote obesity and cause negative cardiovascular effects.<sup>2</sup> Can we obtain healthier edible foams from unsaturated oils? Can the stabilising mechanism proposed in ref. 119 be applied to other oleofoam systems? Is the interfacial TAG crystallization induced by oil-soluble emulsifiers in w/o emulsions applicable to oil foams? What emulsifiers are potential candidates: glycerol esters, sorbitan esters or sucrose esters? Efficient air incorporation into an oil matrix is not always possible for all oleogel systems. In addition, excess heat is generated during vigorous whipping which may trigger the partial melting of oleogels and cause a polymorphic change in the crystal structure. Is it possible to achieve high foamability and long-term stability in the same system at low energy cost? Can certain

hydrocarbon surfactant molecules adsorb readily at air-oil surfaces, *i.e.* exhibit surface activity? If yes, what is the adsorption mode and the interactions therein? How to enhance the stability of oil foams with this surfactant? Is it achievable to prepare novel colloidal materials based on oil foams? Furthermore, is it feasible to fabricate a multitude of colloidal materials using a single edible surfactant? Apart from those, more perspectives can be found in Chapter 8 later. The current research will be carried out based on the above questions.

## 1.5 Presentation of thesis

After a brief overview of oleogels, foams and emulsions, Chapter 2 gives all the materials and experimental methods used throughout this research.

Chapter 3 explores the foaming potential of neat vegetable oils containing long-chain, unsaturated fatty acids, *i.e.* refined peanut oil and extra virgin olive oil, in the absence of any added foaming agent. Firstly, the crystallisation and melting behaviour of neat oils are investigated. Subsequently, the foaming efficiency and stability are evaluated and further correlated to the physicochemical properties of samples prior to whipping. High-melting fat crystals contributing to foaming are extracted and analysed by GC/MS. Finally, the thermo-responsiveness of an initially ultra-stable foam is demonstrated.

Chapter 4 introduces a novel protocol to prepare ultra-stable edible oil foams of high air volume fraction from mixtures of vegetable oil and sucrose ester surfactant. The dispersion characteristics of the lipophilic sucrose stearate surfactant in extra virgin olive oil are described as a function of temperature. Secondly, the effect of whipping temperature and surfactant concentration on the foaming behaviour is studied. Attempts are then made to obtain ultra-stable foams, during which various parameters are optimized including the surfactant concentration, cooling rate and storage temperature. The mechanism of foam formation and stabilization is unveiled. Based on the above, we introduce a home-designed foaming device to produce oil foams from neat oil or mixtures of sucrose ester and oil.

Taking advantage of the mechanism postulated in Chapter 4, Chapter 5 illustrates the possibility of producing stable edible oil foams of high air volume fraction from mixtures of sorbitan esters in rapeseed oil. Comparisons are then made between sucrose esters and sorbitan esters in terms of foamability, foam stability and microstructure. The reasons for the differences are explained.

The effect of HLB and pH on the dispersion and foaming behaviour of a series of sucrose ester surfactants in water is included in Chapter 6. First, the physicochemical properties of sucrose esters in water are investigated as a function of HLB. Subsequently, the foaming behaviour of these dispersions is discussed regarding foamability, foam stability and foam microstructure. Furthermore, the role of pH on the dispersion and foaming properties of two relatively hydrophobic sucrose esters is revealed.

Chapter 7 focuses on fabricating a multitude of colloidal materials using one and the same lipophilic sucrose stearate surfactant.

Finally, Chapter 8 includes a summary of the thesis. Some perspectives for future work are also presented.

## 1.6 References

1. F.D. Gonstone, *The Chemistry of Oils and Fats Sources: Composition, Properties and Uses*, CRC Press, Boca Raton, 2004, ch. 9.
2. A.R. Patel, *Edible Oil Structuring: Concepts, Methods and Applications*, RSC, Cambridge, 2018.
3. A.G. Marangoni and N. Garti, *Edible Oleogels: Structure and Health Implications*, AOCS Press, Urbana, 2011.
4. B. Ruiz-Núñez, D.A.J. Dijck-Brouwer and F.A.J. Muskiet, The relation of saturated fatty acids with low-grade inflammation and cardiovascular disease, *J. Nutr. Biochem.*, 2016, **36**, 1–20.
5. FAO, Food and agriculture organization of the United Nations, fats, and fatty acids in human nutrition - report of an expert consultation, 2008, **91**.
6. L.S.K. Dassanayake, D.R. Kodali and S. Ueno, Formation of oleogels based on edible lipid materials, *Curr. Opin. Colloid Interface Sci.*, 2011, **16**, 432–439.
7. E.D. Co and A.G. Marangoni, Organogels: an alternative edible oil-structuring method, *J. Am. Oil Chem. Soc.*, 2012, **89**, 749–780.
8. K.F. Chaves, D. Barrera-Arellano and A.P.B. Ribeiro, Potential application of lipid organogels for food industry, *Food Res. Int.*, 2018, **105**, 863–872.
9. S. Pakseresht and M.M. Tehrani, Advances in multi-component supramolecular oleogels-a review, *Food Rev. Int.*, 2020, DOI: 10.1080/87559129.2020.1742153.
10. P.K. Okuro, A.J. Martins, A.A. Vicente and R.L. Cunha, Perspective on oleogelator mixtures, structure design and behaviour towards digestibility of oleogels, *Curr. Opin. Food Sci.*, 2020, **35**, 1–9.
11. A. Shakeel, U. Farooq, D. Gabriele, A.G. Marangoni and F.R. Lupi, Bigels and multi-component organogels: an overview from rheological perspective, *Food Hydrocoll.*, 2021, **111**, 106190.
12. S. Murdan, G. Gregoriadis and A.T. Florence, Novel sorbitan monostearate organogels, *J. Pharm. Sci.*, 1999, **88**, 608–614.
13. C.H. Chen, I. Van Damme, and E.M. Terentjev, Phase behaviour of C18 monoglyceride in hydrophobic solutions, *Soft Matter*, 2009, **5**, 432–439.
14. C.H. Chen and E.M. Terentjev, Aging and metastability of monoglycerides in hydrophobic solutions, *Langmuir*, 2009, **25**, 6717–6724.

15. N.K.O. Ojijo, E. Kesselman, V. Shuster, S. Eichler, S. Eger, I. Neeman and E. Shimoni, Changes in microstructural, thermal, and rheological properties of olive oil/monoglyceride networks during storage, *Food Res. Int.*, 2004, **37**, 385–393.
16. M.A. Rogers, A.J. Wright, and A.G. Marangoni, Oil organogels: the fat of the future?, *Soft Matter*, 2009, **5**, 1594–1596.
17. F.G. Gandolfo, A. Bot, and E. Flöter, Structuring of edible oils by long-chain FA, fatty alcohols, and their mixtures, *J. Am. Oil Chem. Soc.*, 2004, **81**, 1–6.
18. H.M. Schaink, K.F. van Malssen, S. Morgado-Alves, D. Kalnin, and E. van der Linden, Crystal network for edible oil organogels: possibilities and limitations of the fatty acid and fatty alcohol systems, *Food Res. Int.*, 2007, **40**, 1185–1193.
19. M. Callau, K. Sow-Kébé, L. Nicolas-Morgantini, and A.L. Fameau, Effect of the ratio between behenyl alcohol and behenic acid on the oleogel properties, *J. Colloid Interface Sci.*, 2020, **560**, 874–884.
20. J. Daniel and R. Rajasekaran, Organogelation of plant oils and hydrocarbons by long chain saturated FA, fatty alcohols, wax esters, and dicarboxylic acids, *J. Am. Oil Chem. Soc.*, 2003, **80**, 417–421.
21. M.A. Rogers, A.J. Wright and A.G. Marangoni, Crystalline stability of self-assembled fibrillar networks of 12-hydroxystearic acid in edible oils, *Food Res. Int.*, 2008, **41**, 1026–1034.
22. A.J. Wright and A.G. Marangoni, Formation, structure, and rheological properties of ricinelaidic acid-vegetable oil organogels, *J. Am. Oil Chem. Soc.*, 2006, **83**, 497–503.
23. K. Higaki, Y. Sasakura, T. Koyano, I. Hachiya, and K. Sato, Physical analyses of gel-like behaviour of binary mixtures of high- and low-melting fats, *J. Am. Oil Chem. Soc.*, 2003, **80**, 263–270.
24. K. Higaki, T. Koyano, I. Hachiya, and K. Sato, In situ optical observation of microstructure of  $\beta$ -fat gel made of binary mixtures of high-melting and low-melting fats, *Food Res. Int.*, 2004, **37**, 2–10.
25. L.S.K. Dassanayake, D.R. Kodali, S. Ueno and K. Sato, Physical properties of rice bran wax in bulk and organogels, *J. Am. Oil Chem. Soc.*, 2009, **86**, 1163–1173.
26. J.F. Toro-Vazquez, J.A. Morales-Rueda, E. Dibildox-Alvarado, M. Charó-Alonso, M. Alonzo-Macias, and M.M. González-Chávez, Thermal and textural properties of organogels developed by candelilla wax in safflower oil, *J. Am. Oil Chem. Soc.*, 2007, **84**, 989–1000.

27. J.A. Morales-Rueda, E. Dibildox-Alvarado, M.A. Charó-Alonso, R.G. Weiss, and J.F. Toro-Vazquez, Thermo-mechanical properties of candelilla wax and dotriacontane organogels in safflower oil, *Eur. J. Lipid Sci. Technol.*, 2009, **111**, 207–215.
28. C.V. Nikiforidis and E. Scholten, Self-assemblies of lecithin and  $\alpha$ -tocopherol as gelators of lipid material, *RSC Adv.*, 2014, **4**, 2466–2473.
29. N. Gaudino, S.M. Ghazani, S. Clark, A.G. Marangoni, and N.C. Acevedo, Development of lecithin and stearic acid based oleogels and oleogel emulsions for edible semisolid applications, *Food Res. Int.*, 2009, **116**, 79–89.
30. M. Perneti, K. van Malssen, D. Kalnin, and E. Flöter, Structuring edible oil with lecithin and sorbitan tri-stearate, *Food Hydrocoll.*, 2007, **21**, 855–861.
31. L.-J. Han, L. Li, L. Zhao, B. Li, G.-Q. Liu, X.-Q. Liu, and X.-D. Wang, Rheological properties of organogels developed by sitosterol and lecithin, *Food Res. Int.*, 2013, **53**, 42–48.
32. M.D. Bin Sintang, S. Danthine, A.R. Patel, T. Rimaux, D. Van De Walle, and K. Dewettinck, Mixed surfactant systems of sucrose esters and lecithin as a synergistic approach for oil structuring, *J. Colloid Interface Sci.*, 2017, **504**, 387–396.
33. P.K. Okuro, I. Tavernier, M.D. Bin Sintang, A.G. Skirtach, A.A. Vicente, K. Dewettinck and R.L. Cunha, Synergistic interactions between lecithin and fruit wax in oleogel formation, *Food Funct.*, 2018, **9**, 1755–1767.
34. M. Aguilar-zárate, B.A. Macias-Rodriguez, J.F. Toro-Vazquez, and A.G. Marangoni, Engineering rheological properties of edible oleogels with ethylcellulose and lecithin. *Carbohydr. Polym.*, 2019, **205**, 98–105.
35. C.V. Nikiforidis, E.P. Gilbert and E. Scholten, Organogel formation via supramolecular assembly of oleic acid and sodium oleate, *RSC Adv.*, 2015, **5**, 47466–47475.
36. A.J. Gravelle, M. Davidovich-Pinhas, S. Barbut and A.G. Marangoni, Influencing the crystallization behaviour of binary mixtures of stearyl alcohol and stearic acid (SOSA) using ethylcellulose, *Food Res. Int.*, 2017, **91**, 1–10.
37. A. Bot, R. den Adel, E.C. Roijers, and C. Regkos, Effect of sterol type on structure of tubules in sterol +  $\gamma$ -oryzanol-based organogels, *Food Biophys.*, 2009, **4**, 266–272.
38. F.R. Lupi, A. Shakeel, V. Greco, N. Baldino, V. Calabrò and D. Gabriele, Organogelation of extra virgin olive oil with fatty alcohols, glyceryl stearate and their mixture, *LWT - Food Sci. Technol.*, 2017, **77**, 422–429.

39. M.D. Bin Sintang, T. Rimaux, D.V. de Walle, K. Dewettinck and A.R. Patel, Oil structuring properties of monoglycerides and phytosterols mixtures, *Eur. J. Lipid Sci. Technol.*, 2017, **119**, 1500517.
40. T. Truong, S. Prakash and B. Bhandari, Effects of crystallisation of native phytosterols and monoacylglycerols on foaming properties of whipped oleogels, *Food Chem.*, 2019, **285**, 86–93.
41. I. Tavernier, K. Moens, B. Heyman, S. Danthine and K. Dewettinck, Relating crystallization behaviour of monoacylglycerols-diacylglycerol mixtures to the strength of their crystalline network in oil, *Food Res. Int.*, 2019, **120**, 504–513.
42. K.R.R. de Godoi, R.C. Basso, C.C. Ming, V.M. da Silva, R.L. da Cunha, D. Barrera-Arellano, and A.P.B. Ribeiro, Physicochemical and rheological properties of soybean organogels: interactions between different structuring agents, *Food Res. Int.*, 2019, **124**, 108475.
43. S. Jana and S. Martini, Physical characterization of crystalline networks formed by binary blends of waxes in soybean oil, *Food Res. Int.*, 2016, **89**, 245–253.
44. G. Fayaz, S.A.H. Goli, M. Kadivar, F. Valoppi, L. Barba, C. Balducci, L. Conte, S. Calligaris and M.C. Nicoli, Pomegranate seed oil organogels structured by propolis wax, beeswax, and their mixture, *Eur. J. Lipid Sci. Technol.*, 2017, **119**, 1700032.
45. T.L.T. da Silva, D.B. Arellano, and S. Martini, Interactions between candelilla wax and saturated triacylglycerols in oleogels, *Food Res. Int.*, 2019, **121**, 900–909.
46. J.K. Winkler-Moser, J. Anderson, F.C. Felker and H.-S. Hwang, Physical properties of beeswax, sunflower wax, and candelilla wax mixtures and oleogels, *J. Am. Oil Chem. Soc.*, 2019, **96**, 1125–1142.
47. D.L. Weaire and S. Hutzler, *The Physics of Foams*, Oxford University Press, Oxford, 1999.
48. P.R. Garrett, *Defoaming: theory and industrial applications*, Marcel Dekker Inc., New York, 1993.
49. J.F. Sadoc and N. Rivier, *Foams and Emulsions*, Springer, Netherlands, 1999.
50. L.L. Schramm, *Emulsions, Foams, and Suspensions: Fundamentals and Applications*, Wiley-VCH, Weinheim, 2005.
51. A. Saint-Jalmes, Y. Zhang and D. Langevin, Quantitative description of foam drainage: transitions with surface mobility, *Eur. Phys. J. E.*, 2004, **15**, 53–60.

52. A. Saint-Jalmes, Physical chemistry in foam drainage and coarsening, *Soft Matter*, 2006, **2**, 836–849.
53. S. Hilgenfeldt, S.A. Koehler and H.A. Stone, Dynamics of coarsening foams: accelerated and self-limiting drainage, *Phys. Rev. Lett.*, 2001, **86**, 4704.
54. E. Rio, W. Drenckhan, A. Salonen and D. Langevin, Unusually stable liquid foams, *Adv. Colloid Interface Sci.*, 2014, **205**, 74–86.
55. T.F. Tadros, *Applied Surfactants: principles and applications*, Wiley-VCH, Weinheim, 2006.
56. J.N. Israelachvili, D.J. Mitchell and B.W. Ninham, Theory of self-assembly of hydrocarbon amphiphiles into micelles and bilayers, *J. Chem. Soc., Faraday Trans. 2*, 1976, **72**, 1525–1568.
57. W.E Ewers and K.L Sutherland, The role of surface transport in the stability and breakdown of foams, *Aust. J. Chem.*, 1952, **5**, 697–710.
58. D.J. Shaw, *Introduction to colloid and surface chemistry*, Butterworths, London, 1968.
59. M.J. Rosen and J.T. Kunjappu, *Surfactants and Interfacial Phenomena*, John Wiley & Sons Ltd., Hoboken, 2012, pp. 336-391.
60. A.L. Fameau and A. Salonen, Effect of particles and aggregated structures on the foam stability and aging, *C.R. Phys.*, 2014, **15**, 748–760.
61. A.L. Fameau, A. Saint-Jalmes, F. Cousin, B.H. Houssou, B. Novales, L. Navailles, F. Nallet, C. Gaillard, F. Boué, and J.P. Douliez, Smart foams: switching reversibly between ultrastable and unstable foams, *Angew. Chem. Int. Ed.*, 2011, **50**, 8264–8269.
62. B.P. Binks, Particles as surfactants-similarities and differences, *Curr. Opin. Colloid Interface Sci.*, 2002, **7**, 21–41.
63. B.P. Binks and T.S. Horozov, *Colloidal particles at liquid interfaces*, Cambridge University Press, Cambridge, 2006, pp. 1–73.
64. T.S. Horozov, Foams and foam films stabilised by solid particles, *Curr. Opin. Colloid Interface Sci.*, 2008, **13**, 134–140.
65. T.N. Hunter, R.J. Pugh, G.V. Franks and G.J. Jameson, The role of particles in stabilising foams and emulsions, *Adv. Colloid Interface Sci.*, 2008, **137**, 57–81.
66. K. Yu, B. Li, H. Zhang, Z. Wang, W. Zhang, D. Wang, H. Xu, D. Harbottle, J. Wang, and J. Pan, Critical role of nanocomposites at air-water interface: From aqueous foams to foam-based lightweight functional materials, *Chem. Eng. J.*, 2021, **416**, 129121.

67. B.P. Binks and R. Murakami, Phase inversion of particle-stabilized materials from foams to dry water, *Nat. Mater.*, 2006, **5**, 865–869.
68. B.P. Binks and T.S. Horozov, Aqueous foams stabilized solely by silica nanoparticles, *Angew. Chem. Int. Ed.*, 2005, **44**, 3722–3725.
69. A. Stocco, E. Rio, B.P. Binks and D. Langevin, Aqueous foams stabilized solely by particles, *Soft Matter*, 2011, **7**, 1260–1267.
70. S. Fujii, P.D. Iddon, A.J. Ryan, and S.P. Armes, Aqueous particulate foams stabilized solely with polymer latex particles, *Langmuir*, 2006, **22**, 7512–7520.
71. L.K. Shrestha, D.P. Acharya, S.C. Sharma, K. Aramaki, H. Asaoka, K. Ihara, T. Tsunehiro and H. Kunieda, Aqueous foam stabilized by dispersed surfactant solid and lamellar liquid crystalline phase, *J. Colloid Interface Sci.*, 2006, **301**, 274–281.
72. L. Zhang, A. Mikhailovskaya, P. Yazhgur, F. Muller, F. Cousin, D. Langevin, N. Wang and A. Salonen, Precipitating sodium dodecyl sulfate to create ultrastable and stimuable foams, *Angew. Chem. Int. Ed.*, 2015, **54**, 9533–9536.
73. L. Zhang, L. Tian, H. Du, S. Rouzière, N. Wang and A. Salonen, Foams stabilized by surfactant precipitates: criteria for ultrastability, *Langmuir*, 2017, **33**, 7305–7311.
74. L. Zhang, H. Wang, B. Zheng, H. Du and A. Salonen, Surfactant crystals as stimuable foam stabilizers: tuning stability with counterions, *J. Surf. Det.*, 2019, **22**, 1237–1245.
75. B.P. Binks and H. Shi, Aqueous foams in the presence of surfactant crystals, *Langmuir*, 2020, **36**, 991–1002.
76. N. Jiang, X. Yu, Y. Sheng, R. Zong, C. Li and S. Lu, Role of salts in performance of foam stabilized with sodium dodecyl sulfate, *Chem. Eng. Sci.*, 2020, **216**, 115474.
77. A.L. Fameau and B.P. Binks, Aqueous and oil Foams stabilized by surfactant crystals: new concepts and perspectives, *Langmuir*, 2021, **37**, 4411–4418.
78. S.E. Friberg and C. Solans, Surfactant association structures and the stability of emulsions and foams, *Langmuir*, 1986, **2**, 121–126.
79. N.M. Kovalchuk, A. Trybala, V. Starov, O. Matar and N. Ivanova, Fluoro- vs hydrocarbon surfactants: why do they differ in wetting performance? *Adv. Colloid Interface Sci.*, 2014, **210**, 65–71.
80. V. Bergeron, J.E. Hanssen and F.N. Shoghl, Thin-film forces in hydrocarbon foam films and their application to gas-blocking foams in enhanced oil recovery, *Colloids Surf. A*, 1997, **123–124**, 609–622.

81. G. Furler and S. Ross, Experimental observations of the rate of ascent of bubbles in lubricating oils, *Langmuir*, 1986, **2**, 68–72.
82. Y. Suzin and S. Ross, Retardation of the ascent of gas bubbles by surface-active solutes in nonaqueous solutions, *J. Colloid Interface Sci.*, 1985, **103**, 578–585.
83. V.C. Suja, A. Kar, W. Cates, S.M. Remmert, P.D. Savage and G.G. Fuller, Evaporation-induced foam stabilization in lubricating oils, *Proc. Natl. Acad. Sci. U.S.A.*, 2018, **115**, 7919–7924.
84. H.W. Fox and W.A. Zisman, The spreading of liquids on low energy surfaces. I. polytetrafluoroethylene, *J. Colloid Interface Sci.*, 1950, **5**, 514–531.
85. H.W. Fox and W.A. Zisman, The spreading of liquids on low-energy surfaces. II. Modified tetrafluoroethylene polymers, *J. Colloid Interface Sci.*, 1952, **7**, 109–121.
86. R. Murakami and A. Bismarck, Particle-stabilized materials: dry oils and (polymerized) non-aqueous foams, *Adv. Funct. Mater.*, 2010, **20**, 732–737.
87. R. Murakami, S. Kobayashi, M. Okazaki, A. Bismarck and M. Yamamoto, Effects of contact angle and flocculation of particles of oligomer of tetrafluoroethylene on oil foaming, *Front. Chem.*, 2018, **6**, 435.
88. B.P. Binks and A. Rocher, Stabilisation of liquid-air surfaces by particles of low surface energy, *Phys. Chem. Chem. Phys.*, 2010, **12**, 9169–9171.
89. B.P. Binks, A. Rocher and M. Kirkland, Oil foams stabilized solely by particles, *Soft Matter*, 2011, **7**, 1800–1808.
90. B.P. Binks and A.T. Tyowua, Influence of the degree of fluorination on the behaviour of silica particles at air-oil surfaces, *Soft Matter*, 2013, **9**, 834–845.
91. B.P. Binks, T. Sekine and A.T. Tyowua, Dry oil powders and oil foams stabilised by fluorinated clay platelet particles, *Soft Matter*, 2014, **10**, 578–589.
92. B.P. Binks, S.K. Johnston, T. Sekine and A.T. Tyowua, Particles at oil-air surfaces: powdered oil, liquid oil marbles, and oil foam, *ACS Appl. Mater. Interfaces*, 2015, **7**, 14328–14337.
93. G. Li, K. Wang, and C. Lu, Wet-etched asymmetric spherical nanoparticles with controllable pit structures and application in non-aqueous foams, *Soft Matter*, 2021, **17**, 4848–4856.
94. K. Achakulwisut, C. Tam, A. Huerre, R. Sammouti, B.P. Binks and V. Garbin, Stability of clay particle-coated microbubbles in alkanes against dissolution induced by heating, *Langmuir*, 2017, **33**, 3809–3817.

95. V. Poulichet and V. Garbin, Cooling particle-coated bubbles: destabilization beyond dissolution arrest, *Langmuir*, 2015, **31**, 12035–12042.
96. S. Ross and G. Nishioka, The relation of foam behaviour to phase separations in polymer solutions, *Colloid Polym. Sci.*, 1977, **255**, 560–565.
97. S.E. Friberg, C.S. Wohn, B. Greene and R. van Gilder, A non-aqueous foam with excellent stability, *J. Colloid Interface Sci.*, 1984, **101**, 593–595.
98. B.P. Binks, C.A. Davies, P.D.I. Fletcher and E.L. Sharp, Non-aqueous foams in lubricating oil systems, *Colloids Surf. A*, 2010, **360**, 198–204.
99. L.K. Shrestha, K. Aramaki, H. Kato, Y. Takase and H. Kunieda, Foaming properties of monoglycerol fatty acid esters in nonpolar oil systems, *Langmuir*, 2006, **22**, 8337–8345.
100. H. Kunieda, L.K. Shrestha, D.P. Acharya, H. Kato, Y. Takase and J.M. Gutierrez, Super-stable nonaqueous foams in diglycerol fatty acid esters-nonpolar oil systems, *J. Disp. Sci. Technol.*, 2007, **28**, 133–142.
101. L.K. Shrestha, R.G. Shrestha, S.C. Sharma, and K. Aramaki, Stabilization of nonaqueous foam with lamellar liquid crystal particles in diglycerol monolaurate/olive oil system, *J. Colloid Interface Sci.*, 2008, **328**, 172–179.
102. R.G. Shrestha, L.K. Shrestha, C. Solans, G. Gonzalez and K. Aramaki, Nonaqueous foam with outstanding stability in diglycerol monomyristate/olive oil system, *Colloids Surf. A*, 2010, **353**, 157–165.
103. G.M. Campbell and E. Mougeot, Creation and characterisation of aerated food products, *Trends Food Sci. Technol.*, 1999, **10**, 283–296.
104. R. Heymans, I. Tavernier, K. Dewettinck and P. van der Meeren, Crystal stabilization of edible oil foams, *Trends Food Sci. Technol.*, 2017, **69**, 13–24.
105. A.L. Fameau and A. Saint-Jalmes, Non-aqueous foams: current understanding on the formation and stability mechanisms, *Adv. Colloid Interface Sci.*, 2017, **247**, 454–464.
106. B.P. Binks, Colloidal particles at a range of fluid-fluid interfaces, *Langmuir*, 2017, **33**, 6947–6963.
107. S.E. Friberg, Foams from non-aqueous systems, *Curr. Opin. Colloid Interface Sci.*, 2010, **15**, 359–364.
108. A.L. Fameau and A. Saint-Jalmes, Recent advances in understanding and use of oleofoams, *Front. Sustain. Food Syst.*, 2020, **4**, 110.
109. B.P. Binks and B. Vishal, Particle-stabilized oil foams, *Adv. Colloid Interface Sci.*, 2021, **291**, 102404.

110. M. Brun, M. Delample, E. Harte, S. Lecomte and F. Leal-Calderon, Stabilization of air bubbles in oil by surfactant crystals: a route to produce air-in-oil foams and air-in-oil-in-water emulsions, *Food Res. Int.*, 2015, **67**, 366–375.
111. D.Z. Gunes, M. Murith, J. Godefroid, C. Pelloux, H. Deyber, O. Schafer and O. Breton, Oleofoams: properties of crystal-coated bubbles from whipped oleogels-evidence for Pickering stabilization, *Langmuir*, 2017, **33**, 1563–1575.
112. R. Heymans, I. Tavernier, S. Danthine, T. Rimaux, P. Van der Meeren and K. Dewettinck, Food-grade monoglyceride oil foams: the effect of tempering on foamability, foam stability and rheological properties, *Food Funct.*, 2018, **9**, 3143–3154.
113. M. Lei, N. Zhang, W.J. Lee, C.P. Tan, O.M. Lai, Y. Wang, and C. Qiu, Non-aqueous foams formed by whipping diacylglycerol stabilized oleogel, *Food Chem.*, 2020, **312**, 126047.
114. K. Mishra, J. Bergfreund, P. Bertsch, P. Fischer and E. J. Windhab, Crystallization-induced network formation of tri- and monopalmitin at the middle-chain triglyceride oil/air interface, *Langmuir*, 2020, **36**, 7566–7572.
115. F. Saremnejad, M. Mohebbi and A. Koocheki, Practical application of nonaqueous foam in the preparation of a novel aerated reduced-fat sauce, *Food Bioprod. Process*, 2020, **119**, 216–225.
116. L. Du, Q. Jiang, S. Li, Q. Zhou, Y. Tan and Z. Meng, Microstructure evolution and partial coalescence in the whipping process of oleofoams stabilized by monoglycerides, *Food Hydrocoll.*, 2021, **112**, 106245.
117. B.P. Binks, E.J. Garvey and J. Vieira, Whipped oil stabilised by surfactant crystals, *Chem. Sci.*, 2016, **7**, 2621–2632.
118. A.L. Fameau, S. Lam, A. Arnould, C. Gaillard, O.D. Velez and A. Saint-Jalmes, Smart nonaqueous foams from lipid-based oleogel, *Langmuir*, 2015, **31**, 13501–13510.
119. S. Mishima, A. Suzuki, K. Sato and S. Ueno, Formation and microstructures of whipped oils composed of vegetable oils and high-melting fat crystals, *J. Am. Oil Chem. Soc.*, 2016, **93**, 1453–1466.
120. B.P. Binks and I. Marinopoulos, Ultra-stable self-foaming oils, *Food Res. Int.*, 2017, **95**, 28–37.
121. Y. Liu and B.P. Binks, Foams of vegetable oils containing long-chain triglycerides, *J. Colloid Interface Sci.*, 2021, **583**, 522–534.

122. L. Goibier, C. Pillement, J. Monteil, C. Faure and F. Leal-Calderon, Emulsification of non-aqueous foams stabilized by fat crystals: towards novel air-in-oil-in-water food colloids, *Food Chem.*, 2019, **293**, 49–56.
123. K. Mishra, D. Dufour and E.J. Windhab, Yield stress dependent foaming of edible crystal-melt suspensions, *Cryst. Growth Des.*, 2020, **20**, 1292–1301.
124. L. Metilli, A. Lazidis, M. Francis, S. Marty-Terrade, J. Ray, and E. Simone, The effect of crystallization conditions on the structural properties of oleofoams made of cocoa butter crystals and high oleic sunflower oil, *Cryst. Growth Des.*, 2021, **21**, 1562–1575.
125. S. Saha, B. Saint-Michel, V. Leynes, B.P. Binks and V. Garbin, Stability of bubbles in wax-based oleofoams: decoupling the effects of bulk oleogel rheology and interfacial rheology, *Rheol. Acta*, 2020, **59**, 255–266.
126. Y. Liu and B.P. Binks, A novel strategy to fabricate stable oil foams with sucrose ester surfactant, *J. Colloid Interface Sci.*, 2021, **594**, 204–216.
127. Y. Liu and B.P. Binks, sucrose ester surfactant: foams, emulsions, foamulsions and aerated emulsions, *Langmuir*, to be submitted.
128. M. Callau, K. Sow-Kébé, N. Jenkins and A.L. Fameau, Effect of the ratio between fatty alcohol and fatty acid on foaming properties of whipped oleogels, *Food Chem.*, 2020, **333**, 127403.
129. C. Qiu, M. Lei, W.J. Lee, N. Zhang and Y. Wang, Fabrication and characterization of stable oleofoam based on medium-long chain diacylglycerol and  $\beta$ -sitosterol, *Food Chem.*, 2021, **350**, 129275.
130. A.G. Marangoni, N. Acevedo, F. Maleky, E. Co, F. Peyronel, G. Mazzanti, B. Quinn and D. Pink, Structure and functionality of edible fats, *Soft Matter*, 2012, **8**, 1275–1300.
131. A.G. Marangoni, *Fat Crystal Networks*, CRC Press, Boca Raton, 2005.
132. K. Larsson, Molecular arrangement in glycerides, *Eur. J. Lipid Sci. Tech.*, 1972, **3**, 136–142.
133. C. Himawan, V.M. Starov and A.G.F. Stapley, Thermodynamic and kinetic aspects of fat crystallization, *Adv. Colloid Interface Sci.*, 2006, **122**, 3–33.
134. K. Sato, S. Ueno and J. Yano, Molecular interactions and kinetic properties of fats, *Prog. Lipid Res.*, 1999, **38**, 91–116.
135. K. Larsson, Classification of glyceride crystal forms, *Acta Chem. Scand.*, 1966, **20**, 2255–2260.

136. B.P. Binks, *Modern Aspects of Emulsion Science*, Royal Society of Chemistry, Cambridge, 1998, ch. 1.
137. A. Aserin, *Multiple emulsion: technology and applications*, John Wiley & Sons Ltd, Hoboken, 2008, ch.1.
138. W.D. Bancroft, The theory of emulsification, *J. Phys.Chem.*, 1913, **17**, 501–519.
139. J. Zhou, X. Qiao, B.P. Binks, K. Sun, M. Bai, Y. Li and Y. Liu, Magnetic Pickering emulsions stabilized by Fe<sub>3</sub>O<sub>4</sub> nanoparticles, *Langmuir*, 2011, **27**, 3308–3316.
140. J. Kim, L.J. Cote, F. Kim, W. Yuan, K.R. Shull and J. Huang, Graphene oxide sheets at interfaces, *J. Am. Chem. Soc.*, 2010, **132**, 8180–8186.
141. S. Abend, N. Bonnke, U. Gutschner and G. Lagaly, Stabilization of emulsions by heterocoagulation of clay minerals and layered double hydroxides, *Colloid Polym. Sci.*, 1998, **276**, 730–737.
142. Q. Zhu, Y. Pan, X. Jia, J. Li, M. Zhang, and L. Yin, Review on the stability mechanism and application of water-in-oil emulsions encapsulating various additives, *Compr. Rev. Food Sci. Food Safety*, 2019, **18**, 1660–1675.
143. D. Rousseau, Aqueous droplets as active fillers in oil-continuous emulsions, *Curr. Opin. Food Sci.*, 2020, **33**, 173–186.
144. S. Ghosh, T. Tran and D. Rousseau, Comparison of Pickering and network stabilization in water-in-oil emulsions, *Langmuir*, 2011, **27**, 6589–6597.
145. S. Ghosh and D. Rousseau, Fat crystals and water-in-oil emulsion stability, *Curr. Opin. Colloid Interface Sci.*, 2011, **16**, 421–431.
146. S. Ghosh and D. Rousseau, Triacylglycerol interfacial crystallization and shear structuring in water-in-oil emulsions, *Cryst. Growth Des.*, 2012, **12**, 4944–4954.
147. R. Rafanan and D. Rousseau, Dispersed droplets as active fillers in fat-crystal network-stabilized water-in-oil emulsions, *Food Res. Int.*, 2017, **99**, 355–362.
148. T. Tran, N. L. Green, S. Ghosh and D. Rousseau, Encapsulation of water-in-oil emulsion droplets within crystal spheroids, *Colloids Surf. A*, 2017, **524**, 1–7.
149. X. Zhao, B. Huang, M. El-Aooiti and D. Rousseau, Demulsification to control solute release from Pickering crystal-stabilized water-in-oil emulsions, *J. Colloid Interface Sci.*, 2018, **509**, 360–368.
150. R. Rafanan and D. Rousseau, Dispersed droplets as tunable fillers in water-in-oil emulsions stabilized with fat crystals, *J. Food Eng.*, 2019, **244**, 192–201.

151. K. Wijarnprecha, A. de Vries, P. Santiwattana, S. Sonwai, and D. Rousseau, Rheology and structure of oleogelled water-in-oil emulsions containing dispersed aqueous droplets as inactive fillers, *LWT - Food Sci. Technol.*, 2019, **115**, 108067.
152. K. Wijarnprecha, A. de Vries, P. Santiwattana, S. Sonwai, and D. Rousseau, Microstructure and rheology of oleogel-stabilized water-in-oil emulsions containing crystal-stabilized droplets as active fillers, *LWT - Food Sci. Technol.*, 2019, **115**, 108058.
153. N.L. Green, S.R. Euston, and D. Rousseau, Interfacial ordering of tristearin induced by glycerol monooleate and PGPR: a coarse-grained molecular dynamics study, *Colloids Surf. B*, 2019, **179**, 107–113.
154. M. El-Aooiti, A. de Vries and D. Rousseau, Displacement of interfacially-bound monoglyceride crystals in water-in-oil emulsions by a non-ionic surfactant, *J. Colloid Interface Sci.*, 2020, **580**, 630–637.
155. S.M. Hodge and D. Rousseau, Continuous-phase fat crystals strongly influence water-in oil emulsion stability, *J. Am. Oil Chem. Soc.*, 2005, **82**, 159–164.
156. B.P. Binks and A. Rocher, Effects of temperature on water-in-oil emulsions stabilised solely by wax microparticles, *J. Colloid Interface Sci.*, 2009, **335**, 94–104.
157. A. Szűts and P. Szabó-Révész, Sucrose esters as natural surfactants in drug delivery systems-a mini-review, *Int. J. Pharm.*, 2012, **433**, 1–9.
158. T. Plat and R.J. Linhardt, Syntheses and applications of sucrose-based esters, *J. Surf. Det.*, 2001, **4**, 415–421.
159. K. Hill and O. Rhode, Sugar-based surfactants for consumer products and technical applications, *Fett/Lipid*, 1999, **101**, 25–33.
160. J.A. Rincón-Cardona, L.M. Agudelo-Laverde, S. Martini, R.J. Candal and M.L. Herrera, In situ synchrotron radiation X-ray scattering study on the effect of a stearic sucrose ester on polymorphic behavior of a new sunflower oil variety, *Food Res. Int.*, 2014, **64**, 9–17.
161. A. Szűts, E. Pallagi, G. Regdon Jr., Z. Aigner and P. Szabó-Révész, Study of thermal behaviour of sugar esters, *Int. J. Pharm.*, 2007, **336**, 199–207.
162. A. Szűts, Z. Makai, R. Rajkó and P. Szabó-Révész, Study of the effects of drugs on the structures of sucrose esters and the effects of solid-state interactions on drug release, *J. Pharm. Biomed.*, 2008, **48**, 1136–1142.

## CHAPTER 2 – EXPERIMENTAL

### 2.1 Materials

#### 2.1.1 Surfactants

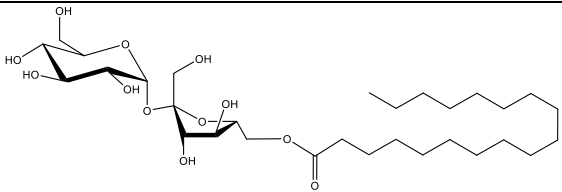
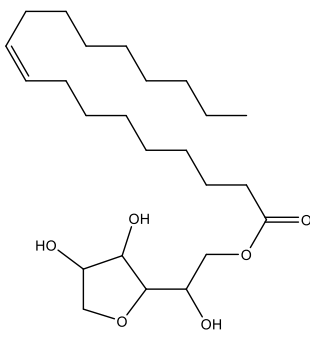
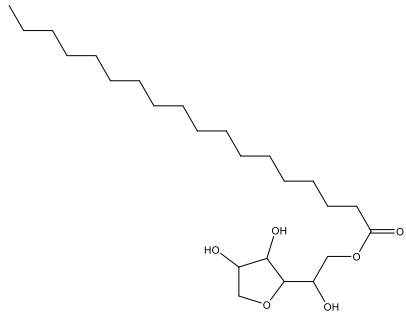
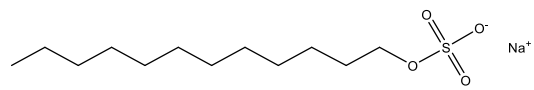
A series of sucrose esters (SE), *i.e.* C-1816 (64168517), C-1811 (66302111), C-1807 (64238516), C-1805 (67022311), C-1803 (6208920A) and C-1802 (53256211), were kindly provided by the Mitsubishi-Kagaku Food Corporation. Number 18 represents the chain length of the major fatty acid esterified with sucrose, *i.e.* stearic acid, and the last two numbers represent the HLB number. Their detailed characteristics are given in Table 2.1.

The nonionic sorbitan esters, *i.e.* sorbitan monooleate (Span 80 HP-LQ-(MH), 0001684768) and sorbitan monostearate (Span 60 HP-PA-(MH), 0001314910), were from Croda, UK & Ireland. Span 80 is a viscous, yellow liquid and Span 60 is white powder at room temperature. The anionic surfactant sodium dodecyl sulfate (SDS, L423392021,  $\geq 98\%$ ) was supplied by BDH Laboratory Supplies. All surfactants were used as received. The chemical structures and types of the surfactants used throughout this research are presented in Table 2.2.

**Table 2.1.** Characteristics of SE used. The samples are listed in increasing hydrophobicity.

Name	HLB number	Fatty acid composition/%	Ester composition/%		Appearance at room temp.
			Monoester	Di-,tri-, polyester	
C-1816	16	70	75	25	White powder
C-1811	11	70	55	45	White powder
C-1807	7	70	40	60	White powder
C-1805	5	70	30	70	White powder
C-1803	3	70	20	80	White powder
C-1802	2	70	10	90	White powder

**Table 2.2.** Type and chemical structure of surfactants used.

Type	Name	Structure
Nonionic	Sucrose monostearate	
	Sorbitan monooleate	
	Sorbitan monostearate	
Anionic	Sodium dodecyl sulfate	

### 2.1.2 Water

Milli-Q water was obtained by firstly passing through an Elgastat Prima reverse osmosis water unit, then through a Millipore Milli-Q reagent water system containing one carbon filter and two ion-exchange filters. The resistivity of Milli-Q water is  $\sim 18 \text{ M}\Omega \text{ cm}$  and its surface tension is  $72.5 \pm 0.2 \text{ mN m}^{-1}$  at  $20^\circ \text{C}$ .

### 2.1.3 Oils

Four vegetable oils were used in our experiments. Extra virgin olive oil (EVOO, SPLI-72120) and rapeseed oil (RO, SPLI-72119) were a gift from Cargill NV, Belgium. High oleic sunflower oil (HOSO, 002/12) and refined peanut oil (RPO, 010/09) are from Eulip. These oils are rich in long-chain unsaturated fatty acids, *e.g.* oleic acid C18:1, in their triglycerides (TAG) and are liquid at ambient temperature.<sup>1</sup> The fatty acid composition of RPO and EVOO in the form of methyl esters (FAMES) was measured by gas chromatography-mass spectrometry

(GC/MS). This method will be introduced later. RPO is abundant in long-chain unsaturated fatty acids (UFAs), *i.e.* oleic (C18:1, 49.7%, O) and linoleic (C18:2, 22.8%, L). It also contains saturated fatty acids (SFAs) being palmitic (C16:0, 12.0%, P), behenic (C22:0, 3.5%, Be), stearic (C18:0, 3.0%, S), lignoceric (C24:0, 1.9%, Lg) and arachidic (C20:0, 1.6%, A). In the case of EVOO, long-chain UFAs dominate as well, being oleic (79.9%) and palmitoleic (C16:1, 0.9%, Po). It contains ~ 17.0% SFAs in total. The fatty acid composition of both oils was comparable to that reported previously.<sup>1,2</sup> All oils were passed through a basic alumina column (Merck kGaA, 0.063 – 0.200 mm) once to purify prior to use unless otherwise stated.

#### 2.1.4 Other materials

Throughout our work, other materials were used as received. Their details including name, use, purity, and supplier are summarised in Table 2.3.

**Table 2.3.** Details of other materials used.

Name	Use	Purity	Supplier
Ethanol absolute	Washing glassware	100%	VWR Chemicals
Ethylene glycol	Preparation of thermostatting liquid	≥ 99%	Fisher Chemicals
Hydrochloric acid (HCl) 37.4%	Adjusting pH	Analytical grade	Fisher Scientific
<i>n</i> -hexane	Removing excess	≥ 97%	VWR Chemicals
Isobutanol	solvent	≥ 99%	Sigma-Aldrich
Potassium hydroxide	Synthesis of fatty	≥ 85%	Fisher Chemicals
Methanol	acid methyl esters (FAMES)	≥ 99.8%	Honeywell
<i>n</i> -hexadecane	Infrared spectral analysis	99%	Sigma-Aldrich

## 2.2 Methods

### 2.2.1 Characterisation of neat surfactants

#### 2.2.1.1 Differential scanning calorimetry (DSC)

DSC is a common technique to investigate the thermal behaviour of a material undergoing crystallisation and melting.<sup>3,4</sup> The theoretical fundamentals of DSC are simplified as follows,

$$\Delta H = \int C_p(T) dT \quad (2.1)$$

where  $\Delta H$  is the enthalpy change of the liquid-crystal phase transition,  $C_p$  is the temperature-dependent heat capacity (*i.e.* the amount of energy required to change the temperature of 1 g of material by 1 °C at constant pressure) and  $T$  is the temperature of the material.

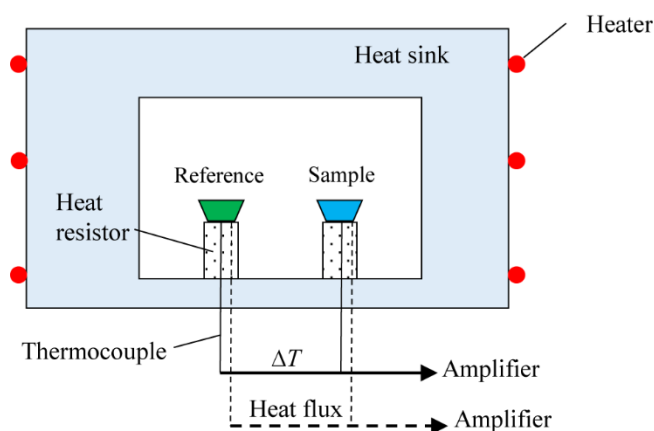
Based on the above, the entropy change of the phase transition can be determined,

$$\Delta S = \frac{\Delta H}{T_m} \quad (2.2)$$

where  $T_m$  is the phase transition temperature at which  $C_p$  reaches a maximum.

There are two basic types of differential scanning calorimeters (DSCs), *i.e.* the heat flux DSC and power compensated DSC, the working principles of which differ. The DSCs used throughout our report belong to the former type. Upon warming or cooling at a constant rate, the heat flows into the sample and reference are the same, so the differential temperature signal is zero. If the sample goes through a phase transition, this steady-state equilibrium is disturbed during which a differential signal is generated which is proportional to the difference between the heat flow rates to the sample and to the reference. The schematic of a heat flux DSC is presented in Figure 2.1.

**Figure 2.1.** Schematic of a heat flux DSC. Adapted from ref. 4.



The melting properties of neat surfactants were investigated using either a Mettler Differential Scanning Calorimeter (822e) with STAR<sup>e</sup> software or a PerkinElmer Differential

Scanning Calorimeter (DSC 4000) with Pyris series software. Nitrogen was used as purge gas. The instruments were calibrated with indium. The samples (3-10 mg) were weighed in aluminium pans using an analytical balance (Mettler Toledo) and then hermetically sealed at room temperature. An empty, sealed aluminium pan was used as reference. The samples were warmed from 20 °C to 80 °C at 5 °C min<sup>-1</sup>, held isothermally for 5 min at 80 °C before cooling to 20 °C at 5 °C min<sup>-1</sup>.

#### 2.2.1.2 X-ray diffraction (XRD)

Crystalline materials are described by the orderly periodic arrangements of atoms. The unit cell is the basic repeating unit that defines a crystal. Parallel planes of atoms intersecting unit cells are used to define directions and distances in the crystal. For a crystalline solid, the waves are scattered by lattice planes separated by the inter-planar distance  $d_{hkl}$ , where h, k and l are the Miller indices of the Bragg plane. When the difference between the path lengths of two waves equals any integer value of the wavelength, the scattered waves interfere constructively where the Bragg law is satisfied (Figure 2.2),<sup>5</sup>

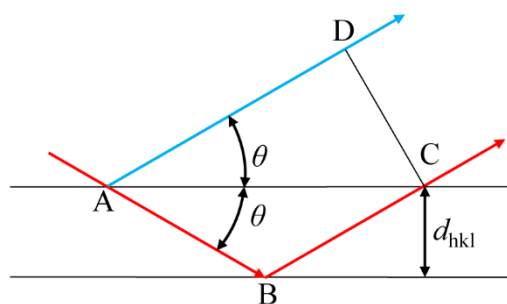
$$AB + BC - AD = n\lambda \quad (2.3)$$

$$2 \frac{d_{hkl}}{\sin\theta} - 2 \frac{d_{hkl}\cos\theta}{\sin\theta} = n\lambda \quad (2.4)$$

$$2d_{hkl}\sin\theta = n\lambda \quad (2.5)$$

where  $n$  is a positive integer (normally equals 1),  $\lambda$  is the wavelength of the incident wave and  $\theta$  is the glancing angle.

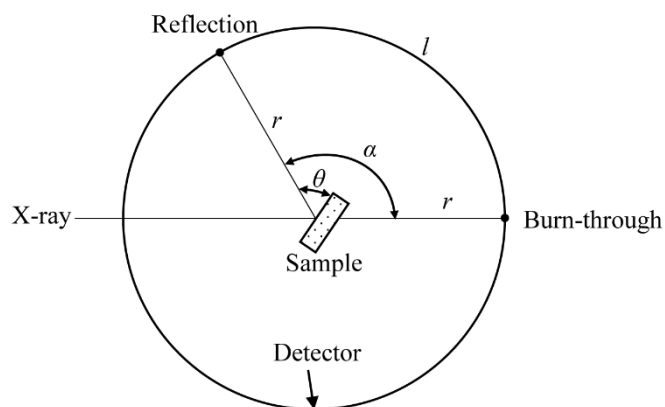
**Figure 2.2.** Schematic of diffraction of X-rays by crystal planes. Adapted from ref. 5.



The crystal structure of a sample was investigated using a Malvern PAN-alytical Empyrean diffractometer with Highscore Plus processing software using a  $\text{CuK}\alpha_1$  radiation source ( $\lambda = 1.5406 \text{ \AA}$ ). The investigated  $2\theta$  ( $\alpha$ ) angles varied from 1.5° to 60° with a step size of 0.02°. The instrument operated in the Bragg-Brentano configuration. The configuration of a powder X-ray diffraction instrument is schematically presented in Figure 2.3. The sample was

mounted with a spatula into a sample holder and then back filled against a polished steel disc to obtain a flat surface. It is known that the short spacing peak appearing at a large diffraction angle reflects the lateral packing order of hydrocarbon chains, whilst the long spacing peak at a small diffraction angle reflects the order and thickness of molecular layers.<sup>6</sup>

**Figure 2.3.** Schematic of a powder X-ray diffractometer. Reproduced from ref. 3.



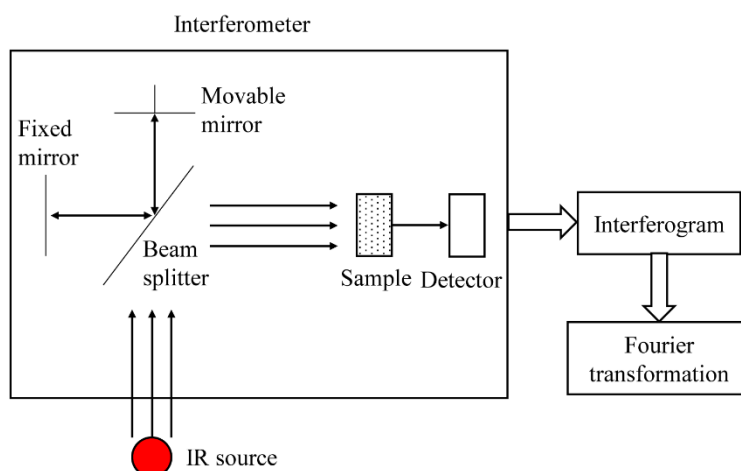
#### 2.2.1.3 Fourier-transform infrared (FTIR) spectroscopy

In FTIR spectroscopy, a sample is exposed to IR radiation. During this process, some of the IR radiation is absorbed by the sample and some of it is transmitted. The resulting spectrum exhibits distinct characteristics of molecular absorption and transmission, creating a spectral fingerprint of the sample.<sup>7</sup> The optical device used in FTIR spectroscopy is called an interferometer. The interferometer employs a beam splitter, which receives the incoming IR beam and then splits it into two beams. One beam reflects off a flat mirror that is fixed, whereas the other one reflects off a flat mirror that is constantly movable within a very short distance from the beam splitter. Subsequently, the reflected two beams will interfere or construct with each other yielding an interferogram. The obtained interferogram from the interferometer however cannot be interpreted directly to identify the functional groups and compounds at specific frequencies. So, a popular mathematical technique, *i.e.* Fourier transformation (FT), is applied to decode the interferogram. The schematic of a FTIR instrument is given in Figure 2.4.

FTIR spectral analysis was carried out using a Nicolet iS-5 FTIR spectrometer equipped with OMNIC software. The samples were measured in the attenuated total reflectance (ATR) mode equipped with a MIRacle ATR accessory at room temperature. Span 80 was loaded directly onto the sampling area of a crystal plate whilst SE powder was loaded using a MIRacle high pressure clamp. Span 60 was ground into powder with a porcelain mortar and pestle before loading. All measurements were performed with 24 scans and background spectra were

subtracted before measurement.

**Figure 2.4.** Schematic of a Fourier transform infrared instrument. Adapted from ref. 7.



### 2.2.2 Preparation of aqueous solutions/dispersions and aqueous foams

A certain mass of a mixture of SE and water was placed into a wide-mouth glass bottle with a screw cap. The mixture was thermostatted at  $\sim 80\text{ }^{\circ}\text{C}$  for  $\sim 30$  min under magnetic stirring (150 rpm), and then cooled gradually to room temperature. Afterwards, the sample was left to mature overnight ( $\sim 12$  h) under gentle magnetic stirring (50 rpm) prior to further experiments. The acidity of SE solutions/dispersions was adjusted using 0.1 M or 0.5 M HCl. The pH value was measured immediately after preparation using a Jenway-3510 pH meter with an InLab Flex-Micro electrode (Mettler-Toledo). SDS solutions/dispersions were prepared by gradually dissolving SDS into water, followed by gentle magnetic stirring (50 rpm) overnight ( $\sim 12$  h).

20 mL of the surfactant-water mixture was transferred to a glass cylinder equipped with a stopper. The tightly sealed glass cylinder was then submitted to vigorous hand shaking for 60 s by the same operator at room temperature. Foam volume was recorded within 10 s after preparation. To quantify foamability, the foamability index  $F$  was defined as the volume ratio of the sample immediately after aeration to that before aeration. Foam stability was characterized in terms of foam half-life  $t_{1/2}$ , time for complete foam collapse and volume ratio of foam on storage to that immediately after preparation.

### 2.2.3 Characterisation of aqueous solutions/dispersions and aqueous foams

#### 2.2.3.1 Dynamic light scattering (DLS) and Zeta potential

DLS is a technique that measures the Brownian motion of particles arising from continuous collision with solvent molecules and relates this to the size of particles. The relationship between the particle size and Brownian motion can be expressed by the Stokes-Einstein equation,<sup>8-10</sup>

$$d_H = \frac{\kappa_B T}{3\pi\eta D} \quad (2.6)$$

where  $d_H$  is the hydrodynamic diameter,  $D$  is the diffusion coefficient,  $\kappa_B$  is the Boltzmann constant,  $T$  is the absolute temperature and  $\eta$  is the dynamic viscosity. During DLS measurements, particles in a cell are illuminated with a laser. To avoid the saturation of a detector, an attenuator is applied to reduce the intensity of the laser source. As particles are moving continuously in a solution, mutually destructive or constructive phases are obtained, corresponding to dark and bright areas, respectively. The detector will measure the scattered light intensity fluctuations as a function of time, *i.e.* the intensity fluctuation rate, which can be used to calculate the particle size. A correlator is designed to determine the extent of similarities between two signals or one signal at different time intervals. If particles are large the signals will fluctuate slowly thus the correlation will remain for a longer period, whilst for small particles which are moving quickly the correlogram will suffer a quick decay (Figure 2.5). The schematic of the configuration of a Zetasizer Nano series NanoZS is presented in Figure 2.6.

A correlation function of the scattered intensity can be expressed as a function of time difference  $\Delta t$  of the correlator,

$$G(\Delta t) = \langle I(t)I(t + \Delta t) \rangle \quad (2.7)$$

For monodisperse particles, it can be fitted to an exponential function of  $\Delta t$ ,

$$G(\Delta t) = A[1 + B \exp(-2\Gamma\Delta t)] \quad (2.8)$$

where  $A$  and  $B$  are the baseline and intercept of the correlation function, respectively.

$$\Gamma = Dq^2 \quad (2.9)$$

$$q = (4\pi\mu/\lambda_0)\sin(\theta/2) \quad (2.10)$$

where  $\mu$  is the refractive index of the solvent,  $\lambda_0$  is the wavelength of the laser and  $\theta$  is the scattering angle.

**Figure 2.5.** Typical correlogram for a sample containing large particles (solid line) and small particles (dotted line). Adapted from ref. 9.

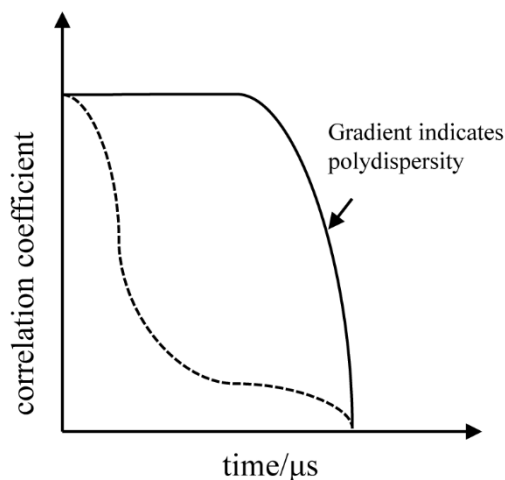
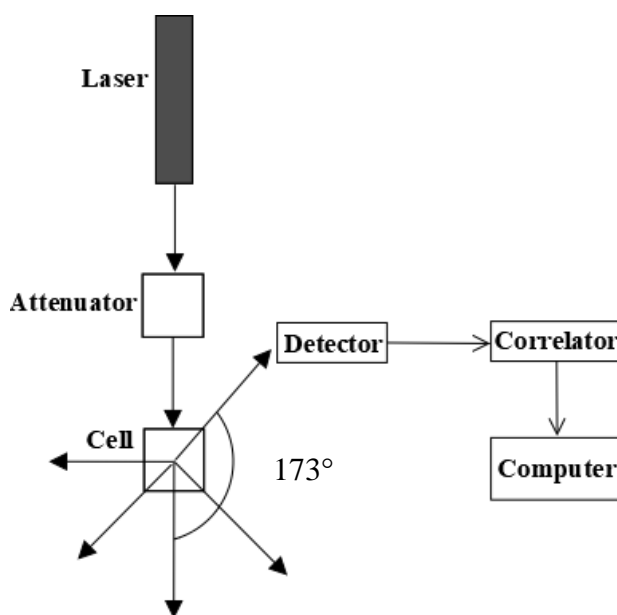


**Figure 2.6.** Optical configuration of a Zetasizer Nano series NanoZS. Adapted from ref. 9.

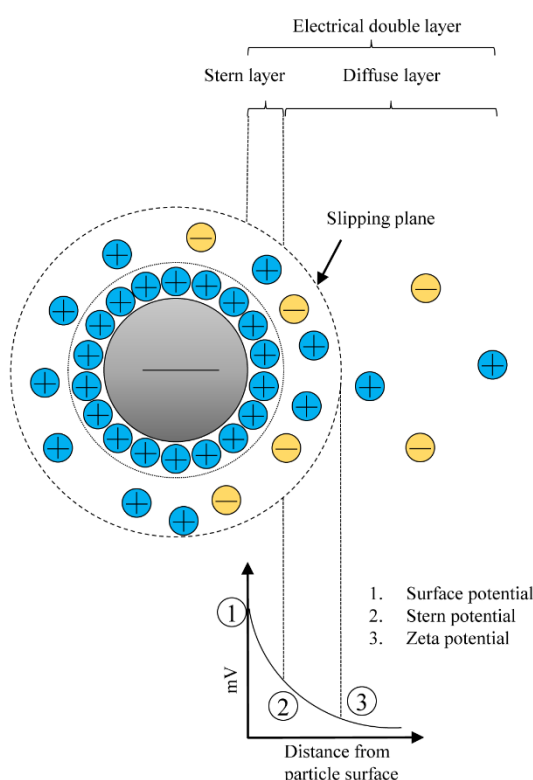


The value of  $D$  can be derived from the fitted correlation function and then it is used to calculate the hydrodynamic diameter ( $d_H$ ) of particles with the Stokes-Einstein equation. Two methods are applied during data analysis, *i.e.* cumulants and distribution analysis. The fundamental size information is the intensity size distribution, which is a plot of the relative intensity of light scattered by particles of various sizes based on the Rayleigh scattering theory.<sup>10</sup> The volume size distribution is converted from the intensity size distribution using the Mie theory, during which the refractive index of the particle is taken into consideration.<sup>10</sup>

An electrical double layer exists surrounding each particle.<sup>9,11</sup> The inner electrical layer is called the Stern layer where ions are strongly bounded to the particle surface, whereas the outer

layer is referred to as the diffuse layer in which ions are less firmly attached. Within the diffusion layer, there exists a boundary inside which ions move as the particle moves, whereas outside which ions do not travel with the particle. This boundary is called the slipping plane and the electric potential at this plane is the Zeta potential. The magnitude of Zeta potential is an indication of the stability of a colloidal system. A system with the magnitude of Zeta potential large than 30 mV is normally regarded as stable. The schematic of the electric double layer for a negatively charged particle suspended in a liquid is given Figure 2.7.

**Figure 2.7.** Schematic of the electric double layer for a negatively charged particle suspended in a liquid. Adapted from ref. 9.



The size of surfactant aggregates formed in water were measured using a Zetasizer Nano-ZS (ZEN3600, Malvern Instruments) equipped with a 4 mW He-Ne laser beam operating at  $\lambda = 633$  nm at a fixed backscattering angle of  $173^\circ$  equipped with Zetasizer software at  $20^\circ\text{C}$ . The applied measuring cell was polystyrene cuvettes ( $10 \times 10 \times 45$  mm, 67.741). The refractive index and viscosity of water at  $20^\circ\text{C}$  are 1.333 and 1 cP, respectively. The intensity size distribution based on the Rayleigh scattering theory<sup>10</sup> was presented for each sample. The zeta potential was measured at  $20^\circ\text{C}$  with the same instrument adopting a universal dip cell (ZEN1002, Malvern Instruments).

### 2.2.3.2 Optical microscopy

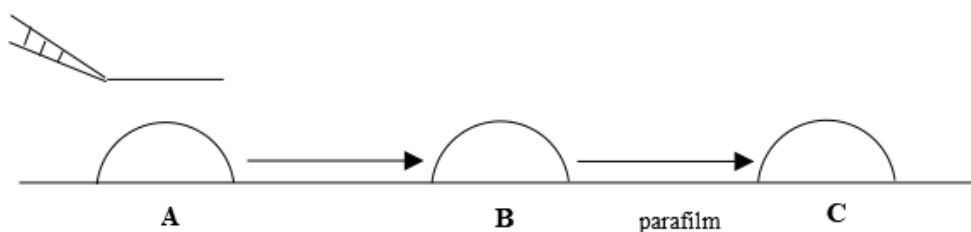
All aqueous samples were observed under an Olympus BX51 microscope mounted with an Olympus DP70 camera. The objective lens used were 20× (LMplan FI), 10× (Upan FI), and 4× (Upan FI). A drop of a sample (~ 10 µL) was spread onto a glass slide (76 mm × 26 mm). Images were taken with Image-Pro plus software. All micrographs were analyzed with ImageJ 1.47V software calibrated with a Pyser-sgi limited graticule. The number average bubble diameter of a foam sample was calculated from at least 150 representative bubbles,

$$D[1,0] = \frac{\sum_{i=1}^n d_i}{n} \quad (2.11)$$

### 2.2.3.3 Transmission electron microscopy (TEM)

The negative staining method<sup>12</sup> was adopted for the staining procedure (Figure 2.8). A carbon film coated copper grid was laid on a drop of sample (10 µL, A) for 2 min, and excess fluid was gently wiped away by filter paper. The copper grid was then laid on a drop of pure water (50 µL, B) for few seconds and excess water was drained off with filter paper. Subsequently, the copper grid was placed into 1% (w/v) aqueous uranyl acetate solution (C) and drained off after 1 min. Lastly, the sample was dried for 24 h at ambient temperature before TEM experiments. TEM images were taken using a Gatan Ultrascan 4000 digital camera attached to a Jeol 2011 Transmission Electron Microscope running at 200 kV. The size distribution of aggregates formed for each sample was calculated from at least 50 representative ones using ImageJ 1.47V software. The diameters of non-spherical aggregates were determined using the Martin's diameter measurement method.<sup>13</sup>

**Figure 2.8.** Schematic illustrating the negative staining method to prepare TEM samples.



### 2.2.3.4 Cryo-scanning electron microscopy (cryo-SEM)

A drop of a sample (~ 10 µL) was mounted onto a channelled aluminium stub by a spatula. The sample was immersed in liquid nitrogen for ~ 2 min and then transferred to a cryo-preparation vacuum chamber (PP3010T, Quorum Technologies Ltd.) at -140 °C. A scalpel was used to fracture the frozen sample. The sample was subsequently transferred to a cold stage in the SEM instrument (Carl Zeiss Evo-60) at -140 °C, and sublimed at -90 °C for ~ 20 min. It

was transferred back to the cryo-preparation chamber and then coated with a thin platinum film ( $\sim 2$  nm). Finally, it was put back onto the SEM cold stage and imaged. Imaging was performed with a LaB6 emitter, 40 micro-amp beam current, 15 kV accelerating voltage and a 35 pico-amp probe current using the secondary electron detector.

### 2.2.3.5 Rheology

For a purely elastic solid, the stress ( $\tau$ ) is proportional to the strain ( $\gamma$ ),

$$\tau = G \times \gamma \quad (2.12)$$

For a Newtonian liquid, the stress ( $\tau$ ) is proportional to the shearing strain rate ( $\dot{\gamma}$ ),

$$\tau = \eta \times \dot{\gamma} \quad (2.13)$$

where  $G$  is the shear modulus and  $\eta$  is the viscosity.

When a sinusoidal oscillating stress is applied to a sample, the corresponding varying strain can be generated. The strain wave is in phase with the stress wave (*i.e.* phase angle  $\delta = 0^\circ$ ) for an elastic solid, whereas  $90^\circ$  out of phase for a Newtonian liquid. For a viscoelastic sample, the phase angle varies between  $0^\circ$ - $90^\circ$  and the stress wave  $\tau$  can be decomposed into two components ( $\tau'$  and  $\tau''$ ): the former one in phase with the strain wave and the latter one  $90^\circ$  out of phase with it (Figure 2.9),<sup>14</sup>

$$\tau = \tau' + \tau'' = \tau'_0 \sin \omega t + \tau''_0 \cos \omega t \quad (2.14)$$

where  $\omega$  is the angular frequency,  $t$  is time and  $\tau'_0$  and  $\tau''_0$  are the maximum stress amplitudes of the elastic and viscous components, respectively.

Based on the above, two dynamic moduli are defined. The elastic modulus ( $G'$ ) and viscous modulus ( $G''$ ) represent the solid and liquid parts of the sample, respectively,

$$G' = \frac{\tau'_0}{\gamma_0} \quad (2.15)$$

$$G'' = \frac{\tau''_0}{\gamma_0} \quad (2.16)$$

where  $\gamma_0$  is the maximum strain amplitude of the viscoelastic sample.

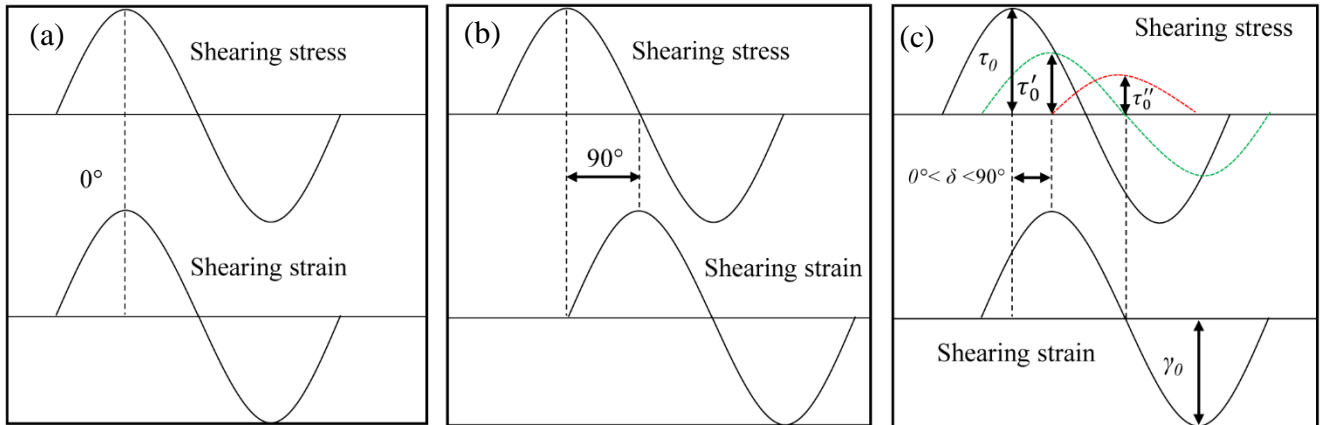
The phase angle  $\delta$  can be written as,

$$\tan \delta = \frac{G''}{G'} \quad (2.17)$$

The complex modulus  $G^*$  is defined to represent the sum of the elastic (storage) modulus  $G'$  and the viscous (loss) modulus  $G''$ ,

$$G^* = G' + iG'' \quad (2.18)$$

**Figure 2.9.** Strain response of (a) elastic solid ( $\delta = 0^\circ$ ), (b) Newtonian liquid ( $\delta = 90^\circ$ ), (c) viscoelastic sample ( $0^\circ < \delta < 90^\circ$ ) under sinusoidal oscillating stress. Adapted from ref. 14.



A Bohlin rheometer (CVO120 High Resolution) with Bohlin software (R6.51.0.3) was used for all rheological measurements. The applied measuring geometry was a cone and plate (CP4/40) of diameter 40 mm and gap 500  $\mu\text{m}$ . The temperature of the lower plate was precisely controlled by a Peltier system ( $\pm 0.1^\circ\text{C}$ ). The viscosity was recorded as a function of shear rate at  $20^\circ\text{C}$  under the viscometry mode.

#### 2.2.3.6 Surface tension

Air-water surface tensions at  $20^\circ\text{C}$  were measured using a Krüss K11 tensiometer and the Wilhelmy plate method (Figure 2.10).<sup>15</sup> 15 mL of an aqueous solution/dispersion with SE was transferred into a Petri dish surrounded by a water jacket in the tensiometer and then maintained at  $20^\circ\text{C}$  for  $\sim 30$  min. Prior to each measurement, the platinum plate was rinsed with ethanol and heated to glowing in a blue Bunsen flame.

For the Wilhelmy plate method, the balance of forces on the plate in scenario (a) is expressed as,

$$F_{\text{external}} + F_{\text{buoyancy}} = F_{\gamma, \text{gas/liquid}} + F_{\gamma, \text{liquid/solid}} + F_{\text{gravity}} \quad (2.19)$$

$$F_{\text{buoyancy}} = \rho_{\text{liquid}} l w h_0 g \quad (2.20)$$

$$F_{\gamma, \text{gas/liquid}} = 2(l + w)\gamma \cos\theta \quad (2.21)$$

$$F_{\gamma, \text{liquid/solid}} = 0 \quad (2.22)$$

$$F_{\text{gravity}} = \rho_{\text{solid}} l w h_1 g \quad (2.23)$$

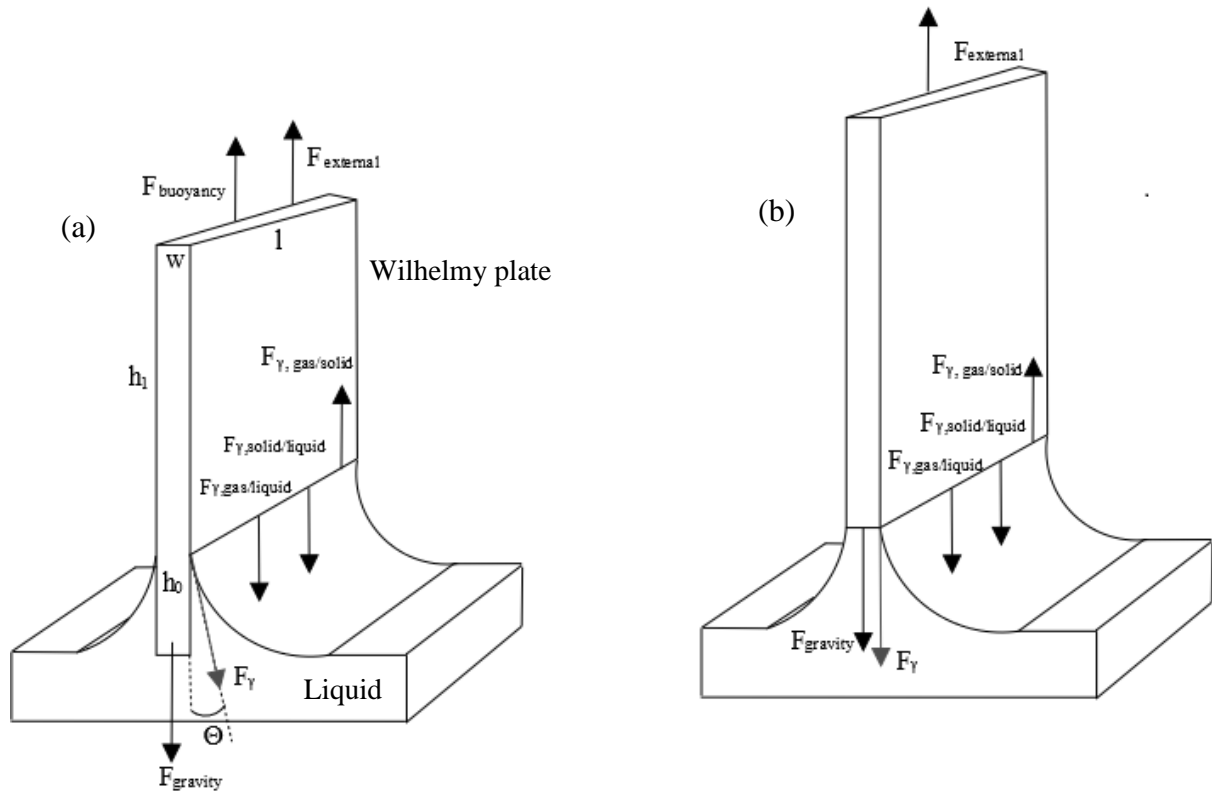
The balance of forces on the plate in scenario (b) is calculated as,

$$F_{\text{external}} = 2(l + w)\gamma + \rho_{\text{liquid}} l w h_0 g \quad (2.24)$$

$$\gamma \approx \frac{F_{\text{external}}}{2(l+w)} \quad (2.25)$$

where  $\gamma_{la}$  is the air-liquid surface tension,  $F_{\text{external}}$  is the external force acting on the plate by the tensiometer,  $F_{\text{buoyancy}}$  is the buoyancy force,  $F_{\gamma, \text{gas/liquid}}$  is the force from the air-liquid surface tension,  $F_{\gamma, \text{liquid/solid}}$  is the force from the liquid-solid interfacial tension and often equals 0 due to high free surface energy of the platinum plate,  $F_{\text{gravity}}$  is the gravitational force,  $l$  and  $w$  are the horizontal length and thickness of the plate, respectively,  $\rho_{\text{liquid}}$  is the liquid density,  $\rho_{\text{solid}}$  is the density of the measuring geometry,  $\theta$  is the contact angle between the liquid meniscus and solid surface measured into the liquid,  $h_0$  is the height of the measuring geometry immersed into the liquid,  $h_1$  is the height of the measuring geometry and  $g$  is the gravitational constant.

**Figure 2.10.** Schematic of the Wilhelmy plate method for measuring the air-liquid surface tension. (a) A plate is slowly pulled out of a liquid. (b) Shortly before the plate is completely pulled out of the surface,  $F_{\text{external}}$  reaches a maximum value at this point. Adapted from ref. 11 and 16.



## 2.2.4 Preparation of oil solutions/dispersions, oil foams, emulsions, foamulsions and aerated emulsions

### 2.2.4.1 Oil solutions/dispersions

The sample preparation methods differed depending on the sample. In the case of neat oil, the oil sample was placed into the well of a thermostat (VWR International) equipped with a MX07R-20 temperature controller. The thermostating liquid was a homogeneous mixture of ethylene glycol and deionized water. All temperatures were measured by an Omega thermocouple ( $\pm 0.1$  °C). Oil samples were pre-heated at 60 °C for  $\sim 30$  min in the thermostat to erase any crystallisation history. Subsequently, they were submitted to different thermal treatment: (i) gradual cooling from 60 °C to the temperature of interest; (ii) rapid cooling to -20 °C and maintaining at this temperature overnight ( $\sim 12$  h), followed by slow heating to the target temperature.

For surfactant-oil mixtures, a certain mass of a mixture was placed in the well of a Grant R1 thermostat. The sample temperature was determined by monitoring the temperature of neat oil in the same water bath. The surfactant-oil mixture was first maintained at  $90 \pm 1$  °C for 10 min under gentle magnetic stirring (150 rpm) yielding a clear, homogeneous solution. It was then cooled gradually to temperatures of interest at  $1$  °C  $\text{min}^{-1}$  until reaching 20 °C. After keeping at 20 °C overnight ( $\sim 12$  h), the sample was heated stepwise at  $1$  °C  $\text{min}^{-1}$  until it turned clear again. Photos of the sample at various temperatures were taken, and the temperature where the mixture first became cloudy upon cooling and the highest temperature at which the cloudiness survived upon warming were recorded.

### 2.2.4.2 Oil foams

#### 2.2.4.2.1 Whipping

Whipping is a common technique to fabricate stable oil foams. Different tempering and whipping protocols were adopted depending on the sample. For neat oil, a glass beaker containing 100 mL of RPO or EVOO was initially maintained at 60 °C in the well of the thermostat to erase history. In the case of the cooling protocol, the oil sample was cooled slowly at a rate of  $0.3$  °C  $\text{min}^{-1}$  until reaching the required temperature. In contrast, the sample submitted to the warming procedure was heated at  $0.4$  °C  $\text{min}^{-1}$  to temperatures of interest after pre-conditioning at -20 °C overnight. This was followed by whipping with a hand-held Vonshef double beater electric whisk at level 1 ( $750 \pm 75$  rpm). The whole whipping procedure lasted for 45 min in total containing 5 min whipping followed by 5 min rest interval, *i.e.* actual

whipping time was 25 min. The variation of the sample temperature before and immediately whipping was  $\pm 2$  °C. Immediately after whipping the homogeneous sample was quickly transferred into two small glass beakers pre-cooled to the aeration temperature. One was stored at the aeration temperature to monitor foam stability (*i.e.* volume of foam, volume of drained oil and foam bubble size *versus* storage time), whilst the other was used for calculating the over-run of the whipped oil. The initial volume of the aerated sample ( $V_{\text{oil+air}}$ ) equals the volume of oil plus entrapped air bubbles, and after warming to room temperature to fully release air bubbles the sample was returned to its initial whipping temperature at which the volume of oil ( $V_{\text{oil}}$ ) before whipping was determined. For comparison, EVOO was passed twice through a basic alumina column to remove potential polar impurities. Subsequently, the columned EVOO was subjected to the same warming procedure followed by the same whipping protocol mentioned above. All glass beakers were sealed with aluminium foil during both whipping and storage to avoid condensation.

For mixtures of surfactant (*i.e.* SE and Span 60) and oil, a glass beaker (250 mL) containing a certain mass of the sample was initially maintained at 90 °C for 10 min under magnetic stirring (150 rpm) to yield a homogeneous solution. The sample was then cooled slowly in a water bath at 1 °C min<sup>-1</sup> until reaching the target temperature and subsequently whipped at level 2 ( $880 \pm 88$  rpm) for 10 min with a single beater. The variation of the sample temperature during whipping was  $\pm 2$  °C. The fresh foams were then stored at the same temperature as the whipping temperature. For comparison, a separate sample was submitted to a different tempering and whipping protocol adapted from a previous method.<sup>17</sup> A homogeneous mixture of surfactant and oil was cooled continuously from 90 °C at 1 °C min<sup>-1</sup>. On reaching 60 °C, foams were produced by whipping the mixture with simultaneous cooling to induce surfactant crystallization. The volume and temperature of the whipped sample were recorded as a function of whipping time.

To obtain ultra-stable foams, fresh oil foams containing SE or Span 60 after 10 min whipping at 80 °C were submitted to different quenching protocols. To investigate the effect of cooling rate, a sample of fresh foam was transferred to room temperature or an ice bath at -5 °C, corresponding to slow and rapid cooling, respectively. To explore the role of storage temperature, the foam for the former was then kept at room temperature, whilst for the latter it was later transferred to a fridge at  $7 \pm 1$  °C or room temperature. To investigate the thermo-responsiveness of the final foams, a volume of foam at 7 °C was transferred into a glass vial pre-cooled to 7 °C and then submitted to a gradual warming at 1 °C min<sup>-1</sup>. Meanwhile, a drop of a separate foam sample was deposited onto a glass slide on the temperature-controlled stage

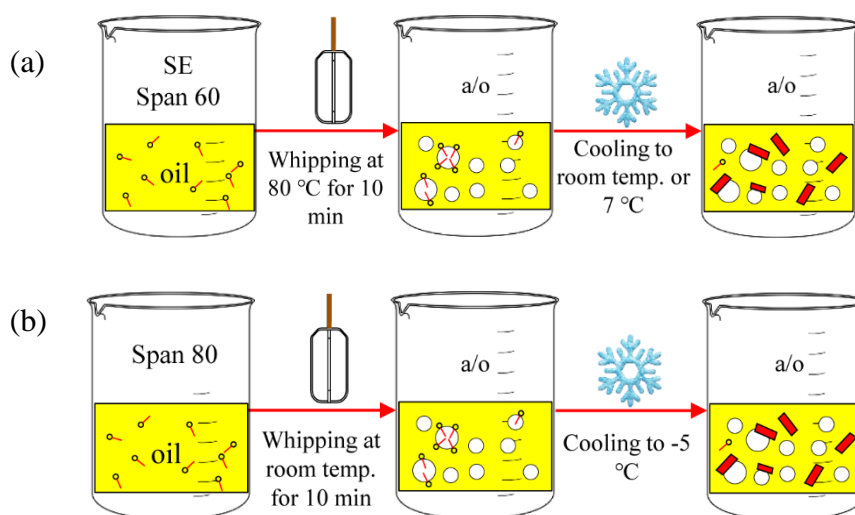
and then covered with a coverslip. Photos and micrographs were taken at different temperatures during heating. The detailed introduction of temperature-controlled optical microscopy is given later.

For Span 80, a glass beaker (250 mL) containing its mixture with oil was initially maintained at room temperature overnight (~ 12 h) under gentle magnetic stirring (50 rpm) to yield a homogeneous solution. The sample was then submitted to whipping at level 2 ( $880 \pm 88$  rpm) for 10 min with a single beater. The fresh foams were then stored at room temperature. To improve foam stability, fresh oil foams after 10 min whipping at room temperature were submitted to rapid cooling in an ice bath at  $-5$  °C, followed by storing at the same temperature.

The appearance of foams during whipping and subsequent storage was recorded photographically and with optical microscopy. The over-run is defined as,

$$\text{over run (\%)} = \frac{V_{oil+air} - V_{oil}}{V_{oil}} \times 100\% \quad (2.26)$$

**Figure 2.11.** Schematic illustrating protocols to prepare stable oil foams with different surfactants. (a) Sucrose esters or Span 60. (b) Span 80.

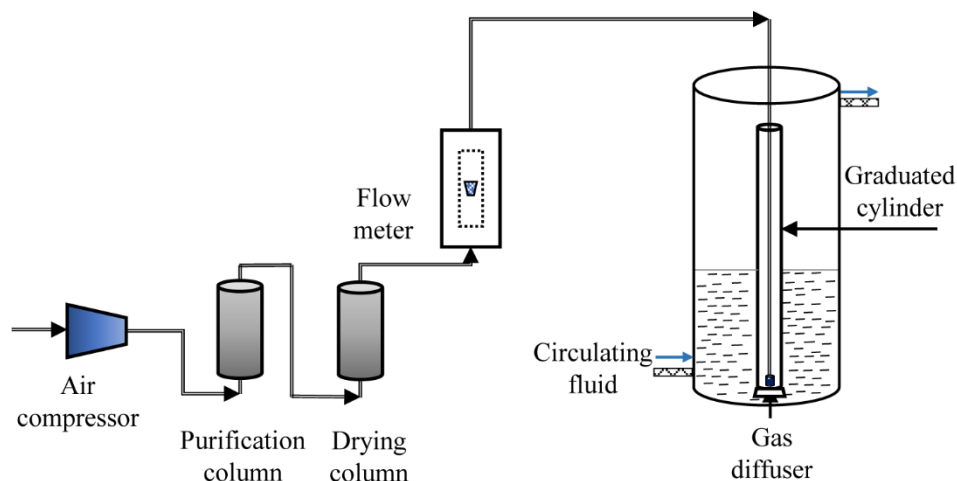


#### 2.2.4.2.2 Bubbling

Whipping has been demonstrated as an effective and reproducible method to produce stable oleofoams.<sup>18,19</sup> The application of whipping is vigorous however, during which comparatively high level of mechanical energy input alongwith viscous energy dissipation are involved.<sup>20,21</sup> In addition, the physiochemical characteristics of pre-formed crystals in oil may alter under whipping, *e.g.* size, morphology and polymorph type, making it difficult to correlate

the properties of the resulting oleofoams with the initial oleogels.<sup>22</sup> Considering this, a home-designed foaming setup was used to produce oil foams through bubbling. It is schematically shown in Figure 2.12, and its detailed description is stated below.

**Figure 2.12.** Schematic of the home-designed foaming setup.



- (i) Compressed air from an air compressor first passed through a purification column filled with activated charcoal. Activated charcoal is a charcoal treated with oxygen to create millions of tiny pores between carbon atoms. It is normally used to remove contaminants and impurities from air.
- (ii) The purified air then passed through a drying tube filled with silica gel. The silica gel has high specific surface area ( $\sim 800 \text{ m}^2 \text{ g}^{-1}$ ), which can adsorb water readily, making it useful as a drying agent. Once the silica gel was saturated with water, it was dehydrated by heating it to  $120^\circ \text{C}$  for 1-2 h.
- (iii) The dried air then went through a flow meter at a flow rate of  $10\text{-}100 \text{ mL min}^{-1}$ . The flow meter consists of a trapped glass tube with a float inside. The upward drag force acting on the float is proportional to the velocity of gas, being balanced by the gravitational force of the float.
- (iv) Finally, the outlet air from the flow meter passed through a Mott diffuser. The mean pore diameter of the Mott diffuser is  $22 \mu\text{m}$ , and its permeability is  $5100 \text{ mL min}^{-1}$  at  $2.45 \text{ KPa}$ .
- (v) A sample was transferred to a glass cylinder (100 mL) surrounded by a silicone oil jacket (Grant R1 thermostat). The applied tempering protocols varied depending on the sample. An oil solution of SE was cooled gradually from  $90^\circ \text{C}$  to  $80^\circ \text{C}$  at  $1^\circ \text{C min}^{-1}$ .

For neat oil, it was cooled directly to -20 °C and maintained at this temperature overnight (~ 12 h). This was followed by being transferred directly to temperatures of interest and equilibrated for ~ 1 h.

- (vi) The gas flow rate was adjusted to a certain value and the Mott diffuser was positioned at the bottom of the sample before bubbling. The sample appearance was recorded as a function of bubbling time and storage time. To describe foamability, the over-run was calculated. For foam stability, normalised foam/drained oil volume was defined as the volume ratio of foam/drained oil on storage to that initially. Note that the gas diffuser was maintained at the vessel bottom after aeration to avoid potential disruption to the foams. The gas diffuser was cleaned with ethanol, rinsed with water and then fully dried prior to use.

#### 2.2.4.3 Emulsions

Equal volumes (5 cm<sup>3</sup>) of water and oil solutions of C-1803 were firstly thermostatted separately at 80 °C in a water bath (Grant R1). Two strategies were then introduced to prepare simple emulsions. (i) The oil solution of C-1803 at 80 °C was transferred to a glass vial (7 cm × 2.5 cm) containing water at the same temperature, and then homogenized with an IKA Digital Ultra Turrax T25 homogenizer with 8 mm head operating at 10,000 rpm for 2 min at 80 °C. The fresh emulsion was then quenched statically to 20 °C, followed by storing at the same temperature. (ii) Two glass vials containing water and the oil solution of C-1803 at 80 °C were cooled gradually to 20 °C, respectively. The latter sample was transferred into the former, followed by homogenizing at 10,000 rpm for 2 min at 20 °C. The emulsion type for the former method is o/w whereas w/o for the latter one by drop test. More information regarding the drop test will be discussed later. The surfactant concentration was calculated as the ratio of surfactant mass to total emulsion volume (10 cm<sup>3</sup>), Figure 2.13(a).

Multiple emulsions (o/w/o) were prepared by introducing an oil dispersion with C-1803 cooled from 90 °C into a glass vessel (50 mL) containing an o/w emulsion stored at 20 °C. The mixture was submitted to magnetic stirring and then stored at 20 °C, Figure 2.13(b).

#### 2.2.4.4 Foamulsions

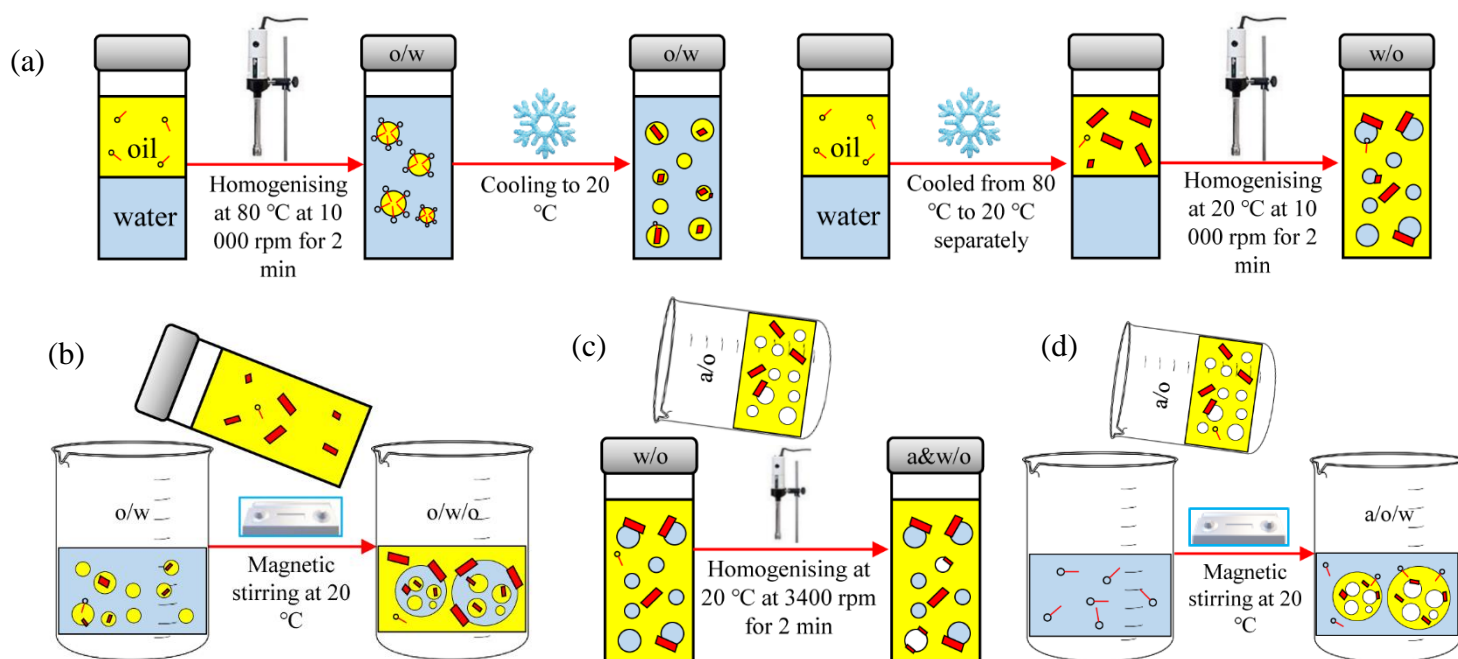
Oil continuous foamulsions (*i.e.* a and w/o) were fabricated as follows. An oil foam (a/o) at 7 °C was transferred to a glass vial (7 cm × 2.5 cm) containing a w/o emulsion prepared at 20 °C, and subsequently homogenised at 3,400 rpm (lowest rotating speed for the

homogeniser used) for 2 min at 20 °C. The resulting foamulsions were stored at 20 °C, Figure 2.13(c).

#### 2.2.4.5 Aerated emulsions

To yield aerated emulsions (a/o/w), a foam stored at 7 °C was progressively introduced into a 50 mL glass beaker containing an aqueous dispersion of C-1803 at 20 °C under gentle manual stirring. Subsequently, the mixture was subjected to magnetic stirring for 2 min and then stored at 20 °C, Figure 2.13(d).

**Figure 2.13.** Schematic illustration of protocols to prepare various colloidal materials. (a) Oil-in-water (left) or water-in-oil (right) emulsions. (b) Oil-in-water-in-oil emulsions. (c) Air and water-in-oil foamulsions. (d) Air-in-oil-in-water emulsions.



### 2.2.5 Characterisation of oil solutions/dispersions, oil foams, emulsions, foamulsions and aerated emulsions

#### 2.2.5.1 DSC

The crystallisation and melting profiles of various colloidal materials were investigated using the same DSC instruments mentioned above. For neat oil, the applied program is summarised as: (i) holding isothermally at 20 °C for 10 min, (ii) cooling from 20 °C to -20 °C at 0.5 °C min<sup>-1</sup>, (iii) holding isothermally at -20 °C for 10 min, (iv) warming from -20 °C to

20 °C at 0.5 °C min<sup>-1</sup>. For mixtures of surfactant and oil, it was initially heated to 90 °C for 10 min, followed by cooling to 20 °C at 3 °C min<sup>-1</sup> (isothermal for 5 min) and subsequent warming to 90 °C at 3 °C min<sup>-1</sup>. In the case of other samples, *e.g.* foams and emulsions, they were subjected to a gradual warming from 20 °C to 90 °C at 3 °C min<sup>-1</sup>.

#### 2.2.5.2 DLS

To detect the possible formation of reverse micelles/vesicles in oil solutions of SE or Span 80, DLS measurements were performed within the one-phase region of the solubility diagram determined by visual observations. The DLS instrument used is the one mentioned above. All oils were passed once through a membrane filter (Sterile, pore size 0.45 µm) to remove potential dust prior to the experiment.

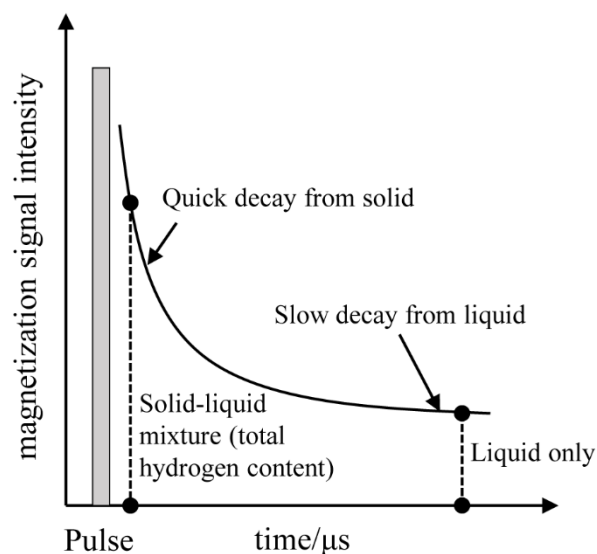
#### 2.2.5.3 Solid fat content (SFC)

The SFC of samples can be determined using pulsed nuclear magnetic resonance (p-NMR).<sup>3,23</sup> The technique is achieved by applying a short intense burst of radio frequency (RF) energy to excite hydrogen protons in a static magnetic field. When a RF pulse is applied to a sample, a magnetization signal is produced. The initial amplitude of this signal is proportional to the total number of hydrogen protons in the sample. The signal decay of protons in a solid is faster than that in a liquid, so signal decays corresponding to different components tend to differ. In Figure 2.14, initially the magnetization signal goes through a quick decay, which is due to the solid fraction. The subsequent slow decay arises from the liquid component. The difference between the signal from the mixed phase and from the liquid phase alone is proportional to the amount of hydrogen protons present in the solid phase. Based on this, the determination of the SFC is achievable,

$$SFC = 100(S_1 - S_2)F/[F(S_1 - S_2) + S_2] \quad (2.27)$$

where  $S_1$  and  $S_2$  represent the signal of the total amount of solid and liquid, respectively and  $F$  is a correction factor allowing for a dead-time in the receiver.

**Figure 2.14.** Magnetization signal decay curve of a solid-liquid mixture for the determination of the SFC using p-NMR. Adapted from ref. 3.



The measurement of the SFC of RPO at different temperatures was performed using a Bruker NMR minispec mqone SFC analyser. First, tubes containing liquid oils were placed on a heating block at 80 °C for 10 min, and then transferred to a 0 °C thermostat and maintained for 1 h. After those pre-conditions, the samples were kept at each temperature for at least 30 min prior to measurements. Groundnut oil from AAK (Hull), also known as peanut oil, was measured for comparison.

#### 2.2.5.4 FTIR spectroscopy

FTIR spectroscopy was done using the FTIR spectrometer mentioned above. For the ambient temperature experiment, the samples were measured in the attenuated total reflectance (ATR) mode equipped with a MIRacle ATR accessory. Neat oil, oil dispersion or oil foam was loaded directly onto the sampling area of a crystal plate. For the high temperature experiment, a quartz cuvette (QX 383) containing an oil solution was positioned carefully in the pathway of the beam from the spectrometer under the adsorption mode. The sample temperature was controlled by a water bath measured by a thermocouple. All measurements were performed with 24 scans and background spectra were subtracted before measurement.

#### 2.2.5.5 Rheology

The rheological measurements were performed using the rheometer mentioned earlier. A serrated parallel plate geometry of diameter 40 mm and gap 1 mm was used to prevent wall slip. The temperature of the lower plate was controlled by the Peltier system ( $\pm 0.1$  °C).

Different programs were applied for temperature sweeps. For neat oil, a temperature sweep was performed from 60 °C to -20 °C or lower, then maintained isothermally at this temperature for 10 min followed by warming gradually to 60 °C with  $f = 0.1$  Hz. The cooling and heating rates were 1 °C min<sup>-1</sup> and the oscillation strain  $\gamma$  was set as 0.05% within the linear viscoelastic region (LVR) of oil gels. To better understand the fat crystal network development upon cooling and warming, four critical temperatures were identified from the temperature ramp curves as:  $T_{cc}$  - crossover temperature ( $G' = G''$ ) of crystallisation during cooling;  $T_{oc}$  - onset temperature of crystallisation during cooling;  $T_{cm}$  - crossover temperature ( $G' = G''$ ) of crystal melting during warming;  $T_{em}$  - end temperature of crystal melting during warming.<sup>17</sup> In the case of mixtures of surfactant and oil, the program for the temperature sweep is summarised as: (a) maintain isothermally at 90 °C for 5 min, (b) cool from 90 °C to 7 °C at 1 °C min<sup>-1</sup>, (c) equilibrate at 7 °C for 5 min, (d) warm from 7 °C to 90 °C at 1 °C min<sup>-1</sup>. The oscillation frequency  $f$  and oscillation stress  $\tau$  were fixed at 1 Hz and 0.1 Pa, respectively. An amplitude stress sweep was performed from 0.01 Pa to 100 Pa at a fixed  $f$  of 1 Hz, from which the stress where  $G' = G''$  is termed the dynamic yield stress ( $\tau_Y$ ). A frequency sweep was done from 0.01 Hz to 10 Hz within the LVR. The measuring geometry was cleaned with ethanol before use.

#### 2.2.5.6 Surface tension

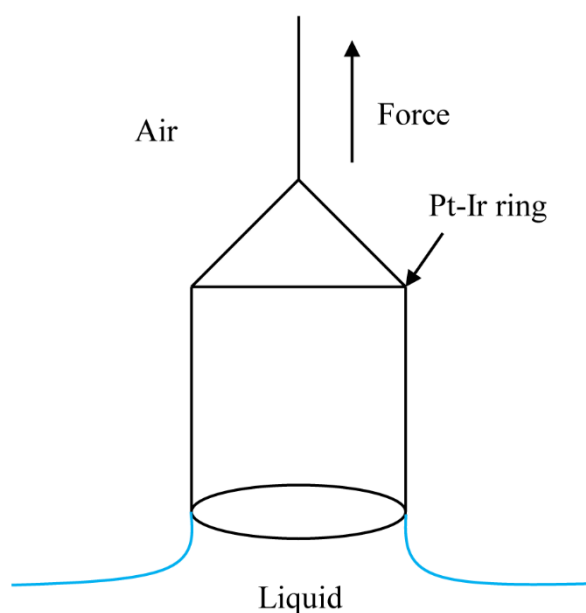
The du Noüy ring<sup>24</sup> is an alternative to the Wilhelmy plate for the determination of surface and interfacial tensions (Figure 2.15). When the ring is pulled up through the interface, the force  $F$  measured by a balance goes through a maximum  $F_{max}$ , which is related to the surface tension of the liquid. The surface tension is given as,

$$\gamma_{la} = \frac{F_{max}}{4\pi r\alpha} \quad (2.28)$$

where  $r$  is the radius of the ring and  $\alpha$  is the correction factor related to the ring geometry and the liquid density.

Air-oil surface tensions at different temperatures were determined using the Krüss K11 tensiometer and the du Noüy ring method. The instrument was calibrated with Milli-Q water of surface tension  $72.5 \pm 0.2$  mN m<sup>-1</sup> at 20 °C. An oil solution/dispersion was first held at the target temperature in a water bath and then transferred into a Petri dish surrounded by a silicone oil jacket in the tensiometer at the same temperature (Grant R1 thermostat). After each measurement, the ring was rinsed with ethanol and heated to glowing in a blue Bunsen flame.

**Figure 2.15.** Schematic of the du Noüy ring method.



#### 2.2.5.7 Contact angle determination

When a drop of liquid is placed on a solid substrate in bulk, *e.g.* gas, there is a relationship between the equilibrium three phase contact angle ( $\theta$ ), the surface tension of the liquid  $\gamma_{la}$ , the surface free energy of the solid  $\gamma_{sa}$  and the interfacial tension between the liquid and solid  $\gamma_{ls}$  (Figure 2.16). This relationship can be described by Young's equation,

$$\cos \theta = \frac{\gamma_{sa} - \gamma_{ls}}{\gamma_{la}} \quad (2.29)$$

When the bulk phase is another liquid *L*, the Young's equation can be expressed as,

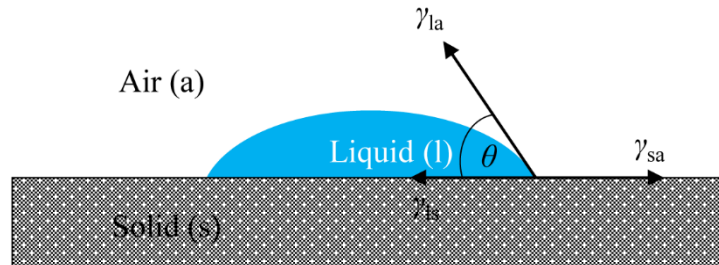
$$\cos \theta = \frac{\gamma_{sL} - \gamma_{ls}}{\gamma_{lL}} \quad (2.30)$$

where  $\gamma_{sL}$  is the interfacial tension between the bulk liquid and solid and  $\gamma_{lL}$  is the interfacial tension between the two liquids.

For irregular and polydisperse particles, it is difficult to directly measure the contact angle at a liquid surface so disks of SE powder (diameter, 13 mm) were made by compressing  $\sim 400$  mg of powder in a steel die using a hydraulic press (Research and Industrial Instrument Co., UK) with a weight of 10 tons. Contact angles were measured using a Krüss DSA Mk 10 apparatus at room temperature. The oil-water contact angle was measured by firstly placing the disk in a cubical quartz cell (dimension,  $2 \times 2 \times 2$  cm) and then filling the cell with oil. Subsequently, a drop of water ( $\sim 10 \mu\text{L}$ ) was gently placed on the surface of the disk and the contact angle was measured through water. For the oil-air contact angle, a drop of oil ( $\sim 10 \mu\text{L}$ )

was added onto the surface of a SE disk and then the contact angle in air was measured through oil. At least five separate measurements were taken.

**Figure 2.16.** Schematic of the three-phase contact angle between a liquid droplet on a solid substrate in air.



#### 2.2.5.8 Temperature-controlled optical microscopy

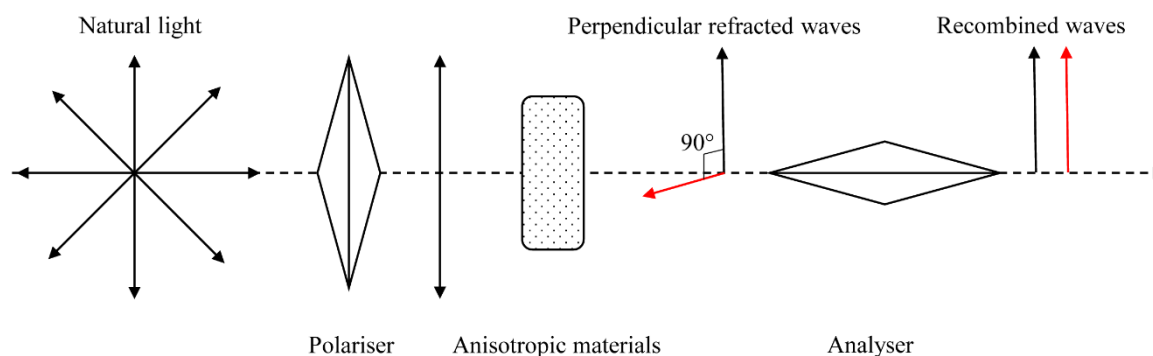
In polarized microscopy, two polarizers are equipped to cross-polarize transmitted light. The first one is set before the sample, whilst the second one also called an analyser is positioned between the sample and eyepiece in the light path.<sup>3,25</sup> The intensity of passed light  $I$  through two polarizers can be quantitatively described by the Malus law,

$$I = I_0 \times \cos^2 \theta \quad (2.31)$$

where  $I_0$  is the intensity of light reaching the first polarizer and  $\theta$  is the angle between the transmission axes of the polarizer and analyser. When the polarisers are crossed (*i.e.*  $\theta = 90^\circ$ ), the intensity of passable light is zero.

During natural light transmission, electromagnetic waves can vibrate in all planes perpendicular to the direction of propagation. After passing through the first polariser, the light vibrates only in the direction parallel to the polariser orientation. Upon travelling through anisotropic materials, it is split into two directions which are perpendicular to each other and to the direction of light propagation. At last, the analyser perpendicular to the polariser can recombine the two beams of waves to achieve maximum contrast, Figure 2.17.

**Figure 2.17.** Schematic illustrating transmission of light through crossed polarisers and anisotropic materials. Adapted from ref. 25.



Optical microscopy was performed using a Leica DME optical microscope mounted with a Leica MC190 HD camera. A polarizer (13596080) and an analyzer were used to cross-polarize transmitted light. Images were acquired by Leica Application Suite 4.12.0 software. A drop of a sample ( $\sim 10 \mu\text{L}$ ) was transferred by a spatula onto the middle of a glass slide ( $76 \text{ mm} \times 26 \text{ mm}$ ) with a single circular cavity ( $15 \text{ mm}$ ), and then covered gently with a thin coverslip ( $24 \text{ mm} \times 24 \text{ mm}$ ) unless otherwise stated. The temperature of the glass slide was adjusted by a temperature-controlled stage (Linkam PE120) connected to a digital controller (Linkam T95PE). All microscopic images were analyzed with ImageJ software (1.47V) calibrated with a Pyser-sgi limited graticule. The number average droplet/bubble diameter was calculated from at least 100 representative droplets/bubbles. To give insight into the microstructure of foam bubbles or emulsion droplets, dilution was applied. A small amount of sample was transferred into a glass vial by a spatula, and continuous phase of the same temperature was then added followed by gentle agitation to ensure the droplets/bubbles were evenly dispersed. The viscosity of the diluted sample was low such that it could be easily spread on the glass slide. Both non-polarised and polarised microscopy images were taken for each sample.

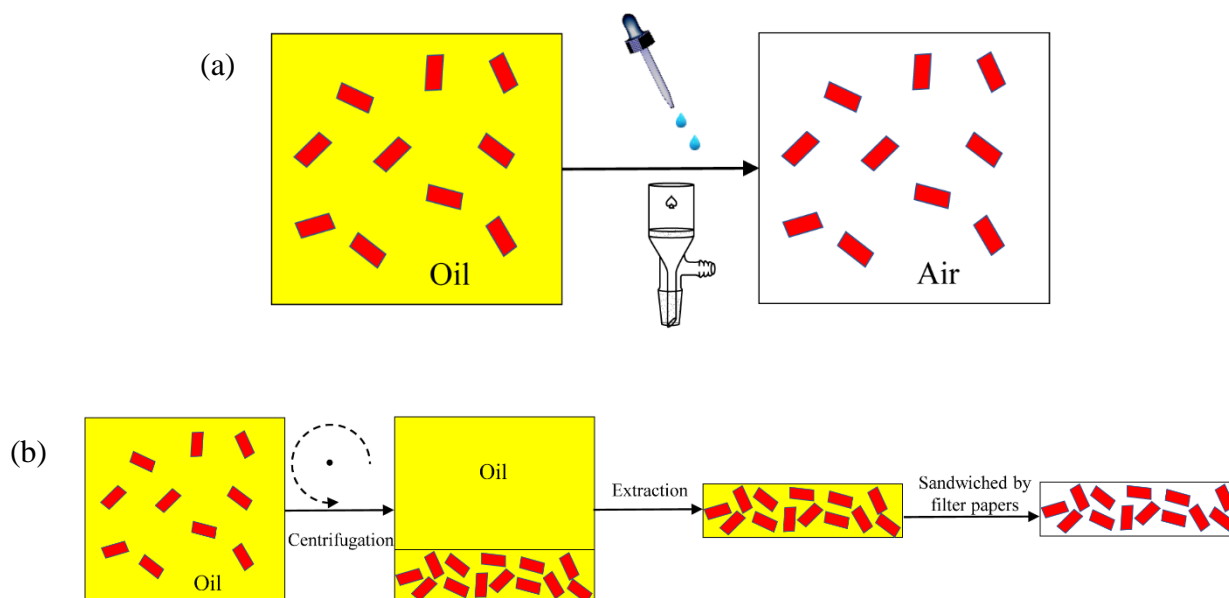
#### 2.2.5.9 Separation of surfactant crystals

##### 2.2.5.9.1 Filtration and solvent washing

The technique of filtration and solvent washing was adapted from refs. 26 and 27. For neat oil, it was maintained at  $-20^\circ\text{C}$  overnight ( $\sim 12 \text{ h}$ ), followed by warming gradually to  $8 \pm 1^\circ\text{C}$  to yield a crystal dispersion. Subsequently, it was filtered through a filter disc (Sartorius 393, diameter:  $70 \text{ mm}$ , pore size:  $1 \mu\text{m}$ ) fitted in a Büchner funnel with a vacuum flask, which

was connected to a portable vacuum pump (Diaphragm MZ 2C, Germany). The whole filtration process was carried out in a cool room of  $7 \pm 1$  °C. The initial solvent-free vacuum filtration lasted for ~ 30 min, and the filtrate was washed gently with *n*-hexane to remove entrained liquid oil and left to dry overnight (~ 12 h). For an oil dispersion containing surfactant crystals, it was transferred onto a filter paper fitted in the Büchner funnel, which was then fixed into the vacuum flask connected to the vacuum pump. To discard excess oil, isobutanol was gradually dropped on the remaining sample (~20:1, v/v) and then left to dry at room temperature for ~ 60 h, Figure 2.18(a).

**Figure 2.18.** Schematic illustrating techniques to separate fat/surfactant crystals. (a) Filtration and solvent washing, (b) centrifugation.



#### 2.2.5.9.2 Centrifugation

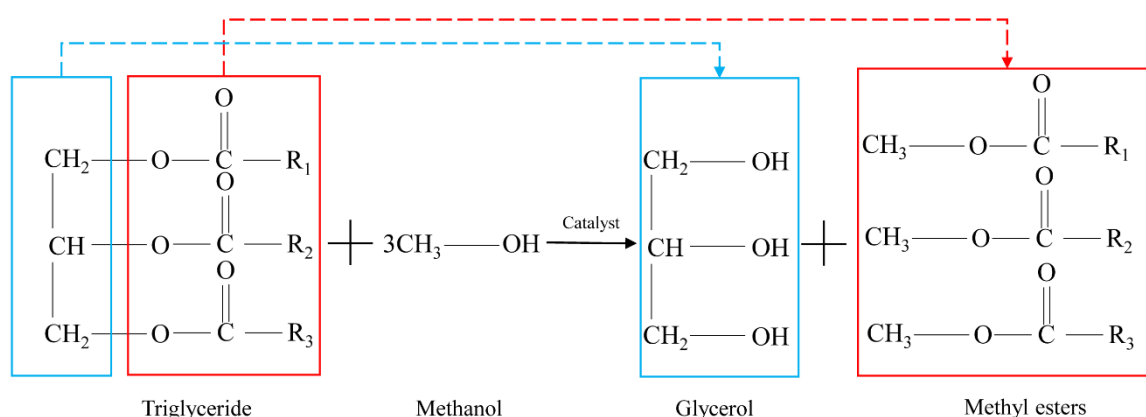
For an oil dispersion or oil foam, a sample tube (Sarstedt, 14 mL) containing the sample was centrifuged (Sorvall Lengend X1, 42124392) at 10,000 rpm for 5 min. The supernatant was discarded, and the remaining part was extracted using a spatula followed by spreading on a filter paper (Sartorius 393). Another filter paper was applied to sandwich the sample, subsequently being compressed gently to remove remaining oil, Figure 2.18(b).

#### 2.2.5.10 Synthesis of FAMES and analysis by GC/MS

FAMES were obtained through the catalytic trans-esterification method as described by the EU official method (Figure 2.19).<sup>28</sup> The FAME samples were submitted to a 1:100 dilution with *n*-hexane before GC/MS analysis. The FAME composition was separated in a Restek Rxi-

5 MS capillary column (30 m (length)  $\times$  0.25 mm (internal diameter)  $\times$  0.25  $\mu\text{m}$  (film thickness)) in an Agilent 6890 + GC coupled to an Agilent 5973 N MSD quadrupole MS. The oven temperature was held initially at 70  $^{\circ}\text{C}$  for 1 min after injection, and adjusted to 300  $^{\circ}\text{C}$  at 15  $^{\circ}\text{C min}^{-1}$  and held for 30 min. The sample was injected at the split injection mode with a split ratio of 25:1, and the carrying gas was helium at a rate of 1  $\text{mL min}^{-1}$ . The injector temperature was 260  $^{\circ}\text{C}$  and the injection volume was 1  $\mu\text{L}$ . MS detector conditions were positive mode electron ionisation at 70 eV, ion source temperature at 210  $^{\circ}\text{C}$  and quad temperature at 150  $^{\circ}\text{C}$ . The MS spectrum was compared with data from the NIST library.

**Figure 2.19.** Schematic illustrating the catalytic trans-esterification method.



#### 2.2.5.11 Cryo-SEM

The preparation protocols varied depending on the sample type. The filter paper containing surfactant crystals was glued on a copper holder and transferred to the cryo-preparation chamber (PP3010T) to freeze at -140  $^{\circ}\text{C}$ . In the case of a foam or an emulsion, a channelled aluminium stub containing the sample was immersed into liquid nitrogen before being transferred to the cryo-preparation chamber at -140  $^{\circ}\text{C}$ . A scalpel was then used to fracture the frozen sample exposing the interior structure. After these initial preparations, the samples were coated with platinum ( $\sim 2$  nm film thickness) and then transferred to the cold stage of the SEM instrument at -140  $^{\circ}\text{C}$  and imaged. Imaging was performed with the LaB6 emitter, 40 microamp beam current, 15 kV accelerating voltage and a 35 picoamp probe current using a secondary electron detector.

#### 2.2.5.12 XRD

XRD was performed using the diffractometer described above and all operating settings remained unchanged. Sample mounting varied depending on the type of the sample. The separated surfactant crystals were mounted as a paste on an aluminium disc. For gelled samples,

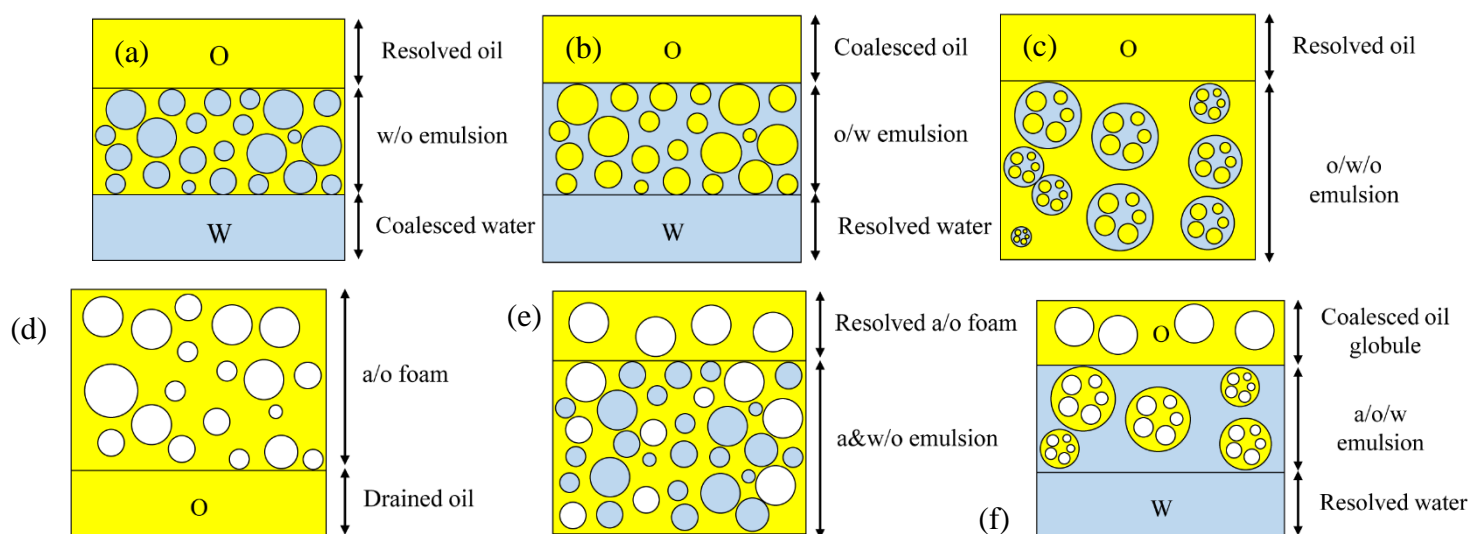
e.g. oil foam, emulsion and foamulsion, it was mounted with a spatula into a sample holder and then back filled against a polished steel disc to obtain a flat surface.

#### 2.2.5.13 Drop test and stability assessment

For various emulsions, such as simple and multiple emulsions, the emulsion type was inferred by the drop test. Oil continuous emulsions disperse in oil and remain as drops in water and *vice versa*. The stability of water continuous emulsions to creaming was assessed by monitoring the position of the clear water-emulsion interface, whilst the extent of coalescence was obtained from the movement of the oil-emulsion boundary. For oil continuous emulsions, the stability to sedimentation was indicated by the downward movement of the oil-emulsion boundary, whereas the position of the water-emulsion interface was recorded as an indicator of coalescence.<sup>29</sup> Meanwhile, the droplet size was recorded as a function of aging time. An increase in the droplet size implied the occurrence of coalescence and/or Ostwald ripening.

In the case of foams, the volume of foam, volume of drained oil and foam bubble size were recorded as a function of storage time. To quantify foam stability, foam half-life  $t_{1/2}$ , time for complete foam collapse and volume ratio of foam/drained oil on storage to that initially were determined. An increase in the bubble size indicated the occurrence of coalescence and/or coarsening. The possible morphologies of various colloidal materials on storage are schematically shown in Figure 2.20.

**Figure 2.20.** Schematic illustrating possible appearance of various colloidal materials during long term storage. (a) w/o emulsion, (b) o/w emulsion, (c) o/w/o emulsion, (d) a/o foam, (e) a and w/o emulsion, (f) a/o/w emulsion.



### *2.2.6 Statistical analysis*

Statistical analysis was performed using IBM SPSS Statistics (ver. 25). All experiments were performed at least 3 times unless otherwise stated and data is expressed as average  $\pm$  standard deviation. Comparisons were made using one-way analysis of variance (ANOVA) or t-test depending on the number of points investigated.  $p < 0.05$  was considered significantly different.

## 2.3 References

1. S. Kurata, K. Yamaguchi and M. Nagai, Rapid discrimination of fatty acid composition in fats and oils by electrospray ionization mass spectrometry, *Anal. Sci.*, 2005, **21**, 1457–1465.
2. G. Beltrán, C. del Rio, S. Sánchez and L. Martínez, Influence of harvest date and crop yield on the fatty acid composition of virgin olive oils from cv. Picual, *J. Agric. Food Chem.*, 2004, **52**, 3434–3440.
3. A.G. Marangoni, *Fat Crystal Networks*, CRC Press, Boca Raton, 2005.
4. G.W.H. Höhne, W.F. Hemminger and H.-J. Flammersheim, *Differential Scanning Calorimetry*, Springer, Berlin, 2003.
5. Y. Waseda, E. Matsubara and K. Shinoda, *X-Ray Diffraction Crystallography: Introduction, Examples and Solved Problems*, Springer, Berlin, 2011.
6. A.C.T. Teixeira, A.R. Garcia, L.M. Ilharco, A.M.P.S. Gonçalves da Silva and A.C. Fernandes, Phase behaviour of oleanolic acid, pure and mixed with stearic acid: interactions and crystallinity, *Chem. Phys. Lipids*, 2010, **163**, 655–666.
7. S. Thomas, R. Thomas, A.K. Zachariah and R.K. Mishra, *Spectroscopic Methods for Nanomaterials Characterization*, 1st ed., Elsevier, 2017, ch. 4.
8. R. Shaw, *Dynamic Light Scattering Training*, Malvern Instruments: Malvern, 2014.
9. *Zetasizer nano user manual*, Malvern, 2010.
10. J. Stetefeld, S.A. McKenna and T.R. Patel, Dynamic light scattering: a practical guide and applications in biomedical sciences, *Biophys. Rev.*, 2016, **8**, 409–427.
11. D.J. Shaw, *Introduction to Colloid and Surface Chemistry*, Butterworths, London, 1968, ch. 7.
12. L.E. Franken, E.J. Boekema and M.C.A. Stuart, Transmission electron microscopy as a tool for the characterization of soft materials: application and interpretation, *Adv. Sci.*, 2017, **4**, 1600476.
13. R.J. Hunter, *Foundation of Colloid Science*, Oxford Press, New York, 2nd ed., 2001.
14. C.W. Macosko, *Rheology: Principles, measurements, and applications*, VCH, New York, 1994.
15. L. Wilhelmy, Ueber die abhängigkeit der capillaritäts-constanten des alkohols von substanz und gestalt des benetzten festen körpers, *Ann. Phys.*, 1863, **195**, 177–217.
16. C.D. Volpe and S. Siboni, The Wilhelmy method: a critical and practical review, *Surf. Innov.*, 2018, **6**, 120–132.

17. A.L. Fameau, S. Lam, A. Arnould, C. Gaillard, O.D. Velez and A. Saint-Jalmes, Smart nonaqueous foams from lipid-based oleogel, *Langmuir*, 2015, **31**, 13501–13510.
18. B.P. Binks, E.J. Garvey and J. Vieira, Whipped oil stabilised by surfactant crystals, *Chem. Sci.*, 2016, **7**, 2621–2632.
19. Y. Liu and B.P. Binks, Foams of vegetable oils containing long-chain triglycerides, *J. Colloid Interface Sci.*, 2021, **583**, 522–534.
20. D.Z. Gunes, M. Murith, J. Godefroid, C. Pelloux, H. Deyber, O. Schafer and O. Breton, Oleofoams: Properties of crystal-coated bubbles from whipped oleogels-evidence for Pickering stabilization, *Langmuir*, 2017, **33**, 1563–1575.
21. K. Mishra, D. Dufour and E.J. Windhab, Yield stress dependent foaming of edible crystal-melt suspensions, *Cryst. Growth Des.*, 2020, **20**, 1292–1301.
22. A.L. Fameau and A. Saint-Jalmes, Recent advances in understanding and use of oleofoams, *Front. Sustain. Food Syst.*, 2020, **4**, article 110.
23. M.C.M. Gribnau, Determination of solid/liquid ratios of fats and oils by low-resolution pulsed NMR, *Trends Food Sci. Technol.*, 1992, **3**, 186–190.
24. P.L. du Noüy, A new apparatus for measuring surface tension, *J. Gen. Physiol.*, 1919, **1**, 521–524.
25. D.B. Murphy and M.W. Davidson, *Fundamentals of Light Microscopy and Electronic Imaging*, 2nd ed., Wiley-Blackwell, New Jersey, 2013.
26. N.C. Acevedo and A.G. Marangoni, Characterization of the nanoscale in triacylglycerol crystal networks, *Cryst. Growth Des.*, 2010, **10**, 3327–3333.
27. A.M. Fitzgerald, O.J. Barnes, I. Smart and D.I. Wilson, Measurement of particle size distribution of tripalmitin crystals in a model solution using a laser diffraction method, *J. Am. Oil Chem. Soc.*, 2001, **78**, 1013–1020.
28. European Union Commission. Regulation EEC 2568/91 on the characteristics of olive oil and olive pomace and their analytical methods, 1991.
29. B.P. Binks and S.O. Olusanya, Pickering emulsions stabilized by coloured organic pigment particles, *Chem. Sci.*, 2017, **8**, 708–723.

## CHAPTER 3 – FOAMS OF VEGETABLE OILS CONTAINING LONG-CHAIN TRIGLYCERIDES

### 3.1 Introduction

Recently, oil foams find applications in the food industry because of their potential in reducing saturated fat intake, providing more desirable mouthfeel, and reducing delivery costs.<sup>1,2</sup> The approaches for preparing ultra-stable edible oil foams are developed on the basis of oleogels, during which a homogeneous solution of an edible emulsifier in vegetable oil is first submitted to a specific tempering procedure to yield an oleogel, followed by mechanical energy input to generate an air-in-oil foam stabilized by pre-formed crystals.<sup>2,3</sup> The potential stabilizing agents can be crystals of mono- and/or diglycerides,<sup>4-8</sup> fatty alcohols,<sup>9</sup> fatty acids,<sup>10</sup> high-melting triglycerides (TAGs)<sup>11-15</sup> and their mixtures.<sup>7,16,17</sup> The first study on the stabilization of vegetable oil foams by high-melting fat crystals was reported by Mishima *et al.*<sup>11</sup> Small  $\beta$ -fat crystals were proven to be a pre-requisite for preparing well-whipped salad oil. More importantly, the arrangement of TAG crystals near the air-oil interface was determined by synchrotron radiation microbeam X-ray diffraction (SR- $\mu$ -XRD). Later, Binks and Marinopoulos<sup>12</sup> reported on the foaming potential of neat coconut oil and other vegetable oils composed of medium-chain fatty acids, in the absence of any additive. Oil foams are not necessarily the final products, however. Most recently, oil foams formed from anhydrous milk fat were used as intermediates to prepare air-in-oil-in-water emulsions, which paved the way for developing novel oil foam-based colloidal systems with new functionalities.<sup>13</sup> All the above-mentioned cases involving the preparation of edible oil foams were dependent on pre-formed crystals.

Up to now, investigations on oil foams stabilized by high-melting fat crystals are still limited, and the stabilization mechanisms are far from well understood. In this chapter, we explore the possibility of foaming neat vegetable oils containing long-chain, unsaturated fatty acids, *i.e.* refined peanut oil (RPO) and extra virgin olive oil (EVOO), in the absence of any added foaming agent. RPO is abundant in unsaturated fatty acids (UFAs), including oleic (C18:1, O) and linoleic (C18:2, L). It also contains saturated fatty acids (SFAs) being palmitic (C16:0, P), stearic (C18:0, S) and behenic (C22:0, Be). EVOO is mainly composed of oleic and palmitoleic (C16:1, Po). The main triglycerides are OOL, OLL, OOO, POO and POL for RPO whilst OOL, OOO, POO, POL plus SLL for EVOO.<sup>18,19</sup> The size, morphology, polymorph type and concentration of crystals play a dominant role in foam formation and stabilisation,<sup>2,3</sup> so we first apply different temperature-time dependent tempering protocols to

induce the formation of high-melting fat crystals within a continuous liquid oil phase. Different methods including visual observation, differential scanning calorimetry, solid fat content, rheology and microscopy are utilised to give insight into the characteristics of crystal dispersions or oil gels before whipping. Subsequently, the foaming efficiency and stability are evaluated as a function of aeration temperature, and further correlated to the physicochemical properties of samples before whipping. High-melting fat crystals contributing to foaming are extracted and analysed by GC/MS. Finally, we investigate the influence of temperature on an initially ultra-stable foam as it approaches the melting point of triglyceride crystals.

## 3.2 Crystallisation and melting behaviour of vegetable oils

### 3.2.1 Appearance

The effect of temperature on the crystallisation and melting of the oils was preliminarily investigated by visual observations. The samples were either cooled gradually from 60 °C at 0.3 °C min<sup>-1</sup> or warmed at 0.4 °C min<sup>-1</sup> from -20 °C in the water bath. Photos of RPO at representative temperatures upon cooling and warming are shown in Figure 3.1(a) and Figure 3.2(a), respectively. On cooling, it is a clear, yellowish liquid above 5 °C. The first evidence of crystallisation appears at 4 °C ( $T_{\text{crystal,onset}}$ ) where the sample turns slightly cloudy. With further supercooling ( $\Delta T = T - T_{\text{crystal,onset}}$ , where  $T$  is the target temperature)<sup>20</sup>, it becomes more turbid and viscous. On reaching the minimum gelling temperature ( $T_g$ )<sup>21</sup> of ~ -5 °C, the sample does not flow when the vessel is inverted. There is no further change in sample appearance when cooling down to -20 °C. Upon warming, the sample remains gelled up to 3 °C, although it gradually softens. A noticeable change occurs at ~ 4 °C where it becomes a flowing viscous dispersion. As the temperature increases further, the sample becomes less turbid, and finally transits back to a clear liquid at 13 °C and higher.

The appearance evolution of EVOO with temperature is illustrated in Figure 3.1(b) and Figure 3.2(b). As expected, the first sign of solidification occurs at a lower temperature compared to RPO, *i.e.* ~ -9 °C, due to a higher proportion of unsaturated fatty acids (UFAs) in the former. It then develops into an oil gel at -12 °C, a few °C lower than the crystallisation temperature  $T_{\text{crystal,onset}}$ . When heating, the transition from a firm gel to a flowing dispersion occurs around 8 °C, followed by the appearance of a clear, dark yellow liquid at 11 °C. Hysteresis exists between cooling and warming of both oils, as reported earlier.<sup>12</sup> This is due to the fact that TAG nucleation during cooling requires an activation energy which is absent for TAG crystal melting.<sup>22,23</sup> Additionally, the transitions between different crystal polymorphs induced by different tempering protocols may account for this difference.<sup>22,23</sup> The driving force

for fat crystallization can be characterised by the difference between the crystallization temperature and the global melting temperature, *i.e.* the highest temperature at which solid phases can survive upon warming.<sup>23</sup> It appears that the driving force for EVOO crystallisation ( $\sim 19\text{ }^{\circ}\text{C}$ ) is significantly larger than that for RPO crystallisation ( $\sim 8\text{ }^{\circ}\text{C}$ ).

**Figure 3.1.** Appearance of vials containing (a) RPO and (b) EVOO upon cooling from  $60\text{ }^{\circ}\text{C}$  at  $0.3\text{ }^{\circ}\text{C min}^{-1}$ . Inset: tilted vial. Scale bars = 1 cm.

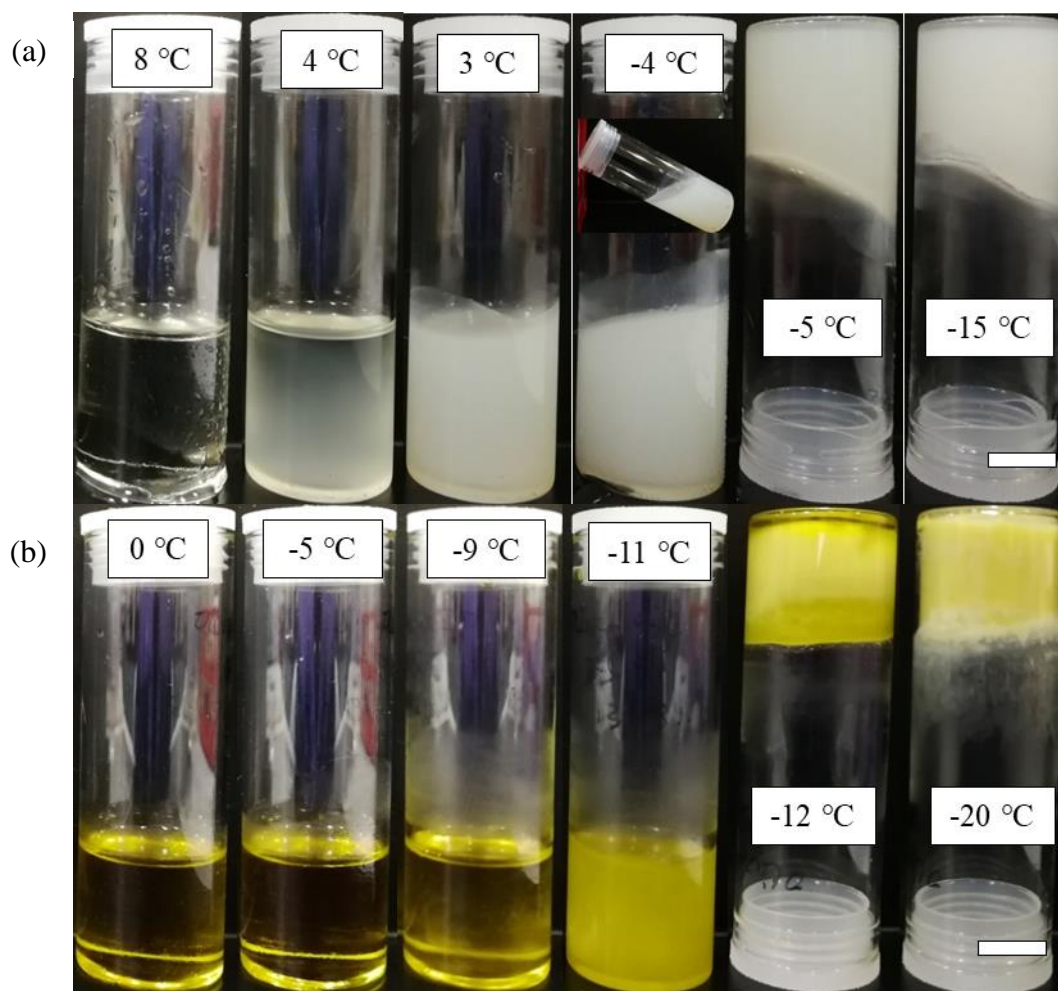
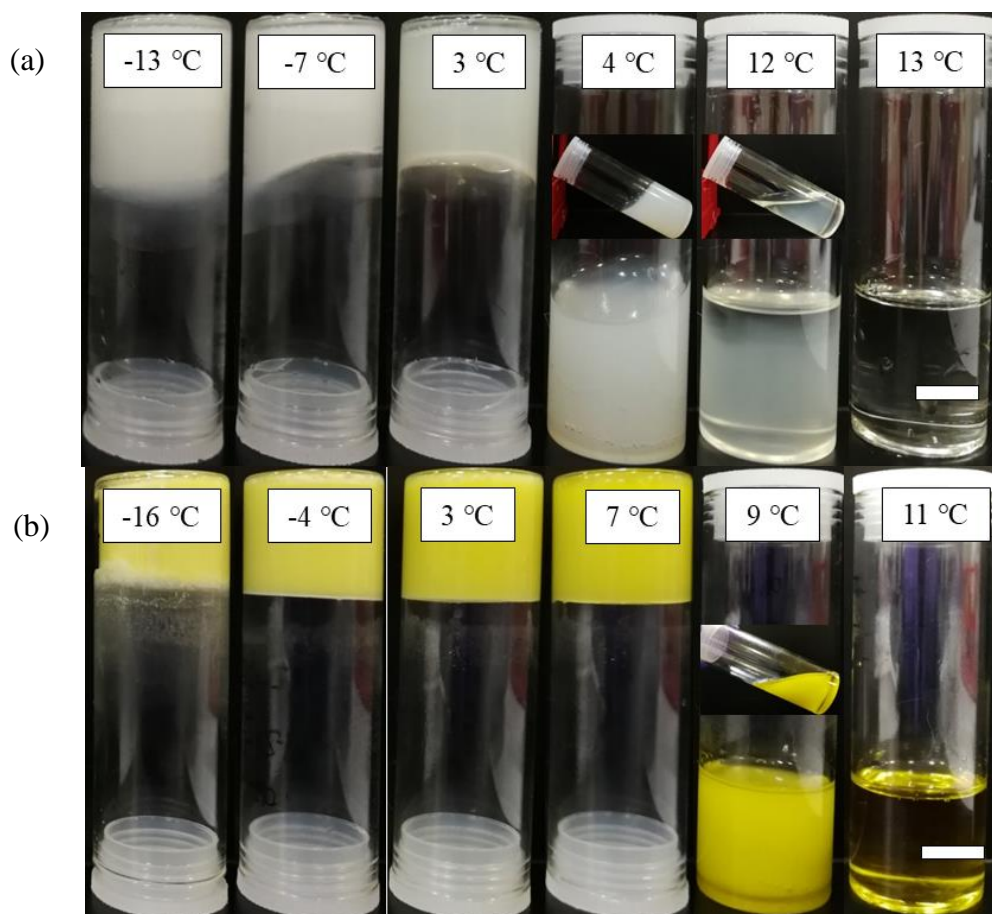


**Figure 3.2.** Appearance of vials containing (a) RPO and (b) EVOO upon warming from -20 °C at 0.4 °C min<sup>-1</sup>. Inset: tilted vials. Scale bars = 1 cm.



### 3.2.2 Thermal properties and SFC

Thermal analysis was carried out using DSC as shown in Figure 3.3(a) for RPO and Figure 3.3(b) for EVOO. In the case of RPO, the first exothermic event occurs at 2.6 °C during cooling, implying the onset of crystallisation. One distinct exothermic peak is observed at -0.2 °C which is mainly attributed to the crystallization of high-melting, di-saturated triglyceride fractions,<sup>24,25</sup> e.g. PPL, PPO, PSL, PSO, PLBe.<sup>18</sup> Three distinguishable endothermic peaks can be detected from the melting curve. The prominent one occurs at 10.5 °C, whereas the two minor ones are at -16.9 °C and -2.6 °C, respectively. Chen Man and Tan<sup>26,27</sup> reported similar phase transition temperatures of peanut oil at 1 °C min<sup>-1</sup>. Nevertheless, the polymorphic forms of peanut oil crystals during phase transitions are still unclear. The cooling thermogram of EVOO displays one distinct exothermic peak but at a lower temperature of -14.3 °C, and the first crystallisation event starts at -11.5 °C.<sup>24-27</sup> This phenomenon implies the emergence of  $\beta'$  polymorph crystals during cooling.<sup>25</sup> Upon heating, two well-defined endothermic peaks are

identified at 6.6 °C and -6.0 °C. A less evident endothermic peak is also observed at 2.6 °C. The peak at -6.0 °C indicates the transformation of the metastable  $\beta'$  form into the more stable  $\beta$  form during warming, whilst the other two peaks represent the melting of  $\beta'$  crystals.<sup>25</sup> The thermal properties of RPO and EVOO are summarised in Table 3.1.

**Figure 3.3.** DSC curves for (a) RPO and (b) EVOO upon cooling (lower) and subsequent warming (upper). Cooling and warming rates were 0.5 °C min<sup>-1</sup>.

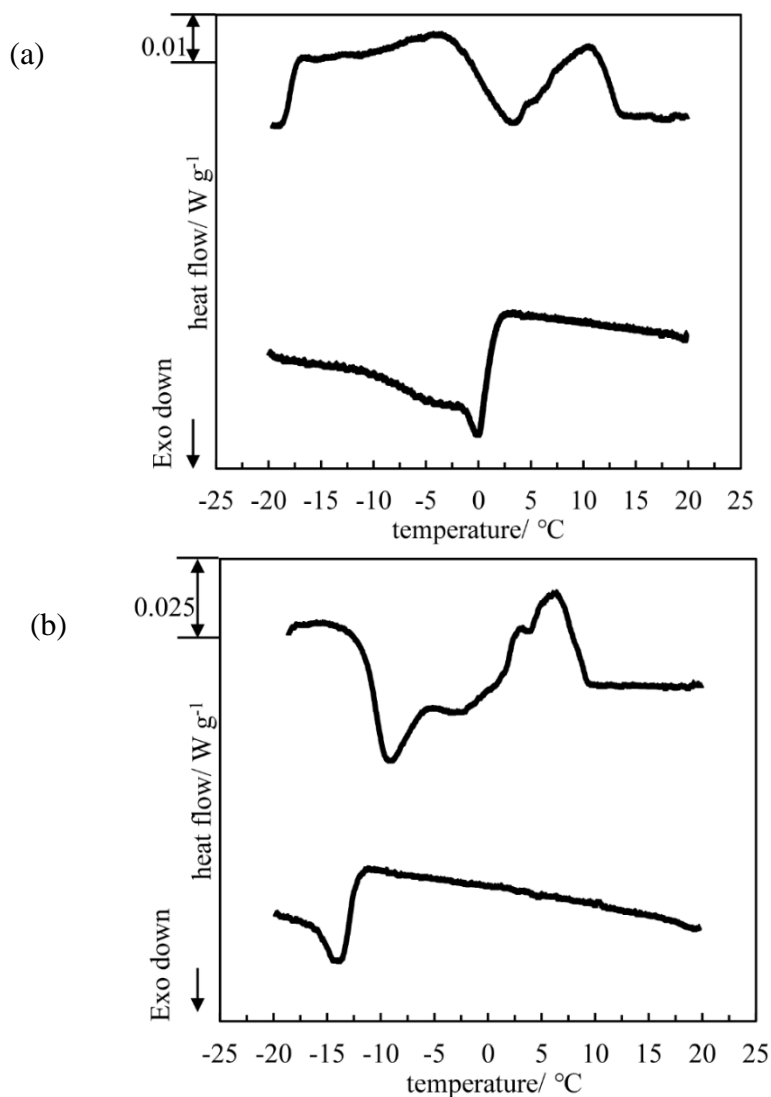


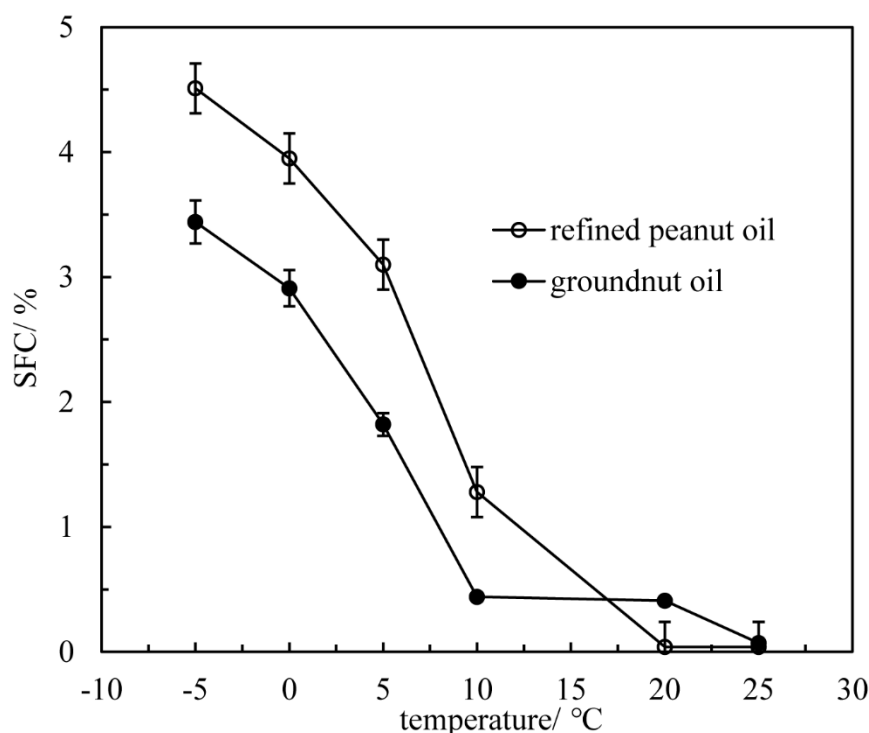
**Table 3.1.** Thermal properties of RPO and EVOO.

Crystallisation				Melting			
$T_{\text{peak}}/^{\circ}\text{C}$	$\Delta H/\text{J g}^{-1}$	$T_{\text{peak}}/^{\circ}\text{C}$			$\Delta H/\text{J g}^{-1}$		
		Peak 1	Peak 2	Peak 3	Peak 1	Peak 2	Peak 3
R <sup>a</sup>	-0.20±0.15    -1.99±0.18	-16.9±0.10	-2.60±0.06	10.52±0.04	—	0.89±0.08	1.81±0.03
E <sup>b</sup>	-14.25±0.64    -1.27±0.15	-6.02±0.42	2.60±0.19	6.60±0.14	0.32±0.04	0.14±0.00	0.89±0.16

<sup>a</sup> RPO; <sup>b</sup> EVOO

In order to quantify the mass fraction of fat crystals at different temperatures for one of the oils, pulsed-NMR was applied. Figure 3.4 shows that the SFC values of RPO and groundnut oil increase with a decrease in temperature, especially at temperatures lower than 10 °C. This is because a higher degree of supercooling tends to accelerate the kinetics of triglyceride nucleation and growth.<sup>22,23</sup> The minimum SFC to form an oil gel for RPO is ~ 4.5%, similar to the values ( $\leq 5\%$ ) of other oleogel systems.<sup>10,21,28</sup>

**Figure 3.4.** Variation of SFC with temperature for RPO (open points) and groundnut oil (filled points).



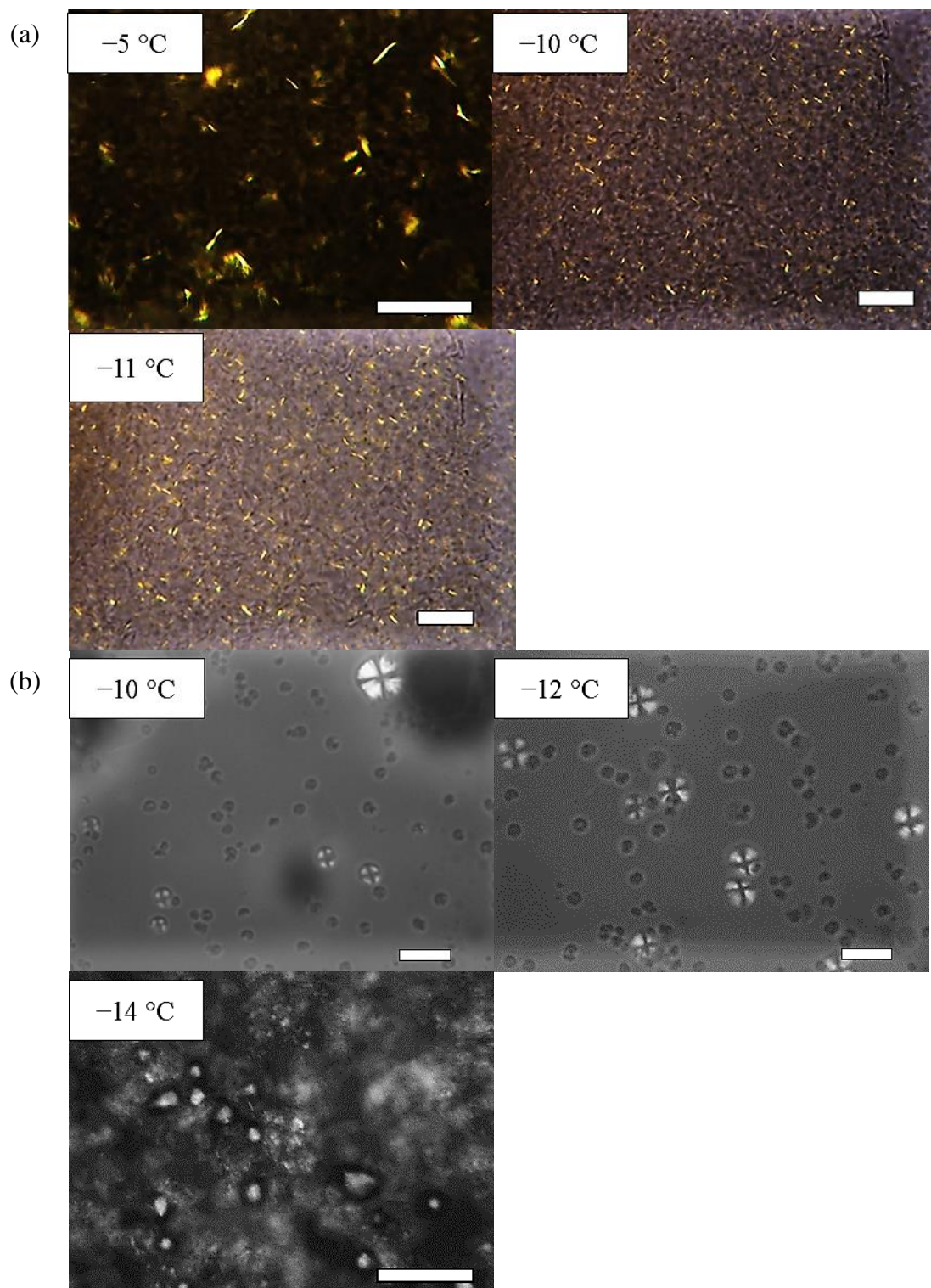
### 3.2.3 Crystal morphology and rheological properties

Figure 3.5(a) presents the polarised micrographs of RPO obtained at different temperatures cooled slowly from 60 °C. RPO crystals are revealed as needle-like in geometry, as observed previously with groundnut oil,<sup>29</sup> of size smaller than 10  $\mu\text{m}$ . With decreasing temperature more crystals tend to form and disperse within the isotropic liquid oil due to a higher degree of supercooling. Upon reaching temperatures below  $T_g$  of -5 °C, individual fat crystals interact with each other mainly through van der Waals forces, producing a three-dimensional crystal network or an oil gel.

EVOO crystals are different to those of RPO, as seen in Figure 3.5(b). No crystal forms at -6 °C (not shown), but further cooling leads to polydisperse spherical crystals of size between

5 and 40  $\mu\text{m}$  with characteristic Maltese crosses, reminiscent of anhydrous milk fat crystals reported by Goibier *et al.*<sup>13</sup>

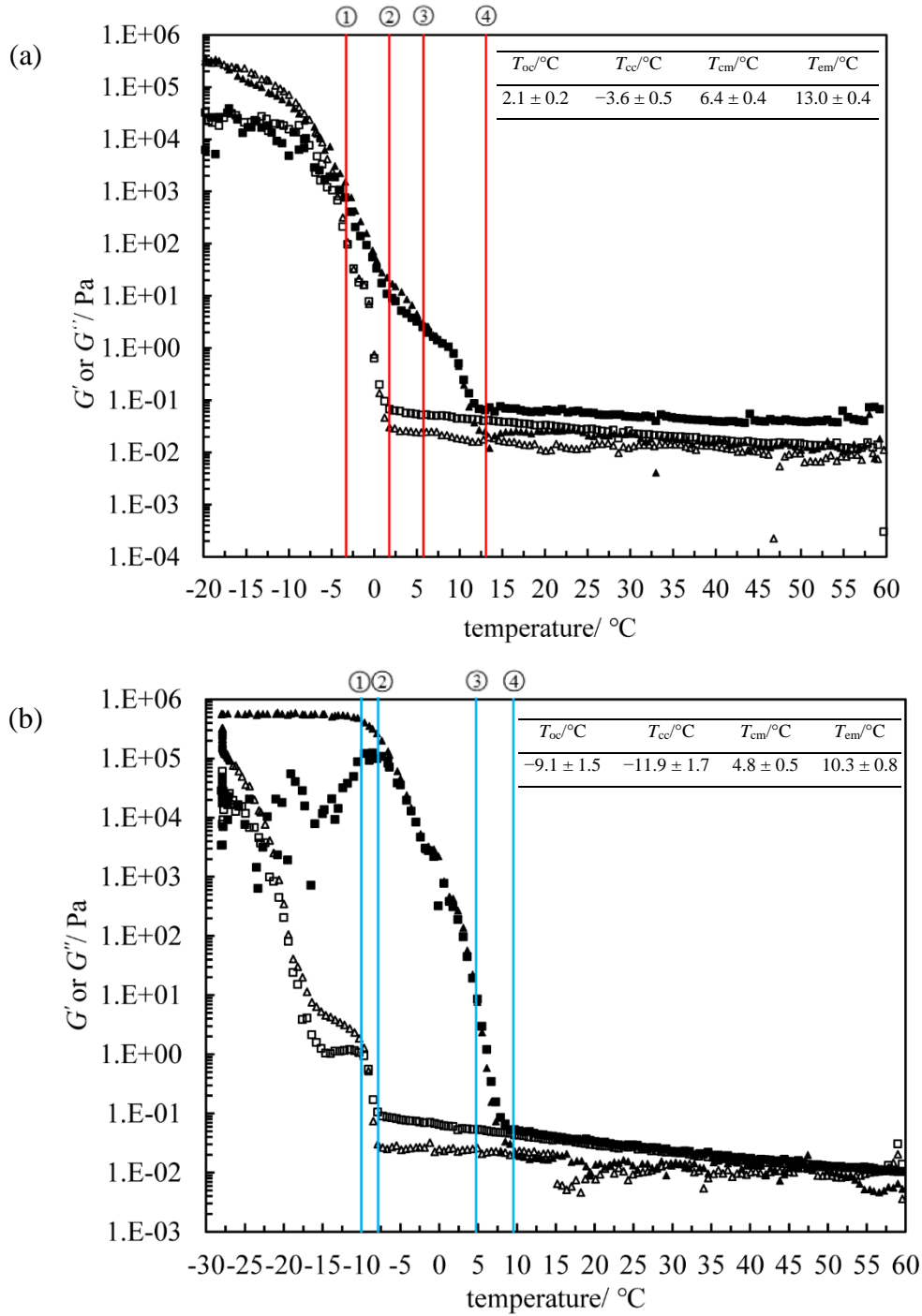
**Figure 3.5.** Polarised micrographs of (a) RPO and (b) EVOO at certain temperatures upon cooling from 60  $^{\circ}\text{C}$  at 0.3  $^{\circ}\text{C min}^{-1}$ . Scale bars equal 50  $\mu\text{m}$  except for the first one which is 25  $\mu\text{m}$ .



The rheological properties of neat oils were investigated by cooling from 60 °C to -20 °C or lower at 1 °C min<sup>-1</sup>, maintaining isothermally at low temperature for 10 min before warming to 60 °C at 1 °C min<sup>-1</sup> in a temperature-controlled rheometer using parallel plates. The viscoelasticity ( $G'$  and  $G''$ ) of RPO is recorded as a function of temperature in Figure 3.6(a). During cooling, initially both  $G'$  and  $G''$  are low ( $< 0.1$  Pa) with  $G' < G''$  corresponding to a weak liquid. A sudden increase in both parameters at  $\sim 2$  °C denotes the onset of crystallisation, followed by a monotonic increase with decreasing temperature during which the sample transforms gradually from liquid-like ( $G' < G''$ ) to solid-like ( $G' > G''$ ). The extracted crossover temperature of  $G'/G''$  ( $T_{cc}$ ) is comparable to  $T_g$  obtained from visual observations. Finally, for temperatures  $< -8$  °C,  $G'$  increases slowly until it reaches around  $5 \times 10^5$  Pa. In this region, the value of  $G''$  is approximately one order of magnitude smaller than  $G'$ , and almost independent of temperature. This viscoelastic development is similar to that reported by Ojijo *et al.* for monoglyceride/olive oil mixtures.<sup>30</sup> Upon heating from -20 °C,  $G'$  and  $G''$  firstly exhibit a progressive decrease, followed by an abrupt decrease until eventually remaining constant in the range of 0.1 Pa. The sample deteriorates from an elastic solid ( $G' > G''$ ) into a viscous liquid with ( $G' < G''$ ) during heating, arising from the gradual melting of triglyceride crystals.

The variation of  $G'$  and  $G''$  with temperature for EVOO is shown in Figure 3.6(b). EVOO is a weak liquid initially with  $G'$  and  $G'' < 0.1$  Pa. Crystallisation starts at  $\sim -9$  °C as evidenced by a sudden increase in both parameters. Subsequently they increase significantly down to the final temperature of -28 °C, and are still developing during the isothermal period. When submitted to heating,  $G'$  remains almost constant at temperatures  $< -11$  °C with  $G' > G''$  possibly arising from the absence of melting events (see Figure 3.3(b)), which is different from the melting behaviour of RPO. Further heating leads to an abrupt decrease in  $G'$  and  $G''$ , and finally a liquid-like state where both values are  $< 0.1$  Pa. Based on the above analysis, we conclude that the crystallisation and melting behaviour determined by different methods are in agreement.

**Figure 3.6.** Variation of  $G'$  (triangles) and  $G''$  (squares) upon cooling (open points) and subsequent warming (filled points) of (a) RPO and (b) EVOO. Cooling and warming rates were  $1\text{ }^{\circ}\text{C min}^{-1}$ . Lines are: ①  $T_{cc}$  - crossover temperature ( $G' = G''$ ) of crystallisation during cooling; ②  $T_{oc}$  - onset temperature of crystallisation during cooling; ③  $T_{cm}$  - crossover temperature ( $G' = G''$ ) of crystal melting during warming; ④  $T_{em}$  - end temperature of melting during warming. Inset: critical temperatures summarised from three independent tests.



### 3.3 Preparation and characterisation of vegetable oil foams

Oil samples of 100 mL were either cooled from 60 °C or warmed from -20 °C to temperatures of interest. Subsequent whipping was applied with a double beater electric whisk for 45 min in total, *i.e.* 5 min whipping followed by 5 min rest interval. We first evaluated the foaming ability as a function of whipping time. Then, the effect of whipping temperature on both foamability and foam stability was studied.

#### 3.3.1 Effect of whipping time

When subjected to cooling, the aeration of RPO was first carried out at four representative temperatures (6 °C, 3 °C, -5 °C and -21.5 °C) corresponding to different stages of crystallisation (liquid, fluid dispersion, soft gel and firm gel respectively). Figure 3.7(a) and Figure 3.8(a) present the appearance evolution of aerated RPO at 3 °C and at the other temperatures, respectively. Clear oil at 6 °C is unwhippable, with no change in volume upon whipping. For the fluid crystal dispersion at 3 °C and the soft gel at -5 °C, a milky white appearance becomes more pronounced as whipping proceeds due to an increasing extent of air incorporation. At -21.5 °C however, whipping initially involves breaking the firm gel into a viscous paste, followed by introducing air into the viscoelastic matrix. In the case of EVOO, the appearance with whipping time at selected temperatures during cooling can be seen in Figure 3.7(b) and Figure 3.8(b). Between -4 °C and -8 °C, the starting samples are clear, dark yellow liquids. Upon cooling gradually from -10 °C to -14 °C, they develop from a slightly turbid dispersion to a soft gel and then a firm gel. Upon whipping, no change in appearance occurs at -4 °C. For lower temperatures, the samples are initially yellow and become increasingly white as more air is incorporated. To quantitatively describe the extent of air incorporation during whipping, Figure 3.7(c) and Figure 3.7(d) plot the over-run as a function of whipping time for RPO and EVOO, respectively. For the former system, the over-run increases at first and then levels off at -21.5 °C and -5 °C, while for 3 °C the value increases continuously up to 45 min, similar to the aeration behaviour of coconut oil at 23 °C.<sup>12</sup> The over-run is zero at 6 °C where no fat crystals are present, in agreement with the non-foaming behaviour of coconut oil<sup>12</sup> and anhydrous milk fat<sup>13</sup> above their crystallisation temperatures. Thus, molecules of triglyceride in these oils are not surface-active at the oil-air surface. The variation of the over-run of EVOO with whipping time is also temperature dependent. At -8 °C the over-run increases progressively with whipping time. At all other temperatures except -4 °C, the over-run exhibits a significant increase up to 35 min, followed by no further change.

**Figure 3.7.** Appearance of oils as a function of whipping time at representative temperatures cooled from 60 °C at 0.3 °C min<sup>-1</sup>. (a) RPO at 3 °C and (b) EVOO at -10 °C. The degree of supercooling  $\Delta T = -1$  °C for both systems. Inset: photos taken from above. Scale bars = 1 cm. Over-run *versus* whipping time for (c) RPO and (d) EVOO at particular temperatures cooled from 60 °C at 0.3 °C min<sup>-1</sup>.

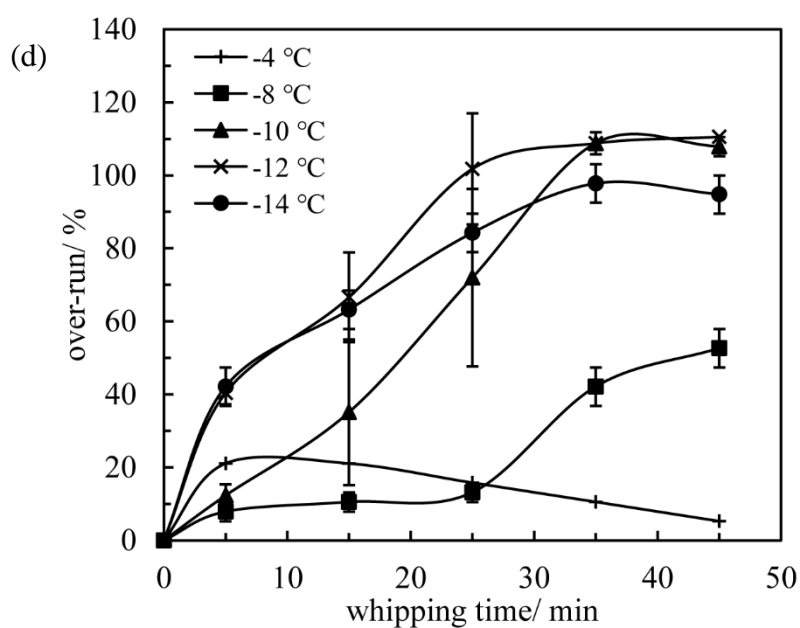
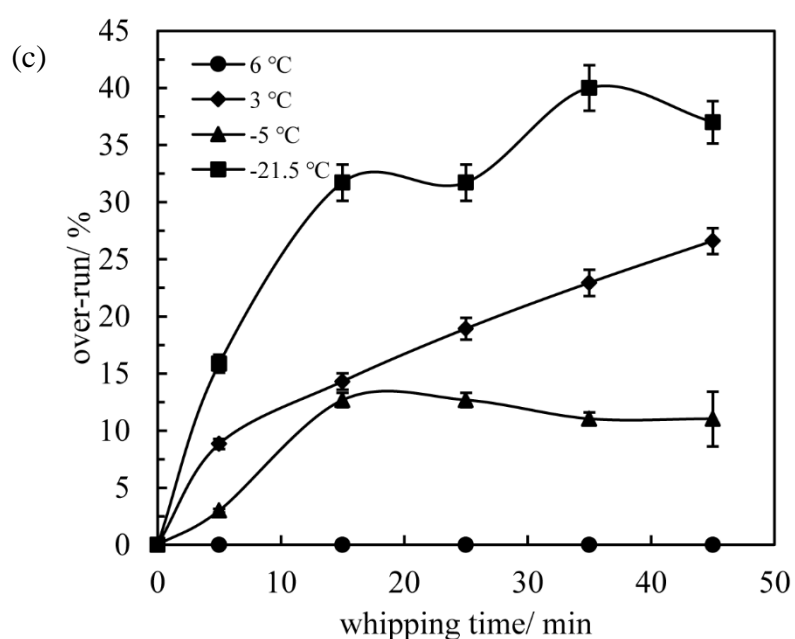
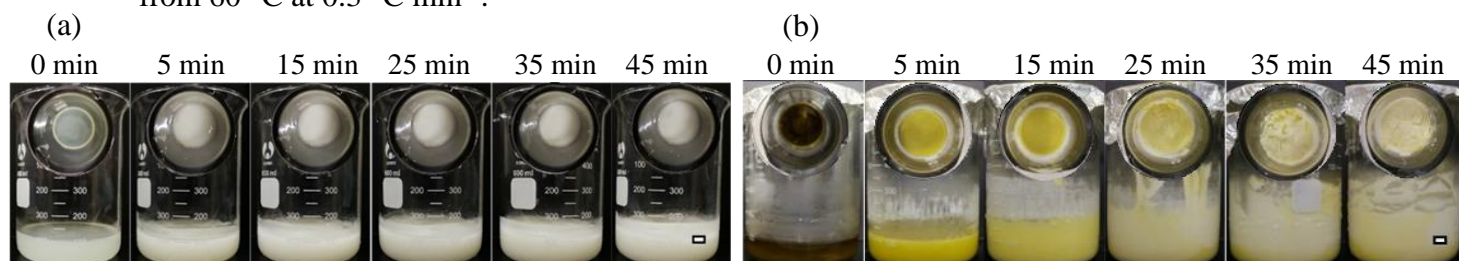
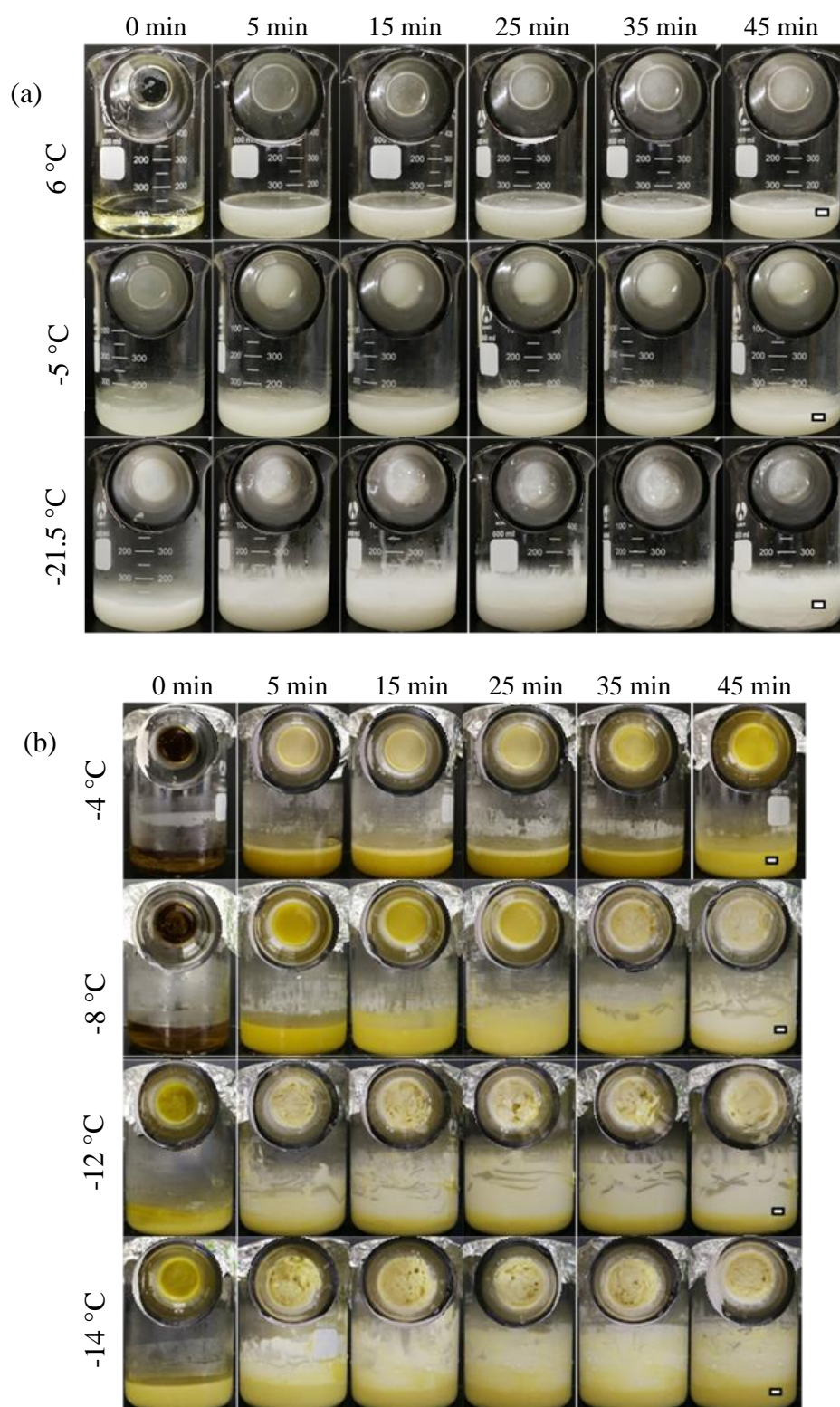


**Figure 3.8.** Appearance of (a) RPO and (b) EVOO as a function of whipping time at particular temperatures cooled from 60 °C at 0.3 °C min<sup>-1</sup>. Inset: photos taken from above. Scale bars = 1 cm.



For a cold sample of RPO subjected to warming, their appearance and over-run values during whipping are given in Figure 3.9. Similar to the whipping of the firm gel at -21.5 °C during cooling, the energy input from the double beater is mainly involved in softening the gel prior to enabling effective air incorporation at -20 °C. At the other temperatures, foaming is achieved once whipping is started. The over-run values of whipped RPO at 3 °C show a gradual increase with aeration time, whereas for the fluid dispersion at 6 °C it increases to a plateau followed by a slight decrease as a result of inefficient network stabilisation in the continuous oil phase against drainage and coalescence during whipping.<sup>5</sup> At the other two temperatures, the over-run increases up to 15 min and then remains almost constant up to 45 min. The maximum over-run is ~ 38% at -20 °C.

For EVOO during heating (see Figure 3.10), at -12 °C and -6 °C the first 15 min whipping serves to soften the firm gel, but subsequent whipping is responsible for effective air incorporation. The soft oil gels at 0 °C and 6 °C can be whipped easily, and the over-run values increase up to 15 min then remain constant. No air incorporation occurs at 12 °C as expected. The maximum over-run is ~ 110% at -12 °C to -6 °C.

**Figure 3.9.** (a) Appearance of RPO as a function of whipping time at particular temperatures warmed from  $-20\text{ }^{\circ}\text{C}$  at  $0.4\text{ }^{\circ}\text{C min}^{-1}$ . Inset: photos taken from above. Scale bars = 1 cm. (b) Over-run *versus* whipping time for systems in (a).

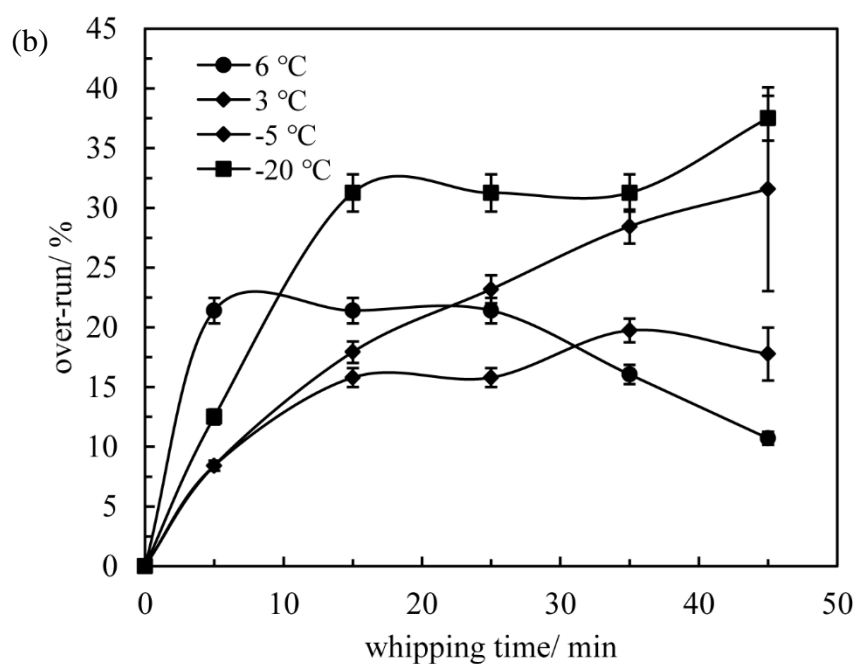
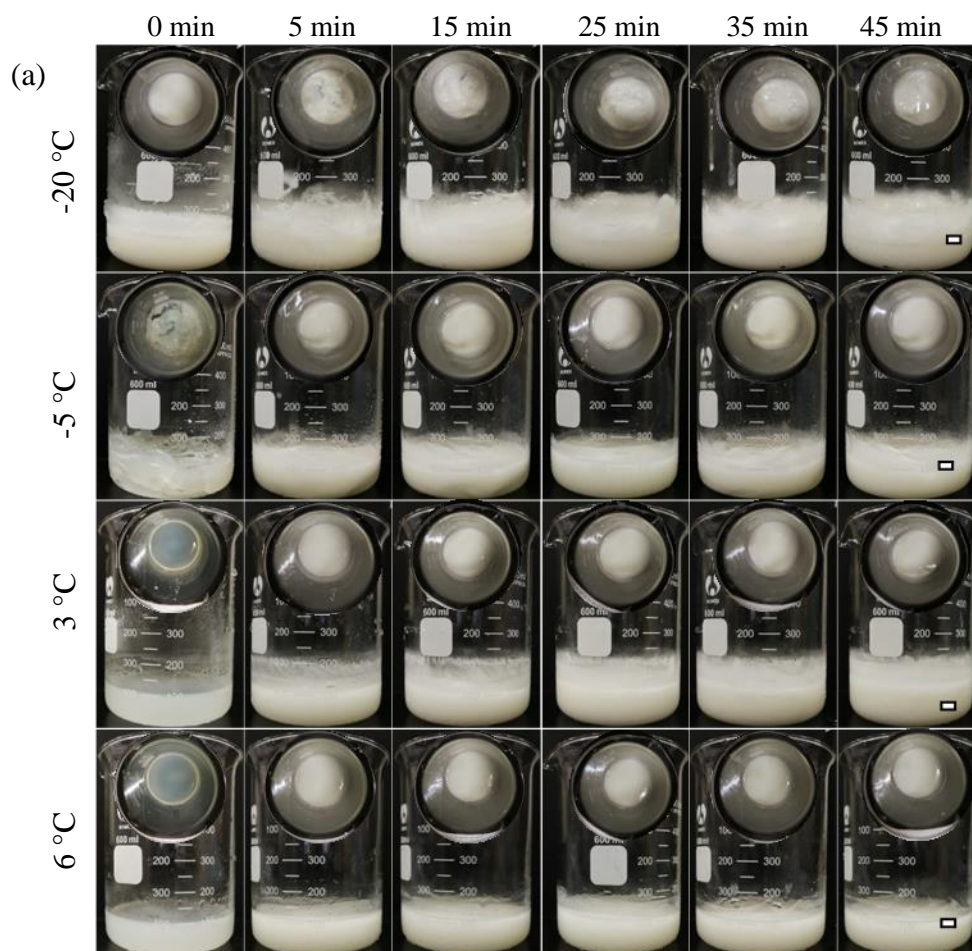
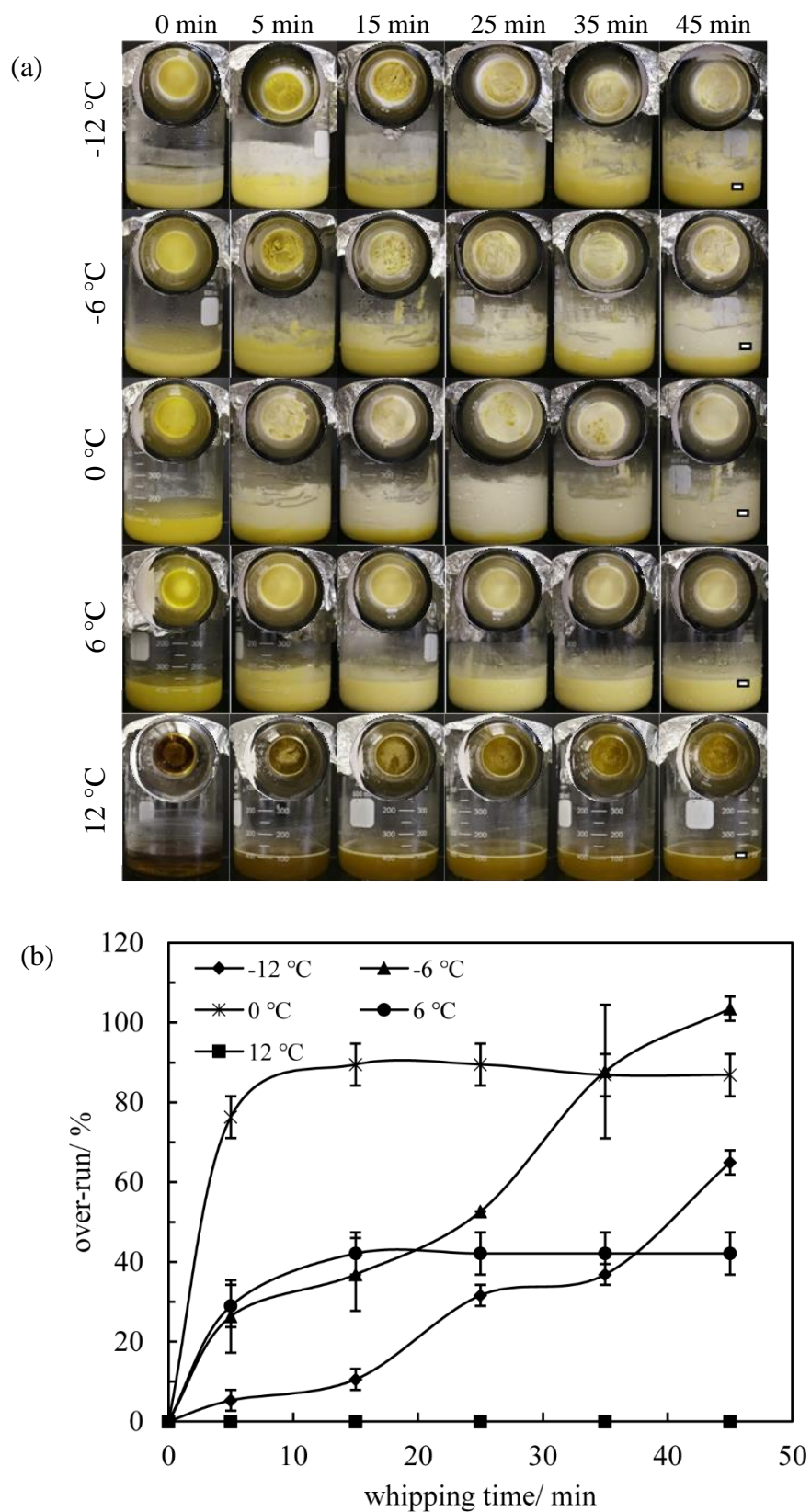


**Figure 3.10.** (a) Appearance of EVOO as a function of whipping time at particular temperatures warmed from  $-20\text{ }^{\circ}\text{C}$  at  $0.4\text{ }^{\circ}\text{C min}^{-1}$ . Inset: photos taken from above. Scale bars = 1 cm. (b) Over-run *versus* whipping time for systems in (a).

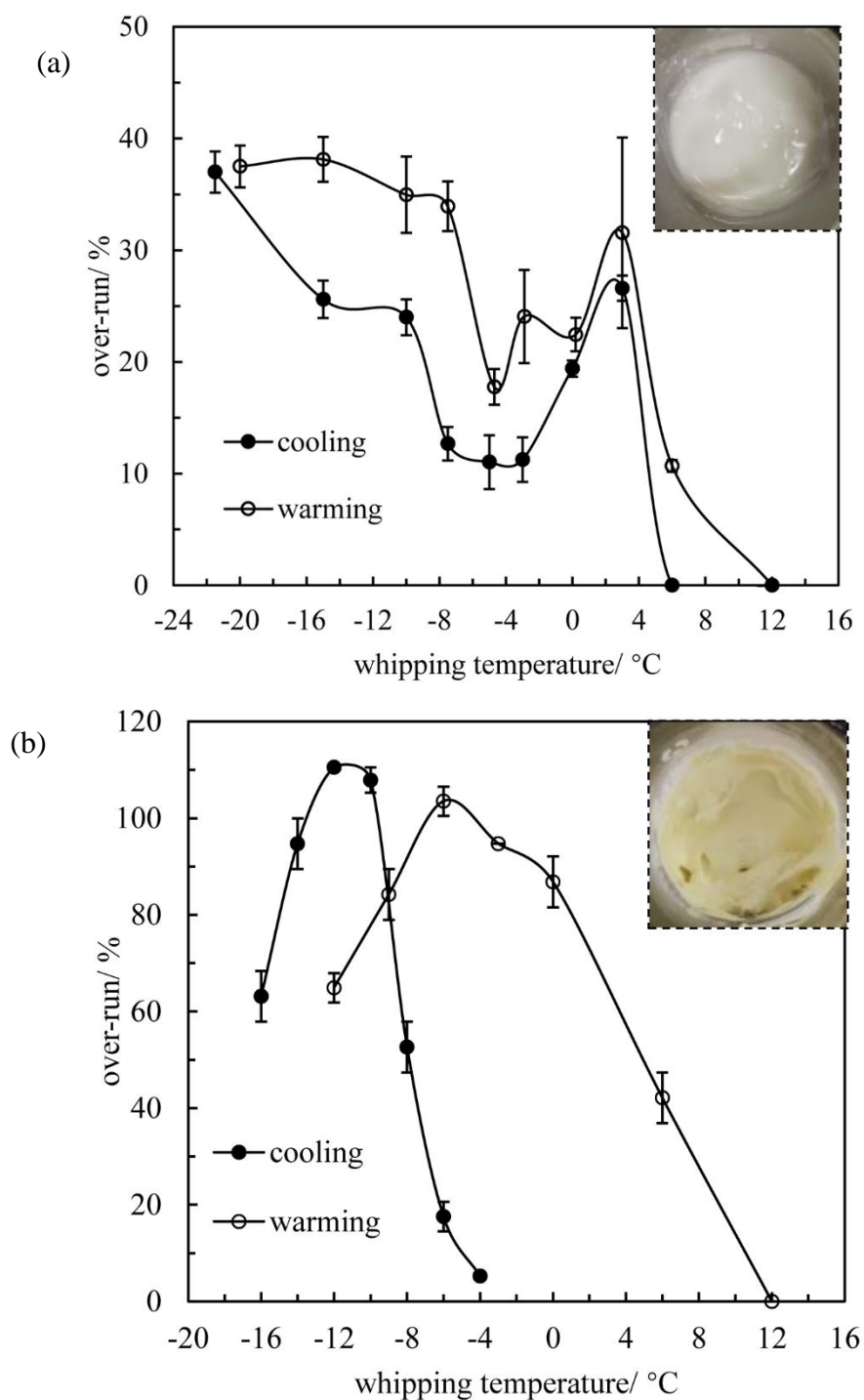


### 3.3.2 Effect of whipping temperature

The over-run of aerated RPO immediately after 45 min whipping is plotted as a function of aeration temperature in Figure 3.11(a) for samples cooled and warmed. The inset in Figure 3.11(a) is a photograph of RPO foam produced at  $-15\text{ }^{\circ}\text{C}$  upon cooling. Not surprisingly, no foam is obtained above the crystallisation temperature during cooling (filled points) since triglyceride molecules are not surface-active at the air-oil interface.<sup>11-13</sup> A marked maximum in foamability occurs at  $\sim 3\text{ }^{\circ}\text{C}$  from a fluid crystal dispersion where the degree of supercooling  $\Delta T = -1\text{ }^{\circ}\text{C}$ .<sup>20</sup> This is in line with the findings of Heymans *et al.*<sup>6</sup> where the best foaming was achieved from partially crystallised monoglyceride in sunflower oil, but contradicts the conclusions of Gunes *et al.*<sup>5</sup> where weak gels were unable to provide effective continuous oil phase stabilisation against drainage and coalescence during whipping for monoglyceride/high oleic sunflower oil mixtures. Some plausible explanations exist for this discrepancy. Firstly, a less viscous crystal dispersion enables more effective air incorporation during whipping.<sup>31</sup> Secondly, the introduction of new air-oil interfaces upon whipping can provide locations where nucleation and crystal growth of triglyceride molecules can occur, thus protecting incorporated air bubbles.<sup>32,33</sup> Last but not least, our observations can be rationalised by an abrupt increase in the air-oil surface tension near the onset of crystallisation as described by Mishra *et al.*<sup>20</sup> arising from the adsorption of solid triglyceride. When the sample was cooled below  $3\text{ }^{\circ}\text{C}$ , we notice a dramatic decrease in the over-run until near  $T_g$  ( $-5\text{ }^{\circ}\text{C}$ ,  $p < 0.05$ ). This is because a significant increase in the viscosity of the continuous phase hinders air incorporation.<sup>10,31</sup> Further cooling down to  $-21.5\text{ }^{\circ}\text{C}$  results in a noticeable increase in the over-run from  $\sim 10\%$  to  $\sim 37\%$  ( $p < 0.05$ ). The effect of gel rheology on the foaming of monoglycerides in vegetable oils was studied by Gunes *et al.*<sup>5</sup> and Heymans *et al.*<sup>6</sup> The former found that the most suitable range of  $G'$  for foaming was  $10^5 - 10^7\text{ Pa}$ , whereas the latter found that a gradual increase in  $G'$  from  $10^3\text{ Pa}$  to  $10^5\text{ Pa}$  resulted in higher air fraction from 5 min whipping. We suggest that in our case increased foamability at lower temperatures ( $< -5\text{ }^{\circ}\text{C}$ ) arises from an increase in  $G'$  of oil gels before aeration. In foaming of RPO upon warming (open points), the variation of over-run with aeration temperature is similar but with higher values. The difference may be attributed to different crystal sizes and polymorphs induced by the two tempering procedures, as reported in previous studies<sup>11,28</sup> since melting-mediated tempering tends to yield smaller  $\beta$ -fat crystals resulting in better foamability. The effect of whipping temperature on the over-run of whipped EVOO also displays a maximum as shown in Figure 3.11(b). The highest over-run on cooling ( $\sim 110\%$ ) is achieved near  $T_g$ , *i.e.*  $-12\text{ }^{\circ}\text{C}$  and  $\Delta T = -3\text{ }^{\circ}\text{C}$ . During heating, foaming can be

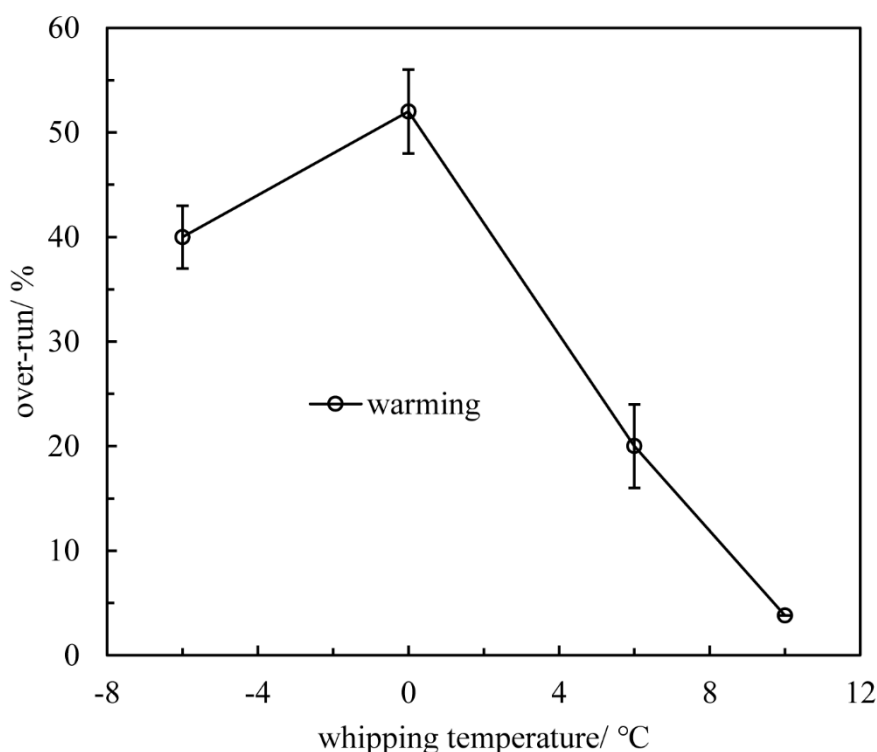
achieved over a wider range of temperature, and the maximum is shifted to a higher temperature. The inset in Figure 3.11(b) is the appearance of EVOO foam fabricated at  $-12\text{ }^{\circ}\text{C}$  during cooling.

**Figure 3.11.** Over-run of (a) RPO foams and (b) EVOO foams after 45 min whipping as a function of whipping temperature upon cooling (filled points) and warming (open points). Inset: photos of RPO foam at  $-15\text{ }^{\circ}\text{C}$  and EVOO foam at  $-12\text{ }^{\circ}\text{C}$  cooled from  $60\text{ }^{\circ}\text{C}$  at  $0.3\text{ }^{\circ}\text{C min}^{-1}$ .



A noticeable difference exists between RPO and EVOO regarding the foaming capacity. The maximum over-run of whipped EVOO is  $\sim 110\%$ , much higher than that of  $\sim 38\%$  for whipped RPO. The maximum volume fraction of air for EVOO foams is  $\sim 0.55$  which is similar to that in previous work<sup>4,10,12</sup> and close to the random close packing fraction of monodisperse hard spheres of 0.64. One possible reason for the difference is that the size and morphology of RPO and EVOO crystals differ (Figure 3.5).<sup>14</sup> In addition, RPO is refined with minor polar components whereas EVOO is unrefined with a variety of polar components including free fatty acids, monoglycerides and polyphenols.<sup>34</sup> We suggest that the driving force for the adsorption of triglyceride crystals to the air-EVOO interface is larger than that for RPO as the minor components of EVOO probably increase its polarity.<sup>11,35</sup> Moreover, in oil foams stabilised by a mixture of fat and molecular foaming agent, interfacial templating crystallisation occurs, leading to smaller bubble size and improved foam stability.<sup>7</sup> To test this hypothesis, raw EVOO was passed twice through a basic alumina column to remove polar impurities prior to whipping. As expected, whipped columned EVOO exhibits a significantly lower over-run (max.  $\sim 50\%$ , see Figure 3.12) than that of raw EVOO (max.  $\sim 110\%$ ,  $p < 0.05$ ), supporting our suggestion.

**Figure 3.12.** Over-run of foams from columned EVOO after 45 min whipping as a function of whipping temperature warmed from  $-20\text{ }^{\circ}\text{C}$  at  $0.4\text{ }^{\circ}\text{C min}^{-1}$ .



Optical microscopy and cryo-SEM were used to investigate the microstructure of RPO and EVOO foams. As shown in Figure 3.13, RPO foam bubbles are polydisperse and spherical, and their surfaces are slightly rough and textured due to the adsorption of crystals, in line with the findings of Saremnejad *et al.*<sup>8</sup> In the case of EVOO foams, some bubbles are non-spherical however, implying jamming of trapped crystals at their surfaces hindering shape relaxation to spherical.<sup>10,11</sup> In addition, a birefringent layer(s) coating the bubbles can be identified by polarised microscopy. Cryo-SEM images of fresh foams at -10 °C during cooling are given in Figure 3.13(d). They reveal that the surfaces of RPO foam bubbles are less textured than those of EVOO. It further suggests that the coverage of bubbles by crystals is higher for EVOO than RPO (see Figure 3.22 later).<sup>36</sup> The average bubble diameter of aerated RPO decreases with decreasing whipping temperature, from ~ 130 µm at 3 °C to ~ 80 µm at -7.5 °C (Figure 3.14(a)). By contrast, that for EVOO foams is ~ 25 µm and almost independent of aeration temperature (Figure 3.14(b)), similar to that in Brun *et al.*<sup>4</sup> (10 – 50 µm), Mishima *et al.*<sup>11</sup> (20 – 35 µm), Binks and Marinopoulos<sup>12</sup> (20 – 30 µm) and Mishra *et al.*<sup>14</sup>

The arrangement of high-melting triglyceride crystals near the air-oil surface and in the continuous phase has been determined through elegant micro-XRD experiments.<sup>11</sup> The faces of triglyceride crystals at bubble surfaces are oriented parallel to the air-oil surface, whilst those within the continuous oil phase are randomly arranged. According to Friberg *et al.*,<sup>37</sup> the prerequisite for spontaneous adsorption of a particle to an air-oil surface is that its surface energy is lower than that of oil. In fact, the surface tension of methyl groups (-CH<sub>3</sub>) is *ca.* 23 mN m<sup>-1</sup> whilst that of methylene groups (-CH<sub>2</sub>) is *ca.* 28 mN m<sup>-1</sup>. Based on the above, we suggest that an energy-favourable configuration is such that the methyl groups of triglyceride crystal faces interact with both the air and oil phases, whereas their edges mainly composed of methylene and glycerol groups interact with other edges of adjacent adsorbed triglyceride crystals (*via* van der Waals forces and hydrogen bonds), see Figure 3.22 later.

**Figure 3.13.** Non-polarised micrographs of (a) RPO foams and (b) EVOO foams. (c) Polarised micrographs and (d) cryo-SEM images of RPO foams (left) and EVOO foams (right). Scale bars of optical micrographs equal 50  $\mu\text{m}$  for RPO foams and 100  $\mu\text{m}$  for EVOO foams. Oil foams were prepared through 45 min whipping at particular temperatures cooled from 60  $^{\circ}\text{C}$  at 0.3  $^{\circ}\text{C min}^{-1}$ .

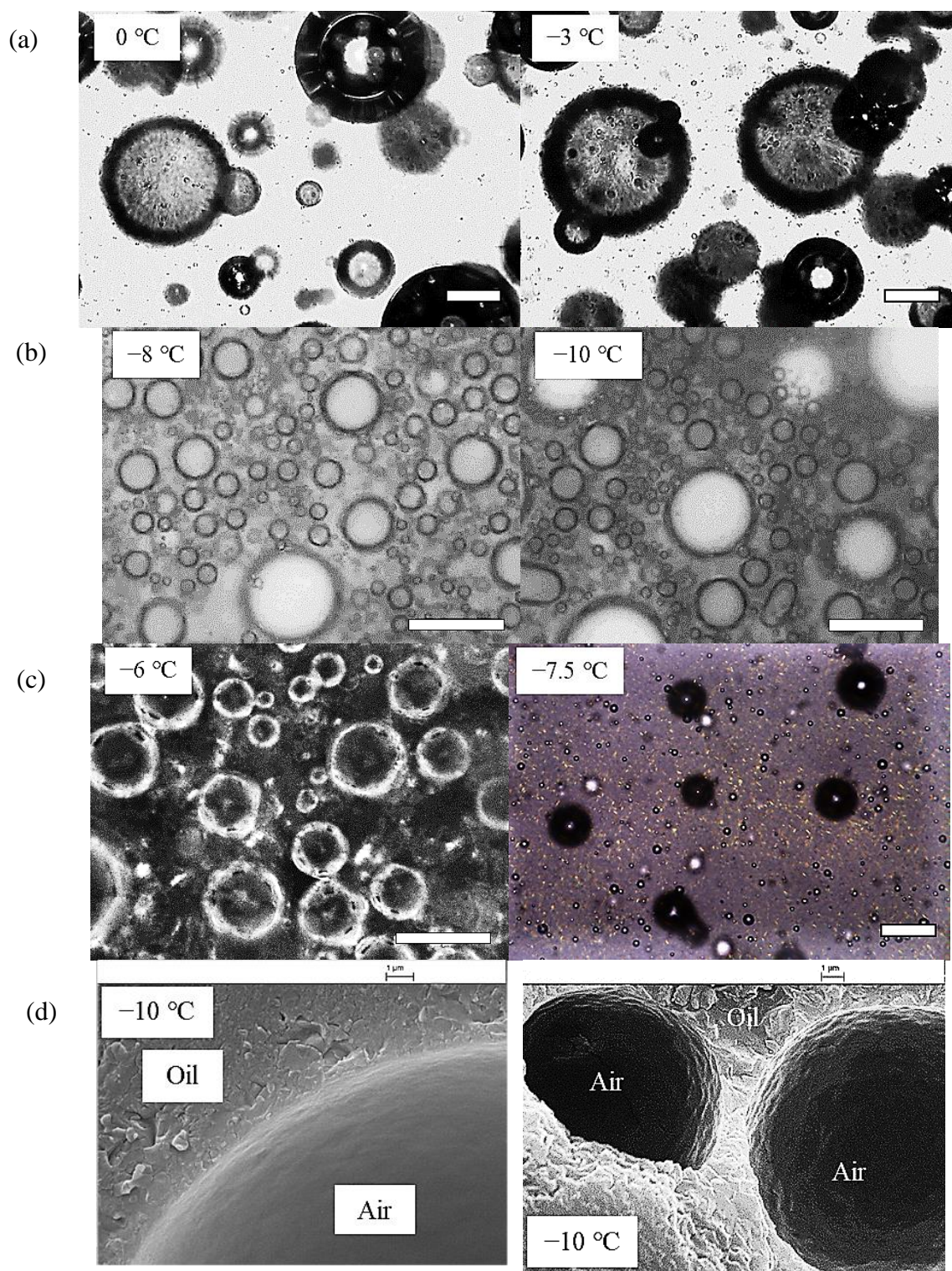
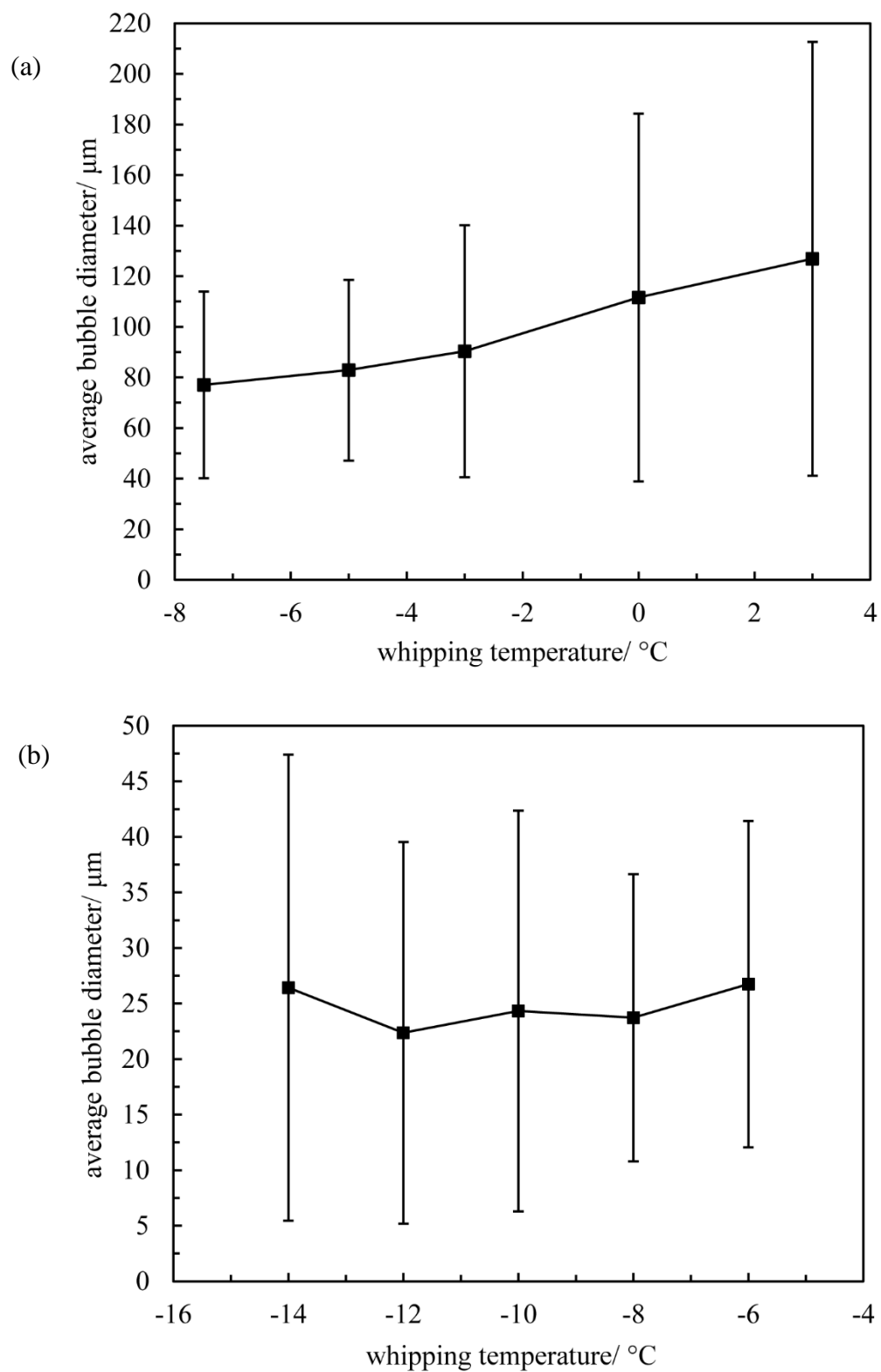


**Figure 3.14.** Average bubble diameter of (a) RPO and (b) EVOO immediately after 45 min whipping with aeration temperature cooled from 60 °C at 0.3 °C min<sup>-1</sup>.



To evaluate foam stability, freshly whipped oils were stored at the respective whipping temperature, and their appearance over one month was recorded photographically and using optical microscopy. The appearance of RPO foams immediately and seven days after preparation is shown in Figure 3.15(a). For foams prepared and stored above  $T_g$  ( $-5\text{ }^{\circ}\text{C}$ ), oil drains and accumulates at the vessel bottom; actually this process ceases within the first 24 h due to the strengthening of the fat crystal network with sintering.<sup>13,23</sup> It is worth noting that the drained oil is slightly turbid, implying that not all the crystals are trapped within the foam. By contrast, no oil drains for oil foams prepared and stored at temperatures  $\leq T_g$ . The relationship between the volume of oil drained after 7 days storage relative to the initial volume of foam and  $G'$  of unaerated samples is shown in Figure 3.15(b). Drainage decreases gradually with increasing  $G'$ , from  $\sim 8\%$  at  $3\text{ }^{\circ}\text{C}$  to zero at  $\leq -5\text{ }^{\circ}\text{C}$  when  $G'$  reaches  $10^3\text{ Pa}$ .<sup>4</sup>

Apart from liquid drainage, foam stability was also evaluated in terms of coarsening/coalescence. Optical micrographs of RPO foams initially and 7 days after preparation are shown in Figure 3.16. No coarsening/coalescence occurs at temperatures  $\leq -5\text{ }^{\circ}\text{C}$  since the bubble size distribution remains similar to that initially ( $p > 0.05$ ), whilst for  $> -5\text{ }^{\circ}\text{C}$  the average bubble size increases gradually with storage time ( $p < 0.05$ ). The evolution in the appearance of EVOO foams up to one month storage can be seen in Figure 3.17 (photos) and Figure 3.18 (micrographs). Although the foams prepared at  $-6\text{ }^{\circ}\text{C}$  during cooling or at  $0\text{ }^{\circ}\text{C}$  during warming exhibit no drained oil, they suffer coarsening/coalescence as evidenced by a noticeable change in bubble size distribution during storage ( $p < 0.05$ ). At temperatures  $\leq -10\text{ }^{\circ}\text{C}$ , oil foams are ultra-stable against drainage, coarsening and coalescence up to at least one month.

**Figure 3.15.** (a) Appearance of RPO foams initially (upper) and 7 days after preparation (lower) at various temperatures cooled from 60 °C at 0.3 °C min<sup>-1</sup>. The storage temperature for all foams was the same as the preparation temperature. Red arrow signifies drained oil. Scale bars = 1 cm. (b) Ratio of volume of drained oil after 7 days storage to volume of initial foam *versus*  $G'$  of oil at different temperatures before whipping.

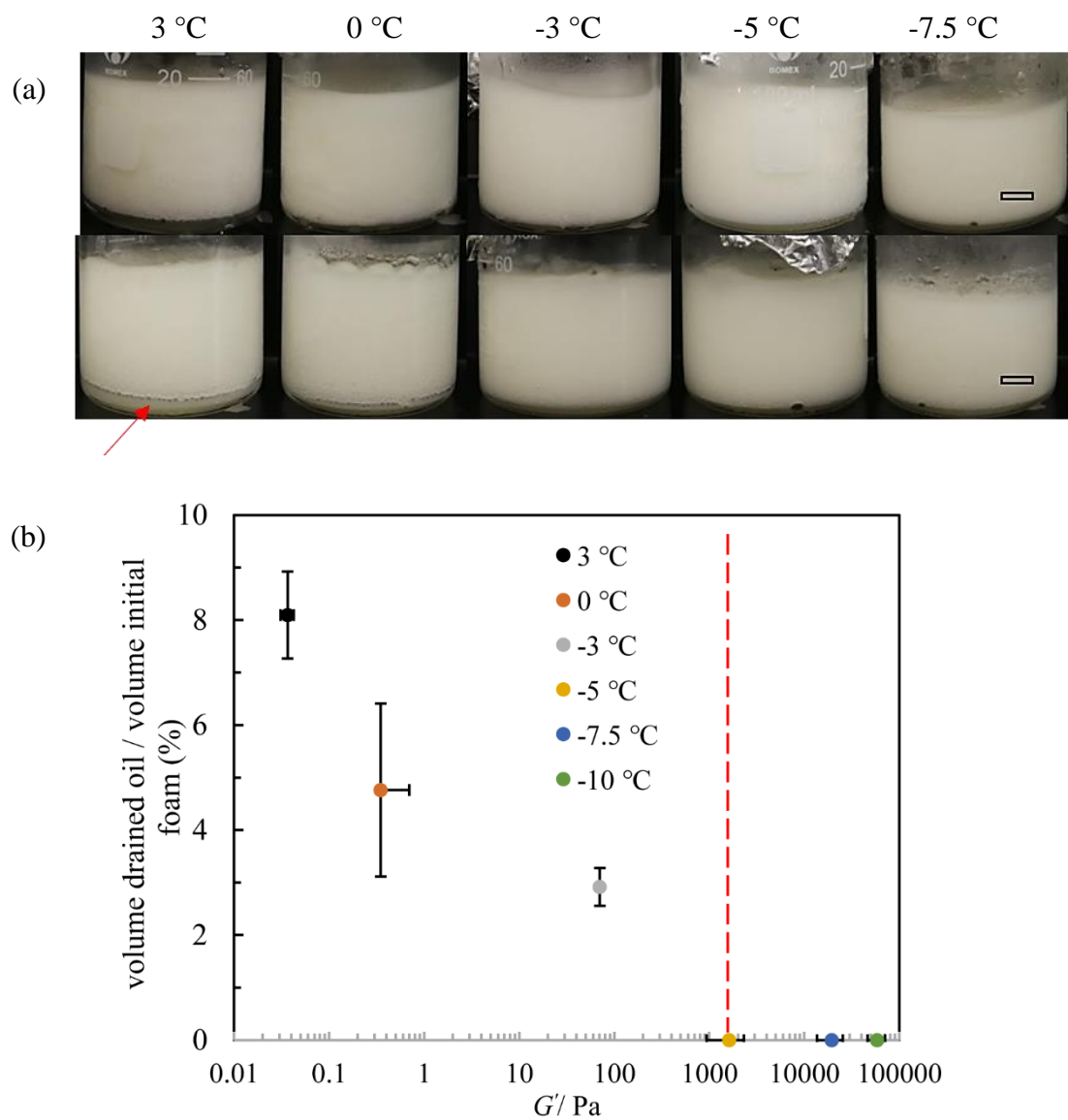


**Figure 3.16.** Optical micrographs of RPO foams initially (left) and 7 days after preparation (right) at various temperatures cooled from 60 °C at 0.3 °C min<sup>-1</sup>. The storage temperature was the same as the preparation temperature. Scale bars = 500 μm.

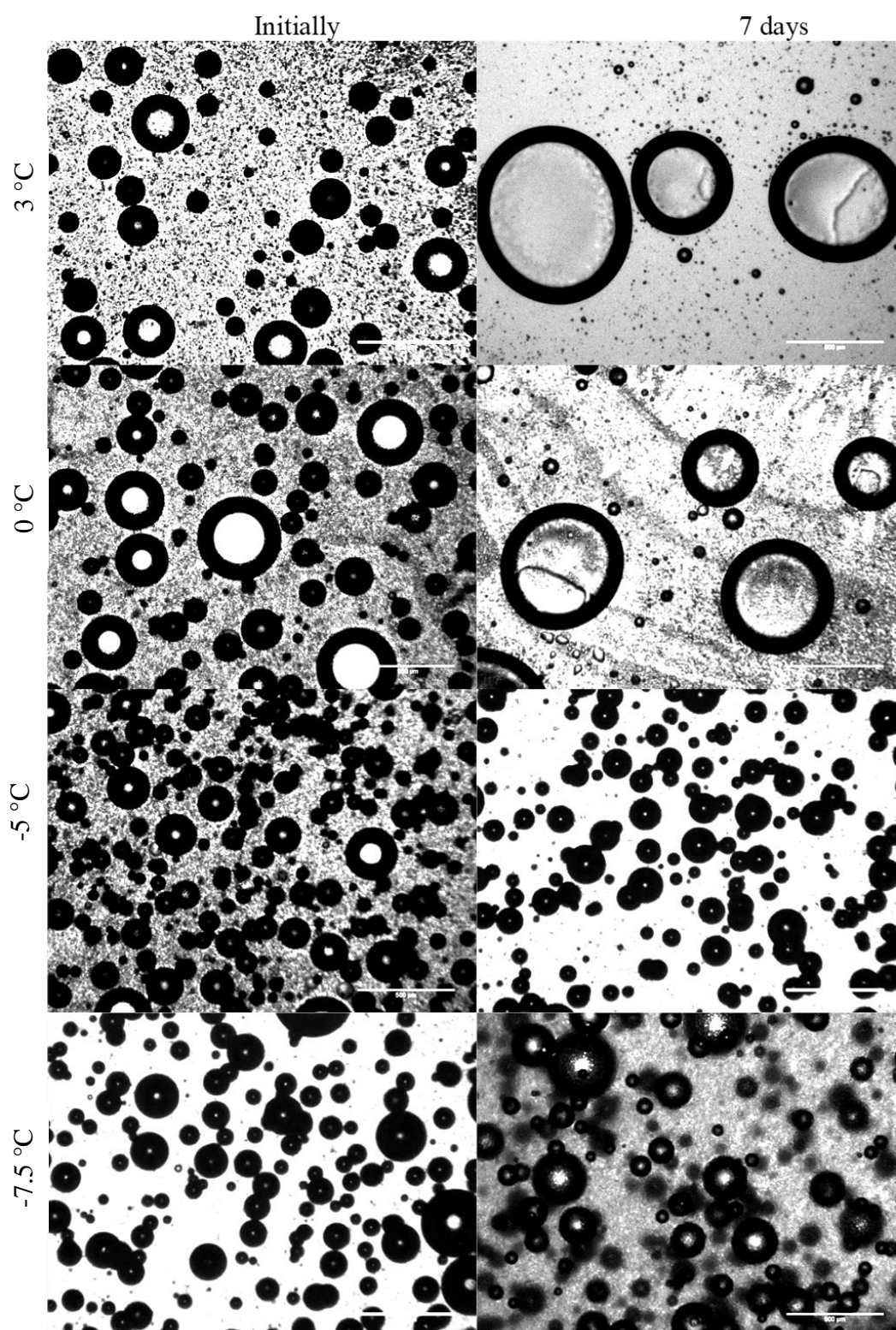


**Figure 3.17.** Appearance of EVOO foams as a function of storage time at various temperatures (a) cooled from 60 °C at 0.3 °C min<sup>-1</sup> or (b) warmed from -20 °C at 0.4 °C min<sup>-1</sup>. The storage temperature was the same as the preparation temperature. Scale bars = 1 cm.

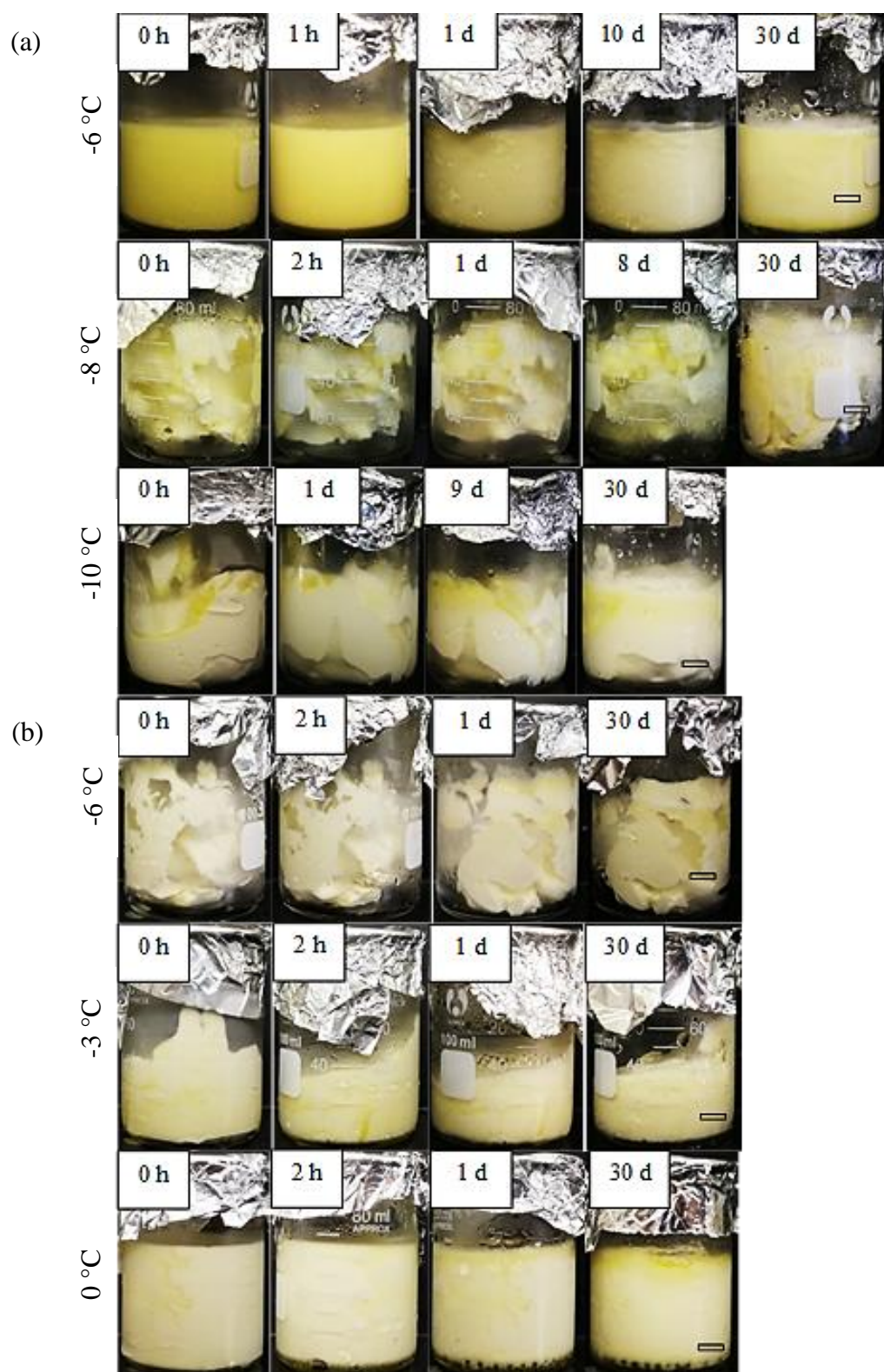
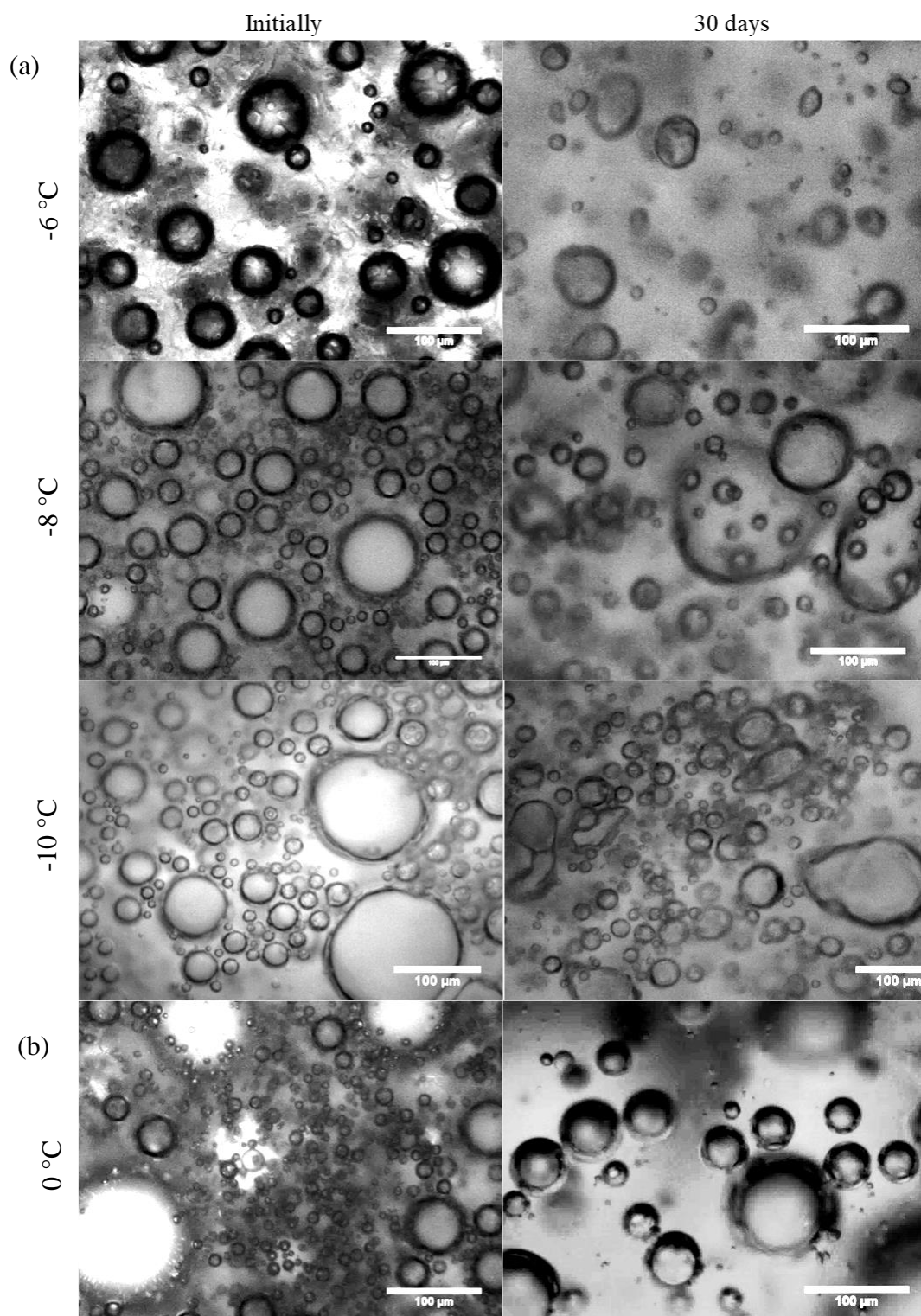


**Figure 3.18.** Optical micrographs of EVOO foams initially (left) and 30 days after preparation (right) at various temperatures (a) cooled from 60 °C at 0.3 °C min<sup>-1</sup> or (b) warmed from -20 °C at 0.4 °C min<sup>-1</sup>. The storage temperature was the same as the preparation temperature. Scale bars = 100 μm.



### 3.4 Thermo-responsiveness of oil foams

Stimuli-responsive foams are of particular interest in industry in the areas of controlled encapsulation, delivery, and release.<sup>38</sup> The stimuli can include pH, temperature, magnetic field, ultrasound *etc.* In our systems, ultra-stable vegetable oil foams are stabilized by triglyceride crystals whose melting profile spans a wide range of temperature. Consequently, it is reasonable to predict that stable oil foams can be rendered unstable on heating, arising from the melting of crystals at both the interface and in bulk. To verify this, we chose to investigate the effect of heating on an otherwise stable RPO foam prepared at -7.5 °C from cooling and an EVOO foam prepared at -6 °C from warming. The foams were warmed progressively to specific temperatures at 1 °C min<sup>-1</sup>. The effect of temperature on the appearance of the foams is shown in Figure 3.19. For RPO foam, there is no observable change in appearance between -7.5 °C and -5 °C. The first sign of drainage occurs at -3 °C at which a minor endothermic peak is observed from the melting profile of neat RPO. Upon warming further, the extent of oil leakage increases slightly. By 11 °C, *i.e.* at the major endothermic peak from the melting profile of neat RPO, the foam network collapses abruptly leaving a small volume of residual foam. The temperature for complete foam collapse is 15 °C where all crystals melt. During heating, an increase in bubble size is evidenced by -3 °C due to either or both of coarsening and coalescence. This is followed by a gradual increase in bubble size with increasing temperature until no bubbles remain at 15 °C or above. In the case of EVOO foam, no drainage is observed between -6 °C and 2 °C. The appearance of oil is first witnessed on the wall interior at 4 °C and the temperature for complete foam collapse is 14 °C. The corresponding microscope images reveal that at temperatures lower than 0 °C, there is virtually no change in bubble size distribution and non-spherical bubbles exist. Upon heating to 4 °C, crystals at both the interface and bulk begin to melt, leading to bubble relaxation into spherical and a significant increase in average bubble diameter from ~ 25 µm to ~ 100 µm. No bubbles exist at or above 14 °C. The variation of the volume of oil foam and that of drained oil with temperature is given in Figure 3.20. When comparing the melting behavior of RPO and EVOO foams, we find that the temperature range during which foams suffer significant collapse is much broader for the latter than the former, whilst the temperatures for complete foam collapse are comparable. Due to the reversible nature of triglyceride crystal melting and crystallization, we chose to cool the molten RPO formed at 50 °C to -7.5 °C and re-whipped it with the same protocol. The resulting over-run was comparable to that found initially, demonstrating the reversibility of the process.

**Figure 3.19.** Effect of temperature on appearance of RPO foam (upper) and EVOO foam (lower). Heating rate was  $1\text{ }^{\circ}\text{C min}^{-1}$ . (a) Photos, scale bars = 1 cm; (b) optical micrographs, scale bars =  $500\text{ }\mu\text{m}$  for RPO foam except at  $50\text{ }^{\circ}\text{C}$  which is  $100\text{ }\mu\text{m}$ , scale bars =  $100\text{ }\mu\text{m}$  for EVOO foam. RPO foam was prepared at  $-7.5\text{ }^{\circ}\text{C}$  after cooling from  $60\text{ }^{\circ}\text{C}$  at  $0.3\text{ }^{\circ}\text{C min}^{-1}$ . EVOO foam was prepared at  $-6\text{ }^{\circ}\text{C}$  after warming from  $-20\text{ }^{\circ}\text{C}$  at  $0.4\text{ }^{\circ}\text{C min}^{-1}$ .

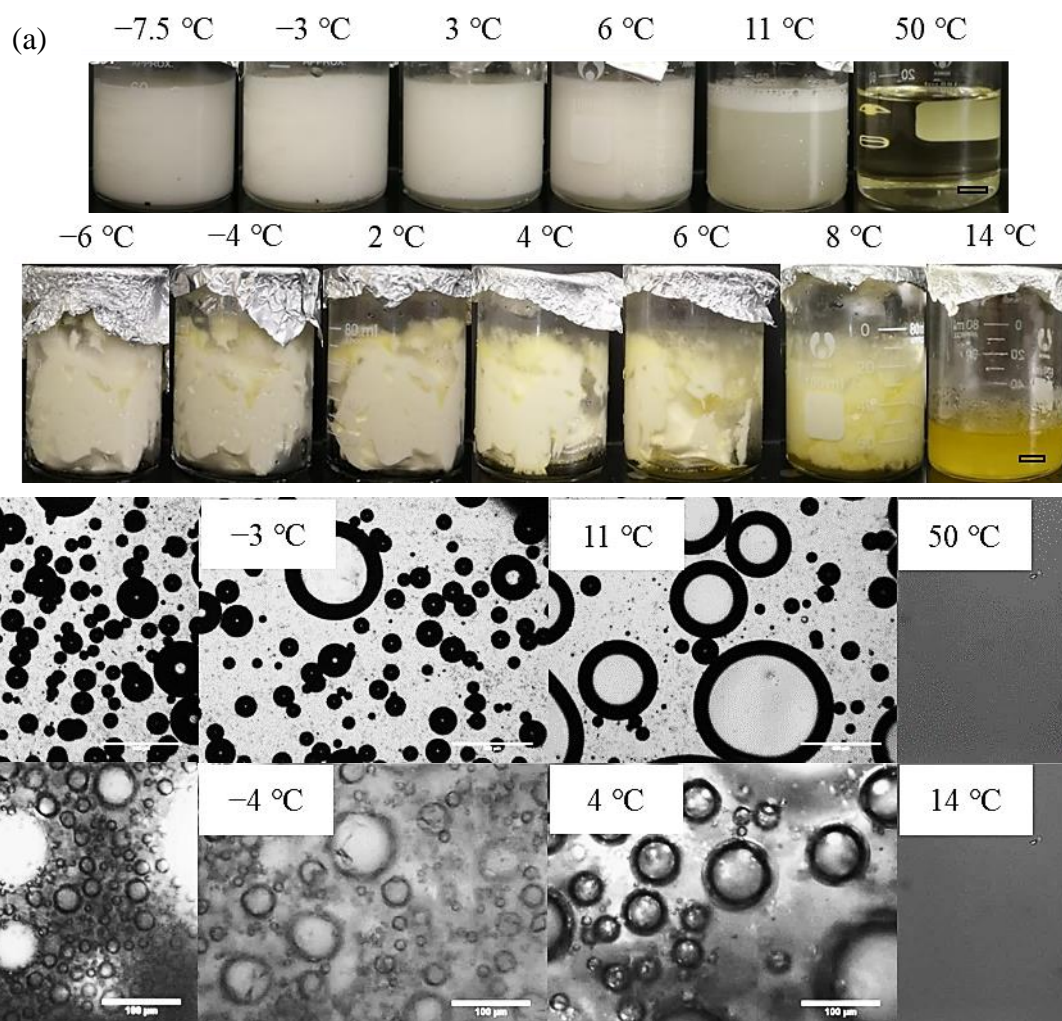
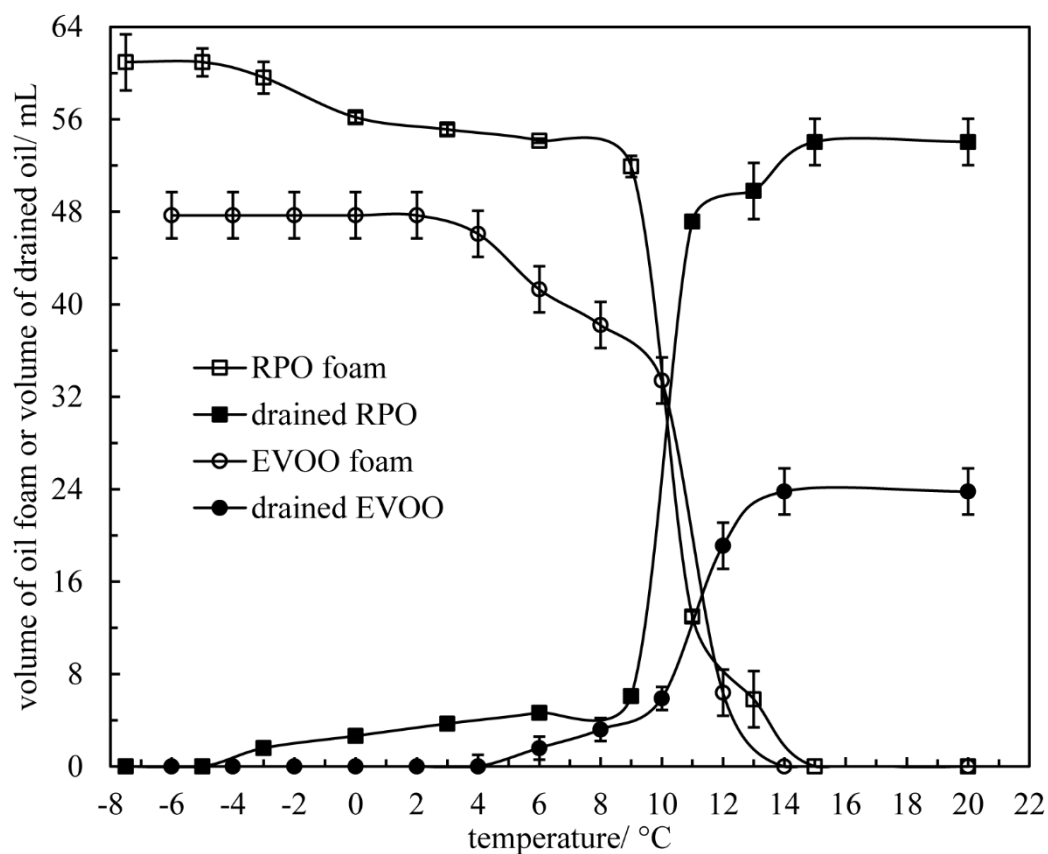


**Figure 3.20.** Variation of volume of foam (open points) and volume of drained oil (filled points) with temperature upon heating. Heating rate was  $1\text{ }^{\circ}\text{C min}^{-1}$ . RPO foams were prepared at  $-7.5\text{ }^{\circ}\text{C}$  after cooling from  $60\text{ }^{\circ}\text{C}$  at  $0.3\text{ }^{\circ}\text{C min}^{-1}$ . EVOO foams were prepared at  $-6\text{ }^{\circ}\text{C}$  after warming from  $-20\text{ }^{\circ}\text{C}$  at  $0.4\text{ }^{\circ}\text{C min}^{-1}$ .



### 3.5 Determination of fatty acid composition in oil crystals

RPO and EVOO are mainly composed of long-chain, unsaturated fatty acids (UFAs) in their triglyceride molecules. By selective crystallization of high-melting triglyceride fractions within low-melting continuous oil, we have shown that such oil dispersions can be aerated producing stable oil foams. Foaming could be achieved over a broad range of temperature in which air bubbles are protected by the adsorption of high-melting triglyceride crystals. However, we do not know the chemical composition of these crystals. In light of the above, we tried to separate the high-melting solid fractions from the liquid ones under vacuum filtration at  $7.5 \pm 1$  °C where the oils were partially crystallized. The recovery of RPO crystals was unsuccessful however since their crystal size was smaller than the pore size of the filter paper used, unlike the case for EVOO crystals. Thus, carefully collected EVOO crystals were subsequently melted and then converted into fatty acid methyl esters (FAMES) by trans-esterification at ambient temperature. GC/MS analysis determined their fatty acid composition. Meanwhile, liquid EVOO was trans-esterified and analyzed for comparison. The overlaid GC-MS chromatograms of liquid EVOO and high-melting EVOO crystals are given in Figure 3.21. They are similar with respect to both intensity and retention time. By comparing their MS spectra with library data (NIST), they are found to possess similar fatty acid types. The fatty acid proportions of both samples are listed in Table 3.2. Original EVOO contains 17.0% SFAs and 80.8% UFAs. For high-melting EVOO crystals, the SFAs increase to 23.0% and that of UFAs decrease to 75.1% ( $p < 0.05$ ). Thus, the ratio of SFA/UFA increases from 21.0 in liquid EVOO to 30.6 in EVOO crystals, an increase of 46%. This means that a higher proportion of SFAs is present in EVOO crystals compared with original EVOO oil,<sup>39,40</sup> in support of our initial hypothesis that high-melting saturated fractions crystallize in a liquid of low-melting triglycerides. However, the TAG profiles of EVOO crystals and liquid EVOO are still unclear.

**Figure 3.21.** GC-MS chromatograms of EVOO (lower) and extracted high-melting EVOO crystals (upper).

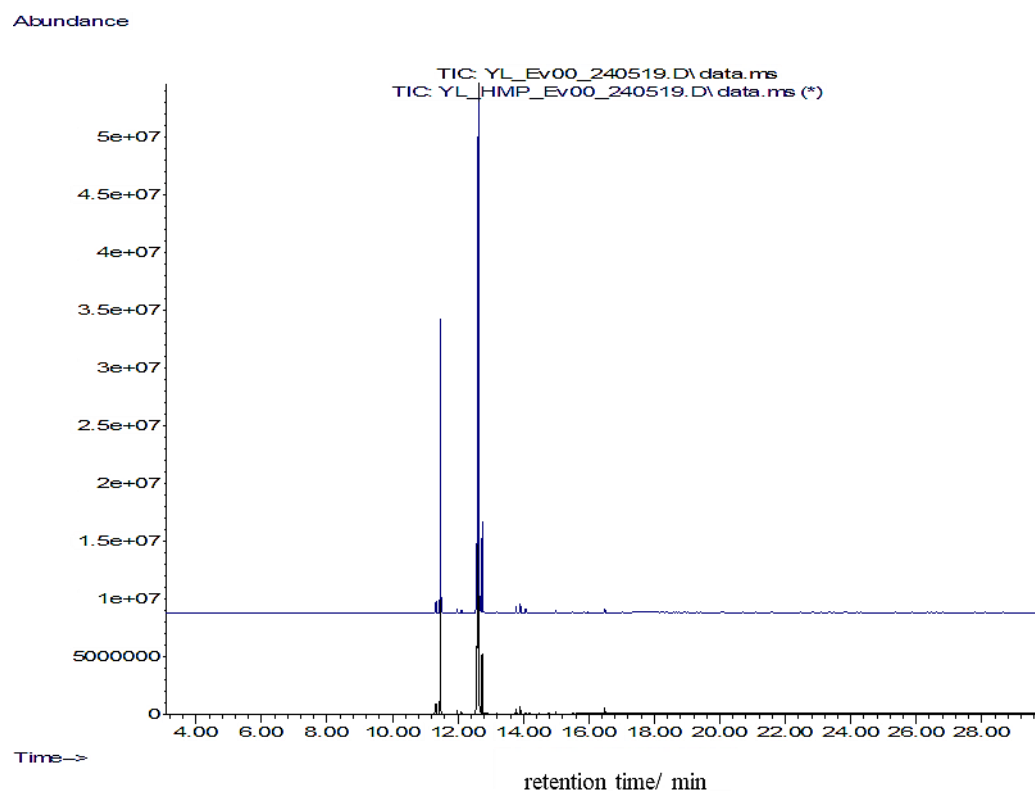


**Table 3.2.** Major fatty acid composition of EVOO and extracted high-melting EVOO crystals.

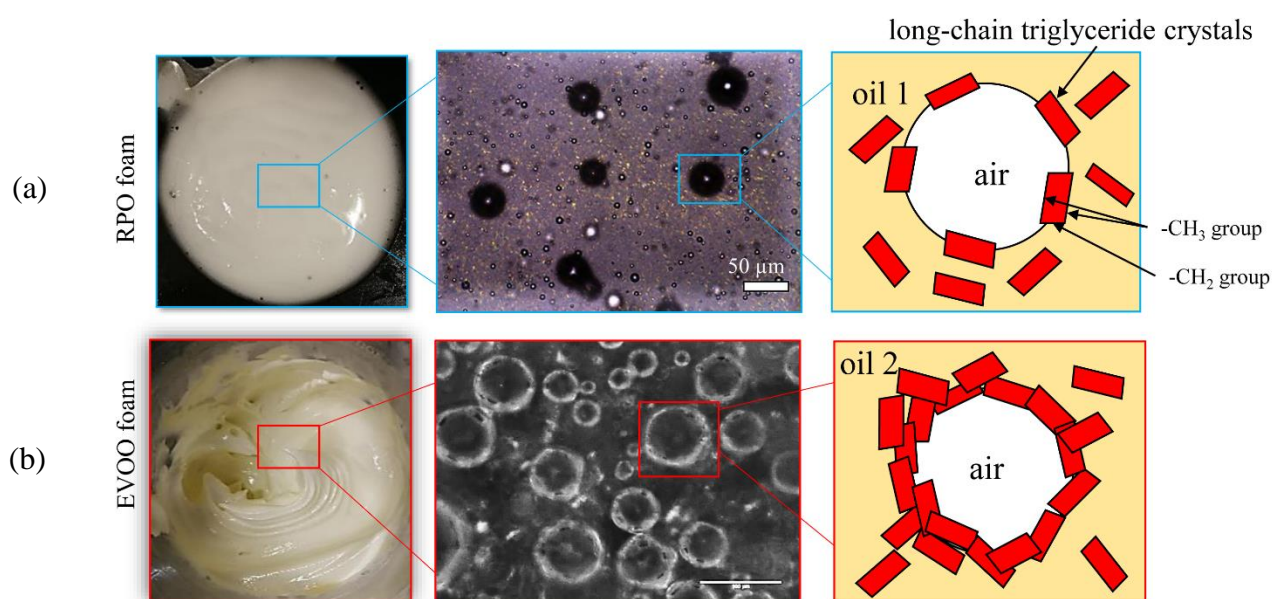
EVOO				High-melting EVOO crystals		
		%	Total/%		%	Total/%
SFA <sup>a</sup>	C16:0	12.2 ± 0.1		C16:0	17.8 ± 0.1	
	C18:0	4.3 ± 0.1	17.0	C18:0	4.7 ± 0.1	23.0
	C20:0	0.5 ± 0.0		C20:0	0.5 ± 0.0	
UFA <sup>b</sup>	C16:1	0.9 ± 0.0		C16:1	0.8 ± 0.0	
	C18:1	79.9 ± 0.2	80.8	C18:1	74.3 ± 0.3	75.1
SFA/UFA			21.0	30.6		

<sup>a</sup> Saturated fatty acid; <sup>b</sup> Unsaturated fatty acid

### 3.6 Conclusions

Our initial hypothesis that a vegetable oil, capable of forming crystals by careful selection of temperature, can be aerated to produce an oil foam has been confirmed. We introduce a new protocol to prepare edible oil foams from vegetable oils containing mainly long-chain, unsaturated fatty acids in their triglyceride molecules in the absence of an added foaming agent. This is in contrast to earlier work in which amphiphilic molecules are added as foaming agent.<sup>4-6,10</sup> Careful temperature control induces the formation of high-melting triglyceride crystals within low-melting continuous liquid oil capable of forming an oleogel. Upon whipping, ultra-stable oil foams containing adsorbed crystals can be fabricated. The highest over-run is  $\sim 40\%$  at  $\leq -16\text{ }^{\circ}\text{C}$  for refined peanut oil and  $\sim 110\%$  at  $-12\text{ }^{\circ}\text{C}$  for extra virgin olive oil. We hypothesise that in RPO foams triglyceride crystals are loosely packed at the interface, whilst in EVOO foams a more coherent crystal layer(s) forms at bubble surfaces (Figure 3.22). It is shown that triglyceride crystals contain a higher proportion of saturated fatty acids than the original oil. Such foams are temperature-responsive and can be rendered completely unstable upon heating to around the melting point of the crystals. We believe that our simple method is versatile and can be applied to a wide range of long-chain vegetable oils differing in fatty acid composition.

**Figure 3.22.** Schematic illustration of the stabilization of air-in-oil foams by TAG crystals. (a) RPO foam, (b) EVOO foam.



### 3.7 References

1. G.M. Campbell and E. Mougeot, Creation and characterisation of aerated food products, *Trends Food Sci. Technol.*, 1999, **10**, 283–296.
2. R. Heymans, I. Tavernier, K. Dewettinck and P. Van der Meeren, Crystal stabilization of edible oil foams, *Trends Food Sci. Technol.*, 2017, **69**, 13–24.
3. A.L. Fameau, S. Lam and A. Arnould, Non-aqueous foams: Current understanding on the formation and stability mechanisms, *Adv. Colloid Interface Sci.*, 2017, **247**, 454–464.
4. M. Brun, M. Delample, E. Harte, S. Lecomte and F. Leal-Calderon, Stabilization of air bubbles in oil by surfactant crystals: a route to produce air-in-oil foams and air-in-oil-in-water emulsions, *Food Res. Int.*, 2015, **67**, 366–375.
5. D.Z. Gunes, M. Murith, J. Godefroid, C. Pelloux, H. Deyber, O. Schafer and O. Breton, Oleofoams: properties of crystal-coated bubbles from whipped oleogels-evidence for Pickering stabilization, *Langmuir*, 2017, **33**, 1563–1575.
6. R. Heymans, I. Tavernier, S. Danthine, T. Rimaux, P. Van der Meeren and K. Dewettinck, Food-grade monoglyceride oil foams: the effect of tempering on foamability, foam stability and rheological properties, *Food Funct.*, 2018, **9**, 3143–3154.
7. M. Lei, N. Zhang, W.J. Lee, C.P. Tan, O.M. Lai, Y. Wang and C. Qiu, Non-aqueous foams formed by whipping diacylglycerol stabilized oleogel, *Food Chem.*, 2020, **312**, 126047.
8. F. Saremnejad, M. Mohebbi and A. Koocheki, Practical application of nonaqueous foam in the preparation of a novel aerated reduced-fat sauce, *Food Bioprod. Process*, 2020, **119**, 216–225.
9. A.L. Fameau, S. Lam, A. Arnould, C. Gaillard, O.D. Velez and A. Saint-Jalmes, Smart nonaqueous foams from lipid-based oleogel, *Langmuir*, 2015, **31**, 13501–13510.
10. B.P. Binks, E.J. Garvey and J. Vieira, Whipped oil stabilised by surfactant crystals, *Chem. Sci.*, 2016, **7**, 2621–2632.
11. S. Mishima, A. Suzuki, K. Sato and S. Ueno, Formation and microstructures of whipped oils composed of vegetable oils and high-melting fat crystals, *J. Am. Oil Chem. Soc.*, 2016, **93**, 1453–1466.
12. B.P. Binks and I. Marinopoulos, Ultra-stable self-foaming oils, *Food Res. Int.*, 2017, **95**, 28–37.

13. L. Goibier, C. Pillement, J. Monteil, C. Faure and F. Leal-Calderon, Emulsification of non-aqueous foams stabilized by fat crystals: towards novel air-in-oil-in-water food colloids, *Food Chem.*, 2019, **293**, 49–56.
14. K. Mishra, D. Dufour and E.J. Windhab, Yield stress dependent foaming of edible crystal-melt suspensions, *Cryst. Growth Des.*, 2020, **20**, 1292–1301.
15. L. Metilli, A. Lazidis, M. Francis, S. Marty-Terrade, J. Ray and E. Simone, The effect of crystallization conditions on the structural properties of oleofoams made of cocoa butter crystals and high oleic sunflower oil, *Cryst. Growth Des.*, 2021, **21**, 1562–1575.
16. T. Truong, S. Prakash and B. Bhandari, Effects of crystallisation of native phytosterols and monoacylglycerols on foaming properties of whipped oleogels, *Food Chem.*, 2019, **285**, 86–93.
17. M. Callau, K. Sow-Kébé, N. Jenkins and A.L. Fameau, Effect of the ratio between fatty alcohol and fatty acid on foaming properties of whipped oleogels, *Food Chem.*, 2020, **333**, 127403.
18. N.K. Andrikopoulos, Triglyceride species compositions of common edible vegetable oils and methods used for their identification and quantification, *Food Rev. Int.*, 2002, **18**, 71–102.
19. F.M. Haddada, H. Manaï, I. Oueslati, D. Daoud, J. Sánchez, E. Osorio, and M. Zarrouk, Fatty acid, triacylglycerol, and phytosterol composition in six Tunisian olive varieties, *J. Agric. Food Chem.*, 2007, **55**, 10941–10946.
20. K. Mishra, J. Bergfreund, P. Bertsch, P. Fischer and E.J. Windhab, Crystallization-induced network formation of tri- and monopalmitin at the middle-chain triglyceride oil/air interface, *Langmuir*, 2020, **36**, 7566–7572.
21. F. Valoppi, S. Calligaris and A.G. Marangoni, Structure and physical properties of oleogels containing peanut oil and saturated fatty alcohols, *Eur. J. Lipid Sci. Technol.*, 2017, **119**, 1600252.
22. A.G. Marangoni, *Fat Crystal Networks*, CRC Press, Boca Raton, 2005.
23. C. Himawan, V.M. Starov and A.G.F. Stapley, Thermodynamic and kinetic aspects of fat crystallization, *Adv. Colloid Interface Sci.*, 2006, **122**, 3–33.
24. E. Chiavaro, E. Vittadini, M.T. Rodriguez-Estrada, L. Cerretani, M. Bonoli, A. Bendini and G. Lercker, Monovarietal extra virgin olive oils: correlation between thermal properties and chemical composition, *J. Agric. Food Chem.*, 2007, **55**, 10779–10786.

25. L. Barba, G. Arrighetti and S. Calligaris, Crystallization and melting properties of extra virgin olive oil studied by synchrotron XRD and DSC, *Eur. J. Lipid Sci. Technol.*, 2003, **115**, 322–329.
26. Y.B. Che Man and C.P. Tan, Comparative differential scanning calorimetric analysis of vegetable oils: II. Effects of cooling rate variation, *Phytochem. Anal.*, 2002, **13**, 142–151.
27. C.P. Tan and Y.B. Che Man, Comparative differential scanning calorimetric analysis of vegetable oils: I. Effects of heating rate variation, *Phytochem. Anal.*, 2002, **13**, 129–141.
28. K. Higaki, T. Koyano, I. Hachiya and K. Sato, *In situ* optical observation of microstructure of  $\beta$ -fat gel made of binary mixtures of high-melting and low-melting fats, *Food Res. Int.*, 2004, **37**, 2–10.
29. A. Devi and B.S. Khatkar, Effects of fatty acids composition and microstructure properties of fats and oils on textural properties of dough and cookie quality, *J. Food Sci. Technol.*, 2018, **55**, 321–330.
30. N.K. Ojijo, I. Neeman, S. Eger and E. Shimoni, Effects of monoglyceride content, cooling rate and shear on the rheological properties of olive oil/monoglyceride gel networks, *J. Sci. Food Agric.*, 2004, **84**, 1585–1593.
31. A. Bals and U. Kulozik, The influence of the pore size, the foaming temperature and the viscosity of the continuous phase on the properties of foams produced by membrane foaming, *J. Membr. Sci.*, 2003, **220**, 5–11.
32. N. Krog and K. Larsson, Crystallization at interfaces in food emulsions – a general phenomenon, *Eur. J. Lipid Sci. Technol.*, 1992, **94**, 55–57.
33. M. Douaire, V. di Bari, J.E. Norton, A. Sullo, P. Lillford and I.T. Norton, Fat crystallisation at oil-water interfaces, *Adv. Colloid Interface Sci.*, 2014, **203**, 1–10.
34. P. Inglese, F. Famiani, F. Galvano, M. Servili, S. Esposto and S. Urbani, Factors affecting extra-virgin olive oil composition, *Horticultural Rev.*, 2011, 83–147.
35. A. de Vries, Y.L. Gomez, E. van der Linden and E. Scholten, The effect of oil type on network formation by protein aggregates into oleogels, *RSC Adv.*, 2017, **7**, 11803–11812.
36. F. Gautier, M. Destribats, R. Perrier-Cornet, J. Dechézelles, J. Giermanska, V. Héroguez, S. Ravaine, F. Leal-Calderon and V. Schmitt, Pickering emulsions with stimuable particles: from highly- to weakly-covered interfaces, *Phys. Chem. Chem. Phys.*, 2007, **9**, 6455–6462.

37. S.E. Friberg, I. Blute and H. Kunieda, Stability of hydrophobic foams, *Langmuir*, 1986, **2**, 659–664.
38. S. Fujii and Y. Nakamura, Stimuli-responsive bubbles and foams stabilized with solid particles, *Langmuir*, 2017, **33**, 7365–7379.
39. M.A. Bootello, R. Garcés, E. Martínez-Force and J.J. Salas, Dry fractionation and crystallization kinetics of high-oleic high-stearic sunflower oil, *J. Am. Oil Chem. Soc.*, 2011, **88**, 1511–1519.
40. O. Zaliha, C.L. Chong, C.S. Cheow, A.R. Norizzah and M.J. Kellens, Crystallization properties of palm oil by dry fractionation, *Food Chem.*, 2004, **86**, 245–250.

## CHAPTER 4 – A NOVEL STRATEGY TO FABRICATE STABLE OIL FOAMS WITH SUCROSE ESTER SURFACTANT

### 4.1 Introduction

As mentioned in chapter 3, stable edible oil foams were prepared from pre-formed lipid crystals. The major drawback of the existing systems however is that whipping a firm oleogel involves a comparatively high level of mechanical energy input and viscous energy dissipation<sup>1,2</sup> and efficient air incorporation is not always possible. Also, relatively slow adsorption kinetics for the migration of crystals towards air-oil interfaces tends to limit foaming capacity compared to surfactant molecules. Is it feasible to achieve high foamability and long-term stability in a similar system at low energy cost?

Sucrose esters (SE) are nonionic surfactants consisting of sucrose as the hydrophilic group and fatty acid chains as the hydrophobic groups. A sucrose molecule has 8 free hydroxyl groups. By optimizing the degree of esterification and nature of the alkyl chains, SE of different hydrophobicity can be obtained. Commercial grade SE of varying hydrophile–lipophile balance (HLB) number are mixtures of mono-, di-, tri- and polyesters with varying ester composition. SE are tasteless, odourless, non-toxic and biodegradable, making them perfect candidates in the areas of food, cosmetics and pharmaceuticals.<sup>3-5</sup> Up to now, a paucity of literature has been available regarding the physicochemical and functional properties of SE. In the neat state, the thermal properties and crystal structures of commercial SE of various HLB number tend to differ.<sup>6</sup> When dissolved in aqueous or non-aqueous solvents, various lyotropic liquid crystalline phases can be formed. For relatively hydrophilic SE, they can be dissolved in water at high temperature and then self-organise into different aggregate structures depending on their molecular structure, concentration and temperature.<sup>7-9</sup> Upon dispersing lipophilic SE into non-polar oils, *e.g.* n-decane, several types of reverse lyotropic liquid crystals may form.<sup>7</sup> SE can also form viscous reverse worm-like micelles when lecithin is present in the non-polar oil.<sup>10</sup> Different grades of SE with a full range of HLB number ranging from 1 to 16 exhibit versatile functionalities, *e.g.* emulsification and foaming,<sup>11-13</sup> solubilization/dissolution improvement,<sup>14</sup> controlled/sustained release<sup>15</sup> and crystal modification.<sup>16</sup> Zhang *et al.*<sup>11</sup> found that the foaming and emulsification properties of pure SE were affected by the fatty acid chain length and the degree of esterification. It is only recently that studies on the role of the lipophilic SE in edible oil structuring yielding oleogels are appearing because of their potential for many applications in food.<sup>17-19</sup> SE alone were not effective structuring agents, so additional cosurfactant was needed to aid structuring of edible oils. A limited number of mixed SE-

surfactant systems has been investigated including sucrose stearate (HLB number = 3)-capsaicin in medium chain TAGs,<sup>17</sup> sucrose stearate (HLB number = 2)-lecithin in sunflower oil<sup>18</sup> and sucrose stearate-ascorbyl palmitate in menhaden oil or home-synthesised lipid.<sup>19</sup> To the best of our knowledge, no publication exists concerning the fabrication of oleofoams of SE alone.

Herein we report on the foaming potential of a range of vegetable oils in the presence of one SE of HLB number = 5 (C-1805). Initial experiments investigate the effect of aeration temperature and surfactant concentration on foaming. Desirable foaming can be obtained from one-phase oil solutions of surfactant molecules after only several min of whipping, but foams of limited stability ensue. This finding is in contrast to that reported in all previous oleofoam systems in which pre-formed lipid crystals were a pre-requisite for oil foaming (see refs. 1,2, 20 – 31). Due to foam instability, we advance a two-stage protocol to prepare ultra-stable oil foams. Vigorous whipping is applied to a one-phase oil solution at high temperature followed by rapid quenching to trigger both interfacial and bulk crystallisation of surfactant molecules *in situ* before foam aging occurs. Foams are then stored at comparatively low temperature. In this way, foam bubbles are endowed with a compact layer(s) of surfactant crystals. Although the continuous phase is a weak gel, the colloidal network of bubbles and excess crystals can arrest oil drainage and long-term oil foams stable to drainage, coarsening and coalescence can be obtained. The obtained foams possess impressive thermal and mechanical properties. We also elucidate the underlying mechanisms of foam formation and subsequent stabilisation.

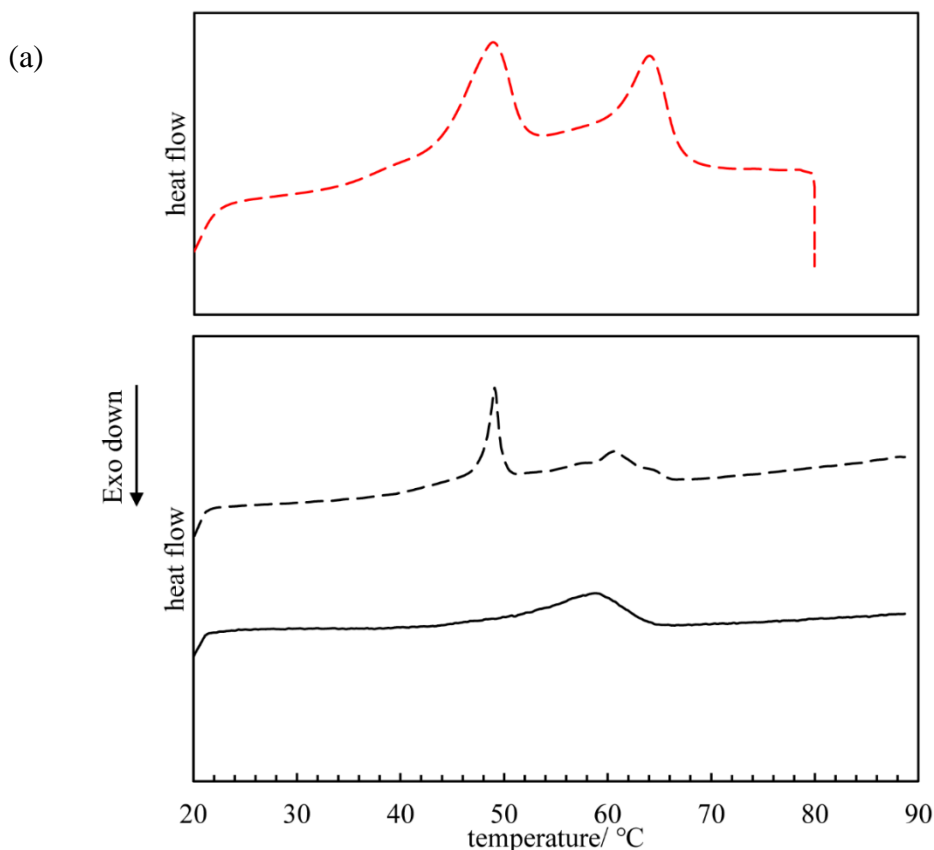
Based on the above, we explore the foaming potential of vegetable oil containing another more lipophilic SE of HLB number = 2. Two methods are introduced to prepare oil foams, *i.e.* whipping and bubbling. Comparisons are then made between the resulting foams from these two methods, regarding foamability, foam stability and foam morphology.

## 4.2 Cooling and warming mixtures of sucrose ester and oil

### 4.2.1 Visual observations and thermal properties

As mentioned in chapter 2, C-1805 is composed of 30% sucrose monoester and 70% sucrose di-, tri-, polyester. Before being dissolved in oil, the thermal behaviour of a powdered sample of neat C-1805 was investigated by DSC (Figure 4.1 and Table 4.1). When heating at  $5\text{ }^{\circ}\text{C min}^{-1}$ , the thermogram exhibits two distinct endothermic peaks at  $48.5\text{ }^{\circ}\text{C}$  and  $63.6\text{ }^{\circ}\text{C}$ , respectively. Subsequent cooling at  $5\text{ }^{\circ}\text{C min}^{-1}$  sees a major exothermic peak at  $57.8\text{ }^{\circ}\text{C}$  and one minor peak at  $41.6\text{ }^{\circ}\text{C}$ . These transitions agree with an earlier report during which SE with low HLB of 3 also exhibited two endothermic peaks during melting.<sup>15</sup> Similarly, Sintang *et al.*<sup>18</sup> reported two exothermic peaks during cooling for SE with low HLB of 2. The low-melting peaks correspond to the melting of mono-, di- and triester, whilst the high-melting peaks represent the melting of tetra- and pentaester fractions.<sup>15</sup>

**Figure 4.1.** (a) Melting and (b) cooling thermograms of C-1805 powder (---), EVOO foam (---) and EVOO dispersion (—) containing 10 wt.% C-1805 stored at ambient temperature. Temperature change rate was  $3\text{ }^{\circ}\text{C min}^{-1}$  for EVOO foam and EVOO dispersion,  $5\text{ }^{\circ}\text{C min}^{-1}$  for C-1805 powder.



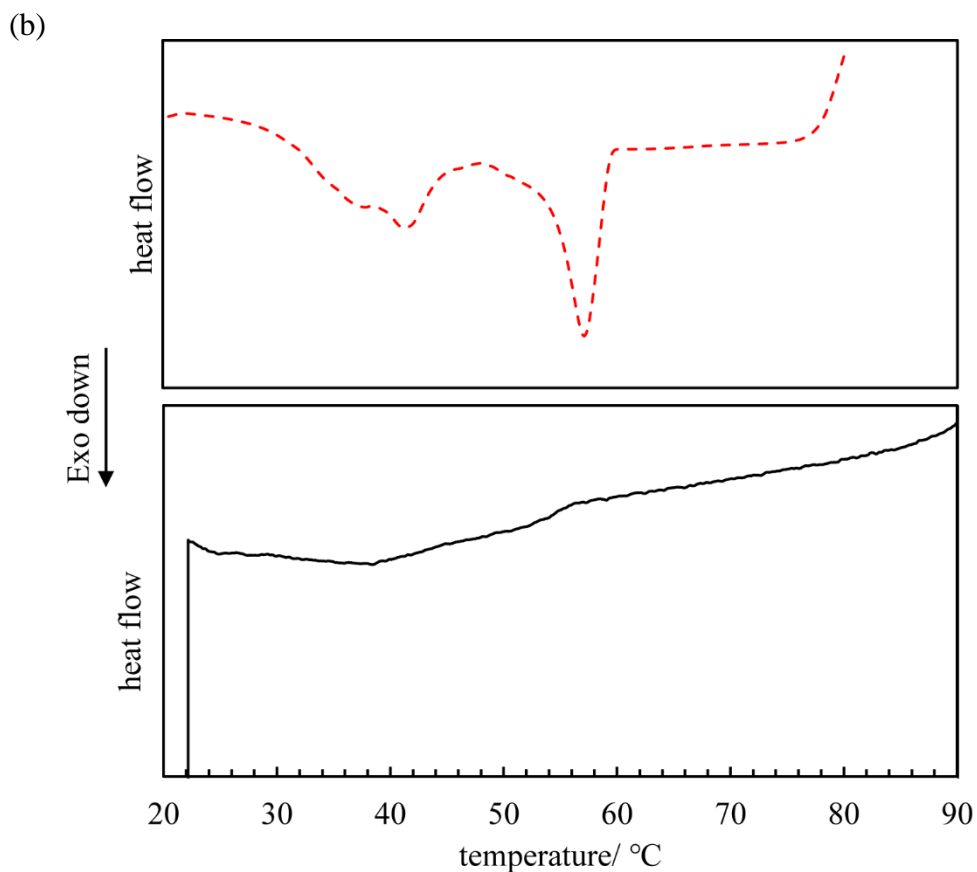


**Table 4.1.** Thermal properties of materials from Figure 4.1.

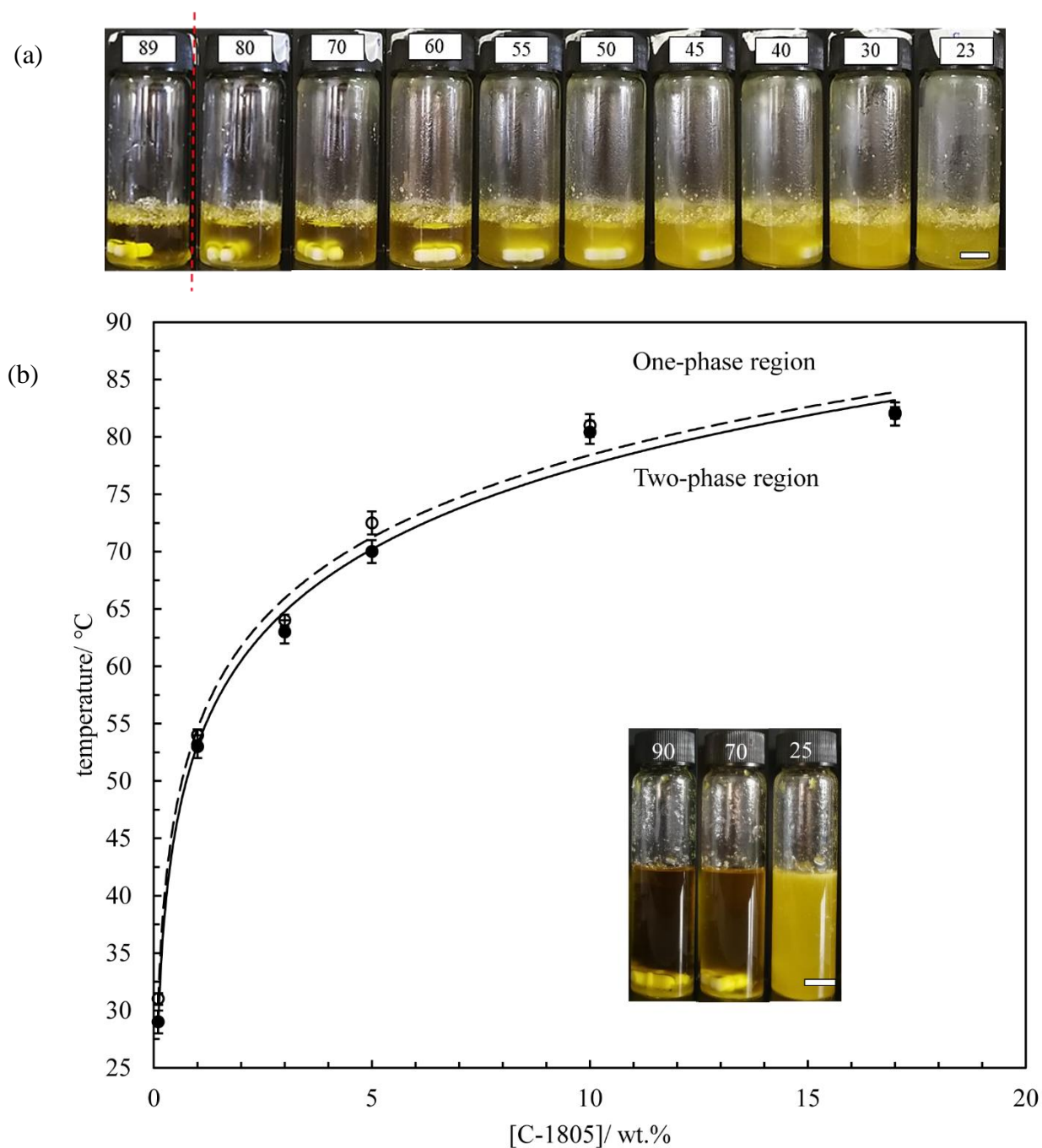
	Crystallisation				Melting			
	$T_{\text{peak}}/\text{°C}$		$\Delta H/\text{J g}^{-1}$		$T_{\text{peak}}/\text{°C}$		$\Delta H/\text{J g}^{-1}$	
	Peak 1	Peak 2	Peak 1	Peak 2	Peak 1	Peak 2	Peak 1	Peak 2
P	$41.58 \pm 0.13$	$57.75 \pm 0.11$	$-11.46 \pm 0.82$	$-11.14 \pm 0.06$	$48.51 \pm 0.20$	$63.59 \pm 0.17$	$8.82 \pm 0.99$	$8.67 \pm 0.43$
F	—	—	—	—	$49.20 \pm 0.10$	$60.70 \pm 0.20$	$0.69 \pm 0.18$	$0.33 \pm 0.10$
D	$38.50 \pm 0.05$	N/A	$-1.21 \pm 0.10$	N/A	$58.84 \pm 0.05$	N/A	$0.63 \pm 0.05$	N/A

P-powder; F-foam; D-dispersion

The effect of temperature on the appearance of C-1805-EVOO mixtures was examined by visual observations. Mixtures were kept at 90 °C under gentle magnetic stirring to create a clear, homogeneous one-phase solution. The mixtures were then submitted to a gradual cooling and subsequent warming at 1 °C min<sup>-1</sup> in a water bath. Figure 4.2(a) shows the appearance of a sample containing 10 wt.% C-1805 as a function of temperature during cooling. The first sign of cloudiness occurs around 80 °C. Upon cooling further, the sample becomes increasingly turbid as a result of the decreasing affinity between the solute and solvent.<sup>32,33</sup> After leaving at 20 °C overnight, the sample was then warmed gradually at 1 °C min<sup>-1</sup> during which it becomes less turbid and finally clear at ~ 81 °C (not shown). Based on the visual observations at different surfactant concentrations, a solubility phase diagram results as in Figure 4.2(b). The critical phase transition temperatures of cooling and warming increase with C-1805 concentration, as in monostearin/hazelnut oil mixtures reported by Chen *et al.*<sup>34</sup> Slight thermal hysteresis exists between cooling and warming. This is due to the instability of the mixtures at the phase transition temperatures and the difference in the energy barrier involved during crystallisation and melting.<sup>34</sup> The inset photos in Figure 4.2(b) show an EVOO solution/dispersion containing 5 wt.% C-1805 at certain temperatures during cooling. It is a transparent liquid at 90 °C in the one-phase region, slightly cloudy at 70 °C near the phase boundary and a turbid viscous dispersion at 25 °C within the two-phase region where surfactant crystals coexist with an oil solution of surfactant at its solubility limit.

DSC was also carried out on a 10 wt.% C-1805 in EVOO dispersion by heating to 90 °C for 10 min, followed by cooling to 20 °C at 3 °C min<sup>-1</sup> (hold for 5 min) then warming to 90 °C at 3 °C min<sup>-1</sup>. During cooling (Figure 4.1(b)), the thermogram displays a broad crystallisation peak centred at 38.5 °C. The onset temperature of crystallisation is 56.0 °C, much lower than the visual phase transition temperature of ~ 80 °C, albeit for different cooling rates. The reason for this difference can be explained as follows. When cooling gradually from the isotropic one-phase region, sucrose mono-, di- and triester fractions may favour the formation of reverse micelles in EVOO, during which no enthalpy change is involved, see Figure 4.26(b) later.<sup>18,33</sup> Upon cooling further, crystallisation gradually develops. The melting profile is given in Figure 4.1(a). It exhibits one peak at 58.8 °C and melting is over at 65.0 °C. The thermal behaviour determined here is in line with that of SE (HLB no. = 2) in sunflower oil described by Sintang *et al.*<sup>18</sup>

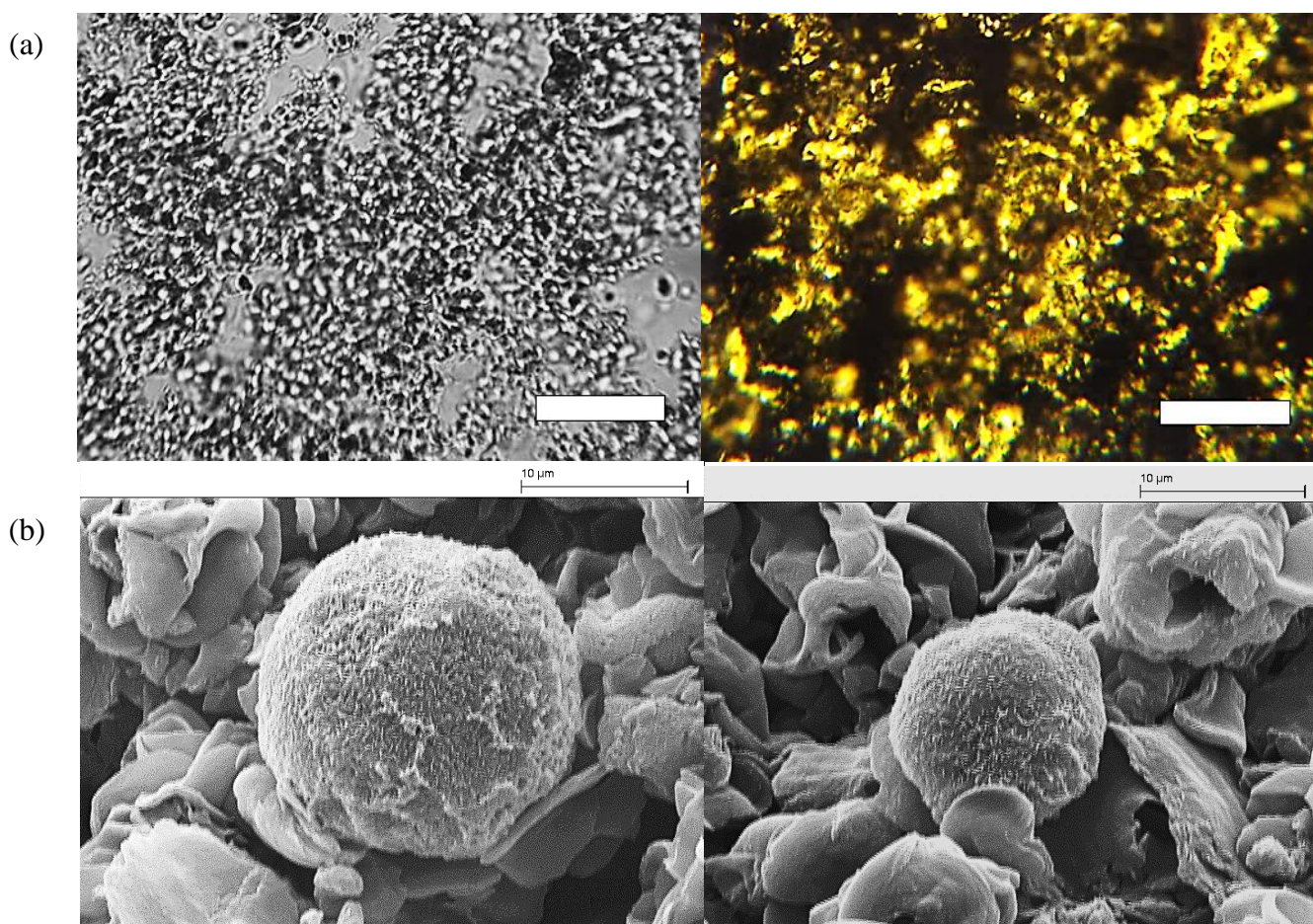
**Figure 4.2.** (a) Appearance of vials containing 10 wt.% C-1805 in EVOO at various temperatures in °C upon cooling at 1 °C min<sup>-1</sup>. (b) Solubility diagram of C-1805 in EVOO based on visual observations; cooling (●) and warming (○) rates were 1 °C min<sup>-1</sup>. Inset: photos of vials containing 5 wt.% C-1805 in EVOO at three temperatures in °C upon cooling. Scale bars = 1 cm.



#### 4.2.2 Crystal morphology and molecular interactions

The microstructure of an EVOO dispersion at room temperature was first visualized by optical microscopy. Non-polarized and polarized light microscopy images of 10 wt.% C-1805 in EVOO are shown in Figure 4.3(a). A dense population of anisotropic C-1805 crystals (bright) exist within the isotropic oil matrix (black). For better visualization, cryo-SEM images were obtained, and the representative ones are given in Figure 4.3(b). C-1805 crystals are spherical and polydisperse with diameters  $\leq 20\ \mu\text{m}$ .<sup>18</sup>

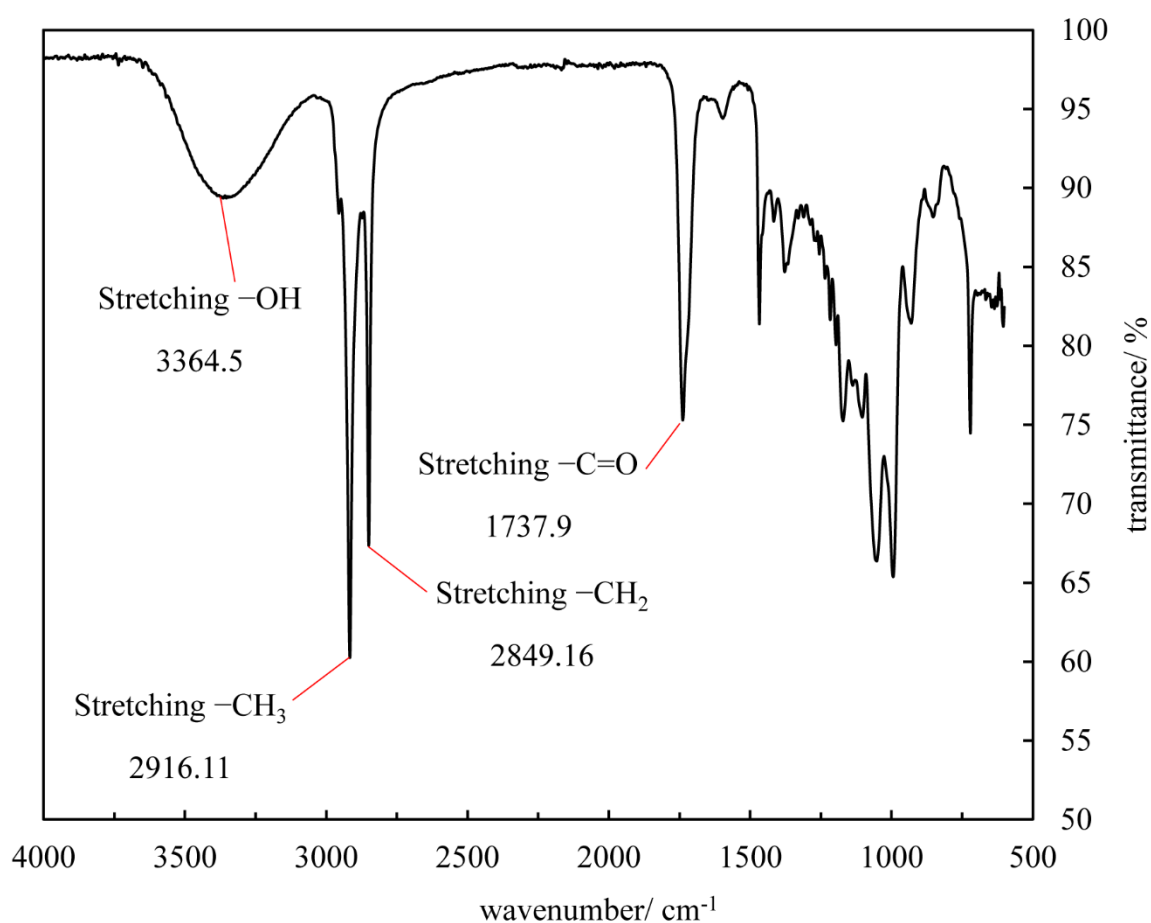
**Figure 4.3.** (a) Non-polarized (left) and polarized (right) micrographs of 10 wt.% C-1805 in EVOO at room temperature, scale bars = 50  $\mu\text{m}$ . (b) Cryo-SEM images of surfactant crystals.



A sucrose molecule is hydrophilic with 8 hydroxyl groups. When esterified with fatty acids, the hydrophobicity increases during which new carbonyl groups are formed at the expense of  $-\text{OH}$  groups. According to the literature, the existence of hydrogen bonding (intramolecular or intermolecular) can broaden the infrared absorption band and lower the absorption frequency for hydroxyl groups.<sup>35</sup> Figure 4.4 shows the FT-IR spectrum at room temperature for C-1805 powder. A particular interest is in the region  $3000\ \text{cm}^{-1}$  to  $4000\ \text{cm}^{-1}$ .<sup>36</sup>

The  $\nu_{\text{OH}}$  peak of  $-\text{OH}$  groups appears at  $3364\text{ cm}^{-1}$  which is much lower than that of free  $-\text{OH}$  groups ( $\sim 3600\text{ cm}^{-1}$ ), implying the formation of intermolecular and/or intramolecular hydrogen bonds among unsubstituted  $-\text{OH}$  groups and ester carbonyl groups.<sup>35-37</sup> The two peaks at  $2916\text{ cm}^{-1}$  and  $2849\text{ cm}^{-1}$  are indicative of  $-\text{CH}_3$  and  $-\text{CH}_2$  stretching vibrations, respectively.<sup>38</sup> The  $\text{C}=\text{O}$  stretching peak can be identified at  $1738\text{ cm}^{-1}$ .<sup>39</sup> The representative functional groups herein are the same as those of Youan *et al.*<sup>38</sup>

**Figure 4.4.** FTIR spectrum of C-1805 powder at room temperature.

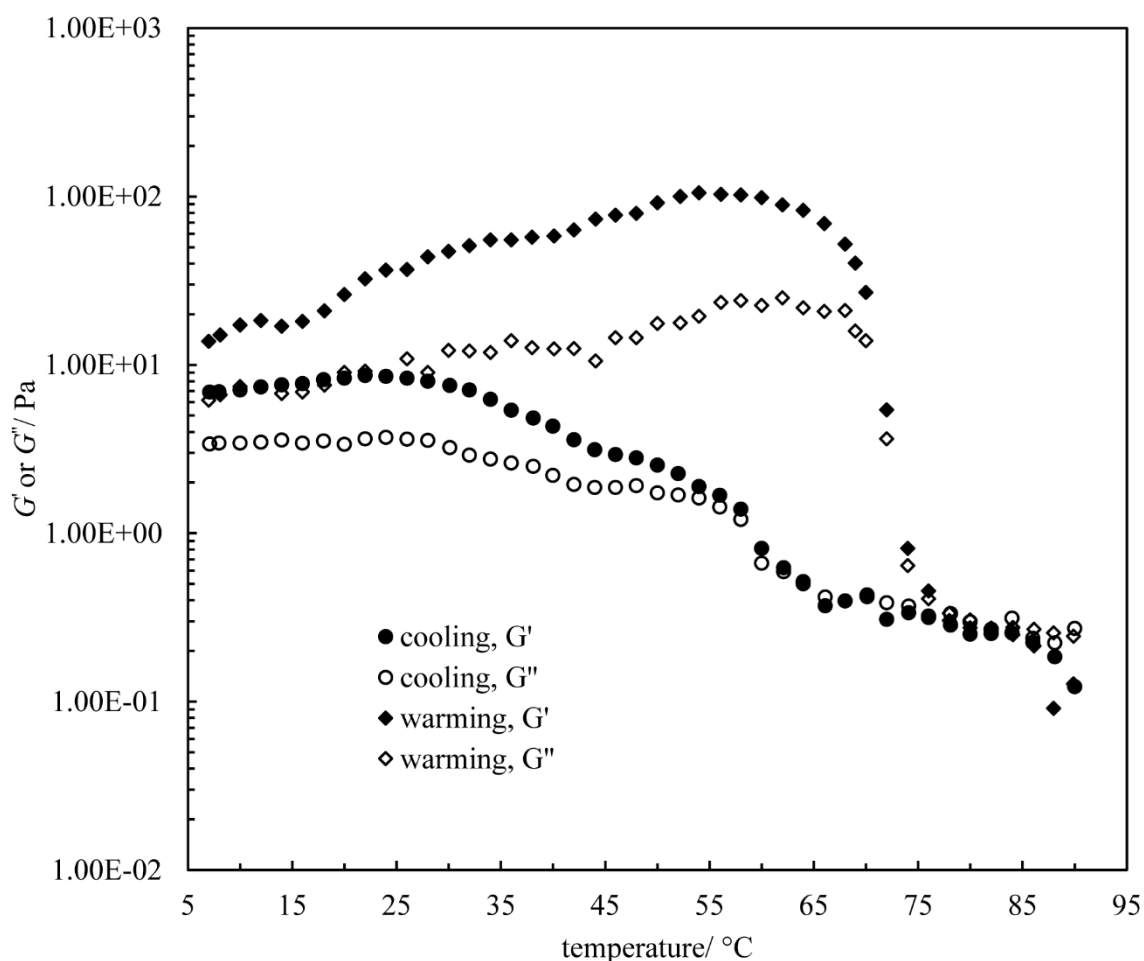


#### 4.2.3 Rheology

The rheological evolution of a mixture of C-1805 and EVOO was investigated by temperature sweep under a small deformation oscillation mode. An EVOO solution of 10 wt.% C-1805 at  $90\text{ }^{\circ}\text{C}$  was cooled stepwise to  $7\text{ }^{\circ}\text{C}$  at  $1\text{ }^{\circ}\text{C min}^{-1}$  (5 min aging) followed by heating at  $1\text{ }^{\circ}\text{C min}^{-1}$  with  $f = 1\text{ Hz}$  and  $\tau = 0.1\text{ Pa}$ . The variation of  $G'$  (storage modulus) and  $G''$  (loss modulus) is shown in Figure 4.5 as a function of temperature. At high temperature, the values of  $G'$  and  $G''$  are low ( $< 1\text{ Pa}$ ) with  $G' < G''$  typical of a liquid. On cooling, both values increase

slowly until  $G' = G''$  at  $\sim 64$  °C, below which they increase more rapidly levelling off with  $G' > G''$ . The sample appears as a weak, viscous gel at 7 °C. During warming, the values of  $G'$  and  $G''$  first increase possibly due to the strengthening of the crystal network by sintering between adjacent crystals.<sup>21</sup> Subsequently both parameters suffer a slow decay from  $\sim 60$  °C followed by an abrupt decay from  $\sim 69$  °C, arising mainly from the melting of the crystals. The macroscopic structure deteriorates from solid-like ( $G' > G''$ ) into liquid-like ( $G' < G''$ ). We note that oleogels at low temperature are relatively soft compared to other systems in the literature, reflecting strong affinity of the solute for the solvent through H-bonding (later).<sup>18</sup>

**Figure 4.5.**  $G'$  (filled points) and  $G''$  (open points) as a function of temperature upon cooling (circles) and subsequent warming (diamonds) at 1 °C min<sup>-1</sup> for 10 wt.% C-1805 in EVOO. Measurements were done at a fixed stress  $\tau$  of 0.1 Pa and a fixed frequency  $f$  of 1 Hz.



### 4.3 Whipping mixtures of sucrose ester and oil

#### 4.3.1 Foams prepared and stored at same temperature

The foaming of C-1805-EVOO solutions/dispersions was studied as a function of surfactant concentration and aeration temperature. Samples were heated to 90 °C and then submitted to gradual cooling at 1 °C min<sup>-1</sup>. Upon reaching the temperature of interest, the mixtures were whipped continuously using a single beater electric whisk for 10 min. Figure 4.6(a) shows the change in appearance for 5 wt.% C-1805 in EVOO upon whipping at four representative temperatures. The sample at 80 °C before whipping is a clear solution, which becomes a slightly cloudy dispersion at 70 °C and more turbid at the other two temperatures. The best foaming occurs at 80 °C with the foam volume increasing progressively with whipping time. A significant decline in foam volume occurs at 70 °C near the phase boundary. Very little or no foam is produced at 60 °C or 50 °C in the two-phase region. Whipping was performed for other surfactant concentrations at various temperatures in the one-phase or two-phase regions. All photos of the samples before and immediately after whipping are displayed in Figure 4.7. The foamability increases with increasing aeration temperature with good foaming achievable in the one-phase region and poor foaming within the two-phase region. This finding contrasts that in all earlier work where oil foaming was only possible in the two-phase region in the presence of surface-active lipid crystals and not from one-phase molecular solutions.<sup>1,2,20-31</sup> This will be discussed later.

The influence of whipping temperature and surfactant concentration on the over-run is shown in Figure 4.6(b). Increasing the surfactant concentration results in a gradual increase in the over-run up to a certain level. The highest volume fraction of air incorporated is 0.63, corresponding to random close packing of monodisperse hard spheres. A separate oil sample containing 5 wt.% C-1805 was whipped from 60 °C while simultaneously cooled to induce crystallization. The over-run decreases gradually on lowering the temperature, Figure 4.6(b).

**Figure 4.6.** (a) Appearance of 5 wt.% C-1805 in EVOO as a function of whipping time at various aeration temperatures cooled from 90 °C. Scale bars = 1 cm. (b) Variation of over-run with whipping temperature for different concentrations of C-1805 in EVOO. Filled points - whipping done isothermally cooling from 90 °C. Open squares - whipping performed from 60 °C with simultaneous cooling. All cooling rates were 1 °C min<sup>-1</sup>.

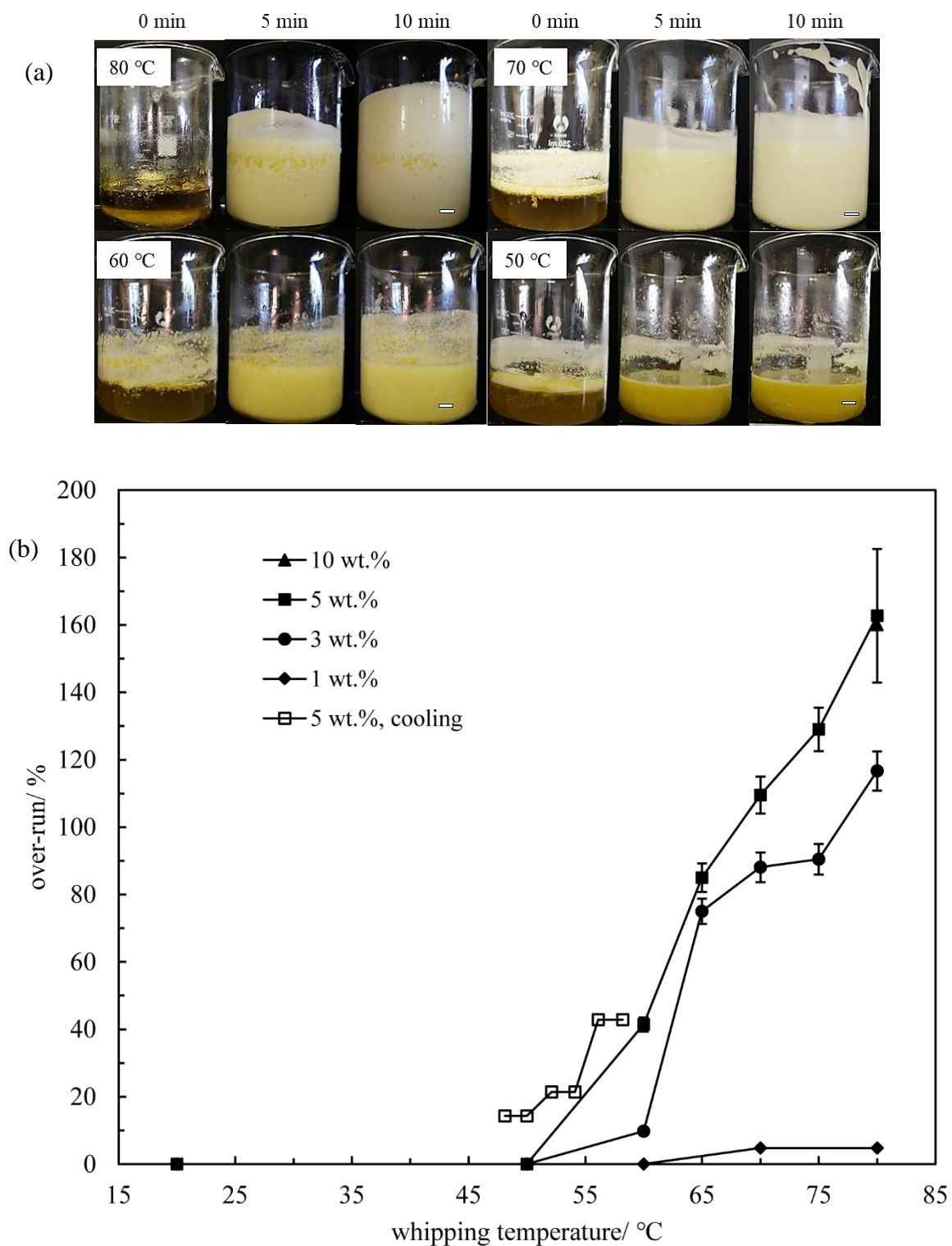
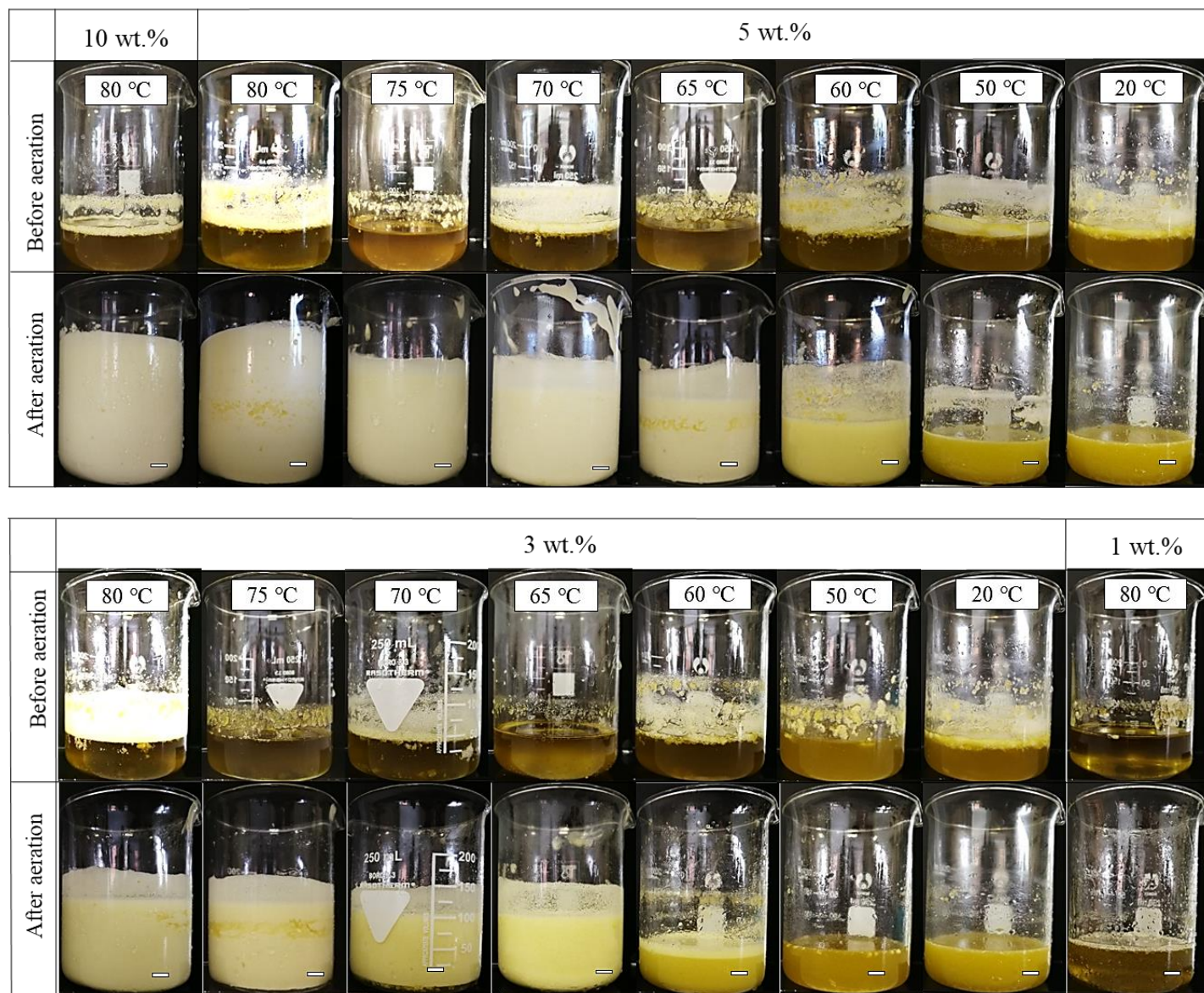


**Figure 4.7.** Photos of vessels containing different concentrations of C-1805 in EVOO before (upper) and immediately after 10 min whipping (lower) at specified aeration temperatures upon cooling at  $1\text{ }^{\circ}\text{C min}^{-1}$ . Scale bars = 1 cm.



Oil foams were stored at respective whipping temperature. Photos of the foams during storage are given in Figure 4.8 (3 wt.%) and Figure 4.9 (5 wt.%). Oil drainage occurs immediately after preparation leading to a dry foam within the first few hours. Foams also gradually decay completely *via* coarsening/coalescence.

**Figure 4.8.** Appearance of EVOO foams containing 3 wt.% C-1805 as a function of storage time at various temperatures. (a) 80 °C, (b) 75 °C, (c) 70 °C and (d) 65 °C. Storage temperature was the same as preparation temperature. Scale bars = 1 cm.

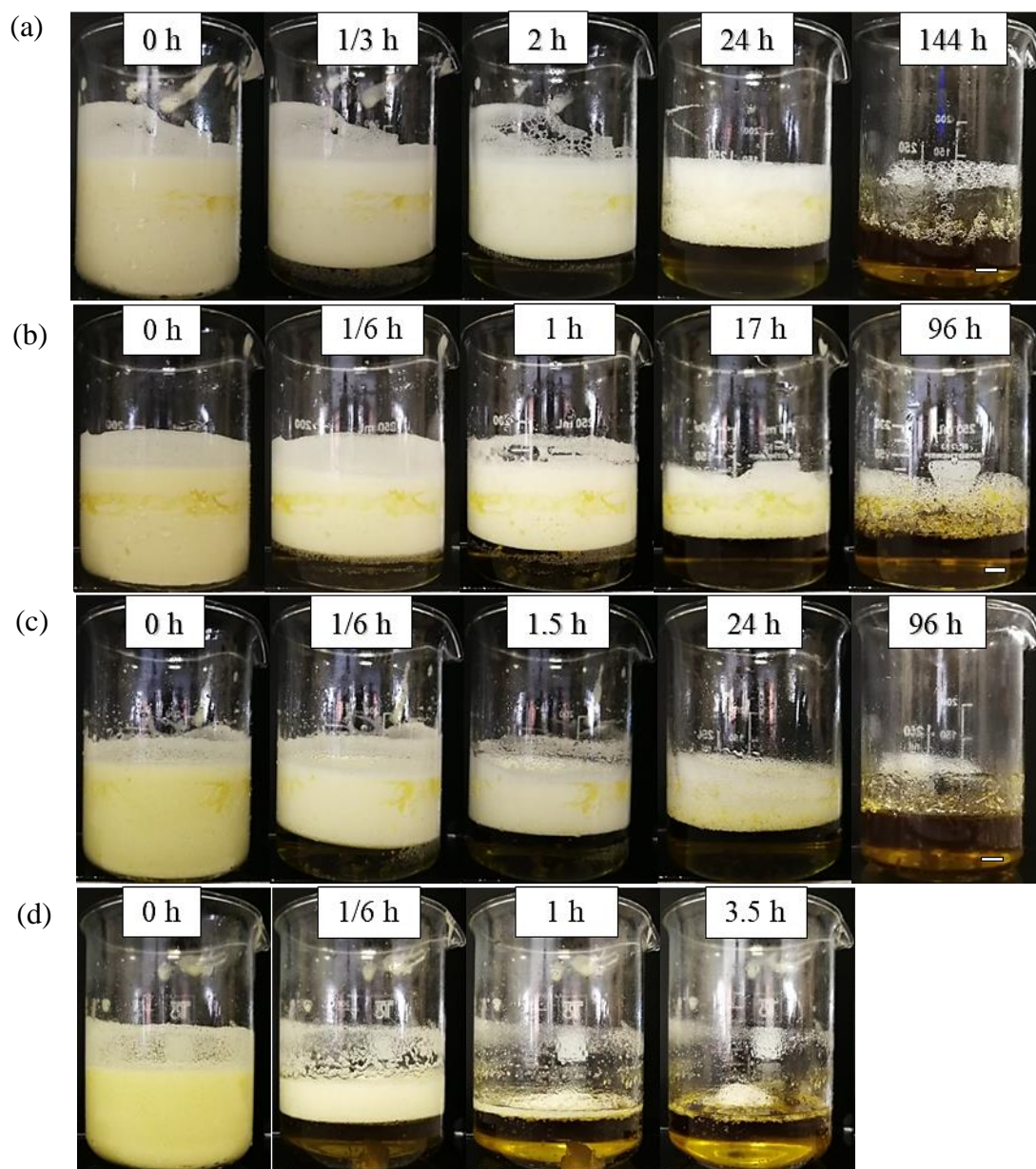
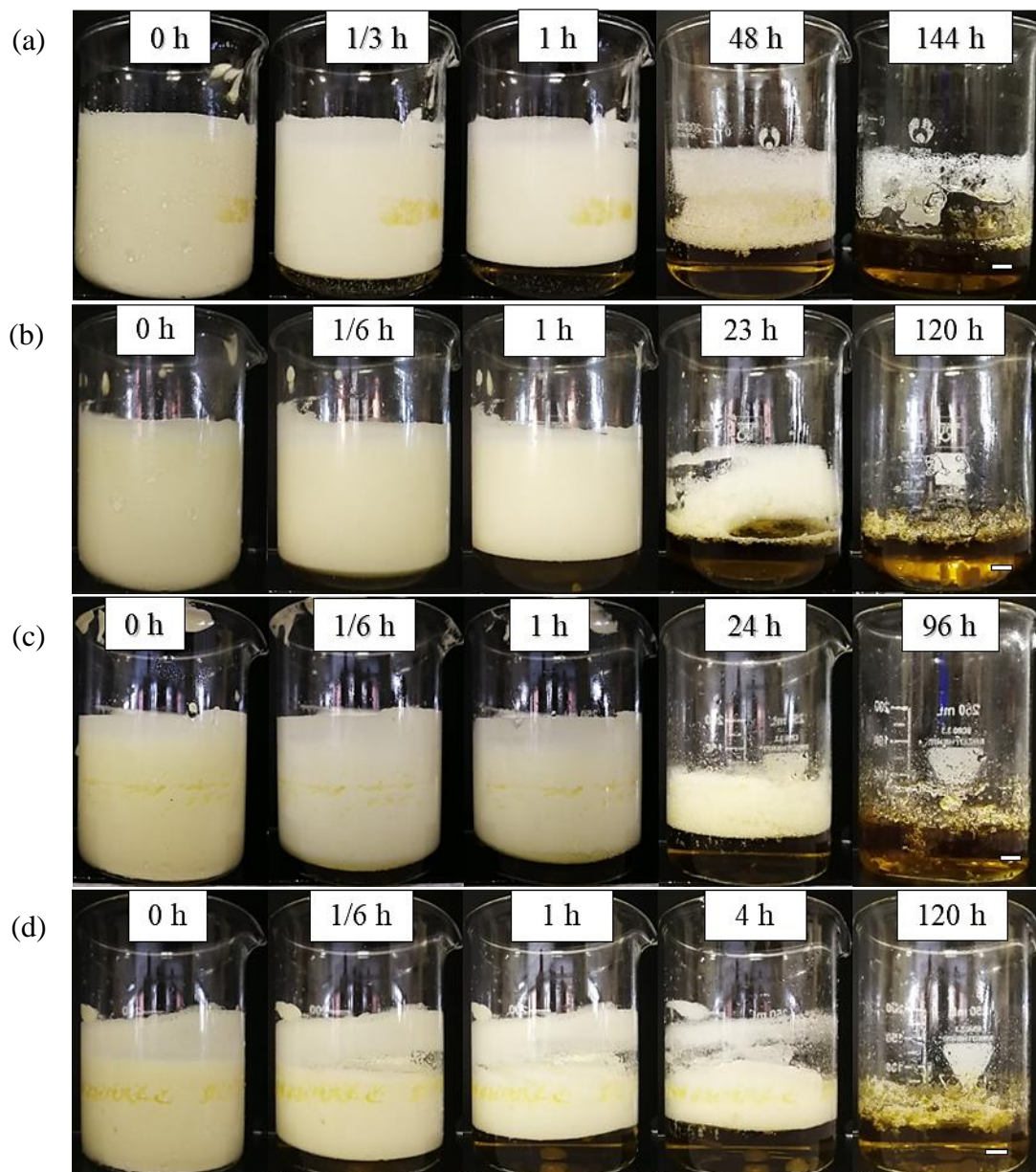
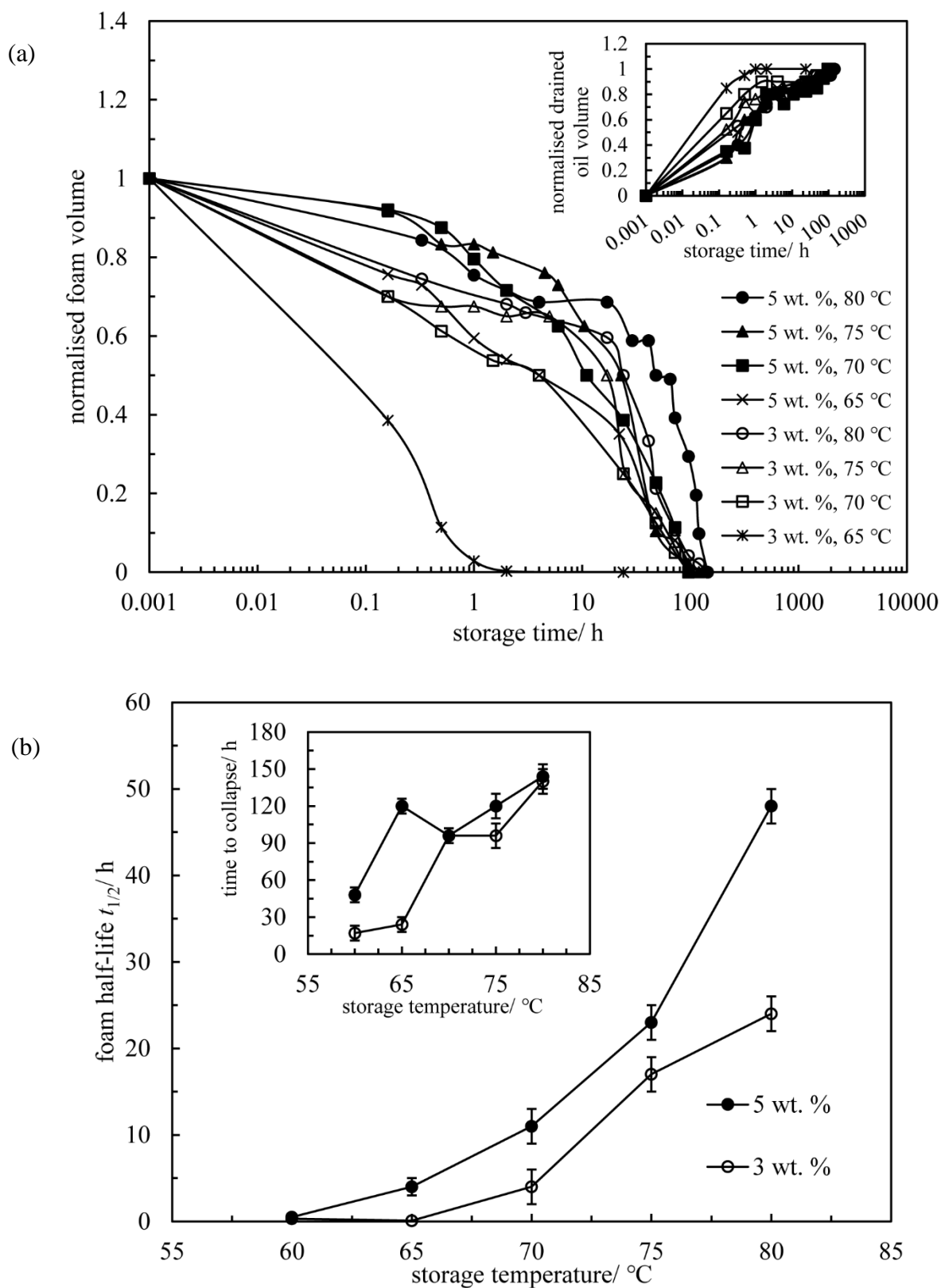


**Figure 4.9.** Appearance of EVOO foams containing 5 wt.% C-1805 as a function of storage time at various temperatures. (a) 80 °C, (b) 75 °C, (c) 70 °C and (d) 65 °C. Storage temperature was the same as preparation temperature. Scale bars = 1 cm.



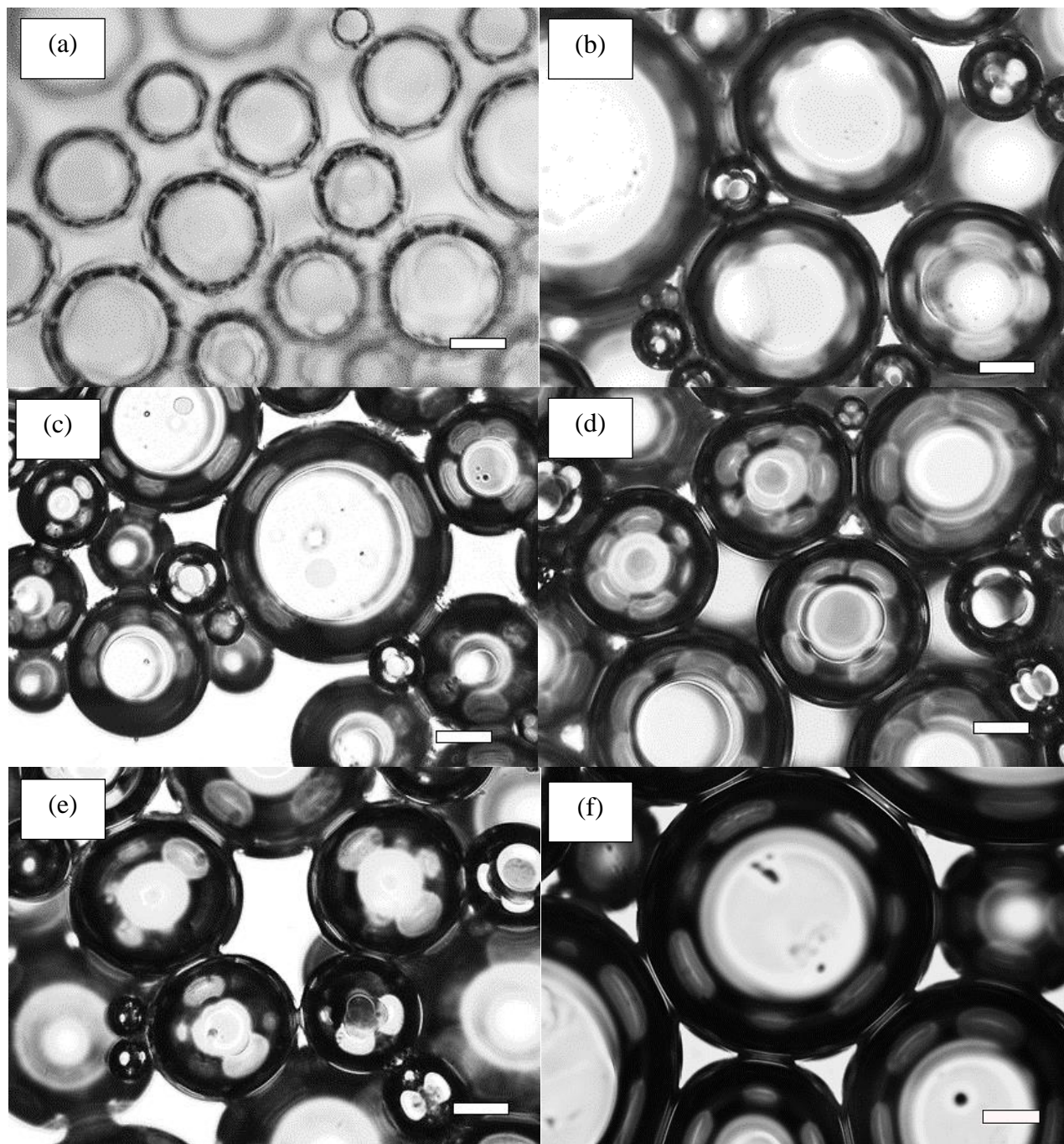
The normalized volume of foam or drained oil, defined as the volume ratio of foam/drained oil during storage relative to that initially, is plotted in Figure 4.10(a) as a function of storage time. The foam half-life ( $t_{1/2}$ ) and the time for complete foam collapse are plotted against storage temperature in Figure 4.10(b). Both foam parameters increase with an increase in temperature and surfactant concentration. However, although foamability is high at high temperature, stability is moderate with no foam remaining after around 5 days.

**Figure 4.10.** (a) Normalised volume of C-1805-stabilised EVOO foam and normalised volume of drained oil (inset) against storage time for systems in Figure 4.6. (b) Foam half-life and time for complete foam collapse (inset) against storage temperature (same as whipping temperature).



Optical micrographs of some foams immediately after preparation and during storage are given in Figure 4.11. The bubbles are polydisperse and spherical possessing smooth surfaces. The increase in bubble size with time is evident.

**Figure 4.11.** Optical micrographs of C-1805-stabilised EVOO foams for systems in Figure 4.6 immediately after whipping for (a) 10 wt.% at 80 °C, (b) 5 wt.% at 80 °C, (c) 5 wt.% at 70 °C, (d) 3 wt.% at 80 °C and (e) 3 wt.% at 70 °C. (f) System (e) after 6 h aging. Scale bars: (a) 50  $\mu\text{m}$ , (b)-(f) 25  $\mu\text{m}$ .



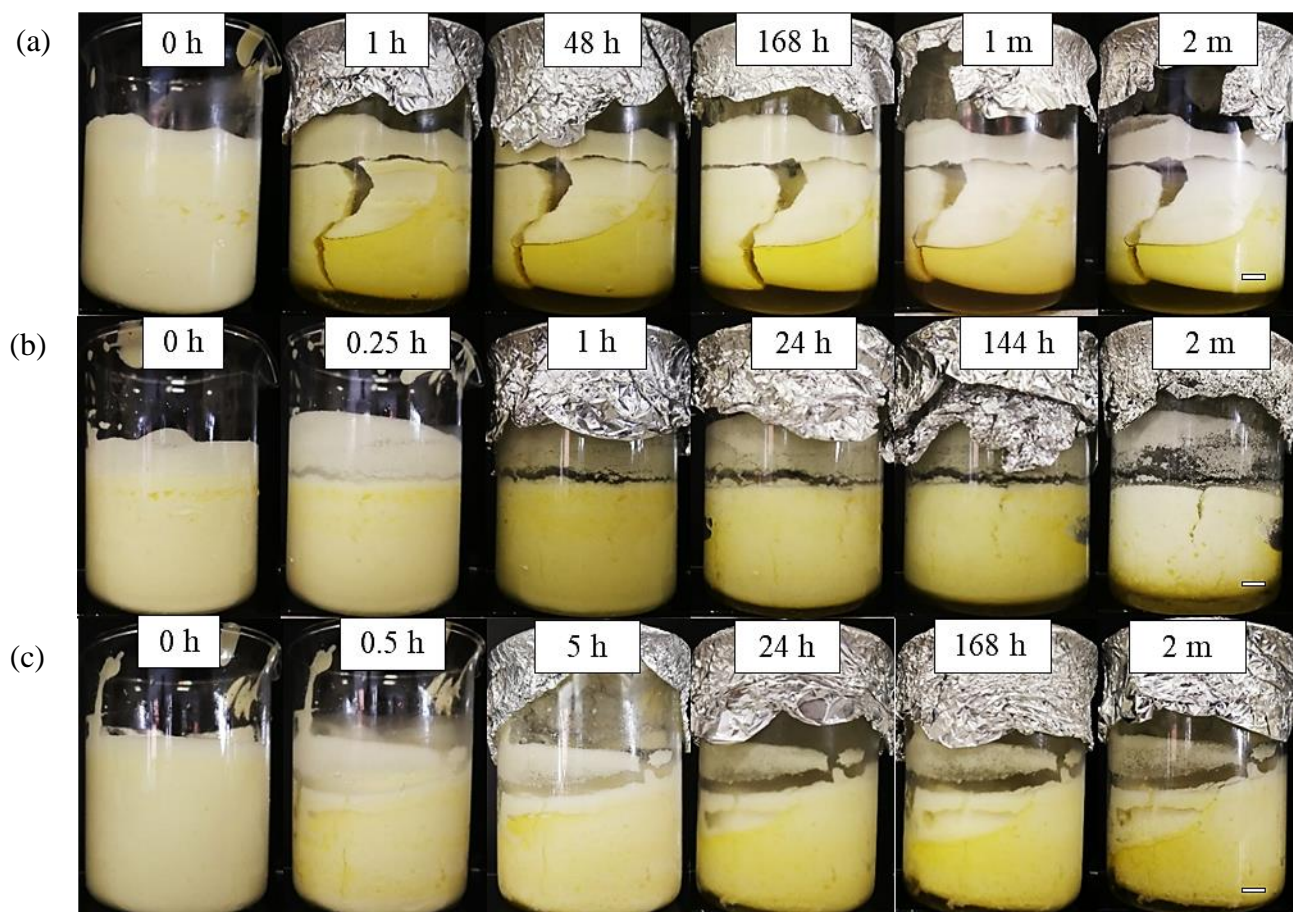
#### 4.3.2 Protocol for fabricating very stable foams

In aqueous foams of the saponin glycyrrhizic acid, cooling can strengthen the intermolecular interactions, *e.g.* hydrogen bonding, between surfactant molecules both at bubble surfaces and in bulk forming a firm three-dimensional (3D) network enhancing foam stability.<sup>40,41</sup> Moreover, increasing the cooling rate can stabilise the foams quickly before aging of the foams commences. On this initiative, we decided on a post-whipping cooling procedure to prevent foam collapse in which various parameters were optimized including cooling rate, storage temperature and surfactant concentration. After foam preparation with 10 min whipping at 80 °C, the foam was quickly transferred to room temperature or an ice bath of - 5 °C, corresponding to slow cooling ( $\sim 1\text{ }^{\circ}\text{C min}^{-1}$ ) or rapid cooling ( $\sim 4\text{ }^{\circ}\text{C min}^{-1}$ ), respectively. Upon reaching either room temperature or 7 °C (fridge), the cooled samples were stored at these temperatures for further investigation.

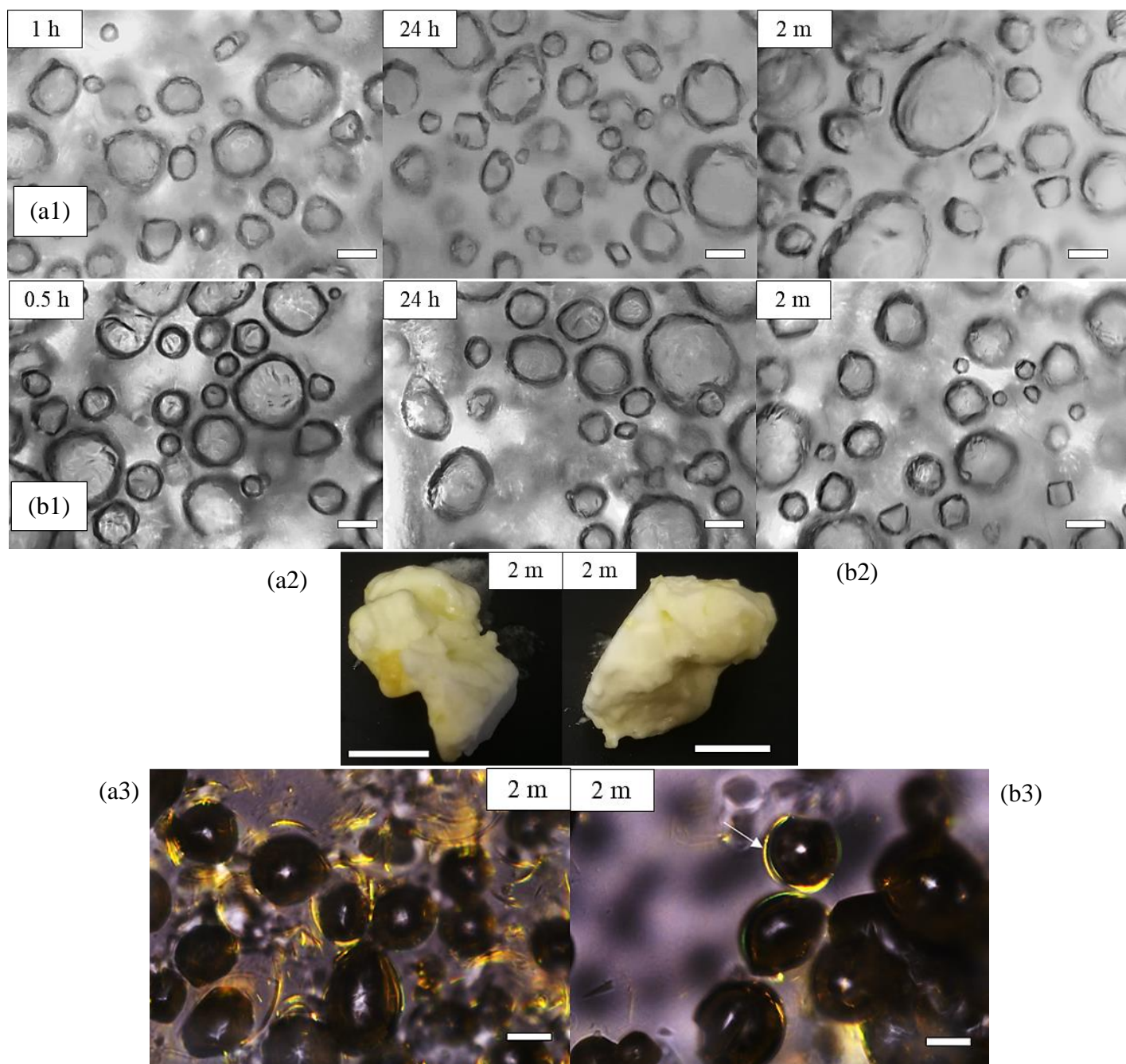
Figure 4.12 illustrates the effect of cooling rate and storage temperature on the stability of EVOO foams containing 5 wt.% C-1805. Compared with foams cooled slowly to room temperature, those subject to rapid cooling exhibit higher stability. This is because faster kinetics of surfactant crystal formation can arrest foam aging more effectively.<sup>41,42</sup> For slow cooling, oil drains quickly at the vessel bottom. In addition, the foam becomes fractured possibly due to its inherent brittleness. For rapid cooling, foams stored at 7 °C exhibit less drainage than those stored at room temperature and are more robust (see Figure 4.12). In fact, the initial average bubble diameter after cooling is  $57 \pm 3\text{ }\mu\text{m}$ , very close to that of  $62 \pm 3\text{ }\mu\text{m}$  at 80 °C, revealing that the foam does not suffer on rapid cooling.

Figure 4.13 reveals the microstructural evolution of EVOO foams after rapid cooling. For the foam stored at room temperature, the average bubble size gradually increases. In contrast, for the foam stored at 7 °C, the bubble size distribution remains unchanged during storage ( $p > 0.05$ ). Many of the bubbles are non-spherical implying solid-like interfaces.<sup>43</sup> In addition, the bubble surfaces at 7 °C are more coherently covered by C-1805 crystals than those at room temperature. A higher extent of interfacial crystallisation increases the rigidity of interfaces and enhances the firmness of an oil foam<sup>1,20,30</sup> or water-in-oil emulsion.<sup>44</sup>

**Figure 4.12.** Appearance of EVOO foams containing 5 wt.% C-1805 submitted to different quenching conditions immediately after 10 min whipping. Foams prepared at 80 °C were subjected to (a) slow cooling to room temperature then stored at room temperature, (b) rapid cooling in an ice bath of -5 °C then stored at room temperature, (c) rapid cooling in an ice bath of -5 °C then stored at 7 °C. Scale bars = 1 cm.

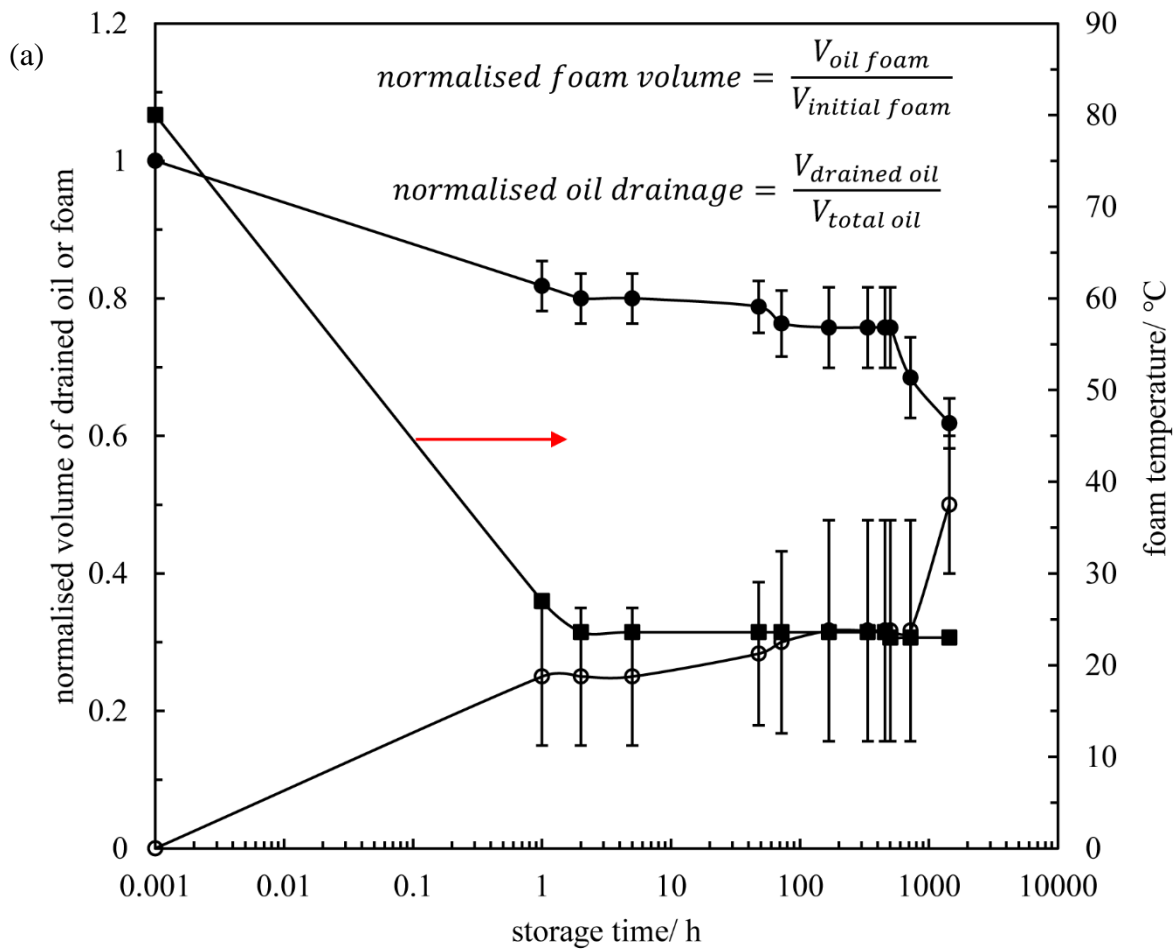


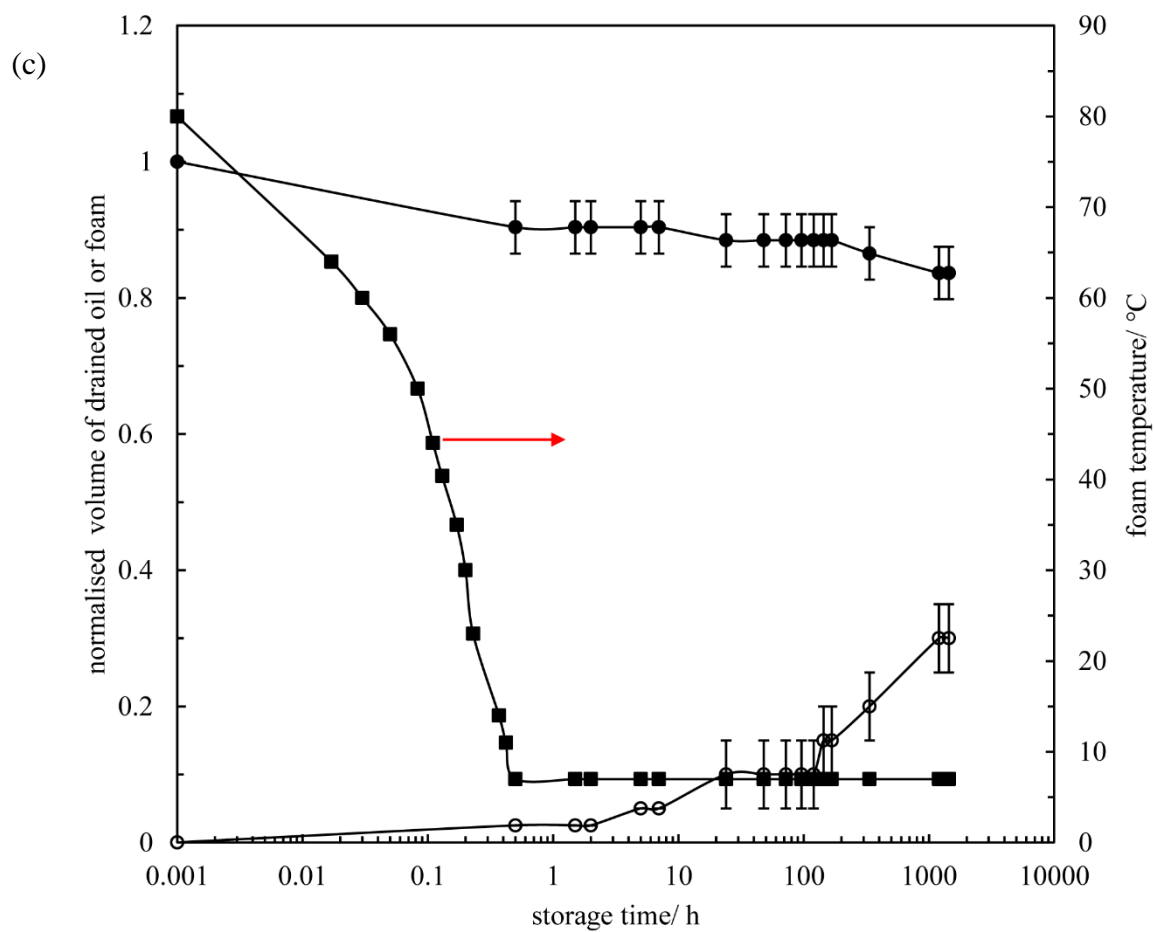
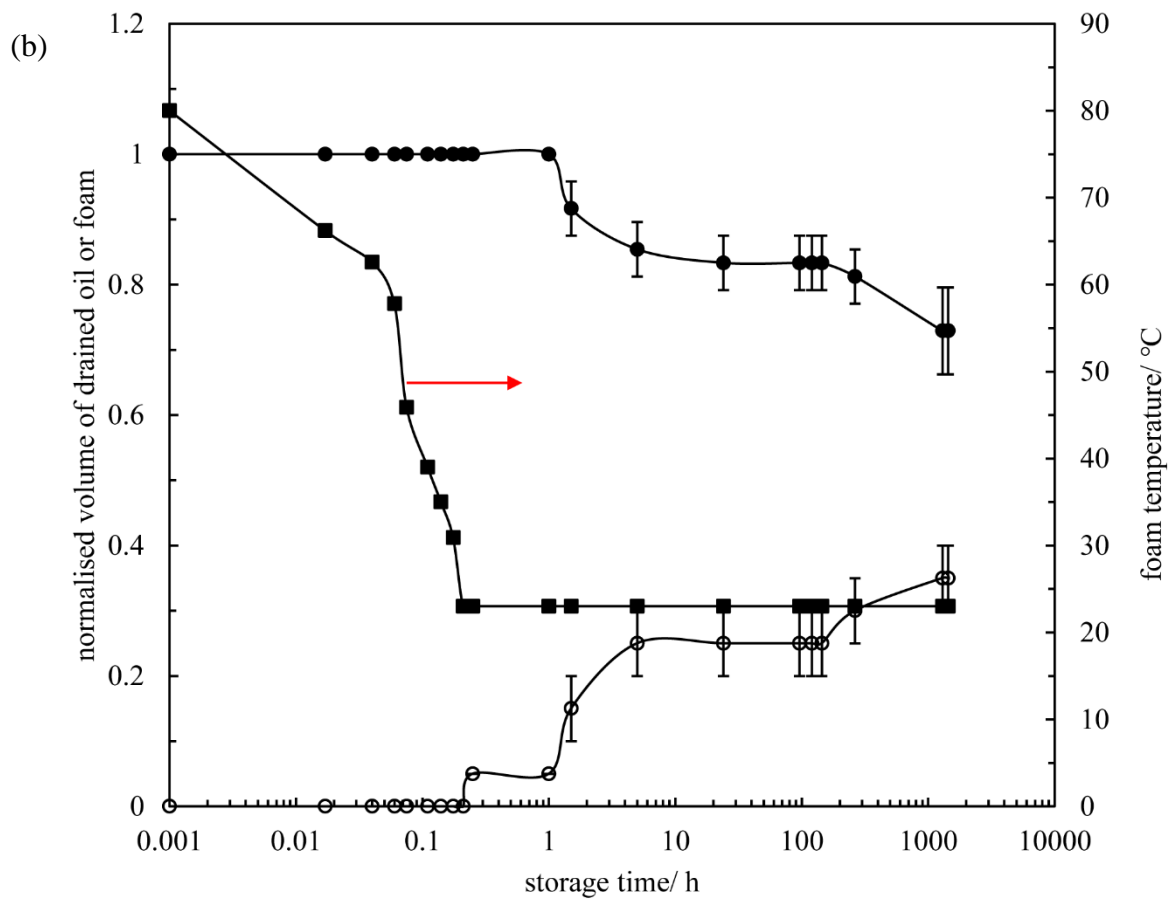
**Figure 4.13.** Microstructural evolution for systems in Figure 4.12 submitted to rapid cooling then storing at (a1) room temperature or (b1) 7 °C. Photos after 2 months storage at (a2) room temperature or (b2) 7 °C. Corresponding polarised microscopy images at (a3) room temperature or (b3) 7 °C. Scale bars equal 1 cm and 50  $\mu$ m for photos and micrographs, respectively. White arrow in (b3) indicates C-1805 crystals at bubble surface.



The normalised volume of foam and drained oil along with foam temperature during cooling is plotted in Figure 4.14 as a function of storage time. The volume fraction of remaining foam after 2 months is ~ 84% at 7 °C and ~ 73% at room temperature compared with only ~ 62% if slow cooled.

**Figure 4.14.** Normalised volume of foam (●) and drained oil (○) and foam temperature (■) as a function of storage time for systems in Figure 4.12. All foams were prepared at 80 °C and either (a) cooled slowly to room temperature, (b) cooled rapidly and stored at room temperature or (c) cooled rapidly and stored at 7 °C.





To study the impact of surfactant concentration on foam stability, EVOO foams containing 10 wt.% C-1805 prepared at 80 °C were subjected to rapid cooling and subsequent storage at either room temperature (Figure 4.15(a) and Figure 4.16(a)) or 7 °C (Figure 4.15(b) and Figure 4.16(b)). At room temperature, only ~ 5 vol% of oil drains whilst the foam decays slightly until ~ 98 vol% remains within 2 h or so. The average bubble diameter (40 – 50  $\mu\text{m}$ ) remains more or less unchanged on storage, indicating the absence of coarsening and coalescence (Figure 4.17). A photo' of the foam after 2 months storage at room temperature alongwith a polarised microscopy image is also given in Figure 4.16(a). Non-spherical bubbles are enclosed by a compact crystal layer(s), characteristic of Pickering-type stabilisation (*i.e.* solid particle stabilised).<sup>1</sup> More importantly, for the foam stored at 7 °C it remains completely stable for at least 2 months. Moreover, it behaves as a firm gel which can withstand its own weight without deformation when inverted (inset in Figure 4.15(b)). The higher surfactant concentration results in an increase in the volume fraction of crystals both at bubble surfaces and in bulk oil. The former leads to more effective interfacial stabilisation, whilst the latter increases the bulk viscosity suppressing buoyancy-driven creaming.<sup>25</sup> We conclude that ultra-stable oil foams which do not drain, coarsen or coalesce can be fabricated at high surfactant concentration at high temperature followed by rapid cooling to a low storage temperature.

**Figure 4.15.** Appearance of EVOO foams containing 10 wt.% C-1805 submitted to rapid cooling immediately after whipping. Foams prepared at 80 °C were cooled in an ice bath of - 5 °C followed by storing at (a) room temperature or (b) 7 °C. Scale bars = 1 cm.

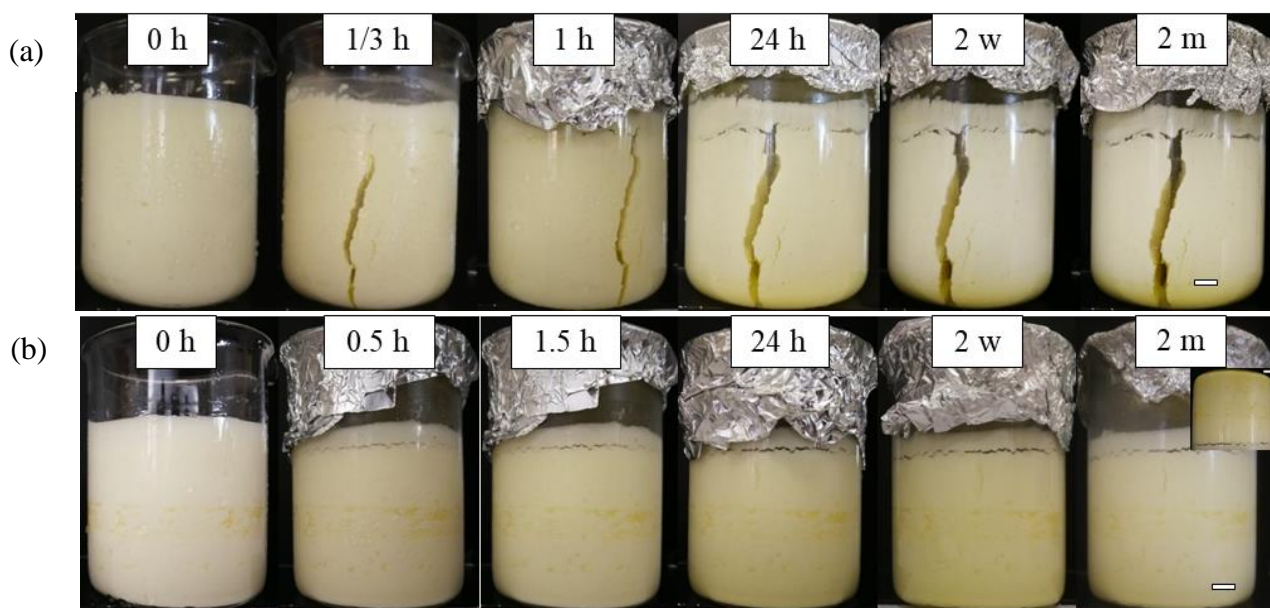


**Figure 4.16.** Normalized volume of foam (●) and drained oil (○) and foam temperature (■) as a function of aging time for systems in Figure 4.15. Foams prepared at 80 °C were cooled in an ice bath of -5 °C followed by storing at (a) room temperature or (b) 7 °C. Inset in (a): photo' and polarized microscopy image of the foam after 2 months storage at room temperature. White arrow indicates crystalline C-1805 layer at bubble surface. Inset in (b): photo' of the foam after 2 months storage at 7 °C.

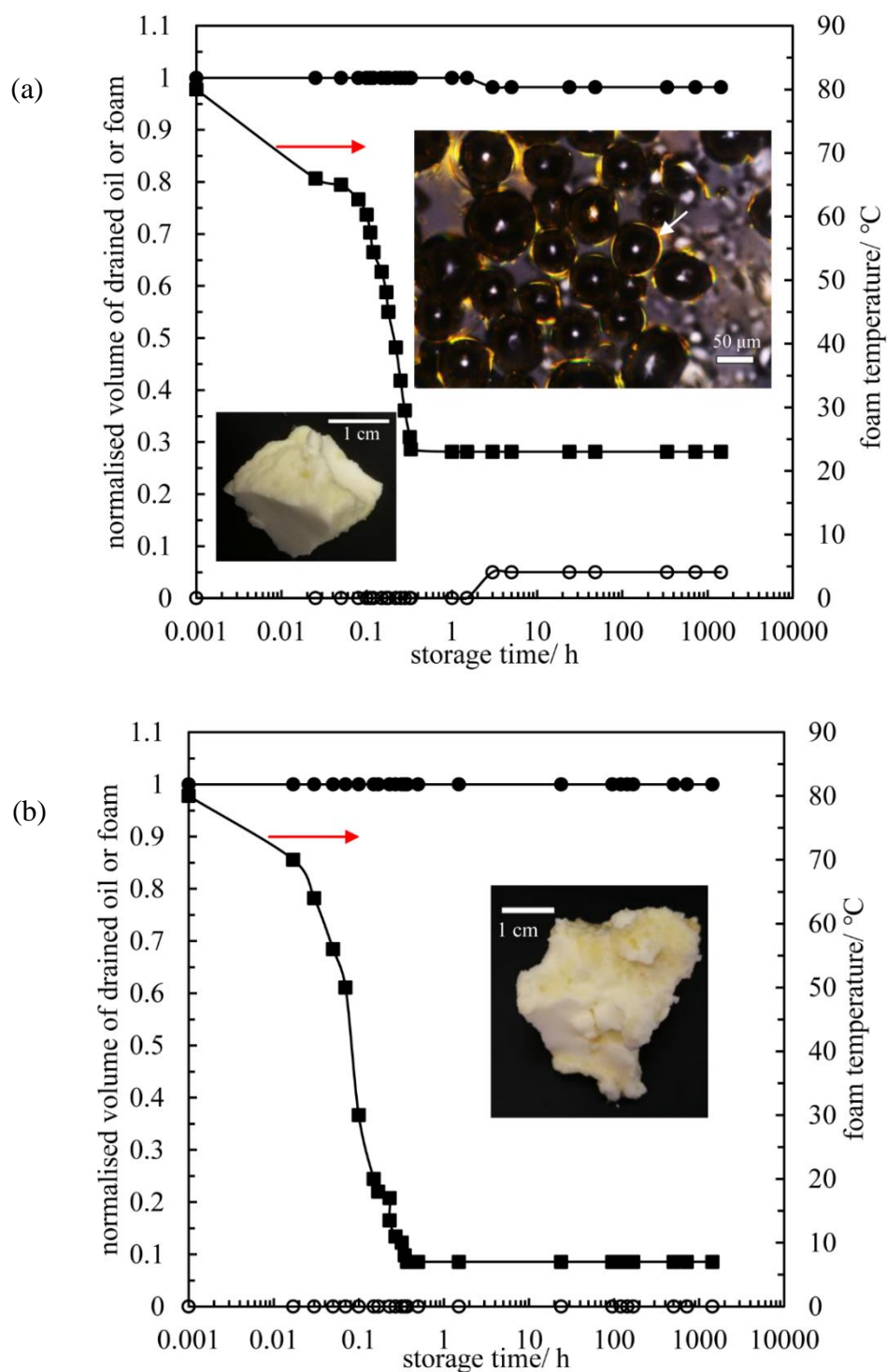
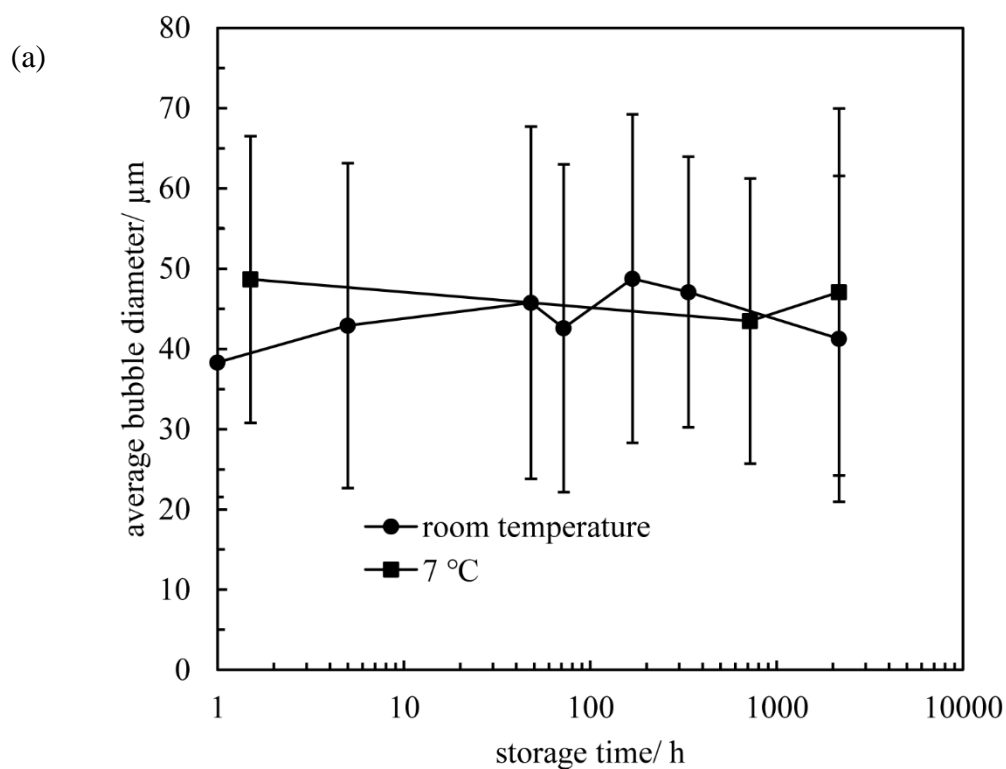
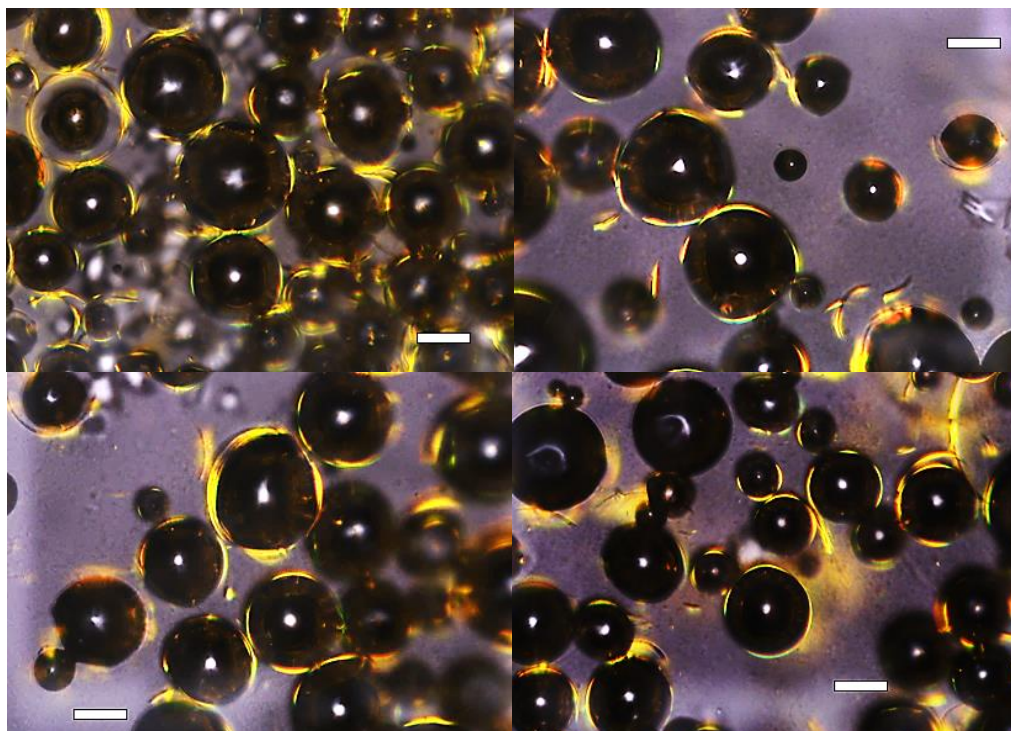


**Figure 4.17.** (a) Variation of average bubble diameter with storage time for systems in Figure 4.15 (10 wt.% C-1805 in EVOO) submitted to rapid cooling then storing at room temperature (●) or 7 °C (■). The bubble diameter is the average value of at least 200 representative bubbles. (b) Polarized micrographs of the foam after 2 months storage at 7 °C. Scale bars = 50  $\mu\text{m}$ .



(b)



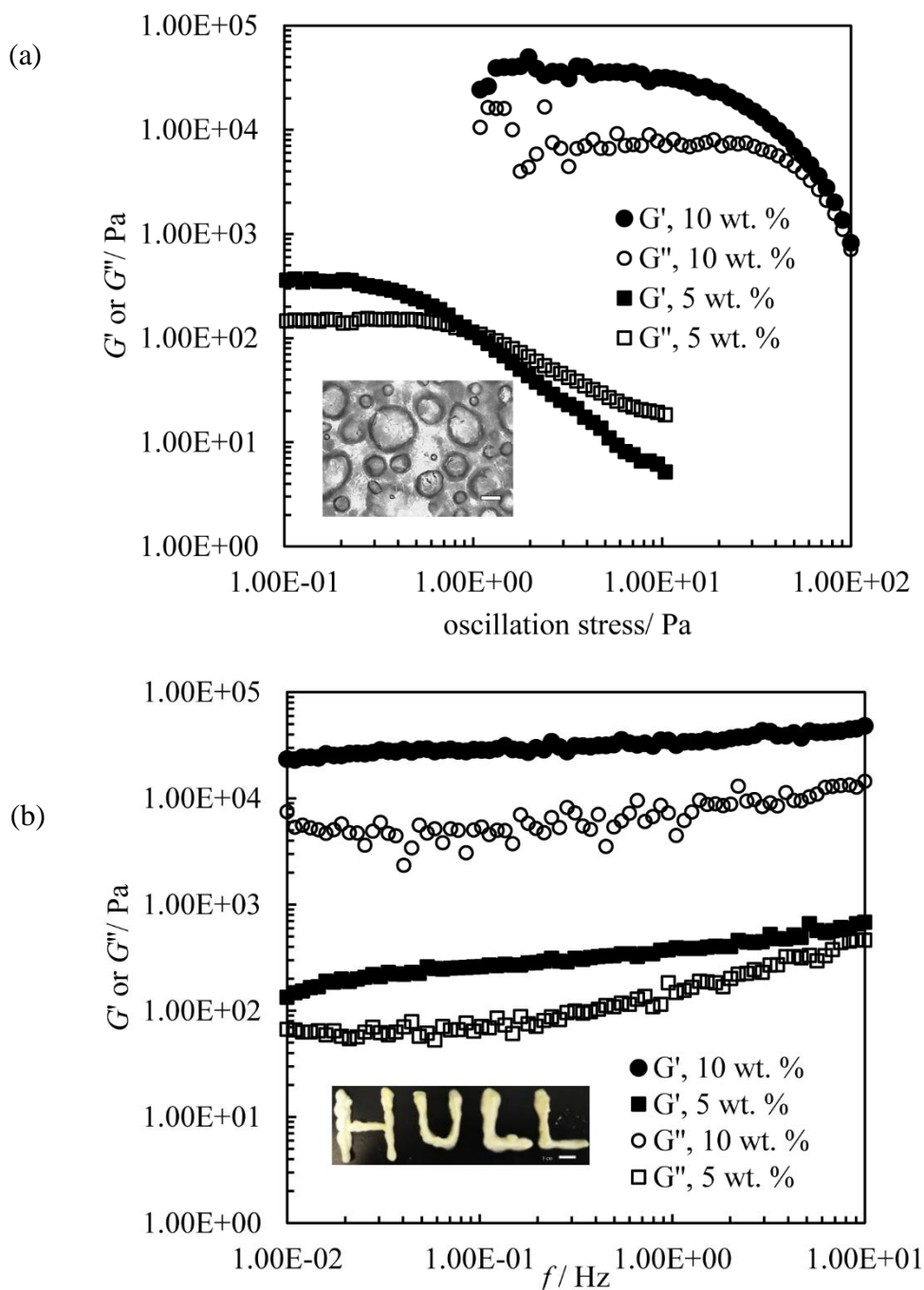
### 4.3.3 Rheology of stable foam

The rheological properties of the resulting foams at 7 °C were studied by amplitude sweep and frequency sweep experiments in an oscillation mode. For the amplitude sweep (Figure 4.18(a)), the elastic modulus ( $G'$ ) is always higher than the viscous modulus ( $G''$ ) within the linear viscoelastic region, indicative of an elastic solid-like network. Then both parameters decay gradually since the transient colloidal network bounded by non-covalent forces is unable to withstand the applied external stress degrading irreversibly into a viscous, liquid dispersion. Bubbles remain intact after the sweep (inset in Figure 4.18(a)). The yield stress ( $\tau_Y$ ) where  $G' = G''$  and  $G'$  within the linear viscoelastic region both increase with surfactant concentration (1 Pa for 5 wt.% and 100 Pa for 10 wt.%), indicating an enhancement in the elasticity of the foam network.<sup>45</sup> To fully arrest oil drainage,  $\tau_Y$  of the foam network should be much higher than the local gravity-induced stress ( $\tau_g = \frac{4}{3}r\rho_{oil}g$ ), where  $r$  is the average bubble radius,  $\rho_{oil}$  is the oil density at 7 °C and  $g$  is the acceleration due to gravity.<sup>20,46</sup> The estimated value of  $\tau_g$  for the 5 wt.% foam is 0.4 Pa comparable to  $\tau_Y$  (1 Pa), whilst  $\tau_g$  for the 10 wt.% foam is 0.3 Pa which is significantly lower than  $\tau_Y$  (100 Pa). The estimates correlate well with our observations.

To determine the viscoelasticity of a foam sample, a frequency sweep was performed at a fixed oscillation stress within the linear viscoelastic region (Figure 4.18(b)). Here  $G'$  is dominant over  $G''$  over the studied frequency range. In addition,  $G'$  for a 10 wt.% C-1805 foam ( $2 \times 10^4$  Pa) is virtually independent of frequency indicating a firm gel, whereas that for 5 wt.% C-1805 varies with frequency ( $10^2 - 5 \times 10^2$  Pa) being a weaker gel.

We also notice that  $G'$  of 10 wt.% C-1805 in EVOO dispersion at 7 °C is only  $\sim 10$  Pa (see Figure 4.5), much lower than that of the foam. A plausible explanation for this contrast is that the crystal-coated air bubbles in the foam act as 'active fillers' that can interact with the surrounding crystal matrix and adjacent air bubbles *via* interfacial crystallisation and sintering, leading to an enhancement in the firmness of the foam network.<sup>20,44,47</sup> The word 'HULL' made by forcing a 10 wt.% C-1805 foam through a syringe at room temperature demonstrates the processability and structural recovery of these stable foams.

**Figure 4.18.** Rheology of EVOO foams containing 5 wt.% (squares) or 10 wt.% (circles) C-1805 after 2 months storage at 7 °C. (a) Amplitude sweep at a fixed frequency of 1 Hz. Inset: micrograph of EVOO foam containing 5 wt.% C-1805 after amplitude sweep, scale bar = 50  $\mu\text{m}$ . All bubbles possess textured surfaces and some of them are non-spherical. (b) Frequency sweep at fixed stress of 0.1 Pa (5 wt.%) or 10 Pa (10 wt.%). Inset: photo of foam containing 10 wt.% C-1805 forced through a syringe. Foams prepared at 80 °C were subjected to rapid cooling in an ice bath of -5 °C then stored at 7 °C.



#### 4.3.4 Thermo-responsiveness of stable foam

One advantage of crystal-stabilised foams is that they should be destabilised upon heating. The effect of heating on the appearance of a foam (prepared at 80 °C, cooled rapidly and stored at 7 °C) containing 5 wt.% C-1805 is shown in Figure 4.19. There is no observable change until 49 °C where the first sign of oil drainage occurs. Further warming leads to more oil leakage alongwith progressive foam collapse. The drained oil is clear, implying that all surfactant crystals remain at bubble surfaces or within the thin liquid films between adjacent bubbles. When reaching and holding at 80 °C (one-phase region), the residual foam stabilised by C-1805 molecules is unstable and collapses completely within 24 h. To capture the microstructural change in the foam on heating, a sample of foam was placed on a glass slide on a microscope hot stage, the temperature of which was increased at 1 °C min<sup>-1</sup>. Initially, all foam bubbles possess rough, textured surfaces and many of them are non-spherical. During heating, many of the bubble surfaces become smoother and bubbles gradually relax into spherical ones especially above 65 °C due to the local dissolution of C-1805 crystals at the interfaces. Interestingly, we notice that the surfaces of some bubbles undergo buckling and crumpling without obvious shedding of crystals before becoming smoother, possibly because air is more soluble in oil at high temperature.<sup>48</sup> This phenomenon is discussed below and schematically shown in Figure 4.20. A significant increase in bubble size can be evidenced above 65 °C, arising from a combination of coarsening and coalescence. At 80 °C or above, the bubbles are close packed, almost spherical and with naked surfaces.

Achakulwisut *et al.*<sup>48</sup> investigated the dissolution dynamics of air bubbles in alkanes stabilized by fluorinated colloidal clay particles during temperature changes. The rate of change of the radius of a bubble as a function of temperature can be described by:

$$\dot{r} = -D\kappa_H RT \left(1 - f + \frac{2\gamma_{lg}}{r p_0}\right) \left(\frac{1}{r} + \frac{1}{\sqrt{\pi D t}}\right) \left(1 + \frac{2}{3} \frac{2\gamma_{lg}}{r p_0}\right)^{-1} + \dot{r}_1(T, r, \gamma_{lg}) \quad (4.1)$$

$$f = \frac{c}{c_s} \quad (4.2)$$

$$c_s = \kappa_H M p_g \quad (4.3)$$

$$\dot{r}_1(T, r, \gamma_{lg}) = \dot{T} \left(p_0 r + 2\gamma_{lg} - 2T \frac{d\gamma_{lg}}{dT}\right) \times \left(3T \left(p_0 + \frac{2}{3} \frac{2\gamma_{lg}}{r}\right)\right)^{-1} \quad (4.4)$$

where  $D$  is the diffusion coefficient,  $\kappa_H$  is Henry's constant,  $R$  is the universal gas constant,  $T$  is temperature,  $c$  is the concentration of dissolved gas in a liquid,  $c_s$  is the saturation concentration of dissolved gas at the liquid-gas interface,  $M$  is the molecular weight of the gas,  $p_g$  is the partial pressure of the gas,  $\gamma_{lg}$  is the interfacial tension between gas and liquid,  $r$  is the

bubble diameter,  $p_0$  is the ambient pressure,  $t$  is time and  $\dot{T}$  is the temperature change rate. The saturation ratio  $f$  is defined as the relative concentration of dissolved gas in the liquid to that at the interface. Of various temperature-dependent parameters, *e.g.*  $D$ ,  $\kappa_H$ ,  $\gamma_{lg}$ , it suggests that  $\kappa_H$  plays the dominant role in controlling bubble dissolution following temperature change.<sup>49</sup>  $\kappa_H$  was found to increase with increasing temperature, thus causing an increase in the saturation concentration,  $c_s$ , thereby making the continuous liquid unsaturated ( $f < 1$ ) and ultimately leading to faster gas dissolution.<sup>48-50</sup>

**Figure 4.19.** Effect of heating on appearance of EVOO foam containing 5 wt.% C-1805 after 2 months storage at 7 °C. (a) Photos, scale bar = 1 cm and (b) optical micrographs of the foam at specified temperatures on the hot stage, scale bars = 50  $\mu\text{m}$ . Heating rate was 1 °C min<sup>-1</sup>. Representative bubbles are selected to show bubble surface evolution (blue circles) and coalescence (black circles) upon heating. Red arrows denote crumpled bubble surfaces.

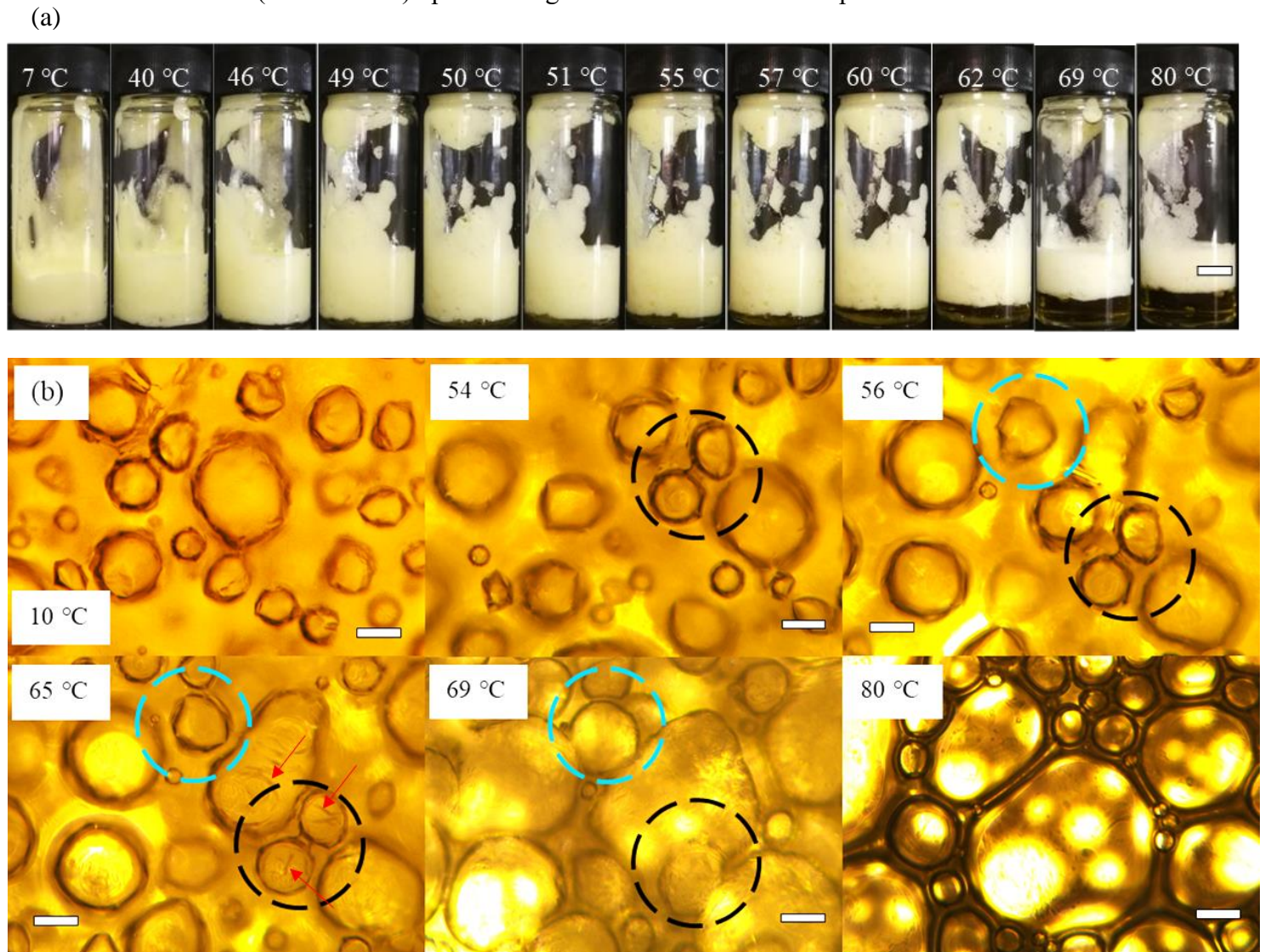
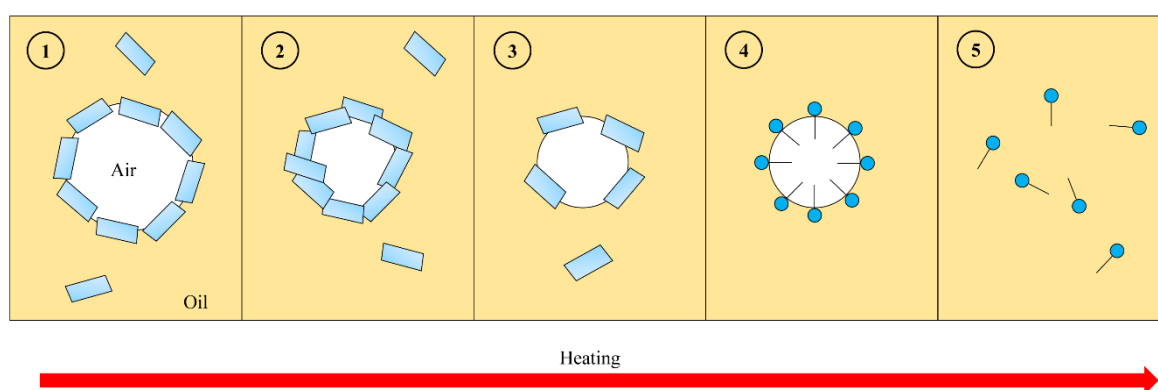


**Figure 4.20.** Sketch illustrating the dissolution behaviour of an air bubble in EVOO upon heating. 1: Initially the air bubble is armoured with a compact layer(s) of crystalline particles, rendering textured bubble surfaces and non-spherical geometry. Bubble dissolution can be arrested when the interfacial elasticity  $E \geq \gamma_{oa}/2$ ,  $\gamma_{oa}$  being air-oil surface tension.<sup>49</sup> 2: Upon increasing temperature, the air bubble is prone to suffer dissolution since the continuous oil phase becomes undersaturated in air.<sup>48,49</sup> The shrinking bubble surface tends to undergo buckling and crumpling without apparent particle shedding due to coherent coating of undissolved crystals. 3: Upon warming above the melting point of crystalline particles, crystals at both the bubble surface and in bulk melt, the bubble surface appears less textured and the shape relaxes gradually into spherical. 4: Above the global melting point, Pickering-type stabilisation transforms into surfactant molecule-stabilised. 5: Air bubbles eventually disappear due to coarsening/coalescence.



The evolution of a foam containing 10 wt.% C-1805 from 7 °C upwards is shown in Figure 4.21. Foam decay and oil drainage occurs gradually with increasing temperature. The variation of the volume of foam and drained oil for both surfactant concentrations is given in Figure 4.22 as a function of temperature. To further unveil the melting behavior of the foam, the melting thermograms were measured by DSC (see Figure 4.1(a)). Two endothermic peaks can be observed at ~ 49 °C and ~ 61 °C, similar to that of neat C-1805 powder. More discussions regarding this can be found in p. 123. The temperature range over which visible foam collapse occurs is consistent with these peak temperatures.

**Figure 4.21.** Effect of heating on appearance of EVOO foam containing 10 wt.% C-1805 stored at 7 °C. (a) Photos, scale bar = 1 cm and (b) optical micrographs of the foam on the hot stage at specified temperatures. Scale bars = 50  $\mu\text{m}$ . Heating rate was 1 °C min<sup>-1</sup>. Representative bubbles are selected to capture bubble shrinkage (red circles), bubble surface change (blue circles) and coalescence (black circles). Red arrows denote crumpled surface.

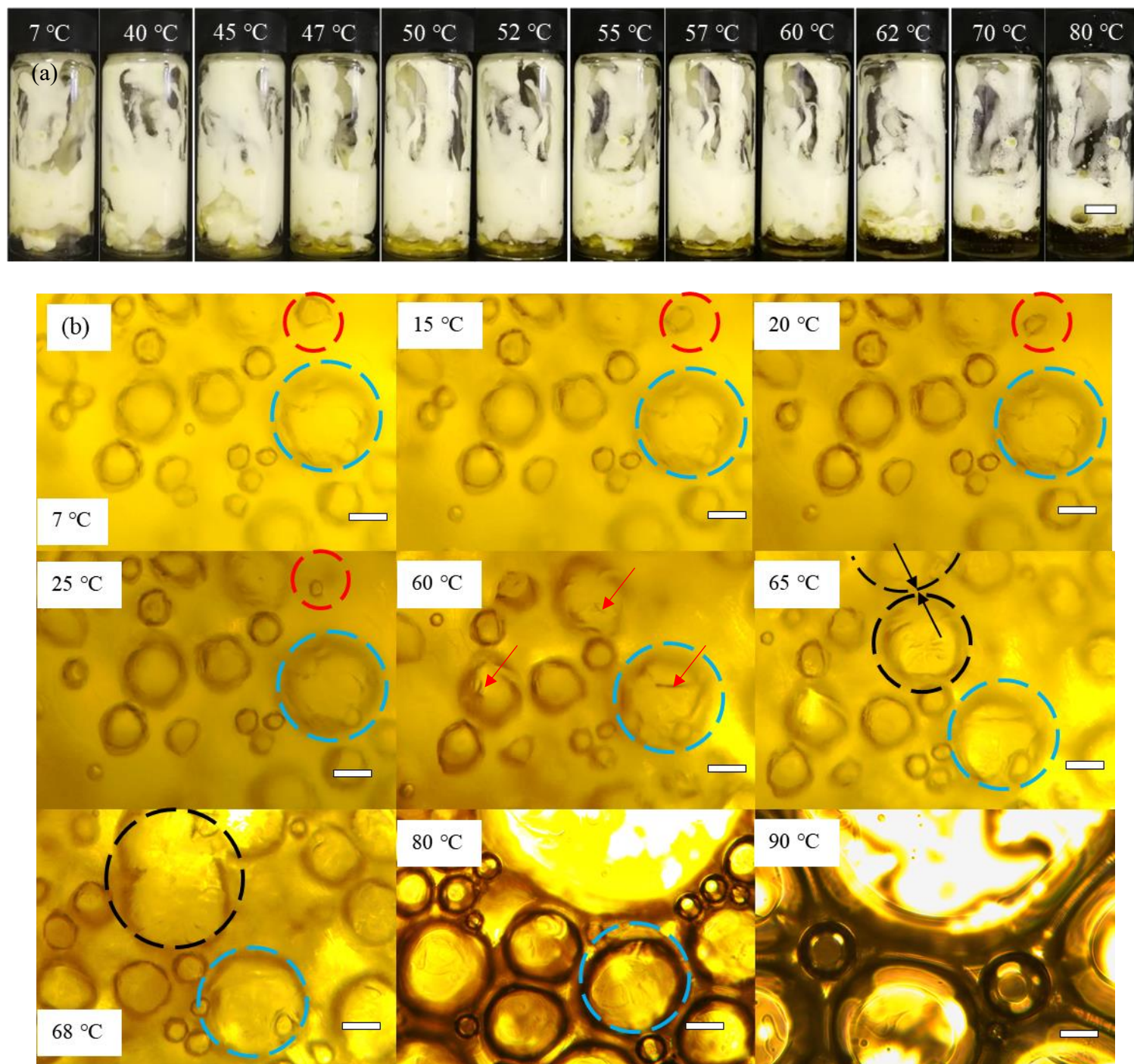
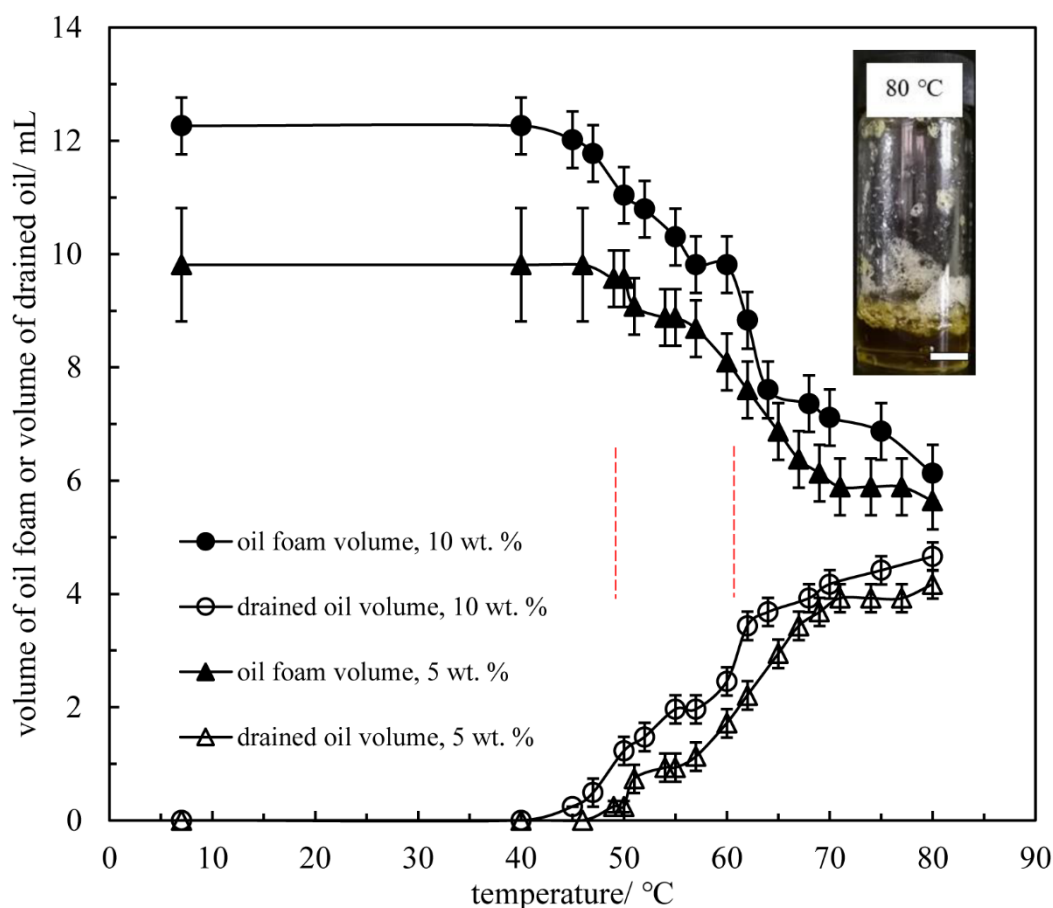


**Figure 4.22.** Variation of volume of oil foam (filled points) and volume of drained oil (open points) with temperature upon heating EVOO foams containing 5 wt.% (triangles) or 10 wt.% (circles) C-1805 stored at 7 °C. Heating rate was 1 °C min<sup>-1</sup>. Red dashed lines indicate the peak temperatures derived from the melting thermograms of EVOO foam containing 10 wt.% C-1805. Inset: photo of foam containing 10 wt.% C-1805 after 21 h storage at 80 °C. Scale bar = 1 cm.

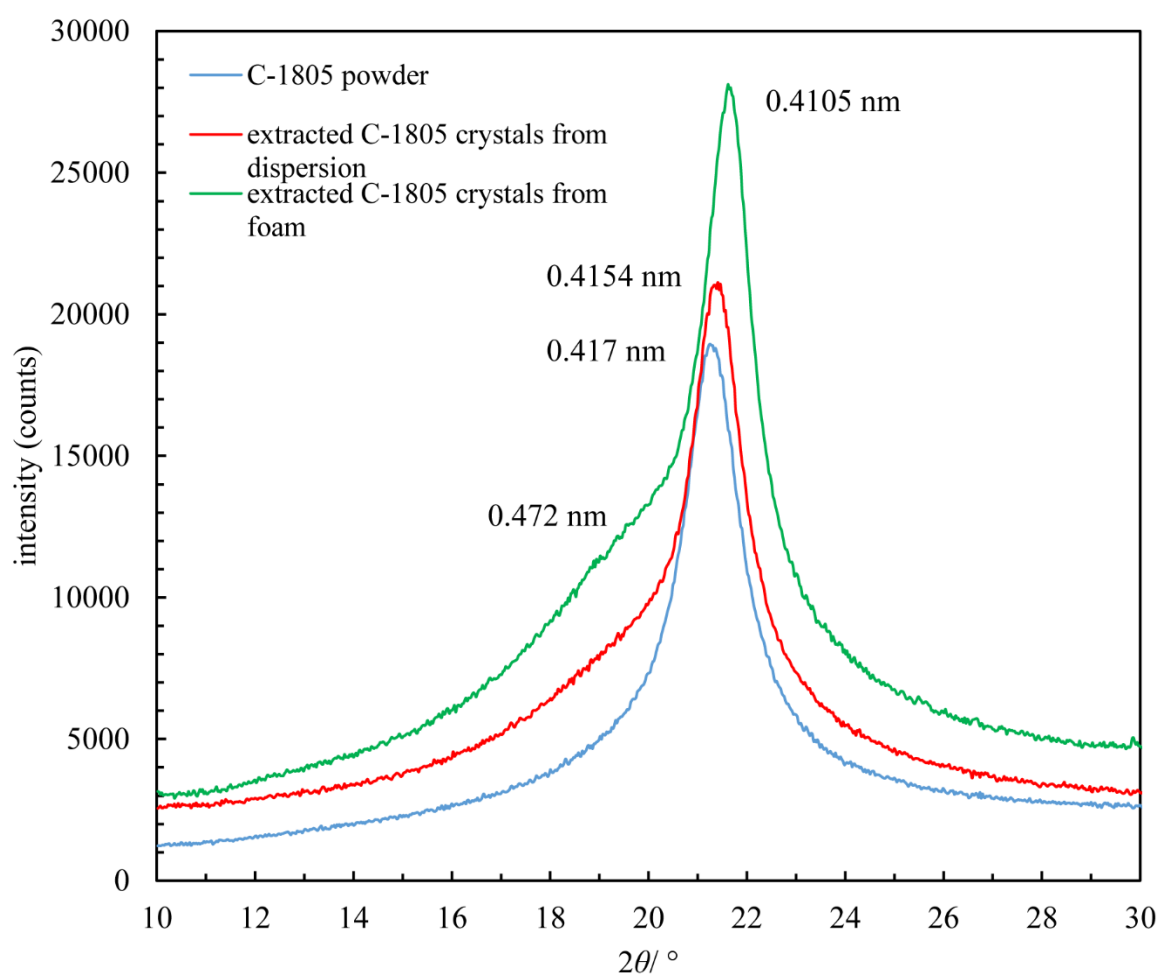


#### 4.3.5 Surfactant crystal structure

Insight into the molecular arrangement within crystals formed within an oil foam (prepared at 80 °C and rapidly cooled to room temperature) was obtained using Wide-Angle X-ray Scattering (WAXS) at room temperature. The scattering spectra of surfactant powder and of surfactant crystals extracted from an oil dispersion are included for comparison. It is known that the short spacing peak appearing at large diffraction angle reflects the lateral packing order of hydrocarbon chains, whilst the long spacing peak at small diffraction angle reflects the order and thickness of molecular layers.<sup>51</sup> From the WAXS spectra in Figure 4.23, neat C-1805 powder and C-1805 crystals of an oil dispersion display a single peak centred

around 0.42 nm, associated with the hexagonal lateral packing of stearyl chains, *i.e.* the  $\alpha$  form.<sup>34,52,53</sup> For C-1805 crystals in a foam, an additional shoulder emerges at around 0.47 nm while the main peak shifts to a lower value of around 0.41 nm, possibly representing a mixture of the  $\beta$  and  $\beta'$  form.<sup>34,52,53</sup> This transition indicates a polymorphic modification of C-1805 crystals during foam preparation.

**Figure 4.23.** Wide angle X-ray scattering (WAXS) region of C-1805 powder (—), C-1805 crystals extracted from EVOO dispersion (—) and EVOO foam (—) containing 10 wt.% C-1805 at room temperature.



#### 4.4 Proposed stabilisation mechanism of oil foam by sucrose ester

Until now, published work reporting stable oil foams has shown that it is only possible to achieve once pre-formed surface-active lipid crystals are present.<sup>1,2,20-31</sup> Interestingly, we discover that impressive foaming can be achieved from a one-phase oil solution at high temperature whilst limited foaming occurs in the presence of surfactant crystals at low temperature. The subsequent introduction of rapid cooling to a foam prepared at high temperature then boosts foam stability yielding oil foams devoid of drainage, coarsening and coalescence. It suggests that the ready incorporation of air bubbles at high temperature is due to rapid adsorption of C-1805 molecules at the air-oil surface and enhanced stability triggered by cooling arises from crystallisation of C-1805 molecules at bubble surfaces and in bulk.

Infrared spectroscopy analysis was carried out on neat EVOO and C-1805 solutions in EVOO at 80 °C in the range 3100 – 4000 cm<sup>-1</sup> pertaining to the stretching modes of –OH groups, Figure 4.24(a).<sup>36</sup> Neat EVOO exhibits a peak at 3474 cm<sup>-1</sup> due to intermolecular H-bonds between TAG carbonyl groups and hydroxyl groups of trace impurity like fatty acid.<sup>54</sup> For surfactant solutions in oil, the peaks centre around 3474 cm<sup>-1</sup> from intermolecular H-bonds formed between carbonyl groups in oil and hydroxyl groups in surfactant.<sup>54,55</sup> Upon increasing the surfactant concentration, the increase in peak broadness is attributed to more –OH groups involved in H-bonding.<sup>56</sup> Based on the multiple minor peaks between 3350 cm<sup>-1</sup> and 3450 cm<sup>-1</sup> above 5 wt.% surfactant, we cannot rule out the formation of intermolecular H-bonds between surfactant molecules themselves.<sup>55</sup> The variation of the absorbance of typical bands as a function of surfactant concentration is given in Figure 4.24(b). The intensities of the bands at 3400 cm<sup>-1</sup> (solute–solute)<sup>55</sup> and 3474 cm<sup>-1</sup> (solute–solvent) increase with concentration and then level off. For comparison, the infrared spectra of pure hexadecane and a solution of C-1805 in hexadecane at 70 °C are shown in Figure 4.25. As expected, no peak corresponding to –OH groups can be observed in pure hexadecane. However, in the surfactant solution there is a broad peak near 3400 cm<sup>-1</sup> indicative of H-bonding between surfactant molecules.

**Figure 4.24.** (a) Infrared spectra of EVOO and C-1805 in EVOO solutions at different concentrations at 80 °C. (b) Infrared absorbance of EVOO solutions at 80 °C as a function of C-1805 concentration at 3,400  $\text{cm}^{-1}$  (H-bonds between surfactant molecules,  $\circ$ ) and 3,474  $\text{cm}^{-1}$  (H-bonds between surfactant and oil molecules,  $\bullet$ ). Inset: hydrogen bond formed between TAG carbonyl group in oil and C-1805 hydroxyl group in surfactant; hydrogen bond formed between C-1805 hydroxyl groups in surfactant.

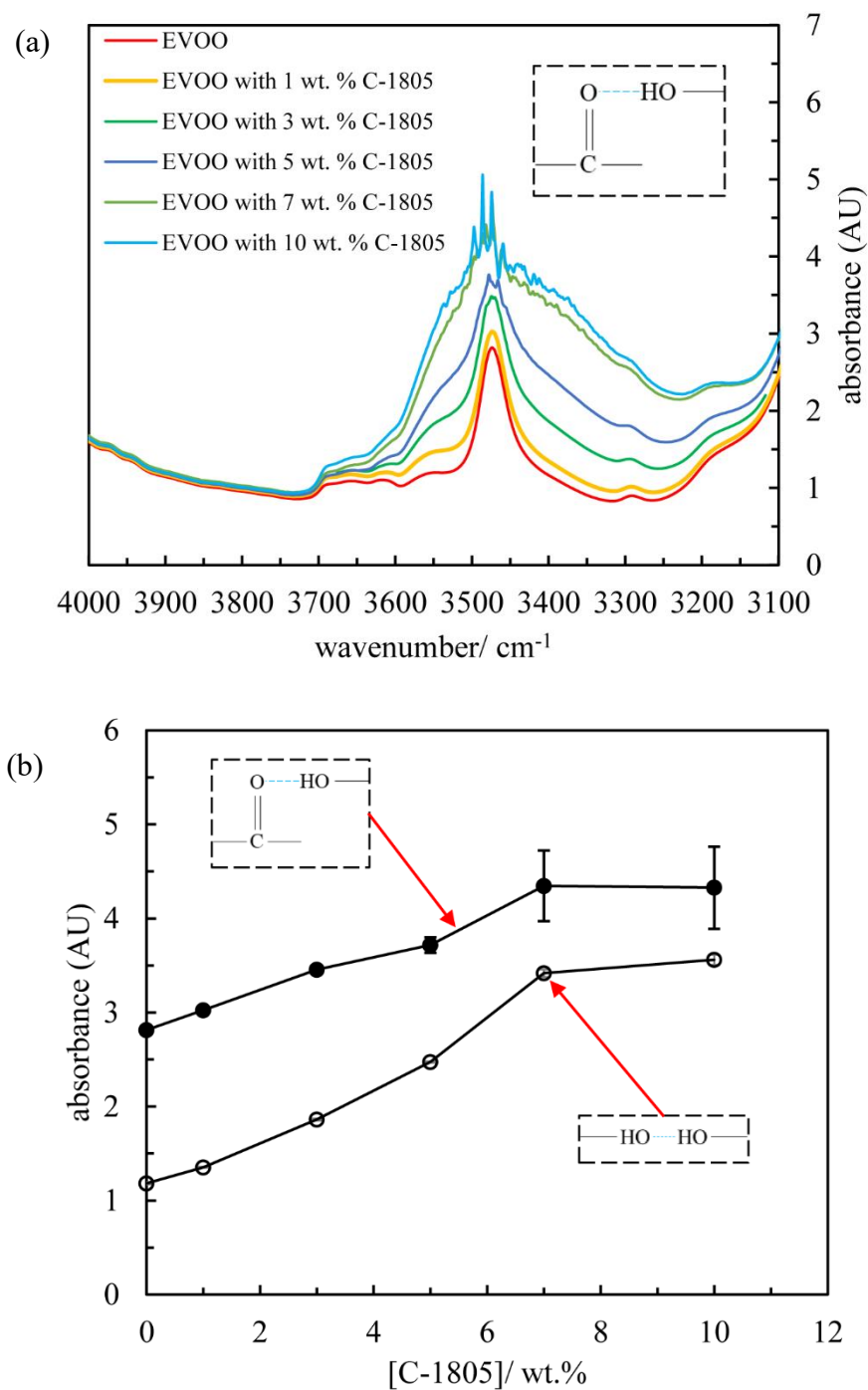


**Figure 4.25.** Infrared spectra of hexadecane (—) and hexadecane containing 3 wt.% C-1805 (—) at 70 °C. The peak at  $\sim 3,400\text{ cm}^{-1}$  in the latter indicates intermolecular H-bonds between surfactant molecules.

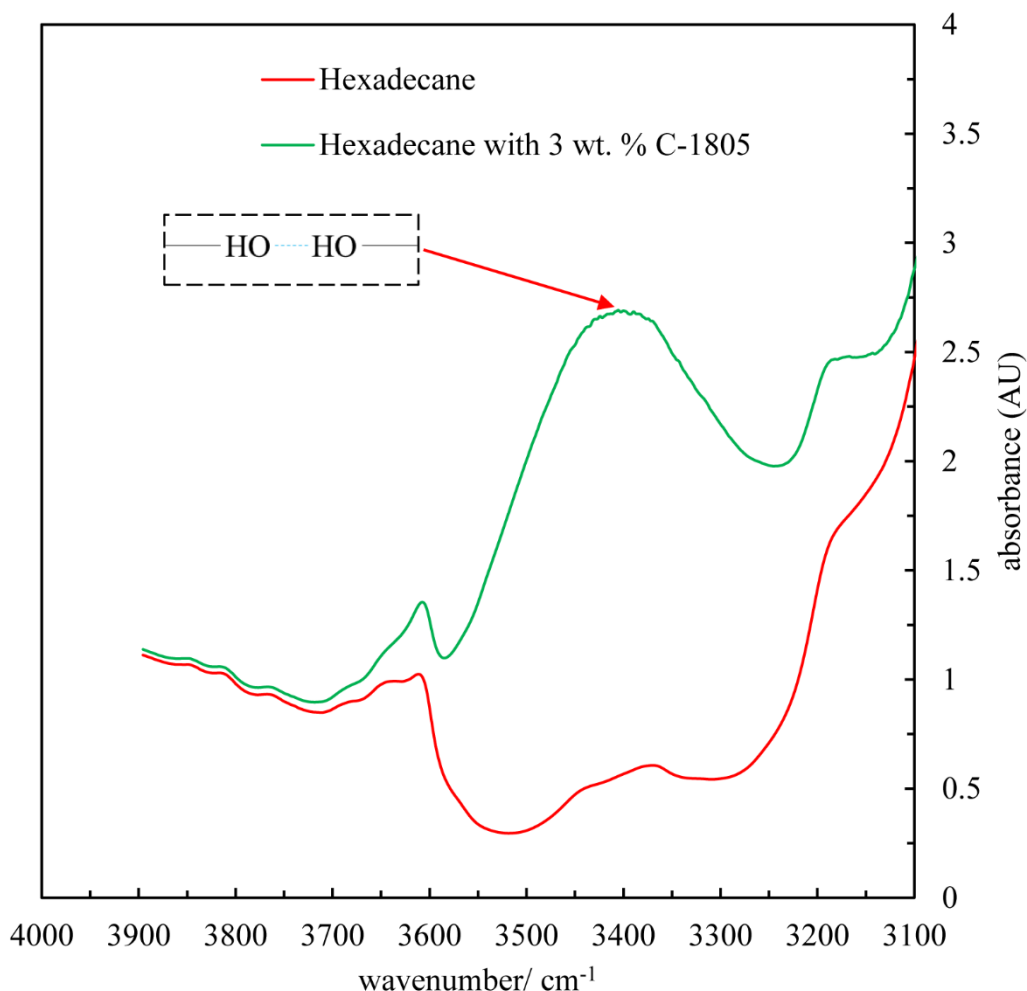
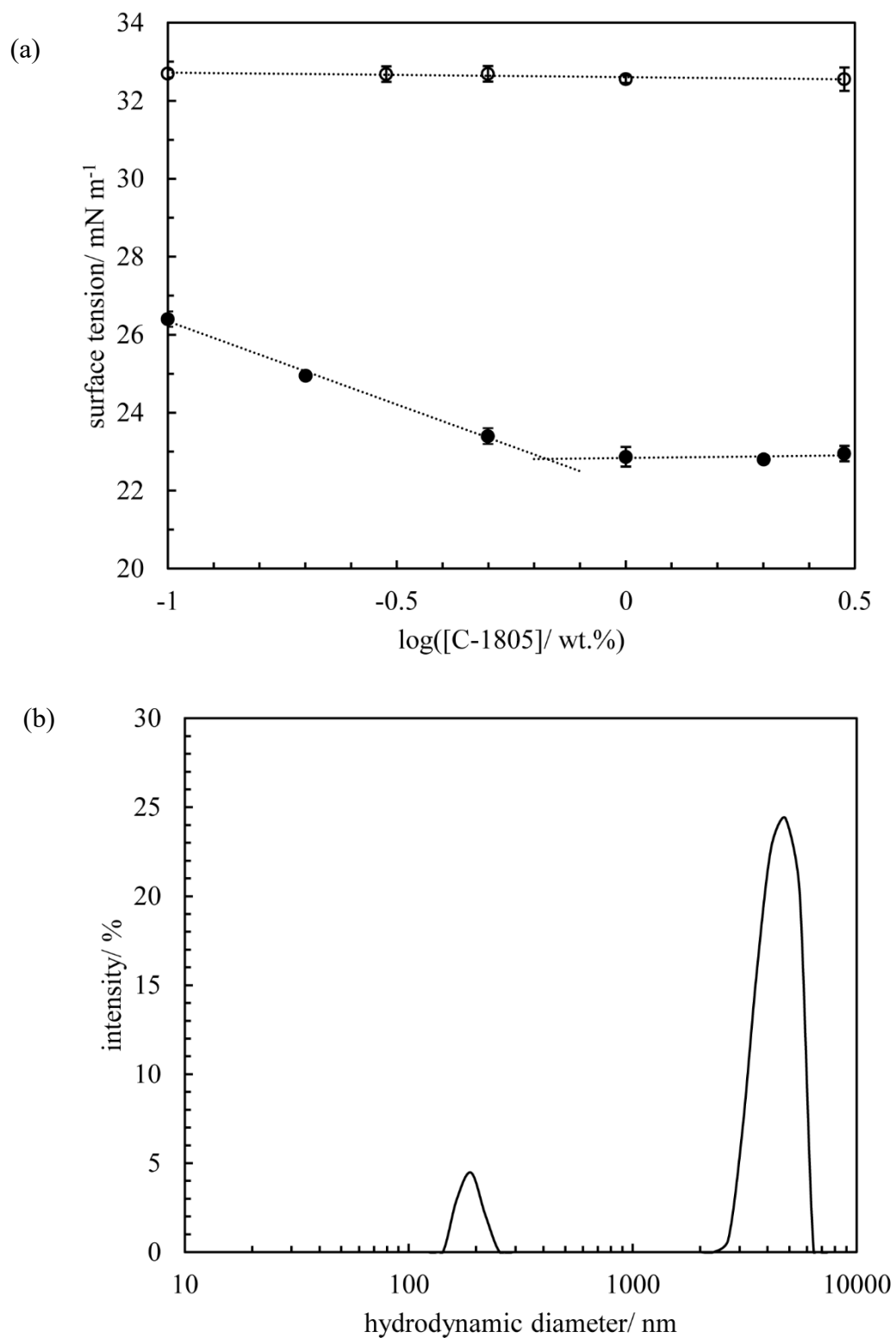


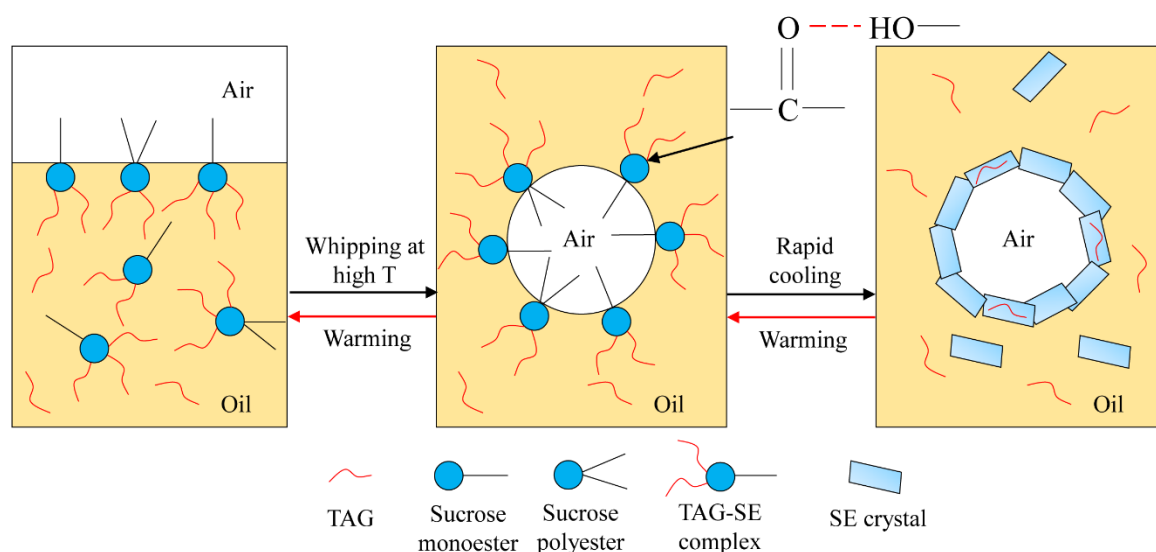
Figure 4.26(a) presents the air-oil surface tension at both 80 °C (one-phase) and 20 °C (two-phase). Our values for neat oil are comparable with those of Xu *et al.*<sup>57</sup> At 80 °C, the surface tension decreases gradually with C-1805 concentration reaching a constant value of  $\sim 23\text{ mN m}^{-1}$  at  $\sim 0.7\text{ wt.}\%$ , confirming our earlier hypothesis. It may be that reverse micelles/vesicles form above the breakpoint; a preliminary dynamic light scattering experiment for 1 wt.% C-1805 in EVOO exhibited a peak at a (spherical) diameter of 175 nm and a larger one at 4  $\mu\text{m}$ , Figure 4.26(b).<sup>58</sup> Further investigation surrounding this is currently underway. On the contrary, at 20 °C the surface tensions of crystal dispersions are the same as that of neat oil implying that C-1805 crystals do not adsorb spontaneously to the air-oil interface or are too large to make any difference.

**Figure 4.26.** (a) Air-oil surface tension of C-1805-EVOO mixtures at 20 °C (○) and 80 °C (●). Surface tension of neat EVOO at 80 °C is 26.5 mN/m. (b) Intensity size distribution of EVOO solution of 1 wt.% C-1805 at 80 °C determined by DLS.



Based on the above, we propose that for an oil solution of C-1805 at high temperature, carbonyl groups of TAG molecules in oil form H-bonds with hydroxyl groups in C-1805 in addition to van der Waals interactions between hydrocarbon chains. The molecular complex is highly surface-active at the air-oil surface facilitating efficient foam formation upon whipping. The noticeable decrease in foamability in the two-phase region is due to several factors. The first is the potential antifoaming effect of the surfactant-rich phase, *e.g.* crystals.<sup>59</sup> Secondly, the pre-requisite for spontaneous adsorption of C-1805 crystals to the air-oil surface is that its surface energy is lower than that of oil.<sup>60</sup> However, by interpolating the data of Szűts *et al.*<sup>61</sup> the solid-air surface energy of C-1805 is estimated to be  $\approx 43 \text{ mN m}^{-1}$  which is significantly higher than that of EVOO, making the adsorption of crystals energetically unfavourable. Thirdly and most importantly, lowering the temperature in the two-phase region results in a reduction in the surfactant monomer concentration in oil, Figure 4.2(b), and less foam forms at lower temperature since monomer molecules are surface-active. Once foams prepared at high temperature undergo rapid quenching however, the molecular complex at bubble surfaces act as a template for heterogeneous nucleation of surfactant molecules from bulk oil followed by crystal growth due to chain-chain ordering between oleyl chains in EVOO and stearyl chains in C-1805. Co-crystallisation of surfactant with some oil cannot be ruled out.<sup>62,63</sup> In this scenario, a compact interfacial crystalline shell(s) covering air bubbles is formed. The postulated mechanism is summarised in Figure 4.27.

**Figure 4.27.** Postulated mechanisms of formation and stabilisation of vegetable oil foams with sucrose ester surfactant.



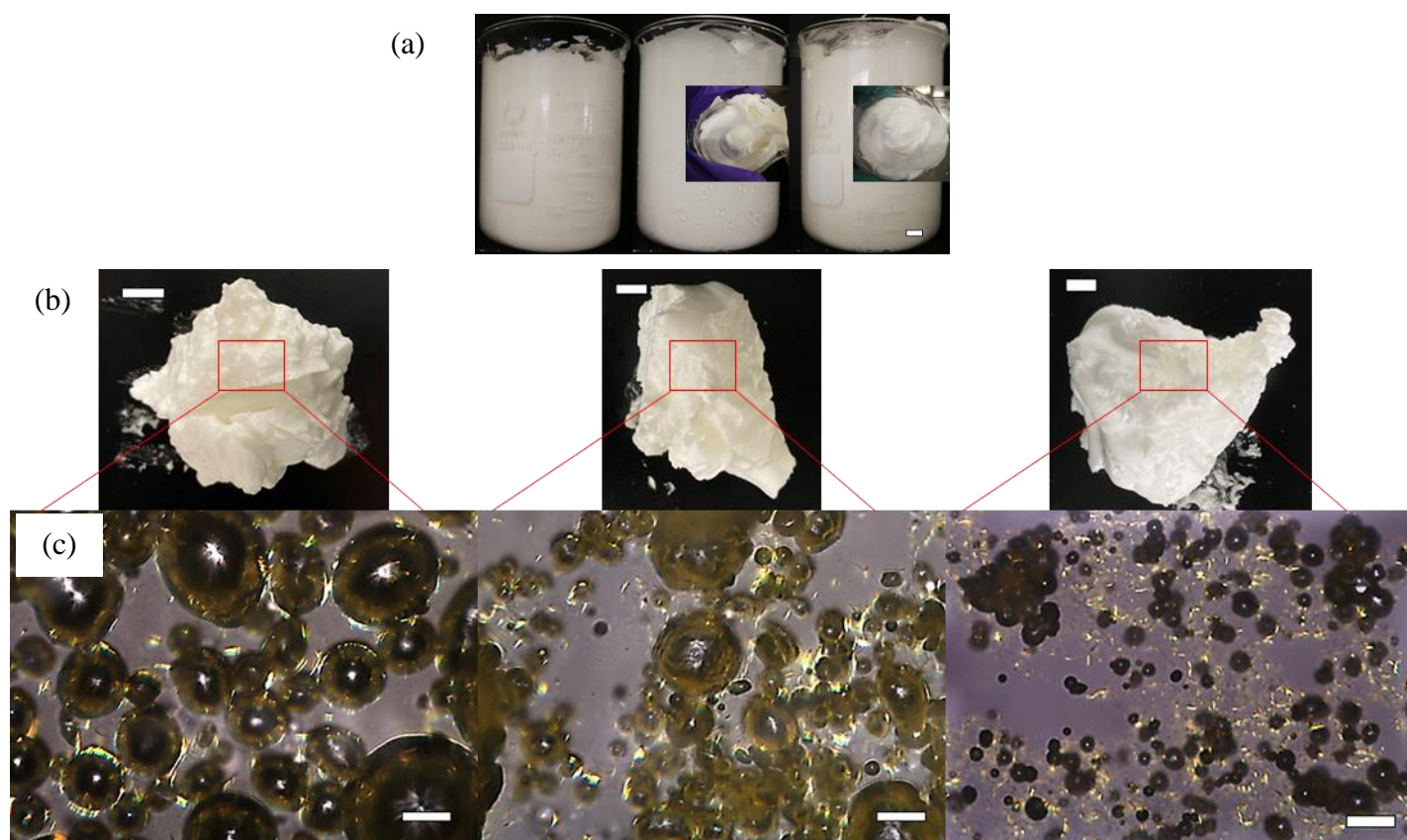
## 4.5 Whipping other vegetable oils and sucrose ester

In order to establish the generic nature of our findings, we chose to whip mixtures of C-1805 and three other vegetable oils, *i.e.* rapeseed oil (RO), high oleic sunflower oil (HOSO) and refined peanut oil (RPO). These oils are rich in long chain unsaturated fatty acids, *e.g.* oleic acid C18:1, in their TAGs and are liquid at ambient temperature.<sup>64</sup> The mixtures were subjected to the same foaming and post-foaming protocols as described earlier. Table 4.2 summarises the foaming properties during whipping and storage. At 80 °C, all oil foams can be generated through whipping with the over-run increasing gradually with time. The values of the over-run after 10 min whipping increase in the order RO < HOSO < RPO. The exceptionally high over-run of 329% (air fraction = 0.77) for RPO with 10 wt.% C-1805 is worth highlighting. Foams containing 5 wt.% C-1805 suffer a gradual decay and finally vanish when stored at 80 °C, however. The corresponding foam half-lives are ~ 45 h and the volume fraction of remaining foam after 24 h aging is ~ 0.55. In contrast, the cooled foams stored at 7 °C possess very high stability with  $92 \pm 3$  vol% of foam remaining after 6 months. Their appearance and microscope images after 6 months storage can be seen in Figure 4.28, in which non-spherical bubbles coated by birefringent crystals are evident. We thus demonstrate that the novel foaming protocol developed can be extended to different vegetable oils so that exceptional foamability and superior foam stability can be achieved.

**Table 4.2.** Foaming properties of other vegetable oil foams stabilized by C-1805. Foams prepared at 80 °C were either stored at the initial whipping temperature or submitted to rapid cooling followed by storage at 7 °C. Stability of residual foam is expressed as ratio of volume of foam during storage to that immediately after whipping.

Oil	Over-run at 80 °C (%)		Foam stability for 5 wt.% C-1805 stored at 80 °C		Foam stability for 10 wt.% C-1805 stored at 7 °C ( $\pm 0.01$ )
	5 wt.%	10 wt.%	$t_{1/2}/\pm 6$ h	Residual foam after 24 h aging	Residual foam after 6 months aging
RO	162	181	47	0.65	0.93
HOSO	167	305	40	0.55	0.95
RPO	210	329	45	0.52	0.89

**Figure 4.28.** (a) Photos with insets of other vegetable oil foams stabilized by 10 wt.% C-1805 immediately after 10 min whipping at 80 °C, scale bar = 1 cm. (b) Photos, scale bars = 0.5 cm and (c) polarized microscopy images of other vegetable oil foams stabilized by 10 wt.% C-1805 after 6 months storage at 7 °C, scale bars = 50  $\mu$ m. RO (left), HOSO (middle) and RPO (right). Foams prepared at 80 °C were submitted to rapid cooling in an ice bath of -5 °C followed by storing at 7 °C.



## 4.6 Whipping or bubbling a second sucrose ester and oil

### 4.6.1 Very stable foams formed by whipping

C-1802 is more lipophilic than C-1805, being composed of 10% monoester and 90% di-, tri- and polyester. Its physicochemical properties are presented below. From the WAXS spectrum in Figure 4.29(a), neat C-1802 powder displays a single peak centred around 0.42 nm, which is comparable to that of neat C-1805 powder, *i.e.* the  $\alpha$  polymorph. The FTIR spectrum in Figure 4.29(b) reveals that the representative functional groups of C-1802 powder are similar to those of C-1805 powder, *i.e.* stretching –OH groups and C=O groups. The thermal properties of C-1802 are illustrated in Figure 4.30 and Table 4.3. The thermograms exhibit one major endothermic peak at 61.6 °C and a major exothermic peak 46.8 °C, which is associated with the melting and crystallisation of sucrose tetra- and pentaester fractions. In addition, the multiple minor peaks are due to the presence of sucrose mono-, di-, and triester.

**Figure 4.29.** (a) Wide angle X-ray scattering (WAXS) region and (b) FTIR spectrum of C-1802 powder at room temperature.

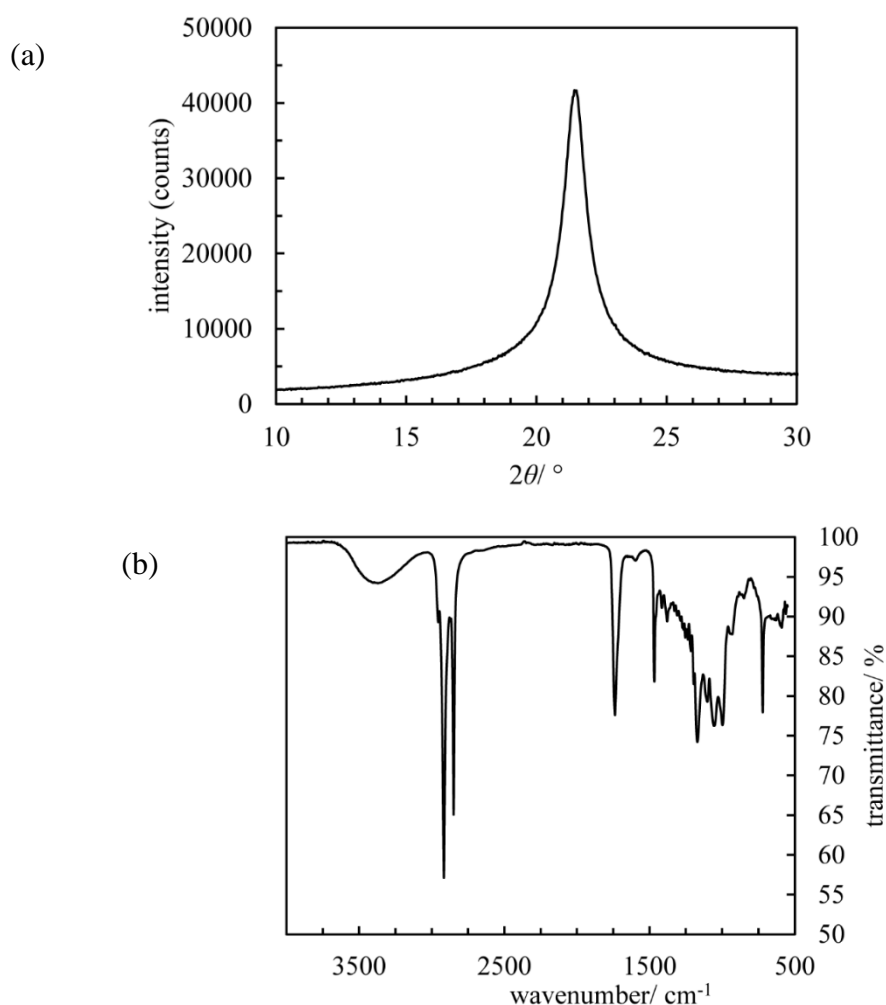


**Figure 4.30.** Melting and cooling thermograms of C-1802 powder. Temperature change rate was 5 °C min<sup>-1</sup>.

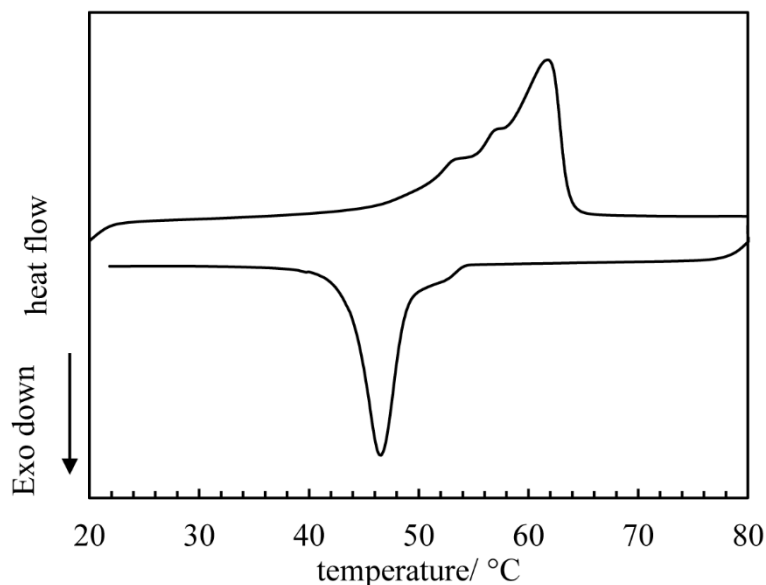
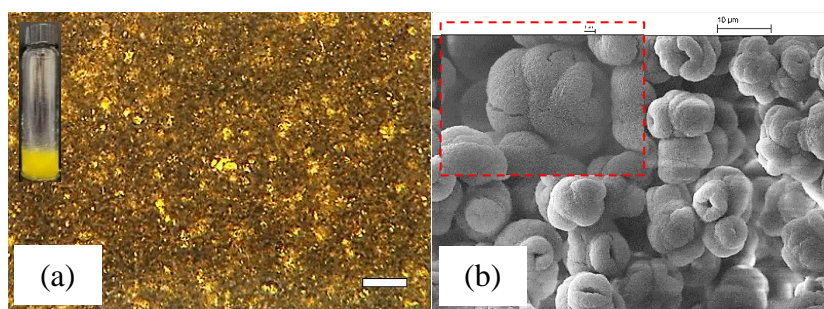


**Table 4.3.** Thermal properties of C-1802 powder.

	Crystallisation		Melting	
	$T_{\text{peak}}/\text{°C}$	$\Delta H/\text{J g}^{-1}$	$T_{\text{peak}}/\text{°C}$	$\Delta H/\text{J g}^{-1}$
C-1802	$46.78 \pm 0.27$	$-59.67 \pm 4.12$	$61.56 \pm 0.21$	$98.05 \pm 3.57$

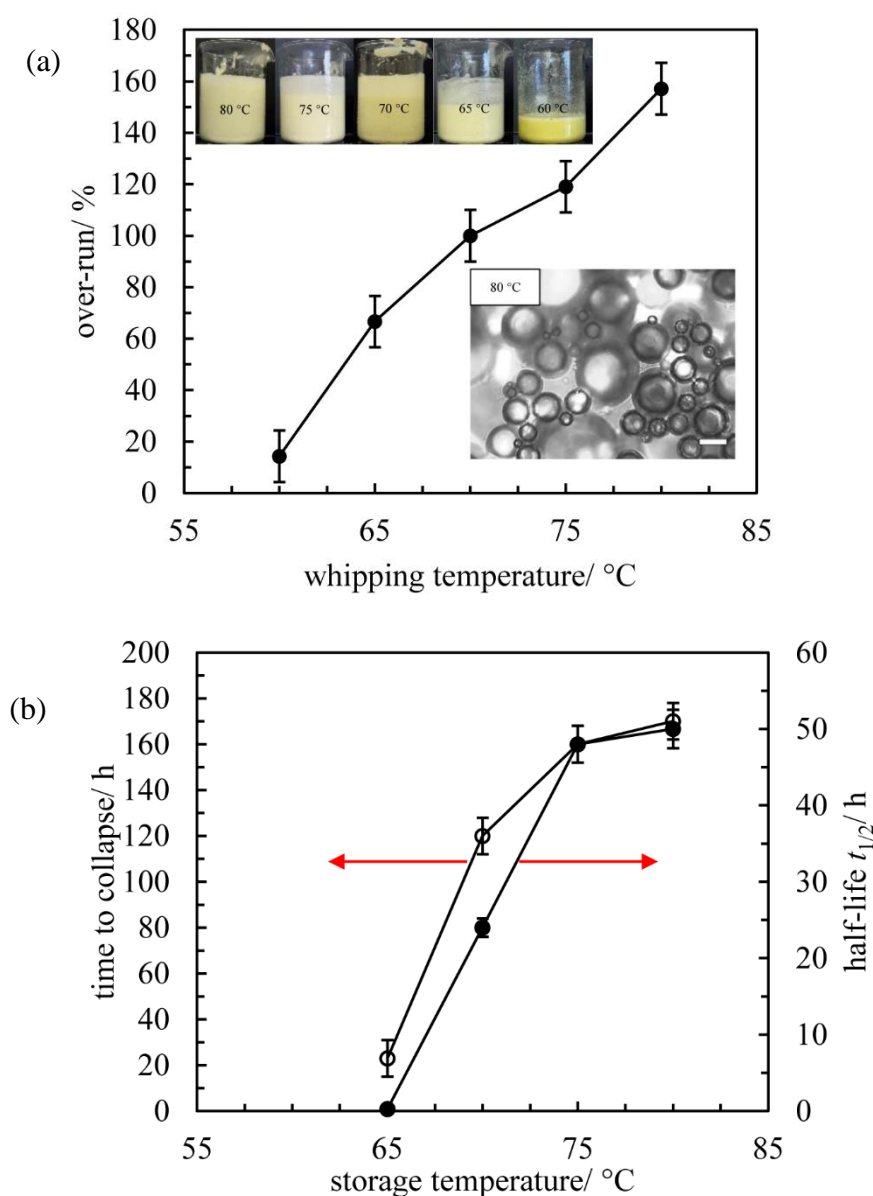
As shown in Figure 4.31(a), the EVOO dispersion containing 5 wt.% C-1802 at 20 °C is a turbid, viscous dispersion. In addition, birefringent surfactant crystals can be identified under polarized microscopy. From the cryo-SEM image in Figure 4.31(b), spherical crystals with diameters < 10 µm possessing openings can be found.

**Figure 4.31.** (a) Polarized micrograph of 5 wt.% C-1802 in EVOO at room temperature, scale bar = 50 µm. Inset: photo of EVOO dispersion containing 5 wt.% C-1802 at room temperature. (b) Cryo-SEM image of surfactant crystals. Inset: enlarged surfactant crystals, scale bar = 1 µm.



The over-run of 5 wt.% of C-1802 in EVOO increases gradually with increasing aeration temperature (Figure 4.32(a)). The highest over-run is  $\sim 160\%$  (*i.e.* volumetric air fraction 0.62) after 10 min whipping at 80 °C. The foam bubbles are polydisperse and spherical, inset in Figure 4.32(a). Oil foams were stored at respective whipping temperature. Both foam parameters (*i.e.* foam half-life and time for complete foam collapse) increase with storage temperature, Figure 4.32(b). No foams remain after around 7 days.

**Figure 4.32.** (a) Variation of over-run with whipping temperature for 5 wt.% C-1802 in EVOO. Inset: photos of EVOO containing 5 wt.% C-1802 immediately after 10 min whipping at given temperatures; optical micrograph of fresh foam at 80 °C, scale bar = 50  $\mu\text{m}$ . (b) Foam half-life (●) and time for complete foam collapse (○) against storage temperature (same as whipping temperature).



To fabricate stable oil foams, mixtures of EVOO and C-1802 were subjected to the same foaming and quenching protocol as mentioned above. An EVOO foam containing 5 wt.% C-1802 prepared at 80 °C was cooled quickly in an ice bath of -5 °C followed by storing at room temperature or 7 °C. For the foam stored at room temperature (Figure 4.33(a)), oil drainage occurs and accumulates gradually at the vessel bottom. The foam network is fractured on storage due possibly to its inherent brittleness. Figure 4.33(b) shows the appearance of the foam stored at 7 °C. Oil drainage occurs as well, but this process ceases within the first 72 h on storage. No crack can be identified within the foam network at 7 °C however, indicating its higher firmness compared with that of the foam at room temperature. The normalised volume of foam and drained oil alongwith foam temperature during cooling and subsequent storage is plotted in Figure 4.34. Approximately 85 vol% foam remains after one month storage for both systems. The inset photos and micrographs in Figure 4.34 reveal its solid-like appearance and interface, respectively.<sup>1</sup>

**Figure 4.33.** Appearance of EVOO foams containing 5 wt.% C-1802 submitted to rapid cooling immediately after whipping. Foams prepared at 80 °C were cooled in an ice bath of -5 °C followed by storing at (a) room temperature or (b) 7 °C. Scale bars = 1 cm.

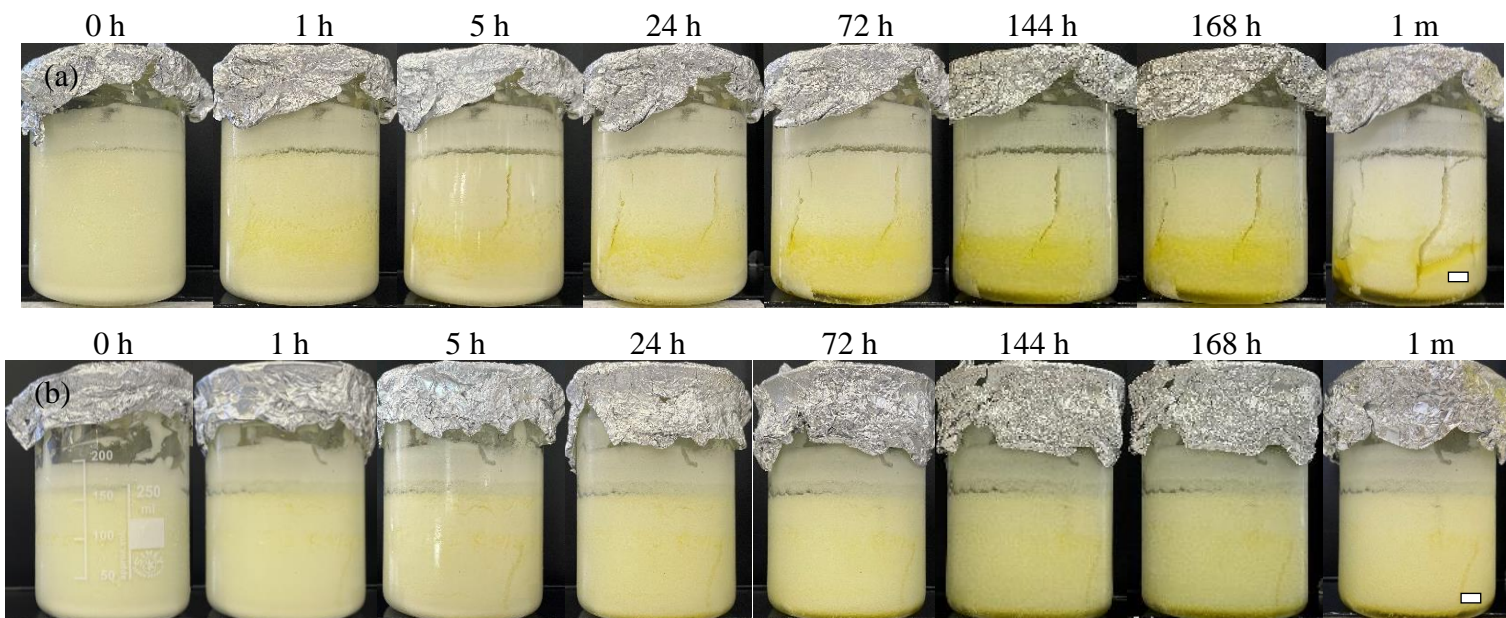


**Figure 4.34.** Normalized volume of foam (●) and drained oil (○) and foam temperature (■) as a function of aging time for systems in Figure 4.33. Inset in (a): photo' and optical micrograph of the foam after 1 month storage at room temperature. Inset in (b): photo' and optical micrograph of the foam after 1 month storage at 7 °C. Scale bars equal 1 cm and 50  $\mu$ m for photos and micrographs, respectively.

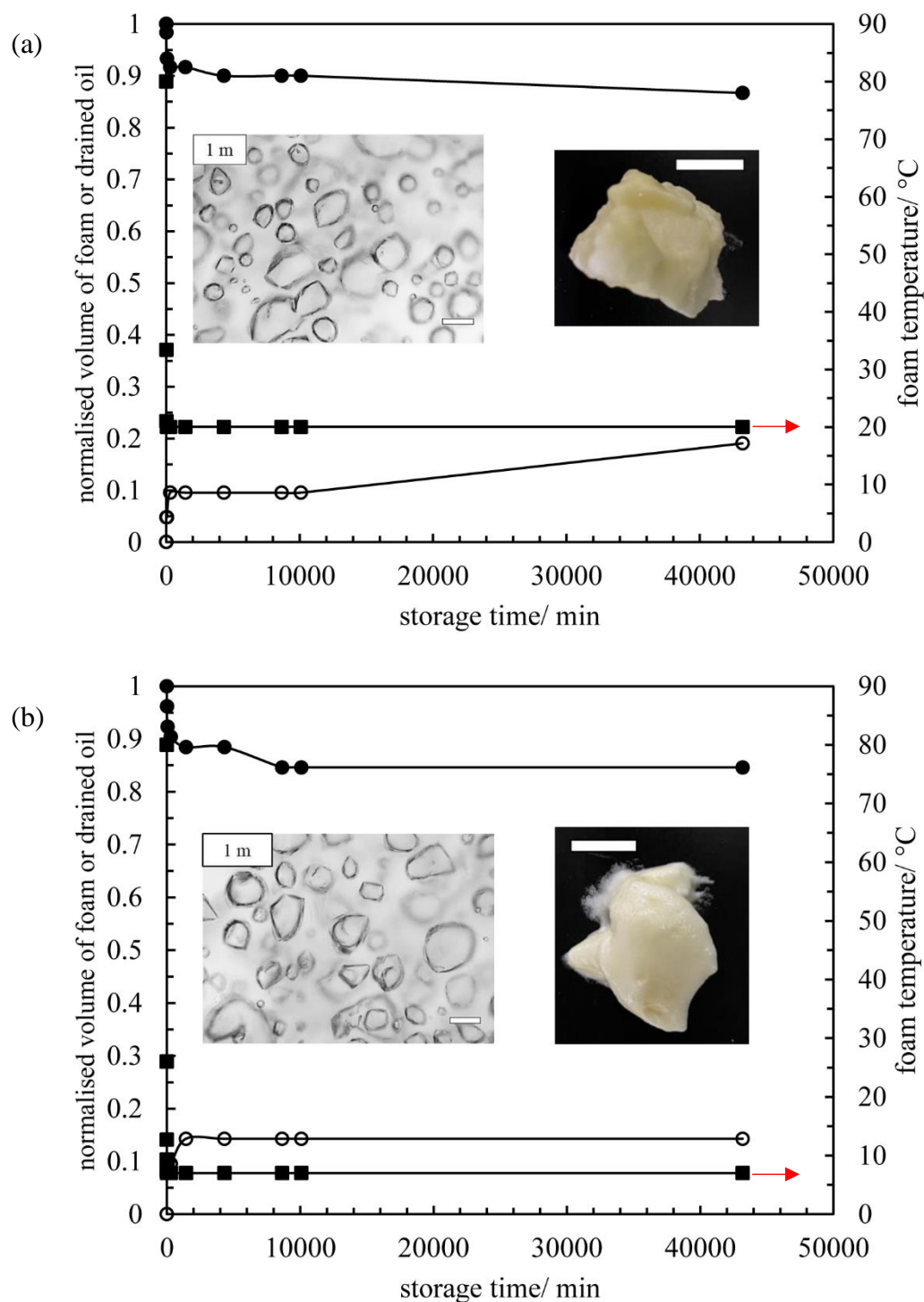
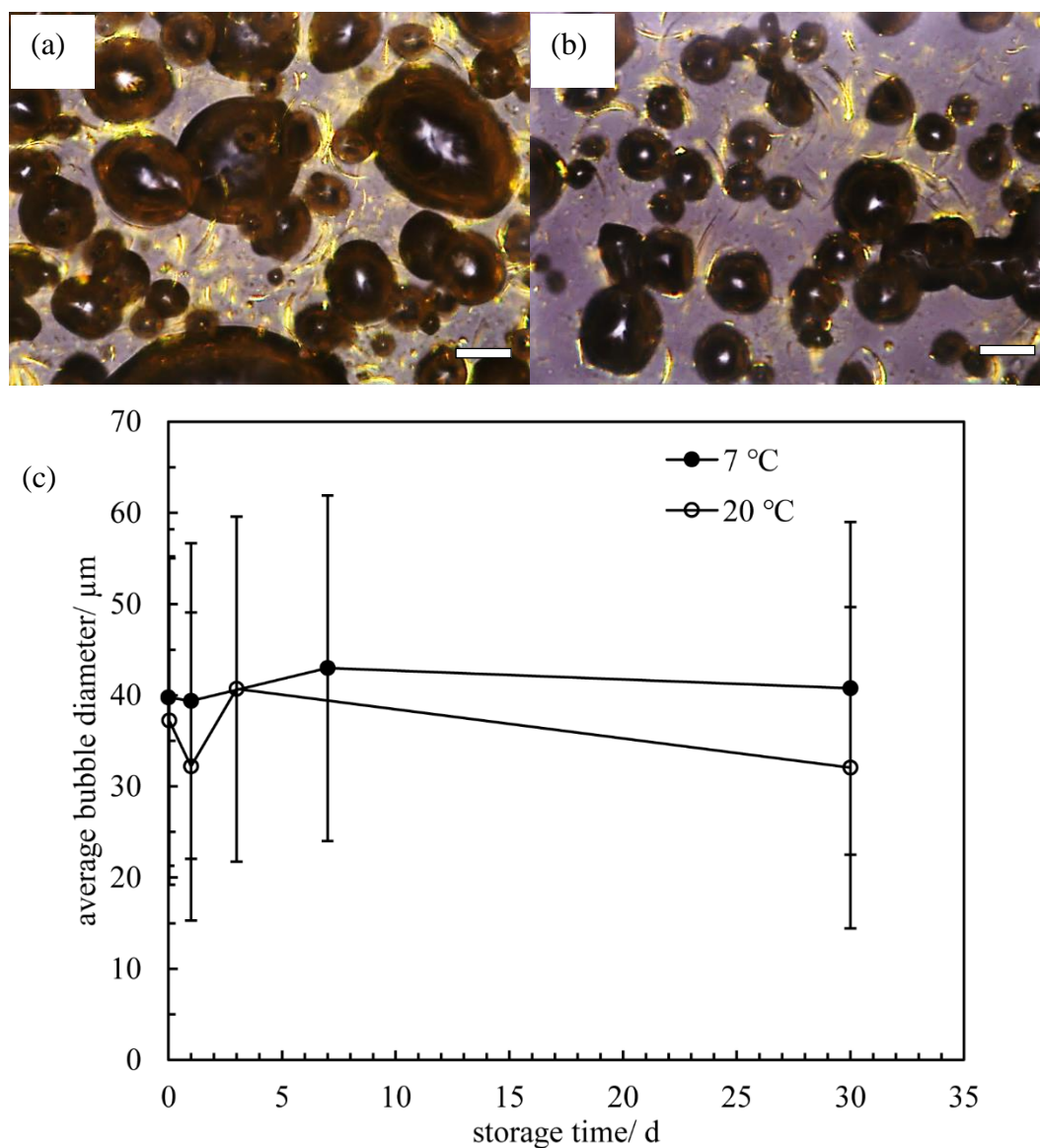


Figure 4.35(a) and Figure 4.35(b) present the polarised microscopy images of the foams containing 5 wt.% C-1802 stored at room temperature and 7 °C, respectively. Birefringent crystals can be identified in continuous oil and at bubble surfaces. Moreover, many bubbles are non-spherical arising from jamming of adsorbed crystals at interfaces. The average bubble diameter of the foams remains more or less constant during storage due to the absence of coarsening/coalescence, Figure 4.35(c). We thus illustrate that the novel foaming protocol can be extended to another sucrose ester system during which both good foamability and long-term stability can be achieved.

**Figure 4.35.** Polarized micrographs of EVOO foams of C-1802 after one month storage at (a) room temperature or (b) 7 °C. Scale bars = 50  $\mu\text{m}$ . (c) Average bubble diameter as a function of storage time for the foams stored at room temperature or 7 °C.



#### 4.6.2 Foams formed by bubbling

All oil foams mentioned earlier are prepared through whipping. In this section, we take advantage of the home-designed foaming setup to produce oil foams *via* bubbling. Firstly, the foaming properties of C-1802-EVOO mixtures are investigated as a function of gas flow rate. Secondly, the foaming behaviour of neat EVOO is explored. Last, comparisons are made between whipping and bubbling regarding foamability, foam stability and foam structure.

##### 4.6.2.1 Bubbling mixtures of sucrose ester and oil

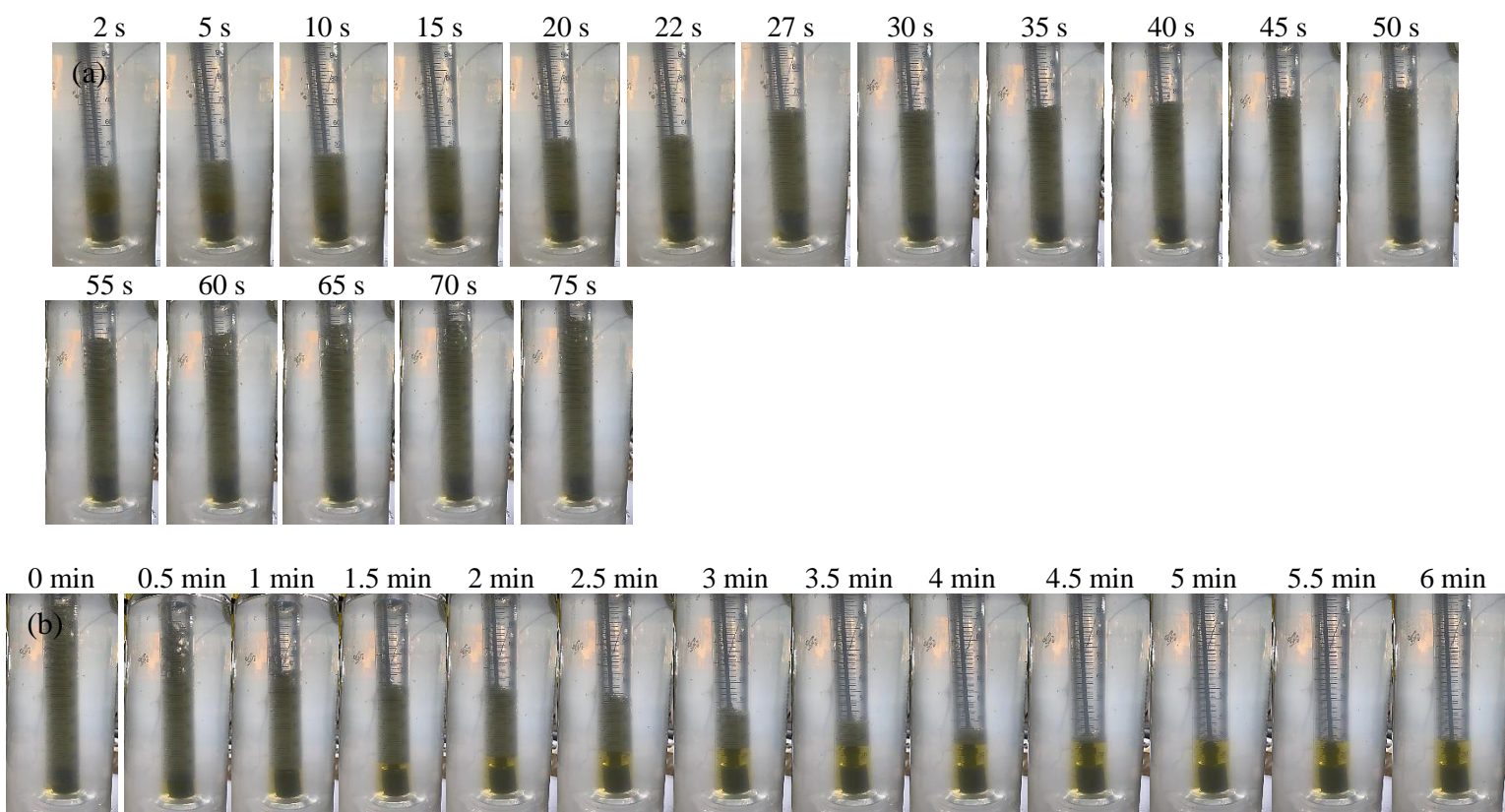
A mixture of EVOO and C-1802 (*ca.* 15 g) was heated to 90 °C under gentle magnetic stirring yielding a clear, homogeneous oil solution. Subsequently, the solution was transferred to a thermostatic circulating tank at 80 °C (one-phase) and then equilibrated at 80 °C for  $\sim 0.5$  h. The gas flow rate was controlled by a flow meter and adjusted to a certain flow rate before aerating. The bubbling process was halted as soon as the total volume of aerated sample ( $V_{\text{air+oil}}$ ) reaches  $100 \pm 2$  mL.

Figure 4.36(a) – Figure 4.38(a) present the appearance of EVOO solutions containing 5 wt.% C-1802 as a function of bubbling time under different gas flow rates, *i.e.* 30 mL min<sup>-1</sup>, 60 mL min<sup>-1</sup> and 100 mL min<sup>-1</sup>, respectively. The foam volume increases gradually with bubbling time. The over-run of the aerated samples is plotted as a function of bubbling time in Figure 4.39(a). As expected, the foamability increases with increasing gas flow rate. The total volume of released air from the gas diffuser is expressed as  $V = Q \times t$ ,  $Q$  being the volumetric flow rate of compressed air and  $t$  being bubbling time. In fact, not all of the air released ( $V$ ) can be entrapped within the oil matrix, so  $V_{\text{air}}$  is normally smaller than  $V$ . Oil foams were then stored at corresponding bubbling temperature. Photos of the foams during storage are displayed in Figure 4.36(b) – Figure 4.38(b). Their stability increases in the order 60 mL min<sup>-1</sup> < 100 mL min<sup>-1</sup> < 30 mL min<sup>-1</sup>, see Figure 4.39(b). The foams decay gradually followed by collapsing completely within 15 min. The inset photo in Figure 4.39(a) illustrates that the foam bubbles are polydisperse with diameters < 1 cm. Further investigations regarding oil samples containing C-1802 bubbled from high temperature while simultaneously cooled to induce surfactant crystallization is now underway.

**Figure 4.36.** (a) Appearance of EVOO solution containing 5 wt.% C-1802 (~ 15 g) as a function of bubbling time at 80 °C. Gas flow rate was 30 mL min<sup>-1</sup>. Bubbling was halted as soon as the total volume ( $V_{\text{air+oil}}$ ) reached  $100 \pm 2$  mL. (b) Appearance of the foam in (a) as a function of storage time. Storage temperature was the same as the preparation temperature. Red arrow denotes the gas diffuser at the vessel bottom.



**Figure 4.37.** (a) Appearance of EVOO solution containing 5 wt.% C-1802 (~ 15 g) as a function of bubbling time at 80 °C. Gas flow rate was 60 mL min<sup>-1</sup>. Bubbling was halted as soon as the total volume ( $V_{\text{air+oil}}$ ) reached  $100 \pm 2$  mL. (b) Appearance of the foam in (a) as a function of storage time. Storage temperature was the same as the preparation temperature.



**Figure 4.38.** (a) Appearance of EVOO solution containing 5 wt.% C-1802 (~ 15 g) as a function of bubbling time at 80 °C. Gas flow rate was 100 mL min<sup>-1</sup>. Bubbling was halted as soon as the total volume ( $V_{\text{air+oil}}$ ) reached  $100 \pm 2$  mL. (b) Appearance of the foam in (a) as a function of storage time. Storage temperature was the same as the preparation temperature.

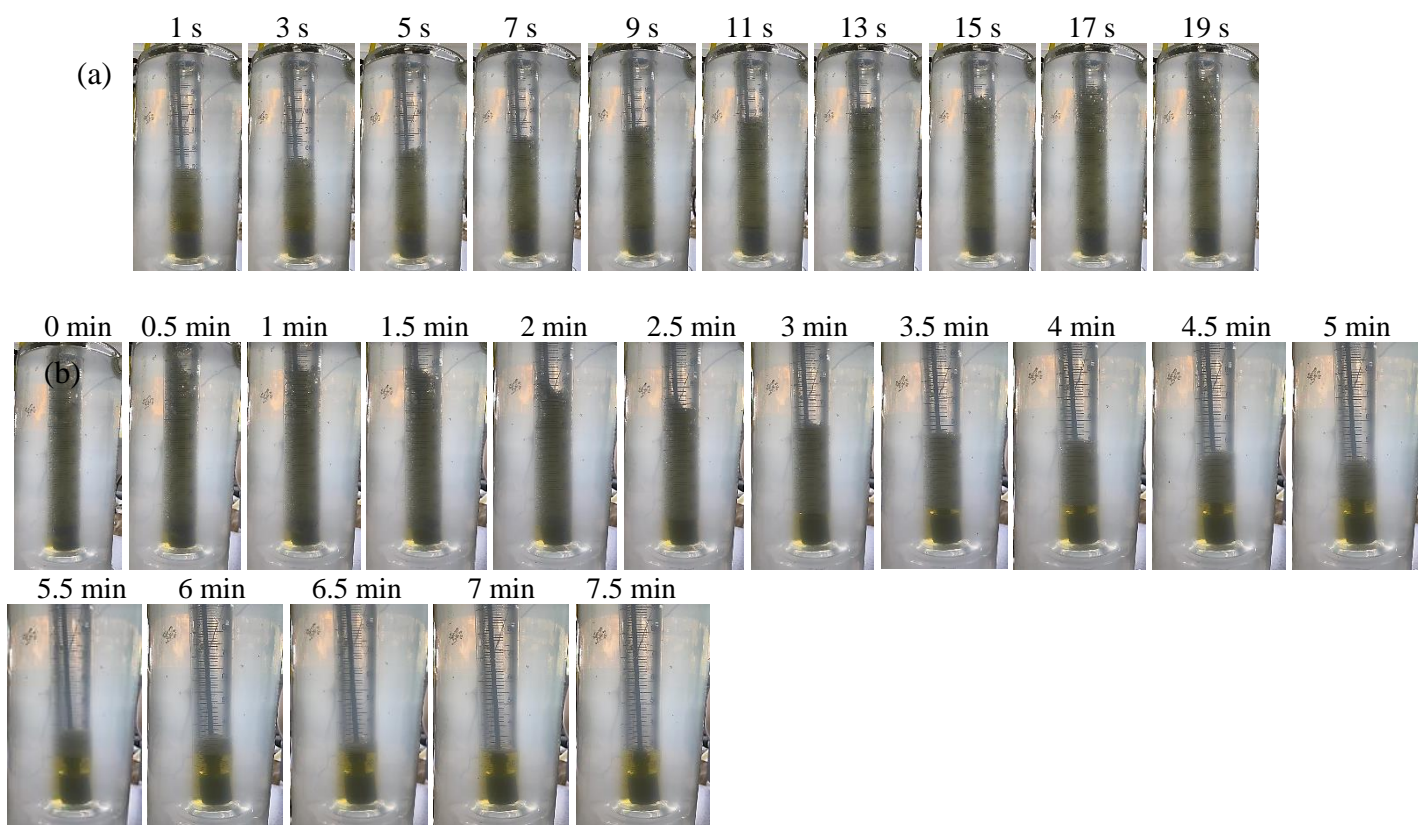
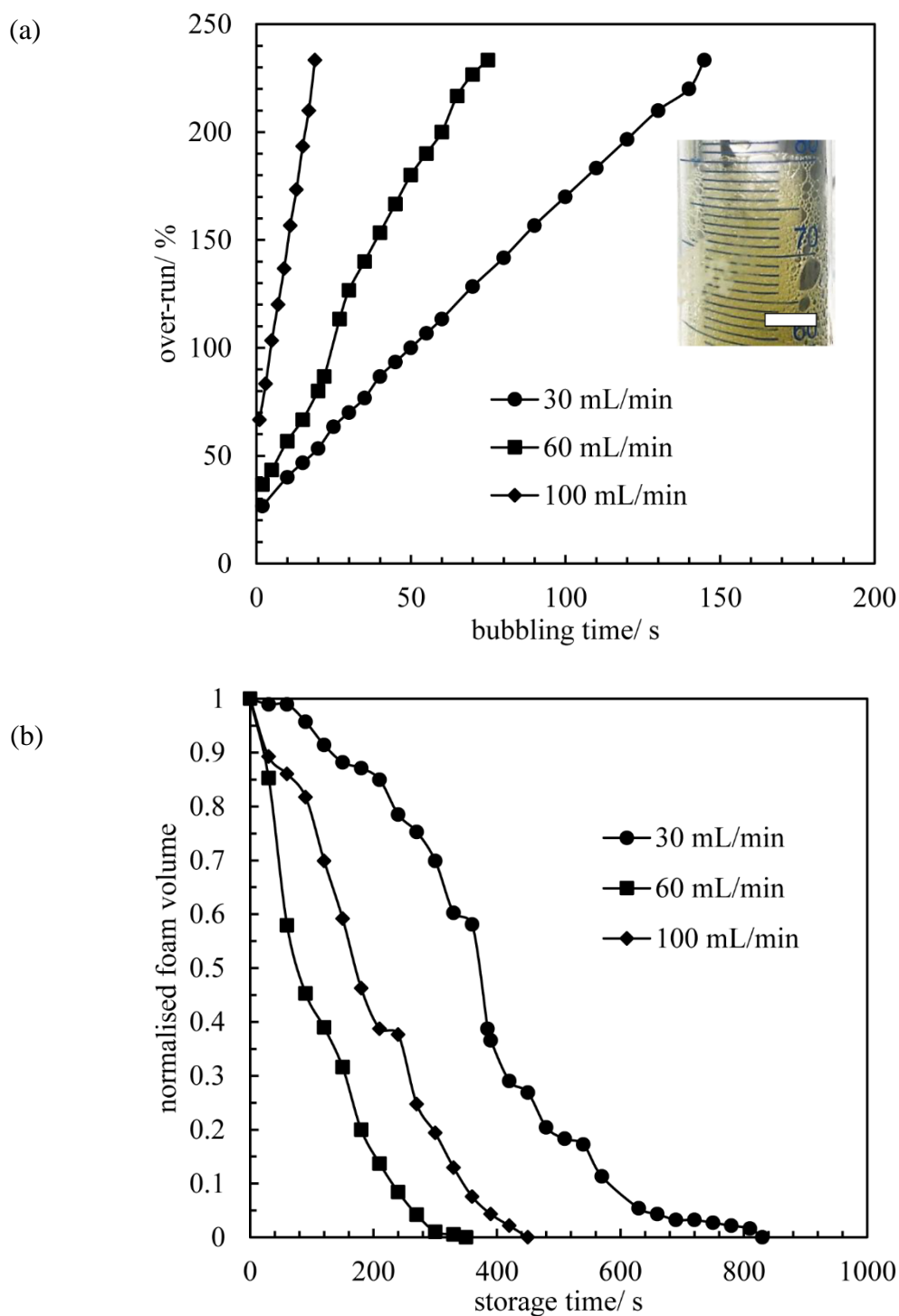


**Figure 4.39.** (a) Over-run as a function of bubbling time for systems in Figure 4.36 – Figure 4.38. Inset: photo of foam upon bubbling at 30 mL min<sup>-1</sup> for 145 s, scale bar = 1 cm. (b) Normalised foam volume as a function of storage time. Storage temperature was the same as the preparation temperature.

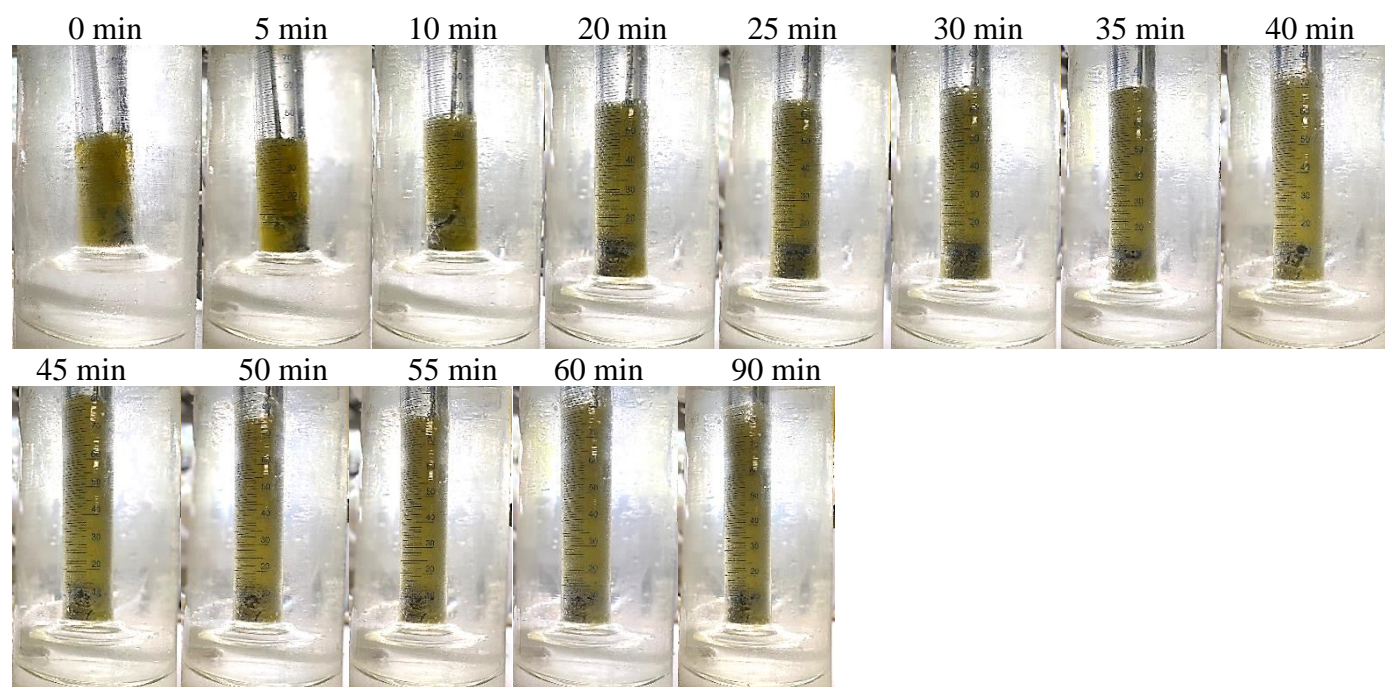


#### 4.6.2.2 Bubbling neat oil

In a recent publication,<sup>30</sup> we succeeded in preparing ultra-stable oil foams from neat EVOO without any additive over a broad range of temperature under vigorous whipping. Herein we aim to explore whether neat EVOO is still foamable under gentle bubbling. Neat EVOO was cooled rapidly to -20 °C and maintained at this temperature overnight (~ 12 h), then transferred directly to temperatures of interest. The tempered samples were then bubbled at a fixed flow rate of 100 mL min<sup>-1</sup>. Figure 4.40 presents the appearance of EVOO during bubbling and subsequent storage at 9 °C. Neat EVOO at 9 °C is a flowable, cloudy dispersion before aeration. During bubbling, the foam volume increases gradually then almost levels off. The bubbled EVOO was then stored at the bubbling temperature. Foam decay and oil drainage both occur on storage. Upon aging for ~ 6 d, the foam network is fractured, making it impossible to record the foam volume. By contrast, neat EVOO at 4 °C is a highly viscous oil dispersion. As shown in Figure 4.41(a), the application of gentle mechanical energy input, *i.e.* bubbling, is not enough to overcome the intrinsic firmness of the fat network due to van der Waals forces, thereby making it rather difficult to introduce air into the oil matrix. In fact, very limited foam can be yielded from this system after 1 h bubbling. Considering this, 2 min whipping was firstly introduced to soften the viscous dispersion into a flowable liquid.<sup>1</sup> Note that some air bubbles may be incorporated into the oil matrix during this softening process. Subsequently, bubbling was applied to the softened dispersion to yield oil foams. The foam volume increases at first, then almost plateaus (Figure 4.41(b)). The resulting foams are ultra-stable devoid of drainage, coarsening and coalescence. The over-run values of various systems as a function of bubbling time are shown in Figure 4.41(c).

**Figure 4.40.** (a) Appearance of neat EVOO as a function of bubbling time at 9 °C. Gas flow rate was fixed at 100 mL min<sup>-1</sup>. Neat EVOO was maintained at -20 °C overnight (~ 12 h) and then warmed to 9 °C. EVOO at 9 °C before aeration is a flowing, cloudy dispersion. (b) Appearance of EVOO foam in (a) as a function of storage time. Storage temperature was the same as the preparation temperature. Red arrow denotes the gas diffuser at the vessel bottom.

(a)



(b)

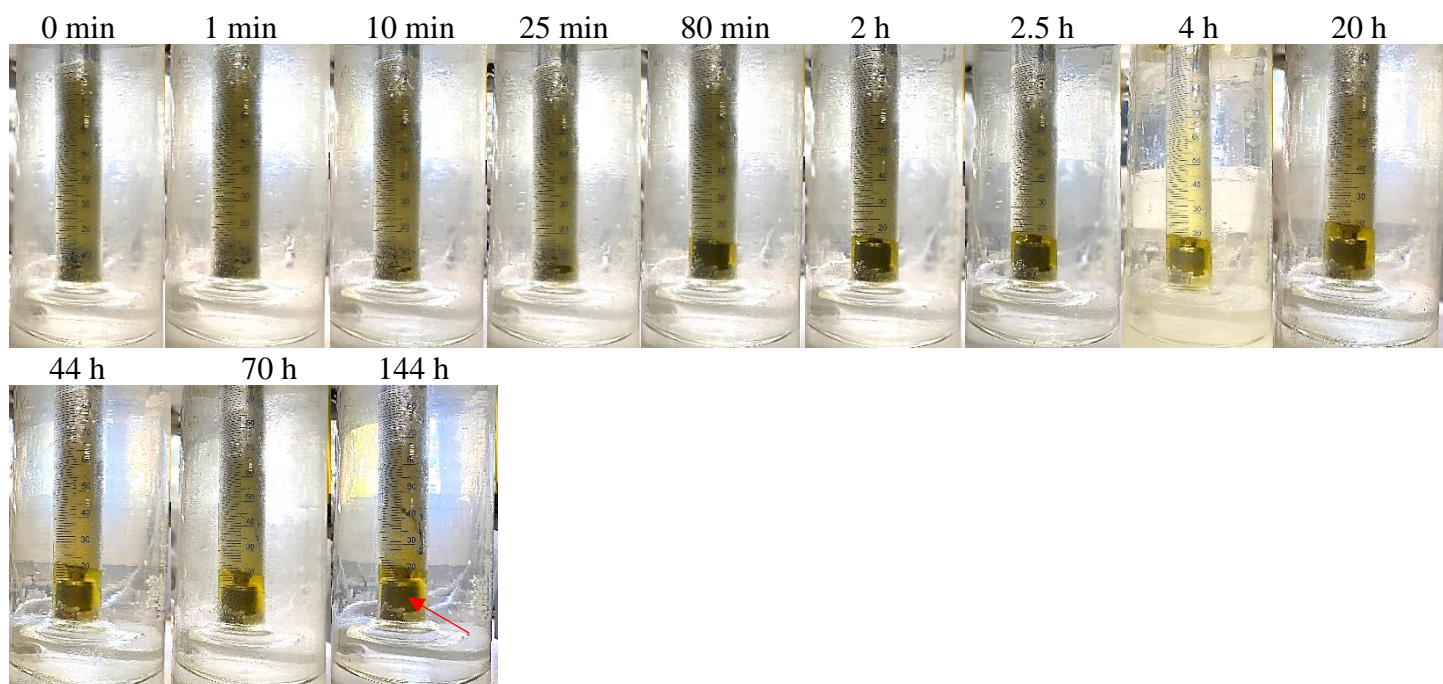


**Figure 4.41.** (a) Appearance of neat EVOO as a function of bubbling time at 4 °C. (b) Appearance of neat EVOO as a function of bubbling time at 4 °C after 2 min whipping at the same temperature. Gas flow rate was fixed at 100 mL min<sup>-1</sup>. Neat EVOO was maintained at -20 °C overnight (~12 h) and then warmed to 4 °C. EVOO at 4 °C before aeration is a viscous turbid dispersion. (c) Variation of over-run as a function of bubbling time for systems in Figure 4.40 and Figure 4.41.

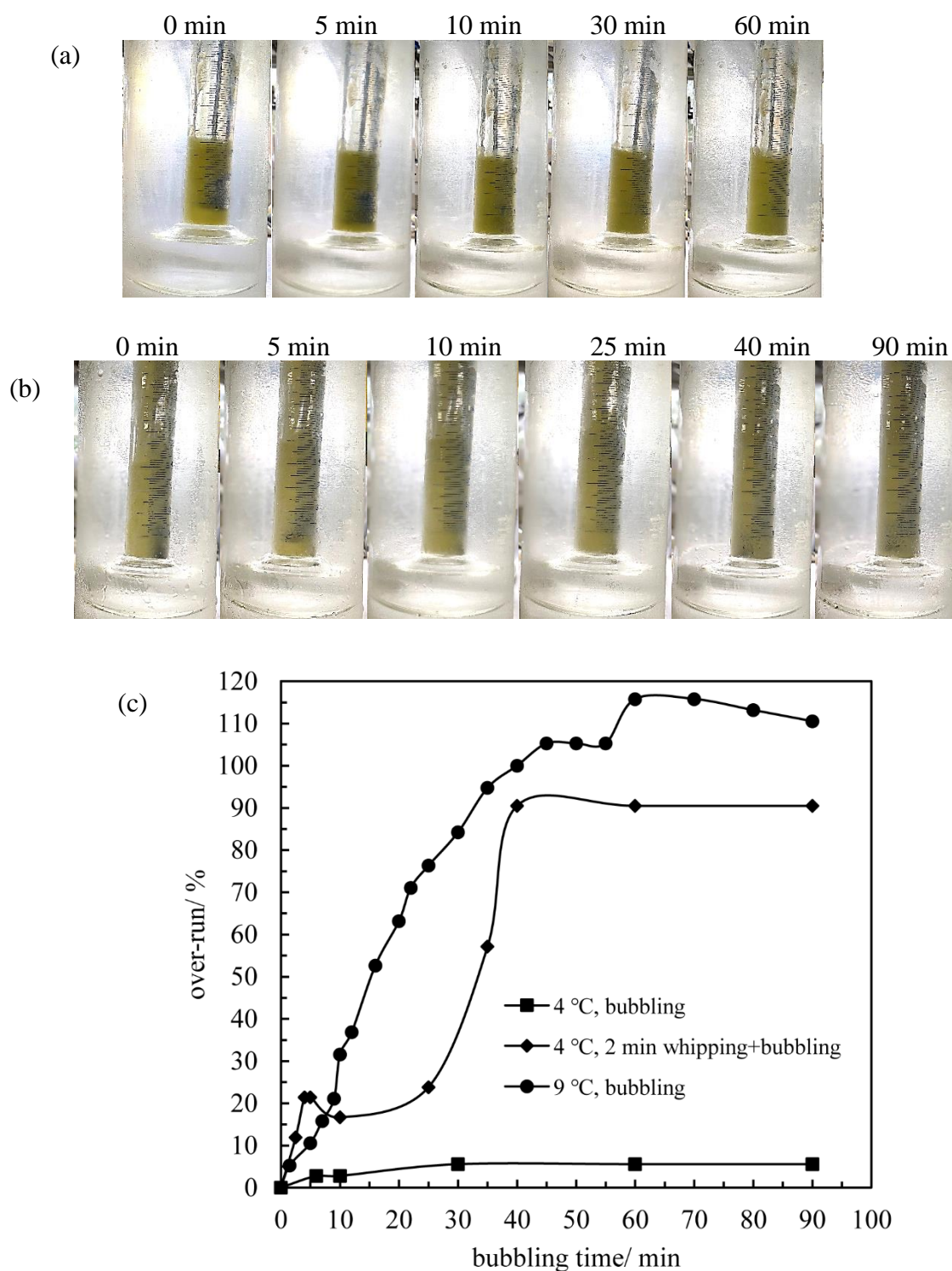
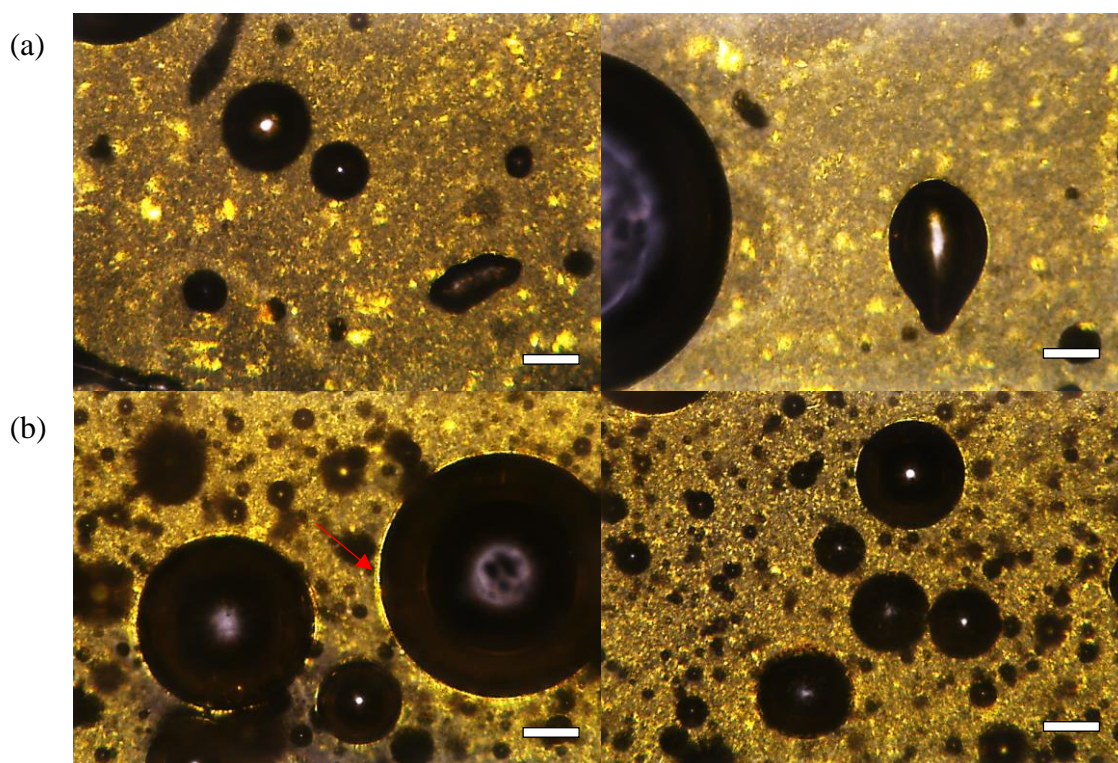


Figure 4.42 shows the polarised micrographs of the foams prepared at 4 °C. Birefringent fat crystals are present both at bubble surfaces and in continuous oil. Besides, some bubbles are non-spherical indicating jamming of crystals at bubble surfaces. More importantly, for a given aeration time more air bubbles can be incorporated into continuous oil for softened EVOO in comparison to that for intact EVOO.

**Figure 4.42.** Polarized micrographs of EVOO foams from systems in Figure 4.41. (a) 45 min bubbling at 4 °C. (b) 45 min bubbling at 4 °C after 2 min whipping at the same temperature. Scale bars = 50  $\mu\text{m}$ . Red arrow denotes crystals at the bubble surface.



#### 4.6.3 Whipping versus bubbling

Oil foams can be produced through either relatively vigorous whipping or gentle bubbling. The foaming characteristics differ however, with regards to foamability, foam stability and foam structure. Firstly, the foaming capacity from bubbling is much higher than that from whipping. For 5 wt.% C-1802 in EVOO at 80 °C, the over-run of bubbled oil can reach  $\sim 230\%$  upon bubbling at  $100 \text{ mL min}^{-1}$  for  $\sim 20 \text{ s}$ , whilst that of whipped oil reaches  $\sim 160\%$  after 10 min whipping. Secondly, the stability of bubbled oil is much poorer compared with that of whipped oil upon storing at respective preparation temperature. The former foams collapse completely within 15 min whereas the latter foams can survive almost several days. Thirdly,

the diameter of bubbled oil can reach  $\sim 1$  cm much larger than that of whipped oil ( $< 100 \mu\text{m}$ ). Detailed comparisons between whipping and bubbling are summarised in Table 4.4.

**Table 4.4.** Comparisons between whipping and bubbling C-1802 in EVOO.

Foaming method	Whipping	Bubbling
Gas type	Natural air	Purified and dehydrated air
Mechanical energy input	Vigorous	Gentle
Temperature variation during foaming	$\pm 2^\circ\text{C}$	$\pm 0.1^\circ\text{C}$
Foamability at $80^\circ\text{C}$ for 5 wt.% C-1802	Over-run of $\sim 160\%$ upon whipping for 10 min	Over-run of $\sim 230\%$ upon bubbling $< 2$ min
Foam stability at $80^\circ\text{C}$ for 5 wt.% C-1802	Collapse completely within 7 days	Collapse completely within 15 min
Foam structure	Less polydisperse; diameter $\leq 100 \mu\text{m}$	Polydisperse; diameter $\leq 1$ cm
Disadvantage	Viscous energy dissipation; crystal properties may alter	Not suitable for foaming highly viscous dispersions

## 4.7 Conclusions

Unlike previous studies,<sup>1,2,20-31</sup> we describe a novel protocol to prepare ultra-stable edible oil foams of high air volume fraction from mixtures of vegetable oil and sucrose ester surfactant. High foamability (over-run up to ~ 330%) is possible in the one-phase region due to rapid adsorption of sucrose ester-triglyceride molecular complexes at the air-oil surface. By contrast, foamability is much reduced in the two-phase region at lower temperature where surfactant crystals form. Our findings confirm the initial hypothesis, and are in contrast to all earlier work in which oil foaming was only possible in the two-phase region in the presence of surface-active lipid crystals and not from one-phase molecular solutions.<sup>1,2,20-31</sup> To enhance the resulting foam stability, a simple method is developed during which aeration is first performed in the one-phase region followed by rapid cooling and then storing at low temperature. The resulting foams, containing crystalline shells of surfactant (/oil) around air bubbles, are completely stable for  $\geq 6$  months and are temperature-responsive possessing impressive mechanical properties. The mechanisms behind foaming and subsequent stabilisation are elucidated. This method is simple but productive and we prove that it can be applied to a wide range of oil-soluble surfactants rich in hydroxyl groups in ester-containing oils.

Compared with vigorous whipping, gentle bubbling can produce oil foams more effectively. However, foam stability is sacrificed. Bubbling is a preferable method to fabricate oil foams from a weak, flowable liquid. However, for a highly viscous dispersion or a firm gel, additional mechanical energy input is needed to soften the bulk phase prior to effective air incorporation. The difference between the surface chemistry of TAG and SE crystals is worthy of further investigations.

## 4.8 References

1. D.Z. Gunes, M. Murith, J. Godefroid, C. Pelloux, H. Deyber, O. Schafer and O. Breton, Oleofoams: properties of crystal-coated bubbles from whipped oleogels-evidence for Pickering stabilization, *Langmuir*, 2017, **33**, 1563–1575.
2. K. Mishra, D. Dufour and E.J. Windhab, Yield stress dependent foaming of edible crystal-melt suspensions, *Cryst. Growth Des.*, 2020, **20**, 1292–1301.
3. A. Szűts and P. Szabó-Révész, Sucrose esters as natural surfactants in drug delivery systems-a mini-review, *Int. J. Pharm.*, 2012, **433**, 1–9.
4. T. Plat and R.J. Linhardt, Syntheses and applications of sucrose-based esters, *J. Surf. Det.*, 2001, **4**, 415–421.
5. K. Hill and O. Rhode, Sugar-based surfactants for consumer products and technical applications, *Fett/Lipid*, 1999, **101**, 25–33.
6. A. Szűts, E. Pallagi, G. Regdon Jr., Z. Aigner and P. Szabó-Révész, Study of thermal behaviour of sugar esters, *Int. J. Pharm.*, 2007, **336**, 199–207.
7. T.M. Herrington and S.S. Sahi, Phase behaviour of some sucrose surfactants with water and n-decane, *J. Am. Oil Chem. Soc.*, 1988, **65**, 1677–1681.
8. N. Becerra, C. Toro, A.L. Zanoeco, E. Lemp and G. Günther, Characterization of micelles formed by sucrose 6-O-monoesters, *Colloids Surf. A*, 2008, **327**, 134–139.
9. Y. Ishigami and H. Machida, Vesicles from sucrose fatty acid esters, *J. Am. Oil Chem. Soc.*, 1989, **66**, 599–603.
10. K. Hashizaki, H. Taguchi and Y. Saito, A novel reverse worm-like micelle from a lecithin/sucrose fatty acid ester/oil system, *Colloid Polym. Sci.*, 2009, **287**, 1099–1105.
11. X. Zhang, F. Song, M. Taxipalati, W. Wei and F. Feng, Comparative study of surface-active properties and antimicrobial activities of disaccharide monoesters, *PLoS One*, 2014, **9**, 1–19.
12. S. Soultani, S. Ognier, J.M. Engasser and M. Ghoul, Comparative study of some surface active properties of fructose esters and commercial sucrose esters, *Colloids Surf. A*, 2003, **227**, 35–44.
13. A. Tual, E. Bourles, P. Barey, A. Houdoux, M. Desprairies and J.-L. Courthaudon, Effect of surfactant sucrose ester on physical properties of dairy whipped emulsions in relation to those of O/W interfacial layers, *J. Colloid Interface Sci.*, 2006, **295**, 495–503.

14. J.D. Ntawukulilyayo, S. Bouckaert and J.P. Remon, Enhancement of dissolution rate of nifedipine using sucrose ester coprecipitates, *Int. J. Pharm.*, 1993, **93**, 209–214.
15. A. Szűts, M. Budai-Szücs, I. Erős, N. Otomo and P. Szabó-Révész, Study of gel-forming properties of sucrose esters for thermosensitive drug delivery systems, *Int. J. Pharm.*, 2010, **383**, 132–137.
16. C. Chen, H. Zhang, Y. Bi and L. Cheong, Effects of sucrose esters on isothermal crystallization of palm oil-based blend, *J. Am. Oil Chem. Soc.*, 2015, **92**, 277–286.
17. M. Lu, Y. Cao, C. Ho and Q. Huang, Development of organogel-derived capsaicin nanoemulsion with improved bioaccessibility and reduced gastric mucosa irritation, *J. Agric. Food Chem.*, 2016, **64**, 4735–4741.
18. M.D.B. Sintang, S. Danthine, A.R. Patel, T. Rimaux, D.V.D. Walle and K. Dewettinck, Mixed surfactant systems of sucrose esters and lecithin as a synergistic approach for oil structuring, *J. Colloid Interface Sci.*, 2017, **504**, 387–396.
19. S.A. Willett and C.C. Akoh, Physicochemical characterization of organogels prepared from menhaden oil or structured lipid with phytosterol blend or sucrose stearate/ascorbyl palmitate blend, *Food Funct.*, 2019, **10**, 180–190.
20. M. Brun, M. Delample, E. Harte, S. Lecomte and F. Leal-Calderon, Stabilization of air bubbles in oil by surfactant crystals: a route to produce air-in-oil foams and air-in-oil-in-water emulsions, *Food Res. Int.*, 2015, **67**, 366–375.
21. R. Heymans, I. Tavernier, S. Danthine, T. Rimaux, P. Van der Meeren and K. Dewettinck, Food-grade monoglyceride oil foams: the effect of tempering on foamability, foam stability and rheological properties, *Food Funct.*, 2018, **9**, 3143–3154.
22. M. Lei, N. Zhang, W.J. Lee, C.P. Tan, O.M. Lai, Y. Wang, and C. Qiu, Non-aqueous foams formed by whipping diacylglycerol stabilized oleogel, *Food Chem.*, 2020, **312**, 126047.
23. F. Saremnejad, M. Mohebbi and A. Koocheki, Practical application of nonaqueous foam in the preparation of a novel aerated reduced-fat sauce, *Food Bioprod. Process*, 2020, **119**, 216–225.
24. A.L. Fameau, S. Lam, A. Arnould, C. Gaillard, O.D. Velez and A. Saint-Jalmes, Smart nonaqueous foams from lipid-based oleogel, *Langmuir*, 2015, **31**, 13501–13510.
25. B.P. Binks, E.J. Garvey and J. Vieira, Whipped oil stabilised by surfactant crystals, *Chem. Sci.*, 2016, **7**, 2621–2632.

26. M. Callau, K. Sow-Kébé, N. Jenkins and A.L. Fameau, Effect of the ratio between fatty alcohol and fatty acid on foaming properties of whipped oleogels, *Food Chem.*, 2020, **333**, 127403.
27. S. Mishima, A. Suzuki, K. Sato and S. Ueno, Formation and microstructures of whipped oils composed of vegetable oils and high-melting fat crystals, *J. Am. Oil Chem. Soc.*, 2016, **93**, 1453–1466.
28. B.P. Binks and I. Marinopoulos, Ultra-stable self-foaming oils, *Food Res. Int.*, 2017, **95**, 28–37.
29. L. Goibier, C. Pillement, J. Monteil, C. Faure and F. Leal-Calderon, Emulsification of non-aqueous foams stabilized by fat crystals: Towards novel air-in-oil-in-water food colloids, *Food Chem.*, 2019, **293**, 49–56.
30. Y. Liu and B.P. Binks, Foams of vegetable oils containing long-chain triglycerides, *J. Colloid Interface Sci.*, 2021, **583**, 522–534.
31. T. Truong, S. Prakash and B. Bhandari, Effects of crystallisation of native phytosterols and monoacylglycerols on foaming properties of whipped oleogels, *Food Chem.*, 2019, **285**, 86–93.
32. S. Murdan, G. Gregoriadis and A.T. Florence, Novel sorbitan monostearate organogels, *J. Pharm. Sci.*, 1999, **88**, 608–614.
33. M. Martínez-Ávila, A. De la Peña-Gil, F.M. Álvarez-Mitre, M.A. Charó-Alonso, and J.F. Toro-Vazquez, Self-assembly of saturated and unsaturated phosphatidylcholine in mineral and vegetable oils, *J. Am. Oil Chem. Soc.*, 2019, **96**, 273–289.
34. C.H. Chen, I. Van Damme, and E.M. Terentjev, Phase behavior of C18 monoglyceride in hydrophobic solutions, *Soft Matter*, 2009, **5**, 432–439.
35. J. Coates, Interpretation of infrared spectra-a practical approach, in *Encyclopedia of Analytical Chemistry*, Meyers, R. A. (ed.), John Wiley and Sons, Chichester, 2000, p.10815–10837.
36. C.H. Chen and E.M. Terentjev, Aging and metastability of monoglycerides in hydrophobic solutions, *Langmuir*, 2009, **25**, 6717–6724.
37. K. Yoza, N. Amanokura, Y. Ono, T. Akao, H. Shinmori, M. Takeuchi, S. Shinkai and D.N. Reinhoudt, Sugar-integrated gelators of organic solvents-their remarkable diversity in gelation ability and aggregate structure, *Chem. Eur. J.*, 1999, **5**, 2722–2729.
38. B.C. Youan, A. Hussain and N.T. Nguyen, Evaluation of sucrose esters as alternative surfactants in microencapsulation of proteins by the solvent evaporation method, *AAPS Pharmsci.*, 2003, **5**, Article 22.

39. F.R. Lupi, A. Shakeel, V. Greco, N. Baldino, V. Calabrò and D. Gabriele, Organogelation of extra virgin olive oil with fatty alcohols, glyceryl stearate and their mixture, *LWT - Food Sci. Technol.*, 2017, **77**, 422–429.
40. Z. Wan, Y. Sun, L. Ma, F. Zhou, J. Guo, S. Hu, and X. Yang, Long-lived and thermoresponsive emulsion foams stabilized by self-assembled saponin nanofibrils and fibrillar network, *Langmuir*, 2018, **34**, 3971–3980.
41. L. Ma, Q. Li, Z. Du, E. Su, X. Liu, Z. Wan and X. Yang, A natural supramolecular saponin hydrogelator for creation of ultrastable and thermostimulable food-grade foams, *Adv. Mater. Interfaces*, 2019, **6**, 1900417.
42. L. Zhang, A. Mikhailovskaya, P. Yazhgur, F. Muller, F. Cousin, D. Langevin, N. Wang and A. Salonen, Precipitating sodium dodecyl sulfate to create ultrastable and stimuable foams, *Angew. Chem. Int. Ed.*, 2015, **54**, 9533–9536.
43. A.B. Subramaniam, M. Abkarian, L. Mahadevan and H.A. Stone, Colloid science: non-spherical bubbles, *Nature*, 2005, **438**, 930.
44. R. Rafanan and D. Rousseau, Dispersed droplets as active fillers in fat-crystal network-stabilized water-in-oil emulsions, *Food Res. Int.*, 2017, **99**, 355–362.
45. C.W. Macosko, *Rheology: principles, measurements, and applications*, VCH, New York, 1994.
46. R.M. Guillermic, A. Salonen, J. Emile and A. Saint-Jalmes, Surfactant foams doped with laponite: unusual behaviours induced by aging and confinement, *Soft Matter*, 2009, **5**, 4975–4982.
47. R. Rafanan and D. Rousseau, Dispersed droplets as tunable fillers in water-in-oil emulsions stabilized with fat crystals, *J. Food Eng.*, 2019, **244**, 192–201.
48. K. Achakulwisut, C. Tam, A. Huerre, R. Sammouti, B.P. Binks and V. Garbin, Stability of clay particle-coated microbubbles in alkanes against dissolution induced by heating, *Langmuir*, 2017, **33**, 3809–3817.
49. V. Poulichet and V. Garbin, Cooling particle-coated bubbles: destabilization beyond dissolution arrest, *Langmuir*, 2015, **31**, 12035–12042.
50. S. Saha, B. Saint-Michel, V. Leynes, B.P. Binks and V. Garbin, Stability of bubbles in wax-based oleofoams: decoupling the effects of bulk oleogel rheology and interfacial rheology, *Rheol. Acta*, 2020, **59**, 255–266.
51. A.C.T. Teixeira, A.R. Garcia, L.M. Ilharco, A.M.P.S. Gonçalves da Silva and A.C. Fernandes, Phase behaviour of oleanolic acid, pure and mixed with stearic acid: Interactions and crystallinity, *Chem. Phys. Lipids*, 2010, **163**, 655–666.

52. S.S. Sagiri, V.K. Singh, K. Pal, I. Banerjee and P. Basak, Stearic acid based oleogels: a study on the molecular, thermal and mechanical properties, *Mater. Sci. Eng. C*, 2015, **48**, 688–699.
53. J. A. Rincón-Cardona, L. M. Agudelo-Laverde, S. Martini, R. J. Candal and M. L. Herrera, In situ synchrotron radiation X-ray scattering study on the effect of a stearic sucrose ester on polymorphic behavior of a new sunflower oil variety, *Food Res. Int.*, 2014, **64**, 9–17.
54. S. Ghosh, T. Tran and D. Rousseau, Comparison of Pickering and network stabilization in water-in-oil emulsions, *Langmuir*, 2011, **27**, 6589–6597.
55. J. Bus, F. Groeneweg and F. van Voorst Vader, Effect of hydrogen bonding on water in oil emulsion properties, *Progr. Colloid Polym. Sci.*, 1990, **82**, 122–130.
56. F.R. Lupi, V. Mancina, N. Baldino, O.I. Parisi, L. Scrivano and D. Gabriele, Effect of the monostearate/monopalmitate ratio on the oral release of active agents from monoacylglycerol organogels, *Food Funct.*, 2018, **9**, 3278–3290.
57. T. Xu, V. Rodriguez-Martinez, S.N. Sahasrabudhe, B.E. Farks and S.R. Dungan, Effects of temperature, time and composition on food oil surface tension, *Food Biophys.*, 2017, **12**, 88–96.
58. L.K. Shrestha, M. Kaneko, T. Sato, D.P. Acharya, T. Iwanaga, and H. Kunieda, Phase behavior of diglycerol fatty acid esters–nonpolar oil systems, *Langmuir*, 2006, **22**, 1449–1454.
59. S. Ross and G. Nishioka, The relation of foam behaviour to phase separations in polymer solutions, *Colloid Polym. Sci.*, 1977, **255**, 560–565.
60. S.E. Friberg, I. Blute and H. Kunieda, Stability of hydrophobic foams, *Langmuir*, 1986, **2**, 659–664.
61. A. Szűts, Z. Makai, R. Rajkó and P. Szabó-Révész, Study of the effects of drugs on the structures of sucrose esters and the effects of solid-state interactions on drug release, *J. Pharm. Biomed.*, 2008, **48**, 1136–1142.
62. P. Wassell, A. Okamura, N.W.G. Young, G. Bonwick, C. Smith, K. Sato, and S. Ueno, Synchrotron radiation macrobeam and microbeam X-ray diffraction studies of interfacial crystallization of fats in water-in-oil emulsions, *Langmuir*, 2012, **28**, 5539–5547.
63. S. Ghosh and D. Rousseau, Triacylglycerol interfacial crystallization and shear structuring in water-in-oil Emulsions, *Cryst. Growth Des.*, 2012, **12**, 4944–4954.

64. S. Kurata, K. Yamaguchi and M. Nagai, Rapid discrimination of fatty acid composition in fats and oils by electrospray ionization mass spectrometry, *Anal. Sci.*, 2005, **21**, 1457–1465.

## CHAPTER 5 – FABRICATION OF OIL FOAMS WITH SORBITAN ESTERS

### 5.1 Introduction

In chapter 4, we demonstrate that the carbonyl groups of TAG molecules in vegetable oil form H-bonds with the hydroxyl groups in sucrose ester. The molecular complexes can adsorb readily at the air-oil surface rendering efficient foam formation upon whipping.<sup>1</sup> Subsequent rapid cooling can induce crystal formation *in situ*, thereby endowing the foam with long term stability.<sup>1</sup> The pre-requisite for this foaming strategy is that the oil-soluble surfactant used is rich in hydroxyl groups. In addition, the alkyl chain length in TAG and surfactant should be comparable to promote interfacial crystallisation on cooling.<sup>2</sup> A sorbitan molecule is rich in free hydroxyl groups and sorbitan esters (Spans) are oil-soluble nonionic surfactants consisting of sorbitan as the hydrophilic group and fatty acid chains as the hydrophobic groups.<sup>3</sup> Are stable oil foams achievable from Span-vegetable oil mixtures?

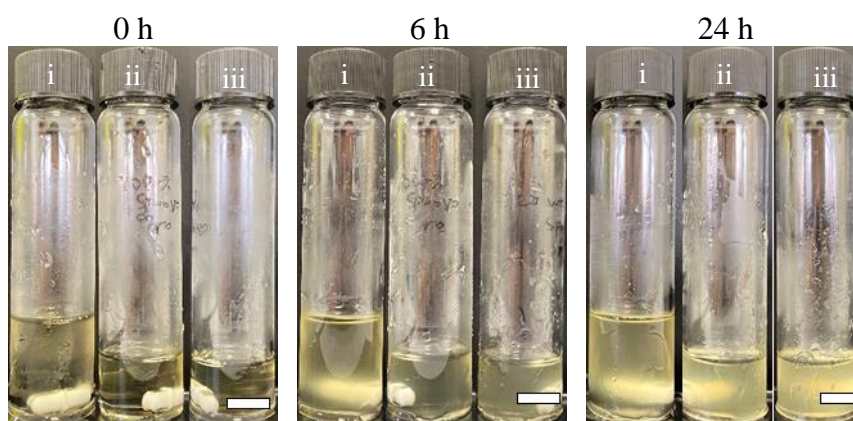
Herein we select two representative sorbitan ester surfactants, *i.e.* sorbitan monostearate (Span 60) and sorbitan monooleate (Span 80), which have been widely used as emulsifiers for stable water-in-oil emulsions.<sup>3</sup> We firstly investigate the dispersion behaviour of Spans in rapeseed oil (RO). Secondly, the effect of surfactant concentration on its foaming behaviour is studied. To prepare stable oil foams, foams prepared at relatively high temperature are submitted to rapid cooling followed by storing at low temperature. Infra-red spectroscopy, surface tension and optical microscopy are used to unveil the underlying mechanisms of the formation and stabilisation of oil foams with sorbitan esters.

## 5.2 Dispersion behaviour of sorbitan monooleate-oil mixtures

### 5.2.1 Visual observations

The melting point of neat Span 80 is  $\sim 1^\circ\text{C}$ , being a viscous, yellow liquid at room temperature.<sup>4</sup> RO remains liquid to at least  $-10^\circ\text{C}$ . Mixtures of Span 80 and RO are submitted to gentle magnetic stirring (50 rpm) at ambient temperature to create a clear, homogeneous oil solution. The mixtures were then cooled gradually in a water bath to  $-5^\circ\text{C}$  (*i.e.* an intermediate temperature between the melting points of neat Span 80 and RO), and the sample appearance is recorded as a function of storage time upon keeping isothermally at  $-5^\circ\text{C}$ . Figure 5.1 presents the appearance evolution of RO solutions/dispersions of three representative concentrations at  $-5^\circ\text{C}$ . Initially, all samples are clear liquid. After  $\sim 6$  h storage, the first sign of cloudiness appears for the samples due possibly to the formation of Span 80 crystals induced by supercooling.<sup>5</sup> The samples turn cloudier after 24 h aging since more crystals are formed.<sup>5</sup> Under the isothermal condition, the crystallization process can be characterized by the induction time ( $t_i$ ), which is the time required for the appearance of the first solid nuclei at the set temperature ( $T_{\text{set}}$ ).<sup>5</sup>  $t_i$  is inversely proportional to the degree of supersaturation or the degree of supercooling  $\Delta T$ ,  $\Delta T = T_m - T_{\text{set}}$  where  $T_m$  is the equilibrium melting temperature of a solute. In our system, the degree of supercooling equals  $\sim 6^\circ\text{C}$ .

**Figure 5.1.** Appearance of vials containing different concentrations of Span 80 in RO as a function of storage time at  $-5^\circ\text{C}$  cooled from room temperature. (i) 5 wt.%, (ii) 10 wt.%, (iii) 20 wt.%. Scale bars = 1 cm.

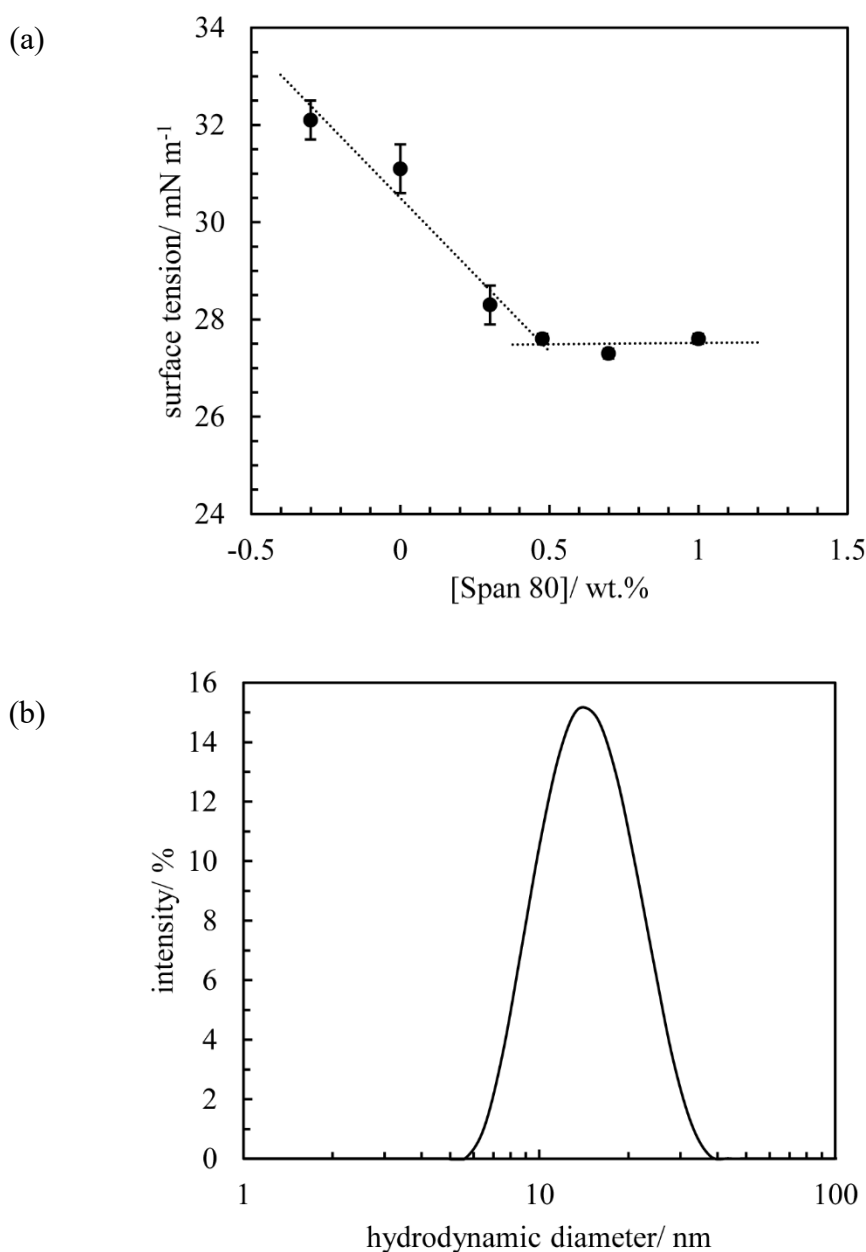


### 5.2.2 Surface tension

Figure 5.2(a) gives the air-oil surface tension of Span 80-RO mixtures at  $20^\circ\text{C}$ . The surface tension value of neat RO at  $20^\circ\text{C}$  is  $33\text{ mN m}^{-1}$ , comparable with that of Sahasrabudhe

*et al.*<sup>6</sup> The surface tension of Span 80-RO mixtures decreases gradually with Span 80 concentration reaching a constant value of  $\sim 27 \text{ mN m}^{-1}$  at  $\sim 3 \text{ wt.}\%$ , similar to the values reported by Xu *et al.*,<sup>7</sup> but larger than those of mixtures of sucrose ester and extra virgin olive oil.<sup>1</sup> From the intensity size distribution of 5 wt.% Span 80 in RO presented in Figure 5.2(b), it exhibits a peak at a hydrodynamic diameter of  $\sim 15 \text{ nm}$ . This is due possibly to the formation of reverse micelles/vesicles above the breakpoint of the surface tension curve.

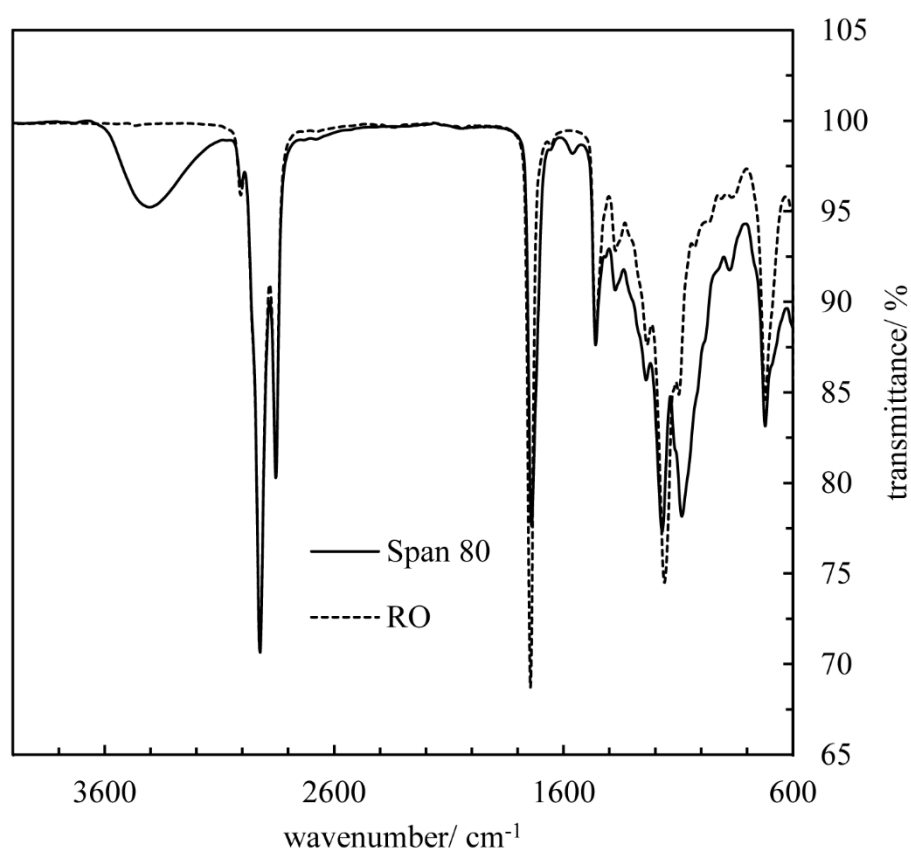
**Figure 5.2.** (a) Air-oil surface tension of Span 80-RO mixtures at 20 °C. Surface tension of neat RO at 20 °C is  $33 \text{ mN m}^{-1}$ . (b) Intensity size distribution of RO dispersion of 5 wt.% Span 80 at 20 °C determined by DLS.



### 5.2.3 Molecular interactions

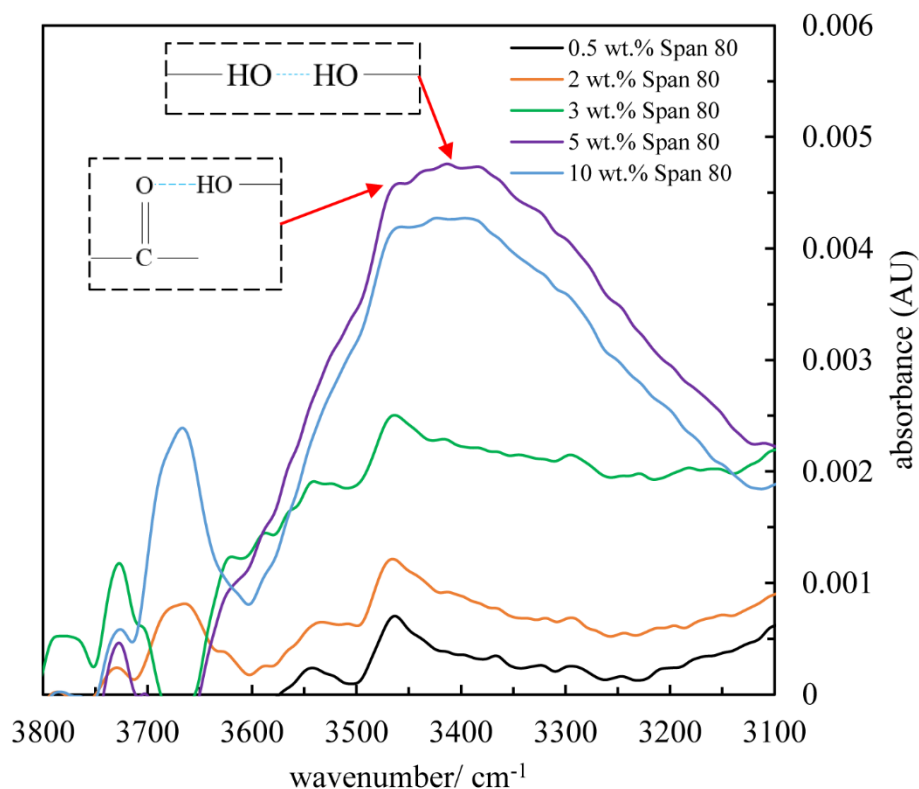
Infrared spectroscopic analysis was carried out on neat RO, Span 80 and Span 80 solutions in RO at 20 °C. In Figure 5.3, neat Span 80 exhibits a peak at  $\sim 3400\text{ cm}^{-1}$  due to intermolecular H-bonds between hydroxyl groups.<sup>8</sup> The results are reminiscent of those of Fu *et al.*<sup>9</sup> In the case of RO, no peak is observed in the range  $3100 - 4000\text{ cm}^{-1}$  pertaining to the stretching modes of  $-\text{OH}$  groups as expected.<sup>10</sup>

**Figure 5.3.** FTIR spectra of Span 80 and RO at 20 °C.



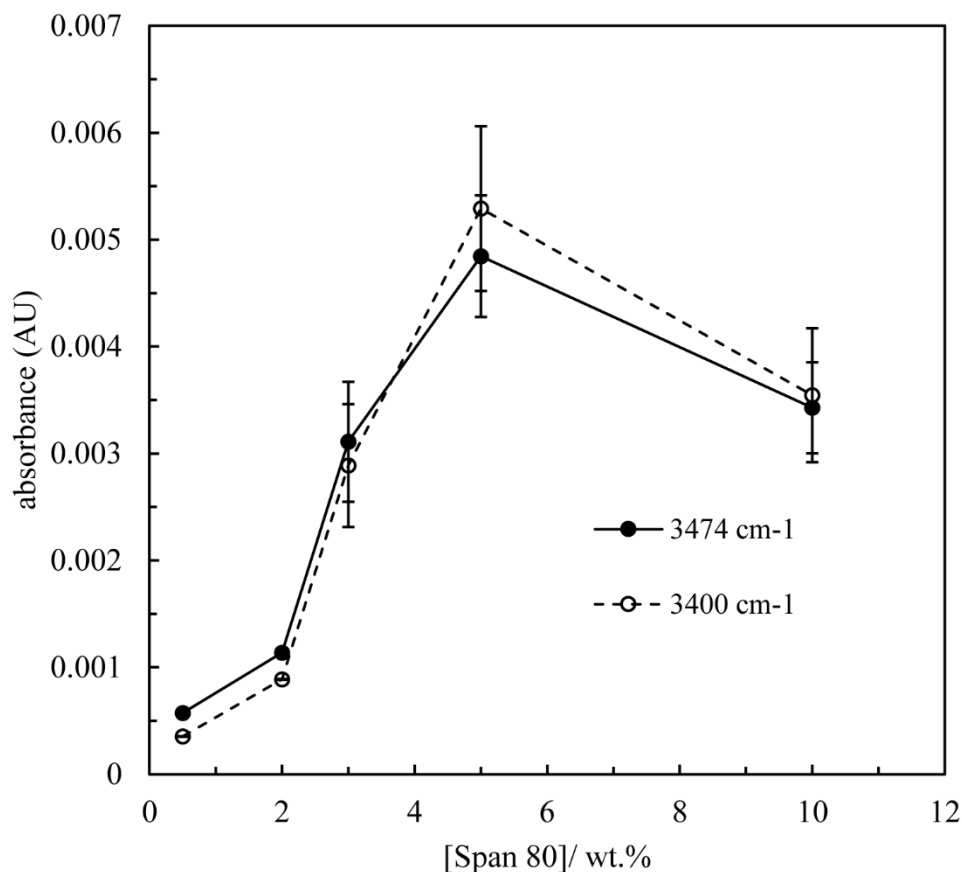
The FTIR spectra of oil solutions of Span 80 are presented in Figure 5.4. With increasing surfactant concentration, the peaks centring around  $3474\text{ cm}^{-1}$  emerge arising from intermolecular H-bonds formed between carbonyl groups in oil and hydroxyl groups in Span 80.<sup>8,11</sup> Upon increasing the surfactant concentration above 3 wt.%, the new broad peaks around  $3400\text{ cm}^{-1}$  signify the formation of intermolecular H-bonds between hydroxyl groups in Span 80 molecules themselves.<sup>8</sup> The appearance of the peaks at  $3474\text{ cm}^{-1}$  is earlier compared to those at  $3400\text{ cm}^{-1}$  as increasing the surfactant concentration, which is possibly because H-bonds formed between carbonyl groups in oil and hydroxyl groups in surfactant are stronger than those between surfactant molecules.<sup>11</sup> Moreover, the increase in peak broadness is attributed to more  $-\text{OH}$  groups involved in H-bonding.<sup>12</sup>

**Figure 5.4.** FTIR spectra of Span 80-RO mixtures at 20 °C. Inset: hydrogen bond formed between TAG carbonyl group in oil and Span 80 hydroxyl group in surfactant; hydrogen bond formed between Span 80 hydroxyl groups in surfactant.



As shown in Figure 5.5, the intensities of the bands at  $3400\text{ cm}^{-1}$  (solute-solute) and  $3474\text{ cm}^{-1}$  (solute-solvent) increase with surfactant concentration peaking at  $\sim 5\text{ wt.}\%$ , followed by a gradual decline. It seems that too high surfactant concentration may disrupt the formation of both solute-solute and solute-solvent molecular interactions. Based on the surface tension and IR data, we propose that for an oil solution of Span 80, both solute-solute and solute-solvent molecular interactions exist in the form of intermolecular H-bonds in addition to van der Waals interactions between hydrocarbon chains. The molecular complexes are highly surface-active at the air-oil surface.

**Figure 5.5.** Infrared absorbance of RO solutions as a function of Span 80 concentration at 3,400  $\text{cm}^{-1}$  (H-bonds between surfactant molecules) and 3,474  $\text{cm}^{-1}$  (H-bonds between surfactant and oil molecules).

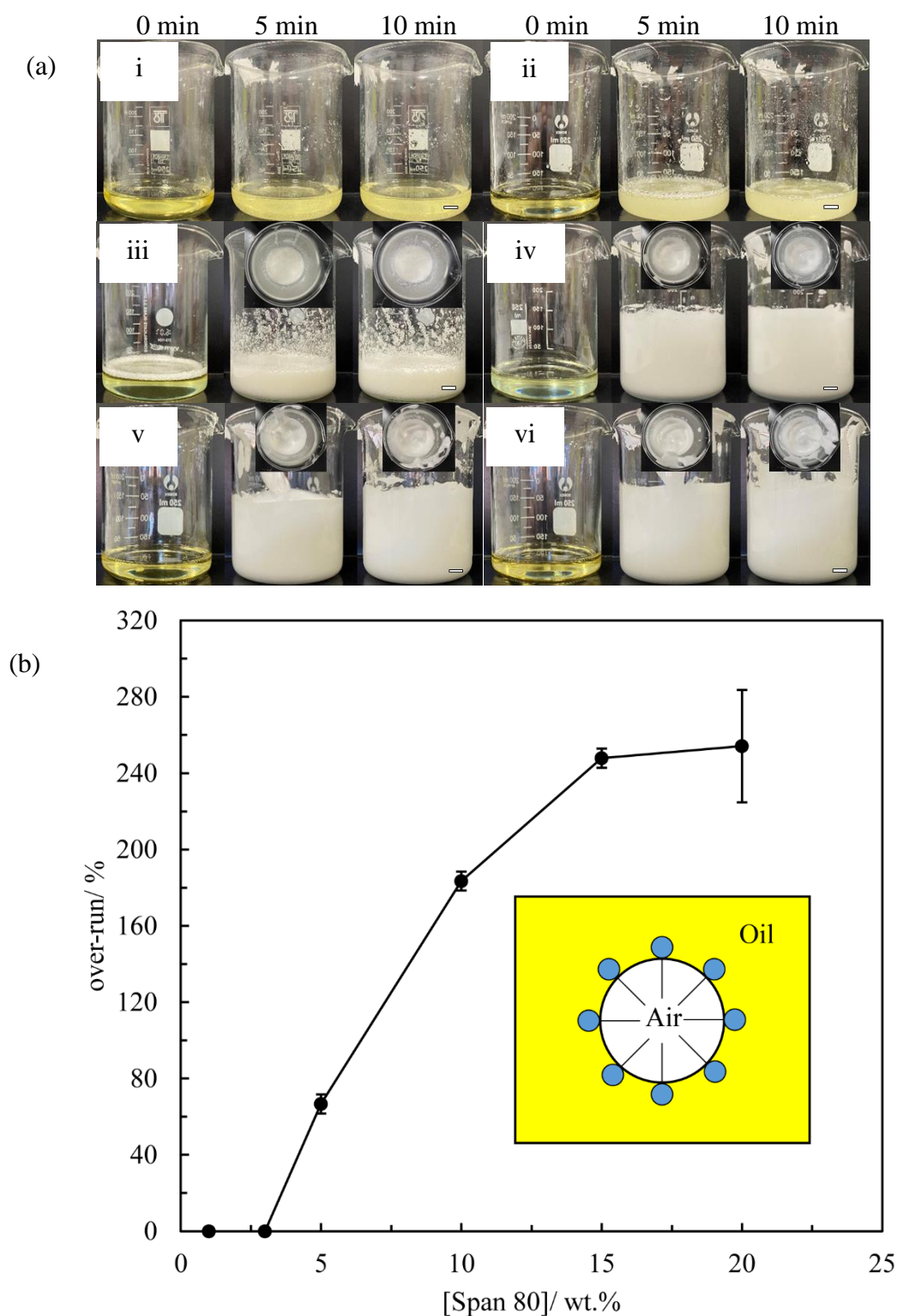


### 5.3 Whipping mixtures of sorbitan monooleate and oil

#### 5.3.1 Foams prepared and stored at same temperature

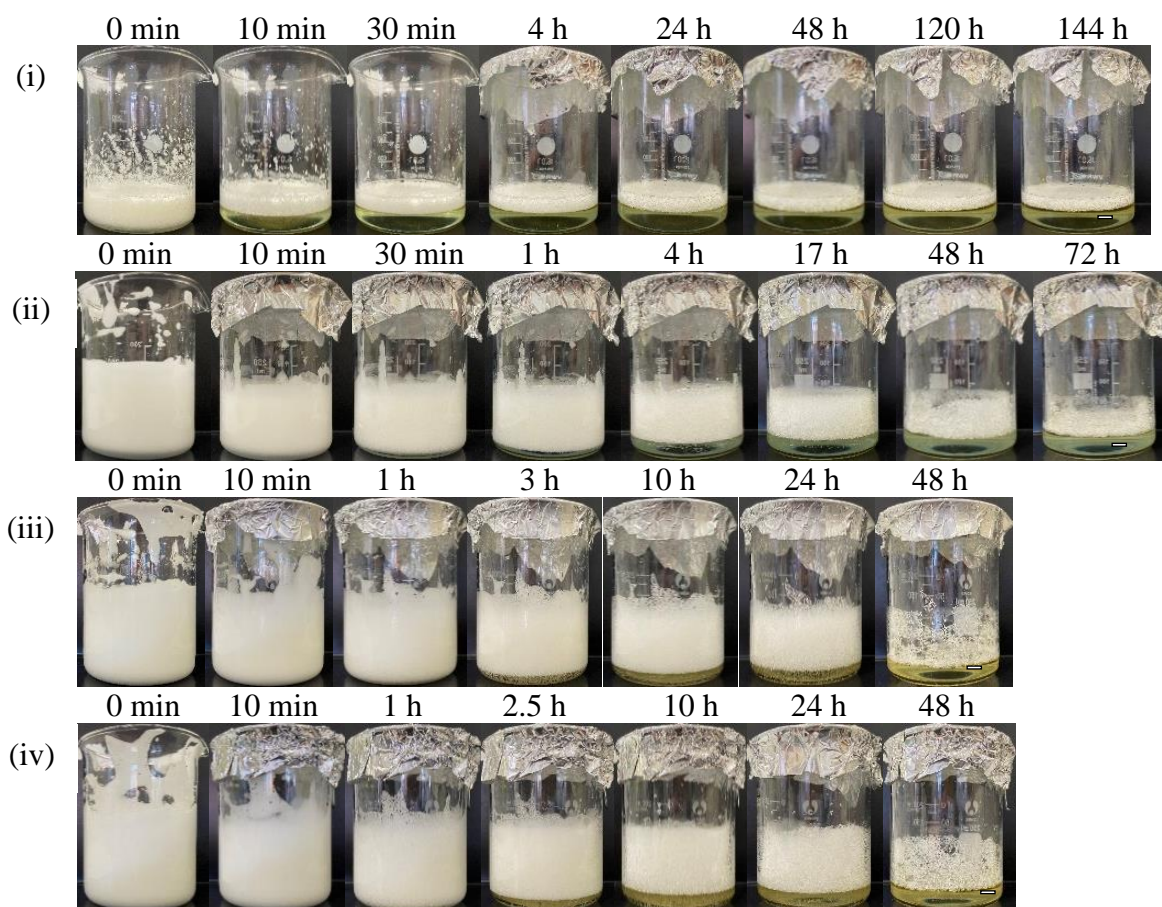
The foaming behaviour of Span 80-RO solutions/dispersions was studied as a function of surfactant concentration. Samples were submitted to gentle magnetic stirring overnight followed by being whipped continuously using a single beater electric whisk for 10 min. Figure 5.6(a) shows the change in appearance for different concentrations of Span 80 in RO as a function of whipping time. All mixtures before whipping are clear liquid. For concentrations  $\leq 3$  wt.%, very little or no foam can be achieved. Upon increasing above 3 wt.%, the foam volume increases with surfactant concentration up to a certain level. The influence of surfactant concentration on the over-run is shown in Figure 5.6(b). The over-run increases with increasing surfactant concentration followed by a constant value. The highest over-run value is 275% for 20 wt.%, corresponding to an air volume fraction of 0.73.

**Figure 5.6.** (a) Appearance of RO containing different concentrations of Span 80 as a function of whipping time at room temperature. (i) 1 wt.%, (ii) 3 wt.%, (iii) 5 wt.%, (iv) 10 wt.%, (v) 15 wt.% and (vi) 20 wt.%. Scale bars = 1 cm. (b) Variation of over-run with Span 80 concentration in RO. Inset: schematic illustrating Span 80-stabilised RO foam.



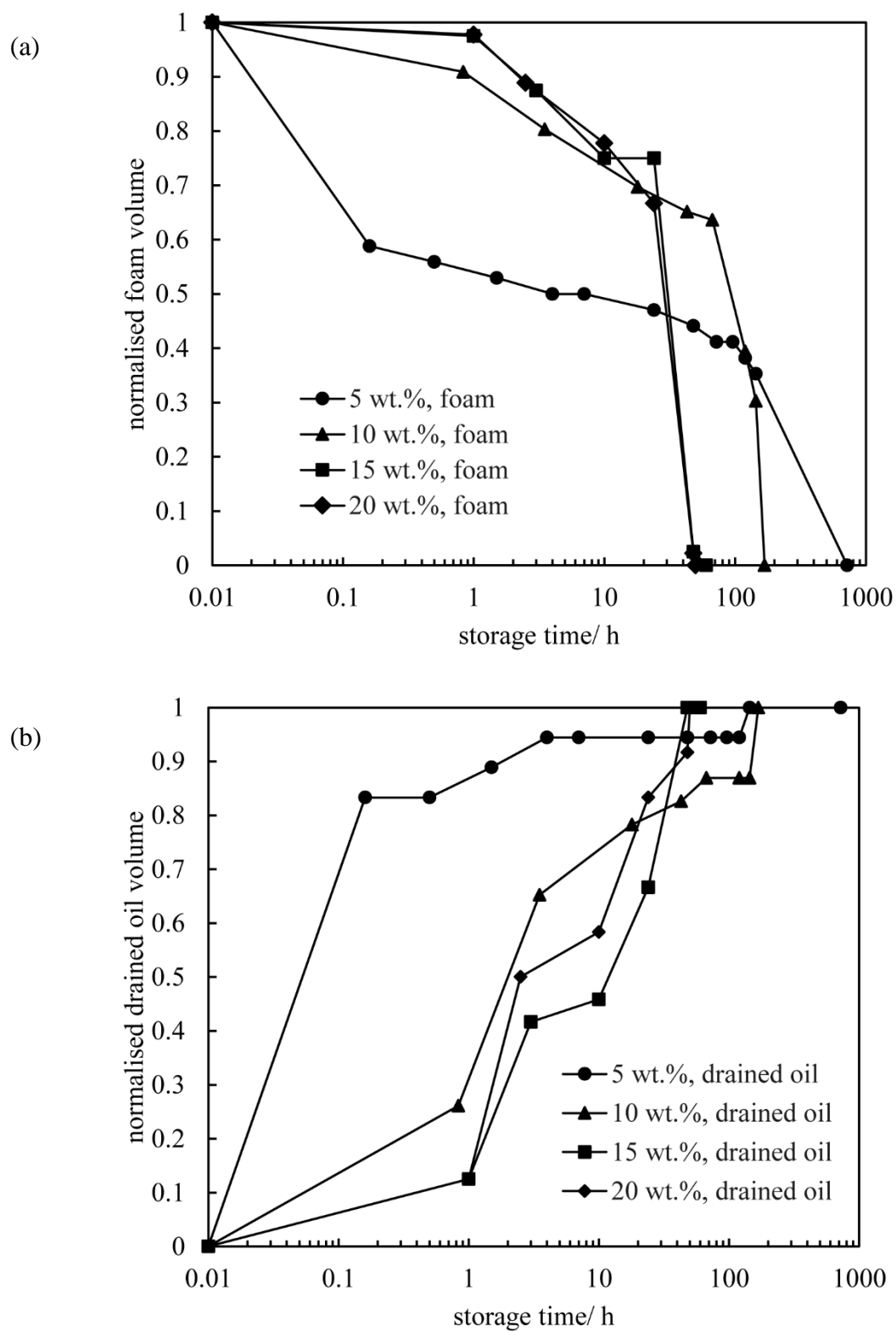
Oil foams were stored at respective whipping temperature. Photos of the foams during storage are given in Figure 5.7. Oil drainage occurs immediately after preparation leading to a dry foam within the first few hours. The foams also gradually decay until collapsing completely through coarsening/coalescence.

**Figure 5.7.** Appearance of RO foams containing different concentrations of Span 80 as a function of storage time for systems in Figure 5.6. (i) 5 wt.%, (ii) 10 wt.%, (iii) 15 wt.% and (iv) 20 wt.%. Storage temperature was the same as the preparation temperature. Scale bars = 1 cm.



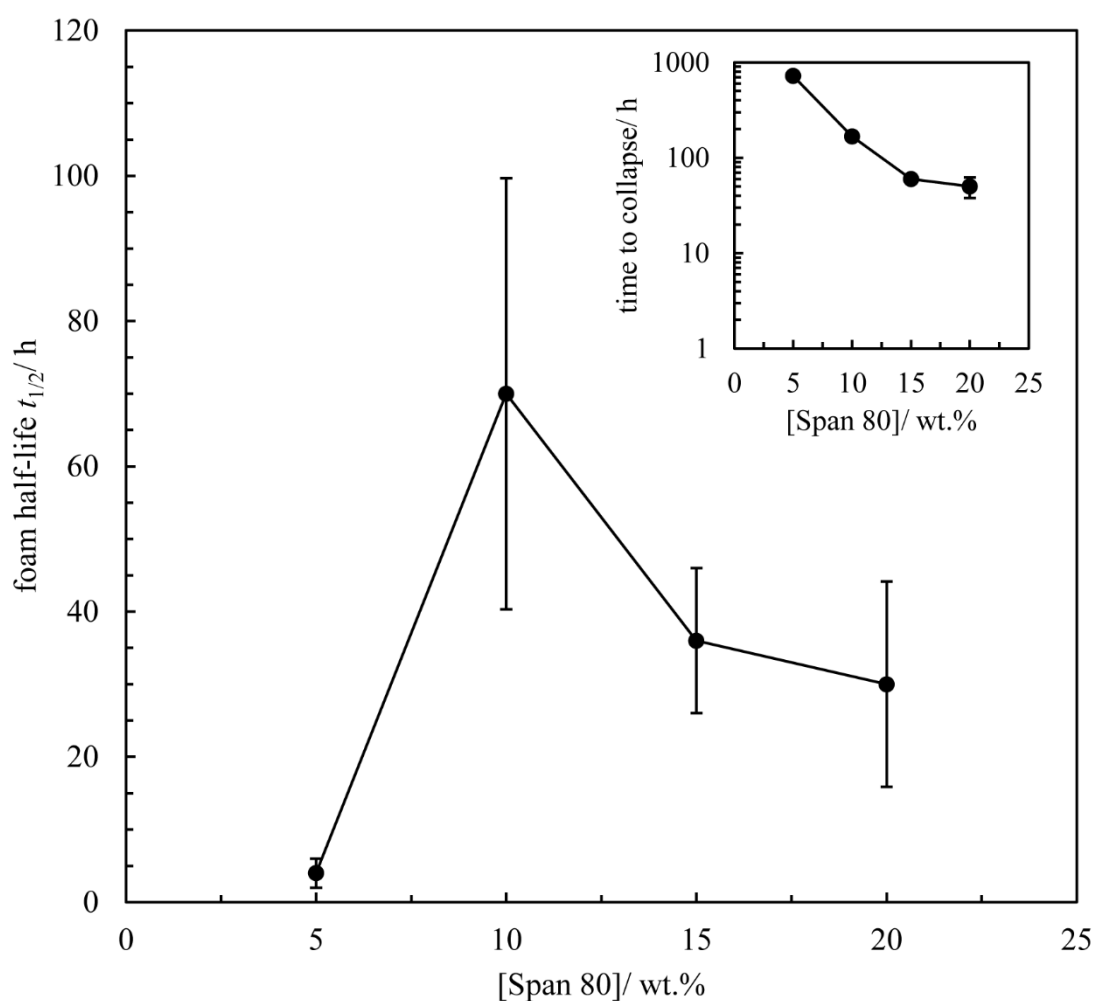
The normalised volume of foam or drained oil, defined as the volume ratio of foam/drained oil during storage relative to that initially, is plotted in Figure 5.8 as a function of storage time. All foams collapse completely within 1 week except the foam stabilised by 5 wt.% Span 80. This is possibly because the intensities of the bands of solute-solute and solute-solvent interactions begin to decay above 5 wt.% as shown in Figure 5.5.

**Figure 5.8.** (a) Normalised volume of Span 80-stabilised RO foam and (b) normalised volume of drained oil against storage time for systems in Figure 5.6.



The foam half-life increases with an increase in surfactant concentration followed by a gradual decline, whilst time for complete foam collapse decreases with surfactant concentration (Figure 5.9). Rousseau *et al.* concluded that the capacity of an oil-soluble lipid emulsifiers to stabilize w/o emulsions strongly depended on how extensively they H-bonded with continuous oil.<sup>2,11</sup> In another study, Liu and Binks highlighted that a pre-requisite for the formation and stabilisation of oil foams was the formation of intermolecular H-bonds between carbonyl groups in oil and hydroxyl groups in surfactant.<sup>1</sup> In our system, we propose that at high surfactant concentration, the adsorption/desorption equilibrium of surfactant molecules at the air-oil surface tends to shift towards desorption due to weaker H-bonding between solute-solute or solute-solvent (see Figure 5.5), thereby leading to poorer foam stability.

**Figure 5.9.** Foam half-life  $t_{1/2}$  and time for complete foam collapse (inset) as a function of Span 80 concentration for systems in Figure 5.6.



Optical micrographs of some foams immediately after preparation and during storage are given in Figure 5.10. The foam bubbles are polydisperse and spherical possessing smooth surfaces. The bubble size increases with storage time because of coarsening/coalescence. The variation of average bubble diameter with surfactant concentration is presented in Figure 5.11. Generally, the average bubble diameter decreases with surfactant concentration.

**Figure 5.10.** Optical micrographs of Span 80-stabilised RO foams for systems in Figure 5.6. Immediately after whipping for (a) 5 wt.%, (b) 10 wt.%, (c) 15 wt.% and (d) 20 wt.% at room temperature. (e) System (a) after 0.5 h aging. Scale bars = 50  $\mu\text{m}$ .

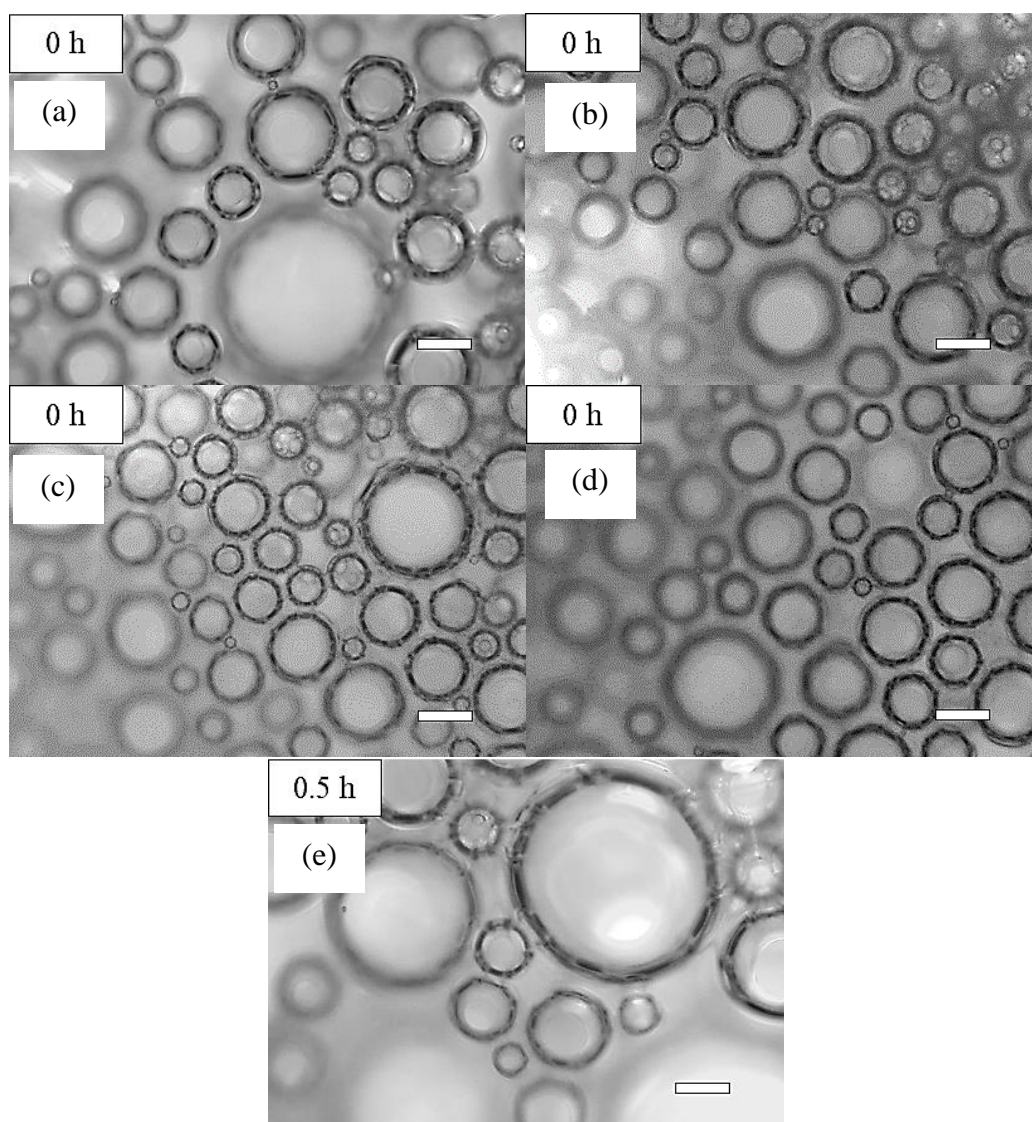
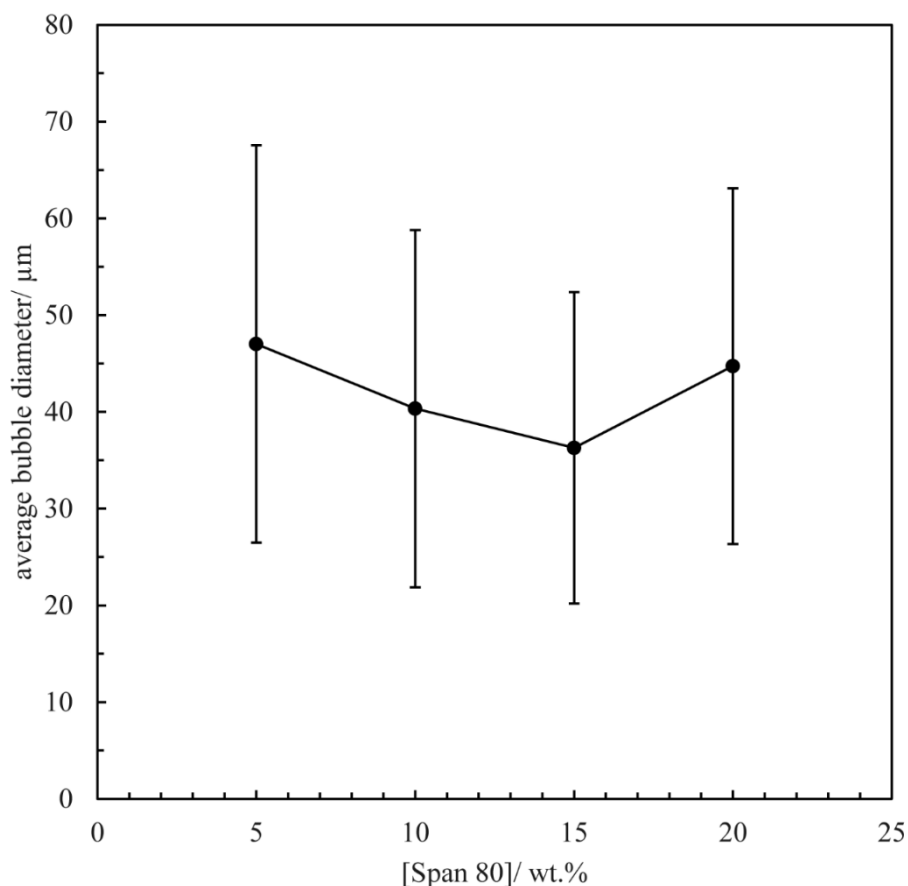


**Figure 5.11.** Variation of average bubble diameter with Span 80 concentration for systems in Figure 5.6 immediately after 10 min whipping at room temperature.



### 5.3.2 Protocol for fabricating stable foams

Due to foam instability, a post-whipping protocol was introduced to enhance the foam stability. Oil foams prepared at room temperature were quickly transferred to an ice bath of  $-5\text{ }^{\circ}\text{C}$ . Upon reaching  $-5\text{ }^{\circ}\text{C}$  (*i.e.* an intermediate temperature between the melting points of neat Span 80 and RO), the quenched samples were stored at this temperature for further investigation.

Figure 5.12 and Figure 5.13 present the appearance of RO foams containing 15 wt.% and 20 wt.% Span 80 subjected to rapid cooling followed by storing at  $-5\text{ }^{\circ}\text{C}$ , respectively. All foams decay gradually within the first 2 weeks on storage, but the residual foams can last for more than one month, being much more stable than the foams stored at room temperature. It seems that ultra-stable foams cannot be achieved based on this system. The possible reasons for this are explained as follows. Firstly, Span 80 cannot gel RO within the investigated quenching and storage temperature range, so a bulk contribution to foam stability is unachievable. Secondly, as shown in Figure 5.14 later, Span 80 crystals formed *in situ* at the

interface are not coherent, which is not sufficient to provide an efficient Pickering stabilisation.

**Figure 5.12.** (a) Appearance of RO foam containing 15 wt.% Span 80 submitted to rapid cooling immediately after 10 min whipping. Foam prepared at room temperature was cooled in an ice bath of  $-5^{\circ}\text{C}$  followed by storing at  $-5^{\circ}\text{C}$ . Scale bar = 1 cm. (b) Corresponding normalized volume of foam (●) and drained oil (○) and foam temperature (■) as a function of aging time.

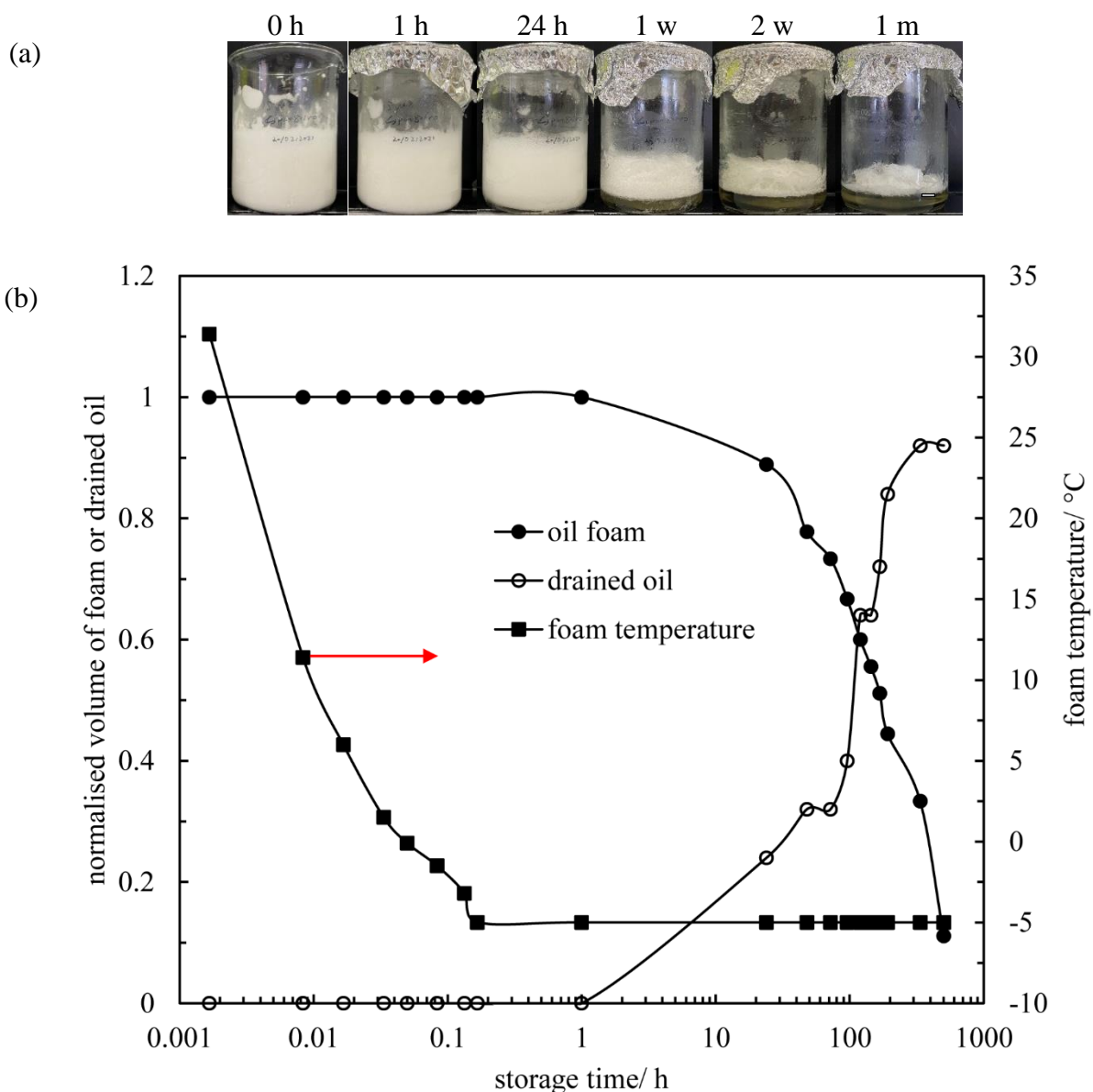


**Figure 5.13.** (a) Appearance of RO foam containing 20 wt.% Span 80 submitted to rapid cooling immediately after 10 min whipping. Foam prepared at room temperature was cooled in an ice bath of -5 °C followed by storing at -5 °C. Scale bar = 1 cm. (b) Corresponding normalized volume of foam (●) and drained oil (○) and foam temperature (■) as a function of aging time.

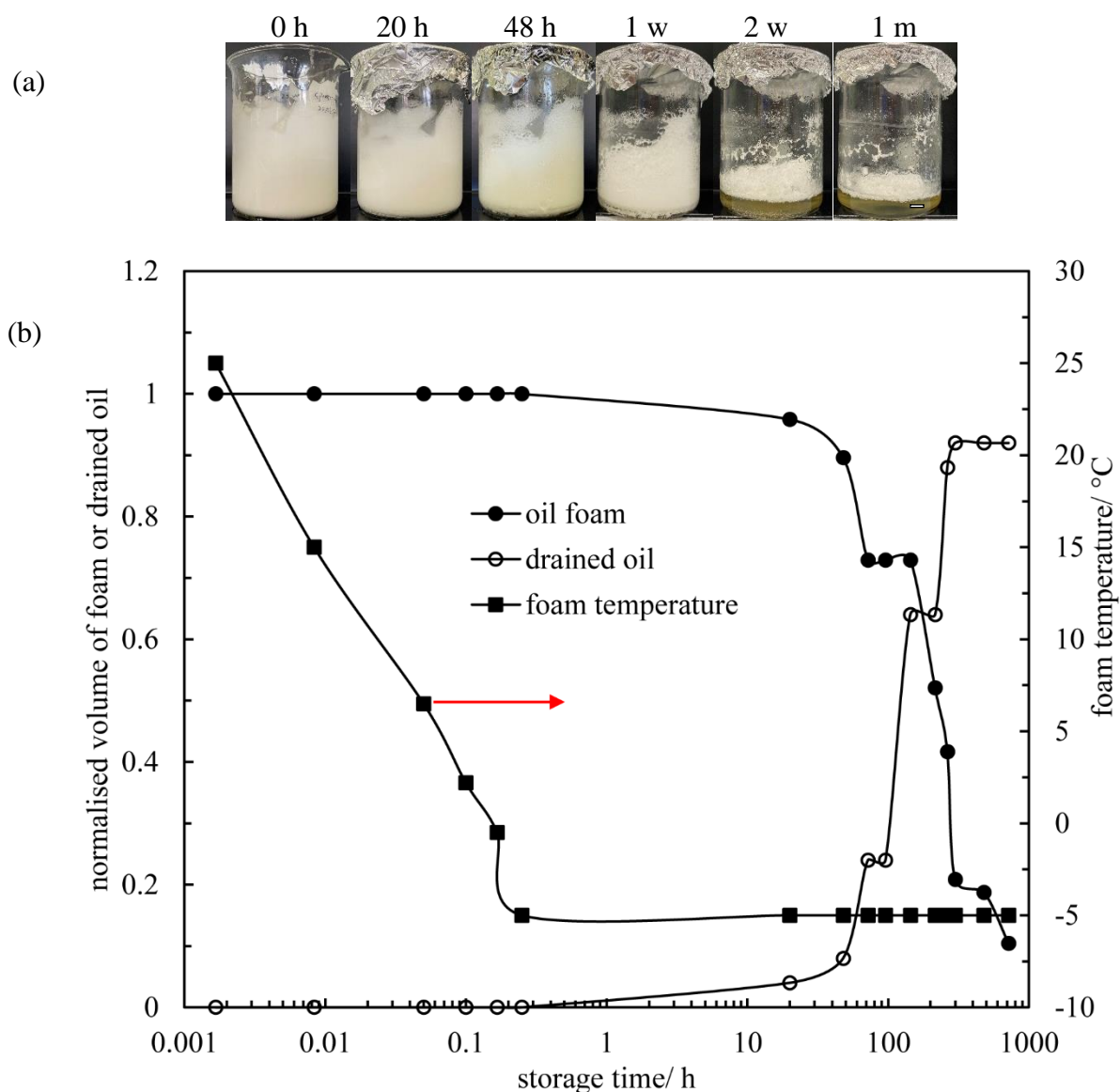
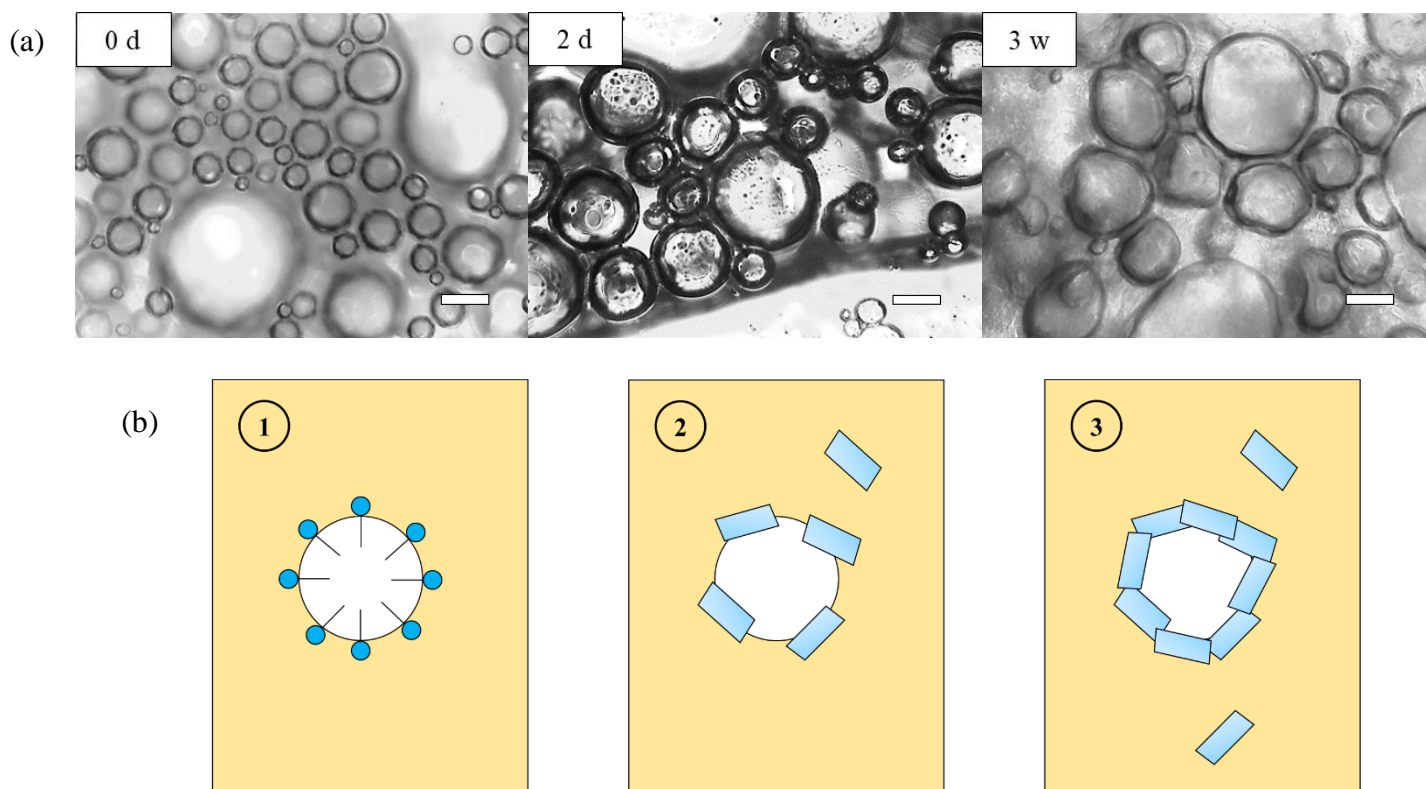


Figure 5.14(a) gives the representative optical micrographs of RO foam containing 20 wt.% Span 80 during storage at -5 °C. The average bubble diameter increases on storage, indicating the occurrence of coarsening and/or coalescence. Meanwhile, the microscopic appearance of RO foam bubbles evolves gradually: (i) initially the air bubbles are spherical and smooth being stabilised by surfactant molecules; (ii) the bubble surfaces turn slightly rough due to the interfacial crystallisation of surfactant molecules *in situ*; (iii) the bubble surfaces

become more rough and textured and some of them are non-spherical due to the interfacial jamming of crystals, Figure 5.14(b). This finding correlates well with the visual observations in Figure 5.1. Future work will concentrate on investigating the effect of storage temperature on foam stability.

**Figure 5.14.** (a) Optical microscopy images of RO foam containing 20 wt.% Span 80 during storage at -5 °C. RO foam prepared at room temperature was cooled in an ice bath of -5 °C followed by storing at -5 °C. (b) Schematic illustrating the appearance of an air bubble in RO in the presence of Span 80 during storage at -5 °C. 1: Initially the air bubble is stabilised by surfactant molecules; 2: the bubble surface appears slightly textured due to interfacial crystallisation *in situ*; 3: the bubble surface becomes more textured and some of them are non-spherical due to the interfacial jamming of crystals.



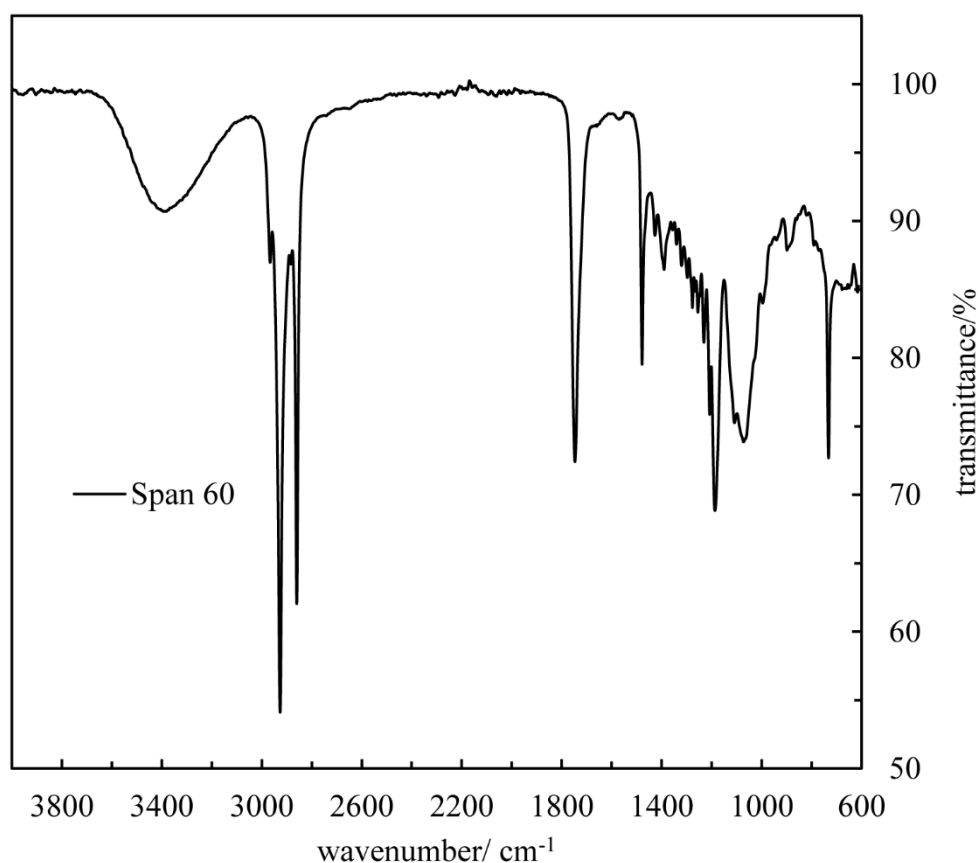
## 5.4 Dispersion behaviour of sorbitan monostearate-oil mixtures

Can we obtain ultra-stable oil foams from mixtures of sorbitan monostearate (Span 60) and vegetable oil? In this section, we firstly study the physicochemical properties of neat Span 60. Secondly, we explore the foaming potential of its mixture with rapeseed oil. Thirdly, the possibility of achieving oil foams with long term stability is investigated.

### 5.4.1 Molecular interactions and thermal properties

Figure 5.15 illustrates the FTIR spectrum of neat Span 60 at room temperature. Neat Span 60 exhibits a peak at  $\sim 3400\text{ cm}^{-1}$  because of intermolecular H-bonds between hydroxyl groups in the surfactant,<sup>8</sup> which is comparable to that of Span 80. The representative C=O stretching peak can be observed at  $1738\text{ cm}^{-1}$ .<sup>13</sup> Fathalla *et al.*<sup>14</sup> also identified two transmittance peaks ( $\sim 3400\text{ cm}^{-1}$  and  $\sim 1738\text{ cm}^{-1}$ ) for Span 60, demonstrating the reliability of our data.

**Figure 5.15.** FTIR spectrum of Span 60 at room temperature.



The thermal behaviour of neat Span 60 was investigated by DSC (Figure 5.16 and Table 5.1). Upon heating at 5 °C min<sup>-1</sup>, the thermogram exhibits one distinct endothermic peak at 53.4 °C. Similarly, Fathalla *et al.*<sup>14</sup> reported a single endothermic peak at ~59 °C with a heating rate of 10 °C min<sup>-1</sup>. The sharp melting endotherm indicates the sample used herein is mono-component, *i.e.* sorbitan monostearate. Subsequent cooling at 5 °C min<sup>-1</sup> sees a major exothermic peak at 48.2 °C and one minor peak at 40.7 °C. To understand the polymorph of the sample, SAXS and WAXS measurements are needed. Further experiments surrounding this are underway.

**Figure 5.16.** Melting and cooling thermograms of Span 60. Temperature change rate was 5 °C min<sup>-1</sup>.

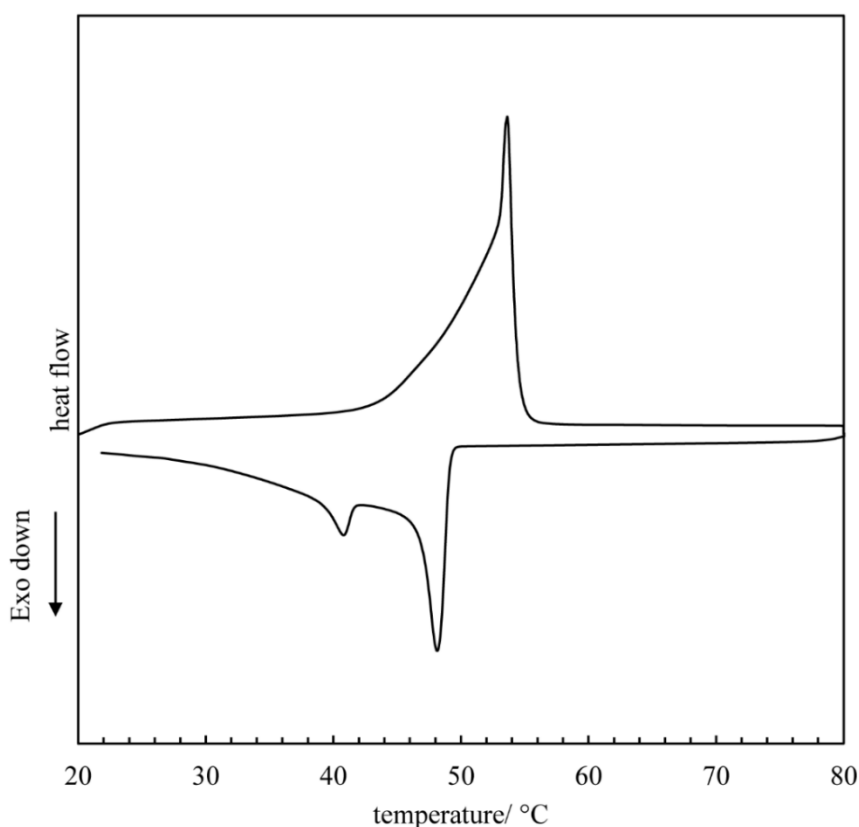


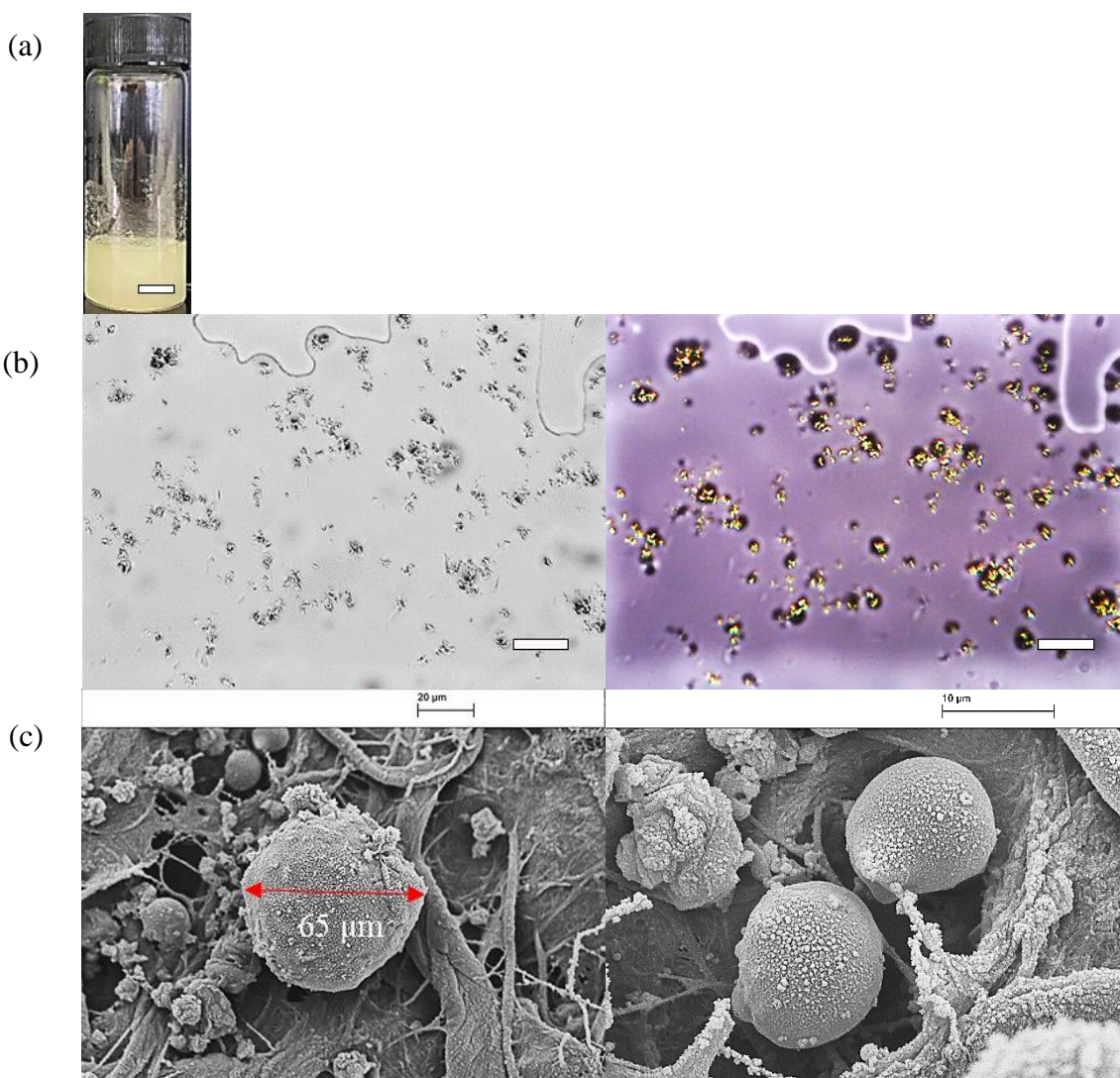
**Table 5.1.** Thermal properties of Span 60.

Crystallisation					Melting	
$T_{\text{peak}}/^{\circ}\text{C}$		$\Delta H/\text{J g}^{-1}$			$T_{\text{peak}}/^{\circ}\text{C}$	$\Delta H/\text{J g}^{-1}$
Span 60	Peak 1	Peak 2	Peak 1	Peak 2	Peak 1	Peak 1
	40.70±0.08	48.20±0.04	-4.93±0.18	-30.31±2.14	53.40±0.20	95.24±2.33

#### 5.4.2 Visual observations and crystal morphology

Figure 5.17(a) presents the appearance of a RO dispersion containing 5 wt.% Span 60 at 20 °C. It is a turbid, viscous dispersion. The non-polarized and polarized microscopy images of the RO dispersion are shown in Figure 5.17(b). Many birefringent Span 60 crystals (bright) exist within the isotropic oil matrix. The cryo-SEM images of Span 60 crystals are given in Figure 5.17(c). Span 60 crystals are spherical and polydisperse with diameters  $\leq 65 \mu\text{m}$ .

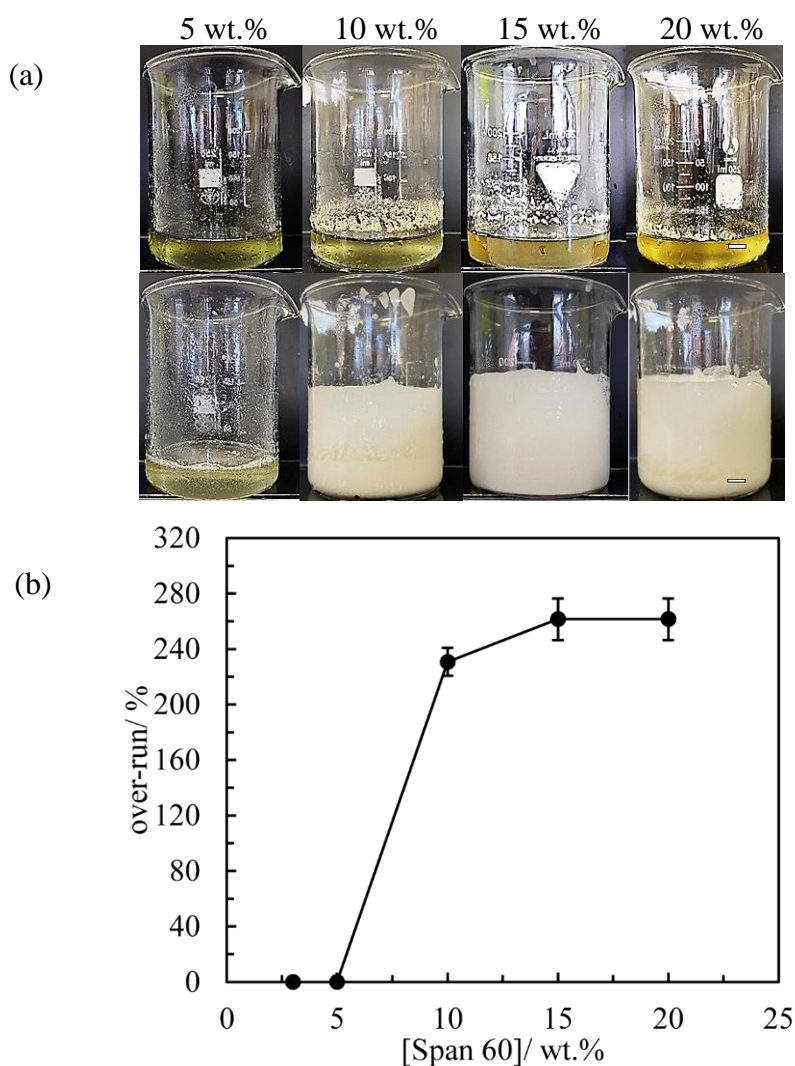
**Figure 5.17.** (a) Photo' of 5 wt.% Span 60 in RO at 20 °C cooled from 90 °C, scale bar = 1 cm. (b) Non-polarized (left) and polarized (right) micrographs of 5 wt.% Span 60 in RO at 20 °C, scale bars = 50  $\mu\text{m}$ . (c) Cryo-SEM images of surfactant crystals.



## 5.5 Whipping mixtures of sorbitan monostearate and oil

The foaming behaviour of Span 60-RO solutions/dispersions was studied as a function of surfactant concentration at 80 °C. Samples were heated to 90 °C and then cooled gradually in a water bath at 1 °C min<sup>-1</sup>. Once reaching 80 °C, the mixtures were whipped continuously using a single beater electric whisk for 10 min. Figure 5.18(a) shows the appearance for different concentrations of Span 60 in RO before and immediately after 10 min whipping at 80 °C. The samples at 80 °C before whipping are a clear solution. The foam volume increases progressively with surfactant concentration to a certain level. The over-run increases with surfactant concentration followed by almost levelling off, Figure 5.18(b). The highest volume fraction of incorporated air is 0.72.

**Figure 5.18.** (a) Appearance of RO containing different concentrations of Span 60 before (upper) and immediately after (lower) 10 min whipping at 80 °C cooled from 90 °C. Scale bars = 1 cm. (b) Variation of over-run with Span 60 concentration for systems in (a).



RO foams containing different concentrations of Span 60 prepared at 80 °C were subjected to rapid cooling followed by storing at 7 °C. Figure 5.19(a) and Figure 5.20(a) present the appearance of RO foams containing 10 wt.% and 15 wt.% Span 60 during cooling and subsequent storage at 7 °C, respectively. A limited extent of oil drainage and foam decay occurs on storage. The normalised volume of foam and drained oil against storage time is displayed in Figure 5.19(b) and Figure 5.20(b). The volume fraction of the remaining foam after 1 month aging relative to that initially is  $\sim 0.85$  for the former system whilst  $\sim 0.94$  for the latter one.

**Figure 5.19.** (a) Appearance of RO foam containing 10 wt.% Span 60 submitted to rapid cooling immediately after 10 min whipping. Foam prepared at 80 °C was cooled in an ice bath of -5 °C followed by storing at 7 °C. (b) Corresponding normalised volume of foam (●) and drained oil (○) and foam temperature (■) as a function of aging time. Inset: photo of the foam after 1 month storage. Scale bars = 1 cm.

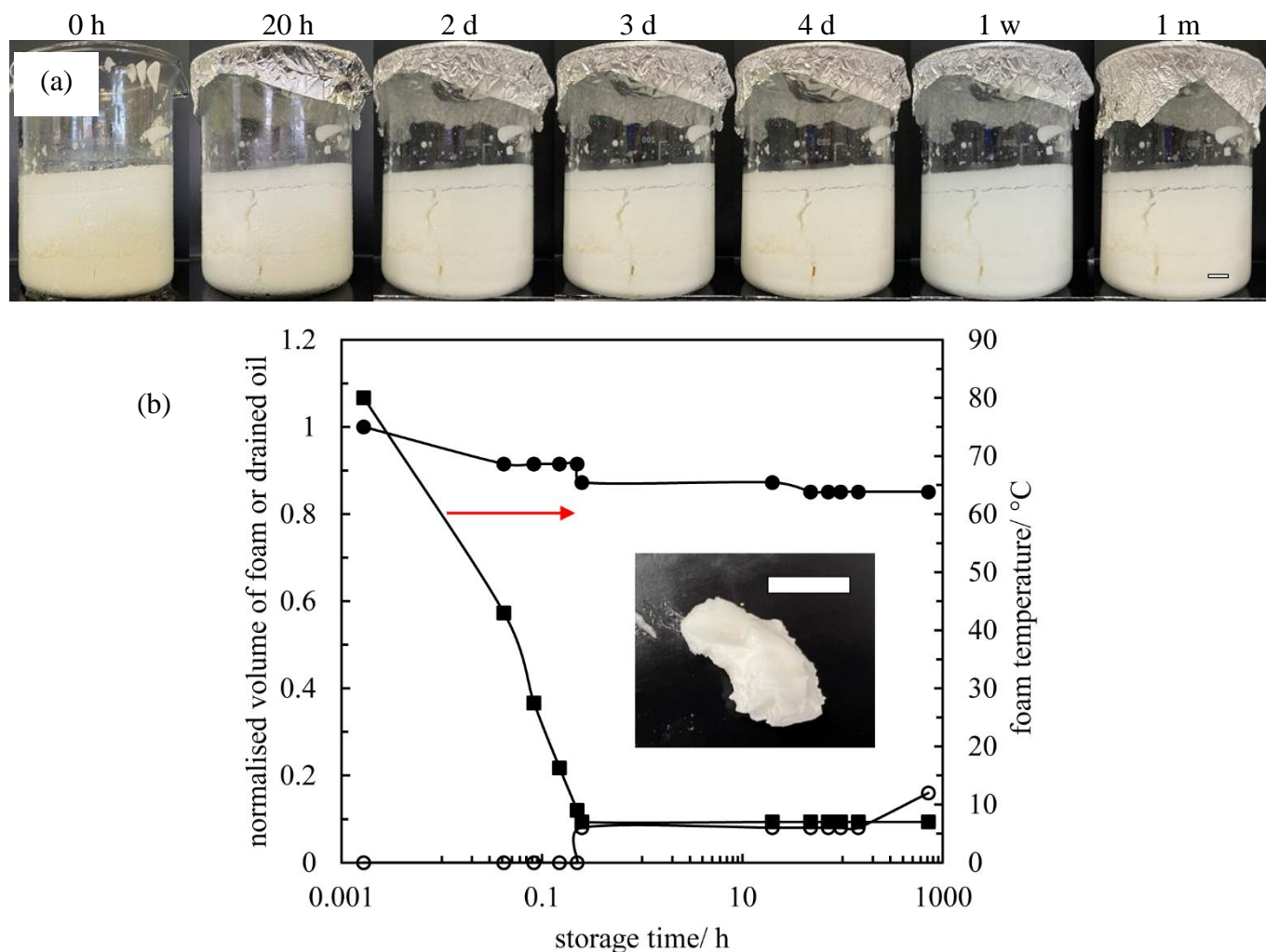
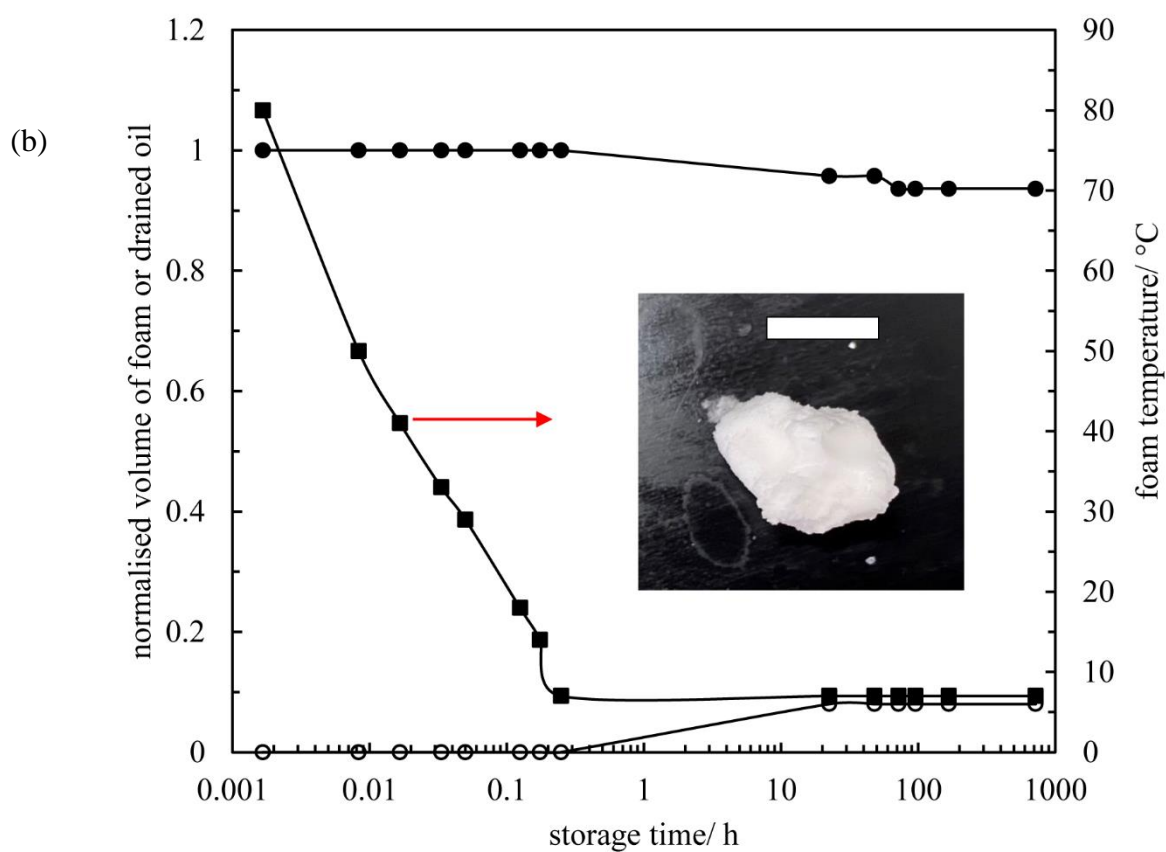
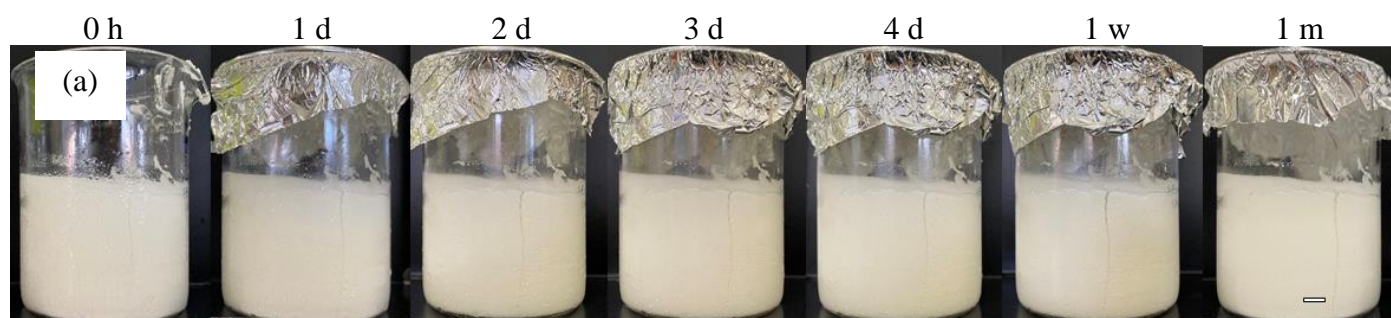
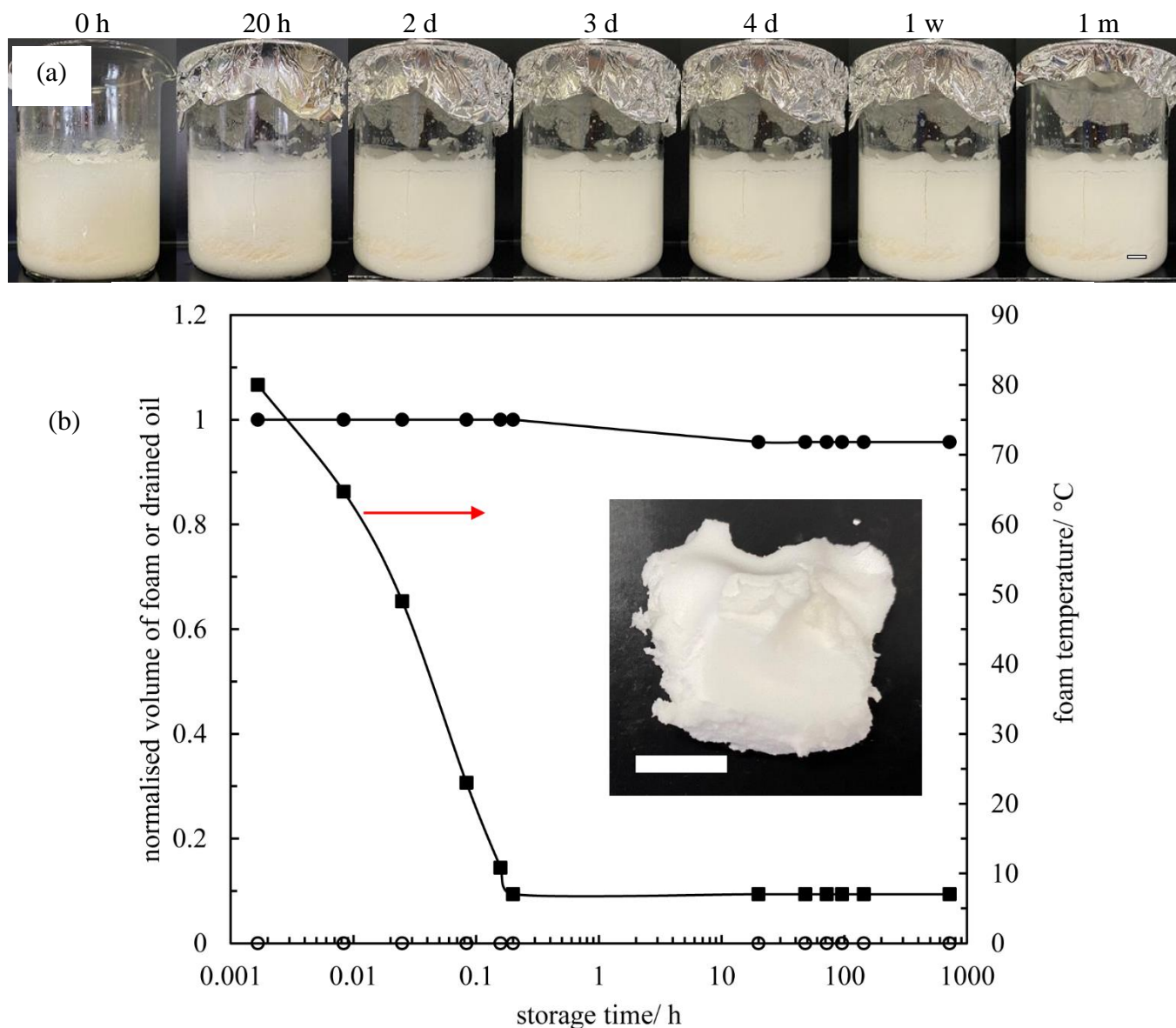


**Figure 5.20.** (a) Appearance of RO foam containing 15 wt.% Span 60 submitted to rapid cooling immediately after 10 min whipping. Foam prepared at 80 °C was cooled in an ice bath of -5 °C followed by storing at 7 °C. (b) Corresponding normalised volume of foam (●) and drained oil (○) and foam temperature (■) as a function of aging time. Inset: photo' of the foam after 1 month storage. Scale bars = 1 cm.



For the foam containing 20 wt.% Span 60 (Figure 5.21), the sample is ultra-stable devoid of drainage with  $\sim 96$  vol% foam remaining after 1 month aging at  $7^\circ\text{C}$ .

**Figure 5.21.** (a) Appearance of RO foam containing 20 wt.% Span 60 submitted to rapid cooling immediately after 10 min whipping. Foam prepared at  $80^\circ\text{C}$  was cooled in an ice bath of  $-5^\circ\text{C}$  followed by storing at  $7^\circ\text{C}$ . (b) Corresponding normalised volume of foam (●) and drained oil (○) and foam temperature (■) as a function of aging time. Inset: photo of the foam after 1 month storage. Scale bars = 1 cm.



The optical microscopy images of the foams containing different concentrations of Span 60 upon storage at 7 °C are given in Figure 5.22 – Figure 5.24. Non-spherical bubbles are enclosed by a compact crystal layer(s) characteristic of Pickering-type stabilisation.<sup>15</sup>

**Figure 5.22.** Optical microscopy images of RO foam containing 10 wt.% Span 60 for system in Figure 5.19 during storage at 7 °C. Scale bars = 50  $\mu\text{m}$ . Both non-polarized (left) and polarized (right) micrographs are presented for the last row.

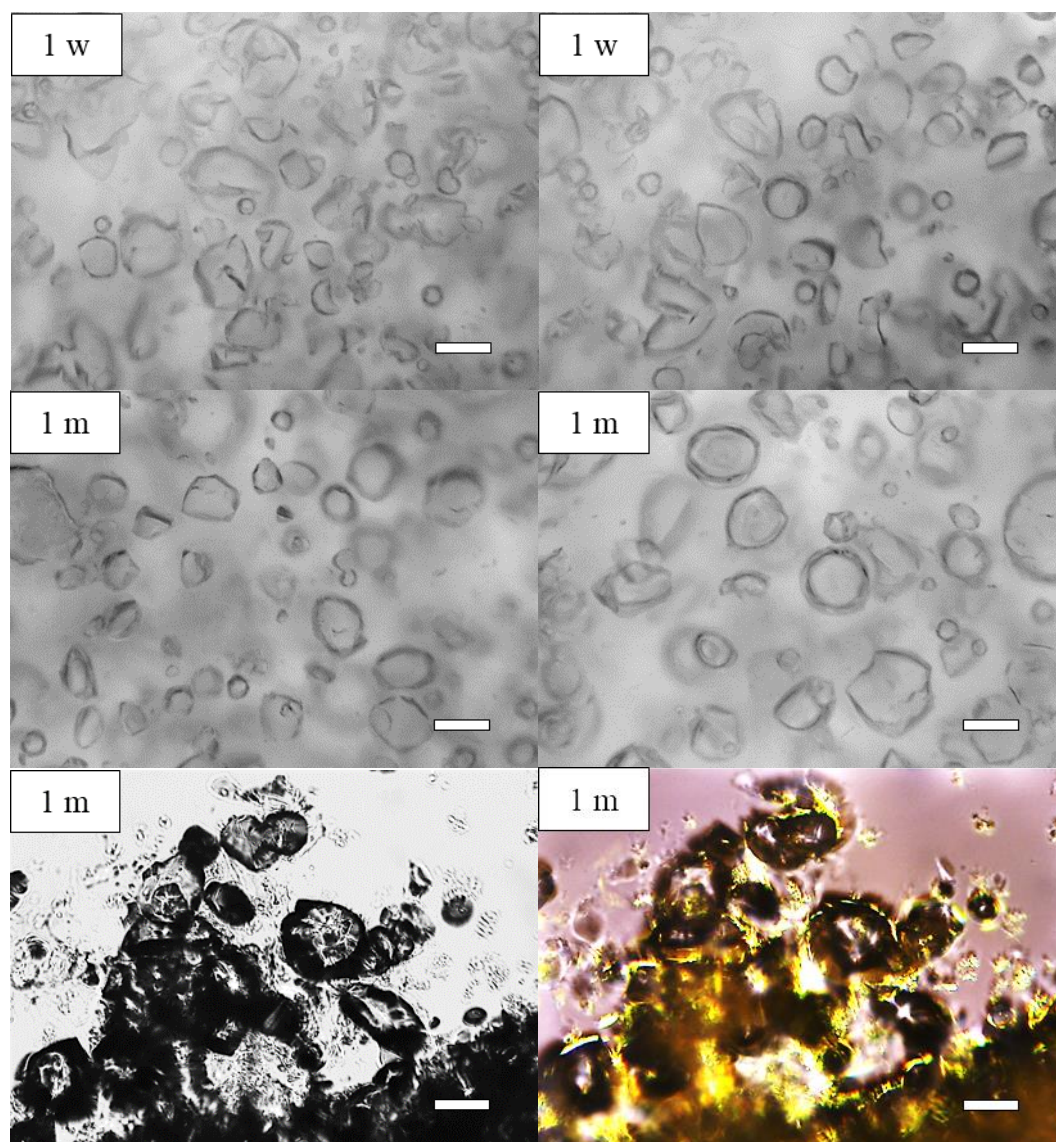


**Figure 5.23.** Optical microscopy images of RO foam containing 15 wt.% Span 60 for system in Figure 5.20 during storage at 7 °C. Scale bars = 50  $\mu\text{m}$ . Both non-polarized (left) and polarised (right) micrographs are presented for the last row.

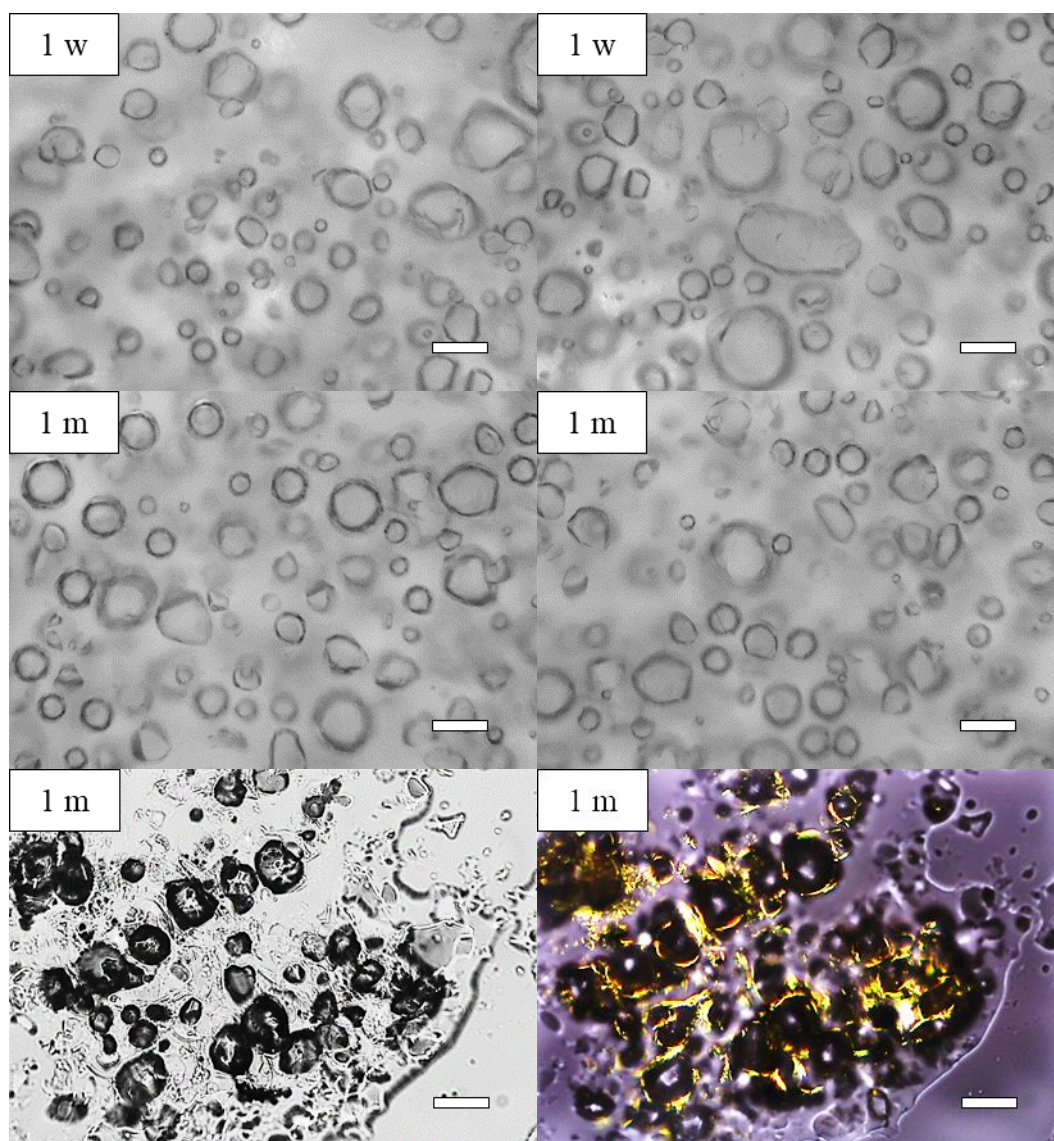
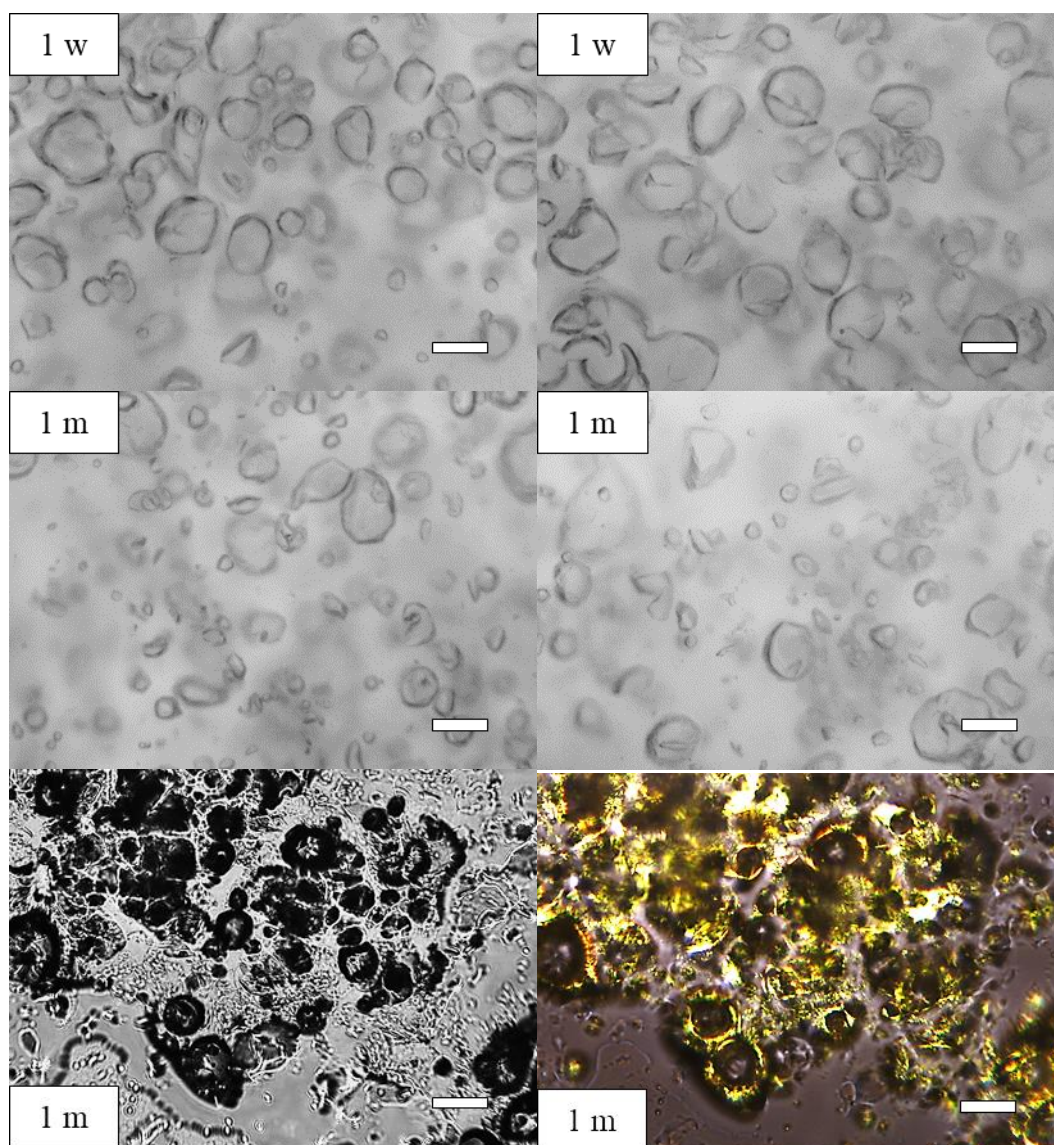
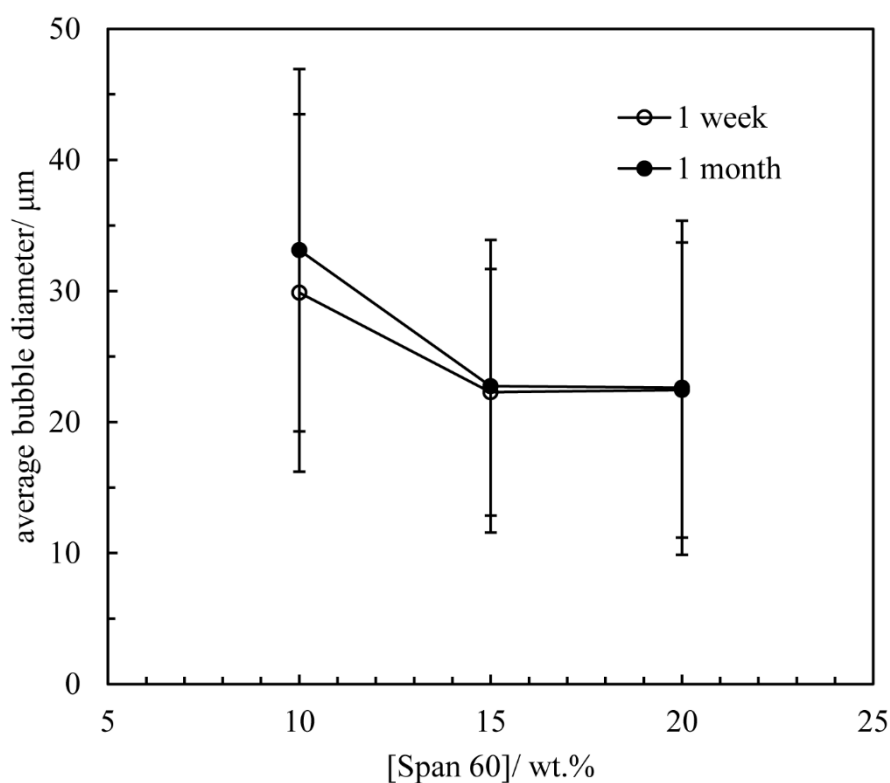


**Figure 5.24.** Optical microscopy images of RO foam containing 20 wt.% Span 60 for system in Figure 5.21 during storage at 7 °C. Scale bars = 50  $\mu\text{m}$ . Both non-polarized (left) and polarised (right) micrographs are presented for the last row.



The average bubble diameter of RO foams containing different concentrations of Span 60 during storage at 7 °C is presented in Figure 5.25. The average bubble diameter increases slightly on storage for the foam containing 10 wt.% Span 60 whereas that of the foam containing 15 wt.% or 20 wt.% Span 60 remains almost unchanged indicating the absence of coarsening/coalescence. Based on the above, we conclude that oil foams with long term stability which do not drain, coarsen or coalesce can be fabricated at high surfactant concentration at high temperature followed by rapid cooling to low storage temperature.

**Figure 5.25.** Average bubble diameter of RO foams as a function of Span 60 concentration after 1 week (○) and 1 month (●) storage at 7 °C. RO foams prepared at 80 °C were cooled rapidly in an ice bath of -5 °C followed by storing at 7 °C.



For certain surfactant concentrations, the cooled foams containing Span 60 at 7 °C are much more stable than those containing Span 80 stored at -5 °C. This contrast arises possibly from the difference in the degree of supercooling  $\Delta T$  between the two systems.  $\Delta T$  equals  $\sim 46$  °C for Span 60 significantly larger than that of  $\sim 6$  °C for Span 80. Firstly, larger  $\Delta T$  can induce faster kinetics of surfactant crystal formation,<sup>5</sup> thus arresting foam aging more effectively.<sup>16,17</sup> Secondly, more crystals can be formed for larger  $\Delta T$ , resulting in an increase in the volume fraction of crystals both at bubble surfaces and in bulk oil.<sup>18</sup>

When recalling the findings of Chapter 4, we find that compared with sucrose esters

the minimum surfactant concentration required for effective oil foaming is unambiguously higher for sorbitan esters. This is due to the fact that more free hydroxyl groups are available in sucrose ester molecules, which can form more H-bonds with carbonyl groups of TAG molecules in vegetable oil adsorbing readily at the air-oil interface upon whipping, thereby yielding foams more effectively.

## 5.6 Conclusions

Herein we apply the protocol developed in Chapter 4 to prepare stable edible oil foams of high air volume fraction from mixtures of vegetable oil and sorbitan esters. Whipping is first performed in the one-phase region followed by rapid cooling and then storing at low temperature. For sorbitan monostearate, the resulting foams containing many crystal-coated air bubbles are completely stable to drainage, coarsening or coalescence. In contrast, for sorbitan monooleate the obtained foams suffer a gradual decay but the residual fractions last for more than one month. This contrast is due mainly to the differences in the kinetics of surfactant crystal formation and the quantity of crystals formed during rapid cooling.

More work surrounding the dispersion and foaming characteristics of sorbitan esters in oil is underway: (a) cooling and warming mixtures of Spans and oil, (b) air-oil surface tensions and FTIR spectra of Span 60-oil mixtures in the one-phase and two-phase regions, (c) foams prepared and stored at the same temperature for Span 60-oil mixtures, (d) surfactant crystal structure and thermal properties of foams, (e) SFC of Spans-oil mixtures *versus* temperature.

## 5.7 References

1. Y. Liu and B.P. Binks, A novel strategy to fabricate stable oil foams with sucrose ester surfactant, *J. Colloid Interface Sci.*, 2021, **594**, 204–216.
2. S. Ghosh and D. Rousseau, Fat crystals and water-in-oil emulsion stability, *Curr. Opin. Colloid Interface Sci.*, 2011, **16**, 421–431.
3. T.F. Tadros, *Applied Surfactants: Principles and Applications*, Wiley-VCH, Weinheim, 2005, ch.1.
4. [https://www.chemicalbook.com/chemicalproductproperty\\_us\\_cb0419567.aspx](https://www.chemicalbook.com/chemicalproductproperty_us_cb0419567.aspx). Accessed 19 April 2021.
5. M.A. Rogers and A.G. Marangoni, Solvent-modulated nucleation and crystallization kinetics of 12-hydroxystearic acid: a nonisothermal approach, *Langmuir*, 2009, **25**, 8556–8566.
6. S.N. Sahasrabudhe, V. Rodriguez-Martinez, M. O'Meara, and B.E. Farkas, Density, viscosity, and surface tension of five vegetable oils at elevated temperatures: measurement and modelling, *Int. J. Food Prop.*, 2017, **20**, 1965–1981.
7. T. Xu, V. Rodriguez-Martinez, S.N. Sahasrabudhe, B.E. Farks and S.R. Dungan, Effects of temperature, time and composition on food oil surface tension, *Food Biophys.*, 2017, **12**, 88–96.
8. J. Bus, F. Groeneweg and F. van Voorst Vader, Effect of hydrogen bonding on water in oil emulsion properties, *Progr. Colloid Polym. Sci.*, 1990, **82**, 122–130.
9. X. Fu, W. Kong, Y. Zhang, L. Jiang, J. Wang and J. Lei, Novel solid–solid phase change materials with biodegradable trihydroxy surfactants for thermal energy storage, *RSC Adv.*, 2015, **5**, 68881.
10. C.H. Chen and E.M. Terentjev, Aging and metastability of monoglycerides in hydrophobic solutions, *Langmuir*, 2009, **25**, 6717–6724.
11. S. Ghosh, T. Tran and D. Rousseau, Comparison of Pickering and network stabilization in water-in-oil emulsions, *Langmuir*, 2011, **27**, 6589–6597.
12. F.R. Lupi, V. Mancina, N. Baldino, O.I. Parisi, L. Scrivano and D. Gabriele, Effect of the monostearate/monopalmitate ratio on the oral release of active agents from monoacylglycerol organogels, *Food Funct.*, 2018, **9**, 3278–3290.
13. F.R. Lupi, A. Shakeel, V. Greco, N. Baldino, V. Calabrò and D. Gabriele, Organogelation of extra virgin olive oil with fatty alcohols, glyceryl stearate and their mixture, *LWT - Food Sci. Technol.*, 2017, **77**, 422–429.

14. D. Fathalla, A. Abdel-Mageed, F. Abdel-Hamid and M. Ahmed, *In-vitro* and *in-vivo* evaluation of niosomal gel containing aceclofenac for sustained drug delivery, *Int. J. Pharm. Sci. Res.*, 2014, **1**, 105.
15. D.Z. Gunes, M. Murith, J. Godefroid, C. Pelloux, H. Deyber, O. Schafer and O. Breton, Oleofoams: properties of crystal-coated bubbles from whipped oleogels-evidence for Pickering stabilization, *Langmuir*, 2017, **33**, 1563–1575.
16. L. Ma, Q. Li, Z. Du, E. Su, X. Liu, Z. Wan and X. Yang, A natural supramolecular saponin hydrogelator for creation of ultrastable and thermostimulable food-grade foams, *Adv. Mater. Interfaces*, 2019, **6**, 1900417.
17. L. Zhang, A. Mikhailovskaya, P. Yazhgur, F. Muller, F. Cousin, D. Langevin, N. Wang and A. Salonen, Precipitating sodium dodecyl sulfate to create ultrastable and stimuable foams, *Angew. Chem. Int. Ed.*, 2015, **54**, 9533–9536.
18. B.P. Binks, E.J. Garvey and J. Vieira, Whipped oil stabilised by surfactant crystals, *Chem. Sci.*, 2016, **7**, 2621–2632.

## CHAPTER 6 – EFFECT OF HLB AND pH ON AQUEOUS DISPERSION AND FOAMING BEHAVIOUR OF SUCROSE ESTERS

### 6.1 Introduction

An aqueous foam is a dispersion of gas in water containing foaming agents, *e.g.* surfactants, polymers, or solid particles.<sup>1</sup> Foams are thermodynamically unstable colloidal systems, which tend to destabilize through drainage, coarsening or coalescence.<sup>1,2</sup> Drainage can be retarded by increasing the viscosity of the continuous phase,<sup>2-4</sup> and slowing down coarsening requires gas with lower diffusion coefficient or the bubble surface with higher compression elastic modulus.<sup>2,4</sup> Coalescence can be suppressed upon increasing the foam film thickness or interfacial elasticity.<sup>2,5</sup> Kinetically stable aqueous foams can be achieved using solid particles or crystalline particles, during which coarsening and coalescence can be hindered or arrested.<sup>6-11</sup> In these systems, small particles (nm to  $\mu\text{m}$ ) with appropriate wettability can irreversibly adsorb at the air-water surface under vigorous mechanical energy input, yielding a solid-like layer(s) of interfacial particles.<sup>12</sup> In specific cases, the formation of the rigid particle network throughout the foam lamella can arrest drainage.<sup>8</sup> The preparation of stable foams with particles however, is more difficult than that with common surfactants, *e.g.* sodium dodecyl sulfate (SDS), arising from comparatively high energy barriers to overcome during the adsorption of particles to the air-water interface.<sup>9</sup> Moreover, the relatively slow adsorption kinetics of particles tend to limit the foaming capacity.<sup>13</sup> A different scenario occurs for common surfactants, during which good foamability is more prone to be achieved but the resulting foam collapses within a day or so. Seeking an appropriate system whereby both good foamability and long-term stability can be yielded is still challenging.

As highlighted in chapter 1, the critical packing parameter (*CPP*) of a surfactant molecule can be used to predict potential self-assembled structures formed when dissolved in water.<sup>14</sup> Several recent studies have focused on the preparation of stable aqueous foams with low molecular weight (LMW) foaming agents that can form large self-assemblies, *e.g.* micron-sized tubes,<sup>13,15,16</sup> vesicles<sup>17-20</sup> and liquid crystalline phases.<sup>21,22</sup> Many of these systems were based on fatty acids or their derivatives.<sup>13,15,16,18-21</sup> Compared with foams formulated from solid particles, these systems possess better foamability and impressive foam stability. Fameau *et al.*<sup>13</sup> found that multilamellar tubes formed from 12-hydroxy stearic acid possessed the pros of both solid particles and LMW surfactants, whereby foams could be obtained easily, and the resulting foams lasted for several months. In another study, Varade *et al.*<sup>18</sup> investigated the foaming behavior of vesicle-forming systems made from mixtures of myristic acid, cetyl

trimethylammonium chloride and water. It was demonstrated that long-lived foams (up to weeks) with good foamability arose from a synergy of viscoelastic interfacial layers and thick liquid lamellas populated with vesicles. Based on the above studies, the morphology and size of surfactant self-assemblies significantly affect foaming properties.<sup>23</sup> Moreover, relatively bulky vesicles or lamellar phases are shown to be a more effective foam stabilizer than small spherical micelles.<sup>23</sup>

Sucrose esters (SE) are omnipresent in the areas of food, cosmetics and pharmaceuticals.<sup>24-26</sup> By now, few studies have been available regarding the physicochemical and functional properties of SE.<sup>27-34</sup> When relatively hydrophilic SE with different alkyl chains were dissolved into water, different structures of mesophases could be formed depending on *CPP*.<sup>30,31</sup> In addition, Zhang *et al.*<sup>34</sup> revealed that the alkyl chain length was the governing factor determining the foaming properties, rather than the degree of esterification. Up to now, there is still a lack of systematic studies focusing on the aqueous dispersion and foaming characteristics of SE with different hydrophobicity. Besides, the underlying interplay between them is still unclear.

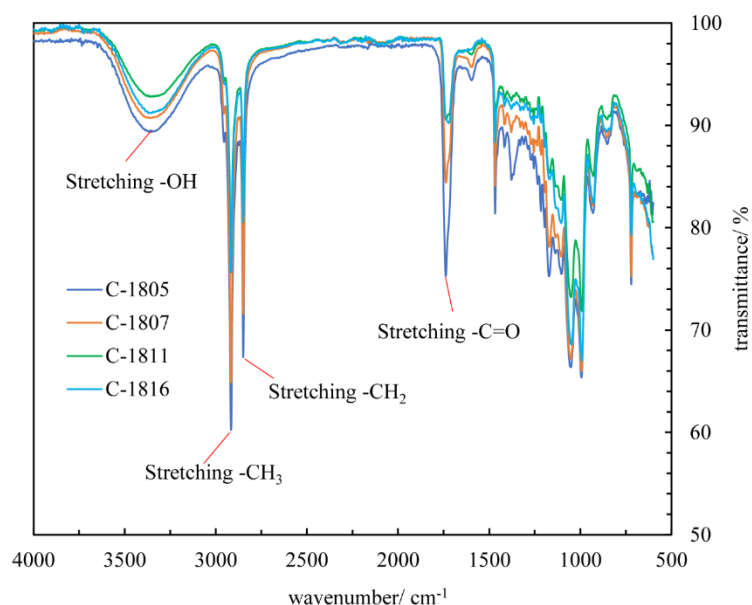
We report here how the physicochemical properties of mixtures of a series of SE and water are correlated to their foaming behaviour, including foamability, foam stability and foam microstructure. We select four commercial grade SE samples with varying HLB as foaming agents. First, the thermal behaviour, polymorphs and molecular interactions for neat SE are investigated. What follows is the characterisation of aqueous solutions/dispersions of SE, resorting to different techniques including DLS, optical microscopy, SEM, TEM, rheology, tensiometer and zeta potential. Subsequently, the influence of surfactant concentration and HLB on foaming properties are discussed. At last, the role of pH on the dispersion and foaming behaviour of the selected SE is elucidated.

## 6.2 Systems with sucrose esters of varying HLB

### 6.2.1 Dispersion behaviour of sucrose ester-water mixtures

The physicochemical properties of neat SE were investigated before being dissolved into water. The FTIR spectra of neat SE of four HLB values are shown in Figure 6.1. Their spectra are similar to each other, indicating comparable functional groups therein.<sup>35</sup> The peaks at  $\sim 3365\text{ cm}^{-1}$  represent hydrogen bonded  $\text{-OH}$  groups in the stretching mode.<sup>36</sup> The peaks at  $\sim 2916\text{ cm}^{-1}$  and  $\sim 2849\text{ cm}^{-1}$  represent  $\text{-CH}_3$  and  $\text{-CH}_2$  stretching vibrations, respectively.<sup>36</sup> The peaks at  $\sim 1738\text{ cm}^{-1}$  are attributed to stretching  $\text{C=O}$  groups.<sup>37,38</sup> Moreover, the transmittance intensities of several stretching peaks (*e.g.*  $\text{-CH}_3$  and  $\text{-CH}_2$ ) tend to strengthen as decreasing the HLB value. This trend is similar to that described by Youan *et al.*<sup>37</sup> Moreover, the representative functional groups determined here are the same as those reported by Youan *et al.*<sup>37</sup>

**Figure 6.1.** FTIR spectra of SE at room temperature.



The thermal profiles of neat SE were determined using DSC (Figure 6.2). The onset temperature of crystallisation on cooling increases as decreasing HLB. In addition, the temperature ranges over which melting and crystallisation occurs are gradually prolonged as lowering the HLB value, alongside a single prominent peak split into multiple smaller ones.<sup>39</sup> The broad and split melting peaks are indicative of multicomponent mixtures of sucrose esters. As stated in chapter 2, C-1811 and C-1816 are mainly composed of sucrose monoester, whilst the compositions of C-1805 and C-1807 are more complex containing sucrose mono-, di-, tri- and polyester.<sup>39</sup> So, it is reasonable to conclude that different ester compositions corresponding

to different HLB are responsible for the discrepancies in the thermal properties. For C-1805 and C-1807, the low-melting peaks reflect the melting of mono-, di- and triester, whilst the high-melting peaks represent the melting of polyester fractions, such as tetra- and pentaester.<sup>39</sup> The critical thermal parameters are summarised in Table 6.1.

**Figure 6.2.** Melting and cooling thermograms of SE. Temperature change rate was 5 °C min<sup>-1</sup>.

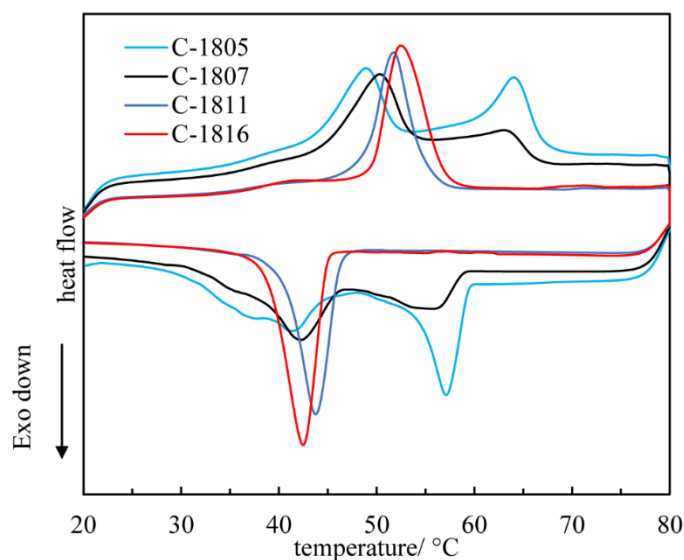


**Table 6.1.** Thermal properties of SE during (a) melting and (b) cooling. The samples are listed in increasing hydrophobicity.

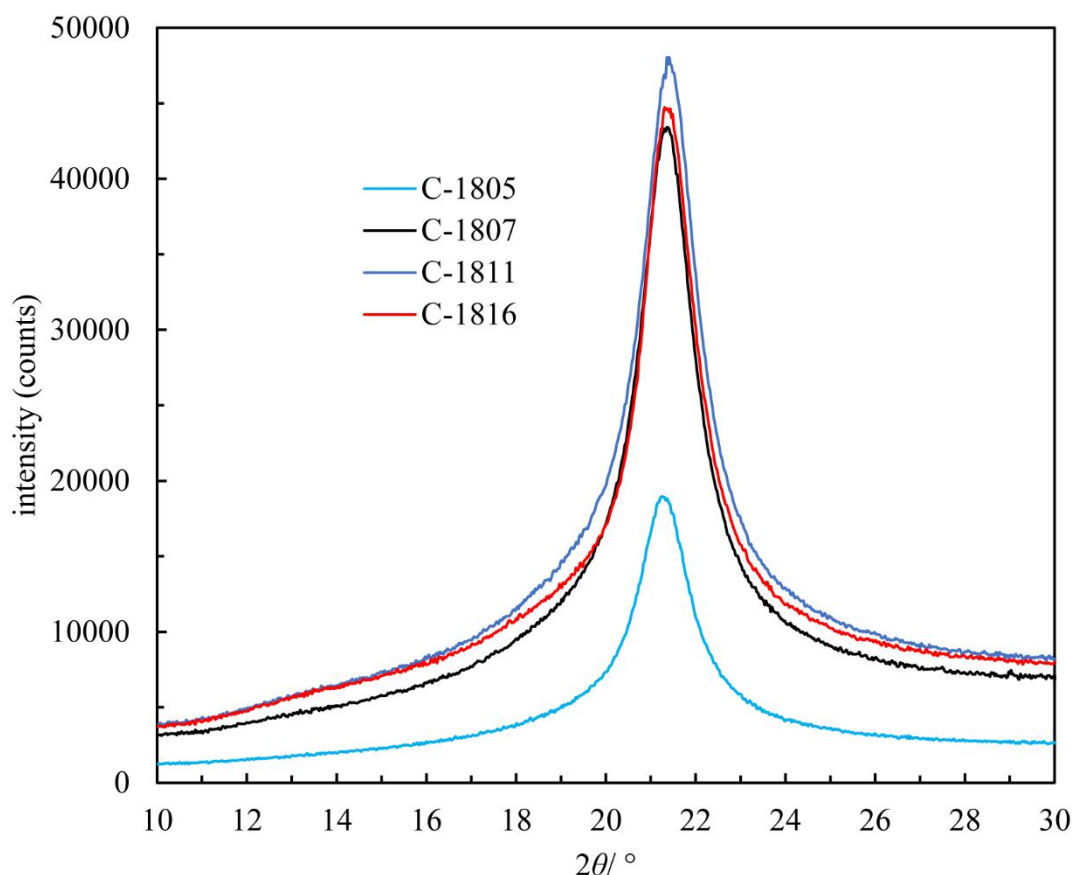
(a)	Name	$T_{\text{peak}}/\text{°C}$		$\Delta H/\text{J g}^{-1}$	
		Peak 1	Peak 2	Peak 1	Peak 2
	C-1816	$49.33 \pm 0.02$	N/A	$28.61 \pm 0.25$	N/A
	C-1811	$51.17 \pm 0.14$	N/A	$29.21 \pm 1.19$	N/A
	C-1807	$50.29 \pm 0.82$	$63.19 \pm 0.34$	$14.21 \pm 0.30$	$4.05 \pm 0.50$
	C-1805	$48.51 \pm 0.20$	$63.59 \pm 0.17$	$8.82 \pm 0.99$	$8.67 \pm 0.43$

(b)	Name	$T_{\text{peak}}/\text{°C}$		$\Delta H/\text{J g}^{-1}$	
		Peak 1	Peak 2	Peak 1	Peak 2
	C-1816	$43.18 \pm 0.02$	N/A	$-32.42 \pm 0.08$	N/A
	C-1811	$46.44 \pm 0.18$	N/A	$-30.45 \pm 0.38$	N/A
	C-1807	$42.52 \pm 0.16$	$56.19 \pm 0.59$	$-12.19 \pm 0.17$	$-6.56 \pm 0.58$
	C-1805	$41.58 \pm 0.13$	$57.75 \pm 0.11$	$-11.46 \pm 0.82$	$-11.14 \pm 0.06$

The wide angle X-ray scattering (WAXS) spectra of SE are shown in Figure 6.3. The short-spacing peaks are all centred around 0.42 nm, related to the hexagonal lateral packing of stearyl chains.<sup>40,41</sup>

**Figure 6.3.** Wide angle X-ray scattering (WAXS) region of SE at room temperature.



A mixture of SE and water was maintained at  $\sim 80\text{ }^{\circ}\text{C}$  under magnetic stirring (150 rpm) to render a homogeneous solution. Subsequently, the mixture was cooled to room temperature followed by aging overnight ( $\sim 12\text{ h}$ ) under gentle magnetic stirring (50 rpm). The photographs of representative aqueous solutions/dispersions of SE are shown in Figure 6.4(a). For 0.01 wt.%, the samples are a transparent liquid. Upon increasing the surfactant concentration to 0.1 wt.%, they are all bluish and turn hazier with decreasing HLB. In the case of 1 wt.%, they evolve gradually from a flowable, bluish liquid to a viscous, turbid dispersion with a decrease in HLB. An increase in turbidity implies the formation of larger aggregates in water. Besides, no visible sedimentation occurs after 6 month storage at room temperature, implying the inherent long term stability of these solutions/dispersions.

To quantify the aggregate size formed in an aqueous mixture, dynamic light scattering

(DLS) experiments were performed. The intensity size distribution and the average hydrodynamic diameter ( $d_H$ ) are presented in Figure 6.4(b) and Table 6.2, respectively. The DLS results for 0.01 wt.% and 1 wt.% SE in water show bimodal or multimodal size distribution, indicating the high polydispersity of aggregates formed. In addition, the major intensity peaks are shifted to a higher value, *i.e.* an increase in the aggregate size, upon increasing SE concentration at fixed HLB or decreasing HLB at fixed concentration, see Table 6.2. This correlates well with the macroscopic observations described above.

**Figure 6.4.** (a) Photos of aqueous solutions/dispersions of SE for given concentrations at room temperature. (i) C-1816, (ii) C-1811, (iii) C-1807 and (iv) C-1805. Scale bars = 1 cm. (b) Intensity size distribution for 0.01 wt.% (left) and 1 wt.% (right) SE in water at 20 °C determined by DLS.

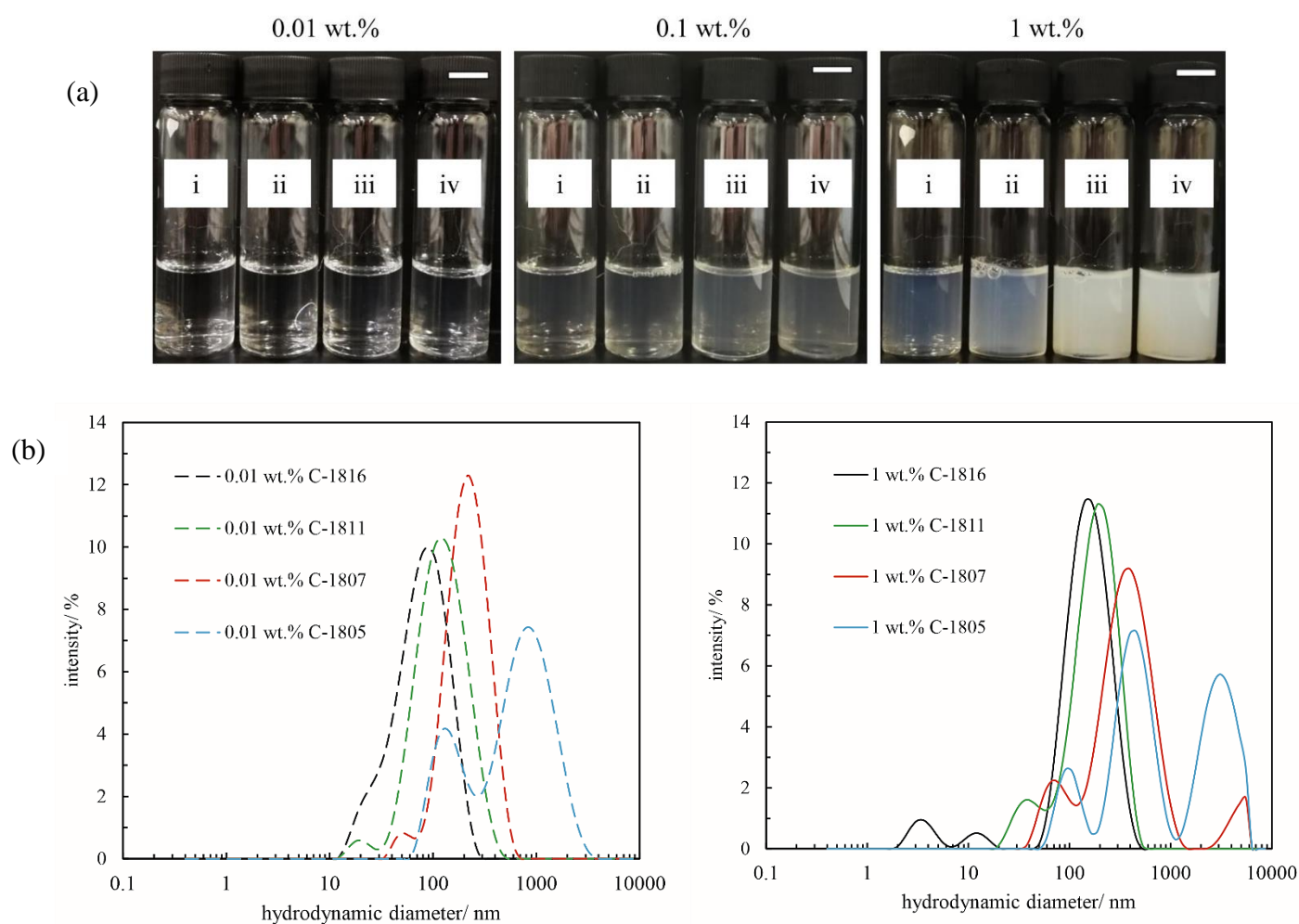
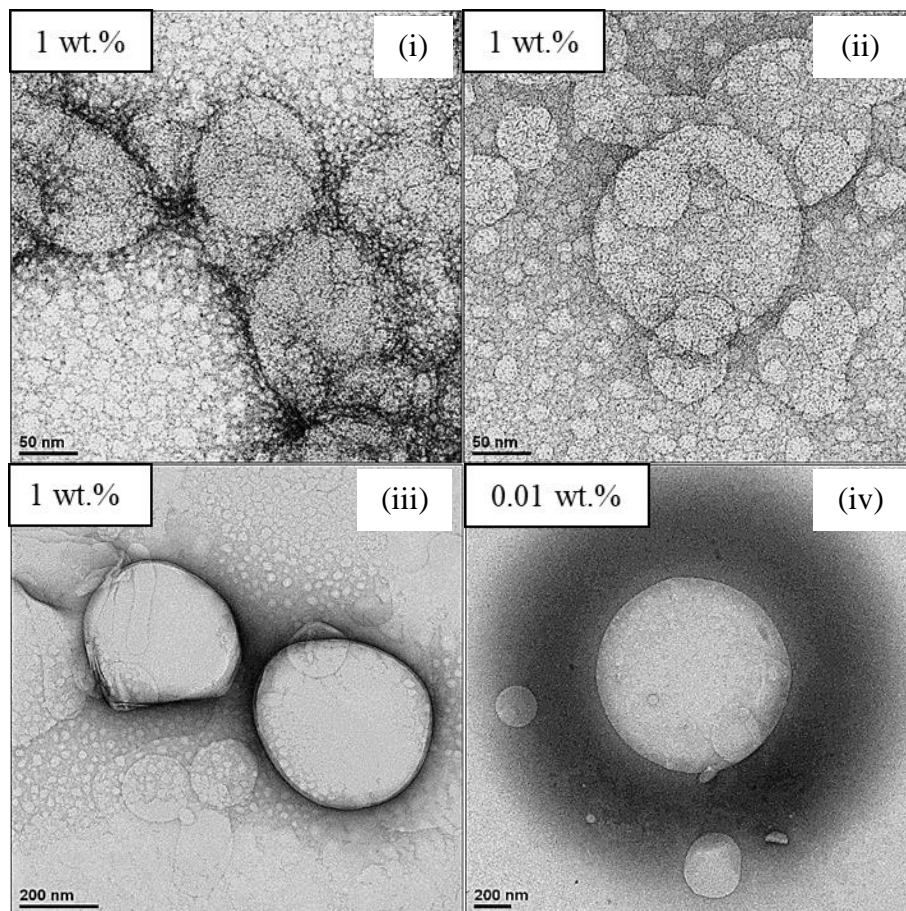


**Table 6.2.** Average hydrodynamic diameter ( $d_H$ ) of aggregates formed in aqueous solutions/dispersions of SE measured by DLS at 20 °C. The samples are listed in increasing hydrophobicity.

		Peak 1	Peak 2	Peak 3
[SE]/wt. %		$d_H/\text{nm}$	$d_H/\text{nm}$	$d_H/\text{nm}$
C-1816	0.01	$98 \pm 10$	$19 \pm 6$	N/A
	0.1	$132 \pm 4$	$15 \pm 5$	$4 \pm 0$
	0.4	$158 \pm 3$	$18 \pm 5$	$4 \pm 1$
	1	$167 \pm 3$	$19 \pm 10$	$4 \pm 1$
C-1811	0.01	$129 \pm 8$	$22 \pm 1$	N/A
	0.1	$131 \pm 4$	$22 \pm 4$	N/A
	0.4	$188 \pm 27$	$44 \pm 12$	N/A
	1	$229 \pm 14$	$41 \pm 11$	N/A
C-1807	0.01	N/A	$270 \pm 19$	$41 \pm 1$
	0.1	N/A	$284 \pm 27$	N/A
	0.4	$4381 \pm 384$	$267 \pm 20$	$46 \pm 2$
	1	$4709 \pm 540$	$500 \pm 162$	$57 \pm 20$
C-1805	0.01	N/A	$825 \pm 120$	$134 \pm 14$
	0.1	$3585 \pm 826$	$886 \pm 232$	$177 \pm 46$
	0.4	$4387 \pm 1145$	$1188 \pm 258$	$179 \pm 55$
	1	$4890 \pm 350$	$1211 \pm 814$	$199 \pm 77$

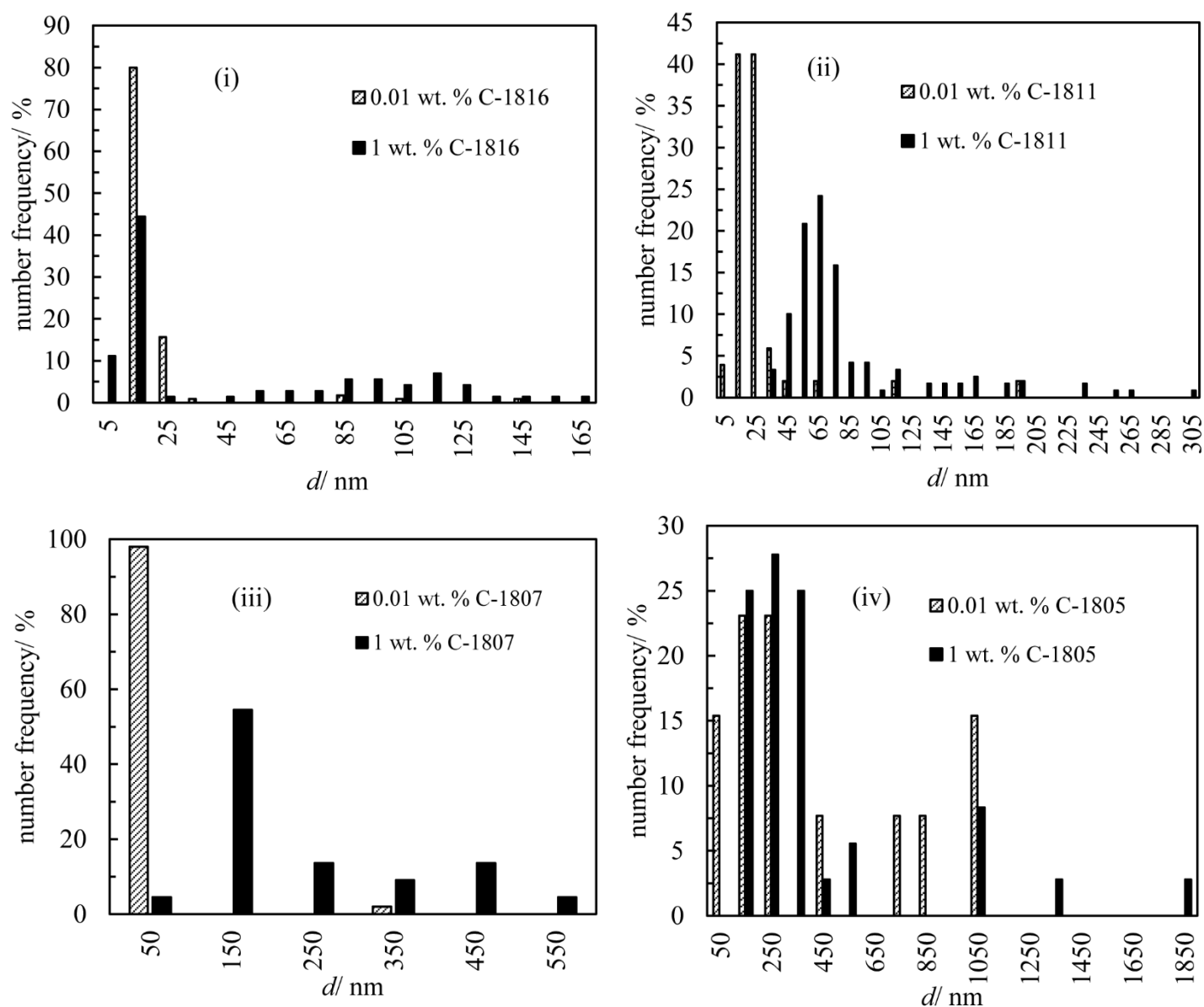
The size and morphology of SE aggregates in water were further studied by TEM. The TEM images in Figure 6.5 illustrate the formation of spherical vesicles for aqueous solutions/dispersions of SE. According to the literature, liposomes can be classified into several categories depending on the size and morphology, *i.e.* small unilamellar vesicles ( $\sim 20$  nm to  $\sim 200$  nm), large unilamellar vesicles ( $\sim 200$  nm to  $\sim 1000$  nm), and giant unilamellar, multilamellar, oligolamellar or multivesicular vesicles ( $> 1000$  nm).<sup>42</sup>

**Figure 6.5.** TEM images of aqueous solutions/dispersions of SE. (i) 1 wt.% C-1816, (ii) 1 wt.% C-1811, (iii) 1 wt.% C-1807 and (iv) 0.01 wt.% C-1805.



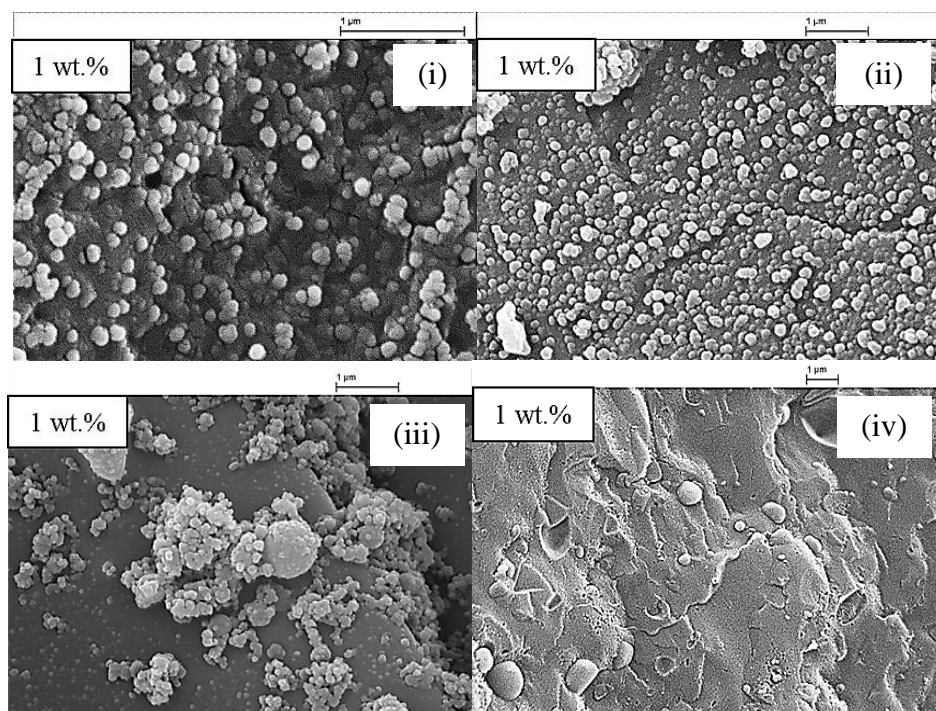
The size distribution of aggregates based on TEM images of 0.01 and 1 wt.% SE in water is shown in Figure 6.6. For C-1816, the diameter of one group centres around 5 nm, implying the existence of spherical micelles. Besides, the diameters of other groups vary between 15-165 nm, characteristics of small unilamellar vesicles. In the case of C-1811, the coexistence of micelles and small unilamellar vesicles is confirmed as well. Moreover, the diameter of 200-305 nm indicates the presence of large unilamellar vesicles. Mixtures of small and large unilamellar vesicles are identified for aqueous C-1807 dispersions, the diameters of which locate within 50-650 nm. The diameters of C-1805-water mixtures span over 50-1850 nm, signifying the mixtures of small unilamellar, large unilamellar, giant unilamellar or multilamellar vesicles. We find that the aggregate size obtained from TEM images is smaller compared to that determined by DLS. This is because DLS determines the hydrodynamic diameters of the dispersed particles whereas TEM presents the projected surface area based on the intensities of incident electrons transmitted through the particles.<sup>43</sup>

**Figure 6.6.** Size distribution of aggregates formed in aqueous solutions/dispersions of SE for systems in Figure 6.5. (i) C-1816, (ii) C-1811, (iii) C-1807 and (iv) C-1805.



From the cryo-SEM images in Figure 6.7, many spherical vesicles can be identified. However, the determination of the vesicle size was not possible except for C-1805 since the vesicles are highly aggregated during which the edge of each vesicle could not be distinguished unambiguously. The change in the aggregate size as a function of HLB for certain concentration can be interpreted based on the model of the critical packing parameter (*CPP*). SE are a mixture of sucrose mono-, di-, tri- and polyesters. Upon decreasing HLB, the fractions of di-, tri- or polyesters increase,  $\frac{V}{a_0}$  and *CPP* tend to increase, thereby favouring larger aggregates with a lower mean spontaneous curvature.<sup>14</sup>

**Figure 6.7.** Cryo-SEM images of aqueous solutions/dispersions of 1 wt.% SE. (i) C-1816, (ii) C-1811, (iii) C-1807 and (iv) C-1805.

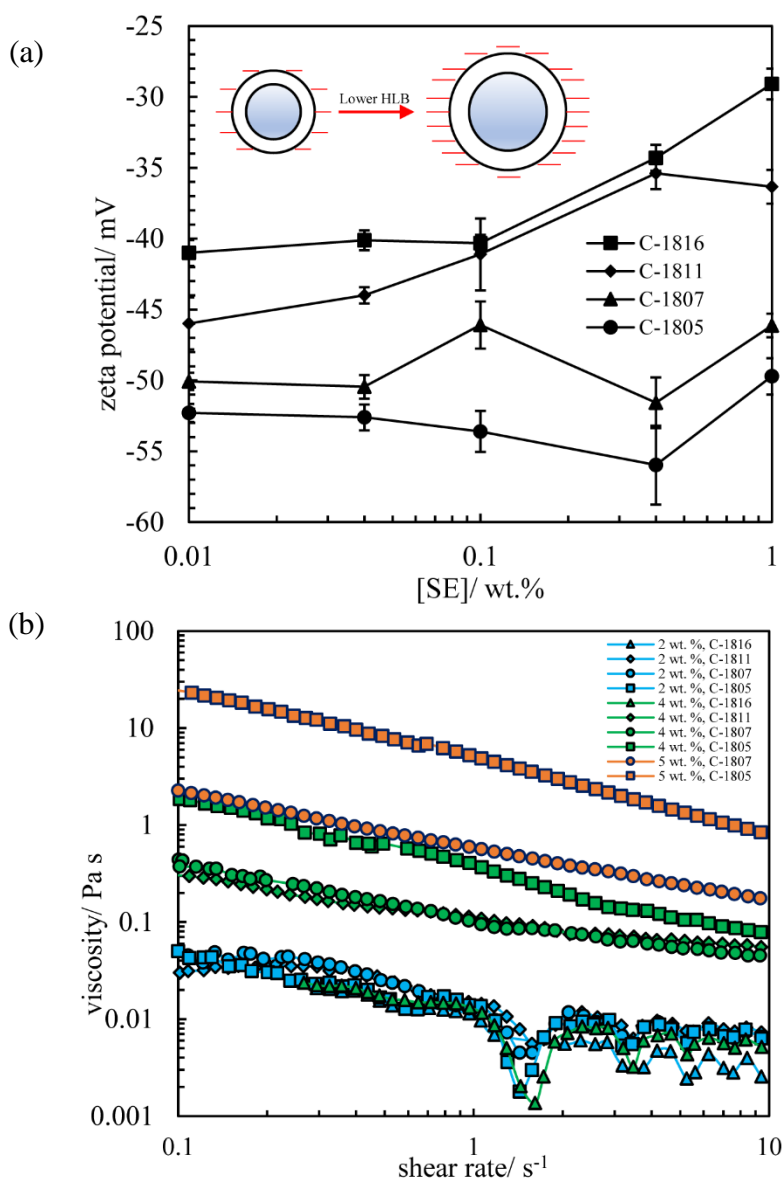


The zeta potentials of aqueous solutions/dispersions of SE at 20 °C are shown in Figure 6.8(a). Despite the nonionic nature of these surfactants, the values of zeta potentials are negative, possibly arising from fatty acid residues during surfactant synthesis.<sup>19,44,45</sup> Free fatty acid molecules became ionized as pH was increased above its  $pK_a$  value.<sup>19,44,45</sup> An increase in the magnitude of the zeta potential can be observed upon lowering HLB at fixed SE concentration, indicating that more deprotonated fatty acid molecules ( $R-COO^-$ ) are present. The schematic illustrating the charged state near the vesicle surface is given in Figure 6.8 as inset. For certain surfactant concentrations, vesicles of low-HLB SE are more negatively charged, thereby electrostatic repulsive forces between adjacent vesicles are stronger ultimately rendering more stable colloidal dispersions according to the DLVO theory.

The rheological properties of aqueous solutions/dispersions of SE are shown in Figure 6.8(b). All samples exhibit shear-thinning behaviour, characteristic of a non-Newtonian liquid. When the shear rate was fixed (*viz.*  $0.5 \text{ s}^{-1}$ ), the shear viscosity remains almost unchanged regardless of HLB for a concentration of 2 wt.% and below. In contrast, for 4 wt.% and above the viscosity increases gradually upon lowering HLB. The shear viscosity depends on concentration as well, and it increases with surfactant concentration except for C-1816. Panizza *et al.*<sup>46</sup> concluded that the viscoelasticity of a vesicle-forming dispersion had two contributions: fluid flow between neighbouring vesicles and flow within a single vesicle itself. The first

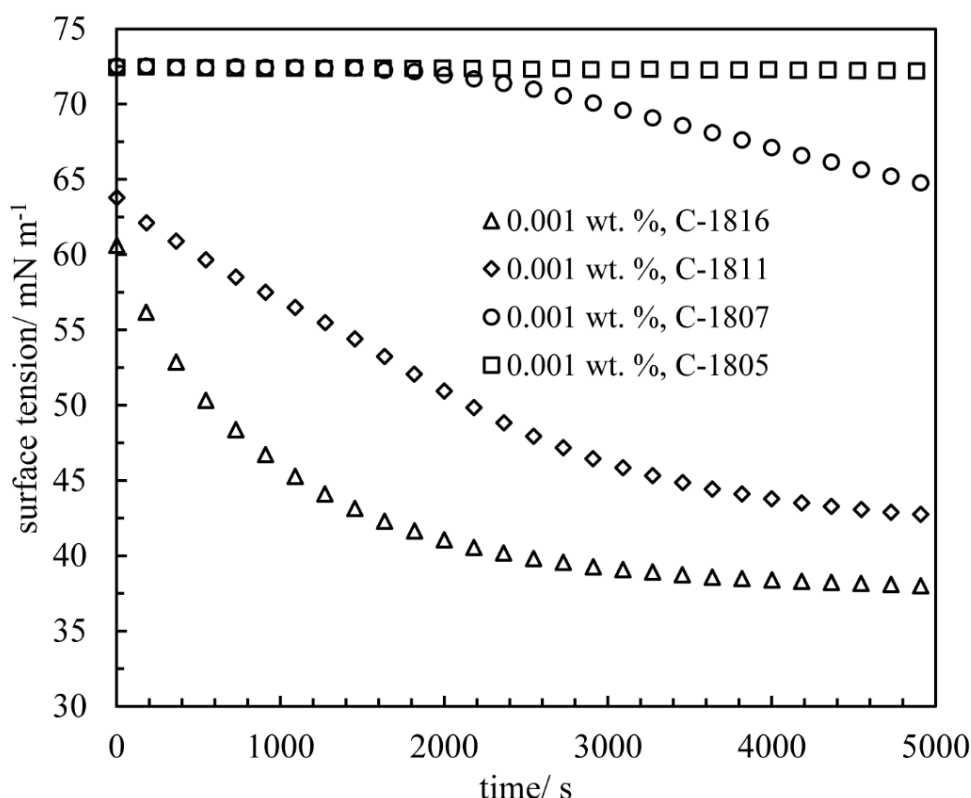
viscosity contribution originated from concentrated shear gradients within the thin solvent lamella between neighbouring vesicles, which could be described as  $\eta_1 \approx \eta_s \frac{r}{h}$ , where  $\eta_s$  is the solvent viscosity,  $r$  is the vesicle radius and  $h$  is the distance between adjacent vesicles. The second contribution arose from the geometry deformation within an individual vesicle, *i.e.*  $\eta_2 \approx \eta_s \left(\frac{r}{h}\right)^x$ ,  $x$  being dependent on the magnitude of  $\eta_1$  compared to that of the measured viscosity and the value of  $r/h$  (normally  $\geq 2$ ). Based on this, it is plausible to conclude that an increase in the viscosity of aqueous solutions/dispersions of SE through either decreasing HLB or increasing surfactant concentration is due to an increase in the value of  $r/h$ .

**Figure 6.8.** (a) Zeta potential and (b) shear viscosity of aqueous solutions/dispersions of SE at 20 °C. Inset: schematic of the charged state near vesicle surface on lowering HLB.



The dynamic surface behaviour of surfactants is an important implication of the potential foaming capacity.<sup>18</sup> The dynamic surface tension curves of SE in Figure 6.9 reveal that the adsorption kinetics of surfactant molecules towards the air-water surface is slower for low HLB. In addition, the final surface tension tends to increase with decreasing HLB.

**Figure 6.9.** Surface tension of aqueous solutions/dispersions of 0.001 wt.% SE as a function of measuring time at 20 °C.



Launois-Surpasl *et al.*<sup>47</sup> put forward a simple theoretical approach to describe the kinetics of surfactant film formation at the interface from liposomes suspensions by two processes: irreversible diffusion of vesicles and subsequent transformation of closed vesicles into destroyed ones. The latter process was much faster than the former one and the overall speed of interfacial film formation was controlled by the slower process, *i.e.* diffusion. For comparatively low concentrations, diffusion control is applicable,

$$n^*(t) = 2c_0 \sqrt{\frac{D}{\pi}} t^{1/2} \quad (6.1)$$

$$D = \frac{\kappa_B T}{6\pi\eta r} \quad (6.2)$$

where  $n^*(t)$  is the number of liposomes near a unit area of subsurface at time  $t$ ,  $r$  is the liposome radius,  $\eta$  is the viscosity of the continuous phase,  $T$  is the absolute temperature,  $\kappa_B$  is

the Boltzmann constant,  $c_0$  is the initial liposome concentration in the bulk phase and  $D$  is the diffusion coefficient. The higher the value of  $n^*(t)$ , the quicker the adsorption of surfactant molecules to the interface. Upon decreasing HLB at fixed concentration, the aggregate size increases and then the diffusion coefficient  $D$  becomes smaller, thereby leading to slower adsorption kinetics to the air-water surface. This prediction correlates well with our observations.

Based on the dynamic surface tension data, we note that the surface tensions for some low concentrations, *e.g.* 0.001 wt.%, do not reach an equilibrium state within the investigated time scale (*i.e.* 5 h). This arises possibly from slow diffusion kinetics.<sup>18</sup> Considering this, the critical aggregation concentration ( $c_{ac}$ ) of SE in water was derived from the break point of the curve of surface tension against concentration;  $\gamma_{cac}$  was defined as the value of surface tension at  $c_{ac}$ . Figure 6.10 presents the variation of surface tension with surfactant concentration at 20 °C for different HLB. As expected, the air-water surface tension decreases gradually reaching an almost constant value with surfactant concentration. The  $c_{ac}$  and  $\gamma_{cac}$  values of SE in water are summarized in Table 6.3. The  $c_{ac}$  values increase in the sequence 0.0007 wt.% < 0.002 wt.% < 0.008 wt.% < 0.01 wt.%, corresponding to C-1816, C-1811, C-1807 and C-1805, respectively. On the other hand, the  $\gamma_{cac}$  values increase gradually (38.1 mN m<sup>-1</sup> < 39.7 mN m<sup>-1</sup> < 43.5 mN m<sup>-1</sup> < 46.0 mN m<sup>-1</sup>). The surface area occupied per SE molecule near the  $c_{ac}$  is unavailable through the Gibbs adsorption equation however, since some of the surface tensions below  $c_{ac}$  did not reach an equilibrium state.

According to the literature, the surface properties are closely linked to the inherent architecture of surfactant molecules,<sup>29</sup> the ionization state of minor fatty acid impurities and the non-covalent forces between different molecular species, *e.g.* electrostatic repulsive forces and H-bonding.<sup>48,49</sup> Regarding the former case, Li *et al.*<sup>29</sup> concluded that more hydrophobic SE molecules were prone to adopt a more bulky, three-dimensional (3D) geometry at the interface, thus reducing the number density of interfacial adsorbed molecules. For the latter one, H-bonding formed between protonated fatty acid molecules (R-COOH) and SE molecules could yield a denser surfactant monolayer at the interface. By contrast, electrostatic repulsions between deprotonated fatty acid molecules (R-COO<sup>-</sup>) led to a looser packing in the surfactant monolayer.<sup>48,49</sup> In our systems, we propose that nonionic SE molecules, protonated and deprotonated fatty acid molecules are all present at the interface (see Figure 6.20(c) inset later), and the synergistic adsorption behavior therein controls the interfacial properties. When the HLB of SE decreases, more deprotonated fatty acid molecules are present at the interface, resulting in a looser packing of surfactant molecules at the interface. Besides, the packing

density of surfactant molecules at the air-water interface is further reduced due to the presence of a higher fraction of relatively bulky sucrose di-, tri- and polyesters. To conclude, low-HLB SE have poor surface activity.

**Figure 6.10.** Surface tension of aqueous solutions/dispersions of SE as a function of [SE] at 20 °C. Open points: non-equilibrium values; filled points: equilibrium values. Arrows denote the cac. Equilibrating time is 18,000 s.

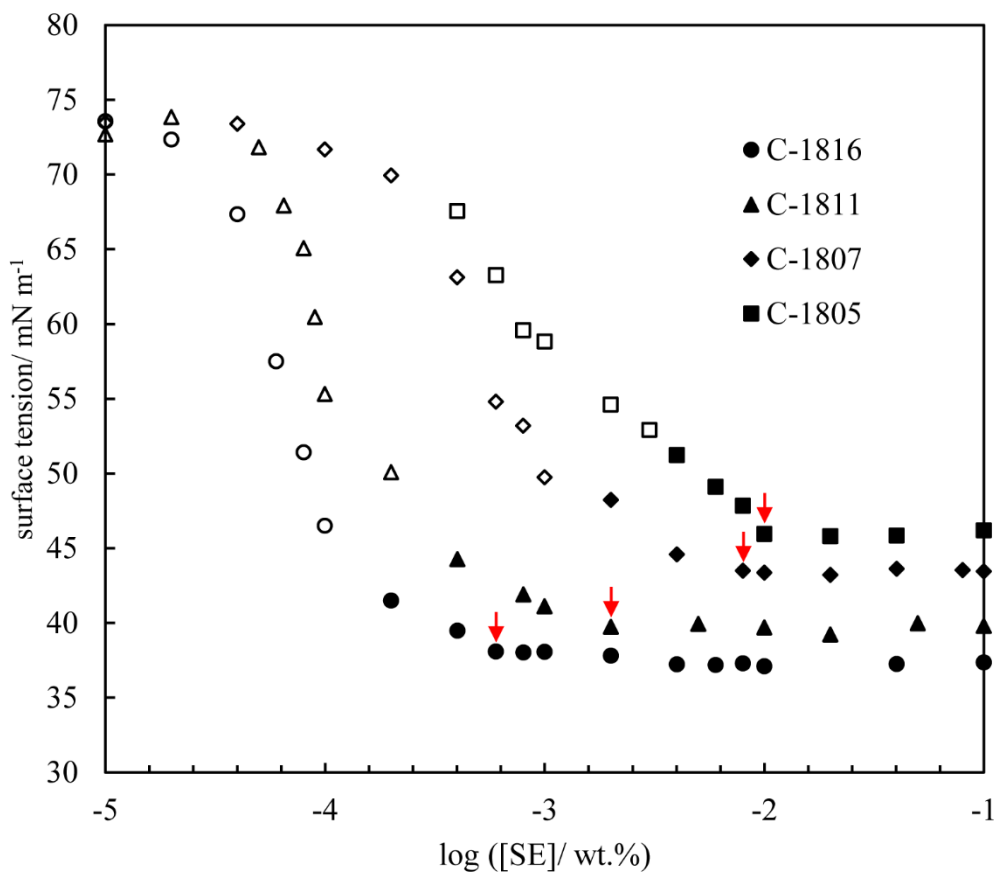


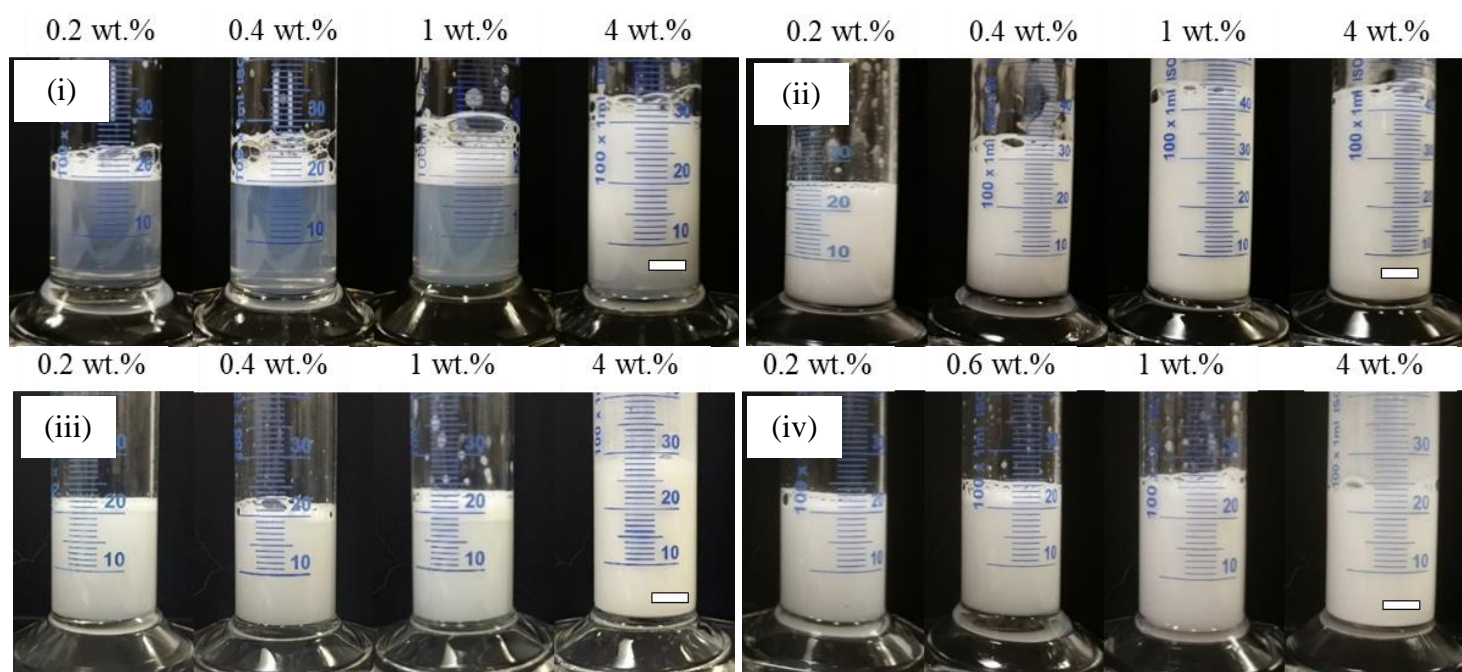
**Table 6.3.** cac and  $\gamma_{\text{cac}}$  values of SE in water at 20 °C.  $\gamma_{\text{cac}}$  is the value of surface tension at cac. Tests were conducted in triplicate.

SE	cac / wt.%	$\gamma_{\text{cac}}$ / mN m <sup>-1</sup>
C-1816	$(7.0 \pm 1.0) \times 10^{-4}$	$38.1 \pm 0.2$
C-1811	$2.0 \times 10^{-3} \pm 5.0 \times 10^{-4}$	$39.7 \pm 0.2$
C-1807	$8.0 \times 10^{-3} \pm 1.0 \times 10^{-4}$	$43.5 \pm 0.2$
C-1805	$1.0 \times 10^{-2} \pm 2.0 \times 10^{-3}$	$46.0 \pm 0.2$

### 6.2.2 Foaming behaviour of sucrose ester-water mixtures

20 mL of aqueous solutions/dispersions of SE were submitted to 60 s handshaking and then stored at room temperature. The sample appearance soon after aeration is shown in Figure 6.11. All fresh foams are a creamy fluid. Increasing the surfactant concentration results in an increase in the total volume ( $V_{\text{air+liquid}}$ ) up to a certain limit for all HLB. Moreover, the freshly aerated samples transit gradually from a foam with relatively high air fraction to a bubbly liquid with comparatively low air fraction, upon reaching a certain concentration except for C-1816 (Figure 6.12 inset). The reason for this is that it is difficult to incorporate air bubbles into a viscous liquid matrix.

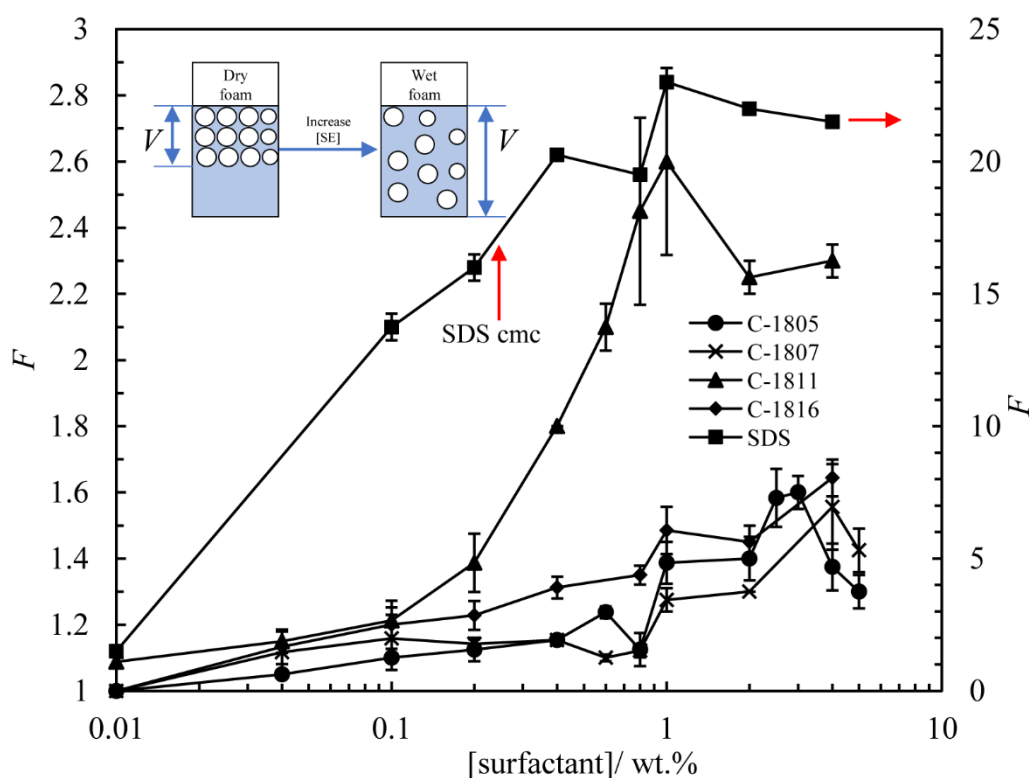
**Figure 6.11.** Photos of vessels containing aqueous solutions/dispersions of SE for given concentrations soon after 60 s hand shaking at room temperature. (i) C-1816, (ii) C-1811, (iii) C-1807 and (iv) C-1805.



To describe the foamability,  $F$  defined as the volume ratio of fresh sample ( $V_{\text{air+liquid}}$ ) relative to that before aeration ( $V_{\text{liquid}}$ ), is plotted in Figure 6.12 as a function of surfactant concentration for different HLB. The foaming behaviour of SDS solutions/dispersions is included for comparison. The critical micelle concentration,  $\text{cmc}$ , of SDS is  $\sim 0.23$  wt.% and its mixture with water is a clear liquid at room temperature.<sup>17</sup> The macroscopic appearance of fresh SDS foams is a dry skeleton composed of polygonal bubbles with diameters up to several cm (not shown). The foamability index  $F$  of SDS increases with surfactant concentration up to  $\sim 1$  wt.% and then almost levels off.<sup>17</sup> In the case of SE, nearly no foam can be obtained below

capacity due to the lower monomer concentration compared to that of SDS. When the surfactant concentration is well above  $cac$ ,  $F$  increases initially followed by a marked drop except for C-1816 during which a continuous increase in  $F$  against concentration can be observed. The downward foaming capacity above a certain concentration is attributed to too high liquid viscosity hindering effective air incorporation.

**Figure 6.12.** Foamability index  $F$  as a function of surfactant concentration for systems in Figure 6.11. Inset: schematic of the transition from dry foam to wet foam with increasing concentration.  $V$  refers to foam volume. Foamability of SDS is included for comparison.

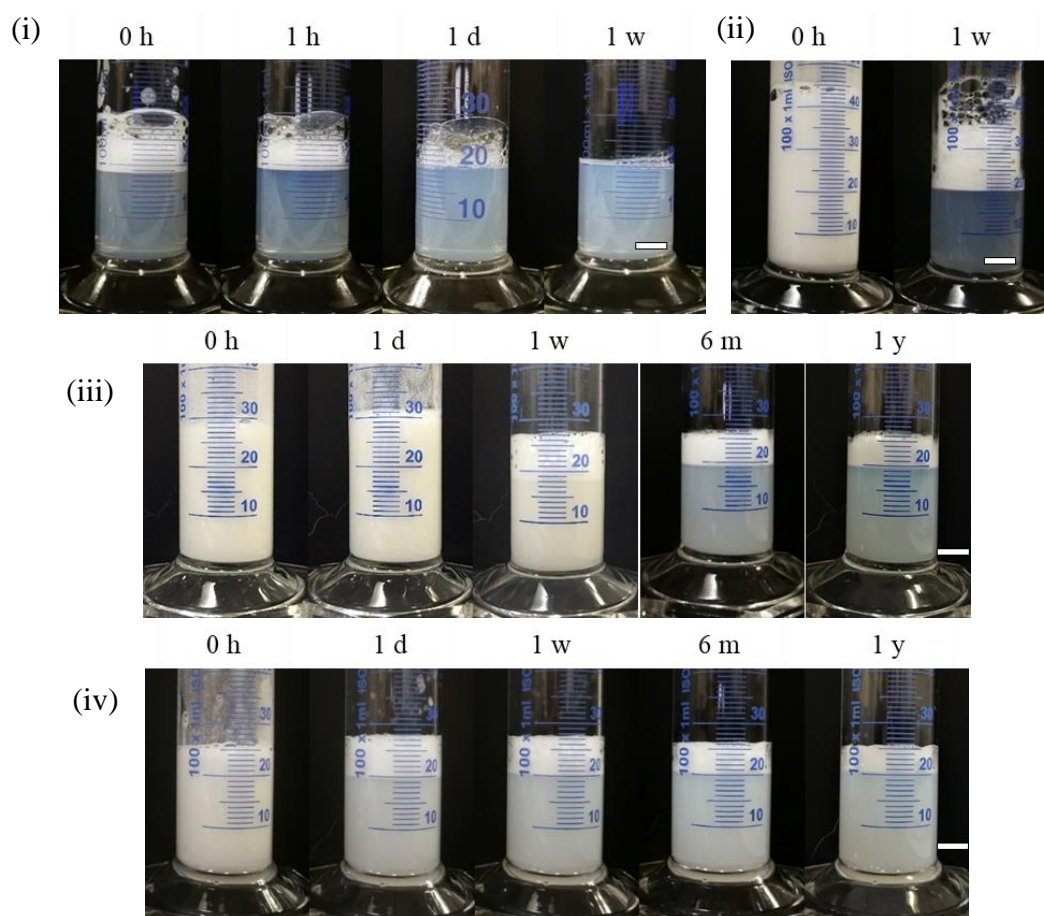


Amidst the investigated SE, C-1811 stands out exhibiting the best foaming capacity. In order to yield good foamability, two criteria should be fulfilled during aeration: (i) rapid adsorption kinetics of foaming agents to the air-water interface; (ii) suppression of different destabilisation processes within a short timescale (typically less than seconds).<sup>23</sup> As described earlier, the adsorption kinetics of SE molecules to the air-water interface increase in the order  $C-1805 < C-1807 < C-1811 < C-1816$ . Conversely, the aggregate size, the magnitude of the zeta potential and the viscosity of the continuous phase decrease following the same order for certain surfactant concentration so drainage, coalescence and coarsening are more likely to occur during foaming. Taken together, we surmise that the optimum foamability for C-1811 originates from reasonably high surface activity alongside limited aging. It demonstrates that

foamability is not only affected by surface activity, but also the bulk characteristics. Besides, the foamability of vesicle-forming SE dispersions is significantly lower in comparison to that of micelle-forming SDS solutions ( $p < 0.05$ ). The former system witnesses relatively slow transport of surfactant molecules towards the air-water interface, corresponding to a low level of dynamic adsorption at the interface thereby yielding low foamability.<sup>50</sup>

The foam stability was recorded as a function of storage time photographically and using microscopy. Figure 6.13 shows the evolution of aqueous foams stabilised by SE at room temperature. All foams suffer liquid drainage immediately after aeration, yet this process ceases within the first few hours on storage. For C-1816 foam, it collapses completely within a week or so, whilst C-1811 foam lasts for several weeks or more depending on the surfactant concentration. In contrast, the foams with C-1805 and C-1807 above a certain concentration can survive more than 1 year.

**Figure 6.13.** Appearance of aqueous foams stabilized by SE as a function of storage time at room temperature. (i) 1 wt.% C-1816, (ii) 1 wt.% C-1811, (iii) 5 wt.% C-1807 and (iv) 2 wt.% C-1805. Scale bars = 1 cm.



The foam half-life ( $t_{1/2}$ ) and the foam stability index  $f$  are plotted in Figure 6.14 against surfactant concentration. With increasing surfactant concentration, the values of  $t_{1/2}$  for SDS, C-1811 and C-1816 foams increase initially and then remain almost constant, whilst those of C-1805 and C-1807 foams go through an increase then an abrupt drop. Additionally,  $t_{1/2}$  of SE foams is at least one order of magnitude higher than that of SDS foams for most of the investigated concentrations. The foam half-life alone cannot fully describe the foam stability. Thus, the foam stability index  $f$  was introduced as the ratio of foam volume after 7 days storage to that immediately after aeration. Apparently, no SDS foams remain (*i.e.*  $f = 0$ ) after 7 days aging, whereas  $f$  for SE foams increases with decreasing HLB except 4 wt.%. The complete collapse time for SDS and C-1816 foams can be found in Figure 6.15.

**Figure 6.14.** Foam stability index  $f$  and foam half-life (inset) as a function of surfactant concentration at room temperature for various SE and SDS.

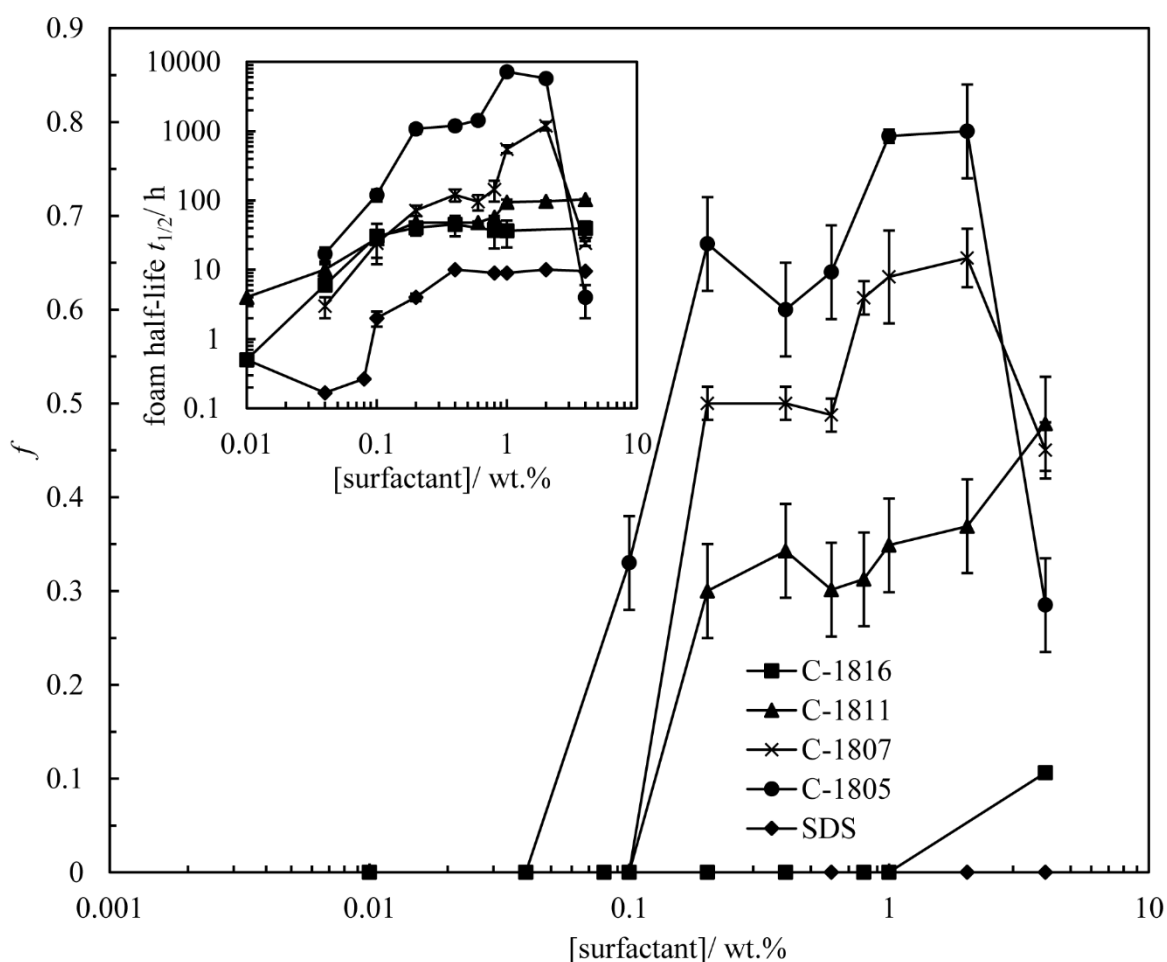
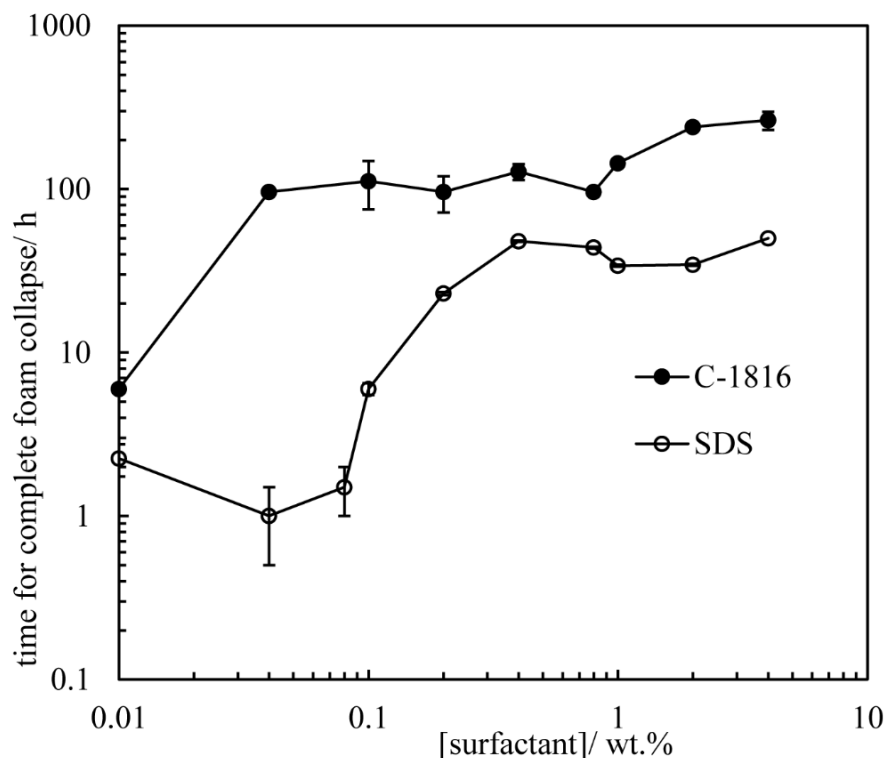


**Figure 6.15.** Variation of time for complete foam collapse with surfactant concentration for C-1816 and SDS at room temperature.



The microstructure of foam bubbles is firstly revealed by optical microscopy, as shown in Figure 6.16. All foam bubbles are spherical possessing smooth surfaces. The average bubble diameters of fresh foams *versus* SE concentration for three HLB are given in Figure 6.17. The bubble diameter goes through a gradual increase reaching a maximum and a slight drop thereafter. This finding can be explained as follows. In the region of low surfactant concentration, more air bubbles which are partially coated by surfactant molecules are involved in coalescence/coarsening with surfactant concentration, thereby leading to an increase in the bubble size.<sup>51</sup> Upon reaching the region of relatively high concentrations, coalescence/coarsening can be suppressed effectively due to a more compact surfactant monolayer at the air-water surface.<sup>51</sup> Meanwhile, more vesicles can be formed reducing drainage, coalescence and inter-bubble gas transfer. The average bubble diameter increases as increasing HLB for almost all concentrations. This is due to the fact that relatively small surfactant aggregates formed and weak electrostatic repulsions for the systems of high-HLB SE in water are more likely to suffer coalescence/coarsening during foaming.<sup>13</sup>

**Figure 6.16.** Optical micrographs of aqueous foams stabilized by SE immediately after aeration (left column) and during storage (right column) at room temperature. (i) 4 wt.% C-1816; (ii) 1 wt.% C-1811; (iii) 5 wt.% C-1807; (iv) 2 wt.% C-1805.

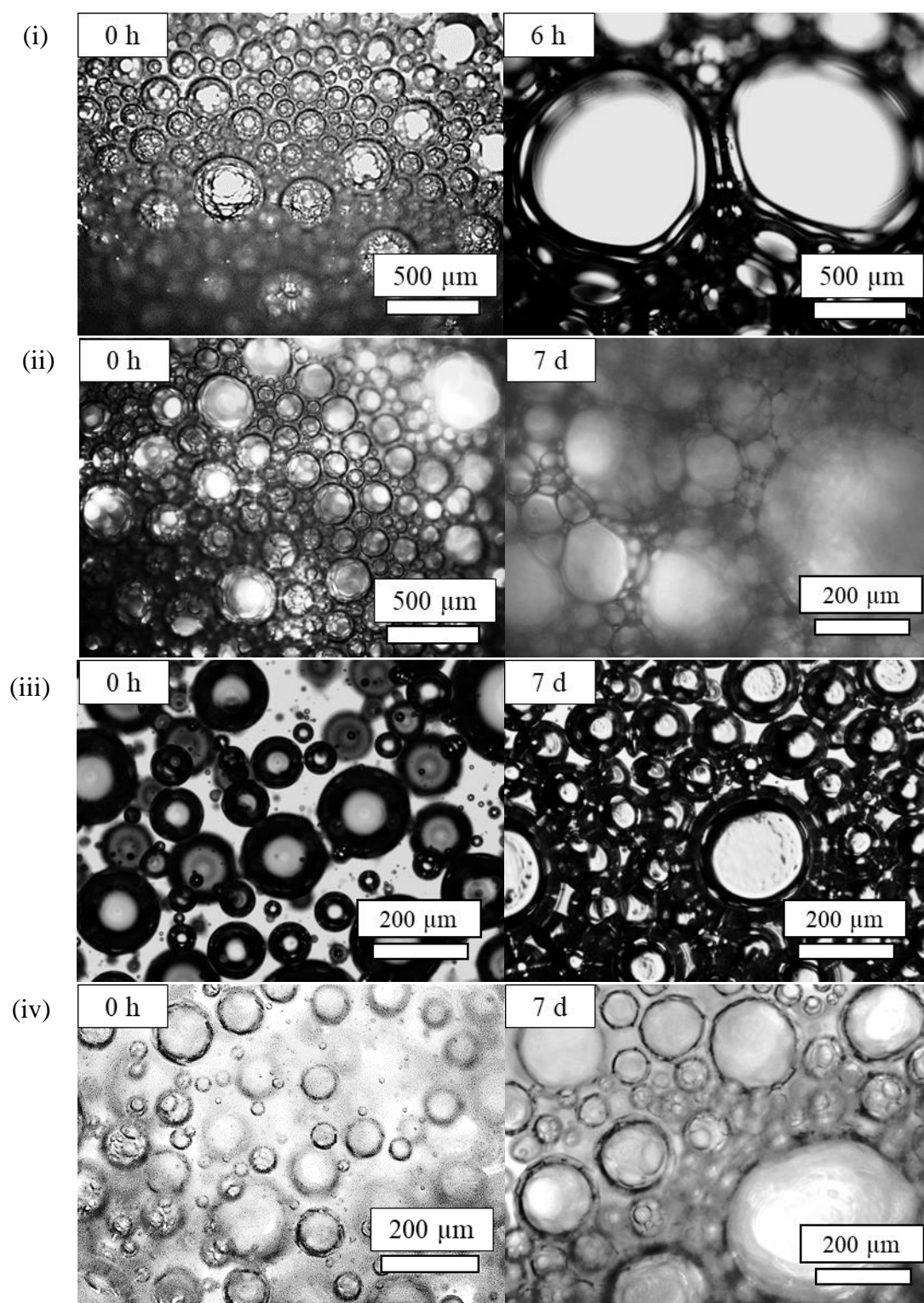
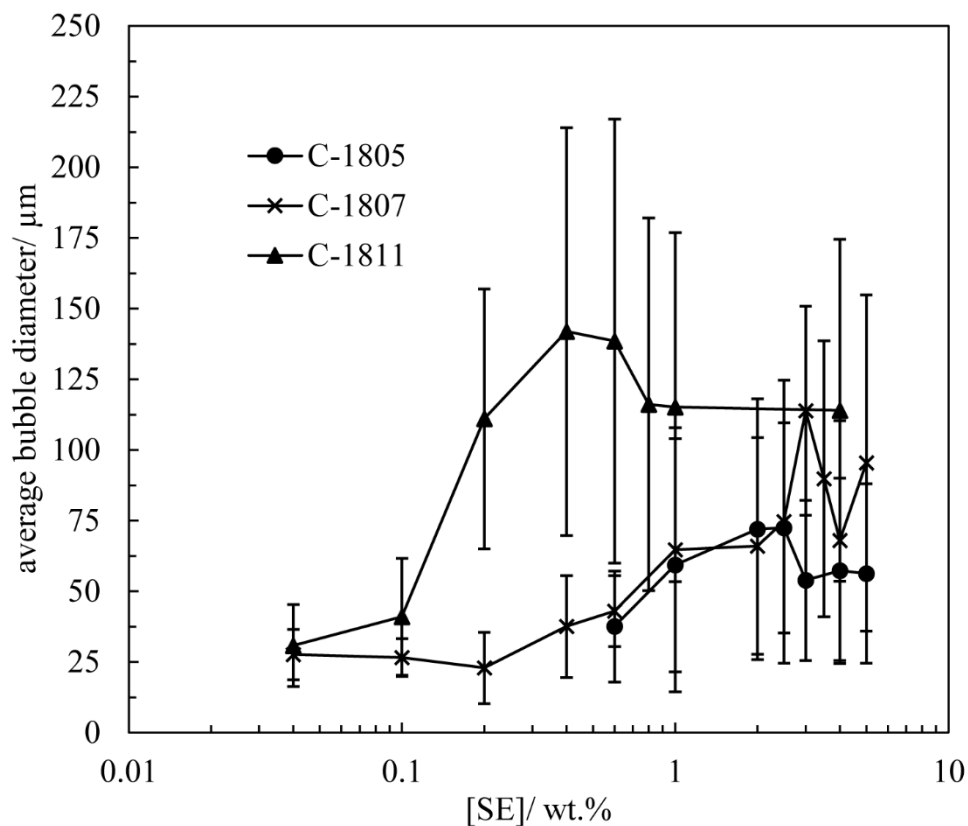


**Figure 6.17.** Variation of average bubble diameter of fresh foams with SE concentration at room temperature.



To further probe into the foam microstructure, the cryo-SEM images of foam bubbles of SE are given in Figure 6.18 (low magnifications) and Figure 6.19 (high magnifications). All bubbles are spherical. Besides, discrete/agglomerated vesicles can be identified within the interstitial areas and in the Plateau borders between neighbouring bubbles. Based on the above, the variation in the foam stability as a function of HLB is explained as follows. First, upon decreasing HLB, the formation of larger surfactant aggregates and the presence of stronger electrostatic repulsions between adjacent aggregates tend to increase the lamella thickness of a foam thus reducing the transport of gas between bubbles and film rupture.<sup>13,52</sup> Secondly, giant aggregates may jam within Plateau borders thereby blocking liquid drainage.<sup>13</sup> Furthermore, smaller and less polydisperse foam bubbles for low HLB are less likely to suffer coarsening driven by the difference in Laplace pressure between bubbles.<sup>2</sup>

**Figure 6.18.** Cryo-SEM images of fresh aqueous foams stabilized by 1 wt.% SE. (i) C-1816, (ii) C-1811, (iii) C-1807 and (iv) C-1805.

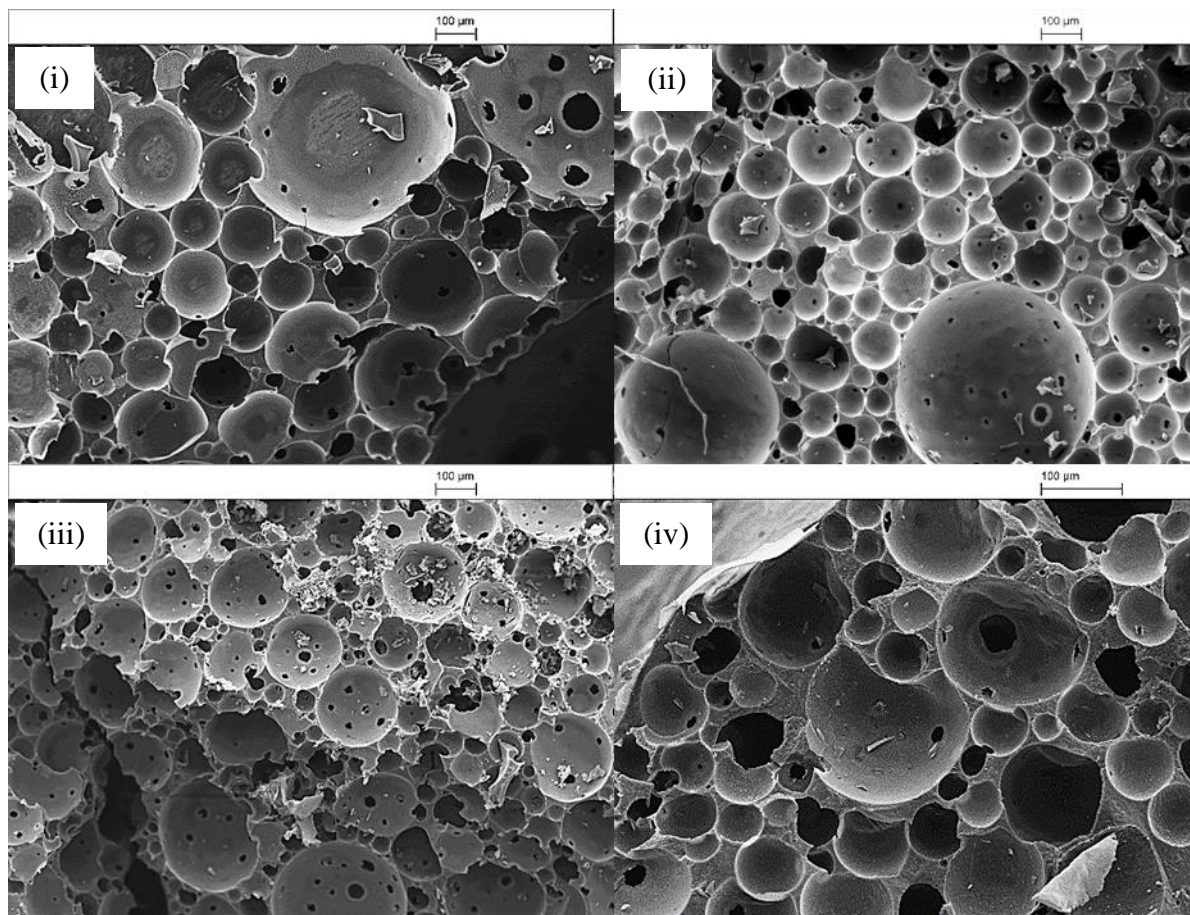
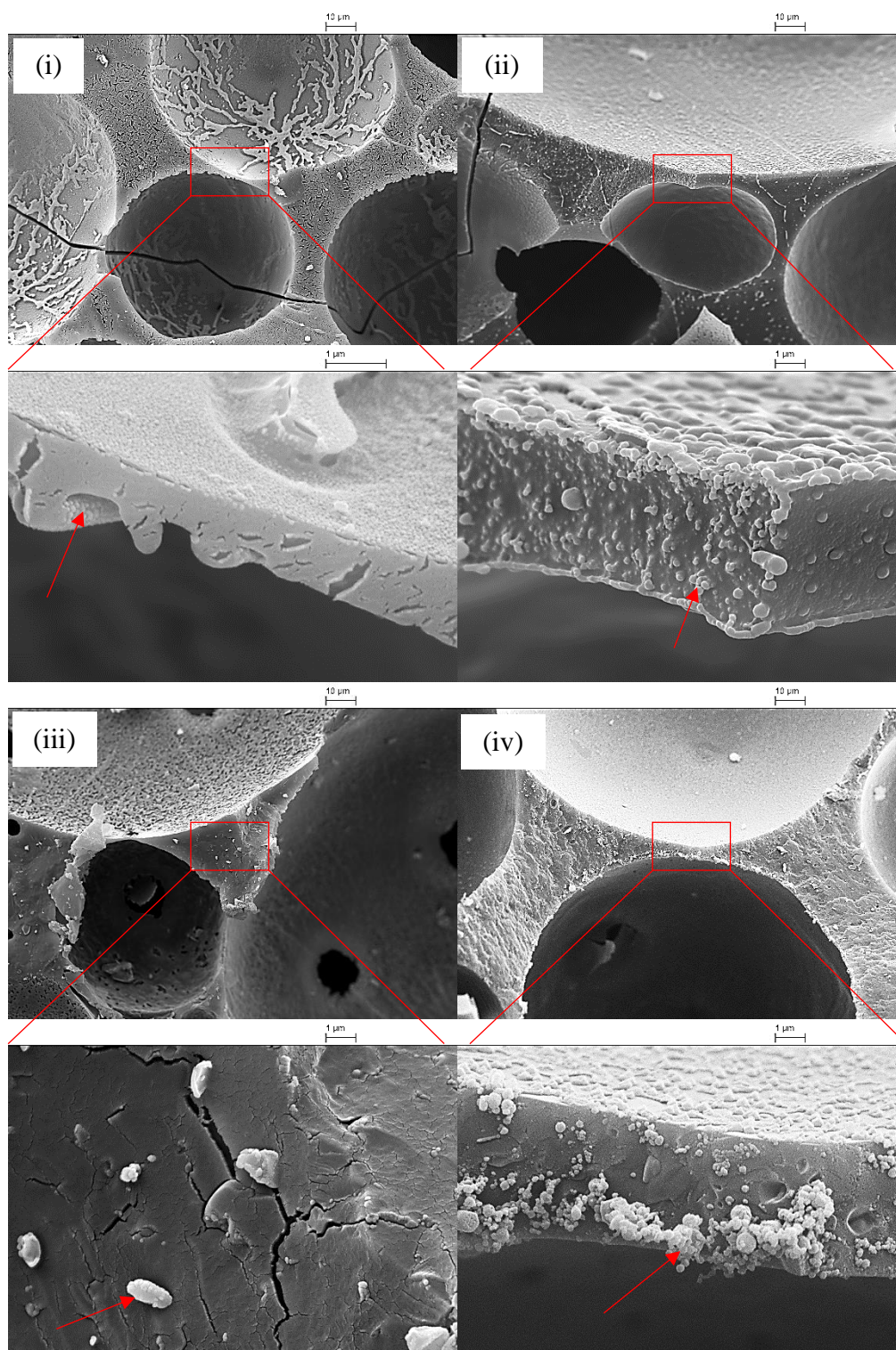


**Figure 6.19.** Cryo-SEM images of fresh aqueous foams stabilized by 1 wt.% SE. (i) C-1816, (ii) C-1811, (iii) C-1807 and (iv) C-1805. Arrows denote vesicles in continuous phase.



### 6.3 Systems with sucrose esters of varying pH

Interestingly, we find that the zeta potentials for aqueous solutions/dispersions of SE are negative despite the nonionic nature of the surfactants used in our experiments. This is possibly because minor fatty acid molecules become deprotonated above the isoelectric point; pKa of the carboxyl group in water is around 4.75.<sup>53</sup> In aqueous systems of the nonionic polyglycerol fatty acid ester,<sup>44,54</sup> lowering pH can improve the surface activity of surfactant molecules yielding better foamability. In addition, an agglomeration of vesicles in the continuous phase can confer the resulting foams with long-term stability.<sup>19</sup> On this initiative, we seek to explore the effect of lowering pH on the aggregate structures, the dynamic adsorption kinetics and foaming behaviour of representative systems, *i.e.* C-1807 and C-1805.

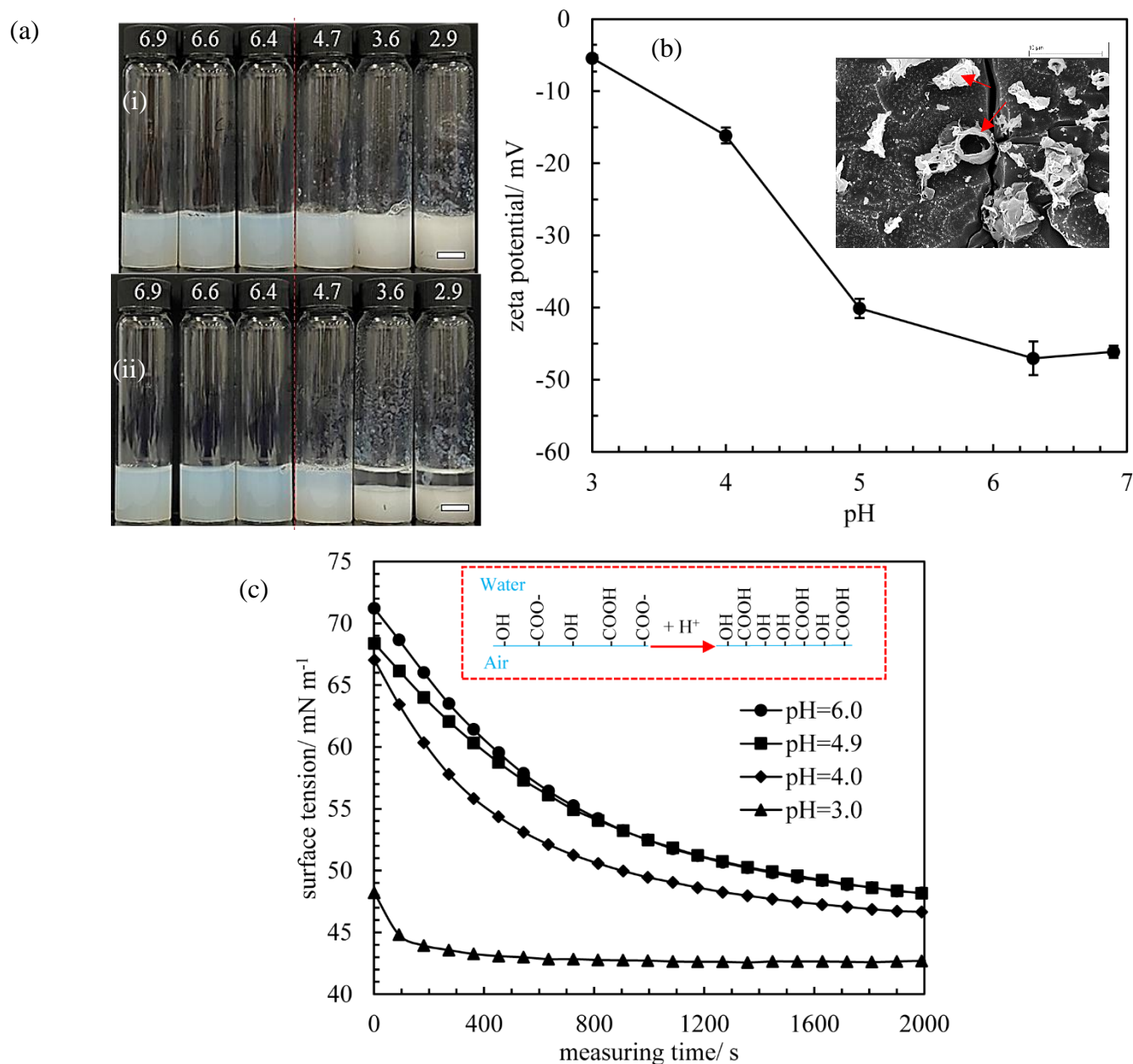
#### 6.3.1 Dispersion behaviour of sucrose ester-water mixtures

Figure 6.20(a) shows the appearance of aqueous dispersions of 1 wt.% C-1807 for different pH freshly prepared and after 48 h storage at ambient temperature. The value of pH for 1 wt.% C-1807 in water at the natural condition is  $\sim 6.9$ . With the addition of acid, there is virtually no change in the sample appearance for  $\text{pH} \geq 6.3$ . Once reaching  $\text{pH} \leq 4.7$ , the sample turns more turbid and viscous on lowering pH. After 48 h storage, sedimentation occurs within the same pH range. The zeta potentials of aqueous dispersions of 1 wt.% C-1807 is shown in Figure 6.20(b) against pH. With a decrease in pH, the magnitude of the zeta potential decreases during which electrostatic repulsion contributing to colloidal stability declines due to charge screening, so aggregates are more likely to flocculate.<sup>19</sup> The cryo-SEM image of a destabilised vesicle dispersion at  $\text{pH} = 3.0$  for 1 wt.% C-1807 is shown in Figure 6.20(b) as inset. Apparently, many vesicles adopt irregular shapes and some of them are ruptured exposing interior structures. The reason for this phenomenon is that osmotic stress caused by excess  $\text{H}^+$  may drive water out of vesicles, causing distortion or even disruption of initially intact vesicles.<sup>44</sup>

The surface tensions of aqueous dispersions of 0.01 wt.% C-1807 for various pH at 20 °C are presented in Figure 6.20(c) as a function of measuring time. The first measurable surface tension decreases with decreasing pH, hinting higher adsorption kinetics of surfactant molecules to the air-water interface.<sup>54</sup> On the other hand, at the end of surface tension measurements, *i.e.* 2000 s, the surface tension decreases on lowering pH as well implying higher surface activity. The reasons for this are explained as follows. Firstly, partially open vesicles driven by osmotic stress at low pH allow for the fast transport of SE monomers to the interface.<sup>54</sup> Secondly, the number ratio of protonated fatty acid molecules to deprotonated ones

adsorbed at the interface tends to increase at low pH, which decreases electrostatic repulsive forces and increases H-bonding forces. This will increase the packing density of adsorbed molecules at the interface.<sup>48</sup> Therefore, lowering pH can improve surface activity.

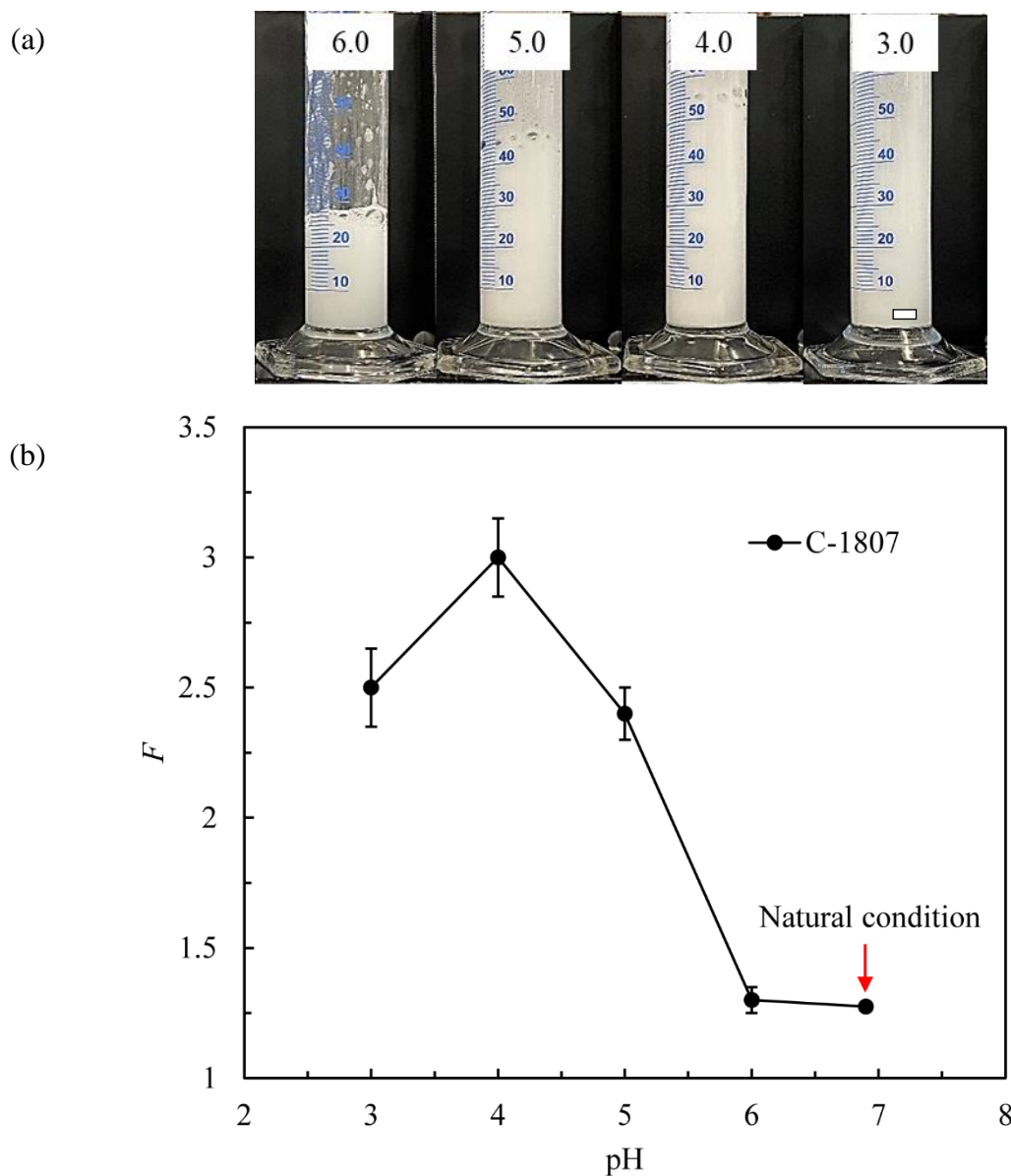
**Figure 6.20.** (a) Photos of aqueous dispersions of 1 wt.% C-1807 against pH at room temperature. (i) Fresh, (ii) 48 h storage. Scale bars = 1 cm. (b) Zeta potential of aqueous dispersions of 1 wt.% C-1807 as a function of pH at 20 °C. Inset: cryo-SEM image of aqueous dispersion of 1 wt.% C-1807 for pH = 3.0. (c) Surface tension of aqueous dispersions of 0.01 wt.% C-1807 *versus* measuring time for different HLB. Inset: schematic of changes in the adsorption behaviour of surfactant molecules at the interface upon decreasing pH.



### 6.3.2 Foaming behaviour of sucrose ester-water mixtures

Figure 6.21 presents the appearance of 20 mL aqueous dispersions of 1 wt.% C-1807 for varying pH immediately after 60 s hand shaking at room temperature. With a decrease in pH, the foaming capacity of C-1807 in water increases appreciably at first, followed by a drop due to too high viscosity of the continuous phase hindering effective air entrainment. The highest foamability index  $F$  is  $\sim 3$  for  $\text{pH} = 4$ , significantly higher than that for the neutral condition ( $\sim 1.3$ ,  $p < 0.05$ ).

**Figure 6.21.** (a) Photos of aqueous dispersions of 1 wt.% C-1807 against pH soon after 60 s hand shaking at room temperature. Scale bar = 1 cm. (b) Corresponding foamability index  $F$  as a function of pH.



The appearance evolution of aqueous foams containing 1 wt.% C-1807 for different pH as a function of storage time can be found in Figure 6.22. The volume fractions of the remaining foams after 7 d storage relative to that initially vary between 0.45-0.75, see Figure 6.23. Despite electrostatic stabilizing forces being significantly reduced at low pH, the resulting foams are reasonably stable possibly arising from an agglomeration of vesicles within the interstitial areas of the foam (see Figure 6.24).<sup>19</sup>

**Figure 6.22.** Appearance of aqueous foams stabilised by 1 wt.% C-1807 as a function of storage time for varying pH at room temperature. (a) pH = 6.0; (b) pH = 5.0; (c) pH = 4.0; (d) pH = 3.0. Scale bars = 1 cm.

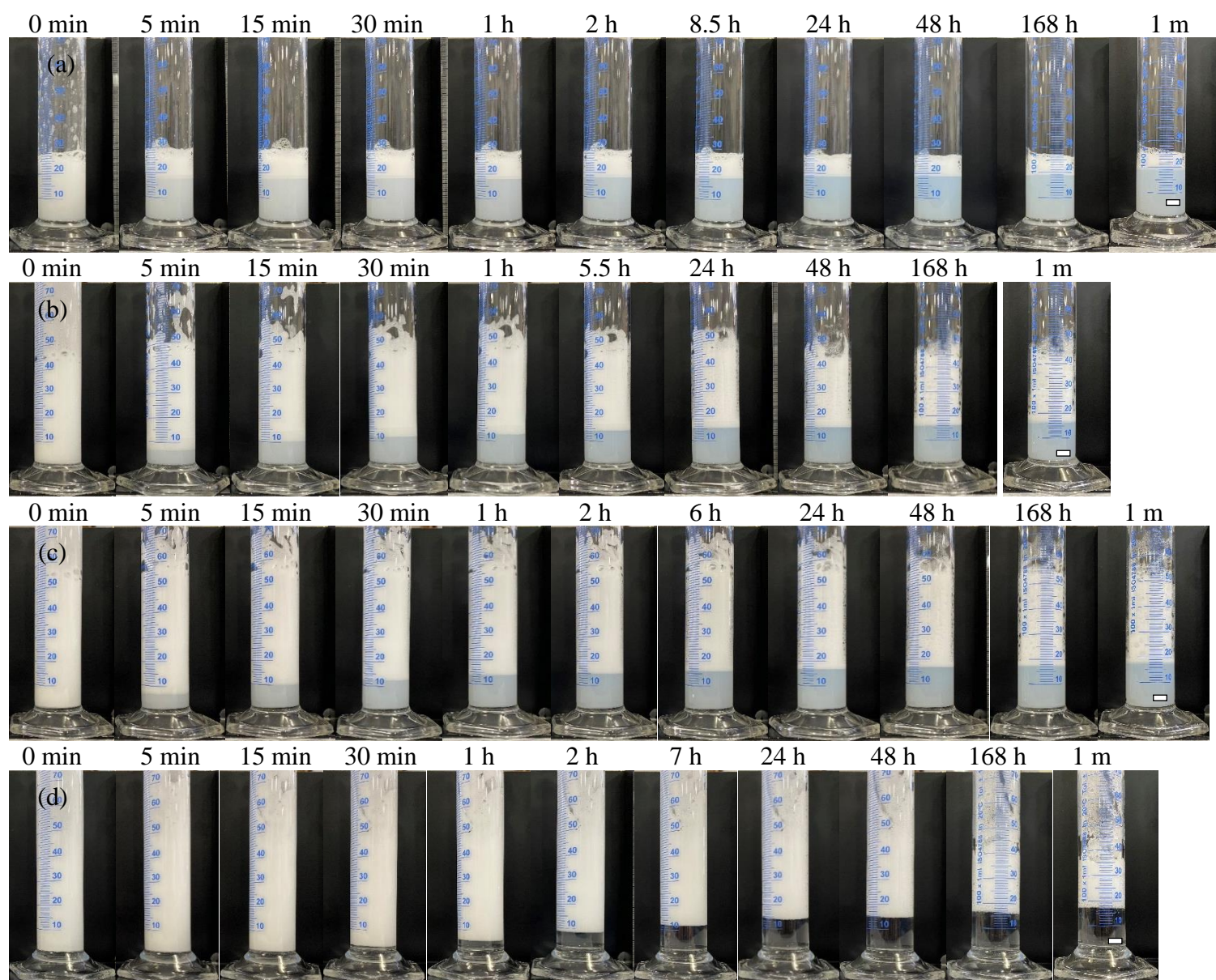
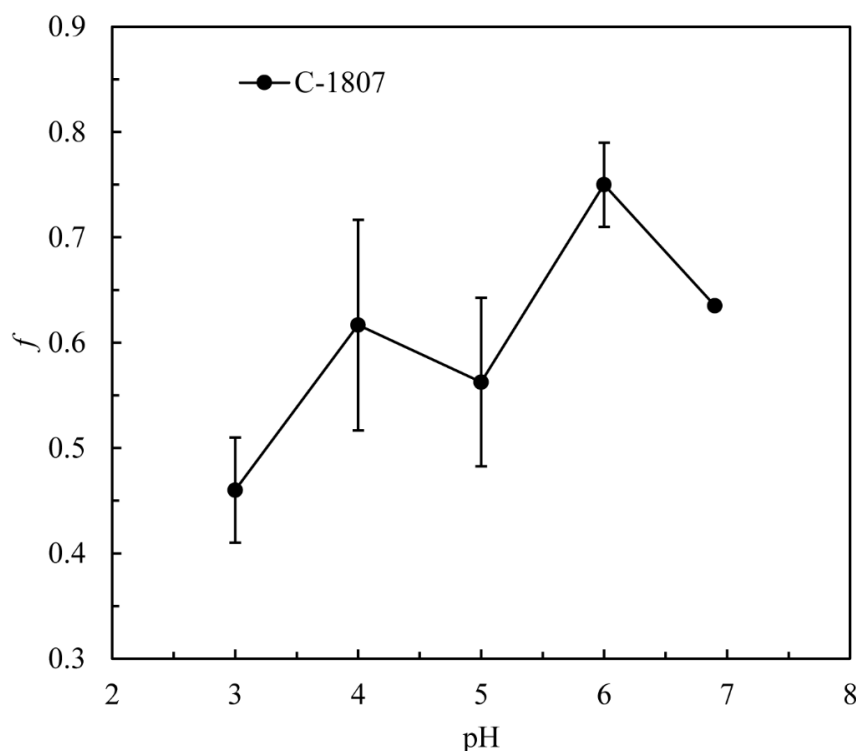


**Figure 6.23.** Foam stability index  $f$  as a function of pH for systems in Figure 6.21.



The cryo-SEM images of a foam containing 1 wt.% C-1807 freshly made for pH = 3.0 are given in Figure 6.24. Many distorted or disrupted vesicles can be identified in the liquid lamella of the foam, the morphology of which is reminiscent of that from the aqueous dispersion before aeration (Figure 6.20(b)). Moreover, the vesicles in the highly agglomerated state can be captured. These results can be compared to the earlier ones in polyglycerol fatty acid ester-water systems,<sup>19,44,54</sup> during which more stable foams can be produced at low pH compared to the neutral condition. This finding can also be applied to the system of C-1805, see Figure 6.25 and Figure 6.26.

**Figure 6.24.** Cryo-SEM images of fresh aqueous foam stabilized by 1 wt.% C-1807 for pH = 3.0. Red arrow indicates disrupted vesicles.

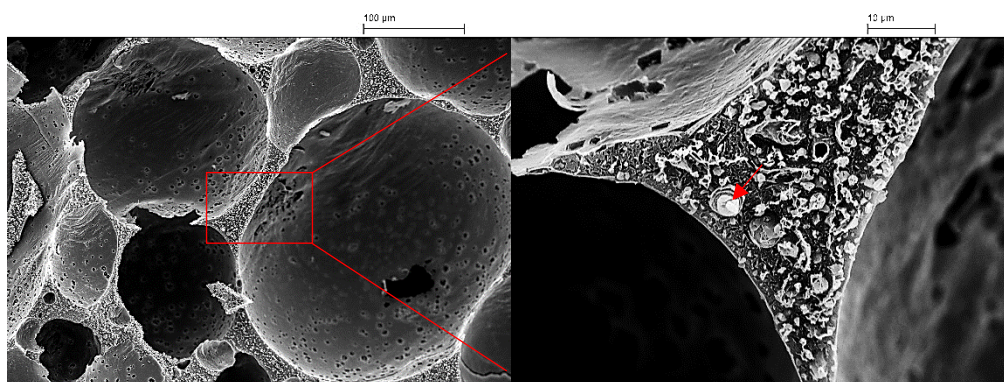


**Figure 6.25.** (a) Photos of aqueous dispersions of 1 wt.% C-1805 against pH soon after 60 s hand shaking at room temperature. Scale bar = 1 cm. (b) Corresponding foamability index  $F$  as a function of pH.

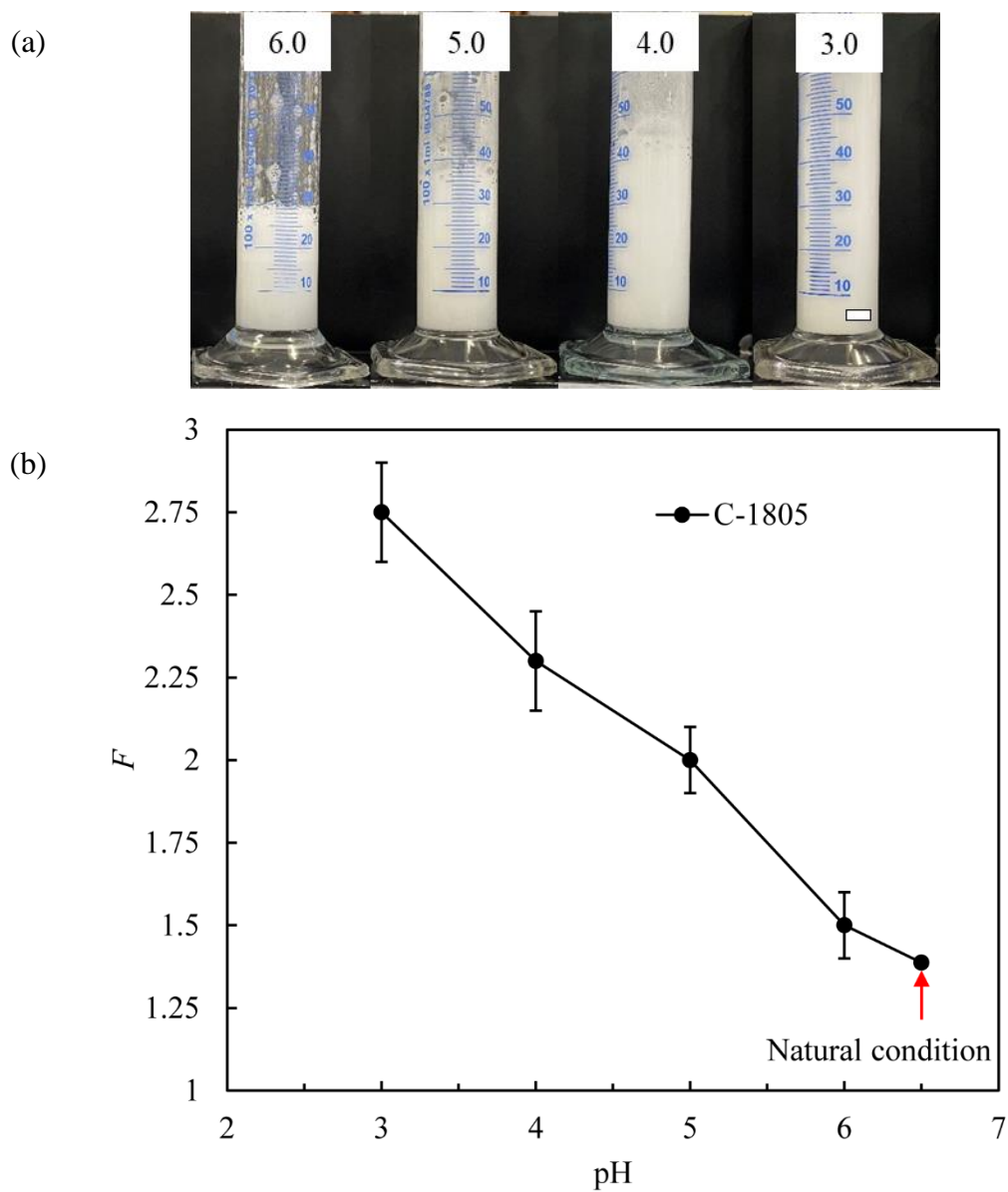
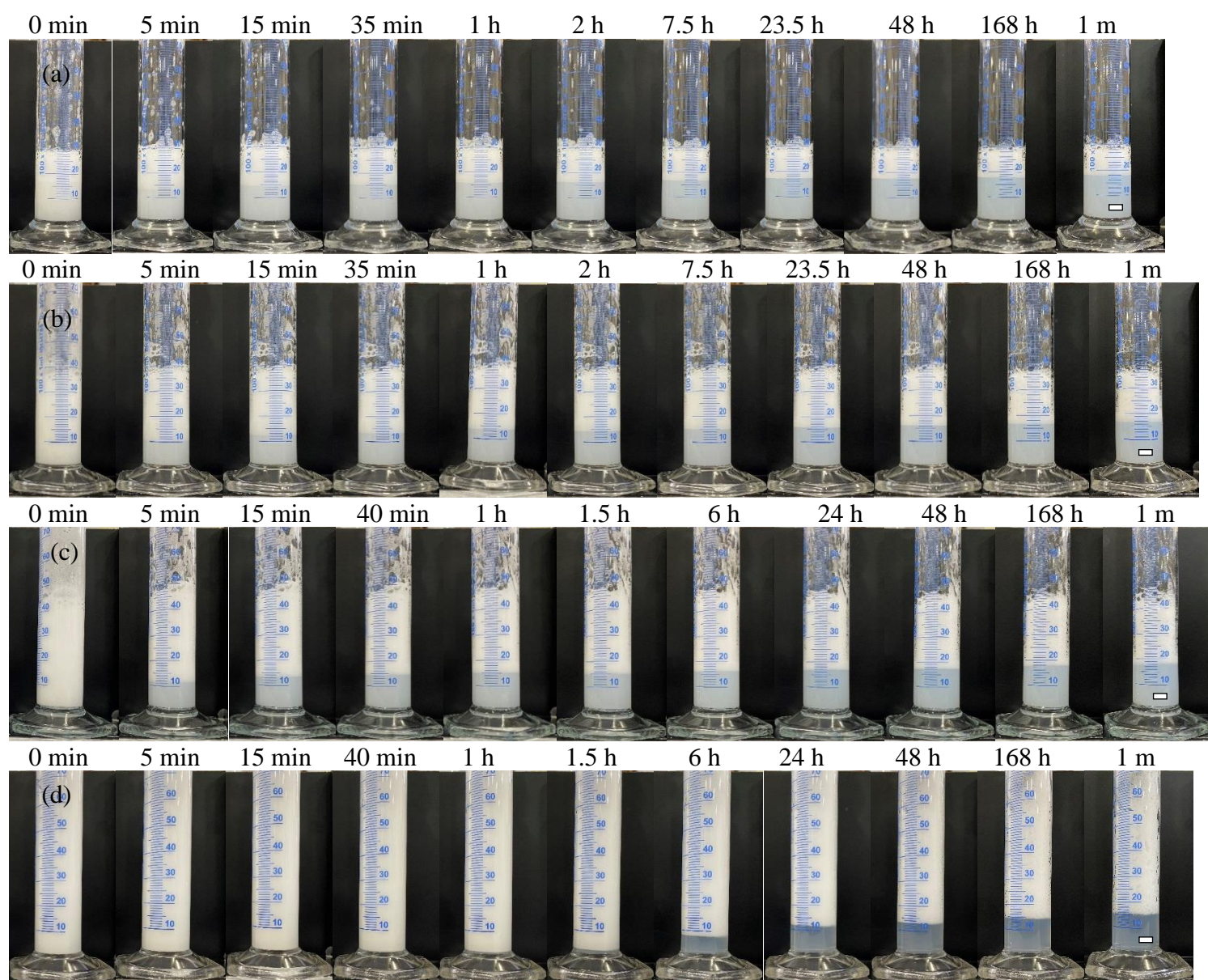


**Figure 6.26.** Appearance of aqueous foams stabilised by 1 wt.% C-1805 as a function of storage time for varying pH at room temperature. (a) pH = 6.0; (b) pH = 5.0; (c) pH = 4.0; (d) pH = 3.0. Scale bars = 1 cm.



## 6.4 Conclusions

In this chapter we carry out a systematic study on the aqueous dispersion and foaming behavior of a series of sucrose stearate esters with different HLB. The physicochemical properties of aqueous solutions/dispersions of SE vary significantly with HLB, including the macroscopic appearance, the size and morphology of surfactant aggregates formed, rheology and surface tension. The foamability of aqueous solutions/dispersions containing SE passes through a maximum followed by a decline as decreasing HLB, much lower than that of popular SDS. In contrast, the stability of resulting foams is much higher than that of SDS and long-lived foams above certain concentrations for C-1807 and C-1805 can survive for up to one year or so. The superior stabilization is attributed to the steric hindrance of bulky vesicles in the foam lamella alongside strong electrostatic repulsion between adjacent vesicles. The variation of foaming functionality as a function of HLB can be well correlated to the dispersion properties prior to aeration.

Comparable to a previous work,<sup>44</sup> the effect of lowering pH on the dispersion and foaming properties of the representative systems is investigated. It is interesting to note that decreasing pH can lead to a change in the vesicle morphology. Meanwhile, the foaming capacity can be improved significantly due to the faster adsorption kinetics of surfactant molecules to the air-water interface. The focus of further work should be on the role of different ionic species, *e.g.* salts and free fatty acids, on the dispersion and foaming properties of sucrose esters in water.

## 6.5 References

1. D.L. Weaire and S. Hutzler, *The Physics of Foams*, Clarendon Press, Oxford, 2005.
2. E. Rio, W. Drenckhan, A. Salonen and D. Langevin, Unusually stable liquid foams, *Adv. Colloid Interface Sci.*, 2014, **205**, 74–86.
3. D.J. Shaw, *Introduction to Colloid and Surface Chemistry*, Butterworths, London, 1968, ch.10.
4. A. Saint-Jalmes, Physical chemistry in foam drainage and coarsening, *Soft Matter*, 2006, **2**, 836–849.
5. D. Langevin, Coalescence in foams and emulsions: similarities and differences, *Curr. Opin. Colloid Interface Sci.*, 2019, **44**, 23–31.
6. B.P. Binks, Particles as surfactants-similarities and differences, *Curr. Opin. Colloid Interface Sci.*, 2002, **7**, 21–41.
7. B.P. Binks and T.S. Horozov, Aqueous foams stabilized solely by silica nanoparticles, *Angew. Chem. Int. Ed.*, 2005, **44**, 3722–3725.
8. U.T. Gonzenbach, A.R. Studart, E. Tervoort and L.J. Gauckler, Ultrastable particle-stabilized foams, *Angew. Chem. Int. Ed.*, 2006, **45**, 3526–3530.
9. A. Stocco, E. Rio, B.P. Binks and D. Langevin, Aqueous foams stabilized solely by particles, *Soft Matter*, 2011, **7**, 1260–1267.
10. L. Zhang, A. Mikhailovskaya, P. Yazhgur, F. Muller, F. Cousin, D. Langevin, N. Wang and A. Salonen, Precipitating sodium dodecyl sulfate to create ultrastable and stimuable foams, *Angew. Chem. Int. Ed.*, 2015, **54**, 9533–9536.
11. B.P. Binks and H. Shi, Aqueous foams in the presence of surfactant crystals, *Langmuir*, **2020**, **36**, 991–1002.
12. A.B. Subramaniam, M. Abkarian, L. Mahadevan and H.A. Stone, Colloid science: non-spherical bubbles, *Nature*, 2005, **438**, 930.
13. A.L. Fameau, A. Saint-Jalmes, F. Cousin, B.H. Houssou, B. Novales, L. Navailles, F. Nallet, C. Gaillard, F. Boué, and J.P. Douliez, Smart foams: switching reversibly between ultrastable and unstable foams, *Angew. Chem. Int. Ed.*, 2011, **50**, 8264–8269.
14. J.N. Israelachvili, D.J. Mitchell and B.W. Ninham, Theory of self-assembly of hydrocarbon amphiphiles into micelles and bilayers, *J. Chem. Soc., Faraday Trans. 2*, 1976, **72**, 1525–1568.
15. A.L. Fameau, S. Lam and O.D. Velev, Multi-stimuli responsive foams combining particles and self-assembling fatty acids, *Chem. Sci.*, 2013, **4**, 3874–3881.

16. A.L. Fameau, J. Ventureira, B. Novales and J.P. Douliez, Foaming and emulsifying properties of fatty acids neutralized by tetrabutylammonium hydroxide, *Colloids Surf. A*, 2012, **403**, 87–95.
17. B.P. Binks, S. Campbell, S. Mashinchi and M.P. Piatko, Dispersion behavior and aqueous foams in mixtures of a vesicle-forming surfactant and edible nanoparticles, *Langmuir*, 2015, **31**, 2967–2978.
18. D. Varade, D. Carriere, L.R. Arriaga, A.L. Fameau, E. Rio, D. Langevina and W. Drenckhan, On the origin of the stability of foams made from catanionic surfactant mixtures, *Soft Matter*, 2011, **7**, 6557–6570.
19. C. Curschellas, J. Kohlbrecher, T. Geue, P. Fischer, B. Schmitt, M. Rouvet, E.J. Windhab and H.J. Limbach, Foams stabilized by multilamellar polyglycerol ester self-assemblies, *Langmuir*, 2013, **29**, 38–49.
20. B. Novales, A. Riaublanc, L. Navailles, B.H. Houssou, C. Gaillard, F. Nallet and J.P. Douliez, Self-assembly and foaming properties of fatty acid-lysine aqueous dispersions, *Langmuir*, 2010, **26**, 5329–5334.
21. L.K. Shrestha, D.P. Acharya, S.C. Sharma, K. Aramaki, H. Asaoka, K. Ihara, T. Tsunehiro and H. Kunieda, Aqueous foam stabilized by dispersed surfactant solid and lamellar liquid crystalline phase, *J. Colloid Interface Sci.*, 2006, **301**, 274–281.
22. Z. Briceño-Ahumada, A. Maldonado, M. Impérator-Clerca and D. Langevin, On the stability of foams made with surfactant bilayer phases, *Soft Matter*, 2016, **12**, 1459–1467.
23. A.L. Fameau and A. Salonen, Effect of particles and aggregated structures on the foam stability and aging, *C. R. Phys.*, 2014, **15**, 748–760.
24. K. Hill and O. Rhode, Sugar-based surfactants for consumer products and technical applications, *Fett/Lipid*, 1999, **101**, 25–33.
25. T. Plat and R.J. Linhardt, Syntheses and applications of sucrose-based esters, *J. Surfactants Deterg.*, 2001, **4**, 415–421.
26. A. Szűts and P. Szabó-Révész, Sucrose esters as natural surfactants in drug delivery systems-a mini-review, *Int. J. Pharm.*, 2012, **433**, 1–9.
27. S. Soultani, S. Ognier, J.M. Engasser and M. Ghoul, Comparative study of some surface active properties of fructose esters and commercial sucrose esters, *Colloids Surf. A*, 2003, **227**, 35–44.

28. G. Garofalakis, B.S. Murray and D.B. Sarney, Surface activity and critical aggregation concentration of pure sugar esters with different sugar headgroups, *J. Colloid Interface Sci.*, 2000, **229**, 391–398.
29. Y. Li, S. Zhang, Q. Wang and J. Yang, Study on surface activity and critical aggregation concentration of sucrose esters containing different isomers of mono-, di- and polyesters, *Tenside Surfact. Det.*, 2004, **41**, 26–30.
30. T.M. Herrington and S.S. Sahi, Phase behavior of some sucrose surfactants with water and n-decane, *J. Am. Oil Chem. Soc.*, 1988, **65**, 1677–1681.
31. N. Becerra, C. Toro, A.L. Zanolco, E. Lemp and G. Günther, Characterization of micelles formed by sucrose 6-O-monoesters, *Colloids Surf. A*, 2008, **327**, 134–139.
32. J. Krawczyk, Aggregation properties of sucrose fatty acid esters and some other sugar-based surfactants at different temperatures, *J. Mol. Liq.*, 2018, **271**, 610–620.
33. X. Zhang, W. Wei, X. Cao and F. Feng, Characterization of enzymatically prepared sugar medium-chain fatty acid monoesters, *J. Sci. Food Agric.*, 2015, **95**, 1631–1637.
34. X. Zhang, F. Song, M. Taxipalati, W. Wei and F. Feng, Comparative study of surface-active properties and antimicrobial activities of disaccharide monoesters, *PLoS One*, 2014, **9**, 1–19.
35. J. Coates, Interpretation of infrared spectra-a practical approach, in *Encyclopedia of Analytical Chemistry*, Meyers, R. A. (ed.), John Wiley and Sons, Chichester, 2000.
36. K. Yoza, N. Amanokura, Y. Ono, T. Akao, H. Shinmori, M. Takeuchi, S. Shinkai and D.N. Reinhoudt, Sugar-integrated gelators of organic solvents-their remarkable diversity in gelation ability and aggregate structure, *Chem. Eur. J.*, 1999, **5**, 2722–2729.
37. B.C. Youan, A. Hussain and N.T. Nguyen, Evaluation of sucrose esters as alternative surfactants in microencapsulation of proteins by the solvent evaporation method, *AAPS Pharmsci.*, 2003, **5**, Article 22.
38. F.R. Lupi, A. Shakeel, V. Greco, N. Baldino, V. Calabrò and D. Gabriele, Organogelation of extra virgin olive oil with fatty alcohols, glyceryl stearate and their mixture, *LWT - Food Sci. Technol.*, 2017, **77**, 422–429.
39. A. Szűts, E. Pallagi, G. Regdon Jr., Z. Aigner and P. Szabó-Révész, Study of thermal behaviour of sugar esters, *Int. J. Pharm.*, 2007, **336**, 199–207.
40. S.S. Sagiri, V.K. Singh, K. Pal, I. Banerjee, and P. Basak, Stearic acid based oleogels: a study on the molecular, thermal, and mechanical properties, *Mater. Sci. Eng. C*, 2015, **48**, 688–699.

41. C.H. Chen, I. Van Damme, and E.M. Terentjev, Phase behaviour of C18 monoglyceride in hydrophobic solutions, *Soft Matter*, 2009, **5**, 432–439.
42. A. Jesorka and O. Orwar, Liposomes: technologies and analytical applications, *Annu. Rev. Anal. Chem.*, 2008, **1**, 801–832.
43. S. Bhattacharjee, DLS and zeta potential – what they are and what they are not?, *J. Control. Release*, 2016, **235**, 337–351.
44. N. Duerr-Auster, T. Eisele, R. Wepf, R. Gunde and E.J. Windhab, Influence of pH on colloidal properties and surface activity of polyglycerol fatty acid ester vesicles, *J. Colloid Interface Sci.*, 2008, **327**, 446–450.
45. S.J. Choi, E.A. Decker, L. Henson, L.M. Popplewell, H. Xiao and D.J. McClements, Formulation and properties of model beverage emulsions stabilized by sucrose monopalmitate: influence of pH and lyso-lecithin addition, *Food Res. Int.*, 2011, **44**, 3006–3012.
46. P. Panizza, D. Roux, V. Vuillaume, C.-Y.D. Lu, and M.E. Cates, Viscoelasticity of the onion phase, *Langmuir*, 1996, **12**, 248–252.
47. M.A. Launois-Surpas, Tz. Ivanova, I. Panaiotov, J.E. Proust, F. Puisieux and G. Georgiev, Behaviour of pure and mixed DPPC liposomes spread or adsorbed at the air-water interface, *Colloid Polym. Sci.*, 1992, **270**, 901–911.
48. A. Arnould, F. Cousin, A. Salonen, A. Saint-Jalmes, A. Perez and A.L. Fameau, Controlling foam stability with the ratio of myristic acid to choline hydroxide, *Langmuir*, 2018, **34**, 11076–11085.
49. C. Stubenrauch, M. Hamann, N. Preisig, V. Chauhan and R. Bordes, On how hydrogen bonds affect foam stability, *Adv. Colloid Interface Sci.*, 2017, **247**, 435–443.
50. P.R. Garrett and P.L. Gratton, Dynamic surface tensions, foam and the transition from micellar solution to lamellar phase dispersion, *Colloids Surf. A*, 1995, **103**, 127–145.
51. A.T. Tyowua and B.P. Binks, Growing a particle-stabilized aqueous foam, *J. Colloid Interface Sci.*, 2020, **561**, 127–135.
52. K. Yu, H. Zhang, C. Hodges, S. Biggs, Z. Xu, O.J. Cayre and D. Harbottle, Foaming behavior of polymer-coated colloids: the need for thick liquid films, *Langmuir*, 2017, **33**, 6528–6539.
53. A.A. Pashkovskaya, M. Vazdar, L. Zimmermann, O. Jovanovic, P. Pohl and E.E. Pohl, Mechanism of long-chain free fatty acid protonation at the membrane-water interface, *Biophys. J.*, 2018, **114**, 2142–2151.

54. N. Duerr-Auster, R. Gunde, R.Mäder and E.J. Windhab, Binary coalescence of gas bubbles in the presence of a non-ionic surfactant, *J. Colloid Interface Sci.*, 2009, **333**, 579–584.

## CHAPTER 7 – SUCROSE ESTER SURFACTANT: FOAMS, EMULSIONS, FOAMULSIONS AND AERATED EMULSIONS

### 7.1 Introduction

Certain colloidal particles of suitable wettability can adsorb at various fluid interfaces giving rise to kinetically stable oil-water emulsions,<sup>1</sup> oil-oil emulsions,<sup>2</sup> water-water emulsions,<sup>3</sup> aqueous<sup>4</sup> and oil foams<sup>5-8</sup>. Of central significance is the particle wettability by the liquid phase quantified by the three-phase contact angle  $\theta$  measured through the more polar phase.<sup>1</sup> For systems containing equal volumes of oil (o) and water (w), oil-in-water (o/w) emulsions are preferred for relatively hydrophilic ( $\theta < 90^\circ$ ) particles, whereas water-in-oil (w/o) emulsions are stabilized with relatively hydrophobic ( $\theta > 90^\circ$ ) particles.<sup>9</sup> In the case of air (a) and water, partially hydrophobic ( $\theta < 90^\circ$ ) and very hydrophobic ( $\theta > 90^\circ$ ) particles can be used to prepare aqueous foams and aqueous liquid marbles, respectively.<sup>10</sup> In contrast, for mixtures of oil, air and particle, oil foams and oil liquid marbles can be yielded using partially oleophobic ( $\theta < 90^\circ$ ) and very oleophobic ( $\theta > 90^\circ$ ) particles, respectively.<sup>11,12</sup> All the above colloidal systems are prepared by mixing two immiscible fluids. When a third immiscible phase is introduced, *e.g.* gas into emulsions, novel colloidal systems containing oil, water and gaseous phases *i.e.* foamed or aerated emulsions can be fabricated.<sup>13-15</sup>

Recently, the role of oil-soluble surfactants in stabilising oil continuous colloidal systems, *e.g.* w/o emulsions<sup>16-19</sup> and a/o foams,<sup>20-33</sup> has been elucidated. Certain surfactant crystals (prepared *in situ* or pre-formed) can adsorb irreversibly at liquid interfaces, conferring emulsions/foams with ultra-stability to coalescence and coarsening. Moreover, excess crystals present in the continuous oil phase can result in a firm three-dimensional (3D) network, hindering or arresting phase separation. The investigated surfactants include mono- and diglycerides, fatty alcohols and fatty acids, high melting triglycerides (TAGs), sucrose esters or their mixtures.<sup>16-33</sup>

Sucrose esters (SE) are nonionic surfactants, the detailed introduction of which can be found in chapter 4. Up to now, the emulsifying and foaming functionalities of SE alone have been scarcely explored.<sup>32, 34-36, 37-39</sup> In one recent study,<sup>32</sup> the foaming capacity of a mixture of relatively oleophilic SE and vegetable oil has been demonstrated. Interestingly, SE molecules were found to be surface active at the air-oil interface and impressive foaming (highest overrun 330%) could occur upon whipping one-phase oil solutions of SE molecules. The subsequent introduction of cooling could improve the foam stability significantly due to *in situ* formed SE crystals at interfaces and in the continuous phase. From all these studies, SE of

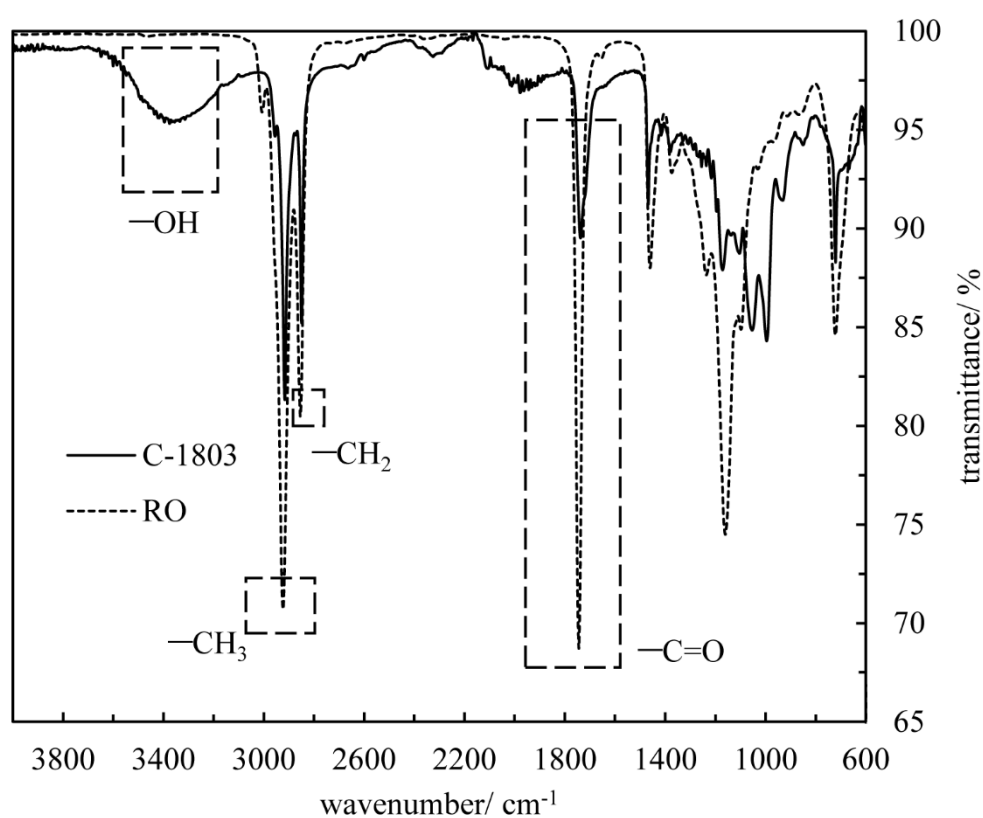
certain omniphobicity in the molecular or crystalline state can adsorb to various fluid-fluid interfaces, *e.g.* air-oil, water-oil and air-water.<sup>32,37-39</sup> One may ask if it is achievable to stabilise multiple interfaces simultaneously with SE alone in the same system, thereby yielding complex colloidal materials? For the first time, we report on the preparation and characterisation of a multitude of colloidal systems, *i.e.* a/o and a/w foams, o/w and w/o emulsions, o/w/o multiple emulsions, a and w/o foamulsions and a/o/w emulsions, using one relatively oleophilic SE sample (HLB number = 3) *via* different protocols.

We first explore the dispersion behaviour of the relatively lipophilic sucrose stearate surfactant (C-1803) in rapeseed oil (RO). Secondly, the interfacial properties of air-oil and water-oil in the presence of C-1803 are studied using surface tension and contact angle measurements. Based on the above, we try to fabricate a multitude of colloidal materials using C-1803 alone. Finally, the physicochemical properties of the colloidal materials are discussed, *e.g.* rheology, polymorphic behaviour and thermal properties.

## 7.2 Dispersion behaviour of sucrose ester-oil mixtures

Before being dissolved in oil, the molecular interactions within and the thermal behaviour of a powdered sample of neat C-1803 were investigated by FTIR and DSC, respectively. Figure 7.1 gives the FTIR spectrum for C-1803 powder at 20 °C. The  $\nu_{\text{OH}}$  peak of –OH groups appears at  $\sim 3400\text{ cm}^{-1}$ .<sup>40</sup> The two prominent peaks locating between  $2800\text{ cm}^{-1}$  and  $3000\text{ cm}^{-1}$  indicate –CH<sub>2</sub> and –CH<sub>3</sub> stretching vibrations, respectively.<sup>41</sup> The peaks representing stretching C=O groups can be found at  $\sim 1700\text{ cm}^{-1}$ .<sup>42</sup> For comparison, the FTIR spectrum for RO is included (broken line).

**Figure 7.1.** FTIR spectra of C-1803 and RO at 20 °C.



The thermograms of C-1803 powder (Figure 7.2) show one minor endothermic peak at 48.2 °C and one major endothermic peak at 63.9 °C during warming, respectively.<sup>43</sup> The reason for the two peaks has been explained in chapter 4 and 6. Subsequent cooling exhibits an exothermic peak at 53.6 °C. The thermal parameters of C-1803 powder can be found in Table 7.1.

**Figure 7.2.** Melting and cooling thermograms of C-1803. Temperature change rate was 5 °C min<sup>-1</sup>.

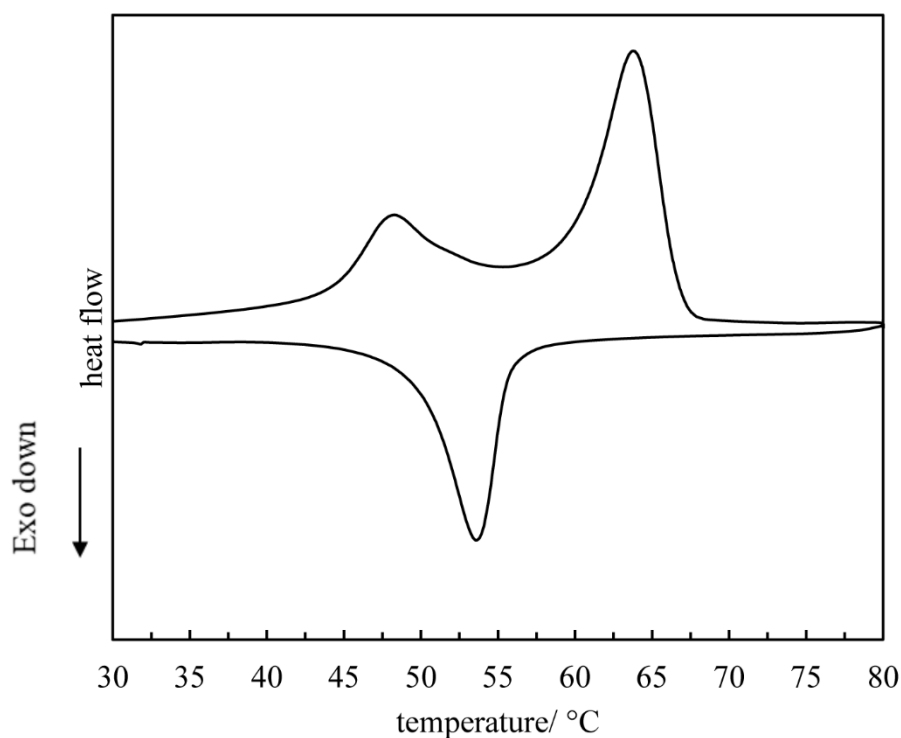
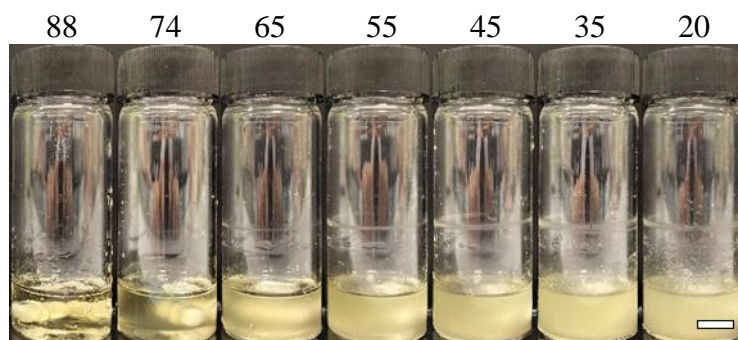


**Table 7.1.** Thermal properties of C-1803.

Crystallisation			Melting			
$T_{\text{onset}}/^{\circ}\text{C}$	$T_{\text{peak}}/^{\circ}\text{C}$	$\Delta H/\text{J g}^{-1}$	$T_{\text{peak}}/^{\circ}\text{C}$		$\Delta H/\text{J g}^{-1}$	
			Peak 1	Peak 2	Peak 1	Peak 2
$55.77 \pm 0.20$	$53.60 \pm 0.15$	$-27.75 \pm 0.20$	$48.19 \pm 0.15$	$63.87 \pm 0.10$	$11.90 \pm 0.20$	$34.00 \pm 0.20$

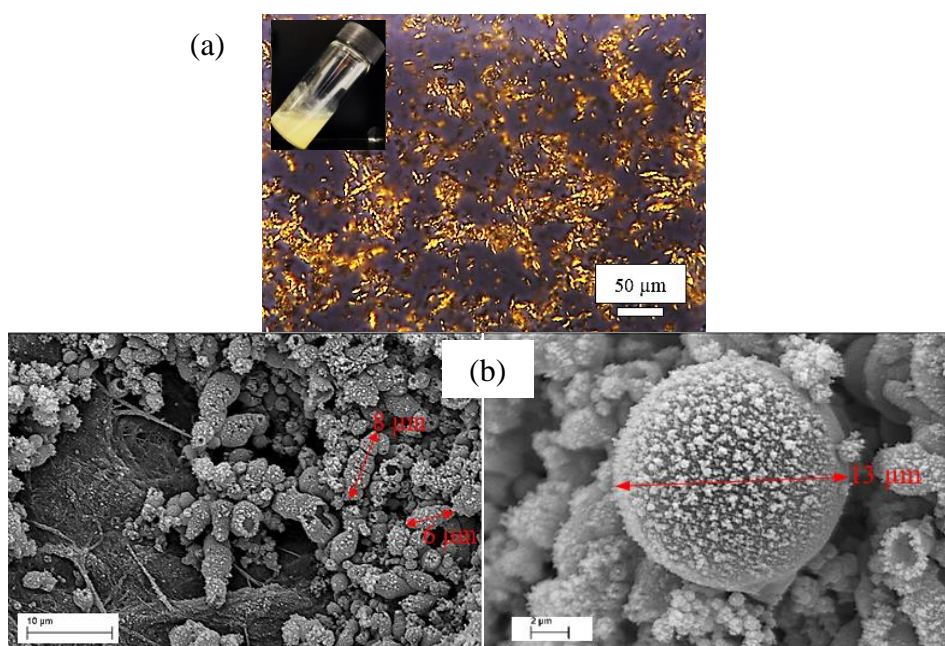
The dispersion behaviour of C-1803 in RO against temperature was first investigated by visual observations. Mixtures of C1803 and RO were thermostatted at 90 °C under gentle magnetic stirring to render a clear, homogeneous one-phase solution. The samples were then cooled gradually at 1 °C min<sup>-1</sup> in a water bath. For 5 wt.% C-1803 in RO (Figure 7.3), the first sign of cloudiness occurs at  $74 \pm 1$  °C. Upon cooling further, the sample becomes more turbid since the miscibility of RO and C-1803 decreases with decreasing temperature.<sup>44</sup> During warming, the sample turns less turbid with temperature until clearing again.

**Figure 7.3.** Appearance of vessels containing 5 wt.% C-1803 in RO at various temperatures in °C upon cooling from 90 °C at 1 °C min<sup>-1</sup>. Scale bar = 1 cm.



The inset photograph and polarised microscopy image of a RO dispersion containing 5 wt.% C-1803 at 20 °C are shown in Figure 7.4(a). Macroscopically, the sample is a flowable, viscous turbid dispersion. From the polarised image, large birefringent C-1803 crystals (bright) can be observed within the isotropic oil matrix (black), but it is impossible to discern the specific morphology and size of a single crystal. Considering this, cryo-SEM images were obtained, and representative ones are presented in Figure 7.4(b). C-1803 crystals exhibit two morphologies, *i.e.* spherical<sup>32</sup> and elongated rod-like. They are polydisperse with spherical diameters  $\leq 13 \mu\text{m}$  and rod-like length  $\leq 10 \mu\text{m}$ .

**Figure 7.4.** (a) Polarised microscopy image of 5 wt.% C-1803 in RO at 20 °C. Inset: tilted vessel containing 5 wt.% C-1803 in RO. (b) Cryo-SEM images of C-1803 crystals.

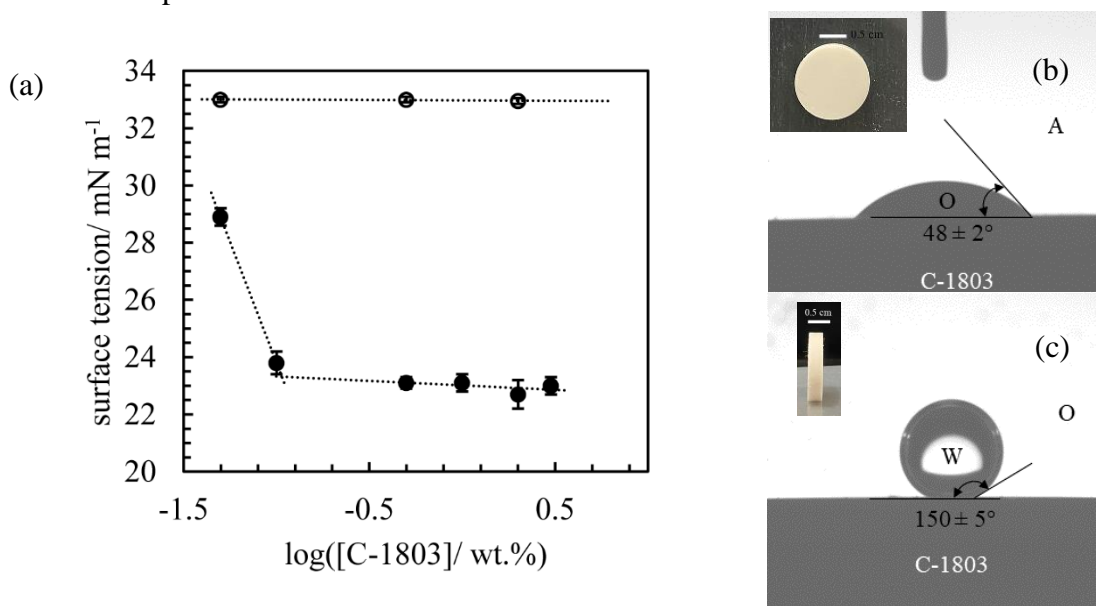


### 7.3 Air-oil surface tension and oil-water (air) contact angle with sucrose ester

To assess the interfacial properties of air-oil and water-oil in the presence of C-1803, surface tension and contact angle measurements were performed. The surface tension of neat RO at 20 °C and 75 °C is 33.0 mN m<sup>-1</sup> and 29.3 mN m<sup>-1</sup>, respectively, similar to the values of Xu *et al.*<sup>45</sup> Figure 7.5(a) gives the air-RO surface tension at both 75 °C (one-phase) and 20 °C (two-phase) as a function of surfactant concentration. At 75 °C, the surface tension decreases gradually with C-1803 concentration until reaching a nearly constant value of ~ 23.0 mN m<sup>-1</sup> at ~ 0.13 wt.%, revealing the potential surface activity of molecular C-1803 at the air-oil interface,<sup>32,45</sup> the interfacial adsorption mode of which has been explained elsewhere.<sup>32</sup> However, at 20 °C the surface tensions of oil dispersions containing crystals are the same as that of neat RO, indicating that C-1803 crystals do not adsorb spontaneously to the air-oil interface or are too large to make any difference.<sup>32</sup>

The contact angle measurements were done using disks of compressed C-1803 powder at 20 °C. The contact angle of a drop of RO in air through RO is *ca.* 48°, implying preference for a/o foams, Figure 7.5(b).<sup>25</sup> The oil-water contact angle measured through water is *ca.* 150° hinting that the favoured emulsion is w/o, Figure 7.5(c).<sup>46</sup>

**Figure 7.5.** (a) Air-oil surface tension of C-1803-RO mixtures at 20 °C (○) and 75 °C (●). Surface tension of neat RO at 20 °C and 75 °C is 33.0 mN m<sup>-1</sup> and 29.3 mN m<sup>-1</sup>, respectively. Contact angle of (b) a RO droplet in air or (c) a water droplet in RO on compressed disks of C-1803 at 20 °C. Inset: photographs of top (upper) and side (lower) view of a compressed disk of C-1803 powder.



## 7.4 Preparation and characterisation of various colloidal materials with sucrose ester

### 7.4.1 Oil and aqueous foams

To prepare stable oil foams, 5 wt.% C-1803 in RO was heated to 90 °C followed by gradual cooling at 1 °C min<sup>-1</sup>. Once reaching 80 °C, the oil solutions of C-1803 molecules were whipped continuously for 10 min. To enhance foam stability, the fresh foams were subjected to rapid cooling ( $\sim 4$  °C min<sup>-1</sup>) followed by storing in a fridge ( $7 \pm 1$  °C).<sup>32</sup> Figure 7.6(a) gives the photographs of RO containing 5 wt.% C-1803 before and soon after 10 min whipping at 80 °C. The sample at 80 °C before whipping is a clear solution. The foam volume increases rapidly as a function of whipping time, and the value of the over-run after 10 min whipping can reach 200% (air volume fraction = 0.67). In terms of the stability of the cooled foam,  $\sim 95$  vol% of the foam remains relative to that initially after 1 month storage at 7 °C. Moreover, the average bubble diameter ( $27.5 \pm 12.5$   $\mu\text{m}$ ) remains almost unchanged on storage, indicating the absence of coarsening/coalescence ( $p > 0.05$ ). A photo of the foam after 1 month storage at 7 °C and a microscopy image are given in Figure 7.6(c1) and (e1), respectively. More microscopy images can be found in Figure 7.7. The creamy foam behaves as a firm gel and non-spherical bubbles encased by a compact crystal layer(s) are evident. To explore the capacity of such stable foams against external mechanical forces, a foam was subjected to relatively vigorous homogenisation (3,400 rpm) for 2 min at 20 °C. The solid-like sample deteriorates into a flowable, viscous paste with the application of homogenisation (Figure 7.6(c2)). In addition, the average bubble diameter decreases from  $27.5 \pm 12.5$   $\mu\text{m}$  initially to  $10.7 \pm 3.3$   $\mu\text{m}$  (Figure 7.6(e2),  $p < 0.05$ ). We admit that some of the air bubbles are sacrificed releasing from the oil matrix during this process, however, many non-spherical bubbles with rough surfaces can still be observed. Furthermore, the letters, *e.g.* ‘A’ and ‘B’, can be created by forcing a foam through a syringe illustrating the processability and structural recovery of those stable foams, Figure 7.6(d).

Attempts were made to prepare aqueous foams from mixtures of C-1803 and water. The mixtures were heated to 80 °C for 30 min under magnetic stirring (150 rpm) and then cooled gradually to 20 °C. C-1803 powder cannot be fully dissolved into water at 80 °C due to its relatively lipophilic nature. However, aqueous foams can still be made from the mixtures containing high enough surfactant concentration at 20 °C. The representative photos of an aqueous foam containing 0.7 wt.% C-1803 during storage at 20 °C are shown in Figure 7.6(b).  $\sim 15$  mL of foam can be generated from 20 mL of aqueous dispersion through 1 min hand shaking. After 1 week aging,  $\sim 9$  mL of the foam remains.

**Figure 7.6.** (a) Photographs of RO containing 5 wt.% C-1803 before and immediately after 10 min whipping at 80 °C. (b) Photographs of aqueous foam containing 0.7 wt.% C-1803 initially and after 1 week storage at 20 °C. Aqueous dispersion of C-1803 was submitted to hand shaking for 1 min then stored at 20 °C. Photographs of RO foams containing 5 wt.% C-1803 (c1) before and (c2) after 2 min homogenisation (3,400 rpm) at 20 °C. RO foam prepared at 80 °C was submitted to rapid cooling in an ice bath of -5 °C followed by storing at 7 °C for 1 month. (d) Photographs of RO foam from (c1) forced through a syringe. Scale bars equal 1 cm for photos. Optical micrographs of (e1) foam from (c1) and (e2) foam from (c2). Inset: schematic illustrating a/o foam with *in situ* formed C-1803 crystals. (f) Optical micrographs of aqueous foam from (b). Inset: schematic illustrating a/w foam with C-1803 molecules.

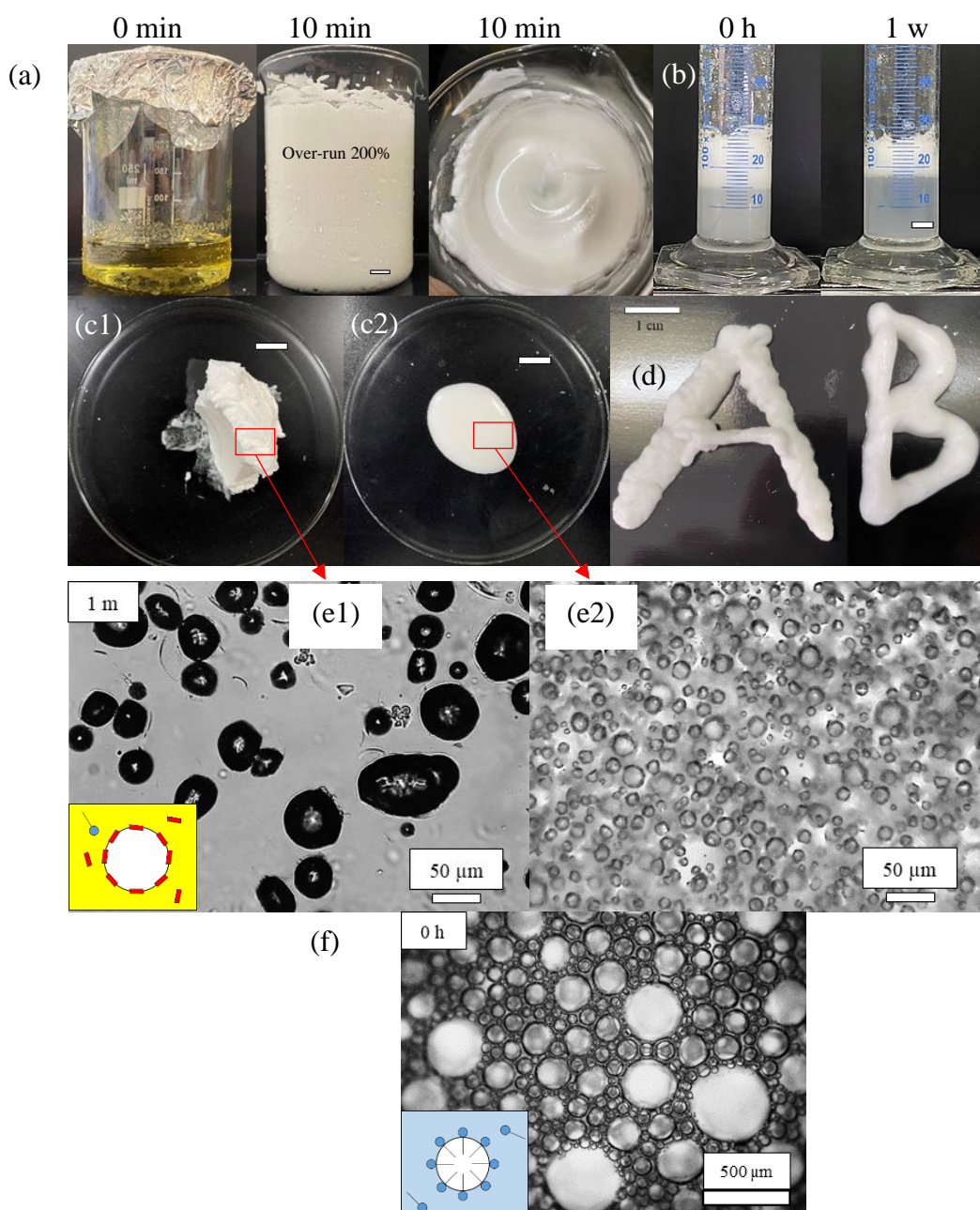
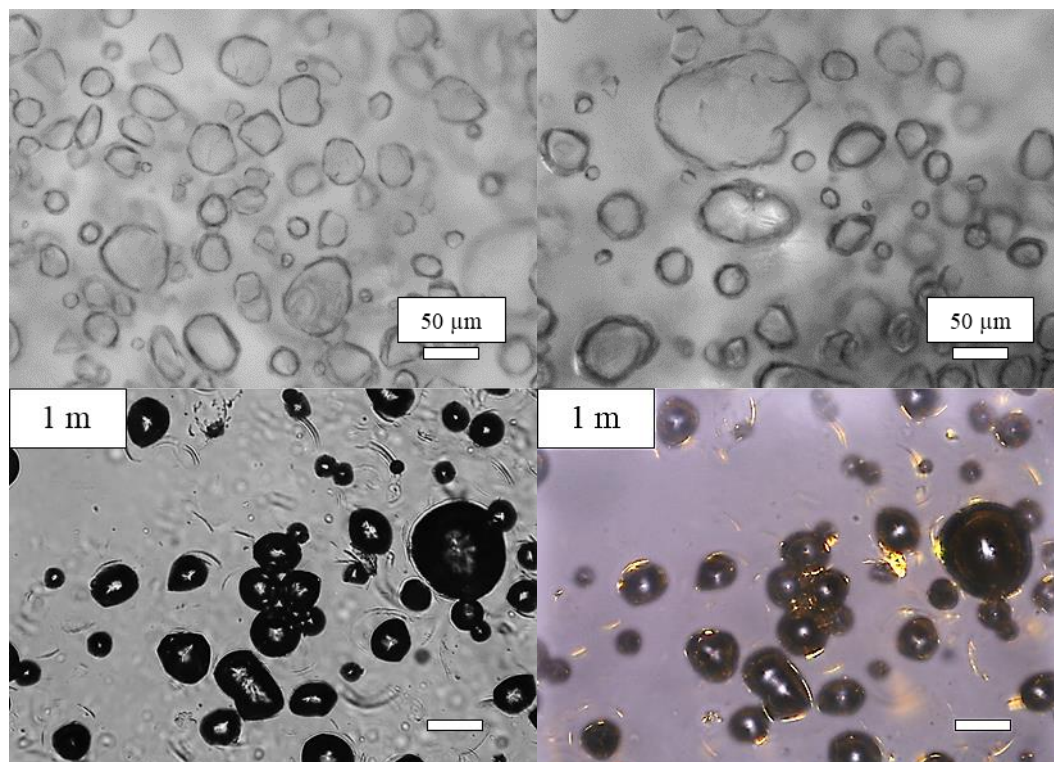
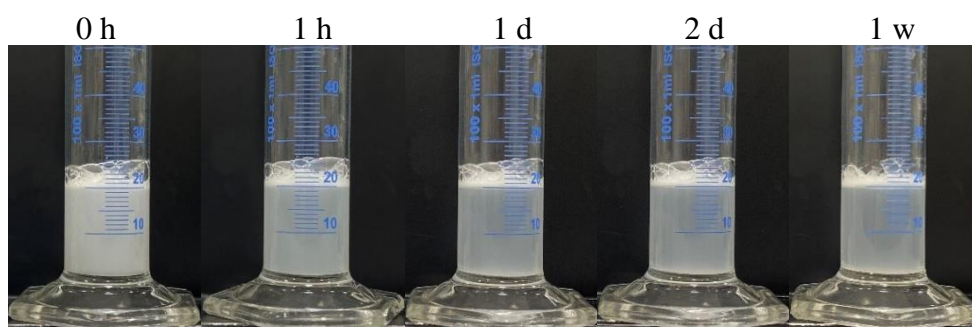


**Figure 7.7.** Optical microscopy images of a/o foam for systems in Figure 7.6(c1) after 1 month storage at 7 °C. Non-polarised (left) and polarised (right) images are presented for the last row.



The appearance of an aqueous foam containing 0.07 wt.% C-1803 is given in Figure 7.8. In comparison with a common anionic surfactant (*e.g.* sodium dodecyl sulfate (SDS)), the foamability of C-1803 in water is much lower. This is due to a lower level of dynamic adsorption of surfactant molecules at the surface.<sup>47</sup> By contrast, the stability of C-1803 foam is far better than SDS foam, possibly arising from the formation of bulky surfactant self-assemblies or crystalline particles in the continuous phase.<sup>47,48</sup> Figure 7.6(f) presents the microscopy image of the foam containing 0.7 wt.% C-1803. The bubbles are polydisperse and spherical with smooth surfaces.

**Figure 7.8.** Appearance of aqueous foam containing 0.07 wt.% C-1803 during storage at 20 °C.



#### 7.4.2 Simple and multiple emulsions

Two strategies were introduced to prepare simple emulsions from equal volumes of water and RO with C-1803. (i) An oil solution of C-1803 at 80 °C was transferred to a glass vial containing water at the same temperature, and then homogenized at 10,000 rpm for 2 min at 80 °C. The fresh emulsion was then quenched statically to 20 °C, followed by storing at the same temperature. (ii) Two glass vials containing water and an oil solution of C-1803 at 80 °C were cooled gradually to 20 °C, respectively. The latter sample was transferred into the former, followed by homogenizing at 10,000 rpm for 2 min at 20 °C.

For emulsions containing 2.5 w/v% C-1803, they are always o/w when prepared at 80 °C then cooled statically to 20 °C, (Figure 7.9(a) and (b)). Emulsion creaming occurs liberating a water phase (10-15 vol.% relative to the total emulsion) within the first 5 min after homogenisation. No resolved oil can be observed for at least 4 weeks, indicating that the emulsion is stable to coalescence.<sup>46</sup> Interestingly, the o/w emulsion behaves as a firm gel without any flow when inverted at 20 °C. This phenomenon will be discussed later. By contrast, the emulsion fabricated at 20 °C cooled from 80 °C is w/o (Figure 7.9(c)), correlating well with the water-oil contact angle results (Figure 7.5(c)). The w/o emulsion can gel within the first week on storage at 20 °C. Nevertheless, sedimentation liberates an upper oil phase (5-10 vol.%) after one week aging. The emulsion is stable to coalescence for at least 4 weeks without resolved water. The relationship between the emulsion type and temperature for systems containing a common nonionic surfactant (pentaethylene glycol monododecyl ether, C<sub>12</sub>E<sub>5</sub>) has been elucidated by Binks.<sup>49</sup> He found that the emulsions were inverted from o/w to w/o with increasing temperature at reasonably high surfactant concentrations, which contradicts our finding herein, *i.e.* w/o to o/w with increasing temperature. This difference is explained as follows. It has been shown that the *in situ* packing parameter of a surfactant at the oil-water interface determines the emulsion type, which can be affected by several factors such as the temperature, salt concentration and oil type.<sup>1</sup> For our systems at high temperature, *e.g.* 80 °C, the sucrose heads of C-1803 show strong affinity for water molecules through the intermolecular H-bonding of hydroxyl groups,<sup>50</sup> thus potentially favouring o/w emulsions. Upon decreasing to a reasonably low temperature, the interactions between sucrose heads and water molecules weaken since the solubility of sucrose in water decreases,<sup>50</sup> alongside the formation of comparatively lipophilic C-1803 crystals (Figure 7.5(c)), thereby preferring w/o emulsions.

As an example, the optical microscopy images of o/w and w/o emulsions containing 2.5 w/v% C-1803 are presented in Figure 7.9(d) and (e), respectively. More images are displayed in Figure 7.10. For the o/w emulsion, spherical oil droplets are in close proximity. In addition, the presence of birefringent crystals is revealed by polarised microscopy. C-1803 crystals (bright) can be identified within the oil droplets because of bulk nucleation and crystallisation induced by rapid cooling.<sup>51</sup> Nevertheless, it is impossible to discern any specific crystallization at the droplet interfaces due to massive crystallisation of C-1803 and relatively small droplet diameter. So, the interfacial nucleation and crystallisation of C-1803 cannot be ruled out.<sup>51</sup> It is worth clarifying that the halos around the oil droplets is due to the wall effect caused by liquid interfaces.<sup>18</sup> During storage, growing C-1803 crystals may protrude through aqueous films causing partial drop-drop coalescence.<sup>51</sup> In the case of the w/o emulsion, water droplet surfaces are rough and textured and some of them are non-spherical due to the adsorption of preformed C-1803 crystals at droplet surfaces.<sup>16-18</sup> Besides, birefringent crystals coating the droplets and partitioning in the continuous phase can be identified by polarised microscopy. The oil droplets of the o/w emulsion are relatively monodisperse and the average droplet diameter initially is  $13.9 \pm 3.5 \mu\text{m}$ . After 2 weeks aging at 20 °C, the droplet diameter increases to  $33.3 \pm 8.0 \mu\text{m}$  on account of partial coalescence/disproportionation ( $p < 0.05$ ).<sup>51</sup> By contrast, the water droplets of the w/o emulsion prepared at 20 °C are more polydisperse with the diameter ( $57.0 \pm 30.8 \mu\text{m}$ ) much larger than that of the former emulsion ( $p < 0.05$ ). Their diameter remains almost unchanged on storage.

Based on the optical microscopy images, the plausible explanations for the gelation phenomenon above are described as follows. For the o/w emulsions, when many oil droplets are in close contact with each other on storage, a 3D colloidal network can be formed during which oil droplets containing *in situ* formed surfactant crystals (*i.e.* solidified droplets) can increase the viscosity dramatically even leading to complete gelation.<sup>51,52</sup> In the case of the w/o emulsions, crystal-coated water droplets may act as ‘active fillers’ that can interact with the surrounding crystal matrix and adjacent droplets *via* interfacial crystallisation and sintering, leading to a more rigid emulsion network.<sup>18,53</sup>

**Figure 7.9.** Appearance of simple emulsions containing 2.5 w/v% C-1803 fabricated through different protocols. (a) Immediately after 2 min homogenisation at 80 °C, (b) 2 min homogenisation at 80 °C then cooled and stored at 20 °C, (c) 2 min homogenisation at 20 °C then stored at the same temperature. Scale bars = 1 cm. Non-polarised (left) and polarised (right) microscopy images. (d) o/w emulsion from (b). Inset: schematic illustrating oil dispersion-in-water emulsion with *in situ* formed C-1803 crystals; photo of fresh o/w emulsion. (e) w/o emulsion from (c). Inset: schematic illustrating water-in-oil emulsion with pre-formed C-1803 crystals (left); photo of fresh w/o emulsion.

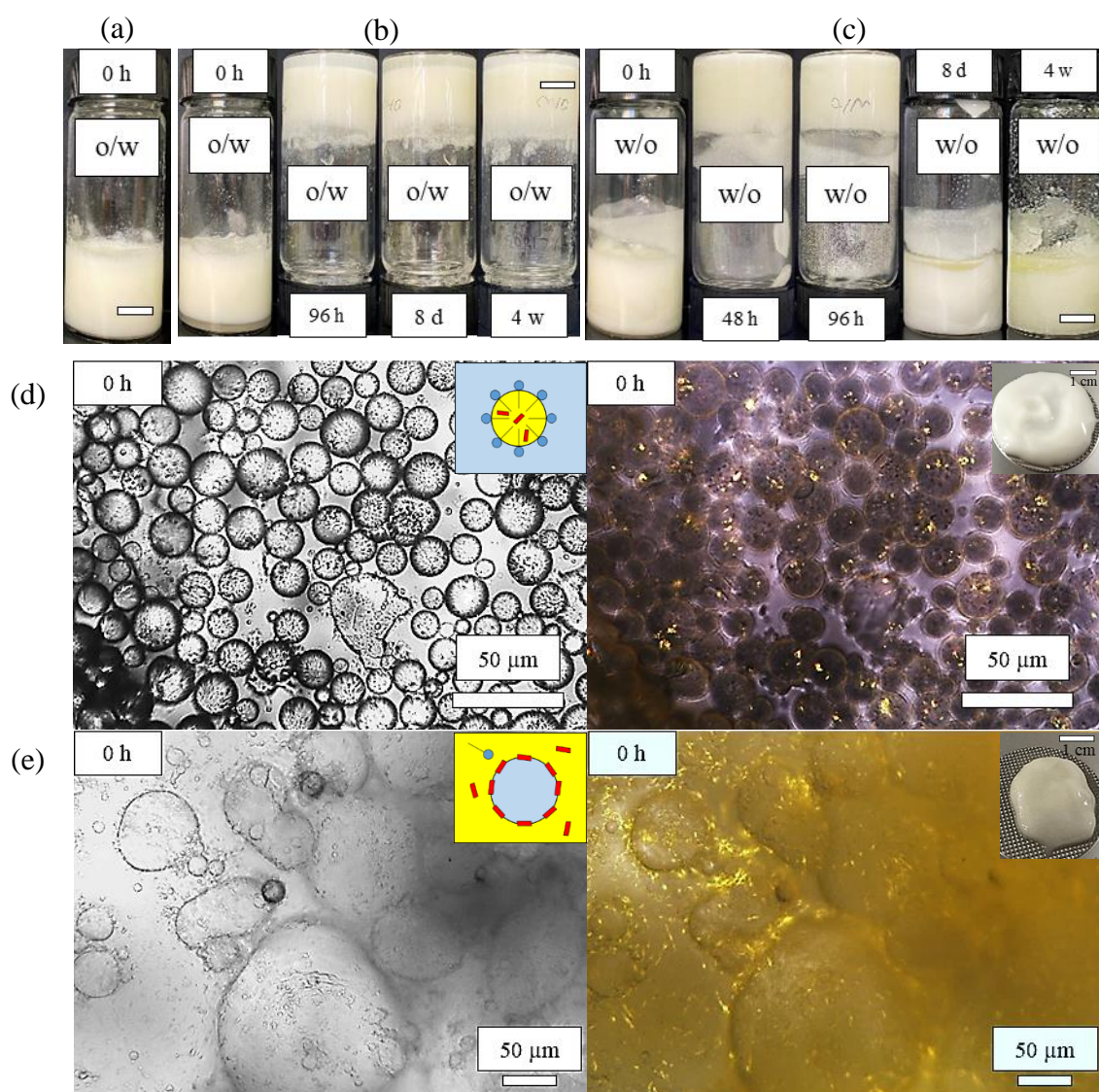
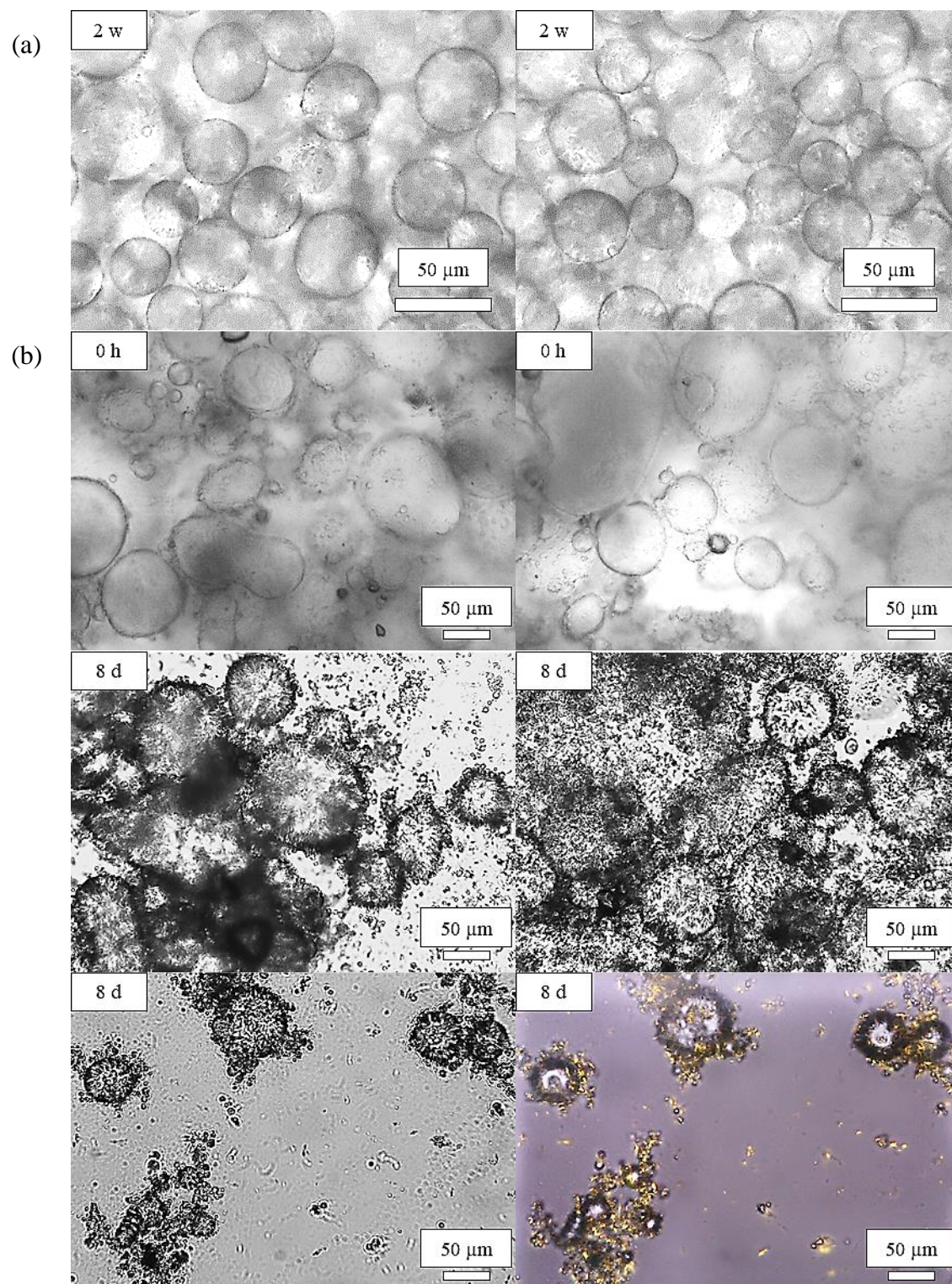


**Figure 7.10.** Optical microscopy images of (a) o/w and (b) w/o emulsions for systems in Figure 7.9. Non-polarised (left) and polarised (right) images are presented for the last row.



Based on the above findings, it is interesting to ask whether multiple emulsions can be made using C-1803 alone. We found that o/w/o emulsions can be fabricated by introducing 5 wt.% C-1803 in RO dispersions to o/w emulsions containing 2.5 w/v% C-1803 (Figure 7.9(b)) at 20 °C, followed by magnetic stirring. Figure 7.11(a) provides the appearance of a multiple emulsion as a function of storage time at 20 °C. Phase separation occurs gradually within the first 48 h on aging liberating a transparent oil phase arising from emulsion sedimentation.<sup>46</sup> Afterwards, no observable change occurs for more than 4 weeks. The normalised volume of multiple emulsion or resolved oil, defined as the volume ratio of emulsion/resolved oil on storage relative to the initial emulsion, is given in Figure 7.11(b) against storage time. The inset microscopy image of the sample reveals that water globules containing oil droplets are polydisperse with the diameter of  $121 \pm 53 \mu\text{m}$ . The average water globule diameter remains more or less unchanged after 2 months storage at 20 °C ( $125 \pm 56 \mu\text{m}$ ), see Figure 7.12. The non-polarised and polarised images of one representative water globule are shown in Figure 7.11(c). Many small oil droplets are encased within the relatively large water globule. The exterior water-oil interface is endowed by a dense population of C-1803 crystals.<sup>16</sup> Moreover, excess crystals in the exterior continuous phase can contribute to bulk stabilisation.<sup>16</sup> More optical microscopy images and one selected cryo-SEM image of the o/w/o emulsion can be found in Figure 7.12 and Figure 7.13, respectively.

**Figure 7.11.** Appearance of o/w/o emulsion during storage at 20 °C. (a) Photographs and schematic. Scale bar = 1 cm. (b) Normalised volume of multiple emulsion (●) and normalised volume of resolved oil (○) against storage time. Inset: optical micrograph; schematic illustrating o/w/o emulsion with C-1803 crystals and molecules. (c) Non-polarised (left) and polarised (right) microscopy images. Mixtures of o/w emulsion from Figure 7.9(b) and 5 wt.% C-1803 in RO dispersion cooled from 90 °C were submitted to magnetic stirring (300 rpm) for 2 min at 20 °C.

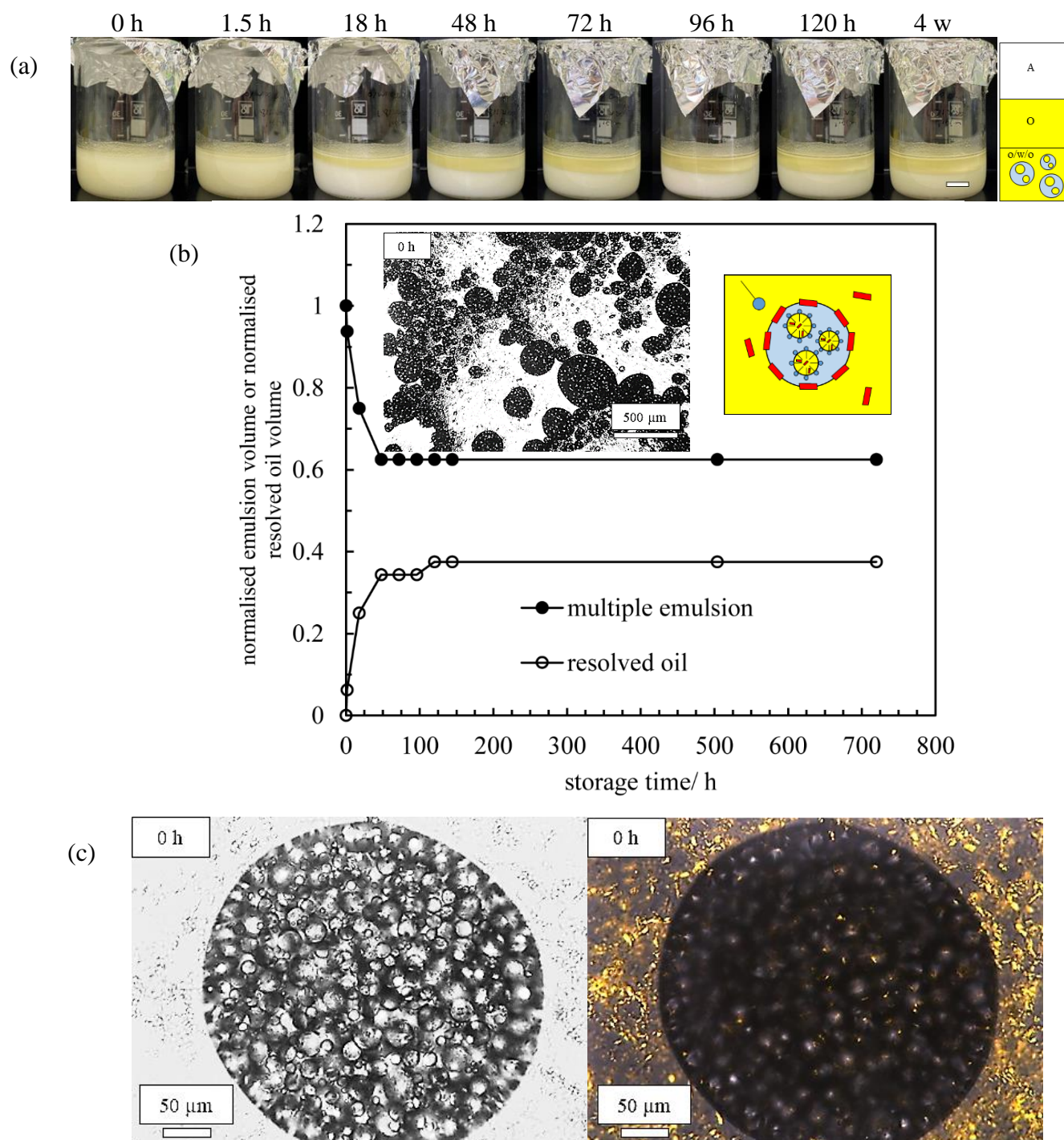


**Figure 7.12.** Optical microscopy images of o/w/o emulsion during storage at 20 °C for systems in Figure 7.11. Both non-polarised (left) and polarised (right) micrographs are presented for row 1-3.

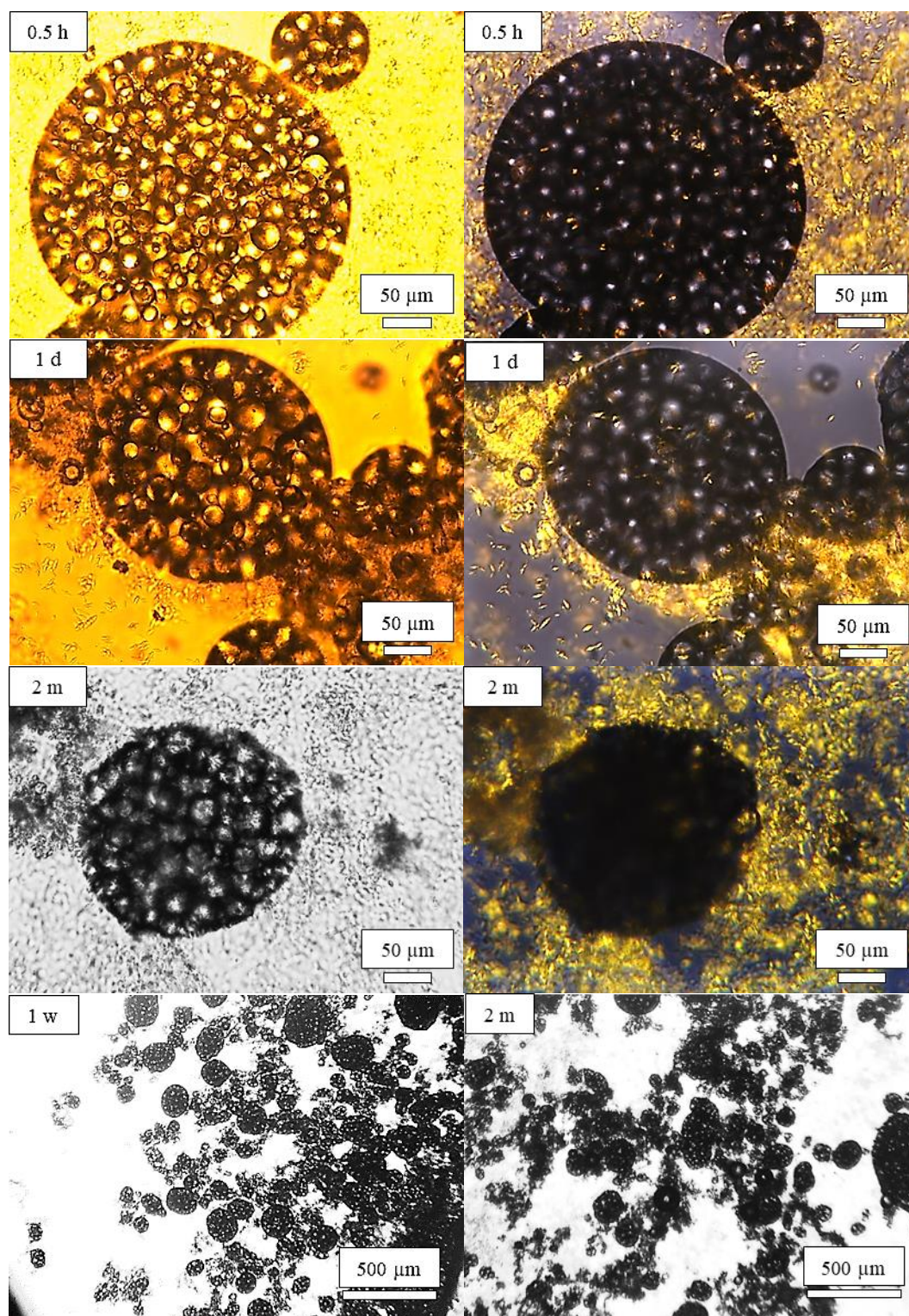
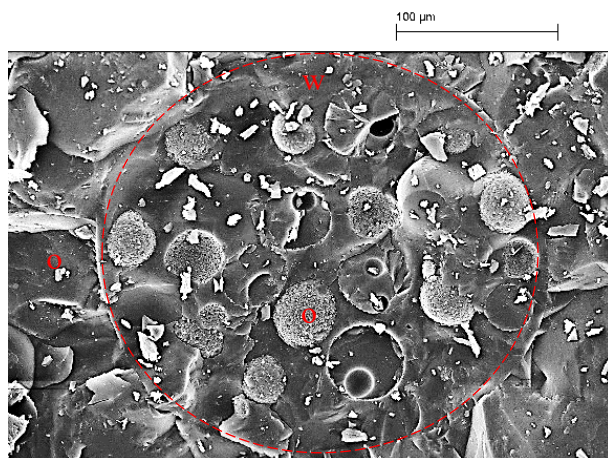


**Figure 7.13.** Cryo-SEM image of o/w/o emulsion for systems in Figure 7.11. One water globule containing small oil droplets is highlighted.



#### 7.4.3 Foamulsions and aerated emulsions

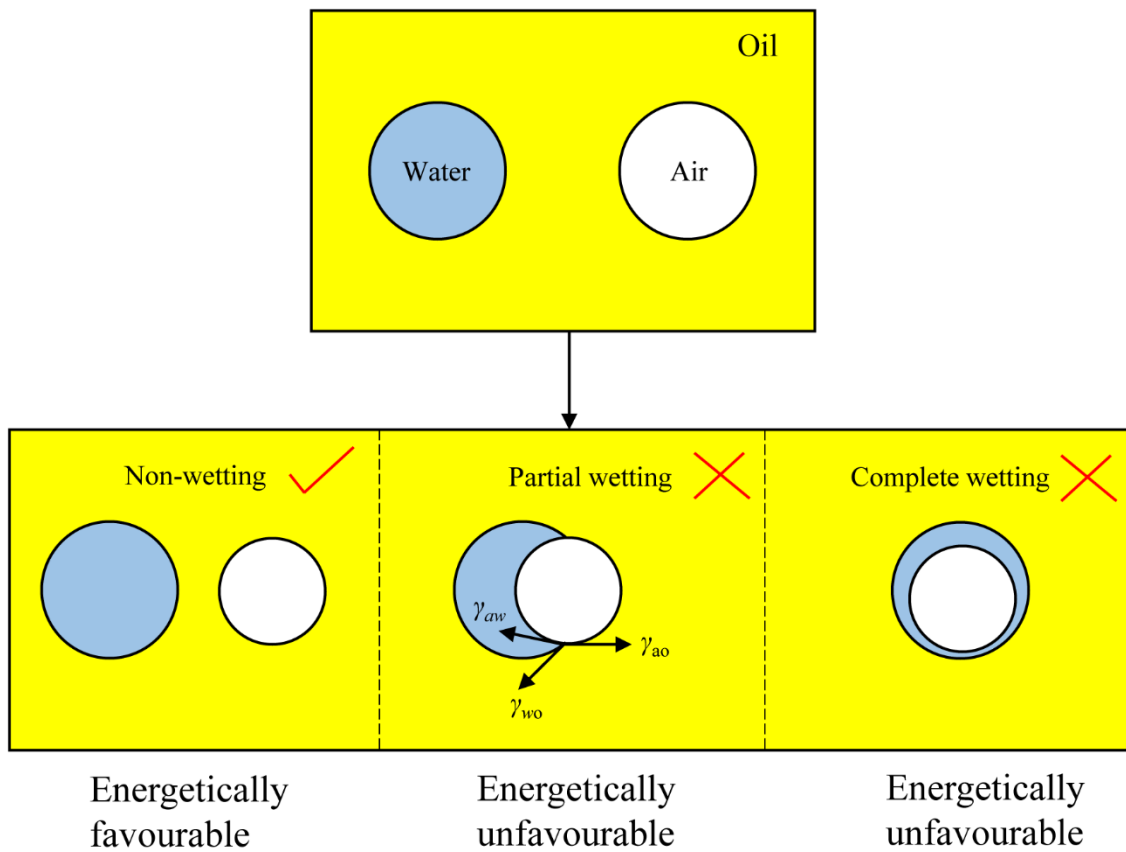
The introduction of air bubbles into emulsions or droplets into foams to make foamulsions is gaining growing interest.<sup>13,14,54</sup> To prepare foamulsions, a single-step or two-step mixing protocol is commonly adopted using a single surfactant or mixtures of stabilisers.<sup>13,14</sup> By now, most of the investigated foamed emulsions are based on the aqueous continuous phase. As mentioned earlier, both stable a/o foams (Figure 7.6) and w/o emulsions (Figure 7.9) by C-1803 crystals can be prepared in our systems. Considering this fact, one may ask if it is feasible to fabricate stable foamed emulsions using C-1803 whereby oil is the continuous phase? Theoretically, the formation of single droplet-bubble mixture in continuous oil is energetically favourable.<sup>54,55</sup> The spreading coefficient of a fluid  $i$  at the interface of two immiscible fluids  $j$  and  $k$  can be expressed as:

$$s_i = \gamma_{jk} - (\gamma_{ij} + \gamma_{ik}) \quad (7.1)$$

If  $s > 0$ , spreading occurs spontaneously. Herein the water-air interface cannot form spontaneously in oil ( $s_o > 0$ ,  $s_w < 0$ ,  $s_a < 0$ ) due to relatively high air-water surface tension. The subscripts a, o and w denote air, oil, and water, respectively. The possible wetting morphology of a water droplet and an air bubble in continuous oil is presented in Figure 7.14. On the other hand, Wan *et al.*<sup>13</sup> reported that stable foamulsions could be produced by emulsifying and aerating in a single step at high temperature followed by rapid cooling for the mixtures of the glycyrrhizic acid, water and sunflower oil. On this initiative, we firstly tried homogenising a mixture of water and RO solutions/dispersions containing 2.5 w/v % C-1803 at 80 °C and 20 °C, respectively (not shown). At 80 °C, aeration and emulsification could be achieved

simultaneously upon homogenisation (10,000 rpm). However, the incorporated air bubbles creamed upwards rapidly resolving an emulsion and then collapsed rapidly after homogenisation (< 1 min). Upon homogenisation at 20 °C, no air bubbles could be incorporated. The initial experiments demonstrate that the one-step protocol to prepare foamulsions is unachievable with our systems.

**Figure 7.14.** Possible wetting behaviour of a water droplet and an air bubble in continuous oil. The spreading coefficient of a fluid  $i$  at the interface of two immiscible fluids  $j$  and  $k$  can be expressed as:  $s_i = \gamma_{jk} - (\gamma_{ij} + \gamma_{ik})$ . If  $s > 0$ , spreading occurs spontaneously. Herein the water-air interface cannot form spontaneously in oil ( $s_o > 0$ ,  $s_w < 0$ ,  $s_a < 0$ ) due to relatively high air-water surface tension. The subscripts a, o and w denote air, oil, and water, respectively. The interfacial tensions of air-water, water-rapeseed oil and air-rapeseed oil at 20 °C are 72.5 mN m<sup>-1</sup>, 20.8 mN m<sup>-1</sup> and 33.0 mN m<sup>-1</sup>, respectively.



$$S_o = \gamma_{aw} - (\gamma_{wo} + \gamma_{ao}) = 72.5 - (20.8 + 33.0) = 18.7 \text{ mN m}^{-1} > 0$$

$$S_w = \gamma_{ao} - (\gamma_{wo} + \gamma_{aw}) = 33.0 - (20.8 + 72.5) = -60.3 \text{ mN m}^{-1} < 0$$

$$S_a = \gamma_{wo} - (\gamma_{ao} + \gamma_{aw}) = 20.8 - (33.0 + 72.5) = -84.7 \text{ mN m}^{-1} < 0$$

Considering this, the multiple-step protocol was adopted. The a/o foams (Figure 7.6) were mixed with the w/o emulsions (Figure 7.9) under gentle magnetic stirring or relatively vigorous homogenisation at 20 °C. The former stirring method was unsuccessful since obvious phase separation occurs immediately after preparation. Surprisingly, stable foamulsions encasing many air bubbles can be rendered for the latter strategy, behaving as a firm gel. Herein we acknowledge that some of the incorporated air bubbles are possibly destroyed during vigorous homogenisation. As an example, a stable foamulsion made by homogenising (3,400 rpm) the mixture of the a/o foam (1.6 g) and the w/o emulsion (8 g) at 20 °C is shown in Figure 7.15(a) and as an inset in Figure 7.15(c). No change in the sample appearance can be observed for more than 1 month. The normalised volume of foamulsion or drained oil, defined as the volume ratio of foamulsion/drained oil during storage relative to the initial foamulsion, is presented in Figure 7.16 as a function of storage time. From the optical microscopy images of the foamulsion (Figure 7.15(c)), water droplets and air bubbles (black halos) can be identified. Besides, their surfaces are wrinkled and many of them are non-spherical. The average bubble diameter of the foamulsion initially and after 1 month storage at 20 °C is  $27.2 \pm 14.8 \mu\text{m}$  and  $30.0 \pm 15.0 \mu\text{m}$ , respectively, comparable to that of the original foam. The determination of the average droplet diameter is unachievable due to the ambiguous interface and the complexity of the mixed system. According to previous studies,<sup>13,18,20</sup> we propose that crystal-coated water droplets and air bubbles in the foamulsions may work synergistically as ‘active fillers’, thereby contributing to an increase in the network rigidity. More discussion regarding this can be found later.

**Figure 7.15.** Photographs and schematic of (a) foamulsion and (b) a/o/w emulsion during storage at 20 °C. Scale bars = 1 cm. (c) Optical micrographs of foamulsion from (a). Inset: schematic illustrating foamulsion with C-1803 crystals; photo' of fresh foamulsion. (d) Optical micrographs of a/o/w emulsion from (b). Inset: schematic illustrating a/o/w emulsion with C-1803 crystals and molecules. The dispersed phase with black halos is air bubbles. For foamulsion, mixtures of w/o emulsion from Figure 7.9(c) and a/o foam from Figure 7.6(c) were homogenised (3,400 rpm) for 2 min at 20 °C. For a/o/w emulsion, mixtures of aqueous dispersion with 5 wt.% C-1803 and a/o foam from Figure 7.6(c) were magnetically stirred (800 rpm) for 2 min at 20 °C.

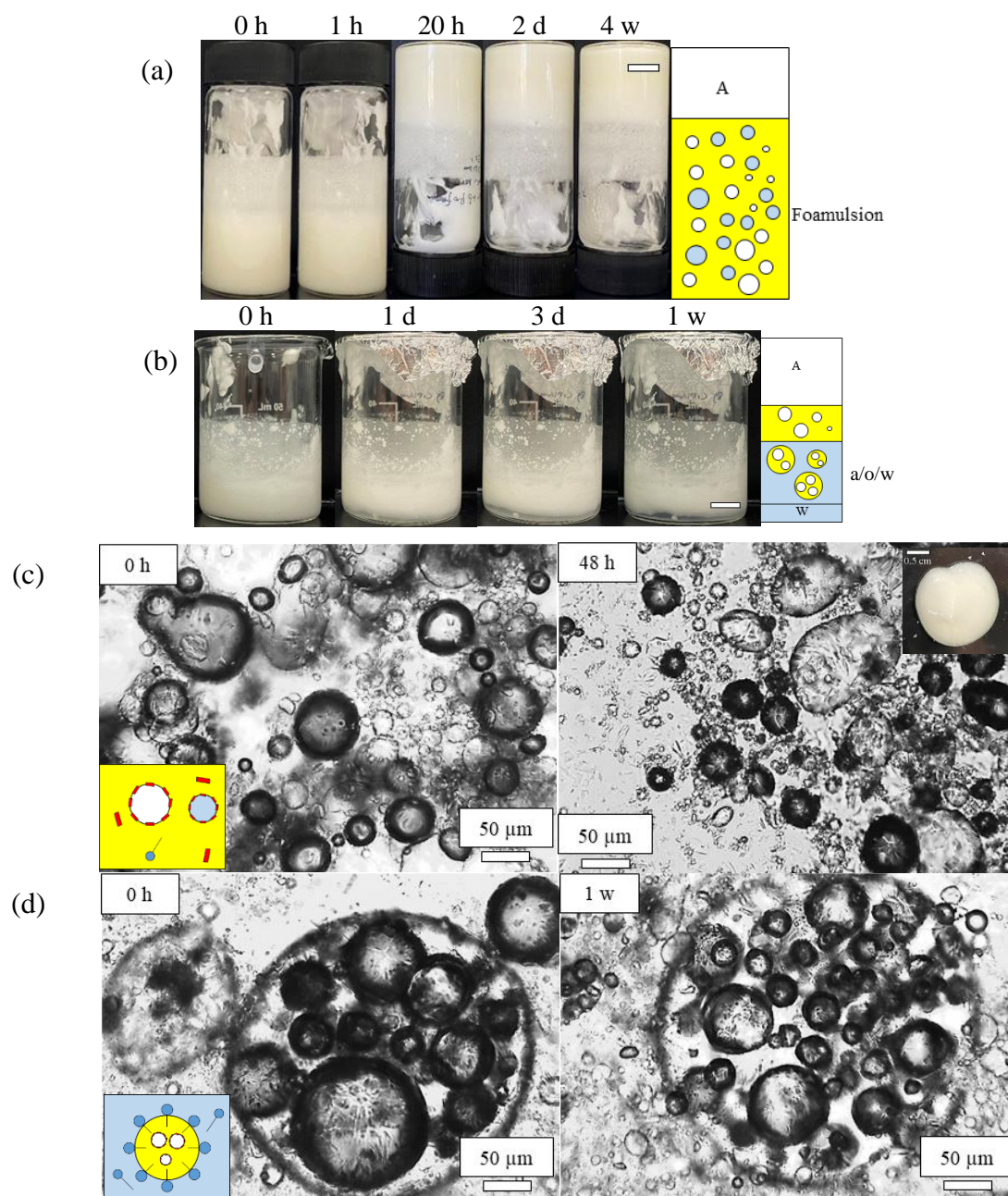
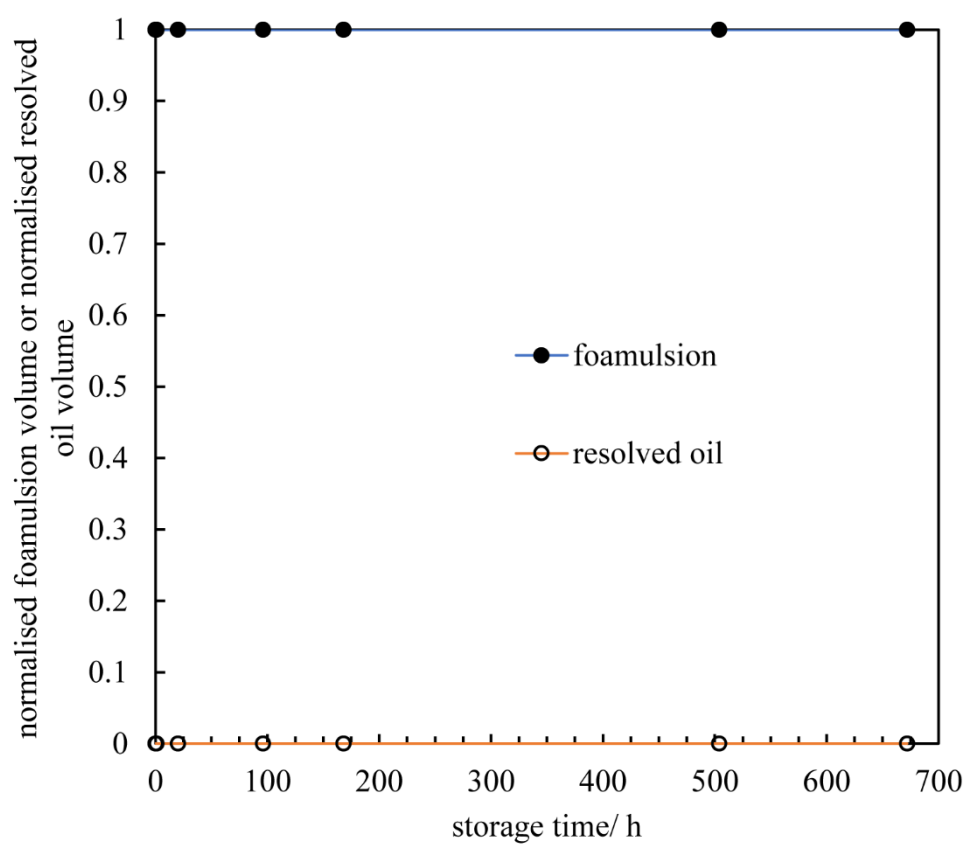
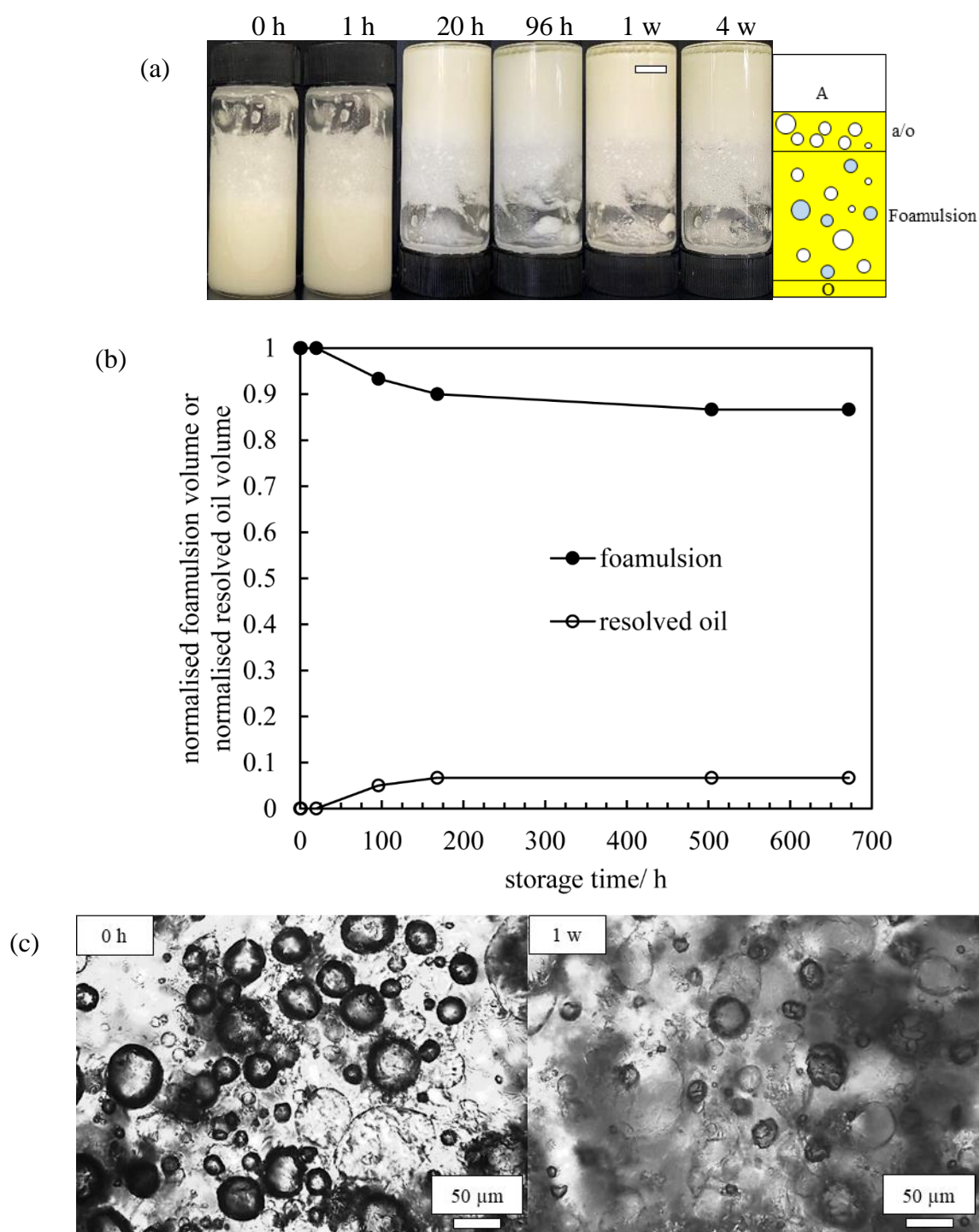


**Figure 7.16.** Normalised volume of foamulsion (●) and normalised volume of resolved oil (○) against storage time for systems in Figure 7.15(a).



When more foam (2.67 g) was homogenised with the w/o emulsion (8 g), a higher volume of gelled foamulsion can be yielded, Figure 7.17. Concerning long-term storage at 20 °C, limited (< 7 vol.%) drained oil and creamed oil foam can be visualised at the bottom and top of the vessel, respectively.

**Figure 7.17.** Appearance of foamulsion during storage at 20 °C. (a) Photographs and schematic. Scale bar = 1 cm. (b) Normalised volume of foamulsion (●) and normalised volume of resolved oil (○) against storage time. (c) Optical microscopy images. Mixtures of w/o emulsion from Figure 7.9(c) and a/o foam from Figure 7.6(c) were homogenised (3,400 rpm) for 2 min at 20 °C.



When dispersing a/o foams stabilised by surfactant crystals into viscous aqueous dispersions containing various hydrophilic emulsifiers and thickening agents, novel a/o/w emulsions were obtained.<sup>20,29</sup> The major drawback of the existing systems however is that so many emulsifiers are involved during the emulsification process, making it difficult to probe into the underlying stabilisation mechanisms; the synergistic interactions between different species are still unclear. Herein we tried on preparing a/o/w emulsions using C-1803 alone. For droplet deformation and rupturing to occur, the applied shear stress  $\eta_c \dot{\gamma}$  must be sufficiently high,  $\eta_c$  being the viscosity of the aqueous phase and  $\dot{\gamma}$  being the applied shear rate.<sup>20,29</sup> However, it should not be excessive to avoid the disruption of air bubbles entrapped within oil globules.<sup>20,29</sup> RO foams containing 5 wt.% C-1803 (1.6 g) cooled from 80 °C were transferred gradually to aqueous dispersions with 5 wt.% C-1803 (8 g) under manual stirring. Subsequently, the mixtures were submitted to magnetic stirring at 20 °C. For the emulsion made at 400 rpm (Figure 7.18), only a limited fraction of the initial oil foam (< 10 vol.%) was dispersed into the external aqueous phase. From the optical microscopy images, few oil globules containing air bubbles can be evidenced. When the shear rate was increased to 800 rpm, most of the oil foam can be dispersed and further stabilised in the aqueous phase. During storage at 20 °C (Figure 7.15(b)), oil globules tend to cream upwards liberating an aqueous phase due to the density mismatch between the globules containing air bubbles and the aqueous phase and the relatively large globule size ( $\leq 500 \mu\text{m}$ ). Moreover, the a/o/w emulsion suffers other types of aging, *e.g.* coalescence and Ostwald ripening between oil globules, air bubbles and globule surfaces.<sup>29</sup> The air-in-oil-in-water morphology can still be observed after 1 week aging at 20 °C, Figure 7.15(d) and Figure 7.19. How to improve the stability of a/o/w emulsions is worthy of further investigation.

**Figure 7.18.** Appearance of a/o/w emulsion during storage at 20 °C. (a) Photographs. Scale bar = 1 cm. (b) Optical microscopy images. Mixtures of aqueous dispersion with 5 wt.% C-1803 at 20 °C and a/o foam from Figure 7.6(c) were magnetically stirred (400 rpm) for 2 min at 20 °C.

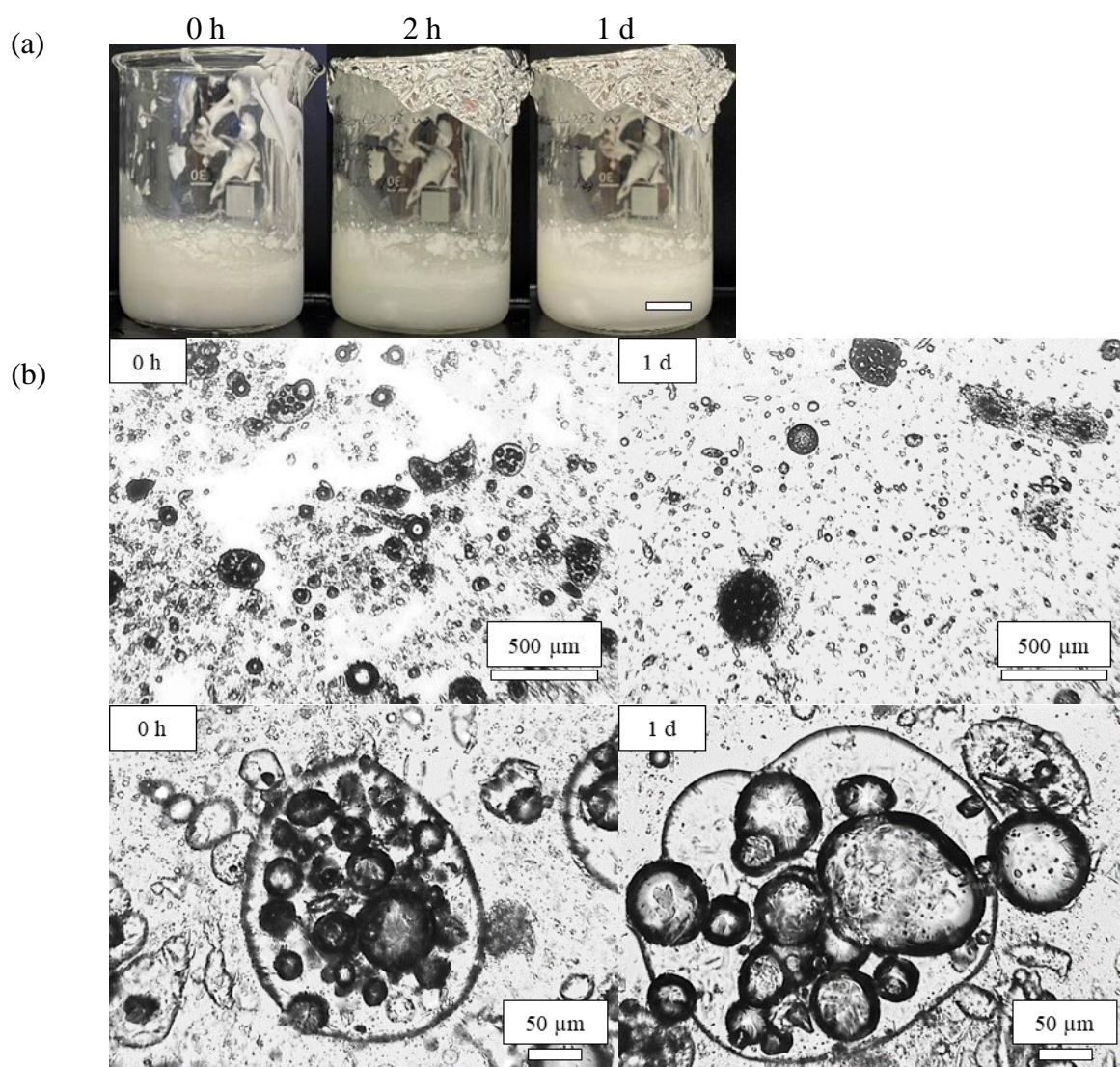
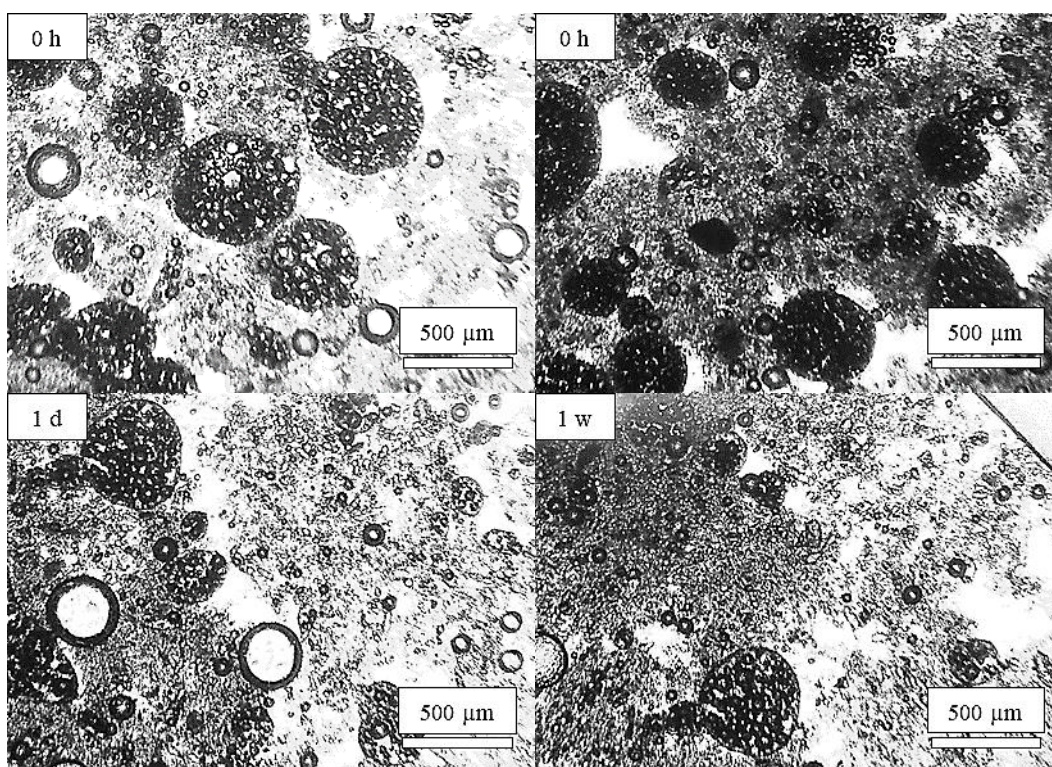


**Figure 7.19.** Optical microscopy images of a/o/w emulsion for systems in Figure 7.15(b).

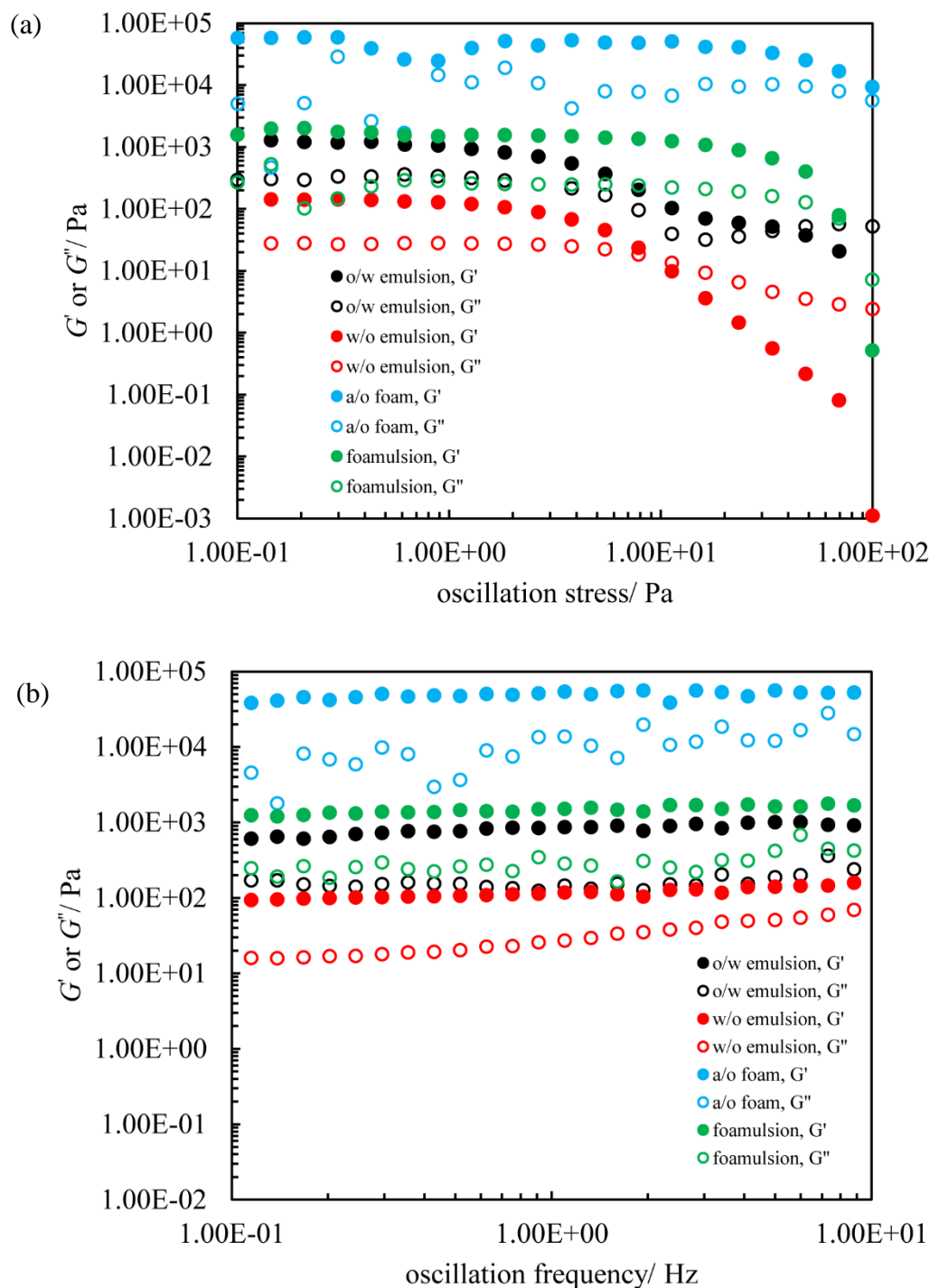


#### 7.4.4 Rheology, polymorphs and thermal properties

The rheological properties of various gelled colloidal materials mentioned above were investigated by amplitude sweep and frequency sweep experiments, Figure 7.20. From the amplitude sweep for all samples, the elastic modulus ( $G'$ ) is always higher than the viscous modulus ( $G''$ ) within the linear viscoelastic region (LVR), indicating the formation of an elastic solid-like network.<sup>56</sup> Above a certain oscillation stress, both parameters decay gradually until reaching  $G' < G''$ , reflecting the gel-sol transition.<sup>56</sup> The yield stress ( $\tau_Y$ ) where  $G' = G''$  and  $G'$  within the LVR both increase in the order w/o emulsions < o/w emulsions < foamulsions < oil foams, mirroring our visual observations. Ducloué *et al.*<sup>57</sup> demonstrated that the elasticity of a foamed emulsion was governed by two dimensionless parameters, *i.e.* the gas volume fraction and the capillary number  $Ca$  quantifying the competition between the elasticity of the emulsion matrix and the deformability of bubbles.  $Ca = \frac{G'_o}{2\gamma_{la}/r}$ , where  $G'_o$  is the elastic modulus of the continuous emulsion phase,  $\gamma_{la}$  is the interfacial tension between air and the continuous phase and  $r$  is the bubble radius. When  $Ca < \sim 0.25$ , the addition of air bubbles would increase the elasticity of the emulsion regardless of the gas volume fraction. In our system, the estimated value of  $Ca$  equal 0.05, implying the elastic modulus of the foamulsion is higher than that of

the w/o emulsion. This estimate correlates well with our rheological results. The frequency sweep reveals that  $G'$  is larger than  $G''$  over the investigated frequency range. In addition,  $G'$  for all samples is almost independent of frequency indicating an elastic gel.

**Figure 7.20.** Rheology of various colloidal materials containing C-1803 at 20 °C. (a) Amplitude sweep at a fixed frequency of 1 Hz. (b) Frequency sweep within the linear viscoelastic region (LVR).



The polymorphs of gelled materials mentioned above were investigated using wide angle X-ray scattering (WAXS), Figure 7.21. Neat C-1803 powder displays a single peak centred around 0.42 nm, related to the hexagonal lateral packing of stearyl chains, *i.e.* the  $\alpha$  form.<sup>58,59</sup> The peak corresponding to stearyl chains is retained in the oil foam, but the peak intensity is significantly weakened due to the presence of non-polar solvent.<sup>58</sup> In the case of the emulsions or the foamulsion, the intensities of the wide-angle peaks are further reduced. In addition, the scattering peaks are shifted to high values hinting a possible change in the crystal polymorph.<sup>58</sup> To know the exact polymorph, SAXS experiments are needed. Figure 7.22 displays the heating thermograms of various colloidal materials including the oil foam, the o/w and w/o emulsions, the o/w/o emulsion and the foamulsion. All samples exhibit two melting endothermic peaks except for the w/o emulsion, comparable to the melting behaviour of neat C-1803 powder. The explanation for the two peaks can be found in chapter 4 and 6. The detailed thermal properties are summarized in Table 7.2.

**Figure 7.21.** Wide angle X-ray scattering (WAXS) region of various colloidal materials with C-1803 at 20 °C. Inset: WAXS region of C-1803 powder.

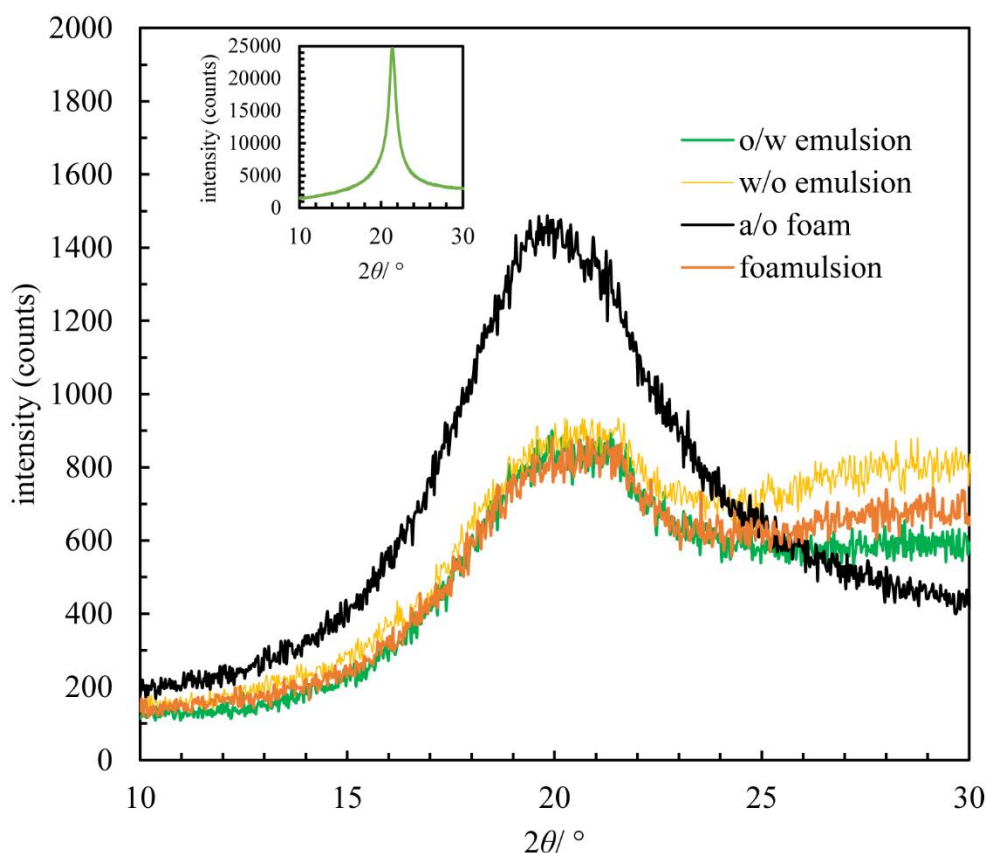


**Figure 7.22.** Melting thermograms of various colloidal materials with C-1803. Temperature change rate was  $3\text{ }^{\circ}\text{C min}^{-1}$ .

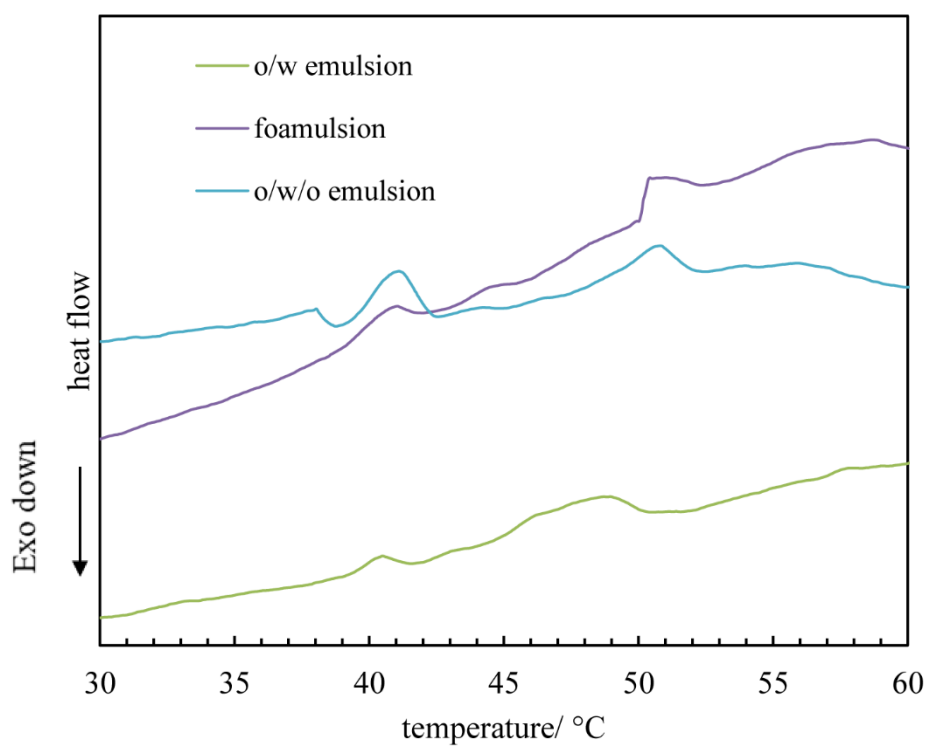
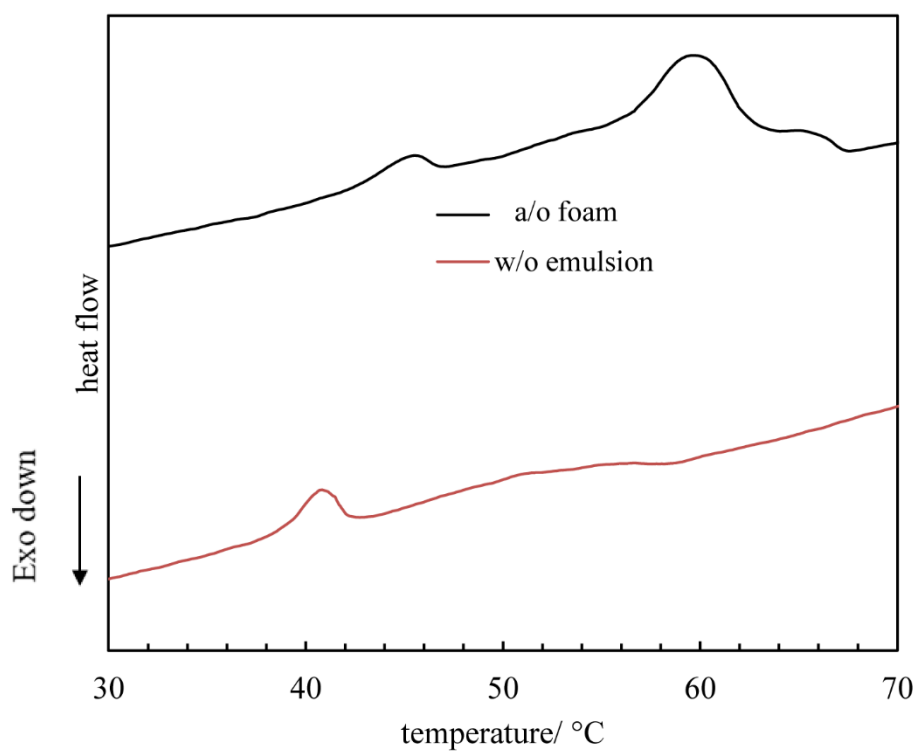


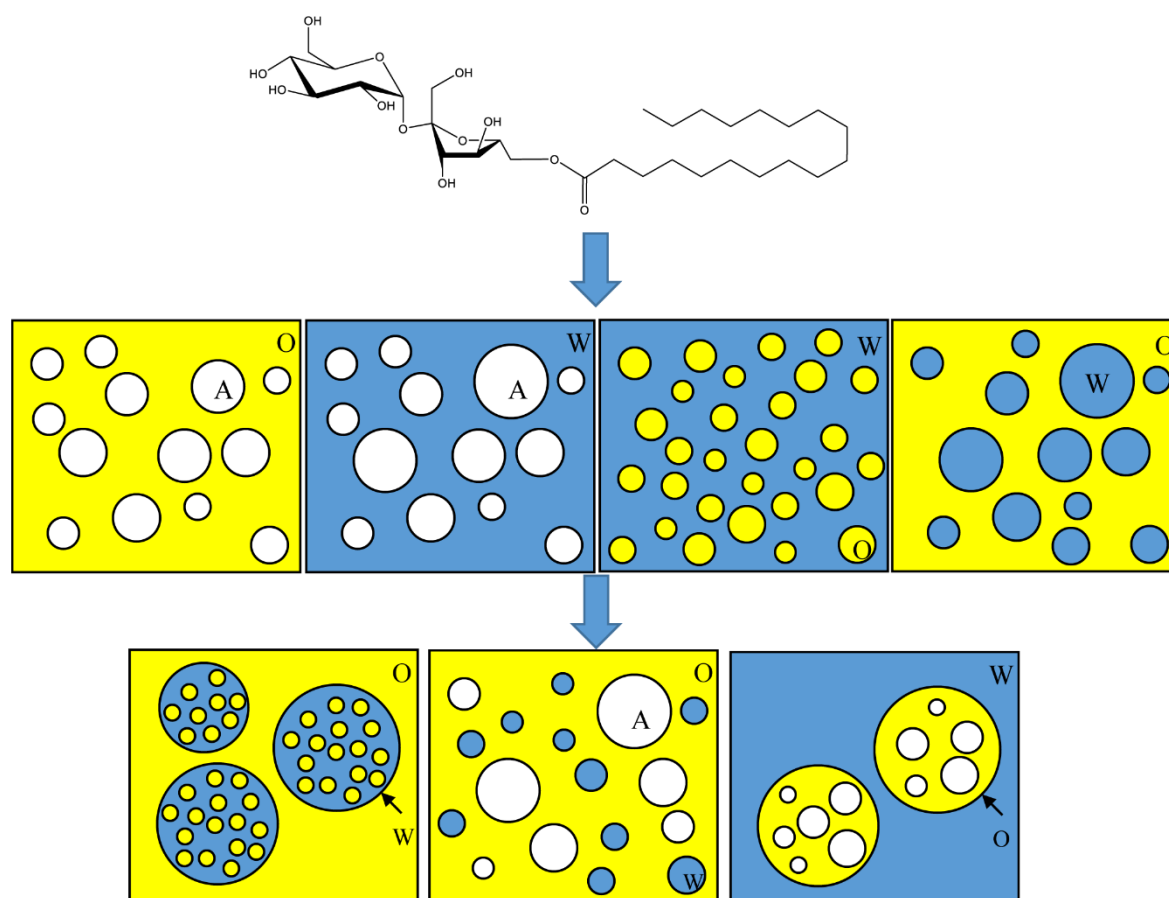
**Table 7.2.** Thermal properties of various colloidal materials with C-1803.

Material	Melting			
	$T_{\text{peak}}/^{\circ}\text{C}$		$\Delta H/\text{J g}^{-1}$	
	Peak 1	Peak 2	Peak 1	Peak 2
a/o foam	$45.64 \pm 0.33$	$59.83 \pm 0.61$	$0.24 \pm 0.10$	$1.45 \pm 0.11$
w/o emulsion	$40.66 \pm 0.08$	N/A	$0.27 \pm 0.13$	N/A
o/w emulsion	$40.46 \pm 0.09$	$48.34 \pm 0.23$	$0.10 \pm 0.03$	$0.15 \pm 0.05$
foamulsion	$40.84 \pm 0.02$	$50.44 \pm 0.02$	$0.09 \pm 0.05$	$0.07 \pm 0.01$
o/w/o emulsion	$41.17 \pm 0.09$	$50.64 \pm 0.16$	$0.13 \pm 0.04$	$0.15 \pm 0.03$

## 7.5 Conclusions

In this chapter, we demonstrate that various colloidal materials, *i.e.* air-in-oil (a/o) and air-in-water (a/w) foams, oil-in-water (o/w), water-in-oil (w/o) and oil-in-water-in-oil (o/w/o) emulsions, air and water-in-oil foamulsions and air-in-oil-in-water (a/o/w) emulsions can be fabricated using sucrose ester surfactant of HLB number = 3 through different protocols, Figure 7.23. First, ultra-stable vegetable oil foams of high air volume fraction are prepared through whipping one-phase oil solutions of sucrose ester at high temperature followed by rapid cooling and storing at low temperature. Secondly, aqueous foams can be made by hand shaking aqueous dispersions of sucrose ester at 20 °C. Two protocols are utilised to prepare simple emulsions: (1) homogenising equal volumes of water and oil solutions of sucrose ester at high temperature and then rapid cooling to 20 °C, *i.e.* post-crystallisation; (2) homogenising equal volumes of water and crystal dispersions at 20 °C cooled from 90 °C, *i.e.* pre-crystallisation. Stable o/w emulsions are created for the former whilst w/o emulsions stabilised by adsorbed crystals are obtained for the latter. Interestingly, when the mixture of the o/w emulsion and an oil dispersion containing C-1803 crystals is submitted to magnetic stirring at 20 °C, a reasonably stable o/w/o emulsion is rendered. Furthermore, a gelled oil continuous foamulsion is prepared through homogenising mixture of a/o foam and w/o emulsion at 20 °C. Last, a/o/w emulsions are yielded upon dispersing the a/o foams into aqueous dispersions of sucrose ester at 20 °C. To the best of our knowledge, this is the first time up to seven colloidal materials are successfully prepared using only one surfactant sample.

**Figure 7.23.** Schematic illustrating the preparation of different colloidal materials with C-1803 alone.



## 7.6 References

1. B.P. Binks, Particles as surfactants-similarities and differences, *Curr. Opin. Colloid Interface Sci.*, 2002, **7**, 21–41.
2. A. Zia, E. Pentzer, S. Thickett and K. Kempe, Advances and opportunities of oil-in-oil emulsions, *ACS Appl. Mater. Interfaces*, 2020, **12**, 38845–38861.
3. Y. Chao and H.C. Shum, Emerging aqueous two-phase systems: from fundamentals of interfaces to biomedical applications, *Chem. Soc. Rev.*, 2020, **49**, 114–142.
4. E. Rio, W. Drenckhan, A. Salonen and D. Langevin, Unusually stable liquid foams, *Adv. Colloid Interface Sci.*, 2014, **205**, 74–86.
5. A.L. Fameau, S. Lam and A. Arnould, Non-aqueous foams: current understanding on the formation and stability mechanisms, *Adv. Colloid Interface Sci.*, 2017, **247**, 454–464.
6. B.P. Binks, Colloidal particles at a range of fluid-fluid interfaces, *Langmuir*, 2017, **33**, 6947–6963.
7. R. Heymans, I. Tavernier, K. Dewettinck and P. Van der Meeren, Crystal stabilization of edible oil foams, *Trends Food Sci. Technol.*, 2017, **69**, 13–24.
8. A.L. Fameau and A. Saint-Jalmes, Recent advances in understanding and use of oleofoams, *Front. Sustain. Food Syst.*, 2020, **4**:110.
9. R. Aveyard, B.P. Binks and J.H. Clint, Emulsions stabilised solely by colloidal particles, *Adv. Colloid Interface Sci.*, 2003, **100–102**, 503–546.
10. B.P. Binks and R. Murakami, Phase inversion of particle-stabilized materials from foams to dry water, *Nat. Mater.*, 2006, **5**, 865–869.
11. B.P. Binks, S.K. Johnston, T. Sekine and A.T. Tyowua, Particles at oil-air surfaces: powdered oil, liquid oil marbles, and oil foam, *ACS Appl. Mater. Interfaces*, 2015, **7**, 14328–14337.
12. R. Murakami and A. Bismarck, Particle-stabilized materials: dry oils and (polymerized) non-aqueous foams, *Adv. Funct. Mater.*, 2010, **20**, 732–737.
13. Z. Wan, Y. Sun, L. Ma, F. Zhou, J. Guo, S. Hu, and X. Yang, Long-lived and thermoresponsive emulsion foams stabilized by self-assembled saponin nanofibrils and fibrillar network, *Langmuir*, 2018, **34**, 3971–3980.
14. A. Salonen, Mixing bubbles and drops to make foamed emulsions, *Curr. Opin. Colloid Interface Sci.*, 2020, **50**, 101381.

15. E. Dickinson, Advances in food emulsions and foams: reflections on research in the neo-Pickering era, *Curr. Opin. Colloid Interface Sci.*, 2020, **33**, 52–60.
16. S. Ghosh, T. Tran and D. Rousseau, Comparison of Pickering and network stabilization in water-in-oil emulsions, *Langmuir*, 2011, **27**, 6589–6597.
17. S. Ghosh and D. Rousseau, Triacylglycerol interfacial crystallization and shear structuring in water-in-oil emulsions, *Cryst. Growth Des.*, 2012, **12**, 4944–4954.
18. R. Rafanan and D. Rousseau, Dispersed droplets as active fillers in fat-crystal network-stabilized water-in-oil emulsions, *Food Res. Int.*, 2017, **99**, 355–362.
19. J. Yang, C. Qiu, G. Li, W.J. Lee, C.P. Tan, O.M. Lai and Y. Wang, Effect of diacylglycerol interfacial crystallization on the physical stability of water-in-oil emulsions, *Food Chem.*, 2020, **327**, 127014.
20. M. Brun, M. Delample, E. Harte, S. Lecomte and F. Leal-Calderon, Stabilization of air bubbles in oil by surfactant crystals: a route to produce air-in-oil foams and air-in-oil-in-water emulsions, *Food Res. Int.*, 2015, **67**, 366–375.
21. D.Z. Gunes, M. Murith, J. Godefroid, C. Pelloux, H. Deyber, O. Schafer and O. Breton, Oleofoams: properties of crystal-coated bubbles from whipped oleogels-evidence for Pickering stabilization, *Langmuir*, 2017, **33**, 1563–1575.
22. R. Heymans, I. Tavernier, S. Danthine, T. Rimaux, P. Van der Meeren and K. Dewettinck, Food-grade monoglyceride oil foams: the effect of tempering on foamability, foam stability and rheological properties, *Food Funct.*, 2018, **9**, 3143–3154.
23. M. Lei, N. Zhang, W.J. Lee, C.P. Tan, O.M. Lai, Y. Wang, and C. Qiu, Non-aqueous foams formed by whipping diacylglycerol stabilized oleogel, *Food Chem.*, 2020, **312**, 126047.
24. A.L. Fameau, S. Lam, A. Arnould, C. Gaillard, O.D. Velez and A. Saint-Jalmes, Smart nonaqueous foams from lipid-based oleogel, *Langmuir*, 2015, **31**, 13501–13510.
25. B.P. Binks, E.J. Garvey and J. Vieira, Whipped oil stabilised by surfactant crystals, *Chem. Sci.*, 2016, **7**, 2621–2632.
26. M. Callau, K. Sow-Kébé, N. Jenkins and A.L. Fameau, Effect of the ratio between fatty alcohol and fatty acid on foaming properties of whipped oleogels, *Food Chem.*, 2020, **333**, 127403.
27. S. Mishima, A. Suzuki, K. Sato and S. Ueno, Formation and microstructures of whipped oils composed of vegetable oils and high-melting fat crystals, *J. Am. Oil Chem. Soc.*, 2016, **93**, 1453–1466.

28. B.P. Binks and I. Marinopoulos, Ultra-stable self-foaming oils, *Food Res. Int.*, 2017, **95**, 28–37.
29. L. Goibier, C. Pillement, J. Monteil, C. Faure and F. Leal-Calderon, Emulsification of non-aqueous foams stabilized by fat crystals: towards novel air-in-oil-in-water food colloids, *Food Chem.*, 2019, **293**, 49–56.
30. K. Mishra, D. Dufour and E.J. Windhab, Yield stress dependent foaming of edible crystal-melt suspensions, *Cryst. Growth Des.*, 2020, **20**, 1292–1301.
31. Y. Liu and B.P. Binks, Foams of vegetable oils containing long-chain triglycerides, *J. Colloid Interface Sci.*, 2021, **583**, 522–534.
32. Y. Liu and B.P. Binks, A novel strategy to fabricate stable oil foams with sucrose ester surfactant, *J. Colloid Interface Sci.*, 2021, **594**, 204–216.
33. T. Truong, S. Prakash and B. Bhandari, Effects of crystallisation of native phytosterols and monoacylglycerols on foaming properties of whipped oleogels, *Food Chem.*, 2019, **285**, 86–93.
34. A. Szűts and P. Szabó-Révész, Sucrose esters as natural surfactants in drug delivery systems-a mini-review, *Int. J. Pharm.*, 2012, **433**, 1–9.
35. T. Plat and R.J. Linhardt, Syntheses and applications of sucrose-based esters, *J. Surf. Det.*, 2001, **4**, 415–421.
36. K. Hill and O. Rhode, Sugar-based surfactants for consumer products and technical applications, *Lipid/Fett*, 1999, **101**, 25–33.
37. X. Zhang, F. Song, M. Taxipalati, W. Wei and F. Feng, Comparative study of surface active properties and antimicrobial activities of disaccharide monoesters, *PLoS One*, 2014, **9**, 1–19.
38. S. Soultani, S. Ognier, J.M. Engasser and M. Ghoul, Comparative study of some surface active properties of fructose esters and commercial sucrose esters, *Colloids Surf. A*, 2003, **227**, 35–44.
39. A. Tual, E. Bourles, P. Barey, A. Houdoux, M. Desprairies and J.-L. Courthaudon, Effect of surfactant sucrose ester on physical properties of dairy whipped emulsions in relation to those of o/w interfacial layers, *J. Colloid Interface Sci.*, 2006, **295**, 495–503.
40. J. Coates, Interpretation of infrared spectra-a practical approach, in *Encyclopedia of Analytical Chemistry*, Meyers, R. A. (ed.), John Wiley and Sons, Chichester, 2000, p.10815–10837.

41. B.C. Youan, A. Hussain and N.T. Nguyen, Evaluation of sucrose esters as alternative surfactants in microencapsulation of proteins by the solvent evaporation method, *AAPS Pharmsci.*, 2003, **5**, Article 22.
42. F.R. Lupi, A. Shakeel, V. Greco, N. Baldino, V. Calabrò and D. Gabriele, Organogelation of extra virgin olive oil with fatty alcohols, glyceryl stearate and their mixture, *LWT - Food Sci. Technol.*, 2017, **77**, 422–429.
43. A. Szűts, E. Pallagi, G. Regdon Jr., Z. Aigner and P. Szabó-Révész, Study of thermal behaviour of sugar esters, *Int. J. Pharm.*, 2007, **336**, 199–207.
44. L.K. Shrestha, M. Kaneko, T. Sato, D.P. Acharya, T. Iwanaga, and H. Kunieda, Phase behaviour of diglycerol fatty acid esters-nonpolar oil systems, *Langmuir*, 2006, **22**, 1449–1454.
45. T. Xu, V. Rodriguez-Martinez, S.N. Sahasrabudhe, B.E. Farks and S.R. Dungan, Effects of temperature, time and composition on food oil surface tension, *Food Biophys.*, 2017, **12**, 88–96.
46. B.P. Binks and S.O. Olusanya, Pickering emulsions stabilized by coloured organic pigment particles, *Chem. Sci.*, 2017, **8**, 708–723.
47. B.P. Binks, S. Campbell, S. Mashinchi and M.P. Piatko, Dispersion behavior and aqueous foams in mixtures of a vesicle-forming surfactant and edible nanoparticles, *Langmuir*, 2015, **31**, 2967–2978.
48. L.K. Shrestha, D.P. Acharya, S.C. Sharma, K. Aramaki, H. Asaoka, K. Ihara, T. Tsunehiro and H. Kunieda, Aqueous foam stabilized by dispersed surfactant solid and lamellar liquid crystalline phase, *J. Colloid Interface Sci.*, 2006, **301**, 274–281.
49. B.P. Binks, Relationship between microemulsion phase behavior and macroemulsion type in systems containing nonionic surfactant, *Langmuir*, 1993, **9**, 25–28.
50. M. Mathlouthi and P. Reiser, *Sucrose: Properties and Applications*, Blackie, Glasgow, 1995, ch. 5.
51. N. Denkov, S. Tcholakova and D. Cholakova, Surface phase transitions in foams and emulsions, *Curr. Opin. Colloid Interface Sci.*, 2019, **44**, 32–47.
52. C. Liu, Z. Zheng, Y. Shi, Y. Zhang and Y. Liu, Development of low-oil emulsion gel by solidifying oil droplets: roles of internal beeswax concentration, *Food Chem.*, 2021, **345**, 128811.
53. R. Rafanan and D. Rousseau, Dispersed droplets as tunable fillers in water-in-oil emulsions stabilized with fat crystals, *J. Food Eng.*, 2019, **244**, 192–201.

54. Y. Zhang, A. Shitta, J.C. Meredith and S.H. Behrens, Bubble meets droplet: particle-assisted reconfiguration of wetting morphologies in colloidal multiphase systems, *Small*, 2016, **12**, 3309–3319.
55. S. Torza and S.G. Mason, Coalescence of two immiscible liquid drops, *Science*, 1969, **163**, 813–814.
56. C.W. Macosko, *Rheology: principles, measurements, and applications*, VCH, New York, 1994.
57. L. Ducloué, O. Pitois, J. Goyon, X. Chateaua and G. Ovarleza, Coupling of elasticity to capillarity in soft aerated materials, *Soft Matter*, 2014, **10**, 5093–5098.
58. C.H. Chen, I. Van Damme and E.M. Terentjev, Phase behavior of C18 monoglyceride in hydrophobic solutions, *Soft Matter*, 2009, **5**, 432–439.
59. S.S. Sagiri, V.K. Singh, K. Pal, I. Banerjee, and P. Basak, Stearic acid based oleogels: a study on the molecular, thermal, and mechanical properties, *Mater. Sci. Eng. C*, 2015, **48**, 688–699.

## CHAPTER 8 – SUMMARY OF CONCLUSIONS AND FUTURE WORK

### 8.1 Summary of conclusions

The primary goal of this thesis is to elucidate the adsorption behaviour of edible surfactants/fats at various fluid-fluid interfaces and their dispersion properties in bulk liquid, based on which various colloidal materials are fabricated including aqueous and oil foams, simple and multiple emulsions, foamed and aerated emulsions. To characterise the materials formed and probe into the stabilisation mechanisms therein, different techniques were applied including differential scanning calorimetry, rheology, X-ray diffraction, infrared spectrometry, surface/interfacial tension, dynamic light scattering, optical and cryo-scanning electron microscopy. Chapters 3-5 include the fabrication of ultra-stable oil foams from neat vegetable oils and mixtures of sugar ester surfactants in vegetable oils. The dispersion and foaming behaviour of sucrose ester surfactants in water as a function of HLB and pH are studied in Chapter 6. Chapter 7 focuses on preparing various colloidal materials with a single sucrose ester surfactant. The conclusions arising from the above systems are summarised below.

Chapter 3 confirms that an oleogel based on a vegetable oil induced by supercooling can be aerated to produce an oil foam. We introduce a new protocol to prepare edible oil foams from vegetable oils containing mainly long-chain, unsaturated fatty acids in their triglyceride molecules in the absence of an added foaming agent. Selected tempering procedures induce the formation of high-melting triglyceride crystals within low-melting continuous liquid oil capable of forming an oleogel. Upon whipping, ultra-stable oil foams containing air bubbles adsorbed by fat crystals can be fabricated. Foamability and foam stability vary depending on the oil type and the degree of supercooling. We demonstrate that in peanut oil foams triglyceride crystals are loosely distributed at the air-oil surface, whilst in olive oil foams a more coherent crystal layer(s) forms at bubble surfaces. It is shown that triglyceride crystals contributing to foaming contain a higher proportion of saturated fatty acids than the original oil. Such foams are temperature-responsive and can be rendered completely unstable upon heating to around the melting point of the crystals. We anticipate that this simple method can be applied to a wide range of long-chain vegetable oils rich in unsaturated fatty acids.

Efficient air incorporation into an oleogel matrix is not always possible. In light of this, Chapter 4 describes a novel protocol to prepare ultra-stable edible oil foams of high air volume fraction from mixtures of vegetable oil and sucrose ester surfactant. High foamability (over-run up to ~ 330%) is possible in the one-phase region due to rapid adsorption of sucrose ester-triglyceride molecular complexes at the air-oil surface. By contrast, foamability is much

reduced in the two-phase region at lower temperature where surfactant crystals form. Our findings are in contrast to all previous work in which oil foaming was only possible in the two-phase region in the presence of surface-active lipid crystals and not from one-phase molecular solutions. To enhance the resulting foam stability, a simple method is developed during which aeration is first performed in the one-phase region followed by rapid cooling and then storing at low temperature. The obtained foams containing closely packed crystal-coated air bubbles, are completely stable for several months and are temperature-responsive possessing impressive mechanical properties. The mechanisms behind foaming and subsequent stabilisation are elucidated *via* infrared spectrometry and surface tension. This method is simple but productive and we prove that it can be applied to a wide range of oil-soluble surfactants rich in hydroxyl groups in ester-containing oils. Compared with vigorous whipping, gentle bubbling can produce oil foams more effectively. However, foam stability suffers.

Taking advantage of the mechanism of foam formation proposed in Chapter 4, Chapter 5 is aimed at preparing stable edible oil foams of high air volume fraction from mixtures of vegetable oil and sorbitan esters. Whipping is first performed in the one-phase region followed by rapid cooling and ultimately storing at low temperature. In the case of high melting sorbitan monostearate, the resulting foams containing populated air bubbles protected by jammed crystals can be completely stable for several months. For low melting sorbitan monooleate, the prepared foams suffer a gradual decay however with the residual parts surviving more than one month. This contrast arises from the differences in the kinetics of surfactant crystal formation and the quantity of crystals formed on rapid cooling. When compared with sucrose ester surfactant, the minimum surfactant concentration required for effective foam formation is higher for sorbitan esters. This is due to the fact that the number of hydroxyl group available for H-bonding is smaller for the latter.

Chapter 6 carries out a comprehensive study on the dispersion and foaming behavior of a series of sucrose stearate esters with different HLB in water. The physicochemical properties of aqueous solutions/dispersions of sucrose esters vary significantly with HLB, such as the macroscopic appearance, the size and morphology of surfactant aggregate formed, viscosity and surface tension. Foamability passes through a maximum on decreasing the HLB number, which is much lower than that of popular sodium dodecyl sulfate (SDS). In contrast, foam stability is much higher than that of SDS whereby some long-lived foams based on relatively hydrophobic surfactants can survive for more than one year. This is attributed to the steric hindrance of bulky vesicles in the foam lamella in combination with strong electrostatic repulsion between neighboring vesicles. The variation of foaming functionality as a function

of HLB number can be well correlated to the property of bulk liquid prior to aeration. Despite the nonionic nature of sucrose ester, the samples used in our experiments are negatively charged in water due possibly to the deprotonation of fatty acid impurities. So, the effect of lowering pH on the dispersion and foaming properties of two representative systems is investigated. Interestingly, decreasing pH can disrupt the vesicle morphology facilitating faster adsorption kinetics of surfactant molecules towards the air-water surface. Thus, foamability is enhanced. Further work should be extended to the role of different ionic species, *e.g.* salts and free fatty acids, on the dispersion and foaming properties of sucrose esters in water.

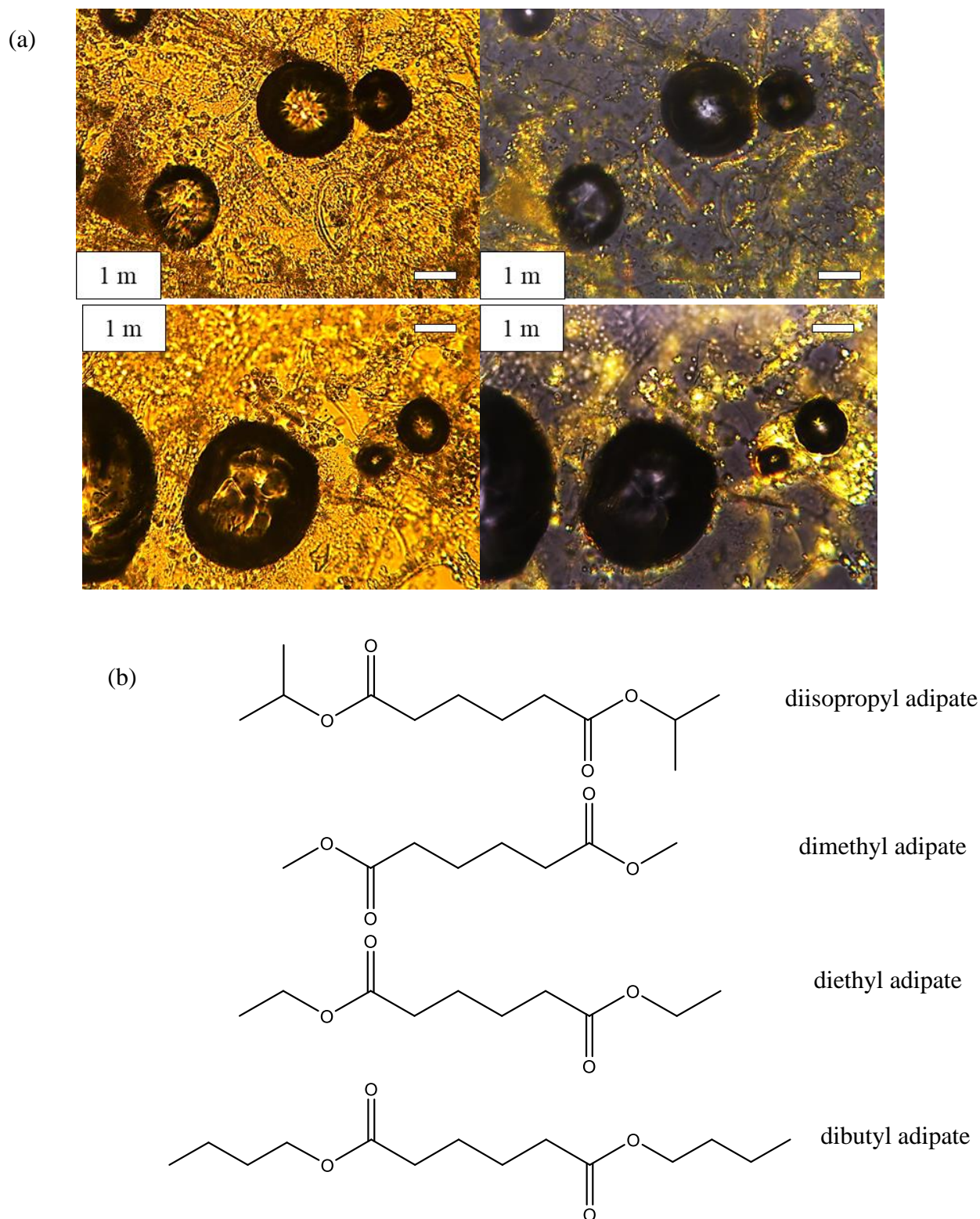
Based on the above sucrose ester-containing systems, Chapter 7 focuses on the fabrication of a range of colloidal materials, using a single sucrose ester surfactant of HLB number = 3 through different protocols, *i.e.* air-in-oil (a/o) and air-in-water (a/w) foams, oil-in-water (o/w), water-in-oil (w/o) and oil-in-water-in-oil (o/w/o) emulsions, air and water-in-oil foamulsions and air-in-oil-in-water (a/o/w) emulsions. First, ultra-stable vegetable oil foams of high air volume fraction are prepared through whipping oil solutions of sucrose ester at high temperature, followed by rapid cooling and storing at a low temperature. Secondly, aqueous foams can be made through hand shaking aqueous dispersions of sucrose ester at 20 °C. Two protocols are utilised to prepare simple emulsions: (1) homogenising equal volumes of water and oil solutions of sucrose ester at high temperature and then rapid cooling to 20 °C, *i.e.* post-crystallisation; (2) homogenising equal volumes of water and crystal dispersions at 20 °C cooled from 90 °C, *i.e.* pre-crystallisation.<sup>1</sup> Stable o/w emulsions are created for the former whilst w/o emulsions stabilised by adsorbed crystals for the latter. Based on the above, when dispersing the o/w emulsion into an oil dispersion containing pre-formed crystals under magnetic stirring at 20 °C, a reasonably stable o/w/o emulsion is rendered. Furthermore, a gelled oil continuous foamulsion can be prepared through homogenising the mixture of the a/o foam and w/o emulsion at 20 °C. Last, an a/o/w emulsion is yielded upon dispersing the a/o foam into an aqueous dispersion of sucrose ester at 20 °C.

## 8.2 Future work

### 8.2.1 Oil foams from mixtures of sugar esters in adipate ester oils

As highlighted above, the carbonyl groups of triglyceride molecules in vegetable oil can form H-bonds with the hydroxyl groups in sugar esters, which are highly surface active at the air-oil surface leading to efficient foam formation upon aeration at high temperature. Can we find other surfactant-ester oil pairs that are highly foamable? Adipate esters ( $\text{ROOC}-(\text{CH}_2)_4-\text{COOR}$ ) are synthesized through esterification of adipic acid with different alcohols, which are commonly applied in plastic products, cosmetics and pharmaceuticals. Binks and Yin reported the stabilisation of oil-in-water Pickering emulsions based on mixtures of water, adipate oils and inherently hydrophilic silica nanoparticles.<sup>2</sup> They found that the adipate oil molecules could act as a surfactant during which hydrogen bonds were formed between the carbonyl groups of the oils and the hydroxyl groups on particle surfaces, thereby increasing the particle hydrophobicity enhancing the resulting emulsion stability. Based on this, we put forward a hypothesis that oil foams of high air volume fraction can be prepared based on a mixture of sugar esters (sucrose or sorbitan esters) and adipate oil. As a proof-of-concept, we chose to whip 5 wt.% sucrose ester surfactant (HLB = 5, C-1805) in diisopropyl adipate at 80 °C, followed by rapid cooling in an ice bath of -5 °C and subsequent storage at room temperature. Although the foam suffers quick decay during the initial quenching period, its residual part can be stable for several months. Some micrographs of the foam after 1 month aging are presented in Figure 8.1(a). Non-spherical bubbles surrounded by surfactant crystals can be identified. The focus of future work will be on the foaming capacity of different adipate oils, *e.g.* dimethyl adipate, diethyl adipate and dibutyl adipate (Figure 8.1(b)), containing sugar esters or other hydroxyl-rich surfactants. Foaming functionality will be investigated as a function of surfactant concentration and carbon number in the oil. Furthermore, we anticipate that upon dispersing such foam into an aqueous dispersion containing hydrophilic silica particles at varying pH under vigorous stirring, a Pickering air-in-oil-in-water emulsion stabilised by the particles is achieved.<sup>2</sup> This is different from all previous air-in-oil-in-water emulsion systems in which various emulsifiers were added.<sup>3-5</sup> How to improve the encapsulation yield of air in oil globules in the aerated emulsion will be explored as well.

**Figure 8.1.** (a) Non-polarised (left) and polarised (right) micrographs of diisopropyl adipate oil foam containing 5 wt.% C-1805 after 1 month storage at room temperature. Scale bars = 50  $\mu\text{m}$ . Foam prepared at 80  $^{\circ}\text{C}$  was submitted to rapid cooling in an ice bath followed by storing at room temperature. (b) Chemical structures of different adipate esters. A single oil molecule has two carbonyl groups.



### 8.2.2 The role of oil-soluble emulsifiers in oil foaming

The foaming potential of natural fats/oils has been well reported.<sup>4,6-10</sup> However, their composition is rather complex, being composed of mainly triglycerides and various minor emulsifier species. The potential effect of those minor components on the oil foaming properties is far from clear. According to a recent review paper,<sup>11</sup> in edible w/o emulsions certain oil-soluble emulsifiers can induce the interfacial crystallization of high melting triglycerides on cooling enabling Pickering-type stabilisation thereby leading to enhanced emulsion stability. We hypothesise that in a/o foams the presence of some emulsifiers may promote the crystallization of high melting triglyceride at bubble surfaces, which may result in an increase in foamability and foam stability. The investigated emulsifiers will be fatty acids, mono- and diglycerides, sorbitan esters and sucrose esters.

### 8.2.3 Using sucrose ester and a second surfactant to prepare foamulsions

In Chapter 7, a multi-step protocol has been developed to prepare stable water and air-in-oil emulsions (*i.e.* foamulsions) using sucrose ester surfactant, during which w/o emulsions and a/o foams are fabricated separately followed by vigorous mixing. Is it feasible to simplify the preparation protocol? In ref. 12, Wan *et al.* reported that gelled foamulsions could be produced by emulsifying and aerating in a single step at high temperature followed by rapid cooling for mixtures of the glycyrrhizic acid, water and sunflower oil. On the other hand, mixing sucrose ester and a second surfactant has been shown to be capable of effective oil gelling.<sup>13</sup> Based on the above, we put forward a simple strategy to fabricate sucrose ester-based foamulsions as shown below. (1) Dissolve sucrose ester and a second surfactant (*e.g.* lecithin or stearic acid) into vegetable oil at high temperature, (2) homogenise the mixture of water and the oil solution at the same temperature during which aeration and emulsification can be achieved simultaneously, (3) rapidly quench the homogenised sample in an ice bath to trigger surfactant crystallisation, (4) store the cooled sample at a low temperature. The effect of varying parameters will be investigated including the mass ratio of sucrose ester: cosurfactant, the volume ratio of oil: water and total surfactant concentration.

### 8.2.4 Preparation of oil-in-water-in-oil emulsions with sucrose esters

In Chapter 7, o/w and w/o emulsions can be obtained from the post-crystallisation and pre-crystallisation protocols, respectively. The reason for this phenomenon is still ambiguous. So, in further work we are going to vary the volume ratio of water: oil in the same system at the same temperature to see if the phenomenon is universal. If not, the critical volume ratio at

which phase inversion occurs will be determined. Based on the above investigations, more systematic work should be carried out on the preparation and characterisation of oil-in-water-in-oil emulsions from the same system. Moreover, the emulsifying behaviour of a more lipophilic sucrose ester surfactant will be studied in detail.

#### 8.2.5 Ascending behaviour of gas bubbles in oil solutions of sucrose ester

The ascending behaviour of air bubbles in complex lubricant-based oil containing various solutes has been reported by Ross and coworkers.<sup>14,15</sup> The presence of surface-active agents at the air-oil surface can create the Marangoni flow improving the interfacial elasticity. The increased interfacial elasticity can hinder an inherent air circulation inside air bubbles, therefore slowing down the rate of bubble rise. In analogy with the above, we anticipate that the ascent rate of an air bubble in a vegetable oil solution of sucrose ester is slower than that in neat oil, due to the adsorption of sucrose ester molecules at the air-oil surface. In relation to this, the effect of bubble size, surfactant concentration and surfactant HLB number will be explored. For comparison, the ascent behavior of an air bubble in an alkane solution of sucrose ester will also be studied.

### 8.3 References

1. D. Rousseau and S.M. Hodge, Stabilization of water-in-oil emulsions with continuous phase crystals, *Colloids Surf. A*, 2005, **260**, 229–237.
2. B.P. Binks and D. Yin, Pickering emulsions stabilized by hydrophilic nanoparticles: *in situ* surface modification by oil, *Soft Matter*, 2016, **12**, 6858–6867.
3. M. Brun, M. Delample, E. Harte, S. Lecomte and F. Leal-Calderon, Stabilization of air bubbles in oil by surfactant crystals: a route to produce air-in-oil foams and air-in-oil-in-water emulsions, *Food Res. Int.*, 2015, **67**, 366–375.
4. L. Goibier, C. Pillement, J. Monteil, C. Faure and F. Leal-Calderon, Emulsification of non-aqueous foams stabilized by fat crystals: towards novel air-in-oil-in-water food colloids, *Food Chem.*, 2019, **293**, 49–56.
5. C. Qiu, M. Lei, W.J. Lee, N. Zhang and Y. Wang, Fabrication and characterization of stable oleofoam based on medium-long chain diacylglycerol and  $\beta$ -sitosterol, *Food Chem.*, 2021, **350**, 129275.
6. S. Mishima, A. Suzuki, K. Sato and S. Ueno, Formation and microstructures of whipped oils composed of vegetable oils and high-melting fat crystals, *J. Am. Oil Chem. Soc.*, 2016, **93**, 1453–1466.

7. B.P. Binks and I. Marinopoulos, Ultra-stable self-foaming oils, *Food Res. Int.*, 2017, **95**, 28–37.
8. Y. Liu and B.P. Binks, Foams of vegetable oils containing long-chain triglycerides, *J. Colloid Interface Sci.*, 2021, **583**, 522–534.
9. K. Mishra, D. Dufour and E.J. Windhab, Yield stress dependent foaming of edible crystal-melt suspensions, *Cryst. Growth Des.*, 2020, **20**, 1292–1301.
10. L. Metilli, A. Lazidis, M. Francis, S. Marty-Terrade, J. Ray, and E. Simone, The effect of crystallization conditions on the structural properties of oleofoams made of cocoa butter crystals and high oleic sunflower oil, *Cryst. Growth Des.*, 2021, **21**, 1562–1575.
11. D. Rousseau, Aqueous droplets as active fillers in oil-continuous emulsions, *Curr. Opin. Food Sci.*, 2020, **33**, 173–186.
12. Z. Wan, Y. Sun, L. Ma, F. Zhou, J. Guo, S. Hu, and X. Yang, Long-lived and thermoresponsive emulsion foams stabilized by self-assembled saponin nanofibrils and fibrillar network, *Langmuir*, 2018, **34**, 3971–3980.
13. M.D.B. Sintang, S. Danthine, A.R. Patel, T. Rimaux, D.V.D. Walle and K. Dewettinck, Mixed surfactant systems of sucrose esters and lecithin as a synergistic approach for oil structuring, *J. Colloid Interface Sci.*, 2017, **504**, 387–396.
14. G. Furler and S. Ross, Experimental observations of the rate of ascent of bubbles in lubricating oils, *Langmuir*, 1986, **2**, 68–72.
15. Y. Suzin and S. Ross, Retardation of the ascent of gas bubbles by surface-active solutes in nonaqueous solutions, *J. Colloid Interface Sci.*, 1985, **103**, 578–585.